POWER ELECTRONIC SYSTEMS DESIGN CO-ORDINATION FOR DOUBLY-FED INDUCTION GENERATOR WIND TURBINES

A thesis submitted to The University of Manchester
for the degree of Doctor of Philosophy
in the Faculty of Engineering and Physical Sciences

2012

MELIKSAH OZAKTURK

School of Electrical and Electronic Engineering

Table of Contents

Table of Contents 1
List of Tables 5
List of Figures 7
List of Abbreviations 13
Abstract 16
Declaration 17
Copyright Statement 18
List of Symbols 19
Dedication 22
Acknowledgements 23

Chapter 1 Introduction 24
1.1 Aims and Objectives of the Research 25
1.2 Outline of the Thesis 26
1.3 Contributions 27

Chapter 2 Research Background 28
2.1 Introduction 28
2.2 Wind Power 28
2.3 Conversion of Wind Power 29
2.4 Wind Turbine Concepts 30
2.4.1 Squirrel Cage Induction Generator Wind Turbines 32
2.4.2 Wound Rotor Induction Generator with Variable Rotor Resistor 32
2.4.3 Variable Speed Wind Turbines with Fully-Rated Converter 33
2.4.4 Variable Speed Wind Turbines with Partly-Rated Converter 33
2.4.5 Stall, Active Stall and Pitch Control 34
2.5 Wind Turbine Components 35
2.6 Mechanical System of Wind Turbine 36
2.6.1 Blades 37
2.6.2 Nacelle 37
2.6.3 Gearbox 38
2.6.4 Tower and Hub 38

2.6.5 Yaw Mechanism 39
2.7 Electrical System of Wind Turbine 39
2.7.1 Generator Topologies 39
2.7.2 Transformers 40
2.7.3 Connection Types to the Network 40
2.7.4 Protection Devices 41
2.8 Power Electronics for Wind Turbines 42
2.8.1 Power Electronics Devices 42
2.8.2 Converter Module Types 44
2.8.3 PWM Techniques 46
2.8.4 Protection Circuits 51
2.9 Review of Prior Art on DFIG Modelling, Control and Protection 52
2.10 Summary 56

Chapter 3 Dynamic Modelling and Control of Doubly-Fed Induction Generator 57
3.1 Introduction 57
3.2 DFIG Modelling 57
3.3 DFIG Equivalent Circuit 58
3.4 Machine Equations 59
3.5 Clarke and Park Transformations 63
3.6 Rotor-side Converter 64
3.7 DC-Link 64
3.8 Grid-side Converter 64
3.9 Generic Rotor-side Converter Control 65
3.9.1 Inner (Current) Loop Control 65
3.9.2 Investigation of Effects of Rotor Voltage Components 69
3.9.3 Tuning of RSC Inner (Current) PI Loop Controller 70
3.10 Generic Grid-side Converter Control 70
3.10.1 Inner (Current) Loop Control 71
3.10.2 Tuning of GSC Inner (Current) PI Loop Controller 73
3.11 Drive Train Modelling 73
3.12 Pitch Control 77
3.13 Summary 79
80

Chapter 4 DC-link Voltage Control – GSC Outer Loop Control

4.1 Introduction 80

4.2 Control Design 81

4.3 Dynamic Stiffness 85

4.4 Tuning Loop for Nominal Operating Point 86

4.5 Operating Point Analysis 87

4.5.1 V_{dco} Sensitivity 89

4.5.2 v_{g_do} Sensitivity 99

4.5.3 i_{g_do} Sensitivity 106

4.6 Summary 113

Chapter 5 System Control and Protection Coordination 114

5.1 Introduction 114

5.2 Controller Loops Segmentation 114

5.3 Protection Coordination 119

5.3.1 Rotor Crowbar Protection 119

5.3.2 DC-link Brake Method 123

5.4 GB Grid Code Fault Ride-Through Requirements 124

5.5 Simulation Results 126

5.5.1 Three-phase Voltage Sag 130

5.5.2 Two-phase Voltage Sag 138

5.5.3 One-phase Voltage Sag 143

5.6 Investigation of the Relation between the Rotor Crowbar and the DC-link Brake Protection Actions 150

5.7 Summary 158

Chapter 6 Improved RSC Outer (Power) Loop Control 159

6.1 Introduction 159

6.2 Choosing a PI Controller 159

6.3 Choosing a PID Controller 161

6.4 Tuning Process of the PID Loop for Nominal Operating Point 163

6.5 Sensitivity Analysis 165

6.5.1 Varying Undamped Natural Frequency 166

6.5.2 Varying Damping Ratio 172

6.5.3 Varying K_D 176

6.5.4 PSCAD Results 181
6.6 Robustness Analysis 183
6.6.1 V_s=0.8pu (Variations in L_{ss} and L_m by ±10%) 184
6.6.2 V_s=1pu (Variations in L_{ss} and L_m by ±10%) 186
6.6.3 V_s=1.2pu (Variations in L_{ss} and L_m by ±10) 187
6.7 Summary 189

Chapter 7 Conclusions and Further Work 190
7.1 Conclusions 190
7.2 Suggestions for Further Work 194

References 195

Appendix 1 Data of Electrical Components 204
Appendix 2 Layout of the DFIG System in PSCAD/EMTDC 206
Appendix 3 Operating Point Sensitivity Analysis and Dynamic Stiffness Assessment of DC-link Voltage Control 207
Appendix 4 Investigation of Protection Coordination 237
Appendix 5 Sensitivity and Robustness Analyses of RSC Power Loop Control 251
Appendix 6 Conference Paper - Modelling and Analysis of DFIG Wind Turbine System in PSCAD/EMTDC 296

Total word count of the main body (including footnotes and endnotes): ***33502***

List of Tables

Table 2.1: Comparison of controllable switches 43

Table 2.2: Switching status of a two-level three-phase SVPWM inverter 51

Table 3.1: The drive train modelling configurations 77

Table 4.1: Selected operating points 88

Table 4.2: Summary of bandwidths obtained from MATLAB results (Bode diagrams) for V_{dc} operating points 97

Table 4.3: Summary of approximate damping ratios obtained from MATLAB results using forward-path transfer function (FpTF) and calculated approximate damping ratios for V_{dc} operating points 97

Table 4.4: Summary of bandwidths obtained from MATLAB results (Bode diagrams) for v_{g_d} operating points (Note that v_{g_d} is phase-rms voltage) 104

Table 4.5: Summary of approximate damping ratios obtained from MATLAB results using forward-path transfer function (FpTF) and calculated approximate damping ratios for v_{g_d} operating points 105

Table 4.6: Summary of bandwidths obtained from MATLAB results (Bode diagrams) for i_{g_d} operating points 111

Table 4.7: Summary of approximate damping ratios obtained from MATLAB results using forward-path transfer function (FpTF) and calculated approximate damping ratios for i_{g_d} operating points 112

Table 4.8: Summary of dynamic stiffness analyses for seven operating points of three variables 112

Table 5.1: Summary of the effects of the voltage sag types on the DC-link voltage, stator active and reactive power 149

Table 6.1: Effects of Independent P, I and D Tuning 164

Table 6.2: Tuning parameters for power (PID) loop controller of the RSC 164

Table 6.3: Full (FTF2), simplified (STF2) and second order approximated (SoATF) transfer functions of the power (outer) loop controller of the RSC 165

Table 6.4: Calculations in Excel for the assessment of varying f_n 166

Table 6.5: Varying f_n - SoATF, STF2 and FTF2 167

Table 6.6: Calculations in Excel for the assessment of varying ζ 172

Table 6.7: Varying ζ - SoATF, STF2 and FTF2 173

Table 6.8: Calculations in Excel for the assessment of varying K_D 176

Table 6.9: Varying K_D - SoATF, STF2 and FTF2 177

Table 6.10: The 'best' tuning parameters of the PID loop 181

Table 6.11: The summary of the effects of varying the tuning parameters 181

Table 6.12: Operating points for robustness analysis 184

Table 6.13: Calculated damping ratios for V_s=0.8pu 184

Table 6.14: Calculated damping ratios for V_s=1pu 186

Table 6.15: Calculated damping ratios for V_s=1.2pu 187

List of Figures

Figure 2.1: Wind turbine types 31

Figure 2.2: A typical configuration of SCIG wind turbine 32

Figure 2.3: WRIG with variable rotor resistance (OptiSlip®) 33

Figure 2.4: Fully-rated variable speed wind turbine (PMSG or WRSG) 33

Figure 2.5: Partly-rated variable speed wind turbine (DFIG) 34

Figure 2.6: The main components of a horizontal axis wind turbine 36

Figure 2.7: A nacelle of a DFIG wind turbine 37

Figure 2.8: Major applications of individual bipolar and unipolar Si and SiC based power electronics devices in terms of the rated blocking voltage 43

Figure 2.9: The applications of discrete power semiconductor devices 44

Figure 2.10: Three-phase two-level six-IGBT switch-based VSC 45

Figure 2.11: Single-phase two-level converter configuration 47

Figure 2.12: Carrier (triangular) waveform (V_{tri}) and reference signal (V_{ref}) 48

Figure 2.13: Two-level sinusoidal PWM method for a three-phase six-switch voltage source converter (VSC) 49

Figure 2.14: Switching vectors for two-level six-switch SVPWM 50

Figure 2.15: A two-level three-phase SVPWM inverter and switching status 50

Figure 2.16: Crowbar configurations 51

Figure 2.17: DC-link brake 52

Figure 3.1: Typical DFIG system 58

Figure 3.2: Standard per-phase DFIG equivalent circuit 58

Figure 3.3: Simplified per-phase DFIG equivalent circuit 59

Figure 3.4: Definitions of angles and the reference frames for the DFIM 60

Figure 3.5: Derivation of transformation angles from *abc* to *dq* 60

Figure 3.6: Decoupled current (inner) loop control of rotor-side converter 66

Figure 3.7: The relation between the rotor currents and the stator active and reactive power 67

Figure 3.8: The step response of the TF and SoATF of the rotor currents in *dq* 68

Figure 3.9: Grid-side converter configuration 70

Figure 3.10: Decoupled inner (current) loop control of the grid-side converter 72

Figure 3.11: Drive train configurations 73

Figure 3.12: Drive train models for wind turbine systems 74
Figure 3.13: Three-mass drive train model including blade and shaft flexibilities 75
Figure 3.14: Representation of the three-mass model in terms of rotor structural dynamics 75
Figure 3.15: Two-mass drive train model 76
Figure 3.16: Block diagram of generic pitch angle control 78
Figure 4.1: The typical DFIG system 80
Figure 4.2: The full control block diagram of the grid-side converter 81
Figure 4.3: DC-link voltage plant 81
Figure 4.4: Full SFSB of the GSC controller 83
Figure 4.5: Outer (V_{dc}) loop control of the grid-side converter 83
Figure 4.6: Extraction of the forward-path transfer function 84
Figure 4.7: Dynamic stiffness 1 (DS1) 85
Figure 4.8: Dynamic stiffness 2 (DS2) 86
Figure 4.9: Bandwidths representation on the full transfer function - Varying V_{dco} 90
Figure 4.10: Bandwidths representation on the transfer function - Varying V_{dco} 90
Figure 4.11: Bandwidths representation on the simplified transfer function - Varying V_{dco} 92
Figure 4.12: Damping ratios representation on the forward-path transfer function - Varying V_{dco} 93
Figure 4.13: Dynamic stiffness analysis of $\Delta i_n/\Delta V_{dc}$ (DS1) - Varying V_{dco} 95
Figure 4.14: Dynamic stiffness analysis of $\Delta v_{g\_d}/\Delta V_{dc}$ (DS2) - Varying V_{dco} 96
Figure 4.15: PSCAD simulation results of V_{dco} sensitivity 98
Figure 4.16: Bandwidths representation on the full transfer function - Varying v_{g_do} 99
Figure 4.17: Bandwidths representation on the transfer function - Varying v_{g_do} 100
Figure 4.18: Bandwidths representation on the simplified transfer function - Varying v_{g_do} 100
Figure 4.19: Damping ratios representation on the forward-path transfer function - Varying v_{g_do} 102
Figure 4.20: Dynamic stiffness analysis of $\Delta i_n/\Delta V_{dc}$ (DS1) - Varying v_{g_do} 103
Figure 4.21: Dynamic stiffness analysis of $\Delta v_{g\_d}/\Delta V_{dc}$ (DS2) - Varying v_{g_do} 104
Figure 4.22: PSCAD simulation results of v_{g_do} sensitivity 105
Figure 4.23: Bandwidths representation on the full transfer function - Varying i_{g_do} 106
Figure 4.24: Bandwidths representation on the transfer function - Varying i_{g_do} 107

Figure 4.25: Bandwidth representation on the simplified transfer function - Varying i_{g_do} 108

Figure 4.26: Damping ratios representation on the forward-path transfer function - Varying i_{g_do} 109

Figure 4.27: Dynamic stiffness analysis of $\Delta i_n/\Delta V_{dc}$ (DS1) - Varying i_{g_do} 110

Figure 4.28: Dynamic stiffness analysis of $\Delta v_{g\_d}/\Delta V_{dc}$ (DS2) - Varying i_{g_do} 111

Figure 5.1: The selection of undamped natural frequency (f_n) and damping ratio (ζ) for the controller loops 115

Figure 5.2: The full SFSB diagram of the GSC controller 118

Figure 5.3: The full SFSB diagram of the RSC controller 118

Figure 5.4: Typical crowbar configurations 120

Figure 5.5: The control algorithm of the crowbar protection scheme 121

Figure 5.6: DC-link brake circuit 124

Figure 5.7: DC-link brake control design 124

Figure 5.8: Fault ride-through requirements of GB grid code for voltage dips lasting greater than 140ms 125

Figure 5.9: 80% (0.8pu) 3-phase voltage sag 127

Figure 5.10: No protection involved during a 0.8pu 3-phase voltage sag 127

Figure 5.11: DC-link brake activation (by increasing the set value of the DC-link voltage - not any voltage sag applied) 128

Figure 5.12: Stator active and reactive power, and rotor-side currents during an increase in the DC-link voltage (from 1kV to 1.5kV between t=2s and t=2.1s) 129

Figure 5.13: Only DC-link brake action taken by introducing voltage sag (the crowbar protection is intentionally suspended) 130

Figure 5.14: 0.2pu three-phase voltage sag 131

Figure 5.15: Rotor-side currents during a 0.2pu three-phase voltage sag 131

Figure 5.16: 0.5pu three-phase voltage sag 132

Figure 5.17: Rotor-side currents during a 0.5pu three-phase voltage sag 133

Figure 5.18: 0.8pu three-phase voltage sag excluding a lock-out time block 134

Figure 5.19: Rotor-side currents during a 0.8pu three-phase voltage sag excluding a lock-out time block 134

Figure 5.20: 0.8pu three-phase voltage sag including a lock-out time (0.01s) block 136

Figure 5.21: Rotor-side currents during a 0.8pu three-phase voltage sag including a lock-out time (0.01s) - Decreasing crowbar switch-on and -off actions 136

Figure 5.22: 0.8pu three-phase voltage sag including a lock-out time (0.045s) block 137
Figure 5.23: Rotor-side currents during a 0.8pu three-phase voltage sag including a lock-out time (0.045s) – Improved results 137
Figure 5.24: 0.2pu two-phase voltage sag 138
Figure 5.25: Rotor-side currents during a 0.2pu two-phase voltage sag 139
Figure 5.26: 0.5pu two-phase voltage sag 140
Figure 5.27: Rotor-side currents during a 0.5pu two-phase voltage sag 140
Figure 5.28: 0.8pu two-phase voltage sag excluding a lock-out time block 141
Figure 5.29: Rotor-side currents during a 0.8pu two-phase voltage sag excluding a lock-out time block 142
Figure 5.30: 0.8pu two-phase voltage sag including a lock-out time block (0.0205s) 142
Figure 5.31: Rotor-side currents during a 0.8pu two-phase voltage sag including a lock-out time block (0.0205s) – Improved results 143
Figure 5.32: 0.2pu one-phase voltage sag 144
Figure 5.33: Rotor-side currents during a 0.2pu one-phase voltage sag 144
Figure 5.34: 0.5pu one-phase voltage sag 145
Figure 5.35: Rotor-side currents during a 0.5pu one-phase voltage sag 146
Figure 5.36: 0.8pu one-phase voltage sag excluding a mono-stable 147
Figure 5.37: Rotor-side currents during a 0.8pu one-phase voltage sag excluding a mono-stable 147
Figure 5.38: 0.8pu one-phase voltage sag including a mono-stable (0.0202s) 148
Figure 5.39: Rotor-side currents during a 0.8pu one-phase voltage sag including a mono-stable (0.0202s) – Improved results 148
Figure 5.40: The DC-link voltage, stator real and reactive power behaviours during a 0.8pu 3-phase voltage sag in the case of no involving any protection 151
Figure 5.41: The DC-link voltage, stator real and reactive power behaviours during a 0.8pu 3-phase voltage sag by activating only DC-link brake protection 151
Figure 5.42: The DC-link voltage, stator real and reactive power behaviours during a 0.8pu 3-phase voltage sag by activating only crowbar protection 151
Figure 5.43: The DC-link voltage, stator real and reactive power behaviours during a 0.8pu 3-phase voltage sag by activating both crowbar and DC-link brake protection 152
Figure 5.44: Rotor-side currents behaviours during a 0.8pu 3-phase voltage sag in the case of no involving any protection 152

Figure 5.45: Rotor-side currents behaviours during a 0.8pu 3-phase voltage sag by activating only DC-link brake protection 153
Figure 5.46: Rotor-side currents behaviours during a 0.8pu 3-phase voltage sag by activating only crowbar protection 153
Figure 5.47: Rotor-side currents behaviours during a 0.8pu 3-phase voltage sag by activating both crowbar and DC-link brake protections 154
Figure 5.48: The DC-link voltage, stator real and reactive power behaviours during a 0.8pu 2-phase voltage sag in the case of no involving any protection 154
Figure 5.49: The DC-link voltage, stator real and reactive power behaviours during a 0.8pu 2-phase voltage sag by activating only DC-link brake protection 155
Figure 5.50: The DC-link voltage, stator real and reactive power behaviours during a 0.8pu 2-phase voltage sag by activating only crowbar protection 155
Figure 5.51: The DC-link voltage, stator real and reactive power behaviours during a 0.8pu 2-phase voltage sag by activating both crowbar and DC-link brake protections 155
Figure 5.52: Rotor-side currents behaviours during a 0.8pu 2-phase voltage sag in the case of no involving any protection 156
Figure 5.53: Rotor-side currents behaviours during a 0.8pu 2-phase voltage sag by activating only DC-link brake protection 157
Figure 5.54: Rotor-side currents behaviours during a 0.8pu 2-phase voltage sag by activating only crowbar protection 157
Figure 5.55: Rotor-side currents behaviours during a 0.8pu 2-phase voltage sag by activating both crowbar and DC-link brake protections 158
Figure 6.1: Outer (power) loop control of the RSC utilising the PI controller 160
Figure 6.2: Outer (power) loop control of RSC utilising the PID controller 162
Figure 6.3: Varying f_n – step responses of SoATF, STF2 and FTF2 ζ=0.7 and K_D=0.1s 168
Figure 6.4: Varying f_n – step responses of SoATF, STF2 and FTF2 ζ=0.8 and K_D=0.1s 169
Figure 6.5: Varying f_n – step responses of SoATF, STF2 and FTF2 ζ=0.9 and K_D=0.1s 170
Figure 6.6: Varying f_n – step responses of SoATF, STF2 and FTF2 ζ=1 and K_D=0.1s 171

Figure 6.7: Varying ζ – step responses of SoATF, STF2 and FTF2 f_n=2Hz and K_D=0.1s 174
Figure 6.8: Varying ζ – step responses of SoATF, STF2 and FTF2 f_n=2.5Hz and K_D=0.1s 175
Figure 6.9: Varying K_D – step responses of SoATF, STF2 and FTF2 f_n=2Hz and ζ=0.9 178
Figure 6.10: Varying K_D – step responses of SoATF, STF2 and FTF2 f_n=2.5Hz and ζ=0.9 179
Figure 6.11: Varying K_D – step responses of SoATF, STF2 and FTF2 f_n=2.5Hz and ζ=1 180
Figure 6.12: The PSCAD results for f_n =2Hz, ζ=0.9 and K_D=0.1s 182
Figure 6.13: The PSCAD results for f_n =2.5Hz, ζ=0.9 and K_D=0.1s 182
Figure 6.14: The PSCAD results for f_n =2.5Hz, ζ=0.9 and K_D=0.2s 183
Figure 6.15: The PSCAD results for f_n =2.5Hz, ζ=1 and K_D=0.1s 183
Figure 6.16: PSCAD results for robustness analysis - V_s=0.8pu 185
Figure 6.17: PSCAD results of $\zeta_1=\zeta_4=\zeta_6$ for robustness analysis - V_s=0.8pu 185
Figure 6.18: PSCAD results for robustness analysis - V_s=1pu 186
Figure 6.19: PSCAD results of $\zeta_7=\zeta_{nom}=\zeta_{11}$ for robustness analysis - Vs=1pu 187
Figure 6.20: PSCAD results for robustness analysis - V_s=1.2pu 188
Figure 6.21: PSCAD results of $\zeta_{12}=\zeta_{15}=\zeta_{17}$ for robustness analysis - V_s=1.2pu 188

List of Abbreviations

AC	Alternating Current
BJT	Bipolar Junction Transistor
BW	Bandwidth
CSC	Current Source Converter
DC	Direct Current
DE	Differential Equation
DFIG	Doubly-Fed Induction Generator
DFIM	Doubly-Fed Induction Machine
DS	Dynamic Stiffness
EMTDC	Electro-Magnetic Transient Direct Current
EU	European Union
EWEA	European Wind Energy Association
FACT	Flexible Alternating Current Transmission
FpTF	Forward-path Transfer Function
FSWT	Fixed-Speed Wind Turbine
FTF	Full Transfer Function
GaN	Gallium Nitride
GSC	Grid-Side Converter
GTO	Gate Turn-off Thyristor
GW	Giga Watt
GWEC	Global Wind Energy Council
HAWT	Horizontal Axis Wind Turbine
HS	High Speed
HVAC	High Voltage Alternating Current
HVDC	High Voltage Direct Current
Hz	Hertz
IEGT	Injection Enhanced Gate Transistor
IGBT	Insulated Gate Bipolar Transistor
JFET	Junction Field Effect Transistor
KCL	Kirchhoff's Current Law
LCC	Line Commutated Converter
LS	Low Speed

MATLAB	Matrix Laboratory
MCT	Metal Oxide Semiconductor Controlled Thyristor
MOSFET	Metal Oxide Semiconductor Field Effect Transistor
MVA	Mega Volt Ampere
MW	Mega Watt
NOVA	Novel Offshore Vertical Axis
OSIG	OptiSlip Induction Generator
PD	Proportional Derivative
PI	Proportional Integral
PID	Proportional Integral Derivative
PLL	Phase Locked Loop
PM	Phase Margin
PMSG	Permanent Magnet Synchronous Generator
PSCAD	Power System Computer Aided Design
pu	Per Unit
PWM	Pulse Width Modulation
RMS	Root Mean Square
RPWM	Random PWM
RSC	Rotor-Side Converter
SBD	Schottky Barrier Diode
SCIG	Squirrel Cage Induction Generator
SCR	Silicon Controlled Rectifier
SFOPWM	Switching Frequency Optimal PWM
SFSB	State-Feedback System-Block
SHEPWM	Selective Harmonic Elimination PWM
Si	Silicon
SiC	Silicon Carbide
SMPS	Switch-Mode Power Supply
SoATF	Second-order Approximated Transfer Function
SPWM	Sinusoidal PWM
SSoATF	Simplified Second-order Approximated Transfer Function
STF	Simplified Transfer Function
SVPWM	Space Vector PWM
TF	Transfer Function
UK	United Kingdom

UPS	Uninterruptible Power Supply
VAWT	Vertical Axis Wind Turbine
VCR	Video Cassette Recorder
VSC	Voltage Source Converter
VSWT	Variable-Speed Wind Turbine
WRIG	Wound Rotor Induction Generator
WRIM	Wound Rotor Induction Machine
WRSG	Wound Rotor Synchronous Generator

ABSTRACT

Wind turbine modelling using doubly-fed induction generators is a well-known subject. However, studies have tended to focus on optimising the components of the system rather than considering the interaction between the components. This research examines the interaction of the control methods for a doubly-fed induction generator (DFIG) in a wind turbine application integrating them with the crowbar protection control and DC-link brake control to make the best use of the converter.

The controls of the rotor-side and the grid-side converters of the DFIG model are both well established and have been shown to work. Typically the crowbar protection is designed in order to protect the rotor-side converter and the power electronic components of the DFIG system from high currents occurring in the rotor due to the faults. The DC-link brake-overvoltage protection is also designed to prevent the overcharging of the DC-link capacitor placed between the rotor-side converter and the grid-side converter. In order to show that these protection schemes work and with thought can co-ordinate with each other, tests consisting of a number of balanced three-, two- and one-phase voltage sags are applied to the network voltage.

The main contributions of this thesis are establishing operational tuning and design limits for the controllers and system subassemblies. This is to minimise the electrical subsystem interaction while maintaining adequate performance, and have an improved DC-link control. This work also includes a full electrical system study of the wind turbine and an essential literature review on significant references in the field of the DFIG wind turbine system modelling, control and protection.

Specifically this research project makes a number of novel contributions to the literature: enhanced DC voltage control including operating point sensitivity analysis and dynamic stiffness assessment, sensitivity and robustness analyses of the power loop control and control loop segmentation by appropriately tuning the controller loops.

Declaration

No portion of the work referred to in this thesis has been submitted in support of an application for another degree or qualification of this or any other university or other institute of learning.

List of Symbols

e= Excitation reference frame (for orientation)

g= General reference frame

o= Operating point

r= Rotor reference frame

s= Slip or stator (stationary) reference frame or second (time)

A= Swept area by rotor blades

R= Rotor radius

d_{HB}, d_{HGB}, d_{GBG}= Hub to blade, hub to gearbox, gearbox to generator mutual damping parameters

d/dt= Rate of change

f_{ref}, f_{tri}= Reference and triangular (carrier) signal frequency

f_n= Undamped natural frequency in Hz

i_{dc}= Direct current

i_n= Noise current

m_a= Amplitude modulation

m_f= Frequency modulation

C_{base}, C_{dc_link} = Base and DC-link capacitance

C_p= Power efficiency coefficient

D_B, D_H, D_{GB}, D_G= External damping components of blade, hub, gearbox and generator

E_g= Output voltage of GSC

G_{inner}= Inner loop gain

I_{cb_abc}= Crowbar current in *abc*

I_g= Grid-side current

I_r, I_s, I_m= Rotor, stator and magnetising (mutual) current

I_{rcc_abc}= Rotor-side converter current in *abc*

J_1= Inertia of flexible blade

J_2= Combined inertia of hub and rigid blade

J_3= Inertia of generator

J_B, J_H, J_G, J_{GB}= Blade, hub, generator and gearbox inertia

K_{2M}= Equivalent shaft stiffness of the two-mass drive train model

K_D= Derivative time constant of power (outer) loop of RSC

K_{HB}, K_{HGB}, K_{GBG}= Hub to blade, hub to gearbox, gearbox to generator spring constants

K_p= Proportional gain of current (inner) loop of RSC

K_{pi}= Proportional gain of current (inner) loop of GSC

K_{po}= Proportional gain of power (outer) loop of RSC

K_{pv}= Proportional gain of voltage (outer) loop of GSC

K_i= Integral time constant of current (inner) loop of RSC

K_{ii}= Integral time constant of current (inner) loop of GSC

K_{io}= Integral time constant of power (outer) loop of RSC

K_{iv}= Integral time constant of voltage (outer) loop of GSC

L_c= Operational transient inductance of rotor winding

L_{12}= Positive sequence leakage reactance between windings 1 and 2 in transformer

L_{13}= Positive sequence leakage reactance between windings 1 and 3 in transformer

L_{23}= Positive sequence leakage reactance between windings 2 and 3 in transformer

L_{gsc}= Coupling self-inductance to the grid-side converter

L_r, L_s, L_m= Rotor leakage, stator leakage and magnetising inductance

L_{rr}, L_{ss}= Rotor and stator self-inductance

L_{rsc}= Coupling self-inductance to the rotor-side converter

N_{GB}= Speed ratio of the gearbox

P_{brake}= DC-link brake power

$P_{converter}$= Real power of the converter

P_g=Real power seen from the grid-side

P_m= Mechanical power on the generator shaft

P_{mech}= Mechanical power

P_r=Rotor active power (real power seen from the rotor-side)

P_s = Stator active (real) power

P_t=Total real power delivered to the external grid

P_{wind}= Wind power

Q_g=Reactive power seen from the grid-side

Q_r=Rotor reactive power (reactive power seen from the rotor-side)

Q_s= Stator reactive power

Q_t=Total reactive power delivered to the external grid

R_{brake}= DC-link brake resistance

R_{cb}= Crowbar resistance

R_r, R_s, R_m= Rotor, stator and magnetising resistance

R_{gsc}= Coupling resistance to the grid-side converter

R_{rsc}= Coupling resistance to the rotor-side converter

S_{base}= Base (rated) apparent (complex) power

T_B= Aerodynamic torque of the blade

T_e= Electromagnetic (generator) torque

T_{shaft}= Torque of the shaft

T_{WT}, T_{wind}= Wind turbine torque

V_{123}= Transformer windings 1, 2 and 3 line-to-line rms voltages.

V_{dc} *or* V_{DC}= DC-link voltage

V_g= Grid-side voltage

V_s= Stator voltage

V_r= Rotor voltage

$V_{control}$, V_{ref}, V_{tri} = Control, reference and triangular (trigger or carrier) signal

V_{grid_abc}= The external grid voltage in *abc*

V_{wind}= Wind speed

X_r, X_s, X_m= Rotor leakage, stator leakage and magnetising reactance

ω= Rotational speed

ω_e= Angular frequency of the excitation reference frame

ω_{gen}= Angular speed of the generator

ω_m= Rotational speed of the blade or mechanical angular frequency of rotor

ω_n= Undamped natural frequency in rad/s

ω_R= Angular speed of the rotor

ω_s= Angular frequency of stator or supply angular frequency

ω_{slip}= Slip frequency ($=\omega_s - \omega_m$)

ω_{tur}= Angular speed of the turbine

ρ_{air}= Air density

ρ_A= Machine pole-pair number

β= Pitch angle

θ_B, θ_{GB}, θ_G, θ_H= Angular positions of the blade, gearbox, generator and hub

Θ_r= Rotor angle

γ= Angle between rotor and excitation reference frames

λ= Tip-speed ratio

μ= Angle between stator and excitation reference frames (stator flux angle)

ζ= Damping ratio

^{m}= Measured value

$\hat{}$ = Peak or estimated value

*= Set value

To my niece, Gökçe.

Acknowledgements

I would like to thank the Ministry of National Education of Republic of Turkey for their financial support during my PhD study.

I would like to express my deepest gratitude to my supervisor Prof Mike Barnes for his constant guidance support, everlasting patience and excellent collaboration. I am also grateful to Dr Judith Apsley who has time to time provided me advice on general matters of a PhD study.

I want to thank all my friends, namely Alper Aktaş and Aslı Tunçay for proving that how a 'best' friend is supposed to be. Special thanks go to the academic staff and postgraduate colleagues at the Power Conversion Group for sharing their knowledge with me. I also wish to acknowledge the administrative staff of the School of Electrical and Electronic Engineering for making life easier.

Lastly, I will greatly appreciate the eternal encouragements of my parents, brother, sister and all my relatives. I would like to thank them for their continual prayers and believing in me that I could accomplish this research.

Chapter 1 Introduction

Wind power today has an increasing importance in power production. Investments in wind energy technologies have been continuously made to generate clean and environmental friendly energy. Apart from construction and decommissioning, these systems never emit carbon dioxide (CO_2) to the atmosphere. However, one of the main disadvantages of using wind power is that the wind speed is unpredictable and very changeable. To alleviate the effect of this drawback, doubly-fed induction generators (DFIGs), which can operate at variable speeds, are widely used in wind conversion applications to maximise power generation and to reduce acoustic noise, converter costs and mechanical loads onto the nacelle [1, 2 and 3]. Hence, DFIG wind turbines currently dominate the market due to their cost-effective provision of variable-speed operation [1]. In particular, independent controllability of active and reactive power, reduced power converter costs and lower mechanical loads make the use of DFIG in wind turbines attractive.

The main source of inspiration of this research is that "better control helps provide high qualitative power". In the light of this motto, a complete model of the DFIG wind turbine system is developed in the simulation programme of PSCAD/EMTDC. Turbine mechanical dynamics and blade pitching control are excluded, since these present a slower set of dynamics, which are considered to be out of interest of this research. Generic current control methods for the rotor-side converter (RSC) and the grid-side converter (GSC) are utilised. Improved power loop control strategy for the RSC and enhanced voltage loop control technique for the GSC are investigated. Relevant sensitivity and robustness analyses for these control strategies are carried out. The integration of the protection schemes (rotor crowbar circuit and DC-link brake) with the overall system control and the coordination relationship between the protection devices are described. The ride-through capability of the DFIG under several balanced voltage sags is worked out. By proposing control loops segmentation, the electrical interaction between sub-controllers is reasonably diminished. The PSCAD simulation results are compared with the mathematical analysis and the MATLAB results to verify that the proposed DFIG system design is shown to work appropriately. An essential literature review on DFIG modelling, control and protection of selected significant references is also included.

1.1 Aims and Objectives of the Research

The main aim of this research is to help improve the power quality of energy generated in DFIG-based wind farms by designing better control techniques – it is from this that the motivation of this work is inspired. Besides, controlling all components of wind farms well needs a great deal of care, since maintenance is expensive and can only be undertaken during part of the year. Thus, another target is to decrease the maintenance costs by designing better control of the DFIG.

This research aims to collate the substantial references chosen in order to present a significant prior to art review on the modelling, control and protection of DFIG system. Enclosing a research background study on wind power, wind turbine concepts, and wind turbine components at a basic knowledge level can be considered as another objective. The key aims and objectives of this thesis are summarised below:

- To establish a comprehensive and coordinated set of DFIG modelling and dynamic machine equations.

- To enhance the DC-link voltage control (outer loop of the GSC) - and to verify this by operating point sensitivity analysis and dynamic stiffness assessments.

- To reduce the electrical interaction between the subsystem controllers by proposing a methodology for controller loops segmentation.

- To use protection schemes (rotor crowbar circuit and DC-link brake) with their improved control algorithms, to establish a protection coordination between these protection devices and to reasonably integrate these protection systems into the overall DFIG system.

- To investigate the behaviour and fault-ride through performance of the DFIG considered in this work under various balanced voltage sags introduced to the network voltage.

- To establish an improved power control (outer loop of the RSC) and to carry out sensitivity and robustness analyses of the power control.

1.2 Outline of the Thesis

The thesis consists of seven chapters:

Chapter 1 presents the aims and objectives of the research and summarises the main contributions made to the field.

Chapter 2 gives an overview of the research background. General wind turbine concepts, a market survey on current use of wind turbine types, the electrical and mechanical system components of a wind turbine and a significant literature review on DFIG modelling, control and protection are covered.

Chapter 3 provides the background to dynamic modelling and the equivalent circuit of DFIG including the dynamic machine equations. This is followed by transformation equations from *abc* reference frame to *dq* coordinates. The generic inner (current) loop controllers of rotor-side and grid-side converters are included as well. Finally, the drive train modelling and pitch control technique are presented.

Chapter 4 proposes a novel investigation of a better DC-link voltage control for the DFIG system. The impacts of disturbance input current and the *d*-component of the grid voltage on the DC-link voltage is investigated by carrying out dynamic stiffness analysis. The sensitivity analysis study is performed for the operating points of the DC-link voltage, and *d*-components of the grid voltage and current.

Chapter 5 presents controller loops segmentation and the designs of protection of power electronics components. The electrical interaction between the outer and inner loop controllers of the rotor-side and grid-side converters is significantly minimised by controller loop segmentation. A rotor crowbar circuit protection against over-current and a DC-link brake protection against over-voltage are explained in detail. Moreover, the protection coordination between these protection devices is described. The protection action relationship between the rotor crowbar and the DC-link brake actions is investigated as well. Lastly, various balanced voltage sags are applied to the system in order to verify that the proposed protection schemes work reasonably.

Chapter 6 investigates an improvement study of the outer (power) loop control of the rotor-side converter. A PI controller is replaced with a PID controller in order to utilise the advantage of controlling both the damping and bandwidth in the case considered in this thesis. A sensitivity analysis for the outer (power) loop control is performed. Furthermore, a robustness analysis for each selected stator voltage is undertaken by taking possible physical changes in the mutual (magnetising) and stator self-inductances into account.

Chapter 7 summarises the key conclusions of this research and presents suggestions for the future work projections related to this research.

1.3 Contributions

The main contributions of this thesis are listed below:

- A critical and essential literature review on DFIG modelling, protection and control.

- Segmentation of system controller loops in order to diminish electrical sub-controller interaction.

- Improved DC-link voltage control containing dynamic stiffness and operating point sensitivity analyses.

- Having a full electrical system assessment of the DFIG wind turbine, but excluding the aero-mechanical dynamics of the turbine which would add extra (and for many studies unnecessary) complexity to the system.

- Designing the rotor-crowbar and DC-link brake protection coordination and investigation of the relationship between these protection schemes actions.

- A novel approach to enhance the outer (power) loop control of the rotor-side converter including the sensitivity and robustness analyses.

Chapter 2 Research Background

2.1 Introduction

The wind has been serving mankind for thousands of years. The initial uses of wind power were to sail ships, grind grains and pump water. Probably, one of the first electric wind turbines, whose capacity was 20 kW, was used to generate electricity as early as 1891 by Dane Poul LaCour, a Danish scientist [4, 5 and 6]. However, the oil crisis in the early 1970s led to wind power drawing great attention as an alternative source to fossil fuels in order to generate cleaner electrical power. Since then wind turbine technology has increasingly evolved year-to-year.

In Chapter 2, the general knowledge on the background of the research will be presented. The main electrical and mechanical components of a wind turbine will be briefly given. Current wind turbine concepts and generator topologies used in wind conversion systems will be described. Chapter 2 will also cover the power electronics for wind turbines, power converter types and their switching control methods. Finally, an essential prior art review on modelling, controlling and protection design of DFIG will be documented.

2.2 Wind Power

Most governments and policy-makers in the world now target a reduction in the carbon dioxide emissions to the atmosphere. In order to achieve their targets, they have started to invest in environmental friendly energy technologies also known as new and renewable energy resources (i.e. hydro, wind, solar, thermal, wave, etc.). Wind, amongst these resources, has been of greatest interest to date to countries with low solar energy resource (like the UK).

The Global Wind Energy Council (GWEC) announced that the total installed wind capacity worldwide reached 197 GW peak in December 2010 [7]. Of this total capacity worldwide, 5.2 GW has been installed in the UK [7 and 8]. The European Wind Energy Association (EWEA) assumes that the installed wind power capacity of the European

Union (EU) however will be raised to 230 GW by 2020 and to 400 GW by 2030 [9]. Wind power is therefore scheduled to become a very significant European industry.

As governments plan to increase their wind power capacity, the size of wind turbines has increased enormously. Currently, 7 MW sized wind turbines are being tested in on and/or off-shore wind farms. In addition to an increase in size, making them more robust, reliable and efficient has always been a challenge. Accessibility and cost-effectiveness of the wind turbines are other issues which need to be carefully considered.

2.3 Conversion of Wind Power

The design of wind turbines is supposed to allow the maximum energy capture from the wind. The power already existing in the wind can be formulated as

$$P_{wind} = \frac{1}{2}\rho_{air} A(=\pi R^2) V_{wind}^3 \tag{2.1}$$

where

P_{wind} : wind power ($kg.m^2/s^3$=Watt)

ρ_{air} : air density (1.225 kg/m^3)

V_{wind} : wind speed (m/s)

A : swept area by rotor blades (m^2)

R : rotor radius (m)

Only a fraction of the wind power is captured by the blades as mechanical power

$$P_{mech} = C_p(\lambda,\beta)\, P_{wind} \tag{2.2}$$

where

C_p : power efficiency coefficient

λ : tip-speed ratio (radian)

β : pitch angle (degree)

The tip-speed ratio, λ, is defined as

$$\lambda=\frac{\omega_m R}{V_{wind}} \qquad (2.3)$$

where

ω_m : rotational speed of the blade (mechanical rad/s)

R : length of the blade or radius of the swept area (m)

Substituting equation 2.1 into equation 2.2, the mechanical power (P_{mech}) captured from wind by wind turbine can be re-written as

$$P_{mech}=\frac{1}{2}\rho_{air}C_p(\lambda,\beta)AV_{wind}^3 \qquad (2.4)$$

Theoretically the maximum value of C_p is restricted to 16/27 (C_{pmax}≈0.593) by Betz's limit, which means that a wind turbine cannot extract more than 59.3% of the power from the wind [2, 5 and 10]. However, the applicable range of maximum C_p values is reasonably 0.25 to 0.45 [10].

2.4 Wind Turbine Concepts

Wind turbines can be divided into two main categories based on the rotating axis direction: vertical axis wind turbines (VAWTs) and horizontal axis wind turbines (HAWTs). Nowadays, the use of VAWTs, which are also known as Darrieus rotor turbines named after their French inventor, is very rare[1]. The most common wind turbine type used in wind conversion systems is the three-bladed, upwind design and either stall or mostly pitch-controlled HAWTs. In Figure 2.1, two types of HAWTs and one type of VAWTs are illustrated.

[1] The Energy Technologies Institute's £2.8m NOVA (Novel Offshore Vertical Axis) project was launched in 2009 by a UK-based consortium to study the feasibility of a NOVA turbine. 5 MW and 10 MW Aerogenerator type turbines are being designed, developed and tested which could in the long term lead to an alternative to HAWTs.

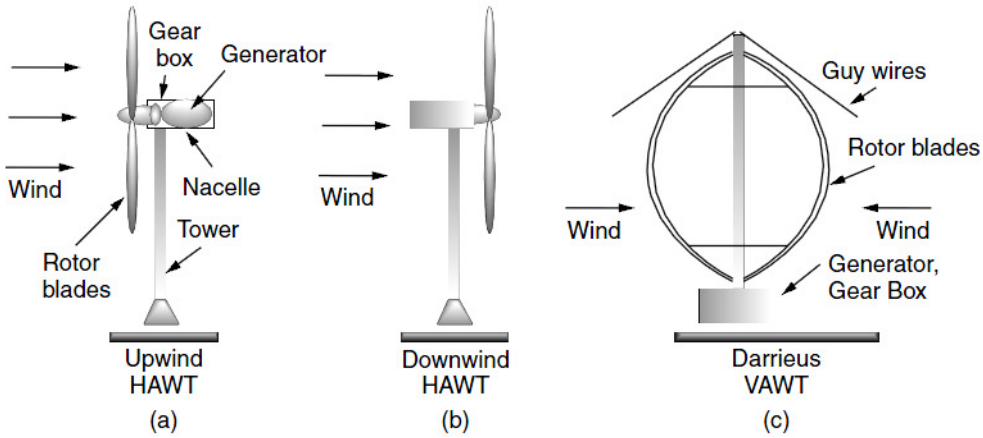

Figure 2.1: Wind turbine types [6]

Wind turbines are further categorised into fixed-speed or variable-speed. This refers to mechanical (shaft) speed. In fixed-speed wind turbines, neglecting the operating slip variation as it is generally below 1%, the wind turbine rotor speed is regarded as fixed and determined by the network frequency [1 and 10]. Although fixed-speed wind turbines (FSWTs) are simple, robust, reliable, and well-proven with a lower cost of electronic components (no frequency converters are used), the major disadvantages are uncontrollable reactive power consumption, higher mechanical stress and poor power quality [1 and 5]. The lack of ability to control active and reactive power independently is another drawback. Because of the fixed-speed operation, any fluctuation in the wind power input is transferred to the generator torque and then lastly reflected through to the electrical power. This system is also very sensitive to voltage dips during grid faults. A squirrel cage induction, wound rotor induction or synchronous generator can be used in fixed-speed wind turbine systems.

The architecture of variable-speed wind turbines (VSWTs) allows the acquisition of maximum aerodynamical efficiency for a certain range of the wind speeds. Over time, since the wind turbine size has become larger, the typically used wind turbine concept has evolved to VSWTs from FSWTs. The attractive advantages of VSWTs are reduction in mechanical loads and stresses, increased energy capture, lower acoustic noise and improved power quality [1, 5 and 10]. With their capability of providing independent active and reactive power control, VSWTs make themselves more favourable and popular. More complexity in control and additional power converter components, which increases both cost and the losses due to power electronics, are the main disadvantages of VSWT systems. Variable-speed wind turbine systems generally employ a wound rotor induction generator with a variable rotor resistor (OptiSlip®), or a wound rotor induction generator with a partially rated converter (DFIG: doubly-fed induction generator), or an induction or synchronous generator (PMSG: permanent magnet synchronous generator, or WRSG: wound rotor synchronous generator) with a fully-rated converter.

2.4.1 Squirrel Cage Induction Generator (SCIG) Wind Turbines

A typical squirrel cage induction generator wind turbine configuration is illustrated in Figure 2.2. This design is known as a fixed speed wind turbine. The generator is directly connected to the network via a transformer. In order to prevent it drawing reactive power from the grid, a capacitor bank is placed to achieve reactive power compensation. This capacitor bank also provides the required reactive power to energise the SCIG. A soft-starter is used to minimise the transient current during the magnetisation of the generator. Thus, the grid connection of the SCIG based wind turbines is made smoother.

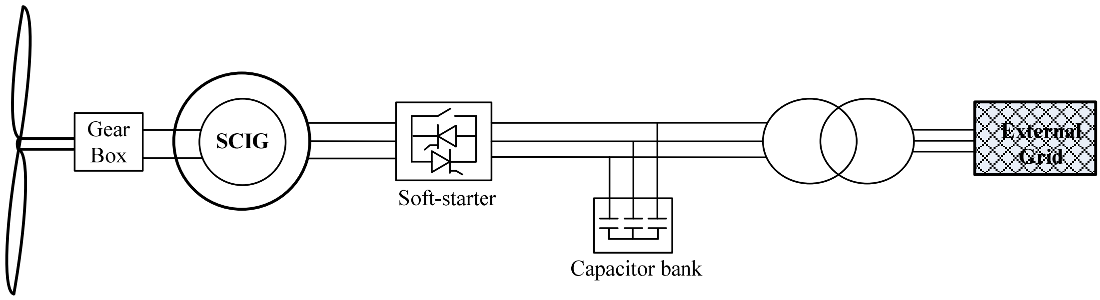

Figure 2.2: A typical configuration of SCIG wind turbine

2.4.2 Wound Rotor Induction Generator with Variable Rotor Resistor (OptiSlip®)

An alternative concept to the fixed speed wind turbines equipped with a squirrel cage induction generator has been developed by Danish manufacturer Vestas to minimise the load and improve power quality. In this concept a wound rotor induction generator coupled directly to the grid via a transformer is used. As in the SCIG wind turbine concept, a soft-starter and a capacitor bank are both used for the same purposes. Using a variable rotor resistance, the variable speed operation is maintained typically up to 10% above synchronous speed [1 and 11]. This concept is shown in Figure 2.3, which is also known as OptiSlip®.

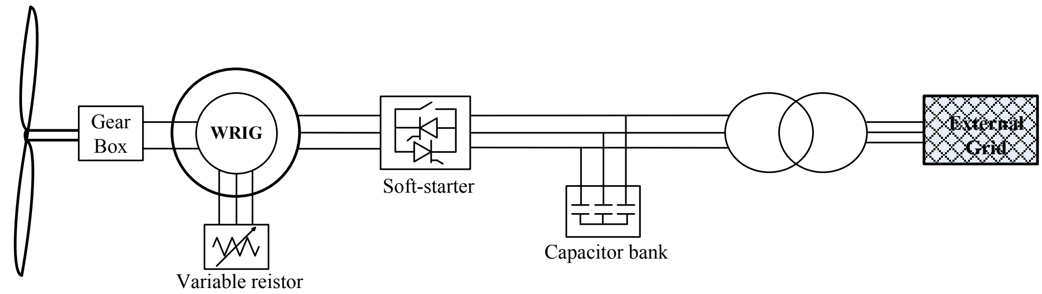

Figure 2.3: WRIG with variable rotor resistance (OptiSlip®)

2.4.3 Variable Speed Wind Turbines with Fully-Rated Converter (PMSG/WRSG)

This configuration employs a squirrel cage induction, permanent magnet or wound rotor synchronous generator with a fully-rated power converter. The generator is connected to the grid via transformer through a fully-rated converter (see Figure 2.4). In this concept, a gearbox may not be required in the case of multi-pole synchronous generators. Being quite expensive and complicated in terms of mechanical design are considered the main drawbacks of this topology. In comparison to induction generators, synchronous generators do not need a magnetising current which is regarded a dominant advantage [1], since it improves efficiency.

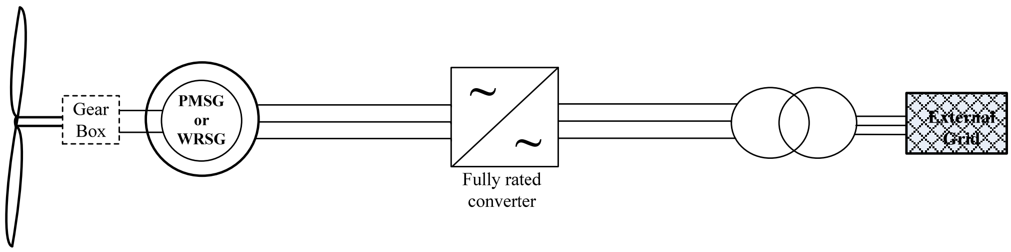

Figure 2.4: Fully-rated variable speed wind turbine (PMSG or WRSG)

2.4.4 Variable Speed Wind Turbines with Partly-Rated Converter (DFIG)

The most dominant of the wind turbine generator concepts in the market is the doubly fed induction generator based wind turbine [1]. With the use of a partly-rated power converter, the converter rating drops to about 30% of the generator rated power. This results in a lower cost and size of converter design. A DFIG typically uses a wound rotor induction generator. The stator winding of the generator is coupled to the grid via a three phase three winding transformer, while the rotor windings are connected by a bi-directional back-to-back partially-rated power converter. The significant advantages of the DFIG are the independent control of stator active and reactive power, reduced mechanical stress, better power quality, lower cost and lower acoustic noise. The requirement of regular maintenance of the slip rings is the disadvantage of using the DFIG based wind turbine topologies. In Figure 2.5, the DFIG concept is depicted.

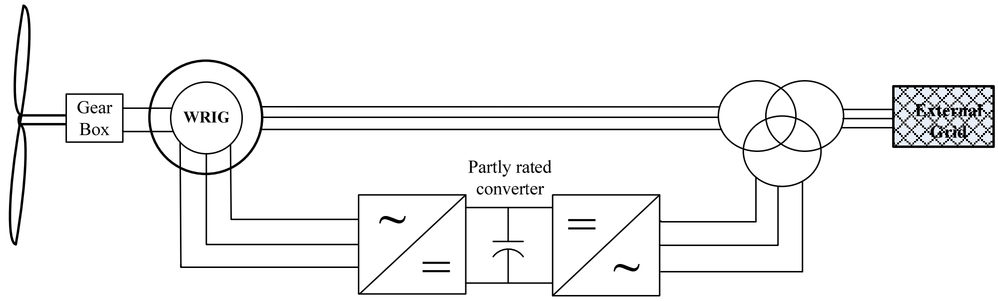

Figure 2.5: Partly-rated variable speed wind turbine (DFIG)

2.4.5 Stall, Active-Stall and Pitch Control [1 and 5]

In this section, References [1 and 5] are reviewed through in order to summarise the appropriate control of the mechanical input power for the wind turbine concepts mentioned in Sections 2.4.1 to 2.4.4. Typically, these common techniques are considered: stall control, active-stall control and variable pitch, variable speed with generator and pitch control. In a stall control scheme, the pitch of the blades to the hub is maintained with a constant angle. If the wind speed exceeds the rated value, the rotor 'stalls' due to its aerodynamic design. Being the most robust, the cheapest and the simplest method can be considered the advantages of this control technique [1]. The main drawbacks are lower efficiency at low wind speeds, lack of assisted start-up and the potential changes in the maximum steady state power as changes in network frequency and the air density occur [5].

In case of that the stall of the blade is being actively controlled by pitching the blades to a greater attack angle, then the so-called active-stall controls method results [1]. Below the rated wind speed, the blades are pitched for optimum power capture. Thus, the maximum power efficiency can then be accomplished. In the case of higher wind speeds, the blades are pitched to a larger attack angle in order to stall the turbine. "In comparison with stall control, active stall control has a smoother limitation of power without large inherent power fluctuations and is able to compensate for air density variations" [1]. Emergency stop and assisted start-up are possible in combination with the pitch mechanism.

The market for larger turbines is currently dominated by variable pitch, variable speed turbines with generator and pitch control. In pitch control, there is no action required to limit the power at low speeds, but the blades are pitched for optimum power yield [1]. When the wind speeds increase and exceed a certain value, then the blades are pitched to a small attack angle to regulate power and to prevent the rotor accelerating too much. Adding extra complexity and a tendency to produce higher inherent power fluctuations are regarded as disadvantages of the pitch control method. Its advantages are a good power control performance, assisted start-up and emergency stop [1 and 5].

The conventional stall control concept in fixed-speed wind turbines was used by many Danish wind turbine companies. Since the dominant wind turbine concept shifted to variable-speed from fixed speed, stall control is no longer used in most wind turbines. Fixed-speed wind turbines with variable pitch operating in wind farms or stand-alone now utilise active-stall control. The market is dominated by variable pitch variable speed wind turbines with partly and fully rated power converter concepts. Specifically, the pitch-controlled DFIG concept is the market leader, while the direct-driven PMSG concept is gaining ground rapidly. It seems that the reign of the DFIG will continue for a few years yet though. Although most large wind turbine manufactures have started to offer a PMSG option in their wind turbines.

2.5 Wind Turbine Components

A typical horizontal axis wind turbine mainly consists of two subsystems, namely a mechanical system and an electrical system. Since this thesis focuses on the control design aspects of the electrical system for the DFIG-based wind turbine, the mechanical system is only touched upon at a basic level. Detailed information on mechanical design of a wind turbine can be found in [2, 4, 6, 12, 13, 14, 15, 16 and 17].

The main components of a horizontal axis wind turbine are given in Figure 2.6. A wind turbine system is comprised of a rotor and its hub, two or mostly three rotor-blades, a nacelle, a gearbox, an electrical generator, the yaw mechanism, sensors and controllers, a tower, the foundations, a protection system, and a transformer.

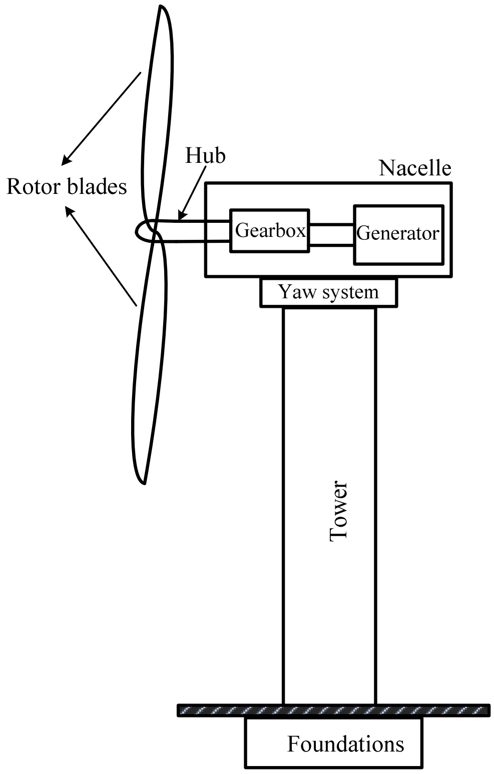

Figure 2.6: The main components of a typical horizontal axis wind turbine

The nacelle is mounted on the tower which is built on the foundations. The drive-train components (low- and high-speed shafts, gearbox, generator, aerodynamic control i.e. stall or pitch control, and a mechanical brake) are placed in the nacelle. The rotor blades are fixed onto the hub and coupled to the rotor and then to the gearbox via a low-speed shaft.

2.6 Mechanical System of Wind Turbine

The mechanical system aspects and their interaction with the electrical system design needs a great deal of care, because all components are nested into a very constrained space on the top of a large tower. Since the generators and power electronics devices are quite expensive, they should be kept in a strong and protective nacelle. Moreover, in case of robust design any structural damage can be avoided during high wind speeds, i.e. gusts. This is so that power is delivered uninterruptedly to the customers. The following components of the mechanical system are of interest: blades, nacelle, gearbox, tower and hub, and yaw mechanism. In Figure 2.7, a nacelle and the components of a DFIG wind turbine designed by Vestas Wind Systems A/S, V112 3MW wind turbine, are shown.

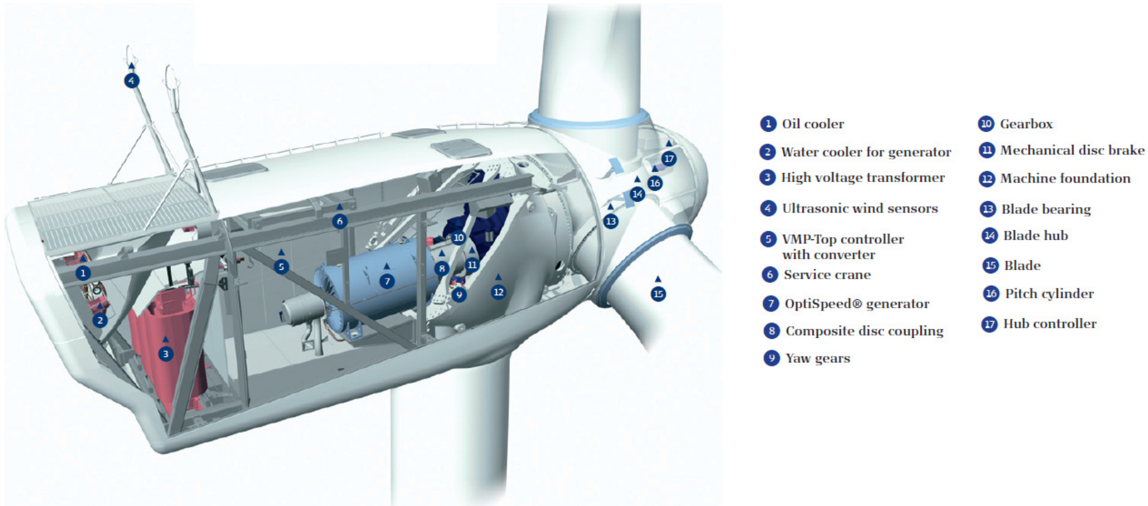

Figure 2.7: A nacelle of a DFIG (V112 3MW) wind turbine [18]

2.6.1 Blades

The blades are the most critical components in a wind turbine system as they extract the kinetic energy of the wind to be converted to the electrical energy via a generator. The aerodynamic design of the blades is significant in order to capture maximum energy.

The blades should withstand the mechanical stress due to centrifugal forces and fatigue loads under perpetual vibrations. The design of the blades then needs a comprehensive effort to avoid blade failures, damage and even breakages which would lead to high maintenance cost.

2.6.2 Nacelle

The construction of the nacelle must be strong enough to be able to protect the major mechanical and electrical components of the wind turbine against any damage due to bad weather conditions. With an increase in the size of the wind turbine, the nacelle also gets bigger and heavier. However, a more powerful wind turbine also means a higher tower to fit the blades. Therefore, the installation of a nacelle at the top of the tower, whose length increases with capacity, becomes difficult and needs progressively more engineering and extra cost. So, the design of the nacelle particularly the need to create a nacelle at a reasonable weight is key – and whole systems design is crucial.

2.6.3 Gearbox

A gearbox is connected to the rotor by a low-speed shaft and increases the rotor speed to a reasonable value. The high-speed shaft couples the gearbox to the generator. The design and choice of gearboxes should be undertaken carefully, as they are expensive and heavy. Initial gearboxes caused a large fraction of long term failures. Thus, careful gearbox design allows the maintenance cost to be reduced. Unless properly designed, the noise sourced from gearboxes can be annoying. However, for example, the materials used in the manufacturing process of the gearbox can be chosen in order to reduce noise. This is a special area for gearbox manufacturers, but shows some of the potential for innovation and system design.

The gearbox use is not necessary for variable speed wind turbines employing multi-pole synchronous generators (i.e. PMSG) with fully rated frequency converters. This reduces the cost spent on the mechanical system, but if the overall system is considered, the DFIG provides a cheaper option than the PMSG does. In DFIG based wind turbines, selecting a gearbox type and ratio are important as any disturbances in the mechanical dynamics (e.g. inertia, torque) are transferred to the generator. According to [2] the efficiency of gearbox varies between 95% and 98%.

2.6.4 Tower and Hub

Tower and hub designs are complex. The structural design of the tower should be capable of carrying the weight of the nacelle and the rotor blades. Due to wind speed fluctuations, the tower vibration could be minimised and eliminated through selecting a robust design of the tower. The typical tower height is 2 to 3 times the rotor radius, however in any case it should be more than 24m [14]. The towers are made of steel, concrete or reinforced concrete. The tower construction in horizontal axis wind turbines could be tubular or lattice. Tubular towers have been commonly used in wind turbine applications.

The hub design is another important issue for HAWTs. There are three common hub types: rigid, teetering and hinged. The most used one amongst them is the rigid hub, since the wind turbines mainly have rigid rotors [14].

2.6.5 Yaw Mechanism [14]

A yaw system is used in most HAWTs in order to keep the rotor oriented in the direction of the wind. Upwind HAWTs have active yaw control, while downwind HAWTs have free yaw control. The yaw mechanism is controlled by an automatic yaw control system including a sensor which traces the wind direction [14]. The yaw control sensors are placed on the surface of the nacelle and are a critical component – failure significantly impairs the turbine performance.

2.7 Electrical System of Wind Turbine

The mechanical turbine rotational energy is converted to electrical energy by means of a complex electrical system in wind farms. The main functions of the electrical system are to generate electricity, but also to maintain telecommunications, protection, and control throughout the whole system, to collect a variety of data and to help improve the system power quality using power electronics devices.

In this section the following components of the electrical system will be covered: generator topologies, transformers, connection types to the grid, and protection devices. Power electronics for wind turbines will be presented itself in another section.

2.7.1 Generator Topologies

Electrical generators are divided into two main groups: DC (direct current) and AC (alternating current) generators. DC generators are today not in use in main-stream wind conversion systems. However, permanent-magnet DC generators are used in very small wind turbines for recharging batteries [15 and 17]. AC generators are categorised into asynchronous (induction) generators and synchronous generators (alternators).

The most used generator type in wind turbines is the induction generator. Induction generators are classified into squirrel cage, where the rotor is short-circuited, and wound rotor induction generators, where the rotor is connected via slip rings to an external circuit. Reactive power for the induction generators can be provided by the network or power electronic equipment. Squirrel cage induction generators are generally used in fixed-speed wind turbines. Wound rotor induction generators can further be categorised into variable-slip (OptiSlip® by Vestas) induction generator (OSIG) and doubly-fed induction generator (DFIG) types. These two configurations are utilised in variable-speed wind turbines.

Synchronous generators are more expensive and require more complex mechanical design than an induction generator. There are two types of synchronous generators being employed in wind turbines, namely the wound rotor synchronous generator (WRSG) and the permanent magnet synchronous generator (PMSG).

Other types of generator have been discussed for wind turbines but are presently not widely used: these include high-voltage generators, switch-reluctance generators, transverse flux generators, and aero-generator concepts (for vertical-axis wind turbines). Detailed information on doubly fed induction generators can be found in [5, 10 and 19]. Variable-speed generators for wind turbines are well-documented in [1, 5, 10, 13 and 20]. In [21 and 22], the electrical machines concepts for each of these are comprehensively reviewed.

2.7.2 Transformers

Transformers are essential auxiliary components in wind turbine systems. Transformers are used to step-up the wind turbine generator voltage, which varies between 400V and 1kV to 11kV-33 kV. In offshore wind farms, since the transformers are located in the nacelle, the design of transformers plays a significant role in reducing the weight of the nacelle and consequently the tower, while they are generally placed in the tower base in onshore wind farms. In the case of offshore wind farms, compact, efficient and reliable transformer designs need to be developed. From the point of the cooling system, the transformers may be classified as liquid (mostly oil)-filled, gas-filled and dry-type. Some doubly-fed induction generator wind turbine concepts are connected to the external grid via a 3-phase 3 winding transformer, while other concepts are coupled through a 3-phase 2 winding transformer.

2.7.3 Connection Types to the Network

Wind farms can be connected to the main network by using high voltage alternating current (HVAC) or high voltage direct current (HVDC). Onshore wind farm connections to the grid are realised by HVAC overhead transmission lines. Initially, offshore wind farms have been coupled to the network by means of HVAC submarine cables. Today, an alternative HVDC connection type is being utilised to connect the offshore wind farms to the shore, at presently on the BorWin 1 farm [23]. Wider use of HVDC is unavoidable since HVAC is not more efficient for most offshore wind farms with a connection of more than around 50 km to shore, and the reactive power compensation used to maintain AC voltage amplitude within the desired value will not be cost-effective [10]. With an increase in distance, shunt capacitance and the cable charging currents will increase, and then result in capacitive losses [16]. Over a 50 km subsea transmission length, HVDC transmission technology is felt preferable.

In HVDC connections, since DC cables are used, no cable charging currents occur during steady-state operation. Moreover, in comparison to HVAC the power loss is low in the cable. There are two HVDC techniques used: voltage source converter (VSC) HVDC using IGBTs, and line-commutated converter (LCC) HVDC based on thyristors. VSC HVDC has a lower size than LCC HVDC does. VSC HVDC has also these advantages over LCC HVDC: no external voltage source required for commutation, thus no need of a synchronous generator or a compensator, independent control of reactive power flow at each AC terminal, independent active and reactive power control [10]. Due to these benefits, VSC HVDC connection is the dominant DC transmission technology in offshore wind industry. Barker [24] has presented detailed information on HVDC connection technology.

2.7.4 Protection Devices

Protection is a very significant issue for wind turbine systems. Protection means different things to different people though. Firstly, to prevent the turbine from over-speeding during strong winds, one of stall, active-stall or pitch control methods is used. These techniques may rapidly stop the turbine or decrease its speed over a period of time based on which wind turbine concept is employed.

Secondly, the surface of the blades and nacelle should be galvanised with an anticorrosive material to protect against adverse weather conditions (icing, humidity, and heat, etc.). For thundery areas, a lighting protection system must be taken into account.

Another protection scheme is needed for the power electronics devices to protect them against over-voltages and other grid faults. The rotor-crowbar protects the power electronic components from high rotor currents occurring in the system. Additionally, the DC-link brake method can be used to prevent the DC-link capacitor overcharging. Thus, the whole system would be protected from the harmful effects of over-voltages in the DC-link. A good example of grid fault ride through work is shown in [25].

2.8 Power Electronics for Wind Turbines

Power electronics is one of the most sensitive components of a wind conversion system. With fast development in power electronics technology, more reliable devices have been designed causing lower power loss in wind farms. This contributes to better power quality and increases overall efficiency of the whole wind turbine system. As wind turbine size increases, so power electronics devices should be able to cope with higher (voltage and current) ratings.

2.8.1 Power Electronics Devices

Rapid development in power semiconductor technology has produced affordable power electronics device designs. Power electronics semiconductor devices can be categorised into three groups regarding their controllability [26 and 27]:

i) Uncontrolled: diodes whose on and off states are controlled by the power circuit
ii) Semi-controlled: thyristors and silicon controlled rectifiers (SCRs) that are controlled by a gate signal to turn on. However, the power circuit is required to turn them off.
iii) Fully-controlled: Controllable switches such as bipolar junction transistors (BJTs), metal-oxide-semiconductor field effect transistors (MOSFETs), gate turn-off (GTO) thyristors, MOS-controlled thyristors (MCTs) and insulated gate bipolar transistors (IGBTs).

In [27], power semiconductor devices are compared in terms of their power capabilities and switching speeds, and presented in Table 2.1.

Device	Power Capability	Switching Speed
BJT	Medium	Medium
MOSFET	Low	Fast
GTO	High	Slow
MCT	Medium	Medium
IGBT	Medium	Medium

Table 2.1: Comparison of controllable switches

To increase the efficiency of the power electronics devices, the use of material of the power semiconductors have also been developed. Although silicon (Si) based power semiconductor devices made improvement in the performance of MOSFETs and IGBTs in the last two decades, further innovative enhancement in power electronic devices is now only possible to a limited degree with this material [28]. Therefore, in some research silicon has been replaced with silicon carbide (SiC) and gallium nitride (GaN) to achieve breakthroughs in increasing the performance of the semiconductors [28 and 29]. A research [28] shows that SiC has 10 times higher breakdown electric field and 3 times higher thermal conductivity than Si does. The main advantages of SiC material are high-voltage blocking capability, low on-resistance, high-temperature operation, fast switching with minimum reverse recovery (little current overshoot) [28]. In terms of rated blocking voltage, the comparison of the major applications of individual bipolar and unipolar Si and SiC based power electronics devices is given in Figure 2.8 [28].

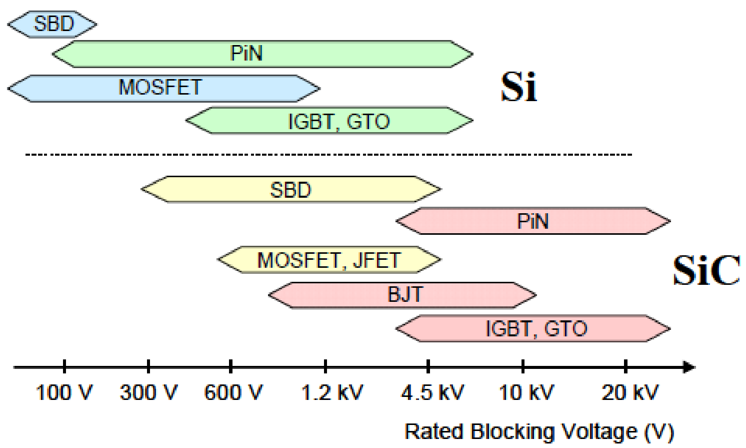

Figure 2.8: Major applications of individual bipolar and unipolar Si and SiC based power electronics devices in terms of the rated blocking voltage [28]

In [29], the application areas of the main power electronics devices are subdivided and shown in Figure 2.9.

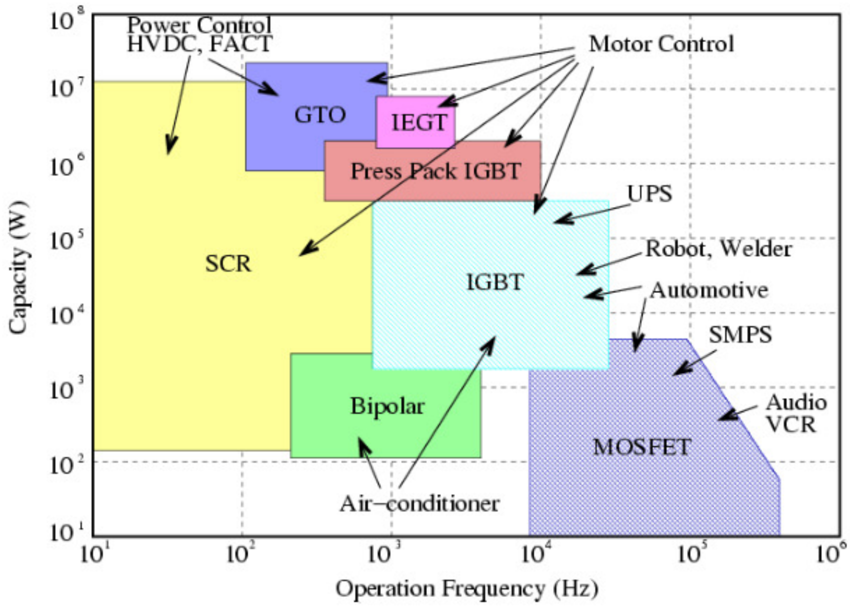

Figure 2.9: The applications of discrete power semiconductor devices [29]

As seen in Figure 2.9, MOSFETs and IGBTs are employed in high-frequency applications, while SCRs and GTOs are used for the purpose of high-power applications. IGBTs or MOSFETs, which are connected series or parallel and inserted in a plastic packaging, can also be used for medium-power, medium-frequency applications [29].

2.8.2 Converter Module Types

The main power electronics components currently being used in wind farms are soft-starters, capacitor banks, converters (rectifiers and inverters), and protection units (crowbar circuits and DC-link brakes).

A soft-starter is used in fixed-speed wind turbines (squirrel cage induction generator based wind turbines) and in wound rotor induction generator with variable rotor resistance based wind turbines (OptiSlip®) to maintain a smooth grid connection by reducing transients during magnetisation. The soft-starter is by-passed right after connection. The advantages of soft-starters are that they are cheap and simple power electronics devices. More information on soft-starters can be obtained from [5, 10 and 30].

In a similar manner, a capacitor bank is used in same wind turbine concepts along with the soft-starter. Therefore, the required reactive power for energisation of the generator is supplied. Today, since variable-speed wind turbine concepts are preferred in wind farms, the presence of soft-starter and capacitor banks are of limited practical interest. Both functions of the soft-starter and capacitor banks can be achieved by controlling the power electronic inverters now being used.

Converters are divided into two main categories in terms of the type of their input source: voltage source converters (VSC) and current source converters (CSC). The conventional phase controlled thyristor based current source converters are used in only high power applications and conventional HVDC systems [27]. Today's variable-speed wind turbine concepts employ partly- or fully-rated frequency converters consisting of voltage source inverters. Three-phase voltage source converters can be divided into two main categories in terms of control methods: Pulse-Width Modulated (PWM) converters and square-wave converters [27]. Since the PWM switching technique is well-proven and has the capability of operating at higher frequencies, it has been dominant in wind turbine industry [26]. In PWM both the magnitude and the frequency of the inverter output voltage can be controlled, while square-wave operation can only control the frequency of the voltage. Given the clear advantages of PWM operation over square-wave, the PWM concept therefore primarily is of interest, and details on it will be presented in section 2.8.3. A three-phase two-level six-switch voltage source converter configuration, which is also used as the rotor- and grid-side converter in this research, is illustrated in Figure 2.10.

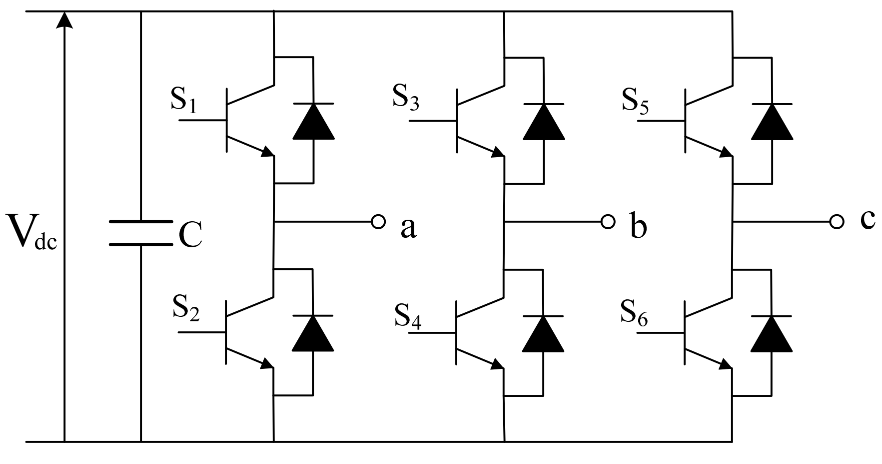

Figure 2.10: Three-phase two-level six-IGBT switch-based VSC

2.8.3 PWM Techniques

In this type of control, the input DC voltage stays almost constant at a certain magnitude. So, the magnitude and the frequency of the output AC voltage need to be controlled by the converter (inverter) itself. To do so, the inverter switches rapidly between the two rail voltages. There are various PWM techniques, such as switching frequency optimal PWM (SFOPWM), selective harmonic elimination PWM (SHEPWM), sinusoidal PWM (SPWM), space vector PWM (SVPWM), harmonic injection modulation, and random PWM (RPWM) [10, 27, 31 and 32]. Amongst them SPWM and SVPWM will be discussed, because they are the most widely used. Note that this section is mostly based on the knowledge presented in [10, 26, 27 and 33].

The advantages of using PWM are that it inherently eliminates the low-frequency harmonics: it keeps the frequency of the first higher order harmonics in the AC output at around the switching frequency. It also allows the converter operate at almost any amplitude or phase angle [5].

The amplitude of the injected AC voltage in terms of the DC voltage can be determined for every single switching voltage output in either Sinusoidal PWM (SPWM) or Space Vector PWM (SVPWM) [16]. The decoupled *d-q* control method is possible with a voltage source converter using the SPWM or SVPWM technique since they provide independent control of the magnitude and the phase of the injected voltage [16]. The PWM switching method therefore allows the independent control of the active (real) and reactive power output of the inverters.

The PWM scheme fundamentally compares a reference signal, V_{ref}, or a control signal, $V_{control}$, which typically varies sinusoidally, with a fixed frequency triangular carrier waveform also known as trigger signal, V_{tri}, in order to form a switching pattern. If an H-bridge converter is used per phase, PWM switching can be either bipolar (both switch pairs controlled together) or unipolar (each switch pair controlled separately).

There are two terms used in PWM inverters: amplitude modulation (m_a) and frequency modulation (m_f). The amplitude modulation is a ratio of the peak value of reference signal to the peak value of the carrier (triangular) signal, while the frequency modulation can be defined as a ratio of the carrier (triangular) signal frequency (f_{tri}) to the reference signal frequency (f_{ref}).

$$m_a = \frac{\hat{V}_{ref}}{\hat{V}_{tri}} = \frac{\text{Peak amplitude of the reference signal}}{\text{Peak amplitude carrier (triangular) signal}}$$

$$m_f = \frac{f_{tri}}{f_{ref}} = \frac{\text{Carrier (triangular) signal frequency}}{\text{Reference signal frequency}}$$

If $m_a \leq 1$, the peak amplitude of the fundamental frequency component in the converter output voltage changes linearly with the amplitude modulation ratio (m_a), as known linear modulation. In other words, the range of m_a between 0 and 1 is considered as the linear range. If m_a is set larger than 1, the fundamental output voltage does not vary linearly since the PWM converter enters in overmodulation mode. Thus, the waveform of the output voltage degenerates into a square wave inverter waveform.

If m_f is less than or equal to 21, the triangular wave and the control signal should be synchronised to each other. Also m_f should be an odd integer number to reduce harmonics. For larger m_f values (m_f >21), synchronisation is not necessary although this is still desirable unless m_f is very large. In three-phase inverters, with low values of m_f ($\leq$21) should be chosen, a multiple of 3, in order to attenuate even harmonics and neutralise the most dominant harmonics in the phase-to-phase voltage. In wind turbine applications, the most used configuration is a typical three-phase two-level six-switch PWM inverter. A three-phase inverter can be formed by connecting three single-phase inverter legs to the same DC link capacitor as shown in Figure 2.10. A single-phase two level converter circuit depicted in Figure 2.11 is used to explain the reference signal and triangular signal (carrier waveform) interaction, which is illustrated in Figure 2.12.

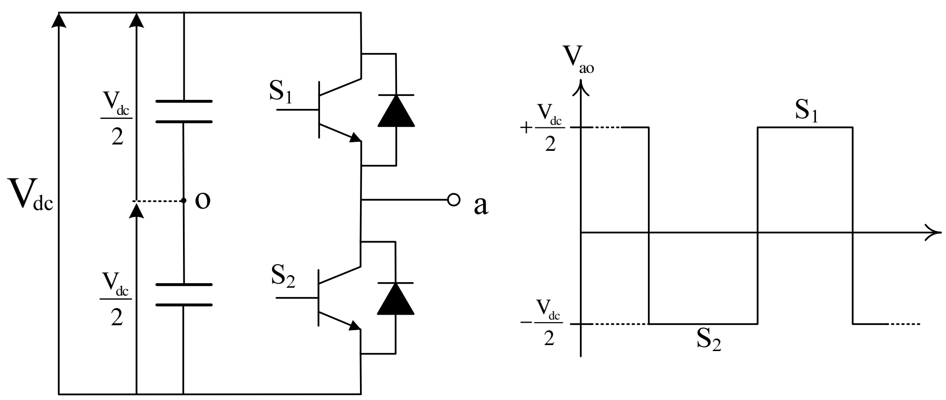

Figure 2.11: Single-phase two-level converter configuration

In this method, S_1 and S_2 switches work as pairs:

$$\text{If } V_{ref} > V_{tri} \quad S_1 = 1 \quad S_2 = 0$$
$$\text{If } V_{ref} < V_{tri} \quad S_1 = 0 \quad S_2 = 1$$

where '1' means the ON state and '0' symbolises the OFF state of the switches.

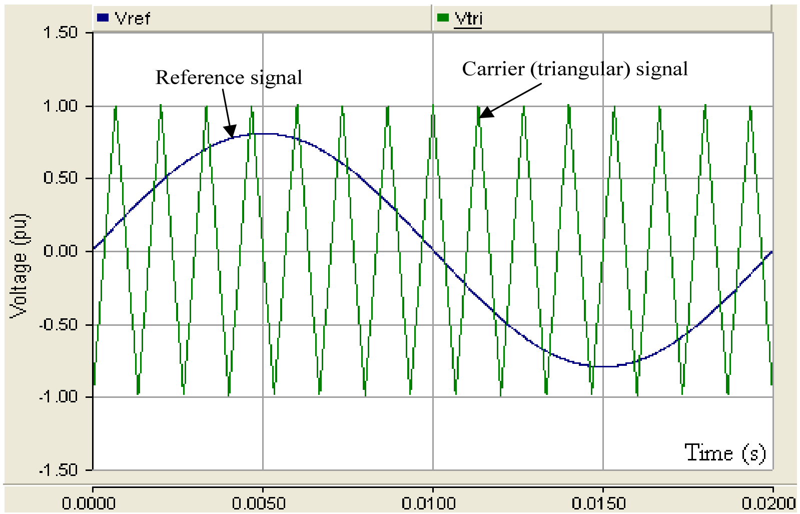

Figure 2.12: Carrier (triangular) waveform (V_{tri}) and reference signal (V_{ref})

Output PWM waveforms and the harmonic spectrum of a three-phase two-level six-switch voltage source converter are taken from [26] and illustrated as an example in Figure 2.13.

Another PWM scheme uses a space vector which represents the switching voltages in the $\alpha\beta$ frame. This is the so-called voltage space vector PWM (SVPWM) as mentioned in [10 and 33]. SVPWM is especially implemented in vector drive control applications [34]. Fitzer et al [33] claims that the SVPWM technique provides good harmonic performance at the range of 1 to 10 kHz inverter switching rate. Being a well-proven switching strategy and easy implementation make the use of SVPWM attractive [33 and 34].

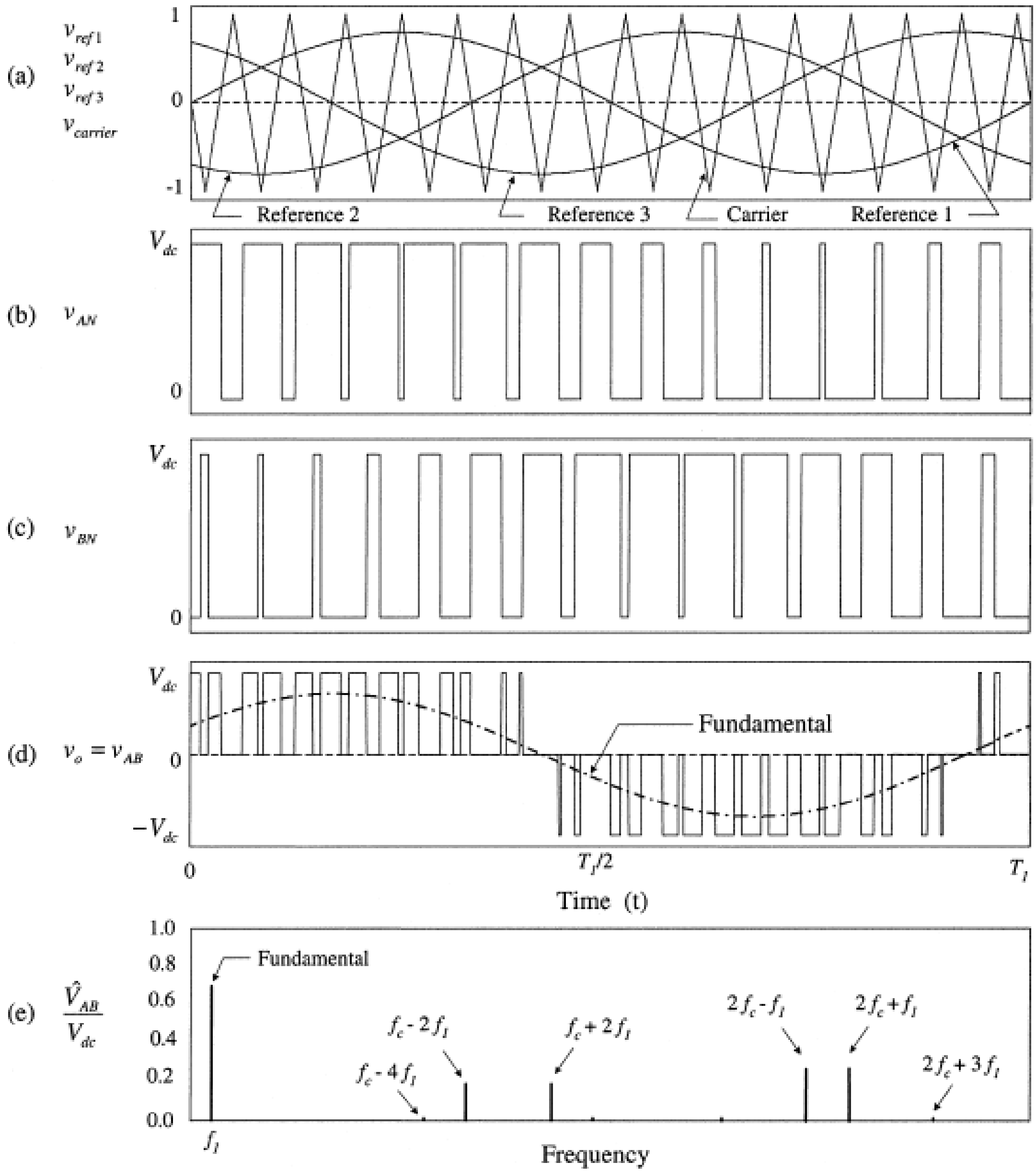

Figure 2.13: Two-level sinusoidal PWM method for a three-phase six-switch voltage source converter (VSC). (a) reference and carrier (triangular) signals (m_f=15 and m_a=0.8) (b) voltage waveform v_{AN} (line-to-neutral voltage A) (c) voltage waveform v_{BN} (line-to-neutral voltage B) (d) phase-to-phase output voltage waveform v_{AB} and (e) normalised harmonic amplitude of the voltage waveform v_{AB} [26].

In the SVPWM method, three-phase supply voltages are converted into one voltage space vector which has *αβ* components with an angular velocity of *ω*. This technique needs a single injection voltage space vector in the *αβ* frame to be transformed back to three injection vectors in the *abc* plane in the form of ready-made switch states [33]. The fundamental basis of SVPWM is to use the states of the core phase voltage of a two-level three-phase inverter to synthesise the injection voltage space vector [33].

Since one leg has two states ON or OFF, in a three phase inverter there are eight possible switching states. Amongst these 8 voltage vectors, V_{s_S0} and V_{s_S7} are two zero (null) voltage vectors, which inject 0V into each phase. V_{s_S1} to V_{s_S6} are the main active voltage space vectors, which inject a variety of active voltages into each phase. The space vector diagram as hexagon for a SVPWM is depicted in Figure 2.14. The magnitude of each active vectors is two-third times the DC-link voltage (V_{DC}). Each vector is adjacent vectors - two active voltage vectors and one (or two) null vectors. Well-defined formulae exist for the length of time each adjacent vector needs to be switched in to generate a vector of particular magnitude and angle.

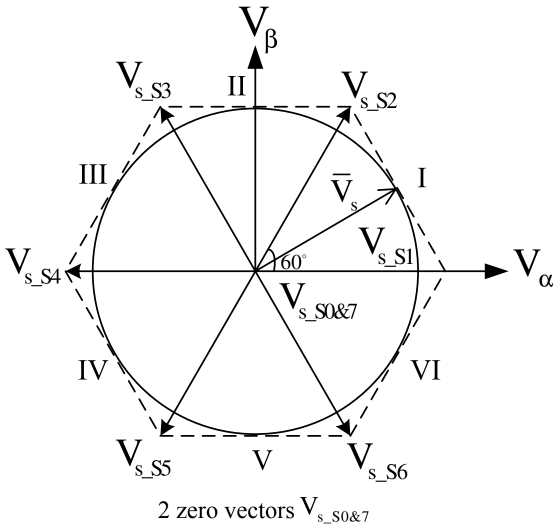

Figure 2.14: Switching vectors for two-level six-switch SVPWM

In the SVPWM method, the sequence of the switching space vectors is chosen in such a manner that only one leg is switched to move from one switching space vector to the next one [10]. The two-level three-phase inverter configuration switched by the SVPWM technique is presented in Figure 2.15 and its switching sequences are demonstrated in Table 2.2.

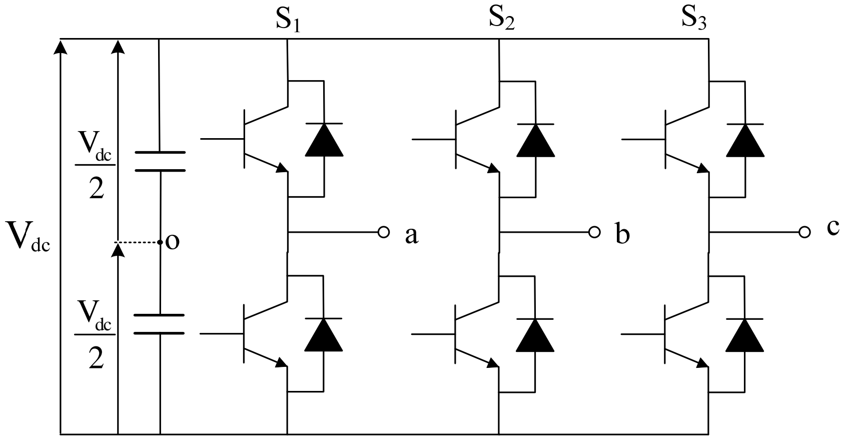

Figure 2.15: A two-level three-phase SVPWM inverter

S_1	S_2	S_3	v_{ao}	v_{bo}	v_{co}	Switching vector
0	0	0	$-V_{dc}/2$	$-V_{dc}/2$	$-V_{dc}/2$	V_{s_S0}
1	0	0	$+V_{dc}/2$	$-V_{dc}/2$	$-V_{dc}/2$	V_{s_S1}
1	1	0	$+V_{dc}/2$	$+V_{dc}/2$	$-V_{dc}/2$	V_{s_S2}
0	1	0	$-V_{dc}/2$	$+V_{dc}/2$	$-V_{dc}/2$	V_{s_S3}
0	1	1	$-V_{dc}/2$	$+V_{dc}/2$	$+V_{dc}/2$	V_{s_S4}
0	0	1	$-V_{dc}/2$	$+V_{dc}/2$	$+V_{dc}/2$	V_{s_S5}
1	0	1	$+V_{dc}/2$	$-V_{dc}/2$	$+V_{dc}/2$	V_{s_S6}
1	1	1	$+V_{dc}/2$	$+V_{dc}/2$	$+V_{dc}/2$	V_{s_S7}

Table 2.2: Switching status of a two-level three-phase SVPWM inverter

2.8.4 Protection Circuits

The system protection circuits, namely a rotor-crowbar circuit and a DC-link brake, are designed in conjunction with the selection of power electronics components so as to protect the power electronics devices placed in the wind turbine system. There are three typical rotor-crowbar circuit configurations:

1. Two anti-parallel thyristors with a series resistance per phase.
2. A rectifier (diode bridge) including a series rotor crowbar resistance and a series thyristor.
3. A diode bridge in series to a rotor crowbar resistance and an IGBT-switch.

These three arrangements are shown in Figure 2.16. Since first two crowbar circuits cannot respond quickly to higher current transients due to faults, the third configuration is widely used to protect power electronics components within the system.

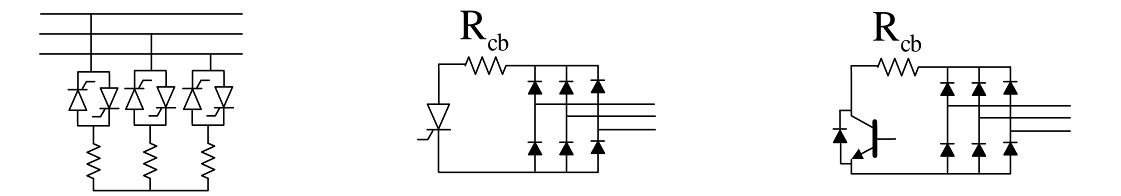

a) Three-phase triac crowbar b) Rectifier and thyristor crowbar c) Rectifier and IGBT crowbar

Figure 2.16: Crowbar configurations

A DC-link brake comprising of a brake resistor and an IGBT-switch is often connected parallel to the DC-link capacitor, also known as chopper circuit. The function of the DC-link brake is to protect the power electronics elements from the harmful effects of over-voltage induced across the capacitor. The DC-link brake design is depicted in Figure 2.17.

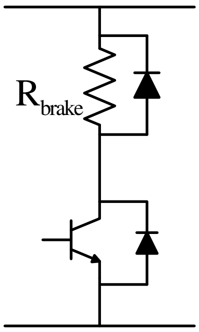

Figure 2.17: DC-link brake

2.9 Review of Prior Art on DFIG Modelling, Control and Protection

Previous sections have looked at fundamental concepts in modelling, control and protection of DFIG wind turbine systems. This introduction will now be supplemented with a review of the state of the art and latest developments. Since it is impossible to cover the entire body of references, significant ones are chosen.

The market survey in [1] shows that most wind turbines operating in on- and offshore wind farms to date have been dominantly equipped with DFIGs. However, permanent magnet synchronous generator (PMSG) wind turbines with gear or gearless (direct-driven) couplings have started to be popular even though they are presently the most expensive option amongst variable speed wind turbine concepts. Getting this technology well-proven however needs lots of time and more practical experiments. Nevertheless, it seems that DFIGs will continue being the market leader for at least the next several years.

The DFIG system modelling in steady-state and for transients is well documented in [13, 19, 35, 36, 37, 38 and 39]. These studies individually cover converter modelling or detailed mechanical system modelling of the wind turbine. Mechanical studies mainly consider the aerodynamic rotor, shaft system and blade-angle control modelling. A transient DFIG electrical model is used for research such as power-voltage stability analyses. However, the full electrical system modelling and the interaction of electrical subassemblies are not widely covered, which could be considered as a drawback from the electrical system aspect of wind turbine systems. Electrical models are usually substantially simplified and focused on one aspect (e.g. transient stability), neglecting most or all others (e.g. protection).

The selection of generator model is an important issue and must be compatible with the reason being used for. The order of the generator indicates the number of state variables in the generator model [5]. Rotor speed, the *d* and *q* components of the stator flux and rotor flux are the state variables of the fifth order model, while the stator flux in *dq* are neglected in the third-order model [5 and 35]. As an example of the simplifications made, a detailed comparison between fifth and third order DFIG wind turbine models is documented in [40 and 41]. In order to get more detailed assessments of the fault current contribution to the system, a fifth order model should be implemented [41]. Moreover, the fifth order model predicts the action of converter more correctly during a short-circuit fault occurring close to the wind turbine terminals [36]. However, the research study results carried out in [40] show that in large power systems, reduced model representation eases the stability analysis, and shortens the computational time [41]. A fifth order model may only be needed if the behaviour of the DFIG-based wind turbines to be investigated, deliberately includes detailed rotor and stator flux transient analyses, since the third order model excludes the details of the stator flux transients [41]. Further discussion on n^{th} order model studies for DFIG can be found in [1, 35, 42 and 43].

Representation of shaft system in terms of lumped mass models is widely evaluated in [10 and 13]. The most common representations of the drive train model are three-mass, two-mass, and single (one or lumped)-mass. If all rotating parts; wind turbine rotor, gearbox and the electrical generator rotor, are modelled as three inertias then this concept is called three-mass model [10, 44 and 45]. By omitting the gearbox, the drive train is represented as two-mass model [16]. Considering all rotating masses as one equivalent inertia gives the single- or lumped mass model [13 and 16]. More than three masses, i.e. large multi mass models are also of interest, such as a six-mass model, but such systems significantly increase complexity [10].

In case of grid disturbances, DFIG wind turbine systems have the risk of shaft system excitation, which causes fatal problems for wind turbine operation with poor damping of the shaft system [13]. Therefore, to avoid complete system design being affected by grid disturbances, a two-mass model shaft system representation is preferable for many studies of DFIG wind turbines in order to get rid of this insufficient damping of shaft torsional oscillations [13]. Thus, at least the use of a two-mass model is required. However, the two-mass model can be reduced to a single-mass or lumped mass model in variable-speed wind turbine applications, since the mechanical and electrical subsystems are decoupled by means of power electronic converters [46]. For a DFIG which has decoupled real and reactive power control, the shaft oscillation can be seen in speed fluctuations but without any effect on the voltage behaviour [13]. From this aspect, the lumped-mass model can be used as a shaft system representation for short-term voltage stability investigations [13]. An example of the lumped mass model is given in [47] to illustrate the possibility of the pitch control method, which is used to supply frequency regulation to the wind turbine. Apart from single and two-mass models; multi-mass, i.e. three-mass, shaft models for the DFIG wind turbine systems are also of interest, which is discussed in [10].

Since DFIGs have more complexity than standard induction machines, precise control is also complex. In order to control the DFIG system, its rotor-side and grid-side converters must be controlled accurately. To do this, the DFIG machine equations presented in [48, 49 and 50] can be used. The rotor currents, and hence the active and reactive power, can be controlled by the rotor-side converter. The general way of controlling the rotor currents is by means of field-oriented control. The stator flux oriented control of DFIG is preferred in [49, 50 and 51] although the stator voltage orientation is adopted in [16]. The disadvantages of stator flux orientation are that the flux-linkages and torque equations exhibit cross-saturation effects [52], and this reference frame shows weak performance in electromagnetic torque control compared with the other controllers [53]. Therefore, the use of airgap flux orientation (or airgap flux reference frame) is suggested by the authors in [52] and the research in [54] used airgap flux orientation. Moreover, rotor flux orientation is defined and discussed in general in [10]. Detailed information about the rotor flux reference frame is supplied in [55]. Direct power control, which is based on the stator flux and requires only the stator resistance as a machine parameter, is proposed in [56]. The authors in [56] claim that direct power control is more effective and more robust since the difficulties in rotor flux estimation are eliminated with the assumption of neglecting the effect of the stator resistance on whole system. It is proposed in [57] that the direct power can be an alternative to field oriented control because of inherently position sensorless operation, insensitivity of the control to the machine parameters, and good control performance.

Alternatively, direct torque control can be also used in [58], although these methods (direct power control and direct torque control) appear not to have attracted widespread attention and implementation in wind turbine control topologies [59].

A good example of rotor-side converter current (inner) loop control is given in [50]. However a robust control was not designed for the power (outer) loop which is comprehensively considered in this thesis. The grid-side converter configuration containing grid-side voltage equations and its controller are described in [60]. This neglects several parameters, and is therefore incomplete, and for the voltage control loop results in limited control for the grid-side converter of the DFIG. A key contribution of this thesis is a more complete DC-link voltage control.

Grid fault ride through techniques for wind turbines employing a DFIG are widely investigated to eliminate the harmful effects of higher voltages and currents to the system in [25, 61 to 77]. The comprehensive fault-ride-through technique comprising a rotor crowbar protection scheme and a DC-link brake is extensively analysed in [25]. Further work to integrate this control into the whole system is needed though. In [61], the performance analysis of a DFIG under network disturbances is carried out by using a passive crowbar consisting of a three-phase diode bridge and a thyristor in series with a resistor. [62, 64 and 72] investigate the ride through of DFIG based wind turbines during a voltage dip. [72] uses a protection scheme of two anti-parallel thyristors with a series by-pass resistors per phase, [64] implements that of inductor based fault emulator, and [25, 65, 66, 68 to 73, 75, 76 and 77] utilise that of a crowbar circuit. As seen from the references, the most dominant protection method against over current is the rotor crowbar design. The advanced crowbar protection configuration amongst variety of crowbar options is one which consists of a diode bridge (rectifier), a rotor crowbar resistance and series IGBT switch (see Figure 2.16.c). Besides the rotor crowbar circuit, extra protection to prevent the DC-link capacitor overcharging is placed between the rotor- and grid-side converters. This is shown in [25] as well by using a DC-link brake. The DC-link brake also helps the grid-side converter keep the DC-link voltage constant at a predefined value.

The protection scheme adapted from [25] is used in this thesis, but the control algorithm of the rotor crowbar protection is further enhanced with a detailed presentation of logic circuits and by considering wider system integration. Thus, improved control for rotor crowbar has been maintained. With the insertion of the rotor crowbar, the sensitive power electronics devices are protected from the high-currents occurring during grid faults. The same DC-link brake configuration found in [25] is also conducted in this thesis with different voltage threshold values.

2.10 Summary

The total installed wind power capacity of the world and the UK was presented. The wind power conversion equations were given. Main wind turbine concepts currently being used in wind farms with their control techniques (stall, active-stall, or pitch control) were briefly summarised. A wind turbine system mainly consists of two subsystems: mechanical and electrical systems, which were covered at a basic knowledge level including their subcomponents. Chapter 2 also focused on power electronics devices for wind turbines, improvements in material of power semiconductors and application areas of power electronics elements. Lastly, a significant literature review on DFIG modelling, control and protection was given.

Chapter 3 Dynamic Modelling and Control of Doubly-Fed Induction Generator

3.1 Introduction

In a wind turbine, for similarly rated machines, the energy capture can be notably improved by using a wound rotor induction machine (WRIM) [78] rather than a squirrel cage machine. The WRIM is also known as a doubly-fed induction generator (DFIG). It has been stated in [1] that the market is dominated by the DFIG based wind turbines as they provide a cheaper option among variable speed wind turbine concepts. The main purpose behind the choice of a variable speed option is not only increased energy capture, but also the possibility of lowering mechanical loads on the drive-train components, significant acoustic noise reduction at low wind speeds, and improved power quality (e.g. low electrical flicker) [2 and 3].

The control of a DFIG is more complicated than that of a standard induction machine. Integrating the various subsystem controllers is also challenging. Aspects of system control have been extensively discussed. As an example, a rotor-side converter control of a DFIG is investigated in [51] while a control design for the grid-side converter is proposed in [60]. A comprehensive fault ride-through method consisting of rotor crowbar protection and the DC-link brake control are well explained in [25]. However, the difficulty to date is that each component has largely been considered individually not as part of a larger or whole system.

3.2 DFIG Modelling

The principal components of a DFIG wind turbine are a back-to-back converter system, i.e. a rotor-side converter and a grid-side converter, a DC-link capacitor placed between these two converters, and the protection of the power electronic components, which are illustrated in Figure 3.1. The DFIG is connected to the grid via a transformer, while its rotor windings are connected to the rotor-side converter via slip rings.

Wind turbine manufacturers and wind farm developers have been employing doubly-fed induction generator based wind turbines, as DFIGs provide maximum power extraction and are suitable for variable speed operation (the speed range is ±33% around the synchronous speed [79]).

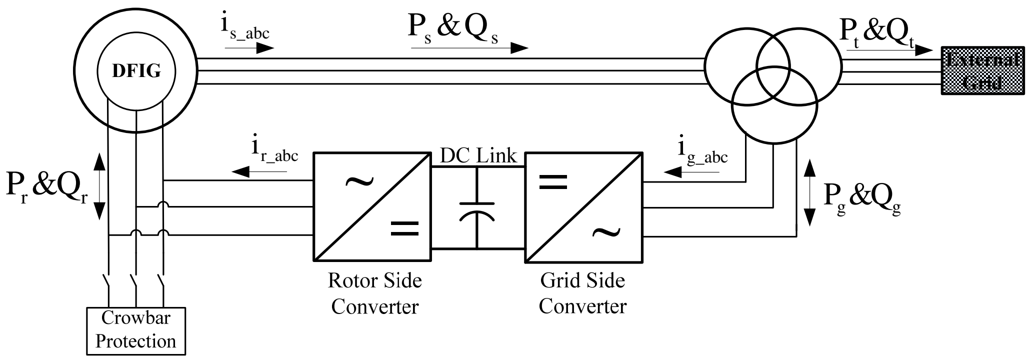

Figure 3.1: Typical DFIG system

The converter topology used in this research is a three-phase voltage source converter (VSC) consisting of insulated-gate bipolar transistors (IGBTs) controlled by a pulse-width modulation (PWM) switching technique.

3.3 DFIG Equivalent Circuit

A standard steady-state per-phase equivalent circuit of a doubly-fed induction generator with the inclusion of phase rotor voltage and magnetising losses (magnetising inductance and resistance) is depicted in Figure 3.2.

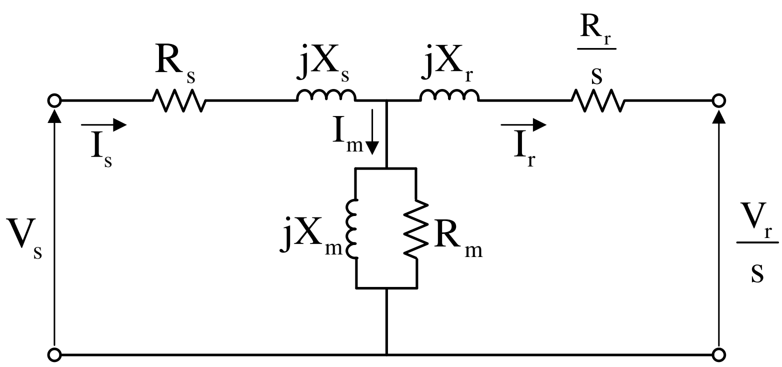

Figure 3.2: Standard per-phase DFIG equivalent circuit

where V_s and V_r are the stator and rotor voltages; I_s, I_r and I_m are the stator, rotor and magnetising currents; R_s, R_r and R_m are the stator, rotor and magnetising resistances; X_s, X_r and X_m are the stator leakage, rotor leakage and magnetising (or mutual) reactances respectively, and s denotes the slip.

Neglecting the magnetising resistance by assuming $X_m >> R_m$, the per-phase equivalent circuit of the DFIG can be simplified to that in Figure 3.3.

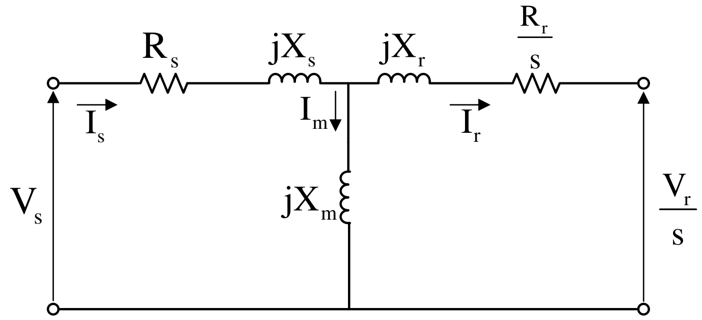

Figure 3.3: Simplified per-phase DFIG equivalent circuit

The simplified representation of the DFIG equivalent circuit is adequate in power system studies for slow dynamics (e.g. some electromechanical oscillation problems). However, this is insufficient for fast electromagnetic transients and here detailed dynamic equations are required.

3.4 Machine Equations [51]

The dynamic machine equations in the excitation reference frame (e-frame) are well known [51], for a wound rotor induction machine where its stator windings are connected to a stiff voltage supply via a transformer. The rotor windings of the machine are connected to a bi-directional power converter.

In [51], the electromagnetic torque of the doubly-fed induction machine (DFIM) in a general ('g') reference frame in space-vector representation is formulated as

$$\begin{aligned} T_e &= -\frac{3}{2}\rho_A \frac{L_m}{L_{ss}}\left(\overline{\Psi}_s^g \times \overline{i}_r^g\right) \\ &= -\frac{3}{2}\rho_A \frac{L_m}{L_{ss}}\left(\Psi_{s\_d}^g i_{r\_q}^g - \Psi_{s\_q}^g i_{r\_d}^g\right) \end{aligned} \tag{3.1}$$

Choosing the stator reference frame to be attached to the stator flux linkage Ψ_s, then T_e in the excitation ('e') frame can be re-written as in equation 3.2.

$$T_e = -\frac{3}{2}\rho_A \frac{L_m}{L_{ss}}\left(\Psi_s^e \times i_{r\_q}^e\right) \tag{3.2}$$

since

$$\Psi^{e}_{s\_q}=0 \quad \text{and} \quad \Psi^{e}_{s\_d}=\left|\overline{\Psi}^{g}_{s}\right|=\Psi^{e}_{s} \tag{3.3}$$

According to equation 3.2, the *q*-component of the rotor current in the e-frame can be used in order to control the torque of the DFIM, where the stator flux is constant. The dynamic machine equations shown in the excitation reference frame are [19 and 51]:

$$\overline{v}^{e}_{s}=R_{s}\overline{i}^{e}_{s}+\frac{d\overline{\Psi}^{e}_{s}}{dt}+j\omega_{e}\overline{\Psi}^{e}_{s} \tag{3.4}$$

$$\overline{v}^{e}_{r}=R_{r}\overline{i}^{e}_{r}+\frac{d\overline{\Psi}^{e}_{r}}{dt}+j(\omega_{e}-\omega_{m})\overline{\Psi}^{e}_{r} \tag{3.5}$$

$$\overline{\Psi}^{e}_{s}=L_{ss}\overline{i}^{e}_{s}+L_{m}\overline{i}^{e}_{r} \tag{3.6}$$

$$\overline{\Psi}^{e}_{r}=L_{rr}\overline{i}^{e}_{r}+L_{m}\overline{i}^{e}_{s} \tag{3.7}$$

The phasor diagram and determination of angles for the DFIM based on [51] are presented in Figure 3.4 and Figure 3.5.

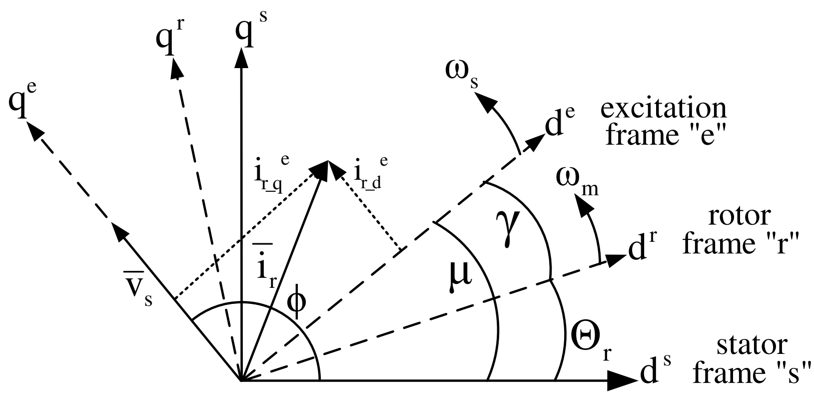

Figure 3.4: Definitions of angles and the reference frames for the DFIM

The transformation angles used to convert the voltage and current quantities from *abc* to *dq* can be derived with the aid of Figure 3.4. This is drawn as a block diagram in Figure 3.5.

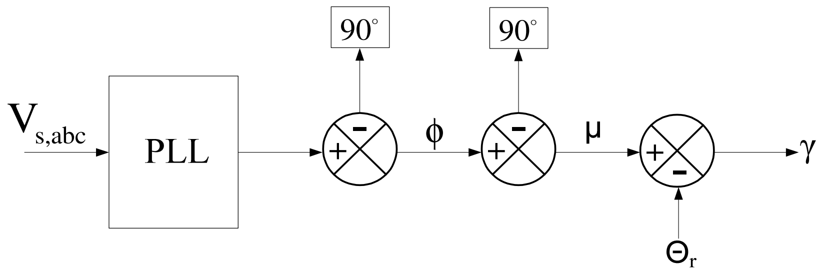

Figure 3.5: Derivation of transformation angles from *abc* to *dq*

Considering the assumption in equation 3.3, re-arranging equation 3.5 and splitting it into *dq* components, the equations of the rotor current components in *dq* reveal the relation between the *dq* components of the stator current and the rotor current components in *dq* coordinates as:

$$i^e_{s\_d} = \frac{1}{L_{ss}} \Psi^e_s - \frac{L_m}{L_{ss}} i^e_{r\_d} \tag{3.8}$$

$$i^e_{s\_q} = -\frac{L_m}{L_{ss}} i^e_{r\_q} \tag{3.9}$$

The stator flux equation in the stator reference frame ("s"):

$$\overline{\Psi}^s_s = L_{ss} \overline{i}^s_s + L_m \overline{i}^s_r \tag{3.10}$$

Splitting equation 3.10 into its *dq*-components, the individual stator flux components in the stator reference frame are then:

$$\Psi^s_{s\_d} = L_{ss} i^s_{s\_d} + L_m i^s_{r\_d} \qquad \overline{\Psi}^s_{s\_q} = L_{ss} i^s_{s\_q} + L_m i^s_{r\_q} \tag{3.11}$$

The stator flux angle, μ, can be determined using of equation 3.3 as

$$\mu = \arctan \frac{\Psi^s_{s\_q}}{\Psi^s_{s\_d}} \tag{3.12}$$

The other possible way to acquire μ can be followed by considering the stator voltage equation in the stator (stationary) reference frame:

$$\overline{v}^s_s = R_s \overline{i}^s_s + \frac{d\overline{\Psi}^s_s}{dt} \tag{3.13}$$

For larger machines, as the stator resistance in comparison to the stator reactance is quite small ($R_s << \omega_s L_{ss}$) [19]. By neglecting the stator resistance equation 3.13 can be simplified to equation 3.14.

$$\overline{v}^s_s \approx \frac{d\overline{\Psi}^s_s}{dt} \tag{3.14}$$

In steady-state conditions, as seen in equation 3.14 the stator reference frame attached to the stator flux has the same angular frequency as the stator voltage does

$$\omega_e = \omega_s = \text{const} \tag{3.15}$$

The magnitude of the stator flux in the excitation ("e") frame can be found out by substituting $\bar{\Psi}_s^s = \left|\bar{\Psi}_s^s\right| e^{j\mu}$ in equation 3.14 and solving the differentiation i.e.:

$$\Psi_s^e \approx \frac{\sqrt{2}V_s}{\omega_s} \tag{3.16}$$

where V_s is the stator phase voltage in rms. The *dq* components of the stator voltage space vector in the excitation frame would then be

$$v_{s\_d}^e = 0 \qquad v_{s\_q}^e = \omega_s \Psi_s^e = \sqrt{2}V_s = \text{constant} \tag{3.17}$$

The stator active and reactive power can be formulated by means of the stator voltage and current in the general reference frame are [51]:

$$P_s = \frac{3}{2}(v_{s\_d}^g i_{s\_d}^g + v_{s\_q}^g i_{s\_q}^g) \tag{3.18}$$

$$Q_s = \frac{3}{2}(v_{s\_q}^g i_{s\_d}^g - v_{s\_d}^g i_{s\_q}^g) \tag{3.19}$$

The stator currents in the *dq* frame in terms of the *dq*-components of the rotor current and the stator flux were given in equations 3.8 and 3.9. Applying the restrictions in equation 3.17 and substituting the stator current in *dq* in equations 3.8 and 3.9 in equations 3.18 and 3.19, the stator active and reactive power equations transform into:

$$P_s = -\frac{3}{2}\frac{\sqrt{2}V_s L_m}{L_{ss}} i_{r\_q}^e \tag{3.20}$$

$$Q_s = \frac{3}{2}\frac{\sqrt{2}V_s}{L_{ss}}\Psi_s^e - \frac{3}{2}\frac{\sqrt{2}V_s L_m}{L_{ss}} i_{r\_d}^e \tag{3.21}$$

In equation 3.20, the negative stator active power means that the active power flow direction is into the grid from the machine. If equation 3.21 gives us positive stator reactive power, then this tells that there is a lagging stator power factor existing which we can compensate with d-axis rotor current. Thus, the inductive power flows from the grid to the machine as excitation power. A negative stator reactive indicates a leading stator power factor.

Equations 3.20 and 3.21 tell us that there is a (linear) relationship between the *q*-component of the rotor current and the stator active power, whereas the stator reactive power is a function of the *d*-component of the rotor current (both in the excitation reference frame), if the stator voltage and the stator flux remain fixed. Thus, the stator active power can be controlled by the *q*-component of the rotor current and the stator reactive power can be controlled by the *d*-component of the rotor current. The full equation of the rotor voltage in the e-frame is:

$$\overline{v}_r^e = R_r \overline{i}_r^e + (L_{rr} - \frac{L_m^2}{L_{ss}}) \frac{d\overline{i}_r^e}{dt} + \frac{L_m}{L_{ss}} \frac{d\overline{\Psi}_s^e}{dt} + j\omega_{slip} (L_{rr} - \frac{L_m^2}{L_{ss}}) \overline{i}_r^e + j\omega_{slip} \frac{L_m}{L_{ss}} \overline{\Psi}_s^e \tag{3.22}$$

3.5 Clarke and Park Transformations [80]

The *dq0* transformation is a conversion of coordinates from the three-phase (*abc*) stationary coordinate system to *dq0* rotating coordinate system, which is realised in two steps:

i) a transformation from the three-phase stationary coordinate system to the two-phase, the so-called *αβ0* stationary frame, and
ii) a transformation from the *αβ0* stationary coordinate system to the *dq0* rotating coordinate system.

This is a method to represent the network AC quantities as nominal DC quantities which are easier to control with classical control theory [80]. Clearly this requires the removal of some position data by means of the transform.

The transformation used to convert the three-phase (*abc*) stationary coordinates to *αβ0* coordinates is known as the Clarke transform:

$$\begin{pmatrix} v_\alpha \\ v_\beta \\ v_0 \end{pmatrix} = k \begin{pmatrix} 1 & -1/2 & -1/2 \\ 0 & \sqrt{3}/2 & -\sqrt{3}/2 \\ 1/2 & 1/2 & 1/2 \end{pmatrix} \begin{pmatrix} v_a \\ v_b \\ v_c \end{pmatrix} \tag{3.23}$$

The inverse Clarke transform is given by

$$\begin{pmatrix} v_a \\ v_b \\ v_c \end{pmatrix} = k \begin{pmatrix} 1 & 0 & 1/2 \\ -1/2 & \sqrt{3}/2 & 1/2 \\ -1/2 & -\sqrt{3}/2 & 1/2 \end{pmatrix} \begin{pmatrix} v_\alpha \\ v_\beta \\ v_0 \end{pmatrix} \tag{3.24}$$

The constant k is a scaling factor. So that a balanced three-phase set, where each phase with a 1pu magnitude, gives 1pu magnitude phasor in *αβ0* space, k=2/3. This is known as the 'magnitude invariant' version of the Clarke transform. If k is for the transform known as 'power invariant', then the value of k is equal to $\sqrt{2/3}$.This gives a simpler power equation. In this research, a magnitude invariant transformation is used.

The transform *αβ0* to *dq0* is known as the Park transform and is given by

$$\begin{pmatrix} v_d \\ v_q \\ v_0 \end{pmatrix} = \begin{pmatrix} \cos\theta & \sin\theta & 0 \\ -\sin\theta & \cos\theta & 0 \\ 0 & 0 & 1 \end{pmatrix} \begin{pmatrix} v_\alpha \\ v_\beta \\ v_0 \end{pmatrix} \tag{3.25}$$

The inverse Park transform is

$$\begin{pmatrix} v_\alpha \\ v_\beta \\ v_0 \end{pmatrix} = \begin{pmatrix} \cos\theta & -\sin\theta & 0 \\ \sin\theta & \cos\theta & 0 \\ 0 & 0 & 1 \end{pmatrix} \begin{pmatrix} v_d \\ v_q \\ v_0 \end{pmatrix} \tag{3.26}$$

3.6 Rotor-side Converter (RSC)

The main function of the rotor-side converter is to control the real and reactive power of the DFIG by controlling the rotor currents. It also provides the required magnetisation power to the generator through the rotor circuit.

3.7 DC-Link

The DC-link capacitor is placed between the rotor-side converter and the grid-side converter in order to maintain the DC-link voltage. The independence of the control loops of the converters can be significantly enhanced by appropriate DC-link circuit design and sizing.

3.8 Grid-side Converter (GSC)

The significant role of the grid-side converter is to keep the DC-link voltage constant at desired value. Additionally, the grid-side converter transfers the rotor power to or from the grid.

3.9 Generic Rotor-side Converter Control

The rotor-side converter plays an essential role in controlling the real and reactive power of the DFIG system. Better control of the rotor-side converter gives better quality in the power delivered to the network.

The rotor-side converter control is constituted by two cascaded-controls, namely the current (inner) loop control and the power (outer) loop control. Both of these controllers should be designed and tuned accurately in order to maintain a good control of the rotor-side converter, which directly influences the quality of the power.

In this thesis, a conventional current (inner) loop control including PI controller is used to control the rotor currents. A new enhanced power (outer) loop control is proposed and presented in Chapter 6.

3.9.1 Inner (Current) Loop Control

A generic current (inner) loop control is designed by splitting the rotor voltage equation given in equation 3.22 into *dq* components namely

$$v^e_{r\_d} = R_r i^e_{r\_d} + L_c p i^e_{r\_d} - \omega_{slip} L_c i^e_{r\_q} + k_L p \Psi^e_{s\_d} \tag{3.27}$$

$$v^e_{r\_q} = R_r i^e_{r\_q} + L_c p i^e_{r\_q} + \omega_{slip} L_c i^e_{r\_d} + \omega_{slip} k_L \Psi^e_{s\_d} \tag{3.28}$$

where $L_c = L_{rr} - \dfrac{L_m^2}{L_{ss}}$, $k_L = \dfrac{L_m}{L_{ss}}$, and $p = \dfrac{\partial}{\partial t}$

Equations 3.27 and 3.28 are utilised in order to create the current control of the rotor-side converter. The block diagram of the decoupled inner loop control of the RSC is depicted in Figure 3.6. As seen in Figure 3.6, the cross coupling terms of $\omega_{slip} L_c i_{r\_q}$ in the *d*-loop, and those of $\omega_{slip} L_c i^e_{r\_d}$ and $\omega_{slip} \dfrac{L_m}{L_{ss}} \Psi_{s\_d}$ in the *q*-loop are nulled. Since the differential term of the *d*-loop, $\dfrac{L_m}{L_{ss}} \dfrac{\partial \Psi_{s\_d}}{\partial t}$, equates to zero in steady-state, it is neglected and not shown in the control block diagram. By nulling the coupling terms, the effects of *d*-components on the *q*-loop current (inner) control and that of *q*-components on the *d*-loop current control would then be eliminated. Thus, fast control of the RSC inner (current) loop can be achieved. However, the reliance on the exact parameter knowledge of nulled quantities is unavoidable. The effectiveness of this nulling method is also subject to the accurate measurement of parameters, errors and noise. In case of small disturbances, the errors of not nulling could be ignored as there should be a little influence of the disturbance on the control response. The corollary of this is that there need not be a 100% accurate nulling control though. In any case complete nulling is only theoretically possible but not practically achievable. The terms $\omega_{slip}L_c i_{r\_q}$ and $\omega_{slip}L_c i_{r\_d}$ existing in the physical plant are nulled by subtracting the control signal of the $\omega_{slip}^m \hat{L}_c i_{r\_q}^m$ from, and by adding the control signal of the $\omega_{slip}^m \hat{L}_c i_{r\_d}^m$ to, respectively, the output of the PI controller. An additional nulling process for the *q*-loop of the current control is done by adding the control signal of the $\omega_{slip}^m \frac{\hat{L}_m}{\hat{L}_{ss}} \hat{\Psi}_s$ to the PI controller output.

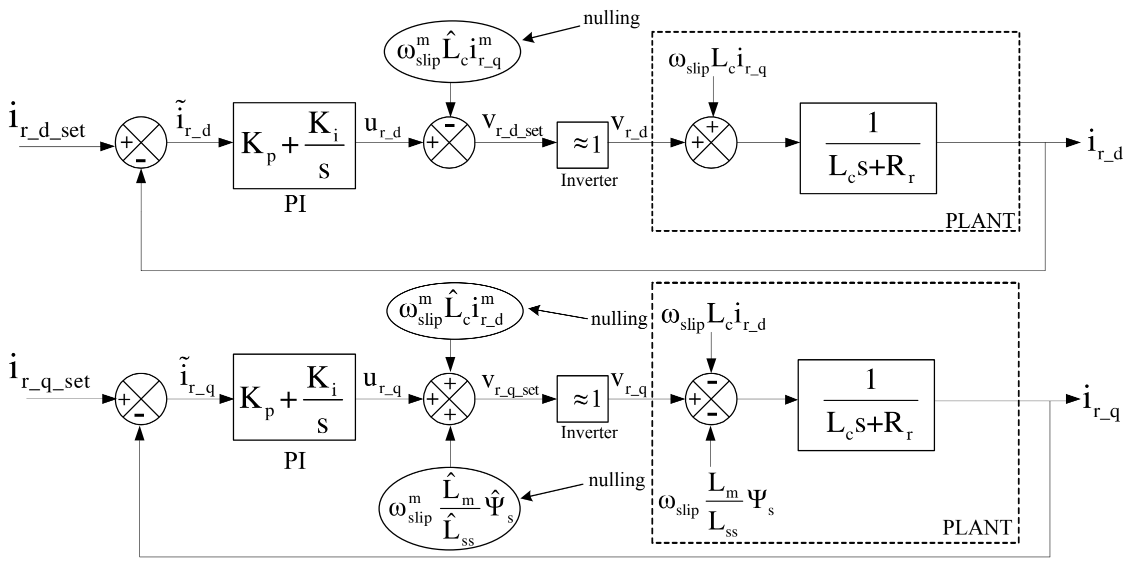

Figure 3.6: Decoupled current (inner) loop control of rotor-side converter

The transfer function (TF) of the current loop of the RSC can be extracted as

$$TF=\frac{i_{r\_d}}{i_{r\_d}^*}=\frac{i_{r\_q}}{i_{r\_q}^*}=\frac{\left(K_p+\frac{K_i}{s}\right)\left(\frac{1}{sL_c+R_r}\right)}{1+\left(K_p+\frac{K_i}{s}\right)\left(\frac{1}{sL_c+R_r}\right)}=\frac{s\left(\frac{K_p}{L_c}\right)+\frac{K_i}{L_c}}{s^2+\left(\frac{K_p+R_r}{L_c}\right)s+\frac{K_i}{L_c}} \tag{3.29}$$

By ignoring the *s* term in the numerator of the full transfer function, TF would become second-order approximated transfer function (SoATF):

$$\text{SoATF}=\frac{\dfrac{K_i}{L_c}}{s^2+\left(\dfrac{K_p+R_r}{L_c}\right)s+\dfrac{K_i}{L_c}}\approx\frac{\omega_n^2}{s^2+2\zeta\omega_n s+\omega_n^2} \tag{3.30}$$

So, the approximate damping ratio and undamped natural frequency can be written down as follows

$$\omega_n^2=\frac{K_i}{L_c}\ \Rightarrow\ \omega_n=\sqrt{\frac{K_i}{L_c}} \tag{3.31}$$

$$2\zeta\omega_n=\left(\frac{K_p+R_r}{L_c}\right)\ \Rightarrow\ \zeta=\frac{K_p+R_r}{2\sqrt{K_i L_c}} \tag{3.32}$$

In order to confirm the relation between the stator active power and the *q*-component of the rotor current, and the relation between the stator reactive power and the *d*-component of the rotor current where the stator voltage and the stator flux stay constant, the DFIG system circuit was constructed and simulated in PSCAD. The simulation results of this, Figure 3.7, are consistent with the theoretical stator active and reactive power equations (see equations 3.20 and 3.21). The inner loop undamped natural frequency (f_n) and damping ratio (ζ) were set to 10Hz and 1, respectively with a simulation smoothing time constant of 25ms.

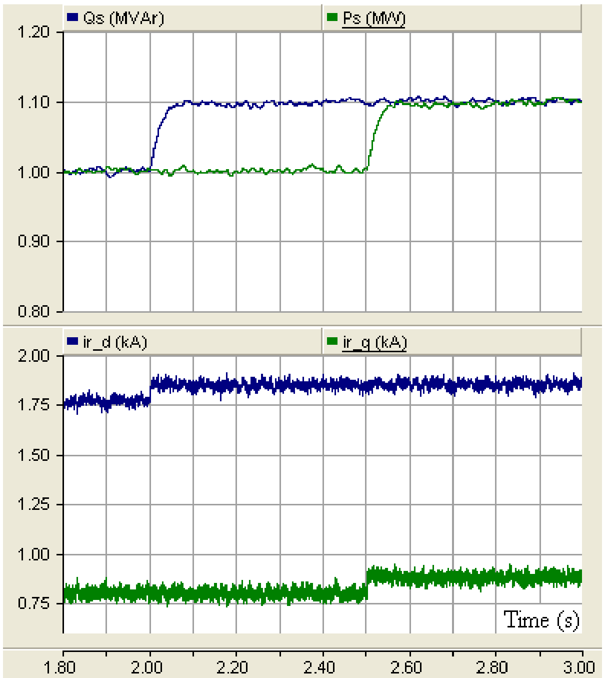

Figure 3.7: The relation between the *dq* rotor currents and the stator active and reactive power

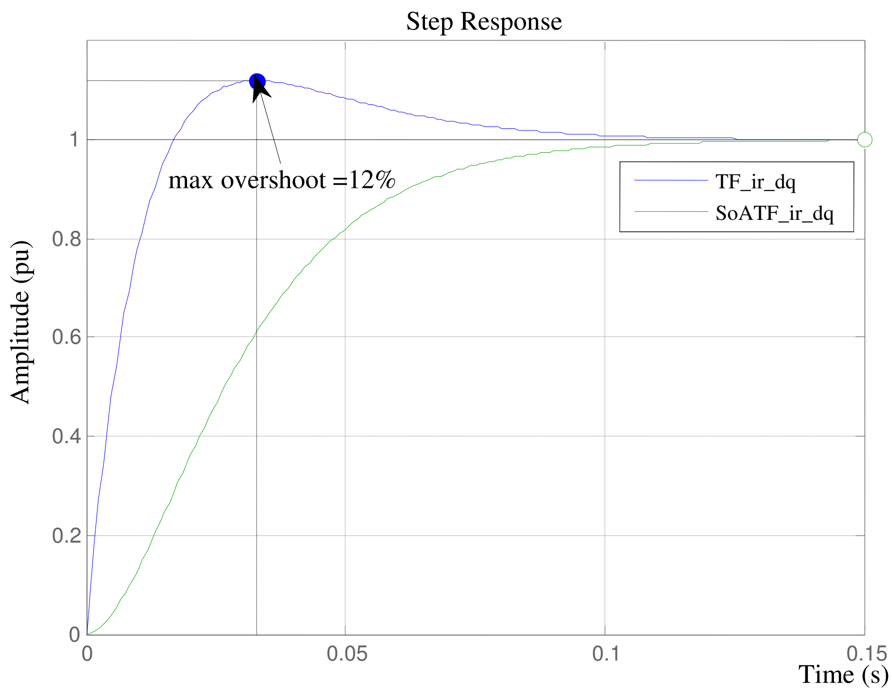

Figure 3.8: The step response of the TF and SoATF of the rotor currents in *dq*

The transfer function (TF) and the second-order approximated transfer function (SoATF) of the inner (current) loop control of the rotor-side converter were given in equations 3.29 and 3.30. In order to compare the simulation results illustrated in Figure 3.7 against the mathematical calculations, the step responses of the TF and SoATF were traced in MATLAB and shown in Figure 3.8. Since the inner loop control is tuned according to SoATF, the damping ratio of the SoATF seen in Figure 3.8 curve is 1 which is exactly compatible with the damping ratio of the tuning parameters. However, the TF has a maximum overshoot of 12% due to the effect of *s* term in the numerator, which means the effective damping ratio is smaller than 1. It can be said that both curves reach the steady-state[2] in almost 0.1s. Then, the bandwidth is calculated as 1/0.1s, which is equal to 10Hz. The value of the bandwidth also matches the tuning parameter of the undamped natural frequency. The DFIG system circuit built in PSCAD is much more complex, and the simulation traces include additional higher frequency oscillations. Therefore, the damping ratio and the undamped natural frequency of the *dq*-rotor current curves in Figure 3.7 should be read as a tuning rule of thumb. However, as seen from Figure 3.7 a damping ratio (ζ) and undamped natural frequency (f_n) of 1 and 10Hz, respectively, are very good starting points. The current response cannot be seen clearly due to switching noise, although you can see a small overshoot and settling after 0.1s particularly in i_{r_q}.

[2] or first downward crossing of the steady state for lower damping ratios

3.9.2 Investigation of Effects of Rotor Voltage Components [59 and 81]

The effects of each term in the rotor voltage equations are widely investigated in [59 and 81]. As a result of these studies, we know that the $v^e_{r\_d}$ component is dominated by the $-\omega_{slip}L_c i^e_{r\_q}$ term in the steady-state, since the voltage drop across the R_r is small and the $\Psi^e_{s\_q}$ is zero (see equation 3.3) due to reference frame orientation. The $v^e_{r\_q}$ component is dominated by the $\omega_{slip}\frac{L_m}{L_{ss}}\Psi^e_{s\_d}$ term as the low L_c (the total leakage inductance) diminishes the effect of the cross coupling terms including the $i^e_{r\_d}$ component. Again note that the $\Psi^e_{s\_q}$ is zero. At fixed mechanical speed (rpm), the cross coupling due to $i^e_{r\_d}$ causes changes in $v^e_{r\_q}$. Generally, the magnitude of the rotor voltage is more dependent on the $v^e_{r\_q}$ component, which is also verified in [82].

The steady-state variation in the rotor current components with regards to the speed-stator reactive power is also investigated in [59 and 81]. The $i^e_{r\_d}$ is higher for the fixed stator power factor at higher speeds due to the increase in the stator reactive power with load torque required to keep the power factor constant. The $i^e_{r\_q}$ component stays almost constant with speed in case of constant torque.

The $-\omega_{slip}L_c i^e_{r\_q}$ term contributes to the $v^e_{r\_d}$ component, while the $\omega_{slip}L_c i^e_{r\_d}$ term constitutes the $v^e_{r\_q}$ component. The $\omega_{slip}L_c i^e_{r\_d}$ component changes with both speed and stator reactive power, e.g. it increases with speed as the load torque increases. At non-synchronous speeds, the $v^e_{r\_d}$ component is mostly dominated by $-\omega_{slip}L_c i^e_{r\_q}$ whose polarity and magnitude are defined by the slip frequency and the torque, respectively.

The $\omega_{slip}\frac{L_m}{L_{ss}}\Psi^e_{s\_d}$ component, whose shape is obviously affected by the ω_{slip}, dominates the quadrature component of the rotor voltage. The term of $-\omega_{slip}\frac{L_m}{L_{ss}}\Psi^e_{s\_q}$ is not shown in the rotor voltage equations due to the alignment of reference frame ($\Psi^e_{s\_q}=0$), however it is noted in [81] that this term contributes to the direct component of the rotor voltage.

3.9.3. Tuning of RSC Inner (Current) PI Loop Controller

A standard PI controller is used to control the current loop of the RSC. The decoupling terms are added to the *q*-loop PI controller outputs and subtracted from the *d*-loop PI controller to eliminate the cross coupling influences and hence the interaction between the *d* and *q* loops. In order to tune the PI controller, the second-order approximated transfer function, SoATF, in equation 3.30 is again utilised. The parameters of the PI controller are calculated by substituting the reference values of undamped natural frequency and damping ratio in equations 3.31 and 3.32, respectively. The reference values are selected as f_n=10Hz and ζ=1.

3.10 Generic Grid-side Converter Control

A grid-side converter is used in variable speed wind turbines primarily to keep the DC-link voltage constant at a pre-set value. This is maintained by the DC-link capacitance. Another function of the grid-side converter is also to convey the rotor power to or from the network. A typical grid-side converter arrangement is illustrated in Figure 3.9.

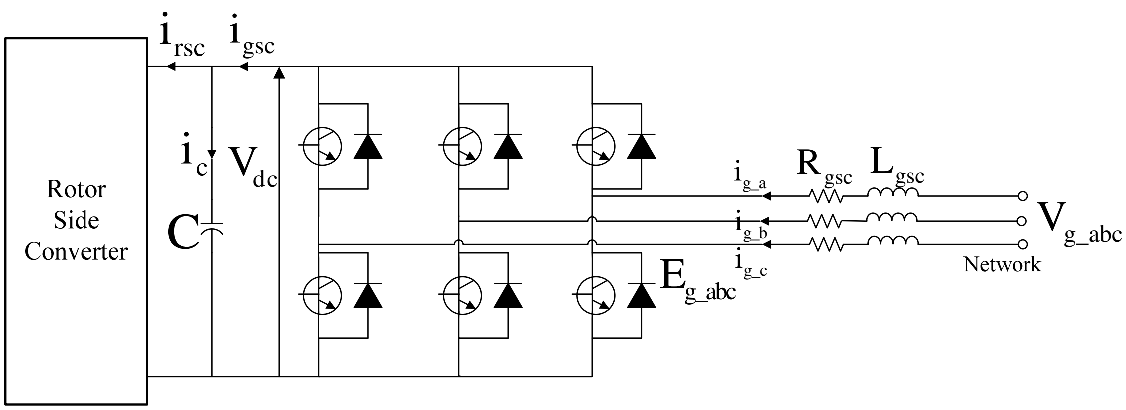

Figure 3.9: Grid-side converter configuration

A traditional control technique for the GSC is adopted which is similar to the current loop control of the RSC. However, a novel, detailed and enhanced DC-link voltage (outer loop) control of the GSC is designed and will be presented in Chapter 4.

The grid-side voltage equations in *dq* can be derived with the aid of the grid-side converter configuration shown in Figure 3.9. The voltage balance across the inductor, L_{gsc}, is depicted in equation 3.33.

$$\begin{aligned} v_{g\_a} &= R_{gsc} i_{g\_a} + L_{gsc} \frac{di_{g\_a}}{dt} + e_{g\_a} \\ v_{g\_b} &= R_{gsc} i_{g\_b} + L_{gsc} \frac{di_{g\_b}}{dt} + e_{g\_b} \\ v_{g\_c} &= R_{gsc} i_{g\_c} + L_{gsc} \frac{di_{g\_c}}{dt} + e_{g\_c} \end{aligned} \tag{3.33}$$

Equation 3.33 can be written in matrix form as

$$\begin{pmatrix} v_{g\_a} \\ v_{g\_b} \\ v_{g\_c} \end{pmatrix} = R_{gsc} \begin{pmatrix} i_{g\_a} \\ i_{g\_b} \\ i_{g\_c} \end{pmatrix} + L_{gsc} \frac{d}{dt} \begin{pmatrix} i_{g\_a} \\ i_{g\_b} \\ i_{g\_c} \end{pmatrix} + \begin{pmatrix} e_{g\_a} \\ e_{g\_b} \\ e_{g\_c} \end{pmatrix} \tag{3.34}$$

where L_{gsc} and R_{gsc} are the coupling inductance and resistance to the grid, respectively. Using the *abc* to *αβ*, and then *αβ* to *dq* transformations, equation 3.34 is re-configured as

$$\begin{pmatrix} v_{\alpha} \\ v_{\beta} \\ v_{0} \end{pmatrix} = \left(R_{gsc} + pL_{gsc} \right) \begin{pmatrix} i_{\alpha} \\ i_{\beta} \\ i_{0} \end{pmatrix} + \begin{pmatrix} e_{\alpha} \\ e_{\beta} \\ e_{0} \end{pmatrix} \tag{3.35}$$

Resolving partial differentials, equation 3.35 transforms into a *dq* reference frame rotating at ω_e (in the case considered in this thesis: ω_e is chosen as the supply angular frequency, ω_s):

$$v_{g\_d} = R_{gsc} i_{g\_d} + L_{gsc} p i_{g\_d} - \omega_e L_{gsc} i_{g\_q} + e_{g\_d} \tag{3.36}$$

$$v_{g\_q} = R_{gsc} i_{g\_q} + L_{gsc} p i_{g\_q} + \omega_e L_{gsc} i_{g\_d} + e_{g\_q} \tag{3.37}$$

3.10.1 Inner (Current) Loop Control

The inner (current) loop control block diagram of the GSC is drawn by the use of equations 3.36 and 3.37 in the *dq* frame. The terms of $\omega_s L_{gsc} i_{g\_q}$ and $\omega_s L_{gsc} i_{g\_d}$ in the physical plant are nulled by adding the control signals of $\omega_s^m \hat{L}_{gsc} i_{g\_q}^m$ and $\omega_s^m \hat{L}_{gsc} i_{g\_d}^m$, respectively, to the output of the PI controller, since the polarity of the PI output is negative. Additionally, in the same manner v_{g_d} and v_{g_q} components are also nulled to eliminate their effects on the inner loop control (see Figure 3.10).

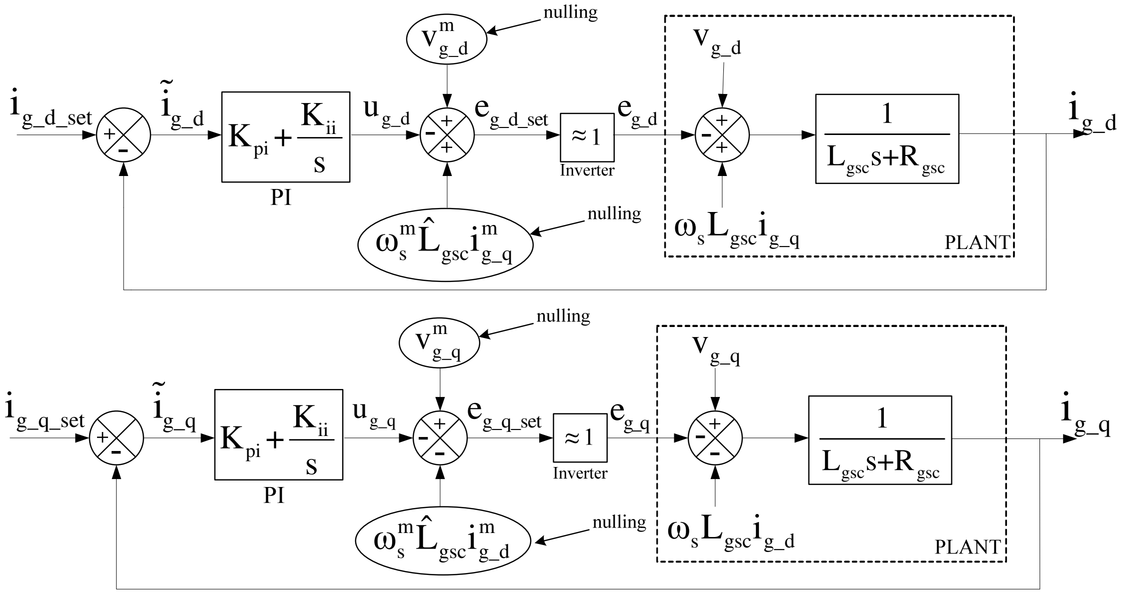

Figure 3.10: Decoupled inner (current) loop control of the grid-side converter

The transfer function (TF) of the inner (current) loop control of the GSC is

$$\mathrm{TF}=\frac{i_{g\_d}}{i_{g\_d\_set}}=\frac{i_{g\_q}}{i_{g\_q\_set}}=\frac{\left(K_{pi}+\frac{K_{ii}}{s}\right)\left(\frac{1}{sL_{gsc}+R_{gsc}}\right)}{1+\left(K_{pi}+\frac{K_{ii}}{s}\right)\left(\frac{1}{sL_{gsc}+R_{gsc}}\right)}=\frac{s\left(\frac{K_{pi}}{L_{gsc}}\right)+\frac{K_{ii}}{L_{gsc}}}{s^2+\left(\frac{K_{pi}+R_{gsc}}{L_{gsc}}\right)s+\frac{K_{ii}}{L_{gsc}}} \tag{3.38}$$

Assuming $K_{ii}>>K_{pi}$ the second order approximated transfer function is

$$\mathrm{SoATF}=\frac{i_{g\_d}}{i_{g\_d\_set}}=\frac{i_{g\_q}}{i_{g\_q\_set}}=\frac{K_{ii}/L_{gsc}}{s^2+\left(\left(K_{pi}+R_{gsc}\right)/L_{gsc}\right)s+K_{ii}/L_{gsc}} \tag{3.39}$$

Equating SoATF to $\frac{\omega_n^2}{s^2+2\zeta\omega_n s+\omega_n^2}$ the tuning parameters can be extracted as

$$\omega_n^2=\frac{K_{ii}}{L_{gsc}} \Rightarrow \omega_n=\sqrt{\frac{K_{ii}}{L_{gsc}}} \tag{3.40}$$

$$2\zeta\omega_n=\left(\frac{K_{pi}+R_{gsc}}{L_{gsc}}\right) \Rightarrow \zeta=\frac{K_{pi}+R_{gsc}}{2\sqrt{K_{ii}L_{gsc}}} \tag{3.41}$$

3.10.2 Tuning of GSC Inner (Current) PI Loop Controller

As in section 3.8.2, a PI controller is added to the current loop of the GSC. To tune the PI controller, second-order approximated transfer function, SoATF, of the inner loop is used. In order to calculate the tuning parameters of the PI controller, the undamped natural frequency, f_n, and the damping ratio, ζ, are determined as 450Hz and 1, respectively. The K_{pi} and K_{ii} are calculated as 0.6906 and 977s, respectively.

3.11 Drive Train Modelling

The drive train in a wind turbine system is mainly comprised of two rotating masses (wind turbine rotor and generator rotor), a low-speed shaft (on the turbine rotor side), a gearbox, a high-speed shaft (on the generator rotor side), a mechanical brake and couplings. Six different drive train configurations documented in [17] are illustrated in Figure 3.11.

Typically, there are four different types of drive train modelling used for power system analysis in wind conversion applications: the six-mass drive train model, three-mass drive train model, two-mass drive train model and single-mass (one-mass or lumped mass) drive train model. These drive train models taken from [83] are shown in Figure 3.12.

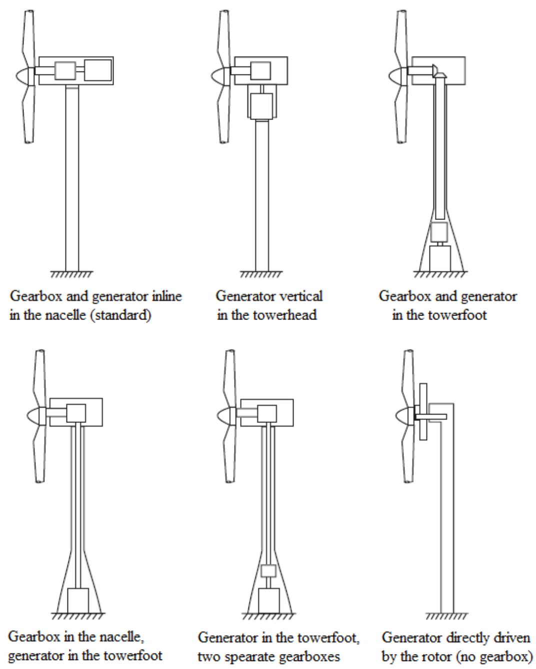

Figure 3.11: Drive train configurations [17]

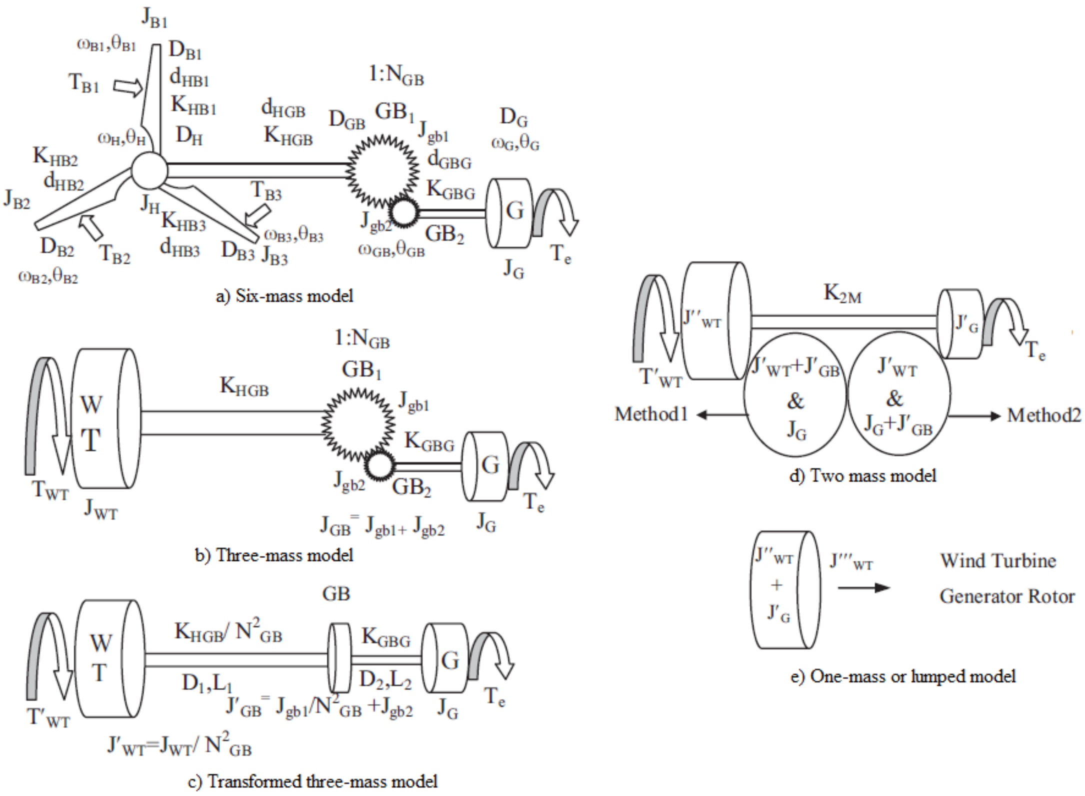

Figure 3.12: Drive train models for wind turbine systems [83]

A six-mass model representation of the drive train in a wind turbine is presented in Figure 3.12a. This system includes six inertias: three blade inertias (J_{B1}, J_{B2}, and J_{B3}), hub inertia (J_H), generator inertia (J_G), and gearbox inertia (J_{GB}). θ_{B1}, θ_{B2}, θ_{B3}, θ_{GB}, θ_G, and θ_H denote the angular positions of the blades, gearbox, generator and hub, respectively. ω_{B1}, ω_{B2}, ω_{B3}, ω_{GB}, ω_G, and ω_H symbolise the angular frequencies of the three blades, gearbox, generator and hub, respectively. K_{HB1}, K_{HB2}, K_{HB3}, K_{HGB}, and K_{GBG} are the spring constants, which define the elasticity between the adjacent masses. The mutual damping parameters between the adjacent masses are determined by d_{HB1}, d_{HB2}, d_{HB3}, d_{HGB}, and d_{GBG}. The external damping components of individual masses, D_{B1}, D_{B2}, D_{B3}, D_H, $D_{GB,}$ and D_G, causes some torque losses [83]. T_e, T_{B1}, T_{B2}, and T_{B3} represent the generator torque and aerodynamic torques of the blades, respectively. Furthermore, the blade torques can be represented as a wind turbine torque, T_{WT}, (T_{WT}=T_{B1}+T_{B2}+T_{B3}). In [83], the aerodynamic torques acting on the gearbox and hub are assumed zero.

If three blade inertias and the hub inertia are integrated with each other to form one inertia (the turbine inertia), the six-mass drive train model turns into three-mass representation. Thus, the mutual damping parameters between the blades and the hub are neglected. This configuration is shown in Figure 3.12b. In case of representing the gears of the gearbox as a lumped equivalent inertia (J'_{GB}), a transformed three-mass drive train model would be designed. This system is also known as simplified three-mass model. A three-mass representation of the wind turbine drive train is presented in a slightly different way in [10], Figure 3.13.

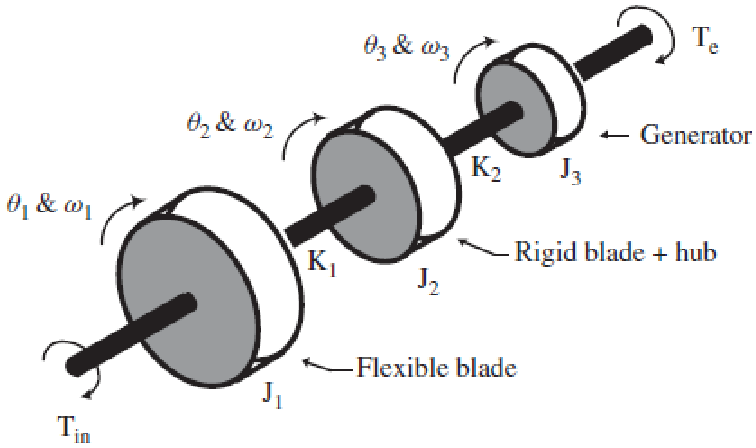

Figure 3.13: Three-mass drive train model including blade and shaft flexibilities [10]

The dynamic equations of the three-mass model in Figure 3.13 using the representation of the rotor structural dynamics shown in Figure 3.14 are given in [10] as:

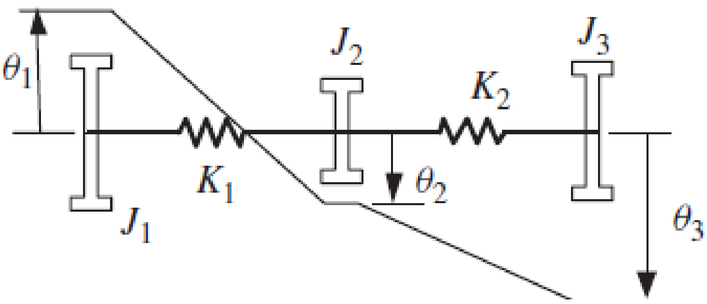

Figure 3.14: Representation of the three-mass model in terms of rotor structural dynamics [10]

$$J_1 \frac{d^2}{dt^2}\theta_1 = -K_1(\theta_1 - \theta_2) \tag{3.42}$$

$$J_2 \frac{d^2}{dt^2}\theta_2 = -K_1(\theta_2 - \theta_1) - K_2(\theta_2 - \theta_3) \tag{3.43}$$

$$J_3 \frac{d^2}{dt^2}\theta_3 = -K_2(\theta_3 - \theta_2) \tag{3.44}$$

By combining the low-speed shaft and the high-speed shaft together into an equivalent shaft, the three-mass model can be reduced to two-mass model which is shown in Figure 3.12d. There are two methods of constituting the two-mass model. In method 1 the wind turbine and the gearbox are lumped together to show the equivalent mass moment of the wind turbine inertia ($J''_{WT}=J'_{WT}+J'_{GB}$), and a generator inertia (J_G) itself, or in method 2 the gearbox is adjacent to the generator to represent the equivalent mass moment of the generator inertia ($J'_G=J_G+J'_{GB}$), plus a wind turbine inertia (J'_{WT}) itself [83]. In the two-mass model, the mutual damping parameters of the generator and gearbox are neglected. In this system, K_{2M} denote the equivalent shaft stiffness of the two-mass drive train model whose equation is [83]:

$$\frac{1}{K_{2M}}=\frac{1}{K_{HGB}/N_{GB}^2}+\frac{1}{K_{GBG}} \tag{3.45}$$

where N_{GB} is the speed ratio of the gearbox.

A different way of showing two-mass drive train model is illustrated in [84] as:

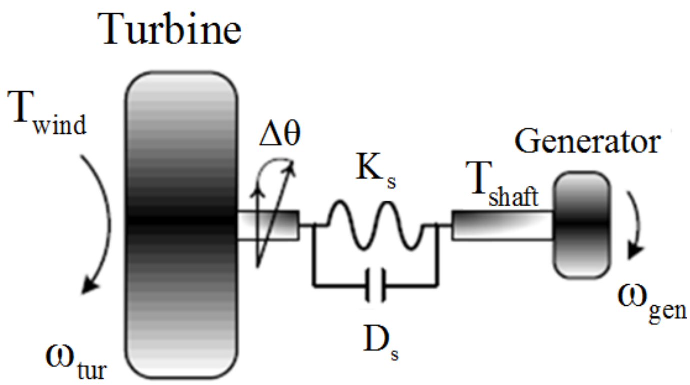

Figure 3.15: Two-mass drive train model [19]

The dynamic equations for the two-mass model of the drive train depicted in Figure 3.15 are given in [84] as:

$$\frac{d\omega_{tur}}{dt}=\frac{T_{wind}-T_{shaft}-D_s\omega_{tur}}{J_{tur}} \tag{3.46}$$

$$T_{shaft}=K_s\Delta\theta+D_s\left(\omega_{tur}-\frac{\omega_{gen}}{\eta_{gear}}\right) \tag{3.47}$$

$$\frac{d(\Delta\theta)}{dt}=\omega_{tur}-\frac{\omega_{gen}}{\eta_{gear}} \tag{3.48}$$

$$P_m=T_{shaft}\frac{\omega_{gen}}{\eta_{gear}} \tag{3.49}$$

where P_m is the mechanical power on the generator shaft.

Further simplification can be made by lumping all masses in a wind turbine system together and representing them as a one-mass (single-mass or lumped-mass) drive train model. The equivalent inertia of a one-mass model is defined by J'''_{WT} ($=J''_{WT}+J'_{G}$) and shown in Figure 3.12e. The dynamic behaviour of this system could be formulated by the following equation [83]:

$$\frac{d\omega_R}{dt} = \frac{T_{WT} - T_E}{J'''_{WT}} \tag{3.50}$$

where J'''_{WT} is the inertia constant of the rotating mass, ω_R is the angular speed of the rotor, T_{WT} is the input mechanical torque applied to the wind turbine rotor, and T_E is the electromagnetic torque of the generator [83].

The drive train modelling can be summarised in a table as in [44]:

3-mass 2-shaft (5^{th} order)	-LS and HS shaft are flexible (2 DE) -*dω/dt* is different for each mass (3 DE)
2-mass 1-shaft (3^{rd} order)	-Equivalent shaft is flexible (1 DE) - *dω/dt* is different for each mass (3 DE)
1-mass no-shaft (1^{st} order)	-All shafts are rigid (no DE) - *dω/dt* is same for each mass (1 DE)

Table 3.1: The drive train modelling configurations [44]

where DE stands for differential equation, ω is rotational speed, LS means low-speed and HS denotes high-speed.

3.12 Pitch Control

In high wind speed conditions (above rated speed) or during any grid disturbance, a proper pitch control should be designed to prevent over-speeding of the wind turbine and maintain the rotational speed at around desired level. Blade angle (pitch) control is the most effective protection against gusts, and is commonly used in large scaled variable speed generators, especially in the DFIG based wind turbines. A generic pitch control block diagram is depicted in Figure 3.16. Below rated speed, there is no need to take any pitch control action. Thus, the minimum blade angle (β_{min}) is kept around approximately 0 degree as an optimum value of the blade angle. However, in light winds the pitch angle can be decreased to a few degrees below zero (i.e. -2°) to capture maximum energy [10]. If the generator rotor speed is below the rated speed, then 'X' in Figure 3.16 is replaced with an electrical quantity of 'P' (active power), which means normal operation (power production control), but at above rated speed, a mechanical quantity, 'ω_{gen}' (generator speed), replaces 'X' (abnormal operation - pitch control mode) [67]. In this case, the pitch controller increases the pitch angle slowly and steadily up to a reasonable value to reduce the mechanical power produced by the wind turbine, and therefore, to prevent the rotor overspeeding. Thus, extra mechanical stresses on the drive train components and any mechanical damage of the turbine would be avoided. In case of pitch regulated variable speed wind turbines, the maximum blade pitching angle (β_{max}) is defined as 90 degrees [13].

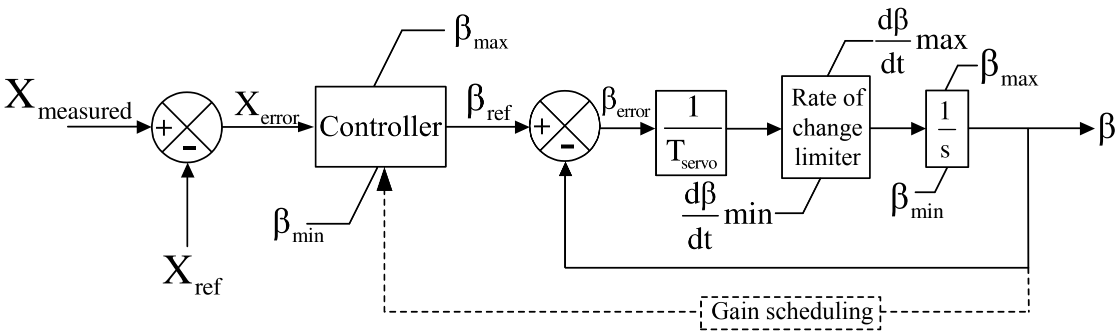

Figure 3.16: Block diagram of generic pitch angle control

In prior art, different controller types were proposed as the pitch controller. For example, a proportional (P-) only control was used in [46], PI controllers were commonly utilised in [13, 67, 75 and 85]. In [84], a PID controller was used to control the pitch angle. Additional PD-controller was developed in [13] just before the main (PI) controller for a better sensitivity. Slootweg et al [46] claims that P-only controller is sufficient since the system never enters the steady-state due to the wind speed variations, and the advantage of the integral control achieving zero steady-state error is not applicable.

In generic pitch control method, the measured generator speed is compared with the reference (or rated) speed and the error signal is sent to the main controller (P-only, PI, or PID). The controller generates the reference blade angle as an output. Again, this reference value of the blade angle is compared to the actual value of the blade angle, and the error is processed in the first order servomechanism model. The blade angle should be kept in the range of between the minimum and the maximum value of the blade angle. In [75, 85 and 86], a gain scheduling control of the blade pitch angle is also included in order to compensate the non-linear aerodynamic characteristics.

3.13 Summary

In this chapter, dynamic modelling, equivalent circuit per-phase and dynamic machine equations of DFIG were given. The *dq*-reference frame layout was depicted including the derivation of the angles required for Clarke and Park transformations. The aims of the usage of the rotor-side converter, the DC-link and the grid-side converter were briefly summarised. Generic current (inner) loop controllers for both rotor-side and grid-side converters were designed and shown to work. The tuning parameters for the controllers were also presented. Furthermore, the effects of each component in the rotor voltage equation were investigated in the lights of [50 and 81]. Finally, the basic knowledge on pitch control and drive train model configurations was added. Since this thesis focuses only on the electrical system control of the DFIG system, the detailed aerodynamic pitch control design is out of the scope of subsequent work in this thesis though.

Chapter 4 DC-Link Voltage Control – GSC Outer Loop Control

4.1 Introduction

In this chapter, an enhanced DC-link voltage control will be established. As discussed in Chapter 3, it is highly desirable to keep the DC-link voltage constant at its pre-defined value in DFIG systems. To do so, a grid-side converter (GSC) is utilised, which is connected to the rotor-side converter by a DC-link capacitor. The only link between the rotor-side converter and the grid-side converter is this capacitor. The inner (current) loop control of the grid-side converter was presented in Section 3.10. This chapter will propose a novel outer (voltage) loop control of the grid-side converter in the DFIG system. The general principle of this control loop has been published previously [60], but disturbance inputs were neglected and simplifications have been made without verifying whether they are acceptable. This chapter attempts a thorough verification. As a reminder, the typical DFIG system is summarised in Figure 4.1.

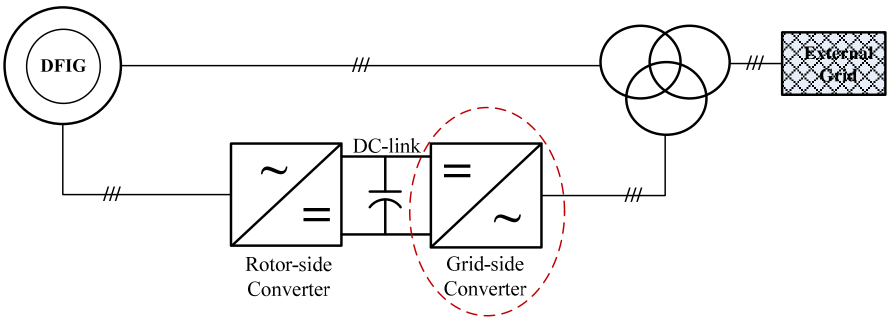

Figure 4.1: The typical DFIG system

A cascaded control block diagram (full representation) that includes the inner *d*-loop and the outer loop of the grid-side converter is depicted in Figure 4.2. Since the undamped natural frequency (f_n) of the inner (current) loop control is far faster than the that of the outer (voltage) loop control (450Hz>>10Hz), a simplification is made in the following sub-sections by assuming that the inner loop gain (G_{inner}) is 1. Thus, the complexity of the inner loop control design is avoided and the time consumed for calculations (e.g. calculation of the tuning parameters of the controller) is minimised.

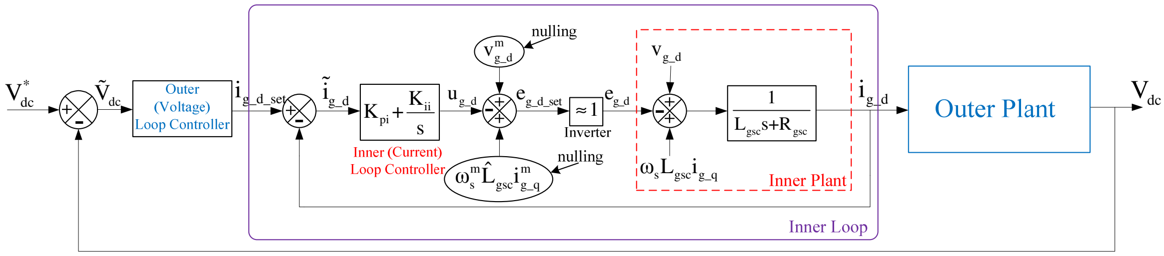

Figure 4.2: The full control block diagram of the d-loop of the GSC

Dynamic stiffness (DS) analyses of both the disturbance input current (i_n) and the *d*-component of the grid voltage (v_{g_d}) with respect to the DC-link voltage (V_{dc}) will be carried out in order to test the controller design. DS is a measure of how 'stiff' a quantity, in this case the DC-link voltage, is to external disturbances. In this case, the disturbances are external current and voltage. Furthermore, sensitivity analysis research will be undertaken for selected operating points (a fraction of the nominal values) of the DC-link voltage, and *d*-components of the grid voltage and current. The flexibility and capability of the designed DC-link voltage controller against the changes in these quantities will be investigated in this chapter. Finally, the results obtained from both MATLAB and PSCAD will be documented and compared to each other, as well.

4.2 Control Design

The grid-side converter shown in the red dotted circle in Figure 4.1 is represented as the DC-link voltage plant, which is illustrated in Figure 4.3, in order to derive the outer (voltage) loop plant model and design the outer (voltage) loop control of the grid-side converter [80]. The outer loop controller depicted in Figure 4.2 will be replaced with a PI controller. The grid voltage is aligned to the *d*-axis, so the *q*-components of the voltage and current quantities are zero for unity power factor converter operation.

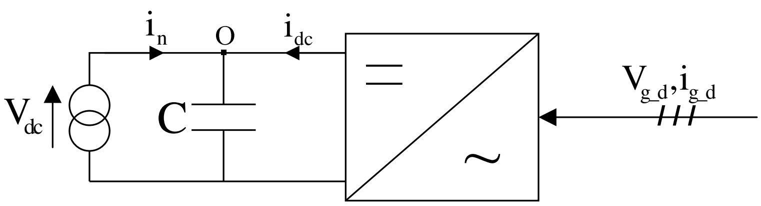

Figure 4.3: DC-link voltage plant

Many physical phenomena in the real word have nonlinear characteristics, but it is often nearly impossible to mathematically model and analyse these systems. Therefore, a small-signal linearisation technique is often used to ease the modelling of non-linear systems by representing them as linear systems within a target operating point range. Thus, a stable system within the limited operating region would be maintained and the controller design for non-linear systems can then be made possible. However, the linearised system will include components which vary with some state variables (i.e. with operating points) [87]. In this research, a small signal linearisation method is utilised to reveal the plant model of the outer loop and to design its controller.

Applying the Kirchhoff's Current Law (KCL) to node 'O' in Figure 4.3,

$$C\frac{dV_{dc}}{dt}=i_n+i_{dc} \tag{4.1}$$

Using the real power invariant principle for the DC-end and AC-end ($P_{AC} = P_{DC}$),

$$v_{dc}i_{dc}=\frac{3}{2}v_{g\_d}i_{g\_d} \tag{4.2}$$

gives the DC-voltage term:

$$\frac{dV_{dc}}{dt}=\frac{i_n}{C}+\frac{3v_{g\_d}i_{g\_d}}{2CV_{dc}}=f \tag{4.3}$$

Taking partial differentials and ignoring all terms apart from the noise term, the direct current term and the DC-voltage term turns the equation into:

$$\Delta\dot{V}_{dc}=\frac{\partial f}{\partial i_n}\Delta i_n+\frac{\partial f}{\partial v_{dc}}\Delta v_{dc}+\frac{\partial f}{\partial i_{g\_d}}\Delta i_{g\_d}+\frac{\partial f}{\partial v_{g\_d}}\Delta v_{g\_d}$$

$$=\frac{1}{C}\Delta i_n-\frac{3v_{g\_do}i_{g\_do}}{2C(v_{dco})^2}\Delta v_{dc}+\frac{3v_{g\_do}}{2Cv_{dco}}\Delta i_{g\_d}+\frac{3i_{g\_do}}{2Cv_{dco}}\Delta v_{g\_d}$$

$$\text{or}\quad C\Delta\dot{V}_{dc}=\Delta i_n-1.5K_vK_s\Delta v_{dc}+1.5K_v\Delta i_{g\_d}+1.5K_s\Delta v_{g\_d} \tag{4.4}$$

where a subscript 'o' indicates an operating point value and

$$K_v=\frac{v_{g\_do}}{v_{dc\_o}}\quad\text{and}\quad K_s=\frac{i_{g\_do}}{v_{dc\_o}}$$

Equation 4.4 gives us the outer loop plant model. Thus, the full state-feedback system-block (SFSB) diagram of the grid-side converter control (including inner-current and outer-voltage loop controllers) of the grid-side converter becomes that shown in Figure 4.4.

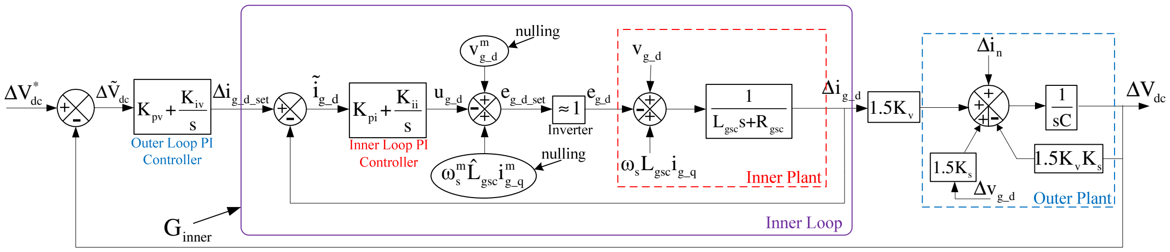

Figure 4.4: Full SFSB of the GSC controller

By ignoring Δi_n (the disturbance current input), the full transfer function (FTF) of the grid-side converter controller depicted in Figure 4.4 $\left(\Delta V_{dc}/\Delta V_{dc}^*\right)$ including the G_{inner} term is

$$\mathrm{FTF}=\frac{\Delta V_{dc}}{\Delta V_{dc}^*}=\frac{s^2 1.5K_v K_{pv} K_{pi}+s[1.5K_v(K_{pv}K_{ii}+K_{pi}K_{iv})]+1.5K_v K_{iv} K_{ii}}{\begin{Bmatrix} s^4 L_{gsc}C+s^3[C(R_{gsc}+K_{pi})+1.5K_v K_s L_{gsc}]+s^2[CK_{ii}+1.5K_v K_s(R_{gsc}+K_{pi}) \\ +1.5K_v K_{pv}K_{pi}]+s[1.5K_v(K_{pv}K_{ii}+K_{pi}K_{iv}+K_s K_{ii})]+1.5K_v K_{iv} K_{ii} \end{Bmatrix}} \qquad (4.5)$$

Assuming the inner loop control is fast (G_{inner}=1), the full SFSB can be simplified to only the outer loop control of the grid-side converter, see Figure 4.5, and then the full transfer function (FTF) can be reduced to the transfer function (TF) shown in equation 4.6.

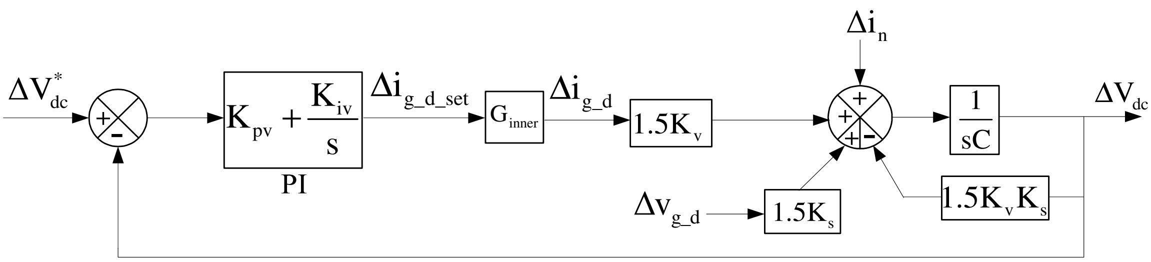

Figure 4.5: Outer (V_{dc}) loop control of the grid-side converter

$$\mathrm{TF}=\frac{\Delta V_{dc}}{\Delta V_{dc}^*}=\frac{1.5K_v K_{pv}s+1.5K_v K_{iv}}{Cs^2+1.5K_v(K_s+K_{pv})s+1.5K_v K_{iv}} \qquad (4.6)$$

The transfer function in equation 4.6 can further be simplified to equation 4.7 by considering K_{pv}>>K_s. This is reasonable because the typical values of K_{pv} and K_s are 9 and 1.95, respectively, for a 4.5MVA machine with a controller undamped natural frequency (f_n) of 10Hz and damping ratio (ζ) of 0.7 for the voltage loop.

$$\text{STF (Simplified Transfer Function)} = \frac{\Delta V_{dc}}{\Delta V_{dc}^{*}} = \frac{1.5K_vK_{pv}s+1.5K_vK_{iv}}{Cs^2+1.5K_vK_{pv}s+1.5K_vK_{iv}} \tag{4.7}$$

The sK_{pv} term in the numerator of equation 4.6 can be neglected by assuming $K_{iv} >> K_{pv}$ (this is reasonable because the typical values of K_{iv} and K_{pv} are 404 and 9, respectively for our system), which gives us the second-order approximated transfer function (SoATF):

$$\text{SoATF}=\frac{\Delta V_{dc}}{\Delta V_{dc}^{*}} = \frac{1.5K_vK_{iv}/C}{s^2+\left(1.5K_v(K_s+K_{pv})/C\right)s+1.5K_vK_{iv}/C} \tag{4.8}$$

Further simplification can be done by neglecting the K_s parameter ($K_{pv}>>K_s$) in the denominator of Equation 4.8 which results in the simplified second-order approximated transfer function (SSoATF) formulated as in equation 4.9.

$$\text{SSoATF}=\frac{\Delta V_{dc}}{\Delta V_{dc}^{*}} = \frac{1.5K_vK_{iv}/C}{s^2+\left(1.5K_vK_{pv}/C\right)s+1.5K_vK_{iv}/C} \tag{4.9}$$

Figure 4.5 can be reconfigured in order to depict the forward-path transfer function. Thus, the approximated damping ratio of the control system on the Bode diagrams in MATLAB can be determined by using the forward-path transfer function (FpTF) of the system. Since the feedback gain, H(s), is 1, this is equivalent to the loop gain. Ignoring the disturbance inputs Δi_n and Δv_{g_d}, as they are of insignificant interest in the forward-path gain, Figure 4.5 transforms into Figure 4.6.

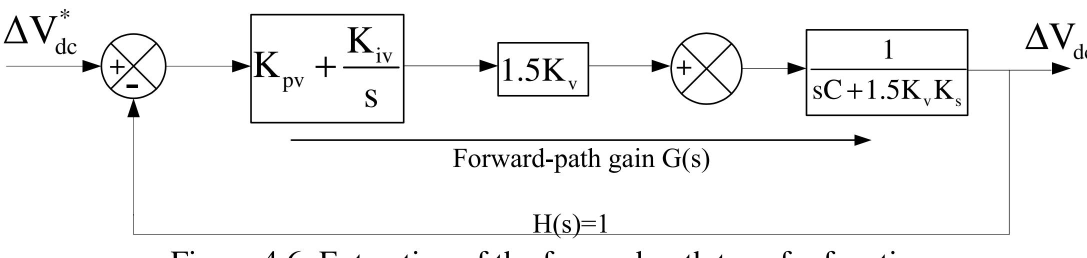

Figure 4.6: Extraction of the forward-path transfer function

The forward-path transfer function (FpTF) of the system can then be written as:

$$\text{FpTF}=G(s).H(s)=\frac{1.5K_vK_{pv}s+1.5K_vK_{iv}}{Cs^2+1.5K_vK_ss} \tag{4.10}$$

4.3 Dynamic Stiffness

The dynamic stiffness indicates how 'stiff' the overall system output is against changes occurring in the system disturbance variables. The impact of these elements on the system response can be investigated and action taken in case of a low DS. A high DS already means that the system is probably stiff enough. In this section, the effects of disturbance current input and the *d*-component of the grid voltage on the DC-link voltage are studied.

The dynamic stiffness of the control system can be tested in terms of two transfer functions. The first technique (DS1) is used to find out the effect of the disturbance input Δi_n on the DC-link voltage (ΔV_{dc}). Figure 4.5 can be re-drawn illustrating Δi_n as an input (see Figure 4.7). In second method (DS2), the relation between Δv_{g_d} and ΔV_{dc} is investigated by reconfiguring Figure 4.5 to depict the dynamic stiffness function (see Figure 4.8).

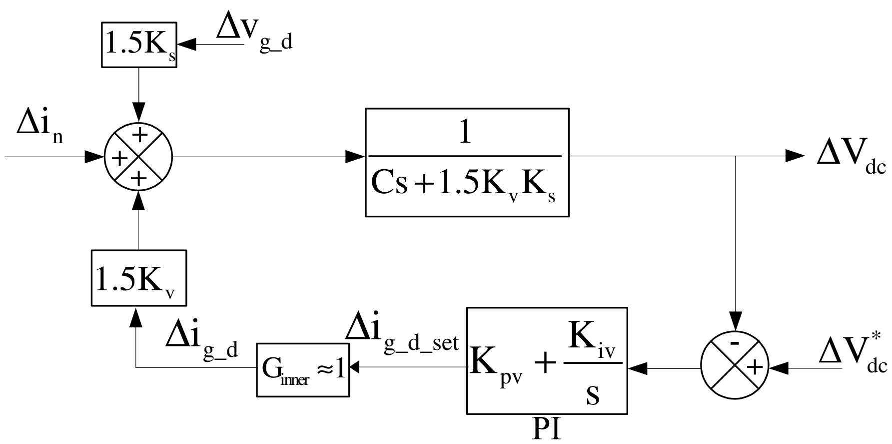

Figure 4.7: Dynamic stiffness 1 (DS1)

Thus we have:

$$\text{Noise Function1} = \left|\frac{\Delta V_{dc}}{\Delta i_n}\right| = \frac{\left(\dfrac{1}{sC+1.5K_vK_s}\right)}{1+\left(\dfrac{1}{sC+1.5K_vK_s}\right)\left(K_{pv}+\dfrac{K_{iv}}{s}\right)(1.5K_v)} \tag{4.11}$$

$$\text{Dynamic Stiffness1} = \left|\frac{1}{\text{Noise Function1}}\right| = \left|\frac{\Delta i_n}{\Delta V_{dc}}\right| = \frac{1+\left(\dfrac{1}{sC+1.5K_vK_s}\right)\left(K_{pv}+\dfrac{K_{iv}}{s}\right)(1.5K_v)}{\left(\dfrac{1}{sC+1.5K_vK_s}\right)}$$

$$\mathrm{DS1}=\left|\frac{\Delta i_n}{\Delta V_{dc}}\right|=\left|\frac{Cs^2+1.5K_v(K_s+K_{pv})s+1.5K_vK_{iv}}{s}\right| \tag{4.12}$$

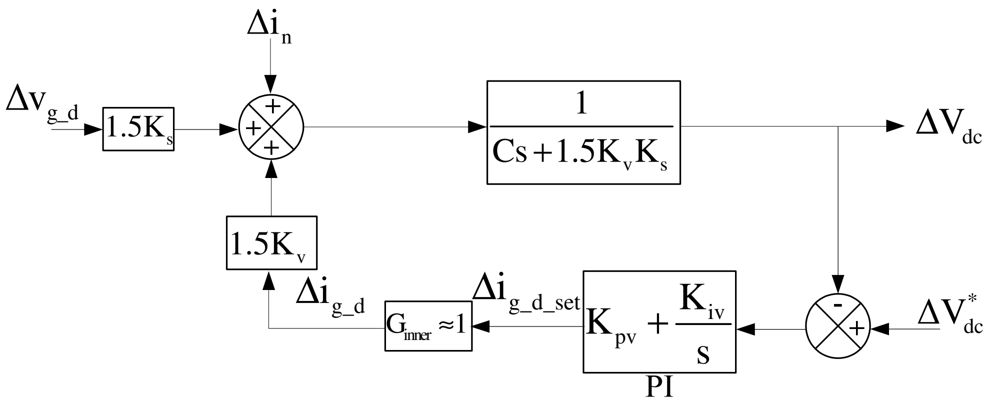

Figure 4.8: Dynamic stiffness 2 (DS2)

and also:

$$\text{Noise Function2}=\left|\frac{\Delta V_{dc}}{\Delta v_{g\_d}}\right|=\frac{(1.5K_s)\left(\frac{1}{sC+1.5K_vK_s}\right)}{1+\left(\frac{1}{sC+1.5K_vK_s}\right)\left(K_{pv}+\frac{K_{iv}}{s}\right)(1.5K_v)} \tag{4.13}$$

$$\text{Dynamic Stiffness2}=\left|\frac{1}{\text{Noise Function2}}\right|=\left|\frac{\Delta v_{g\_d}}{\Delta V_{dc}}\right|=\frac{1+\left(\frac{1}{sC+1.5K_vK_s}\right)\left(K_{pv}+\frac{K_{iv}}{s}\right)(1.5K_v)}{(1.5K_s)\left(\frac{1}{sC+1.5K_vK_s}\right)}$$

$$\mathrm{DS2}=\left|\frac{\Delta v_{g\_d}}{\Delta V_{dc}}\right|=\left|\left(\frac{1}{1.5K_s}\right)\frac{Cs^2+1.5K_v(K_s+K_{pv})s+1.5K_vK_{iv}}{s}\right| \tag{4.14}$$

4.4 Tuning Loop for Nominal Operating Point

In order to extract the tuning parameters of the outer (voltage) PI loop control for the grid-side converter, the simplified second-order approximated transfer function (SSoATF) is equated to $\frac{\omega_n^2}{s^2+2\zeta\omega_n s+\omega_n^2}$. Thus, the equations of undamped natural frequency and the damping ratio can be derived as follows

$$\omega_n^2=\frac{1.5K_vK_{iv}}{C}\ \Rightarrow\ \omega_n=\sqrt{\frac{1.5K_vK_{iv}}{C}} \tag{4.15}$$

$$2\zeta\omega_n=\left(\frac{1.5K_vK_{pv}}{C}\right)\ \Rightarrow\ \zeta=\frac{K_{pv}}{2}\sqrt{\frac{1.5K_v}{CK_{iv}}} \tag{4.16}$$

The undamped natural frequency (f_n) and the damping ratio (ζ) are set to 10Hz (see Chapter 5) and 0.7, respectively, since this is a good balance between response speed and overshoot.. The value of the DC-link capacitor used in the grid-side converter configuration is assigned as 50134μF (3.5pu) [16]. The nominal operating point of the DC-link voltage (V_{dco_nom}) and the base grid voltage ($v_{g\_d\_base}$) are determined as 1kV [10 and 16] and 0.4kV [16], respectively.

Note that the grid voltage is phase-to-phase rms voltage, and needs to be converted to phase peak voltage, ($v_{g\_do\_nom}$) which is approximately 326.6V phase peak. The calculation of the nominal phase peak grid current then is:

$$i_{g\_do\_nom} = \frac{P_{converter}}{\frac{3}{2} v_{g\_d\_base}} = \frac{30\% \text{ x } S_{base}}{\frac{3}{2} v_{g\_d\_base}} = \frac{30\% \text{ x } 4.5\text{MVA}}{\frac{3}{2} \text{x} \underbrace{\left(0.4\text{kVx}\frac{\sqrt{2}}{\sqrt{3}}\right)}_{\text{phase peak voltage}}} \approx 2.76 \text{ kA} \quad \text{phase peak}$$

The nominal values of the constants, K_v and K_s, can be calculated using the nominal operating points of the voltages and currents.

$$K_v = \frac{v_{g\_do\_nom}}{v_{dco\_nom}} = \frac{0.3266\text{kV}}{1\text{kV}} \approx 0.327 \quad \text{and} \quad K_s = \frac{i_{g\_do\_nom}}{v_{dco\_nom}} \approx \frac{2.76\text{kA}}{1\text{kV}} \approx 2.76 \text{ (A/V)}$$

Finally, substituting the value of the K_v in equations 4.15 and 4.16 the tuning parameters, K_{pv} and K_{iv}, of the PI controller can be calculated as 9 and $404s^{-1}$, respectively. The time constant of the PI loop, the T_{iv}, which is the inverse of the K_{iv}, is 2.475ms.

4.5 Operating Point Analysis

The influences of the different operating points of the DC-link voltage, grid voltage and current on the system control response are investigated. Three variables are chosen: V_{dco} (the DC-link voltage), v_{g_do} (the *d*-component of the grid voltage) and i_{g_do} (the *d*-component of the grid current). A fraction of the nominal value is added to or subtracted from the nominal value. Each time, seven different operating points of one quantity in turn is selected while the other two quantities are kept constant at their nominal values. Thus, the effects of varying one parameter in turn on overall system are analysed. In Table 4.1, the selected operating points for the current and voltage quantities are presented. By considering the set value of the nominal undamped natural frequency (f_{n_nom}) of 10Hz and that of the nominal damping ratio (ζ_{nom}) of 0.7, the PI parameter (K_{pv} and K_{iv}) in the equations are calculated and held fixed at their values. Thus for each operating point with one quantity in turn, the different estimated values of f_n and ζ are found. The tuning parameters (K_{pi} and K_{ii}) for the inner (current) loop of the grid-side converter were documented in Section 3..10.2.

In order to estimate the approximated bandwidth of the each operating point in the system, the first frequency where the gain drops below 70.79% (-3dB) of its DC value is used in the Bode diagrams. The forward-path transfer function of each operating point in the system is used to determine its approximated damping ratio. To do so, the phase margin, which is the difference between the phase of the system response and -180° when the gain is unity (0dB), is first calculated by adding 180° to the phase in degrees corresponding the 0dB gain margin in the Bode diagrams of the forward-path transfer function of each operating point. Then, this phase margin is divided by 100 to find out the approximated damping ratio.

% change	**V_{dco} (V)**	**v_{g_do} (V)**	**i_{g_do} (A)**
-30%	700 (V_{dco_min})	228.62 ($v_{g\_do\_min}$)	1928.97 ($i_{g\_do\_min}$)
-20%	800	261.28	2204.54
-10%	900	293.94	2480.11
-nom-	1000 (V_{dco_nom})	326.6 ($v_{g\_do\_nom}$)	2755.68 ($i_{g\_do\_nom}$)
+10%	1100	359.26	3031.24
+20%	1200	391.92	3306.81
+30%	1300 (V_{dco_max})	424.58 ($v_{g\_do\_max}$)	3582.38 ($i_{g\_do\_max}$)

Table 4.1 Selected Operating Points

The equations of full transfer function (FTF), transfer function (TF), simplified transfer function (STF), second-order approximated transfer function (SoATF), simplified second-order approximated transfer function (SSoATF), forward path transfer function (FpTF) and dynamic stiffness equations are given in a clear form in order to help carry out the sensitivity analysis work.

a) $\mathrm{FTF}=\dfrac{\Delta V_{dc}}{\Delta V_{dc}^{*}}=\dfrac{s^2 1.5K_v K_{pv} K_{pi}+s[1.5K_v(K_{pv}K_{ii}+K_{pi}K_{iv})]+1.5K_v K_{iv} K_{ii}}{\begin{array}{c}s^4 L_{gsc}C+s^3[C(R_{gsc}+K_{pi})+1.5K_v K_s L_{gsc}]+s^2[CK_{ii}+1.5K_v K_s(R_{gsc}+K_{pi})\\ +1.5K_v K_{pv} K_{pi}]+s[1.5K_v(K_{pv}K_{ii}+K_{pi}K_{iv}+K_s K_{ii})]+1.5K_v K_{iv} K_{ii}\end{array}}$

b) $\mathrm{TF}=\dfrac{\Delta V_{dc}}{\Delta V_{dc}^{*}}=\dfrac{1.5K_v K_{pv}s+1.5K_v K_{iv}}{Cs^2+1.5K_v(K_s+K_{pv})s+1.5K_v K_{iv}}$

c) $\mathrm{STF}=\dfrac{\Delta V_{dc}}{\Delta V_{dc}^{*}}=\dfrac{1.5K_v K_{pv}s+1.5K_v K_{iv}}{Cs^2+1.5K_v K_{pv}s+1.5K_v K_{iv}}$

d) $\mathrm{SoATF}=\dfrac{\Delta V_{dc}}{\Delta V_{dc}^{*}}=\dfrac{1.5K_v K_{iv}/C}{s^2+\left(1.5K_v(K_s+K_{pv})/C\right)s+1.5K_v K_{iv}/C}$

e) $\mathrm{SSoATF}=\dfrac{\Delta V_{dc}}{\Delta V_{dc}^{*}}=\dfrac{1.5K_v K_{iv}/C}{s^2+\left(1.5K_v K_{pv}/C\right)s+1.5K_v K_{iv}/C}$

f) $\mathrm{FpTF}=G(s).H(s)=\dfrac{1.5K_v K_{pv}s+1.5K_v K_{iv}}{Cs^2+1.5K_v K_s s}$

g) $\mathrm{DS1}=\left|\dfrac{\Delta i_n}{\Delta V_{dc}}\right|=\left|\dfrac{Cs^2+1.5K_v(K_s+K_{pv})s+1.5K_v K_{iv}}{s}\right|$

h) $\mathrm{DS2}=\left|\dfrac{\Delta v_{g\_d}}{\Delta V_{dc}}\right|=\left|\left(\dfrac{1}{1.5K_s}\right)\dfrac{Cs^2+1.5K_v(K_s+K_{pv})s+1.5K_v K_{iv}}{s}\right|$

4.5.1 V_{dco} Sensitivity

The sensitivity analysis of V_{dco} is carried out by choosing seven different operating points, while v_{g_do} and i_{g_do} are fixed at their nominal values, $v_{g\_do\_nom}$ and $i_{g\_do\_nom}$, which are 326.6V and 2.76kA, respectively. The seven operating points selected for V_{dc} are: 700V, 800V, 900V, 1000V, 1100V, 1200V and 1300V. Note that as V_{dc} varies, so do K_v and K_s parameters.

The Bode diagrams for seven operating points of the full transfer function (FTF) and the transfer function (FT) including their bandwidths are shown in Figures 4.9 and 4.10, respectively. In both upper graphs of the figures, the gain is 1 at DC which means that the steady-state error is zero. However, the gain drops dramatically at higher frequencies. In other words, changes in set value do not propagate through well above a given frequency, in this case about 20Hz. This ties in with an undamped natural frequency (f_n) of 10Hz. It is obviously seen from the lower graphs that the bandwidths decrease as V_{dco} increases.

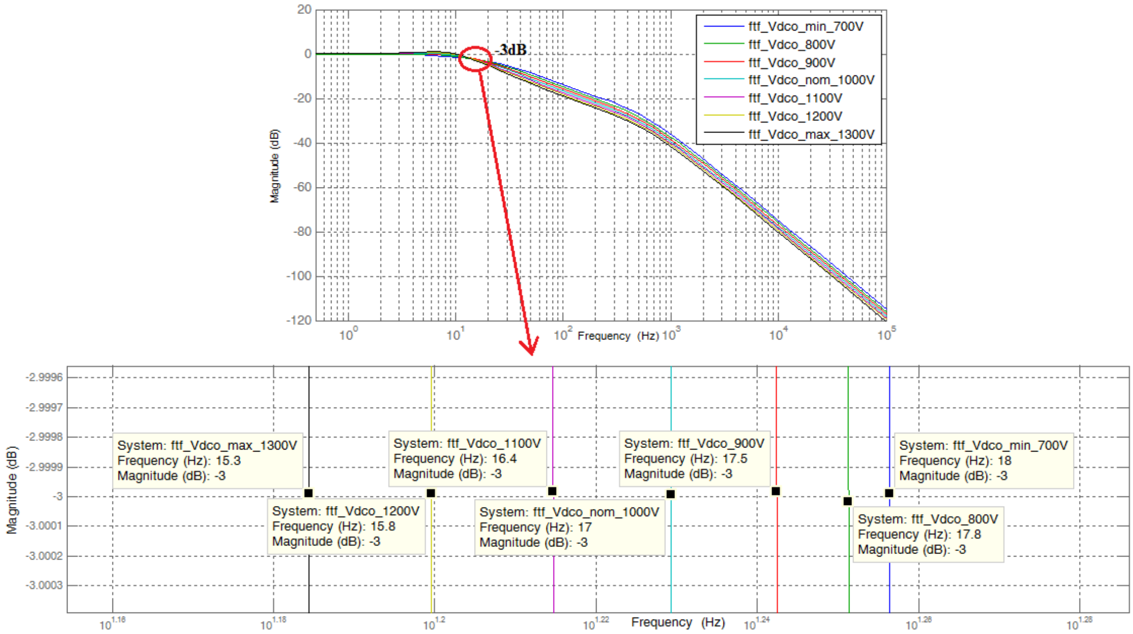

Figure 4.9: Bandwidths representation on the full transfer function - Varying V_{dco}

The bandwidths of the same operating points on the full transfer function and the transfer function bode diagrams (Figure 4.9 and 4.10) are effectively same. Thus, the simplification of the full transfer function (FTF) to the simpler transfer function (TF) is perfectly reasonable by assuming that the inner (current) loop is fast (the inner loop gain was considered as 1). This gives the advantage of decreasing the computational time required for the tuning process.

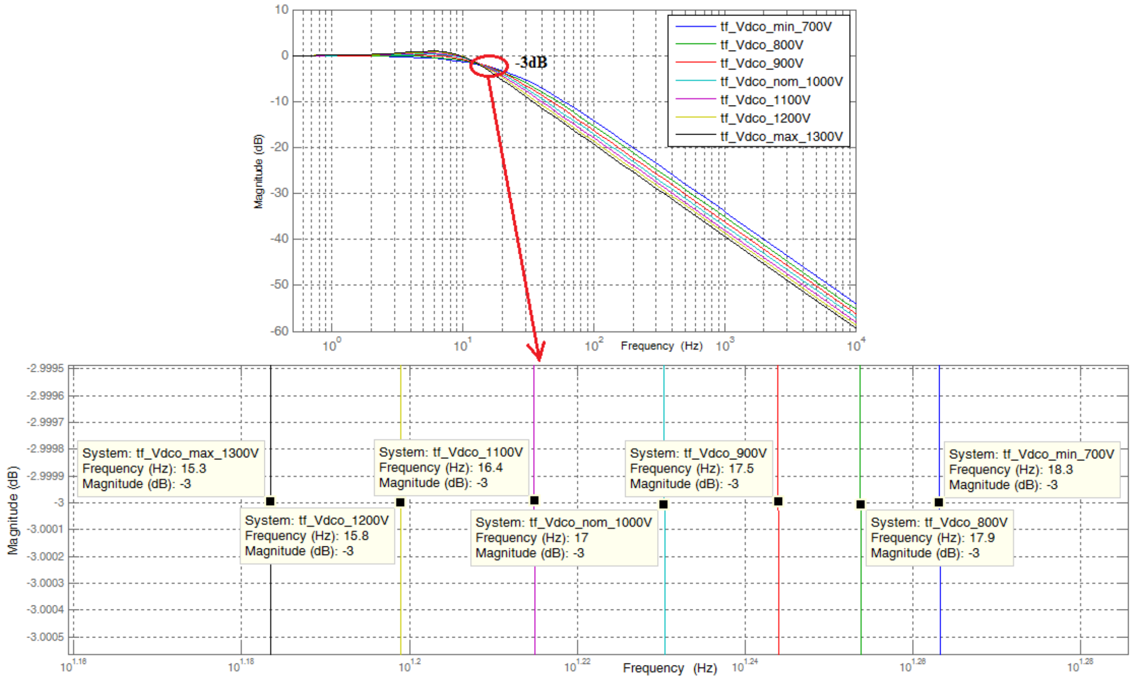

Figure 4.10: Bandwidths representation on the transfer function - Varying V_{dco}

If the equation of the undamped natural frequency (ω_n) (see equation 4.16) is re-written in terms of V_{dco}, then

$$\omega_n = \sqrt{\frac{1.5K_{iv}}{C}\frac{v_{g\_do\_nom}}{V_{dco}}} \qquad 4.17$$

Since only the operating points of V_{dc} change and the remaining parameters ($v_{g\_do\_nom}$, K_{iv}, and C) in the equation 4.17 are kept constant, the ω_n (or f_n) is inversely proportional to $\sqrt{V_{dco}}$. This means that as V_{dco} increases the bandwidth of the system decreases. The MATLAB results shown in the lower graphs of the Figures 4.9 and 4.10 are well-matched the mathematical calculations.

The simplified transfer function (STF) can be derived by neglecting the term including the K_s ($1.5K_vK_ss$) in the mid-term of the denominator of the transfer function (TF). So, the bandwidths corresponding the same operating point of V_{dc} in the STF will be higher than in comparison to those in the TF. However, the relation between the bandwidth of the system and V_{dco} stays same.

Let us examine how change in V_{dco} affects the $1.5K_vK_ss$ term. Consequently, how the change occurring in this term can affect the bandwidths. As a reminder, the equations of these parameters are:

$$K_v = \frac{v_{g\_do\_nom}}{V_{dco}} \quad \text{and} \quad K_s = \frac{i_{g\_do\_nom}}{V_{dco}}$$

Both parameters are inversely proportional to V_{dco}, if v_{g_do} and i_{g_do} are both constant at their nominal values. So, increasing V_{dco} decreases K_v and K_s. The product of the K_vK_s has its highest value at the minimum operating pointof V_{dc}. This means that the difference in bandwidths in percentage is higher at lower V_{dco}. So, the biggest change occurs in 0.7kV operating point of V_{dc} (the bandwidth at 0.7kV of V_{dco} in the TF is 18.3Hz, and that in the STF is 26.7Hz). From an initial tuning point of view and given the simplifications made, this level of deviation may be accurate enough at an initial stage of study. However, this means for a well designed system to get a reasonably accurate value of system bandwidth (BW), the designer needs to use at least the complexity of the simplified second-order approximated transfer function (SSoATF). Since the BW varies with respect to V_{dco}, both the minimum BW, which occurs at maximum DC-link voltage and the maximum BW, which occurs at minimum DC-link voltage, must be checked.

The bandwidths obtained in the STF for seven different operating points of V_{dco} are shown in Figure 4.11. The simulation results for the second-order approximated transfer function (SoATF) and the simplified second-order approximated transfer function (SSoATF) will be shown in Appendix 3.

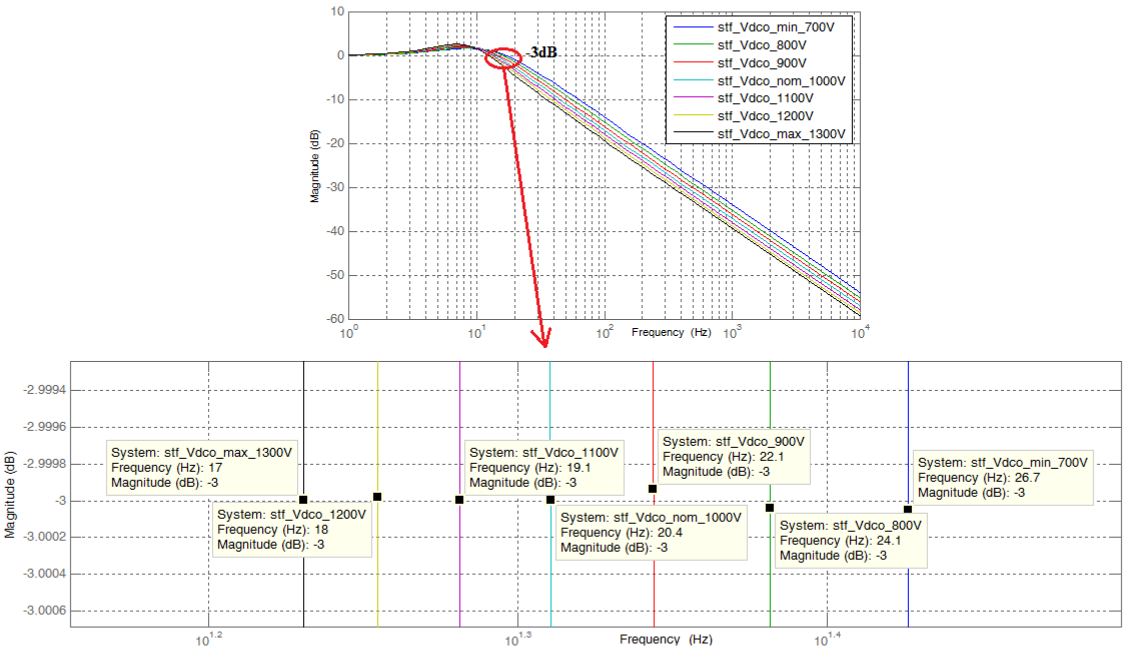

Figure 4.11: Bandwidths representation on the simplified transfer function - Varying V_{dco}

The forward-path transfer function bode diagram is illustrated in Figure 4.12 to read the approximate damping ratio for each operating point of V_{dc}. In Figure 4.12, the 0dB gain region is magnified to obtain the phase margins as well as the damping ratios.

The relation between the damping ratio and V_{dco} can be derived by re-configuring equation 4.16 as

$$\zeta = \frac{K_{pv}}{2}\sqrt{\frac{1.5}{CK_{iv}}\frac{v_{g\_do\_nom}}{V_{dco}}} \tag{4.18}$$

As seen in equation 4.18, the damping ratio is inversely proportional to $\sqrt{V_{dco}}$ if the other parameters ($v_{g\_do\_nom}$, K_{pv}, K_{iv}, and C) are held fixed at their initial or nominal values.

The approximate damping ratio can be estimated from the MATLAB result by using the following equation:

$$\zeta = \frac{PM}{100} \tag{4.19}$$

The phase margin (PM) can be obtained by adding 180° to the phase in degree of each operating point corresponding the 0dB line in Figure 4.12. Therefore, equation 4.19 can be re-written as equation 4.20.

$$\zeta = \frac{180^{\circ} + \text{phase(deg)}}{100} \tag{4.20}$$

As V_{dco} increases the approximate damping ratio decreases (see Figure 4.12), which matches the theory. They are not actually same since the forward-path transfer function does not reflect the precise results. However, the trend relating V_{dco} and the approximate damping ratio calculated with the aid of Figure 4.12 is the same as the mathematical analysis.

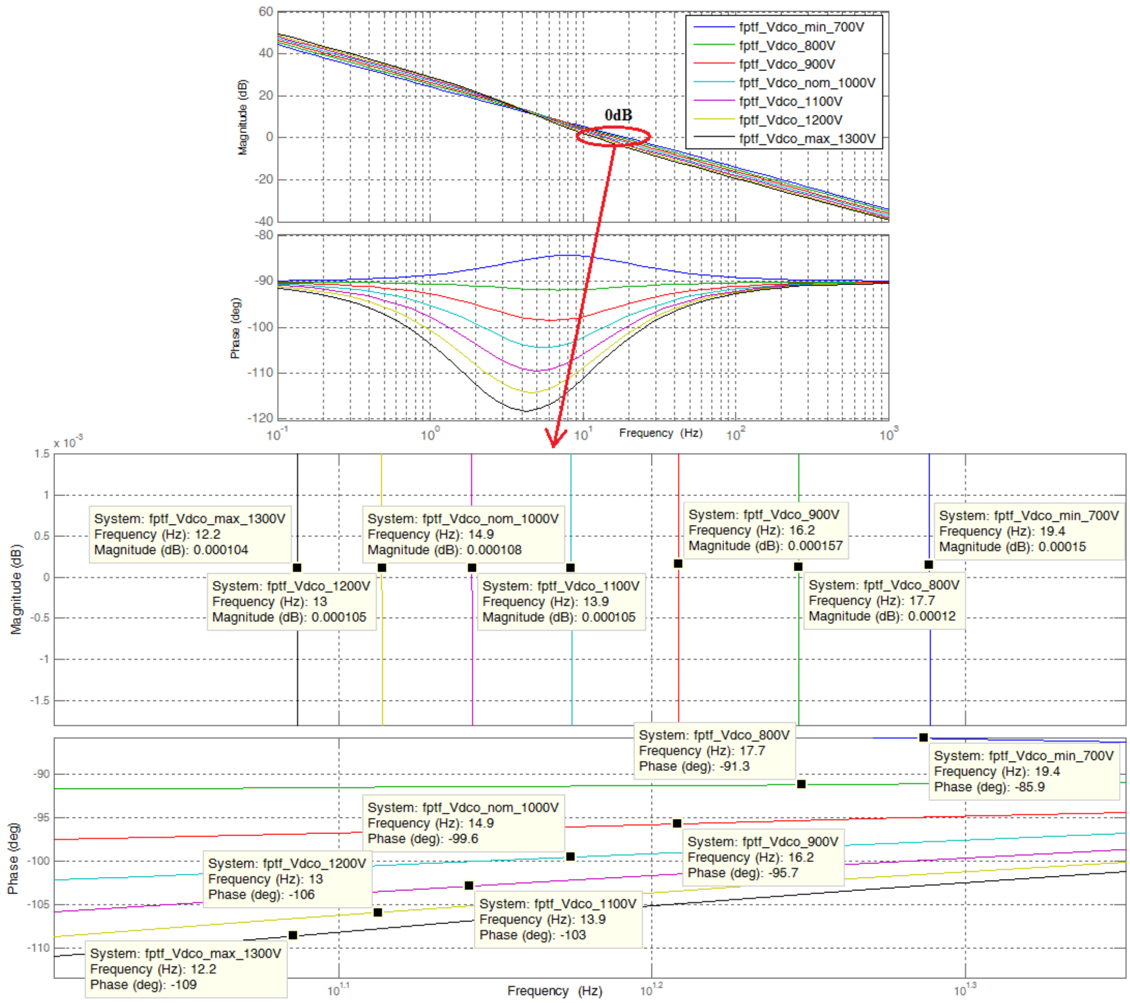

Figure 4.12: Damping ratios representation on the forward-path transfer function - Varying V_{dco}

The dynamic stiffness results are given in Figures 4.13 and 4.14. The stiffness of the system against the disturbance current and the grid voltage is tested. The stiffness analysis of $\Delta i_n/\Delta V_{dc}$ (DS1) tells us that at lower frequencies, increasing V_{dco} causes a less stiff system, while there is no effect of changing V_{dco} on the system stiffness at high frequencies (Figure 4.13).

At low frequencies, by neglecting high and mid- frequency terms the equation of DS1 (see equation 4.12) can then be simplified to:

$$DS1=\left|\frac{\Delta i_n}{\Delta V_{dc}}\right|=\left|\frac{1.5K_vK_{iv}}{s}\right| \quad \text{and} \quad K_v=\frac{v_{g\_do\_nom}}{V_{dco}} \quad \Rightarrow \quad DS1=\left|\frac{1.5v_{g\_do\_nom}K_{iv}}{V_{dco}s}\right| \tag{4.21}$$

At mid-frequencies, the low and high frequency terms are neglected and the DS1 equation becomes:

$$DS1=1.5K_v(K_s+K_{pv}) \text{ and } K_v=\frac{v_{g\_do\_nom}}{V_{dco}} \Rightarrow DS1=1.5\frac{v_{g\_do\_nom}}{V_{dco}}(K_s+K_{pv}) \tag{4.22}$$

Equation 4.21 and 4.22 tell us that at low and mid-frequencies the dynamic stiffness decreases as V_{dco} increases. DS1 is inversely proportional to V_{dco} for both low and mid-frequencies. This relation is also clearly seen in Figure 4.13.

At high frequencies, by ignoring the low and mid- frequency terms the DS1 equation can be re-written as:

$$DS1=\left|\frac{\Delta i_n}{\Delta V_{dc}}\right|=\left|\frac{Cs^2}{s}\right| \quad \Rightarrow \quad DS1=\left|Cs\right| \tag{4.23}$$

In equation 4.23, DS1 is not effectively influenced by changing (increasing or decreasing) V_{dco} at high frequencies (a range from ~40Hz to 1kHz) since there is no V_{dco} term in the equation. This is confirmed in the right-hand side of Figure 4.13. The mathematical calculations carried out for low and high frequencies of the DS1 are consistent with the MATLAB simulation results (see Figure 4.13).

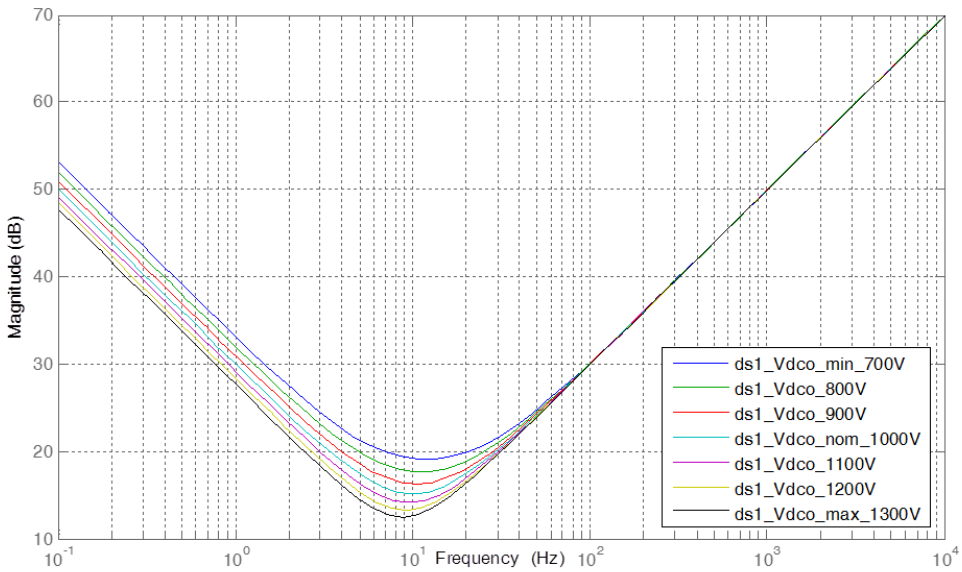

Figure 4.13: Dynamic stiffness analysis of $\Delta i_n/\Delta V_{dc}$ (DS1) - Varying V_{dco}

For the stiffness analysis of $\Delta v_{g\_d}/\Delta V_{dc}$ (DS2), at higher frequencies increasing V_{dco} makes the system much stiffer while changing the operating point of V_{dc} does not affect the stiffness of the system at low frequencies (Figure 4.14).

At low frequencies, by omitting the mid- and high frequencies term in the equation of DS2 (see equation 4.14), the equation of the DS2 can be reduced to:

$$DS2=\left|\frac{\Delta v_{g\_d}}{\Delta V_{dc}}\right|=\left|\left(\frac{1}{1.5K_s}\right)\frac{1.5K_vK_{iv}}{s}\right| \tag{4.24}$$

where

$$K_v=\frac{v_{g\_do\_nom}}{V_{dco}} \quad \text{and} \quad K_s=\frac{i_{g\_do\_nom}}{V_{dco}}$$

By substituting the parameters of K_v and K_s in equation 4.24, DS2 turns into:

$$DS2=\left|\frac{\Delta v_{g\_d}}{\Delta V_{dc}}\right|=\left|\left(\frac{1}{1.5K_s}\right)\frac{1.5K_vK_{iv}}{s}\right|=\left|\left(\frac{1}{1.5\frac{i_{g\_do\_nom}}{V_{dco}}}\right)\frac{1.5\frac{v_{g\_do\_nom}}{V_{dco}}K_{iv}}{s}\right|=\left|\frac{v_{g\_do\_nom}}{i_{g\_do\_nom}}\frac{K_{iv}}{s}\right| \tag{4.25}$$

As seen in equation 4.25, since there is no V_{dco} parameter existing in the equation varying V_{dco} will not influence the dynamic stiffness (DS2) at low frequencies. This is also shown by the simulation results in the left-hand side of Figure 4.14.

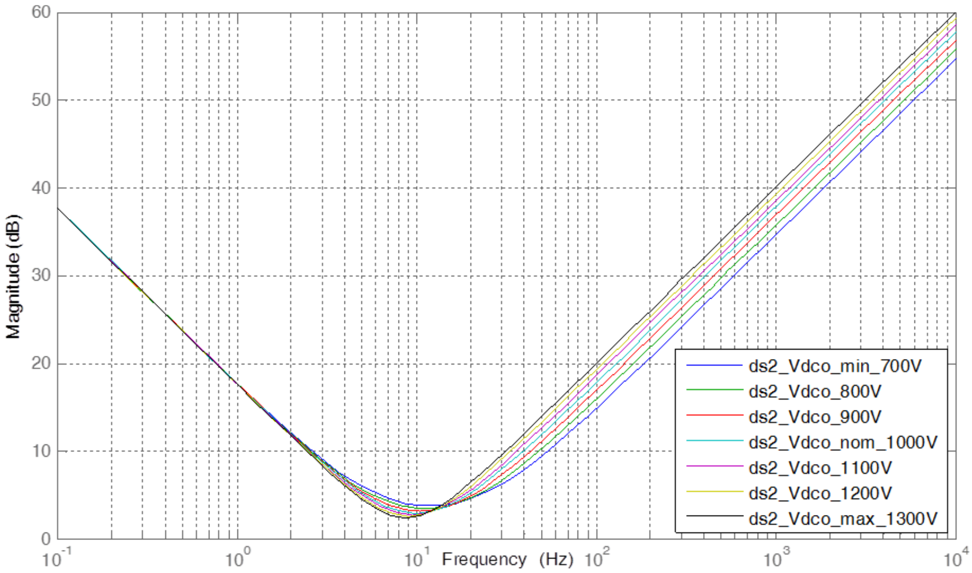

Figure 4.14: Dynamic stiffness analysis of $\Delta v_{g\_d}/\Delta V_{dc}$ (DS2) - Varying V_{dco}

At mid-frequencies, by neglecting the low and high frequency terms and substituting K_s and K_v parameters the DS2 equation will be

$$DS2=\left|\frac{\Delta v_{g\_d}}{\Delta V_{dc}}\right|=\left|\left(\frac{1}{1.5K_s}\right)\frac{1.5K_v(K_s+K_{pv})s}{s}\right|=\left|\frac{v_{g\_do\_nom}}{i_{g\_do\_nom}}\left(\frac{i_{g\_do\_nom}}{V_{dco}}+K_{pv}\right)\right| \tag{4.26}$$

This equation shows that V_{dco} is inversely proportional to DS2 at mid-frequencies, which is also supported by the MATLAB graphs seen in Figure 4.14.

At high frequencies, again by ignoring the low and mid- frequency terms in the equation of DS2, DS2 can then be transformed into:

$$DS2=\left|\frac{\Delta v_{g\_d}}{\Delta V_{dc}}\right|=\left|\left(\frac{1}{1.5K_s}\right)\frac{Cs^2}{s}\right| \text{ and } K_s=\frac{i_{g\_do\_nom}}{V_{dco}} \Rightarrow DS2=\left|\frac{V_{dco}}{i_{g\_do\_nom}}\frac{Cs}{1.5}\right| \tag{4.27}$$

Equation 4.27 tells that DS2 is direct proportional to V_{dco}. Increasing V_{dco} increases the dynamic stiffness (DS2) while decreasing V_{dco} decreases DS2. This relation is perfectly justified in the right-hand side of Figure 4.14.

Finally, the maths calculations and the simulation results in MATLAB undertaken for V_{dco} sensitivity analysis are consistent each other. This shows that the system works correctly.

The sensitivity analysis of varying V_{dco} is summarised in Tables 4.2 and 4.3. In Table 4.2, the bandwidths of seven operating points of V_{dc} for different transfer functions are presented. Table 4.3 shows the approximate damping ratios corresponding the each operating points of V_{dco}.

Transfer Function Types / Varying V_{dco}	Full Transfer Function (FTF)	Transfer Function (TF)	Simplified Transfer Function (STF)	Second-order Approximated Transfer Function (SoATF)	Simplified Second-order Approximated Transfer Function (SSoATF)	
					Read on Bode diagrams	Mathematical Results
700 V (min)	18 Hz	18.3 Hz	26.7 Hz	5.92 Hz	9.82 Hz	11.95 Hz
800 V	17.8 Hz	17.9 Hz	24.1 Hz	6.4 Hz	9.9 Hz	11.18 Hz
900 V	17.5 Hz	17.5 Hz	22.1 Hz	6.85 Hz	10 Hz	10.54 Hz
1 kV (nom)	17 Hz	17 Hz	20.4 Hz	7.24 Hz	10.1 Hz	10 Hz
1.1 kV	16.4 Hz	16.4 Hz	19.1 Hz	7.6 Hz	9.99~ Hz	9.535 Hz
1.2 kV	15.8 Hz	15.8 Hz	18 Hz	7.86 Hz	9.9 Hz	9.129 Hz
1.3 kV (max)	15.3 Hz	15.3 Hz	17 Hz	8.05 Hz	9.81 Hz	8.77 Hz

Table 4.2: Summary of bandwidths obtained from MATLAB results (Bode diagrams) for V_{dc} Operating Points

Varying V_{dco}	Approximate Damping Ratio on Bode diagrams	Calculated Approximate Damping Ratio
700 V (min)	0.941	0.837
800 V	0.887	0.783
900 V	0.843	0.738
1 kV (nom)	0.804	0.7
1.1 kV	0.77	0.666
1.2 kV	0.74	0.639
1.3 kV (max)	0.71	0.614

Table 4.3: Summary of approximate damping ratios obtained from MATLAB results using forward-path transfer function (FpTF) and calculated approximate damping ratios for V_{dc} Operating Points

The V_{dco} sensitivity analysis work is also simulated in PSCAD/EMTDC programme. Seven different graphs are merged together and illustrated in Figure 4.15. The PSCAD simulation results ties up with the mathematical calculations and MATLAB results.

Damping decreases as V_{dco} increases (overshoot becomes larger), and bandwidth also decreases (settling time increases). Care must be taken for the second-order approximated transfer function which does not show this behaviour (see Table 4.2). This may therefore be a simplification too far for detailed analysis.

Note that the PSCAD simulation results are based on a system consisting of the grid-side inverter on its own. Simulations of the full system were undertaken and some example graphs are given in Figure A.3.26, but here other sub-system dynamics interference masks the main behaviour under consideration in Figure 4.15.

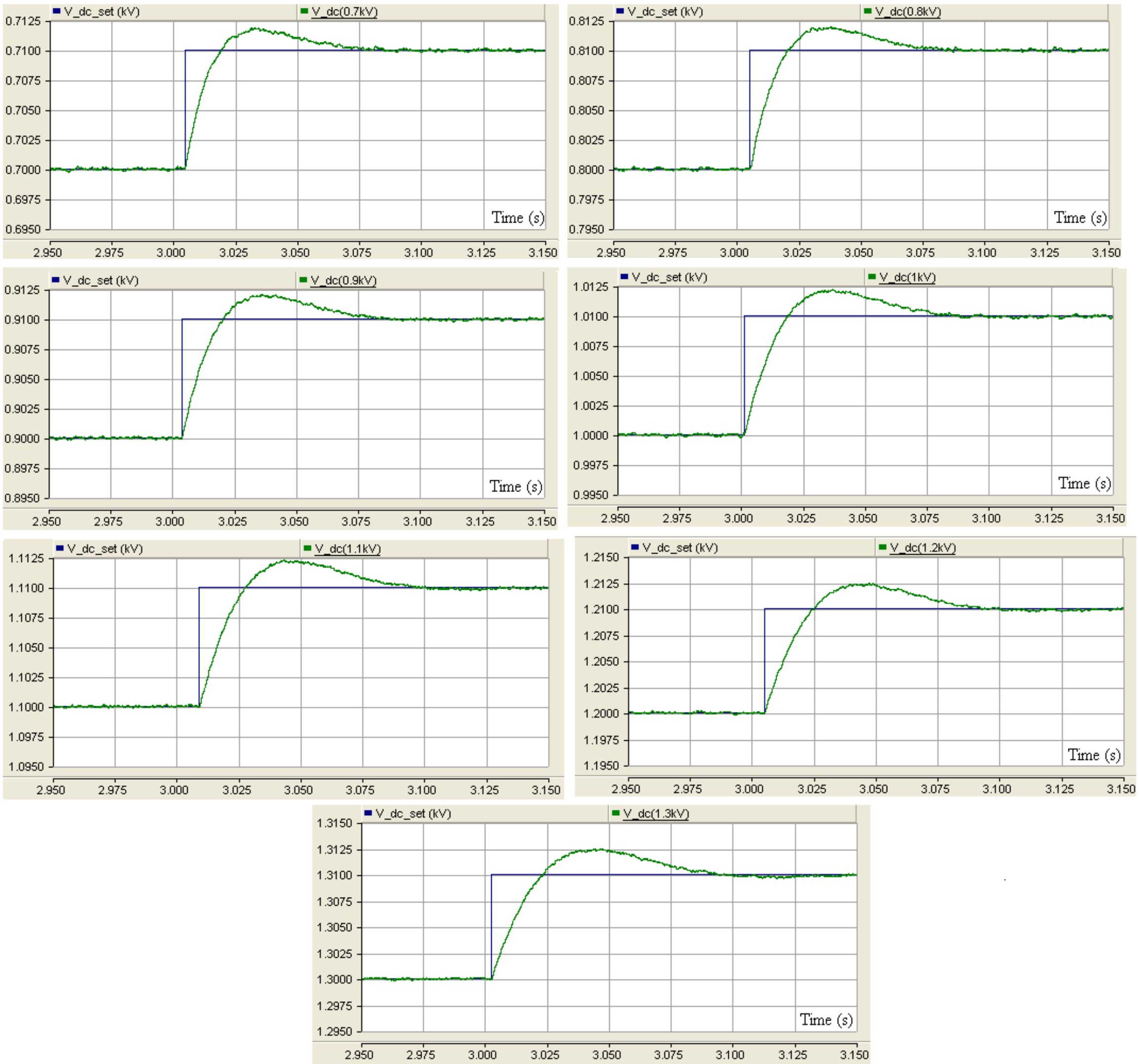

Figure 4.15: PSCAD simulation results of V_{dco} sensitivity

4.5.2 v_{g_do} Sensitivity

The sensitivity analysis of v_{g_do} is undertaken by selecting seven different operating points, while V_{dco} and i_{g_do} are fixed at V_{dco_nom} and $i_{g\_do\_nom}$, which are 1kV and 2.76kA, respectively. The seven operating points chosen for v_{g_do} are: 228.62V, 261.28V, 293.94V, 326.6V, 359.26V, 391.92V, and 424.58V. Note that as v_{g_do} varies, so does the K_v parameter; while K_s remains constant at 2.76 (A/V) for all operating points of v_{g_d} since V_{dco} and i_{g_do} are not varied. It is seen that the K_v is directly proportional to v_{g_do}.

The full transfer function (FTF-including inner loop) and transfer function (TF-neglecting inner loop) in the case of varying only v_{g_do} are depicted as Bode diagrams in Figures 4.16 and 4.17. The bandwidths across the same operating points in the lower graphs of these figures are effectively the same. So, simplifying the full transfer function (FTF) to the transfer function (TF) is feasible and proved by the simulation results.

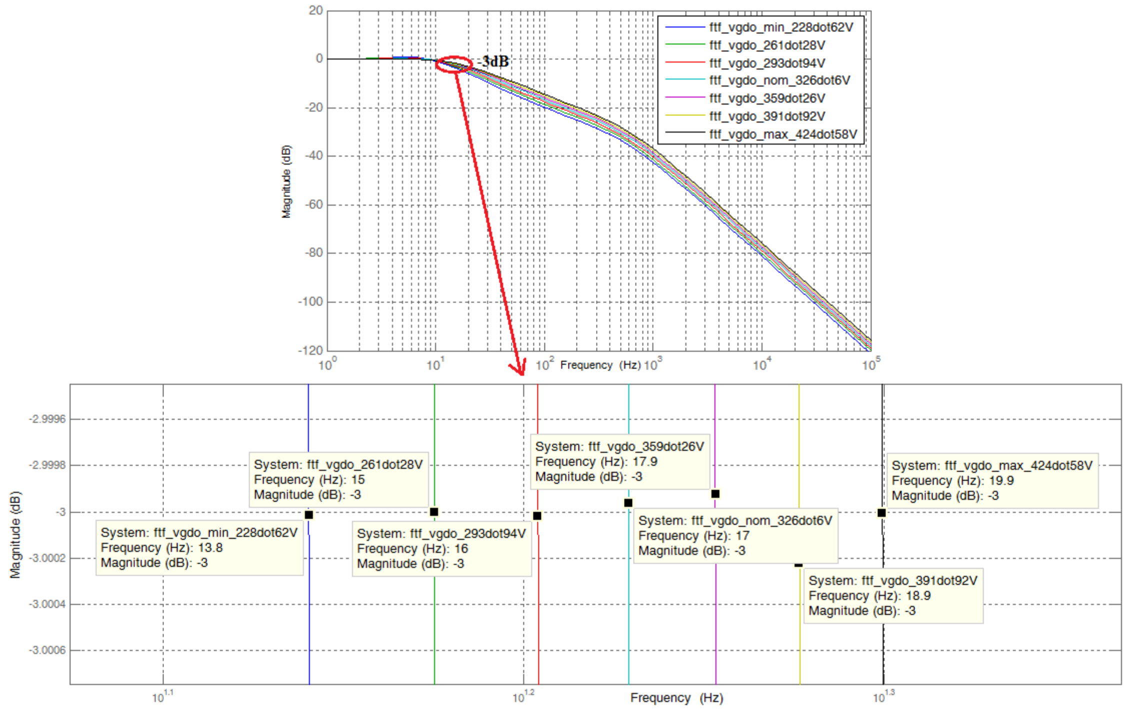

Figure 4.16: Bandwidths representation on the full transfer function - Varying v_{g_do}

In Figures 4.16 and 4.17, as v_{g_do} increases the bandwidth corresponding the operating points also increases. To relate this result to mathematical analysis, the undamped natural frequency (ω_n) equation is derived (see equation 4.17). In equation 4.17, the ω_n is direct proportional to $\sqrt{v_{g\_do}}$. Increasing v_{g_do} noticeably causes an increase in the bandwidth. Therefore, the simulation results are consistent with the mathematical calculations.

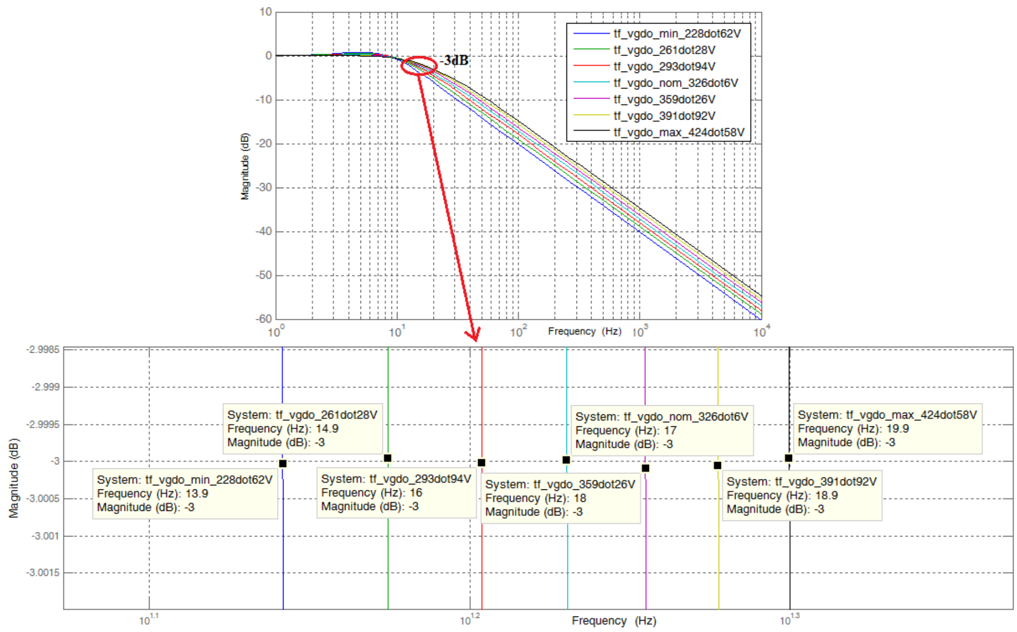

Figure 4.17: Bandwidths representation on the transfer function - Varying v_{g_do}

The K_s term ($1.5K_vK_ss$) in the denominator of the transfer function (TF) is neglected in order to obtain the simplified transfer function (STF). In case of varying v_{g_do}, since only K_v parameter changes (K_s remains constant as it is independent from v_{g_do}) the neglected term ($1.5K_vK_s$) varies less than in case of varying V_{dco} (see section 4.5.1). The relationship between the bandwidth and v_{g_do} is still same as in the Bode diagrams of the full transfer function and the transfer function.

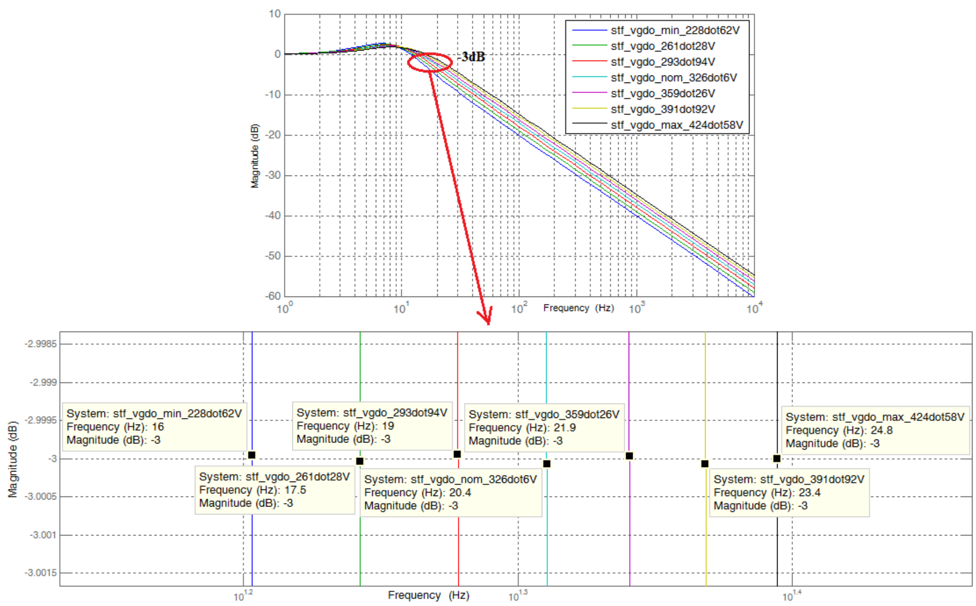

Figure 4.18: Bandwidths representation on the simplified transfer function - Varying v_{g_do}

In Figure 4.18, as v_{g_do} increases the difference in bandwidths corresponding the same operating point for the simplified transfer function (STF) and transfer function (TF) gets bigger. The biggest change occurs in the maximum operating point of v_{g_d} (the bandwidth at $v_{g\_do\_max}$ in the TF is 19.9Hz, and that in the STF is 24.8Hz). Likewise in the operating point analysis of V_{dc}, this variation due to the simplification from the transfer function to the simplified transfer function can reasonably be considered as accurate enough from the viewpoint of an initial tuning study. Since only K_v changes while K_s stays fixed, the $1.5K_vK_ss$ term has less effect on the system in comparison to the V_{dco} sensitivity analysis. Therefore, v_{g_do} affects the system response less than V_{dco} does. The sensitivity analyses of v_{g_do} for the second-order approximated transfer function (SoATF) and the simplified second-order approximated transfer function (SSoATF) will be shown in A.3.2.2.

In order to examine the approximate damping ratio for each operating point of v_{g_d}, the forward-path transfer function is derived and the Bode diagram for that function is illustrated in Figure 4.19. The same equations of phase margin and damping ratio used in section 4.5.1 are also utilised in this section. Equation 4.18 shows a direct relation between the v_{g_do} and the damping ratio. This means that if v_{g_do} increases so does the approximate damping ratio corresponding the operating points. Since the forward-path transfer function is used to estimate the approximate damping ratios on the Bode diagram, the actual calculated damping ratios are slightly different. But, the relationship between the damping ratio and v_{g_do} is same. In both Bode diagrams (see Figure 4.19) and the mathematical analysis, as v_{g_do} increases the damping ratio also increases. Thus, the simulation results match the mathematical calculations.

The dynamic stiffness analyses of the system are tested with respect to the disturbance current and the grid voltage in case of varying v_{g_do}. The Bode diagrams of the dynamic stiffness work (DS1 and DS2) are presented in Figures 4.20 and 4.21. DS1 and DS2 are at low, mid- and high frequencies are investigated.

Equation 4.21 is used in order to examine DS1 at low frequencies:

$$DS1=\left|\frac{1.5v_{g\_do}K_{iv}}{V_{dco\_nom}s}\right|$$

To investigate the dynamic stiffness analysis (DS1) for mid-frequencies, in case the low and high frequency terms are ignored, the DS1 equation (4.22) is used:

$$DS1=\left|\frac{1.5v_{g\_do}(K_s+K_{pv})}{V_{dco\_nom}}\right|$$

At low and mid-frequencies, v_{g_do} is directly proportional to DS1 increases as well. This relation is also seen in Figure 4.20, which means that the simulation results match the theory, and the system analysis works.

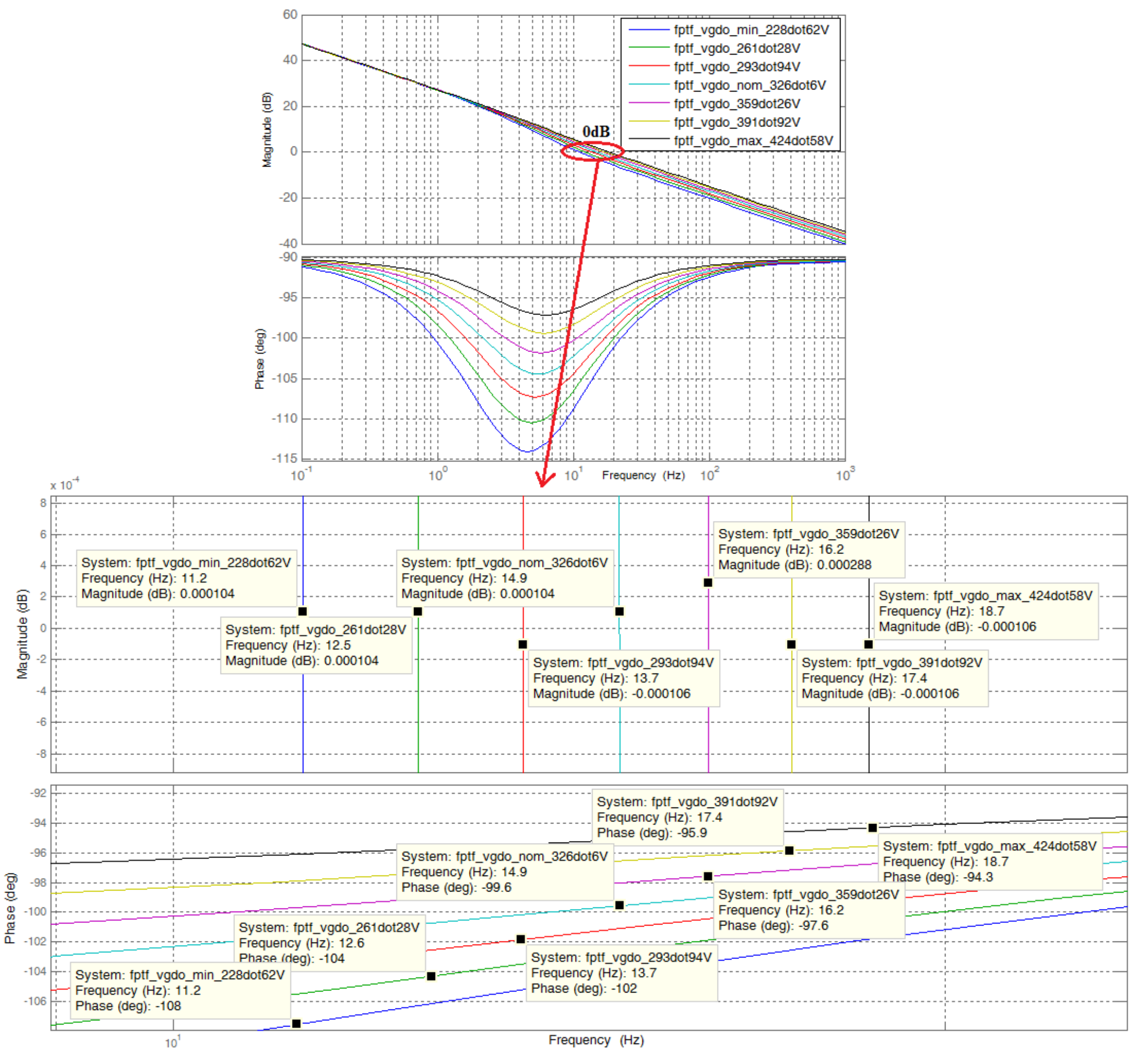

Figure 4.19: Damping ratios representation on the forward-path transfer function - Varying v_{g_do}

At high frequencies, by ignoring the low and mid- frequency terms the DS1 equation turns into equation 4.23, which is:

$$DS1=|Cs|$$

As understood from equation 4.23, at high frequencies there is no effect of varying v_{g_do} on DS1. This is also seen in the right-hand side of Figure 4.20. Again, the theory is consistent with the simulation results.

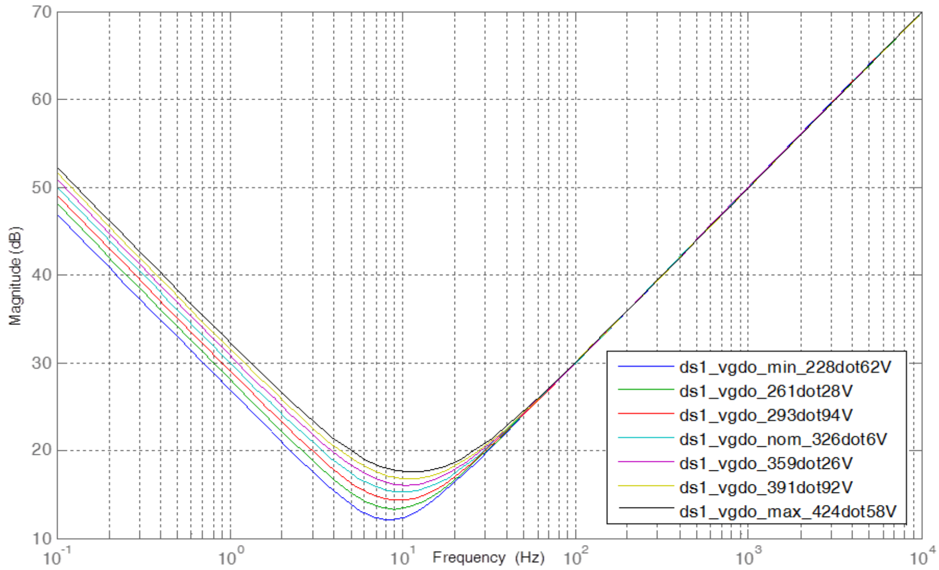

Figure 4.20: Dynamic stiffness analysis of $\Delta i_n/\Delta V_{dc}$ (DS1) - Varying v_{g_do}

For the investigation of DS2 at low frequencies, equation 4.25 is again utilised.

$$DS2=\left|\frac{v_{g\_do}}{i_{g\_do\_nom}}\frac{K_{iv}}{s}\right|$$

At mid-frequencies, by neglecting low and high frequency terms the equation of DS2 is simplified to:

$$DS2=\left|\frac{v_{g\_do}}{i_{g\_do\_nom}}(K_s+K_{pv})\right|$$

The equations of DS2 for both low and mid-frequency investigations reveal a direct relationship between DS2 and v_{g_do}. In other words, increasing v_{g_do} increases the DS2, or deceasing v_{g_do} decreases DS2 at low and mid-frequencies. This relationship can be also seen in Figure 4.21.

At high frequencies, in order to find out the relation between v_{g_do} and the DS2, equation 4.27 can be re-used.

$$DS2=\left|\frac{V_{dco\_nom}}{i_{g\_do\_nom}}\frac{Cs}{1.5}\right|$$

Since there is no v_{g_do} parameter existing in the equation of DS2, increasing or decreasing v_{g_do} does not influence DS2 response at high frequencies. This is clearly seen on the right half of Figure 4.21.

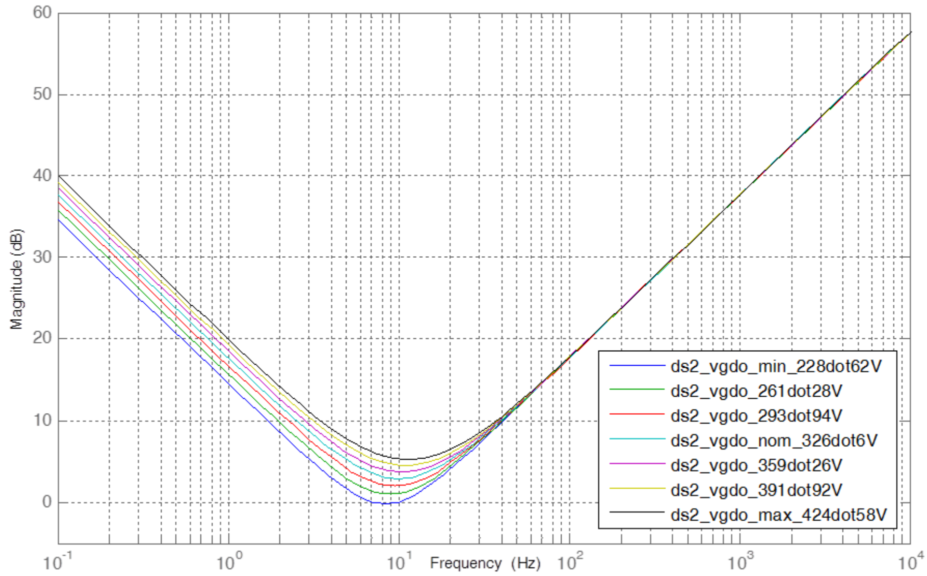

Figure 4.21: Dynamic stiffness analysis of $\Delta v_{g\_d}/\Delta V_{dc}$ (DS2) - Varying v_{g_do}

Tables 4.4 and 4.5 summarise the sensitivity analysis work undertaken for varying v_{g_do}. While Table 4.4 shows the bandwidths of seven operating points of v_{g_do} for different transfer functions, the approximate damping ratios corresponding the each operating points of v_{g_do} are presented in Table 4.5.

Transfer Function Types / Varying v_{g_do}	Full Transfer Function (FTF)	Transfer Function (TF)	Simplified Transfer Function (STF)	Second-order Approximated Transfer Function (SoATF)	Simplified Second-order Approximated Transfer Function (SSoATF)	
					Read on Bode diagrams	Mathematical Results
228.62 V (min)	13.8 Hz	13.9 Hz	16 Hz	7.6 Hz	9.69 Hz	8.367 Hz
261.28 V	15 Hz	14.9 Hz	17.5 Hz	7.54 Hz	9.93 Hz	8.944 Hz
293.94 V	16 Hz	16 Hz	19 Hz	7.38 Hz	9.98 Hz	9.487 Hz
326.6 V (nom)	17 Hz	17 Hz	20.4 Hz	7.24 Hz	10.1 Hz	10 Hz
359.26 V	17.9 Hz	18 Hz	21.9 Hz	7.14 Hz	10 Hz	10.488 Hz
391.92 V	18.9 Hz	18.9 Hz	23.4 Hz	6.99 Hz	9.93 Hz	10.954 Hz
424.58 V(max)	19.9 Hz	19.9 Hz	24.8 Hz	6.86 Hz	9.87 Hz	11.4 Hz

Table 4.4: Summary of bandwidths obtained from MATLAB results (Bode diagrams) for v_{g_d} Operating Points (Note that v_{g_d} is phase-rms voltage)

Varying v_{g_do}	Approximate Damping Ratio on Bode diagrams	Calculated Approximate Damping Ratio
228.62 V (min)	0.72	0.68
261.28 V	0.76	0.71
293.94 V	0.78	0.74
326.6 V (nom)	0.804	0.76
359.26 V	0.824	0.78
391.92 V	0.841	0.8
424.58 V (max)	0.857	0.811

Table 4.5: Summary of approximate damping ratios obtained from MATLAB results using forward-path transfer function (FpTF) and calculated approximate damping ratios for v_{g_d} Operating Points

The v_{g_do} sensitivity analysis work is run in PSCAD/EMTDC programme. For seven different operating points seven graphs are generated and shown together in Figure 4.22. The PSCAD simulation results are consistent with the mathematical calculations and MATLAB results. A few example graphs for full system simulation are presented in Figure A.3.27.

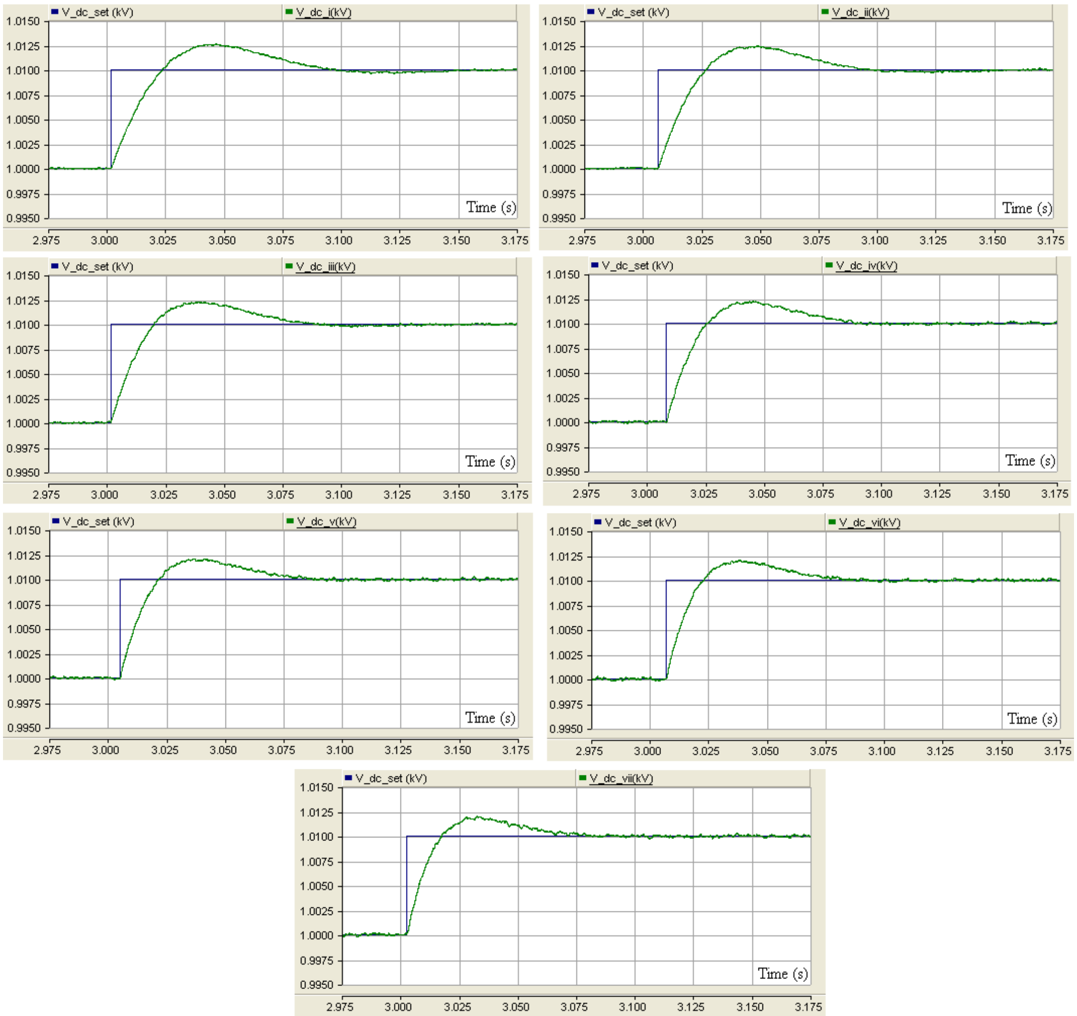

Figure 4.22: PSCAD simulation results of v_{g_do} sensitivity

4.5.3 i_{g_do} Sensitivity

The i_{g_do} sensitivity analysis is realised by adopting seven different operating points, while V_{dco} and v_{g_do} are held constant at V_{dco_nom} and $v_{g\_do\_nom}$, which are 1kV and 326.6V, respectively. The seven operating points selected for i_{g_do} are: 1928.97A, 2204.54A, 2480.11A, 2755.68A, 3031.24A, 3306.81A, and 3582.38A. Note that as i_{g_do} varies so does the K_s parameter; while the K_v remains constant at 0.327 since V_{dco} and v_{g_do} do not change. Therefore, in the case of varying i_{g_do} it is anticipated that the K_s equates to i_{g_do}.

The Bode diagrams of the full transfer function (FTF) and transfer function (TF) for seven operating point of i_{g_d} are depicted in Figures 4.23 and 4.24, respectively. In the denominator of the equations of FTF and TF, the term including the K_s parameter is not neglected. However, to find out the equations of undamped natural frequency (ω_n) and the approximate damping ratio (ζ) (see equations 4.15 and 4.16), the simplified second-order approximated transfer function (SSoATF) excluding the K_s term is used. Therefore, mathematical analysis shows that there is no effect of varying i_{g_do} on the bandwidth (BW) and damping. In fact, there is an interaction between the i_{g_do} and the BW and damping. But, as seen in the lower graphs of Figures 4.23 and 4.24, the biggest change, which occurs between the minimum and maximum operating point of i_{g_d} (minimum and maximum bandwidths are 15.7Hz and 18.2Hz, respectively). Since the difference between the minimum and maximum values of bandwidths is low enough, the relation between the i_{g_do} and the tuning parameters could then be neglected.

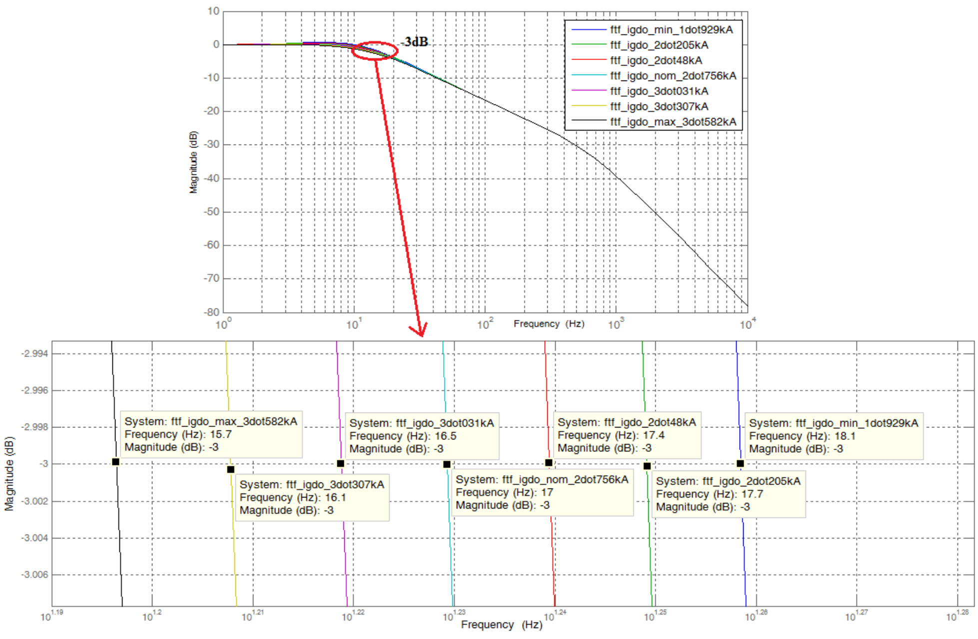

Figure 4.23: Bandwidths representation on the full transfer function - Varying i_{g_do}

By examining the lower graphs of Figures 4.23 and 4.24, it is seen that the bandwidths of each operating points of i_{g_d} are effectively same in the full transfer function and transfer function. So, simplifying the full transfer function to the transfer function derived by assuming that the inner loop gain is 1 can be possible, and the simulation results show that this is reasonable.

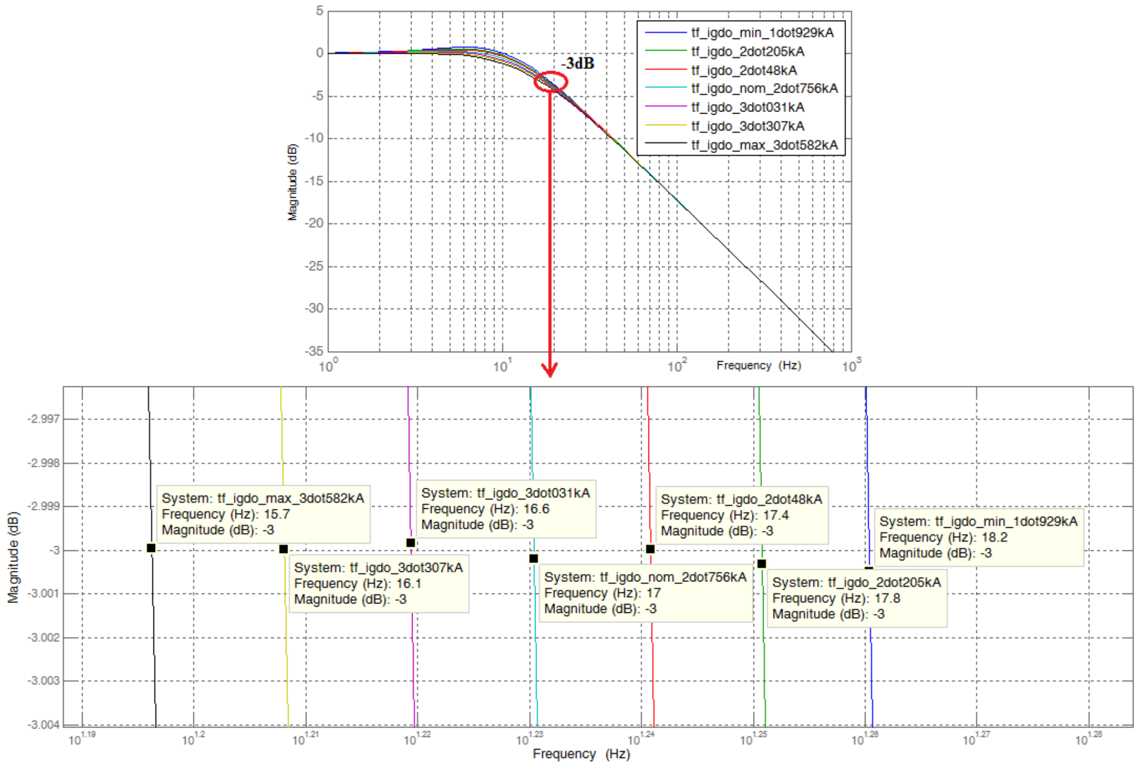

Figure 4.24: Bandwidths representation on the transfer function - Varying i_{g_do}

The simplified transfer function (STF) of the system for seven operating points of i_{g_d} is shown in Figure 4.25. The STF is formed by neglecting the term with the K_s parameter in the transfer function (TF). As i_{g_do} changes the K_s parameter also changes. However, since there is no K_s in the STF, for all seven operating points the bode diagrams of the STF are same as seen in Figure 4.25. The maximum change in bandwidth occurs between the maximum operating point of i_{g_d} in the TF and any operating point of i_{g_d} in the STF (the minimum bandwidth of the TF is 15.7Hz, while the bandwidth of the STF is 20.5Hz). Note that the bandwidth is same for all i_{g_do} points in the STF. Varying i_{g_do} affects the K_s which is already included in the FTF and TF. So, the difference in the bandwidth of FTF (or TF) and STF is slightly higher than that for the v_{g_d} operating point analysis. However, this difference may reasonably be regarded as accurate enough from an initial tuning point of view.

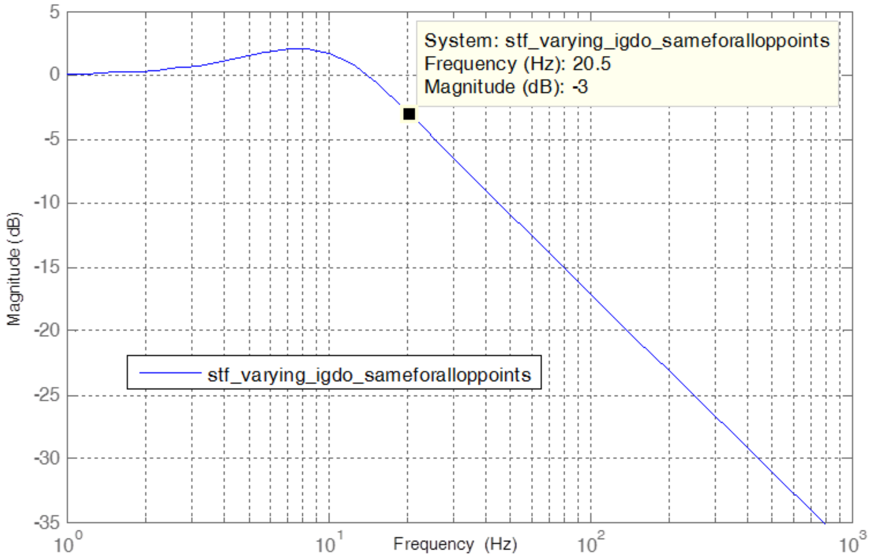

Figure 4.25: Bandwidth representation on the simplified transfer function - Varying i_{g_do}

The forward-path transfer function (FpTF) for i_{g_do} sensitivity analysis is simulated in MATLAB and depicted for all seven operating points of i_{g_d}. The FpTF is used to calculate the damping ratios by reading the phase (deg) of each operating points corresponding the 0dB line in the upper graph of Figure 4.26. As seen in equation 4.18, there is no i_{g_do} term in the equation of the approximate damping ratio. So, varying i_{g_do} does not influence the damping ratio. But, if the full transfer function or transfer function is considered, there is an effect of changing i_{g_do} on the damping ratio. Moreover, the forward-path transfer function cannot show the exact results since some parameters needed to be neglected. In the lower graph of Figure 4.26, the lowest and the highest damping ratios can be calculated as 0.76 and 0.848, respectively. As a reminder, the nominal damping ratio was set to 0.7. The differences between the lowest and highest damping ratios and the nominal damping ratio are 8.57% and 21.14%, respectively. However, there is an 11.58% difference seen between the lowest and the highest damping ratios by taking the lowest damping ratio (0.76) as reference. This percentage could be considered as reasonable in terms of control theory.

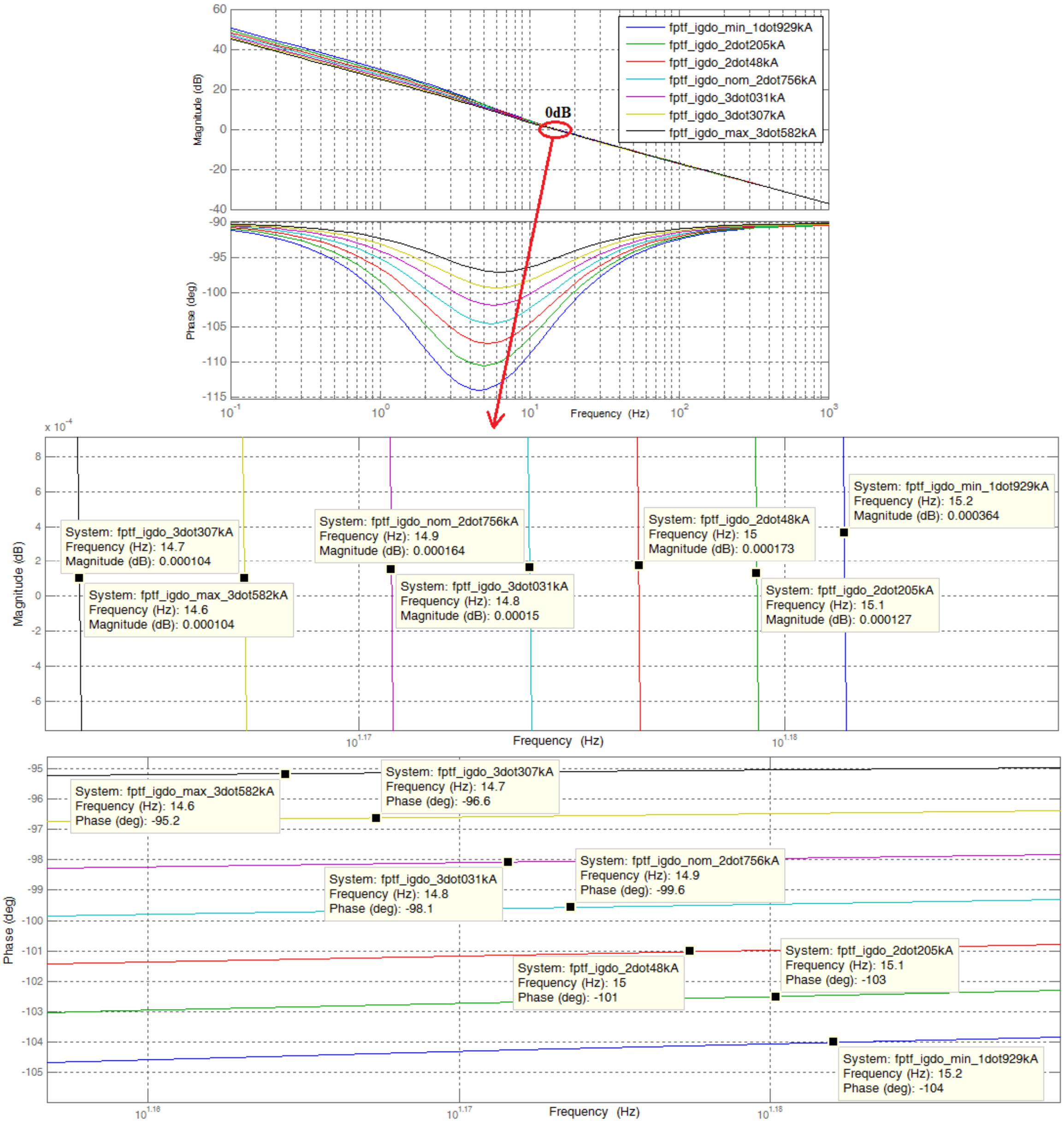

Figure 4.26: Damping ratios representation on the forward-path transfer function - Varying i_{g_do}

At both low (neglecting mid- and high frequency terms) and high frequency (neglecting low and mid-frequency terms) equations 4.21 and 4.23 were derived. In these equations since there is no i_{g_do} term, DS1 is not affected by changing i_{g_do}. This is clearly seen in Figure 4.27. As seen in the right- and left-hand sides of Figure 4.27, DS1 does not change with i_{g_do}. For mid-frequencies, the equation (4.22) of DS1 can be re-written by ignoring low and high frequency terms as:

$$DS1=\left|\frac{\Delta i_n}{\Delta V_{dc}}\right|=\left|1.5K_v(K_s+K_{pv})\right|$$

and by substituting the K_s

$$DS1=\left|1.5K_v\left(\frac{i_{g\_do\_nom}}{V_{dco}}+K_{pv}\right)\right| \tag{4.28}$$

Equation 4.28 shows the direct proportional relationship between DS1 and i_{g_do}. So, for mid-frequencies, increasing i_{g_do} increases DS1, which makes the system stiffer. This relationship is also seen in Figure 4.27. The theory matches the simulation results then.

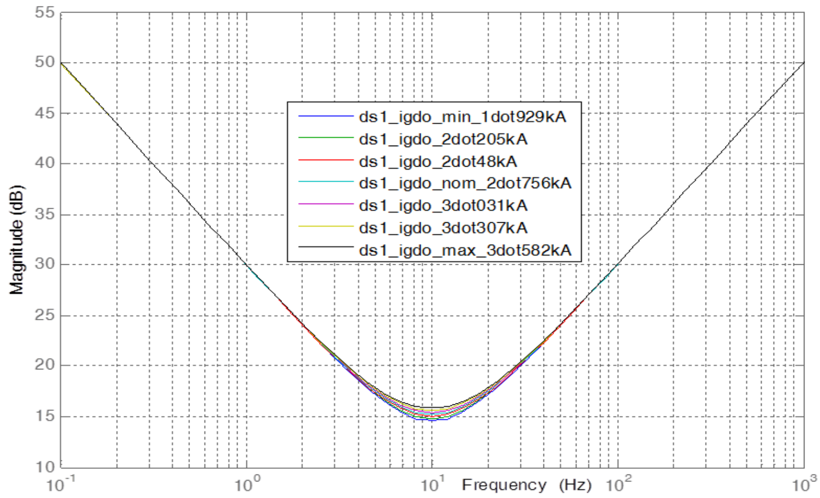

Figure 4.27: Dynamic stiffness analysis of $\Delta i_n/\Delta V_{dc}$ (DS1) - Varying i_{g_do}

In all conditions (at low, mid- and high frequencies), varying i_{g_do} changes DS2. The equations of DS2 in all conditions can be derived by reconfiguring equation 4.14 and substituting the K_s in this equation.

$$DS2=\left|\frac{\Delta v_{g\_d}}{\Delta V_{dc}}\right|=\left|\left(\frac{1}{1.5K_s}\right)\frac{Cs^2+1.5K_v(K_s+K_{pv})s+1.5K_vK_{iv}}{s}\right|$$

$$\text{At low frequency} \Rightarrow \quad DS2=\left|\frac{\Delta v_{g\_d}}{\Delta V_{dc}}\right|=\left|\frac{V_{dco\_nom}}{i_{g\_do}}\frac{K_vK_{iv}}{s}\right| \tag{4.29}$$

$$\text{At mid-frequency} \Rightarrow \quad DS2=\left|\frac{\Delta v_{g\_d}}{\Delta V_{dc}}\right|=\left|\frac{V_{dco\_nom}}{i_{g\_do}}K_vK_{pv}+K_v\right| \tag{4.30}$$

$$\text{At high frequency} \Rightarrow \quad DS2=\left|\frac{\Delta v_{g\_d}}{\Delta V_{dc}}\right|=\left|\frac{V_{dco\_nom}}{i_{g\_do}}\frac{Cs}{1.5}\right| \tag{4.31}$$

At low, mid- and high frequencies, DS2 is obviously inversely proportional to i_{g_do}. So, increasing i_{g_do} decreases DS2 and decreasing i_{g_do} increases DS2. This relation can be seen in Figure 4.28. So, for the sensitivity analysis of i_{g_do}, the simulation results show the consistency with the mathematical calculations.

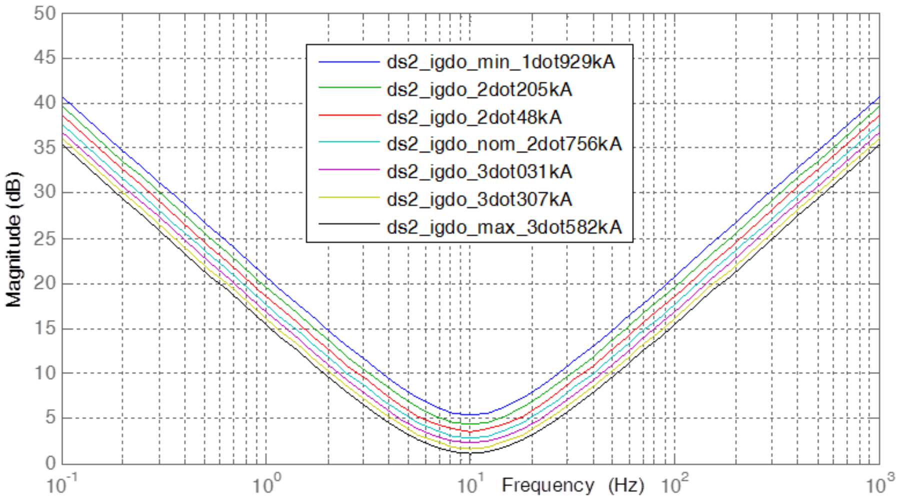

Figure 4.28: Dynamic stiffness analysis of $\Delta v_{g\_d}/\Delta V_{dc}$ (DS2) - Varying i_{g_do}

Operating point sensitivity analyses for V_{dc}, v_{g_d}, and i_{g_d} were carried out. All simulation results for these variables are reasonably consistent with the mathematical calculations. The reasonable differences are sourced from the simplifications of the transfer functions by neglecting the related terms. However, form the point of control theory view, these simplifications could be possible and the differences between the theory and simulation could be acceptable.

The i_{g_do} sensitivity analysis is briefly summarised in Tables 4.6 and 4.7. In these tables, the bandwidths and approximate damping ratios corresponding the each i_{g_d} operating points are given. In the simulation circuit, since it is impossible to manually enter the set values of i_{g_d}, the PSCAD results cannot be shown. Note that i_{g_d} is dependent on the rated power and base grid voltage. The mathematical calculations well match the MATLAB results.

Transfer Function Types / Varying i_{g_do}	Full Transfer Function (FTF)	Transfer Function (TF)	Simplified Transfer Function (STF)	Second-order Approximated Transfer Function (SoATF)	Simplified Second-order Approximated Transfer Function (SSoATF)	
					Read on Bode diagrams	Maths Results
1.929 kA (min)	18.1 Hz	18.2 Hz	20.5 Hz	8.02 Hz	10.1 Hz	10 Hz
2.205 kA	17.7 Hz	17.8 Hz	20.5 Hz	7.73 Hz	10.1 Hz	10 Hz
2.48 kA	17.4 Hz	17.4 Hz	20.5 Hz	7.47 Hz	10.1 Hz	10 Hz
2.756 kA (nom)	17 Hz	17 Hz	20.5 Hz	7.24 Hz	10.1 Hz	10 Hz
3.031 kA	16.5 Hz	16.6 Hz	20.5 Hz	7.02 Hz	10.1 Hz	10 Hz
3.307 kA	16.1 Hz	16.1 Hz	20.5 Hz	6.82 Hz	10.1 Hz	10 Hz
3.582 (max)	15.7 Hz	15.7 Hz	20.5 Hz	6.6 Hz	10.1 Hz	10 Hz

Table 4.6: Summary of bandwidths obtained from MATLAB results (Bode diagrams) for i_{g_d} Operating Points

Varying i_{g_do}	Approximate Damping Ratio on Bode diagrams	Calculated Approximate Damping Ratio
1.929 (min)	0.76	0.7
2.205 kA	0.77	0.7
2.48 kA	0.79	0.7
2.756 kA (nom)	0.804	0.7
3.031 kA	0.819	0.7
3.307 kA	0.834	0.7
3.582 kA (max)	0.848	0.7

Table 4.7: Summary of approximate damping ratios obtained from MATLAB results using forward-path transfer function (FpTF) and calculated approximate damping ratios for i_{g_d} Operating Points

The dynamic stiffness analyses of $\Delta i_n/\Delta V_{dc}$ (DS1) and $\Delta v_{g\_d}/\Delta V_{dc}$ (DS2) for all seven operating points of V_{dc}, v_{g_d}, and i_{g_d} are summarily given in Table 4.8. The relations between these variables and the system dynamic stiffness outputs are reviewed. The MATLAB results are consistent with the mathematical results shown in Table 4.8.

Dynamic Stiffness Analyses		DS1 ($\Delta i_n/ \Delta V_{dc}$)			DS2 ($\Delta v_{g\_d}/ \Delta V_{dc}$)		
		Low Frequency	Mid-Frequency	High Frequency	Low Frequency	Mid-Frequency	High Frequency
Varying V_{dco}	Increasing V_{dco}	Decreasing	Decreasing	No Effective Change	No Effective Change	Decreasing	Increasing
	Decreasing V_{dco}	Increasing	Increasing	No Effective Change	No Effective Change	Increasing	Decreasing
Varying v_{g_do}	Increasing v_{g_do}	Increasing	Increasing	No Effective Change	Increasing	Increasing	No Effective Change
	Decreasing v_{g_do}	Decreasing	Decreasing	No Effective Change	Decreasing	Decreasing	No Effective Change
Varying i_{g_do}	Increasing i_{g_do}	No Effective Change	Increasing	No Effective Change	Decreasing	Decreasing	Decreasing
	Decreasing i_{g_do}	No Effective Change	Increasing	No Effective Change	Increasing	Increasing	Increasing

Table 4.8: Summary of dynamic stiffness analyses for seven operating points of three variables

4.6 Summary

The outer loop (DC-link voltage) control of the grid-side converter was developed. The full transfer function of the controller design was derived and reasonable simplifications were made step by step. The dynamic stiffness analyses of the controller were carried out to find out how stiff the system is against the disturbance current and the grid voltage quantities. Moreover, the operating point sensitivity analyses of the DC-link voltage, grid voltage and current were undertaken in order to estimate which component plays the most important role in the controller design. Lastly, the selected results obtained from both MATLAB and PSCAD simulation programmes are also shown in this chapter to be compared each other and validated against mathematical analysis. It is found out that mathematical calculations are consistent with the MATLAB and PSCAD results. Full MATLAB and selected PSCAD results for all operating points of the three variables can be found in the related appendix section.

Chapter 5 System Control and Protection Coordination

5.1 Introduction

The protection of electronic devices used in the structure of power electronic converters is important in order to protect the overall system from the damaging effects of over-voltage and/or over-current phenomena. These typically occur in the system during the transient process during and after voltage dips or grid faults. Protection allows the cost of replacing the semiconductor devices to be avoided. In most DFIG-based wind turbines, a rotor crowbar circuit is used as an over-current protection circuit while a DC-link brake is used for over-voltage protection. Chapter 5 describes the topologies of the rotor crowbar and DC-link brake protection schemes and how to fit the additional constraints imposed by their control into the overall system. Despite the addition of further generic control algorithms for the rotor crowbar circuit and DC-link brake, the coordination of the protection schemes has been maintained. Enhancements of the protection and control techniques are also included.

The electrical subsystem interaction between the controller loops is minimised by designing control loops so that they do not interfere with each other significantly. Thus, control loop segmentation is realised. Since the system used in this research has significant complexity, the interaction between the loops is not fully eliminated; however, reasonable performance of the system is obtained.

5.2 Controller Loops Segmentation

The principle by which the system control coordination is achieved is by designing the controller loops of the sub-systems (grid-side and rotor-side converters) to be four to ten times slower than the next faster loop. This assumption is used to specify the undamped natural frequency of the control loops. The selection of the undamped natural frequencies (f_n)and damping ratios (ζ) of sub-system controller loops is summarised in Figure 5.1. This system was chosen because it allows simple single-input single-output control formulation for the eventual design engineers in industry. However it does impose f_n constraints on the system, which will be examined in this chapter.

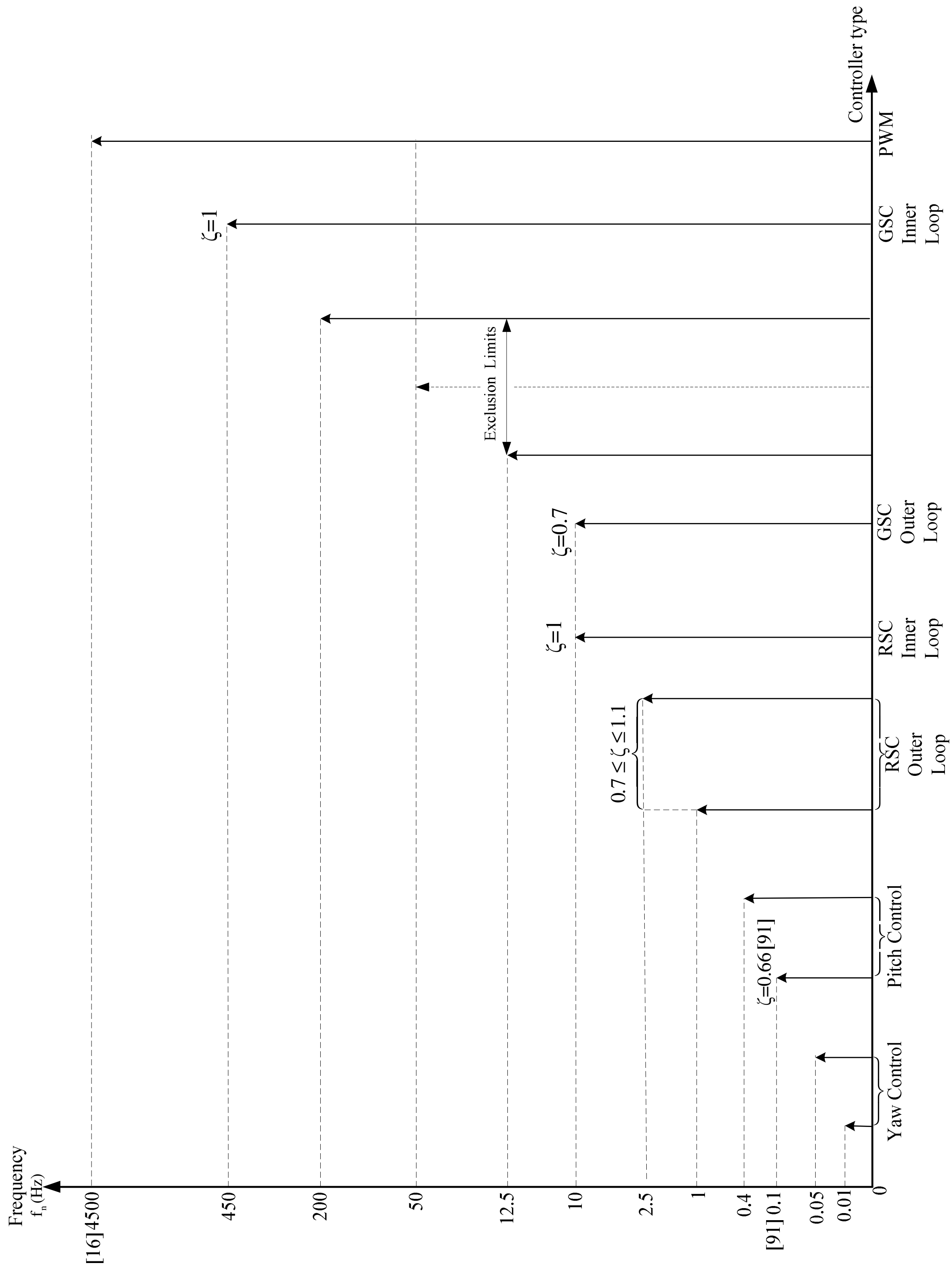

Figure 5.1: The selection of undamped natural frequency (f_n) and damping ratio (ζ) for the controller loops

In a typical second-order closed-loop system, the system response characteristic is function of only dimensionless damping ratio (ζ) and undamped natural frequency (ω_n) since the second-order transfer function includes only ζ and ω_n [88] i.e.:

$$G(s)=\frac{\omega_n^2}{s^2+2\zeta\omega_n s+\omega_n^2}$$

When $\zeta<0$ (negatively damped), the system is unstable. If ζ is 0, then the system is called marginally stable or unstable. These conditions are of interest in control applications only as regions to avoid. When $0<\zeta<1$, the system becomes underdamped which includes oscillatory overshoot, however the system is now stable. Increasing ζ from 0 to 1 decreases the overshoot, and gives less oscillatory response. If ζ is equal to 1, the system is defined as critically damped, which implies the limits between underdamped and overdamped systems. A critically damped system ($\zeta=1$) gives the fastest response without overshoot [89]. The system turns into an overdamped system when $\zeta>1$, and does not have overshoot. However increasing the damping ratio further above 1 (say $\zeta=1.2$ or above) means the system response speed gets slower. Therefore, higher values of the damping ratio should not be chosen if fast response is desired.

In [89], the relationship between the settling time, which defines how fast or slow the system response is, and the system control parameters (ζ and ω_n) are summarised as follows:

- For $\zeta<0.69$, the system settling time is inversely proportional to ω_n and ζ. Having a fast response is possible by increasing ω_n while holding ζ fixed. However, the system response will be more oscillatory. Increasing ζ decreases the overshoot and also gives fewer oscillations in response.

- For $\zeta>0.69$, the system settling time is still inversely proportional to ω_n, but now is also proportional to ζ. Again the settling time can be decreased by increasing ω_n.

The reasonable range of the damping ratios is specified in [89] as being between 0.7 and 1. However, since there is no need to get a very fast rise shape for the power (outer) loop of the RSC controller, a damping ratio of 1.1 is also considered in Figure 5.1.

The fastest component in the system considered in this research is the PWM signal generator whose switching frequency is assigned as 4.5kHz. Typically the switching frequency varies between 2 to 20kHz in power converters of reasonable power using PWM [5]. This range is narrowed to 2.5 – 5kHz in [90] for DFIGs. To get rid of lower order harmonics, the PWM switching frequency should be chosen to be high, although the higher frequency causes more switching losses in the power electronics components. In [25 and 48], the PWM switching frequency is set to 5kHz. In this thesis, the switching frequency of the PWM triangular generator is adopted 4.5kHz as in [16].

The grid-side converter is connected to the grid by a transformer and is responsible for real and reactive power flow regulation to or from the grid. A slower loop than the PWM frequency is necessary for the grid-side converter (GSC) inner (current) loop. The undamped natural frequency (f_n) of the current loop of the grid-side converter is thus defined to be about 10 times slower than the PWM frequency, which is 450Hz. The f_n of the next loop in the cascaded controller, which is the outer (voltage) loop of the grid-side converter, is supposed to be between 112.5Hz (four times slower than the inner loop) and 45Hz (10 times slower than the inner loop). But, if the 50Hz network frequency interference is considered then the f_n of the outer loop of the GSC should be chosen carefully to avoid interactions here. In this work, the exclusion limits are designated four times slower and four times faster than the 50Hz network frequency, which are 12.5Hz and 200Hz. Thus, the f_n of the outer loop of the GSC is selected as 10Hz. So, the outer loop of the GSC is 45 times slower than the inner loop of the GSC, which makes the assumption of neglecting the inner loop (inner loop is fast and G_{inner}=1) reasonable while designing the outer loop control of the GSC. The structure of the inner (current) and outer (voltage) loops of the GSC is shown as a state-feedback system-block (SFSB) diagram in Figure 5.2.

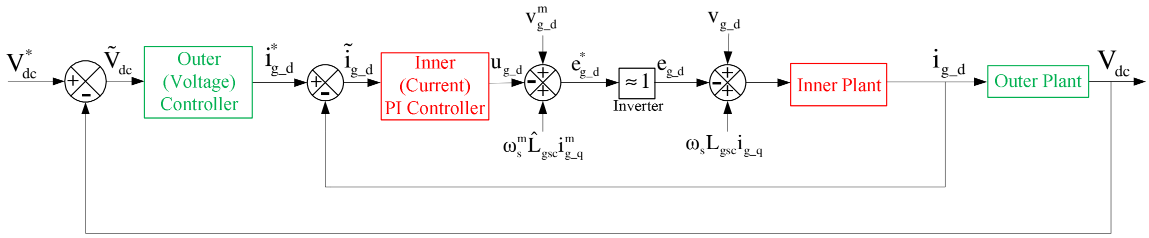

Figure 5.2: The full SFSB diagram of the GSC controller

The rotor-side converter (RSC) mainly controls the active and reactive power of the DFIG by controlling the rotor currents. So, the RSC is supposed to act slower than the GSC, as its control is simplified if it sees a relatively stiff DC-link. It is also controlling the change in aero-mechanical parameters, such as speed and torque, etc. which are generally slower than the 50Hz of the network. Fast action of the rotor-side converter is not desirable if it causes heavy mechanical loading on the drive train. By considering the speed balance of the grid-side converter and the rotor-side converter action, the f_n of the inner (current) loop of the RSC is set to 10Hz which is exactly same as with that of the outer loop of the GSC. This makes it 45 times slower than the comparable (current) loop of the GSC. The f_n of the outer (power) loop of the RSC is then in the range of 1Hz (10 times slower than the inner loop of the RSC) and 2.5Hz (four times slower than the inner loop of the RSC). The power loop of the RSC is then 4 to 10 times slower than the voltage loop of the GSC. The sensitivity analysis of f_n selection for the outer (power) loop of the RSC will be explained in detail in Chapter 6. The full state-feedback system-block (SFSB) diagram of the RSC including both current (inner) and power (outer) loops is depicted in Figure 5.3.

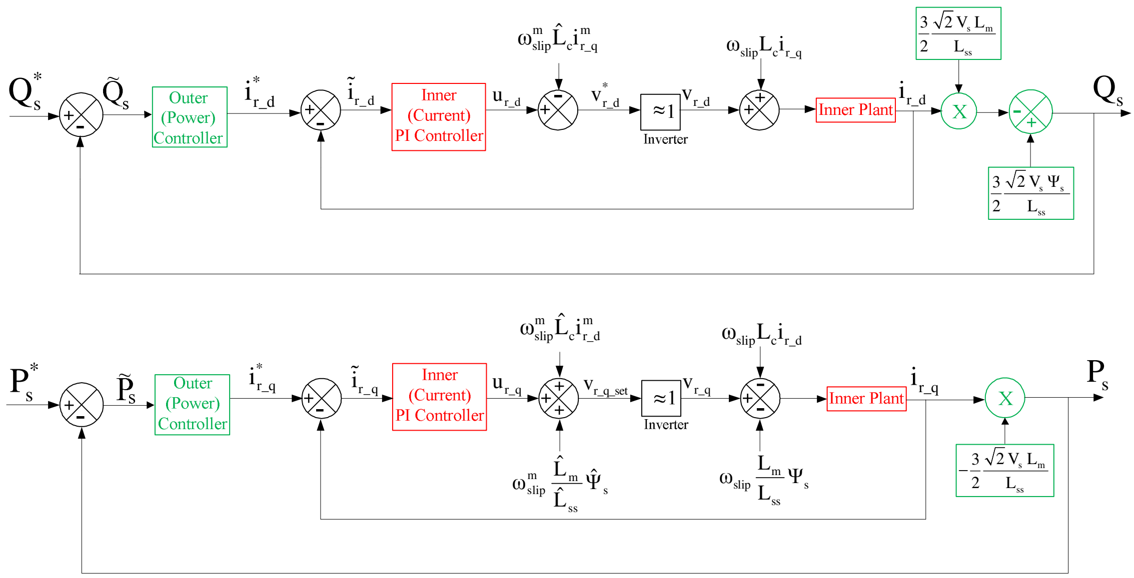

Figure 5.3: The full SFSB diagram of the RSC controller

The slowest controller loop of the whole system is the pitch control, as the pitch angle cannot be changed too quickly. In this work, the pitch control is not designed as it is out of the thesis scope. However, the selection of f_n for the pitch controller loop is also included in Figure 5.1. Typically, the f_n of the pitch control can vary between 0.1Hz and 0.4Hz since it is physically impossible to change or pitch the pitch angle faster. For example, in [91], the f_n of the speed controller using the pitch mechanism is specified as 0.1Hz, which is consistent with the range of f_n for the pitch controller proposed in Figure 5.1. Note that the damping ratio for the pitch controller is set to 0.66 in [91]. The nacelle (e.g. Vestas V164-7.0MW) is approximately 10 times heavier than the blade. So, the yaw control should act slower than the pitch control. Therefore, the f_n of the yaw control can be determined in the range of 0.01Hz and 0.05Hz (Figure 5.1).

It is clear from Figure 5.1 that careful design of the controllers must be used. The pitch control sets a lower frequency limit and the PWM sets an upper frequency limit. The mains frequency sets an exclusion zone. Fitting the controller's undamped natural frequencies into this for the cascaded controllers does not leave much freedom and very careful design coordination is needed. This control needs coordination with the protection systems too.

5.3 Protection Coordination

In case of faults, a rotor crowbar circuit is inserted between the rotor-side converter and the rotor windings. This is to protect the power electronic components of the DFIG system due to over-current occurring in the rotor. A DC-link brake is used to avoid over-voltage in the DC-link capacitor.

5.3.1 Rotor Crowbar Protection

Typically, the function of the crowbar is to short-circuit the rotor through a resistance if the rotor currents exceed threshold values. Once the crowbar protection is activated, the IGBTs of the rotor-side converter are all switched off and integrators of the controllers (e.g. power-outer loop controllers of the RSC) are reset to zero, i.e. the rotor blocks. Consequently, the DFIG system behaves as a squirrel-cage induction generator with a high resistance including additional rotor resistors. The typical crowbar arrangements are shown in Figure 5.4. The crowbar circuit can be designed by placing two pairs of anti-parallel thyristors per phase connected to the rotor terminals (see Figure 5.4.a.) or by using a combination of a diode bridge (rectifier) including a single thyristor and a rotor crowbar resistance (R_{cb}) [92]. The crowbar configurations seen in Figures 5.4.a and b are unable to quickly stop the rotor transient currents limiting the rotor-side converter restarting process. This is considered undesirable from a point of view of the fault ride-through technique [45]. An active crowbar shown in Figure 5.4.c is proposed in [25 and 92] to resolve this. In an active crowbar arrangement, the rotor current can be stopped by using of a forced commutation of the GTO-thyristor or an IGBT [45]. In this work, the crowbar circuit depicted in Figure 5.4.c is used as a rotor crowbar protection of the DFIG-based wind turbine system.

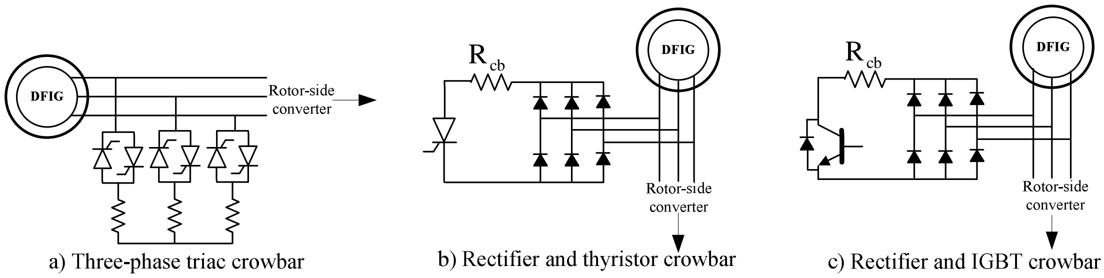

Figure 5.4: Typical crowbar configurations [25]

In [25 and 84], the crowbar is activated if the rotor current exceeds 2pu while this threshold limit is taken down to 1.8pu in [93]. The authors in [94, 95 and 96] propose the crowbar limit as 1.5pu. The control algorithm for the crowbar protection in this work is defined as below and depicted in Figure 5.5.

$$i_{r\_a} \text{ or } i_{r\_b} \text{ or } i_{r\_c} \quad > 2 \text{ pu} \quad \Rightarrow \text{Crowbar ON}$$
$$i_{r\_a} \text{ and } i_{r\_b} \text{ and } i_{r\_c} \quad < 1.9 \text{ pu} \quad \Rightarrow \text{Crowbar OFF}$$

Thus an over-current in any one phase triggers the crowbar. Hysteresis is added and all three phase currents must be less than a lower threshold for the crowbar to be deactivated. In addition, a lock out time may be added which allows the crowbar to stay ON (activated) for a reasonable time. This is maintained by a mono-stable block shown in Figure 5.5. The mono-stable block is used in order to delay the switch-off signal for a desired duration of time. By using this device, once the crowbar triggers it is expected that the crowbar stays switched-on for a fixed time and does not take further switch-on and -off actions. However, if the rotor currents persist exceeding the threshold value, the crowbar can switch on again until the over-current disappears. Nevertheless, reducing the switch-on and off actions of the crowbar can help the whole system become less oscillatory and the switching losses occurring in the system may then be diminished. Moreover, in order to prevent both the crowbar protection and the DC-link brake from being activated at start-up, a time block is added to their control algorithms and causes delay in activation of these protection devices by 0.4s from the beginning of the simulation (Figures 5.5 and 5.7). Therefore, start-up transients inherently existing in the system do not trip protection scheme in error. The difference between inclusion and exclusion of the protection scheme at start-up is presented in Appendix 4 (see Figures A.4.1). The SR (Set-Reset) flip-flop logic diagram and truth table are given in Appendix 4 (see Figure A.4.2). Detailed information on the use of the SR flip-flop logic circuit is documented in [97]. In [25, 95 and 96], the D-type flip flop is used to send the trigger signal to the crowbar switch. However, a manual reset is needed. Therefore, SR-type flip-flops are utilised in the crowbar circuit and the DC-link brake since they have already an automatic reset input.

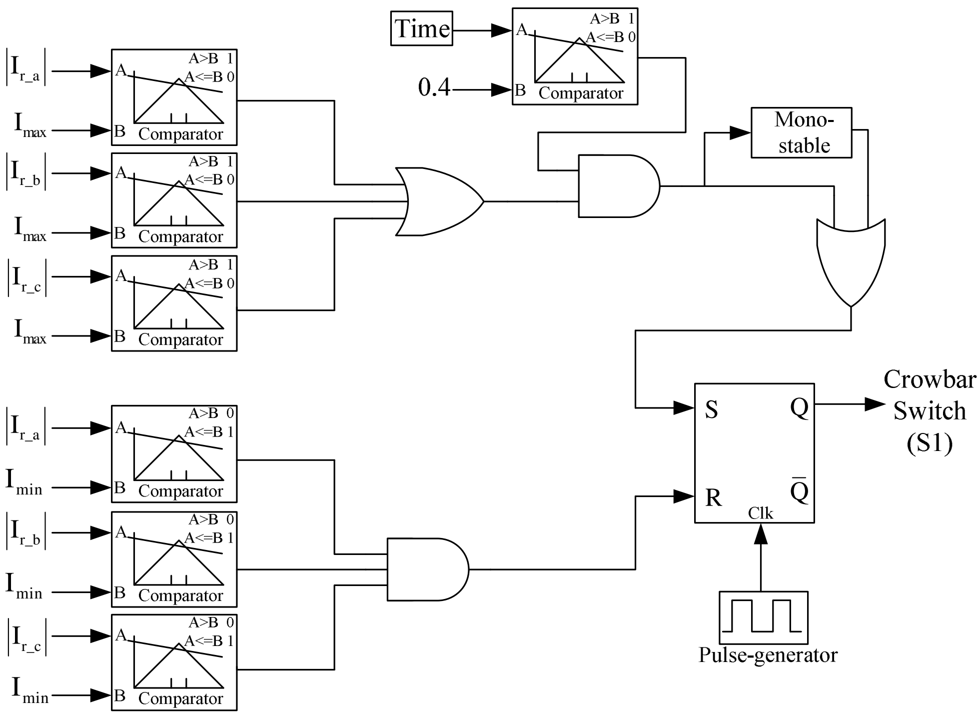

Figure 5.5: The control algorithm of the crowbar protection scheme

In the crowbar protection and the DC-link brake, the signal frequency of the pulse-generator of the SR-type flip flops is set to 4.5kHz, which is same as for the PWM signal generator. In case of over-current and/or over-voltage due to faults, the switches of the protection devices can immediately take action so as to protect the whole system. These protections should activate as fast as the fastest controller of the DFIG system considered in this work (PWM frequency) in order to be able to protect the power electronic devices used in the converters as quickly as the over-current in the rotor and/or over-voltage in the DC-link capacitor are detected. Note that the clock speed of these SR logic circuits employed in the control algorithms of the protection devices should not be set to a frequency higher than the PWM frequency, since in a real application sampling would need to be synchronised with the PWM frequency to reduce noise.

The value of the crowbar resistor, R_{cb}, is typically in the range of 1 to 10 times the rotor resistance, R_r, [36]. However, it is mentioned in [84] that a crowbar resistance higher than $10R_r$ gives satisfactory recovery for the proposed DFIG system. The concern with further increase in crowbar resistance would be very low rotor currents which lead to significant electrical torque reduction and over-speeding of the wind turbine during the disturbance [84].

The equation of the maximum value for the crowbar resistance is formulated in [98] (see equation 5.1).

$$R_{cb} < \frac{V_{r,max} X_s^{'}}{\sqrt{1.6V_s^2 - V_{r,max}^2}} \tag{5.1}$$

where $V_{r,max}$ is the maximum allowable rotor voltage. An approximation of the maximum stator current is derived in [98] as all parameters are transferred to the stator side; therefore the maximum rotor current (reduced on the stator side) will have approximately the same value:

$$i_{s,max} \approx \frac{1.8V_s}{\sqrt{X_s^{'2} + R_{cb}^2}} \tag{5.2}$$

Another way of calculating the rotor crowbar resistance can be found in [25]:

$$i_{cb}R_{cb} < V_{DC} \quad \Rightarrow \quad R_{cb} < \frac{V_{DC}}{1.35 i_r} \tag{5.3}$$

The peak value of stator and rotor currents are given in [25] as

$$\left|\bar{i}_{s,peak}\right| = 1 \big/ \sigma L_{ss} \tag{5.4}$$

$$\left|\bar{i}_{r,peak}\right| = 1 \big/ \sigma L_{rr} \tag{5.5}$$

where

$$\sigma = 1 - \frac{L_m^2}{L_{rr}L_{ss}} \tag{5.6}$$

Substituting equation 5.6 into equations 5.4 and 5.5

$$\left|\bar{i}_{s,peak}\right| = 3.71\text{pu} \approx 4\text{pu} \qquad \text{and} \qquad \left|\bar{i}_{r,peak}\right| = 3.777\text{pu} \approx 4\text{pu}$$

Finally, equation 5.3 turns into equation 5.7 by replacing $i_{r,peak}$

$$R_{cb} < \frac{V_{DC}}{1.35 x 4 i_{r,base}} \quad \Rightarrow \quad R_{cb} < \frac{V_{DC}}{5.4 i_{r,base}} \tag{5.7}$$

The crowbar resistance can then be calculated using equation 5.7 as 0.05Ω.

A typical fault ride-through technique consists of these sequences: fault occurrence (or introducing voltage sag), triggering over-voltage (DC-link brake) and/or over-current protection (crowbar) switch, turning converter off, riding through fault, deactivating the protection and resuming the converter operation, maintaining synchronisation and finally returning to normal operation [45]. This operation needs integration into the rest of the system including the control.

5.3.2 DC-link Brake Method

A DC-link brake circuit is used to prevent the overcharging of the DC-link capacitor. The DC-link voltage is monitored and if it exceeds a certain threshold then the DC-link brake is activated.

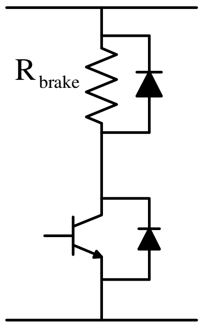

Figure 5.6: DC-link brake circuit

The maximum limit for overvoltage (DC-link) protection was set to 1.5pu in [84 and 94]. There can be a risk of exceeding relay settings by over-current in the rotor circuit and by overvoltage in the DC-link when voltage drops down to 0.5pu or below [13]. In this thesis, the DC-link brake is activated if the DC-link voltage (V_{DC}) exceeds 1.3pu of its nominal value, and if it is equal or less than 1.1pu, then the DC-link brake is deactivated. The control block diagram of the DC-link brake is shown in Figure 5.7. The calculation of the DC-link brake resistor (R_{brake}) is given in Appendix (see A.4.1).

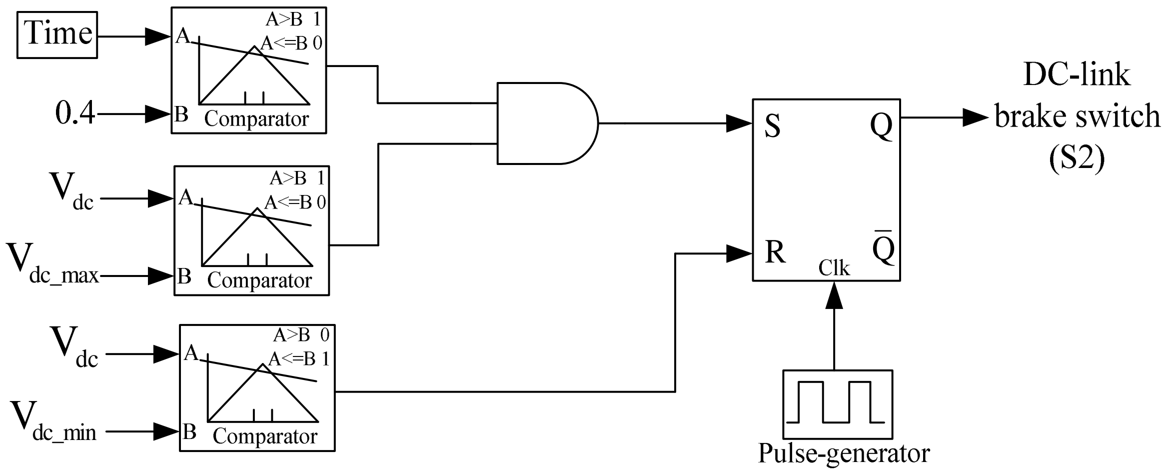

Figure 5.7: DC-link brake control design

5.4 GB Grid Code Fault Ride-Through Requirements [99]

The fault ride-through (FRT) requirements of generating units (in our case: wind farms) for GB the Grid Code are documented in section CC.6.3.15 in [99]. To summarise:

- For short-circuit faults or voltage sags occurring at the "supergrid voltage" lasting up to 140 ms (=total fault clearance time), a wind farm should have the capability of remaining transiently stable and grid-connected. If the duration of the system fault is greater than 140ms, throughout the dip duration on or above heavy black line shown in Figure 5.8 the wind farm again should remain connected to the network without tripping.

- "In case of supergrid voltage dips lasting up to 140ms, within 0.5s of restoration of the supergrid voltage to 90% of nominal or greater, the wind farm should supply the active power to at least 90% of its pre-fault value" [99]. If the grid faults last greater than 140ms, then the time of 0.5s can be extended to 1s.
- "During the grid faults or voltage sag period, a wind farm should provide maximum reactive current without exceeding the transient rating limits of the generating unit" [99].
- If the wind farm generates less than 5% or more than 50% (in case of very high wind speeds) of its rated power in MW, then the wind farm may be tripped.

Other requirements for GB Grid Code are available in [99]. The summaries of some other certain countries' grid codes can be found in [25].

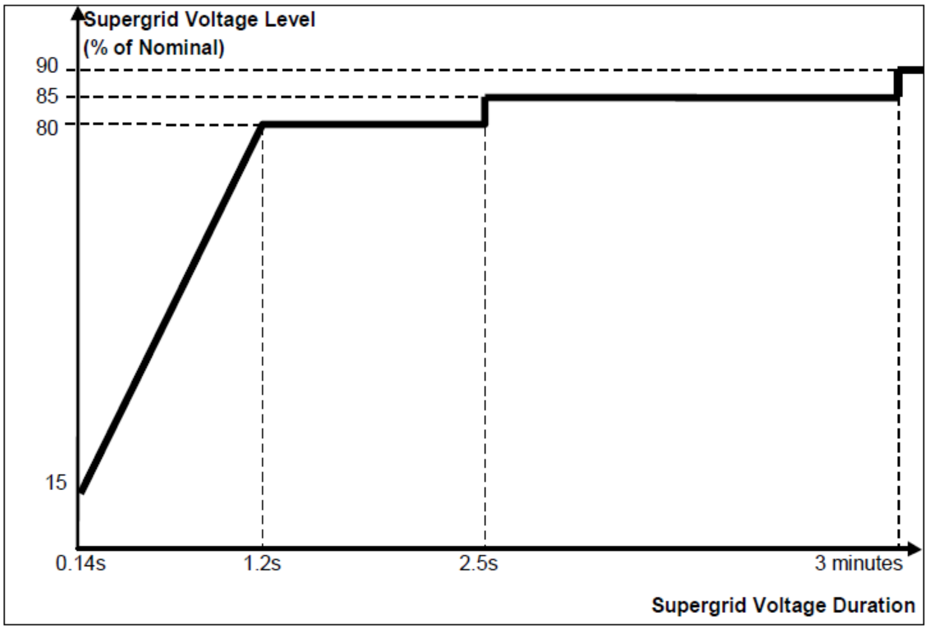

Figure 5.8: Fault ride-through requirements of GB grid code for voltage dips lasting greater than 140ms (Figure CC.A.4A.2 in [99])

5.5 Simulation Results

In order to verify that the protection devices (crowbar and DC-link brake) work sufficiently, a number of voltage sags were applied to the network voltage source at t=2s for a duration of 100ms [75]. 0.8pu (retained voltage 0.2pu), 0.5pu (retained voltage 0.5pu) and 0.2pu (retained voltage 0.8pu) three-phase (Phase A, B and C), two-phase (Phase A and B) and one-phase (Phase A) voltage sags are selected.

As a rule of thumb based on the same principles used to separate inner and outer loop speeds in a cascaded controller, the crowbar should act[3] at least four times faster than the fastest loop (inner-current loop) of the RSC. The speed of crowbar action is then supposed to be 40Hz. However, this number drops into the exclusion limits region (between 12.5Hz and 200Hz - see Figure 5.1). To maintain adequate protection of the power electronics and to avoid the 50Hz interference on the protection schemes, the frequencies of the crowbar and DC-link brake actions should be set to a number greater than 200Hz. The DC-link brake should not only act four to ten times faster than the fastest loop (inner-current loop) of the GSC, but would ideally be at least four times faster than the crowbar action bandwidth to maintain adequate protection of the power electronics. Note that the activation of the protection schemes (DC-link brake and rotor crowbar circuit) should not be faster than the PWM frequency (4.5kHz). Since there is not much of freedom, fitting these protection frequencies into Figure 5.1 needs precise assessment. Furthermore, the lock-out time for the mono-stable block used in the crowbar circuit should be chosen accurately in order to avoid crowbar taking several switch-on and off actions. An appropriate delaying time is required.

Firstly, the DFIG system under the more severe three-phase voltage sag (0.8pu) introduced between 2s and 2.1s is simulated without considering any protection. The simulation file of the DFIG system in PSCAD was run with initial parameters: P_s^*=4.5MW (rated power), Q_s^*=0MVAr, V_{dc}^*=1kV (DC-link voltage) and the 3-phase grid voltage= 33kV L-L, RMS. The 0.8pu three-phase voltage sag applied to the grid voltage is shown in Figure 5.9.

[3] The crowbar is activated very quickly (<ms) after a fault is detected. 'Act' in this case refers to the typical frequency at which lockouts and delays allow the protection to trip, reset and trip again.

During the voltage sag period, the crowbar and the DC-link brake are intentionally suspended. As seen in Figure 5.10 without taking any protection the system is left very sensitive to severe voltage dips. The worst case happens for the stator active and reactive power outputs, and the DC-link voltage starts to fluctuate and falls down to 0V. These results show the importance of including any protection design in the DFIG systems during grid faults. Figure trace labels are defined on the diagram presented in Appendix 2 (see Figure A.2.1).

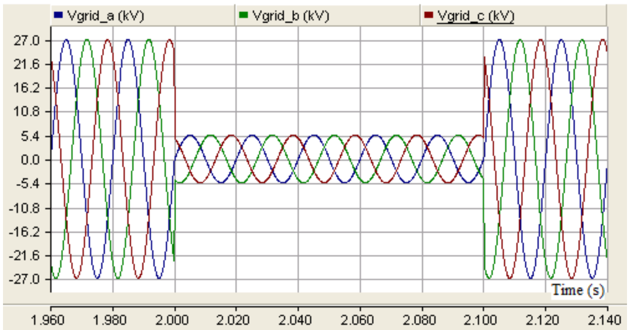

Figure 5.9: 80% (0.8pu) 3-phase voltage sag

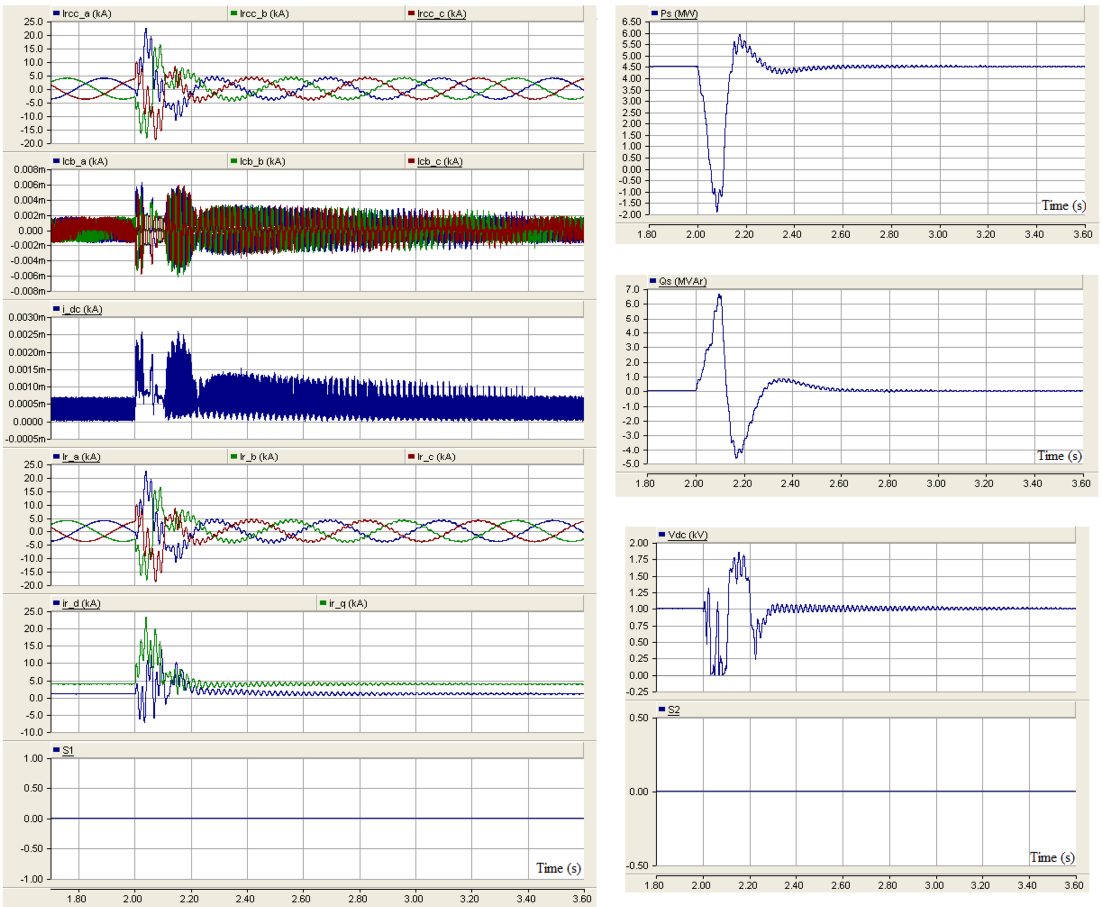

Figure 5.10: No protection involved during a 0.8pu 3-phase voltage sag

The DC-link brake is tested in the simulation programme by manually increasing the set value of the DC-link voltage from its nominal value of 1kV (1pu) to 1.5kV (1.5pu) between 2s and 2.1s. In Figure 5.11, the DC-link brake is not activated exactly at 2s because the DC-link voltage has not yet exceeded the maximum threshold (1.3pu=1.3kV). As soon as it detects (at around 2.0094s) an over-voltage across the DC-link capacitor, which means that the DC-link voltage is greater than 1.3kV, then the DC-link brake switch (S2) immediately triggers. If the voltage drops below 1.1kV (1.1pu-lower threshold) then the DC-link brake is resumed. So, the DC-link brake and its logic are shown to work in Figure 5.11.

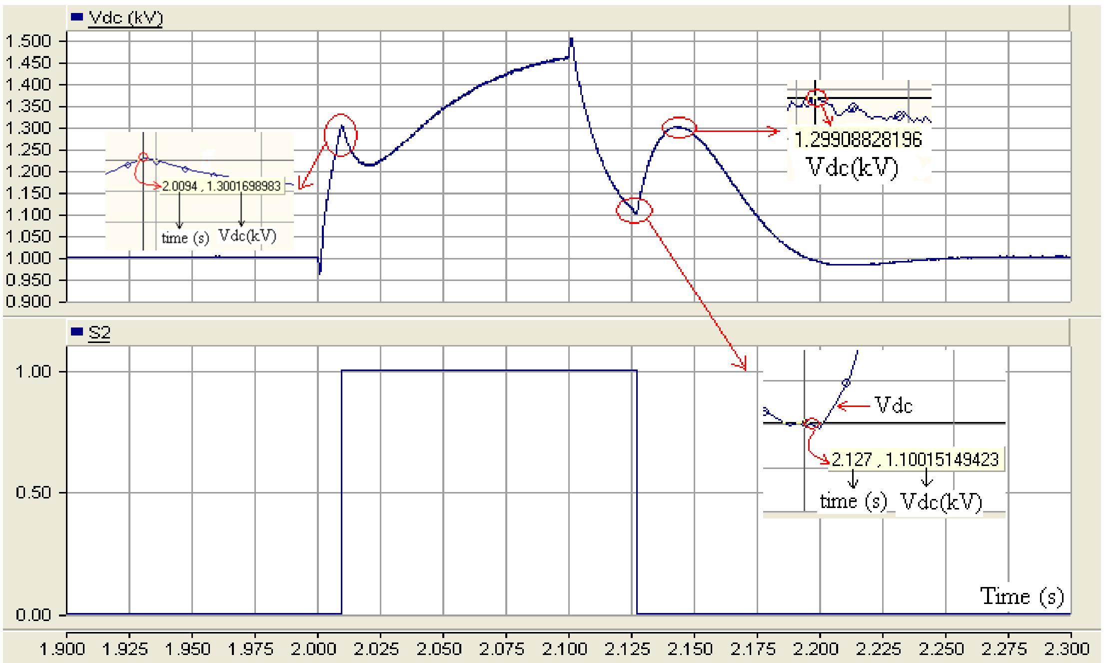

Figure 5.11: DC-link brake activation (by increasing the set value of the DC-link voltage - not any voltage sag applied)

The effects of changing the DC-link voltage on the rotor side quantities are also shown in Figure 5.12. Infinitesimal change in the rotor currents occurred and hence there was no need for any possible crowbar action. The stator reactive power (approximately +4% and -6% variations) is more influenced rather than the stator active power (approximately +0.35% and -0.28% variations). However, these changes can be ignored.

Figure 5.12 shows that varying the DC-link voltage (from 1kV to 1.5kV) has almost no effective impact on the rotor-side quantities. The crowbar switch (S1) was not triggered since any phase current of the rotor did not exceed the upper threshold. The rectified (direct) current (i_dc) is almost zero amperes. Because of not activating the crowbar, the rotor-side converter gates were not switched off. Therefore, the rotor-converter currents (I_{rcc_abc}) are exactly the same as the rotor currents (I_{r_abc}) flowing into the rotor. While the DC-link brake was engaged, the crowbar protection circuit remained turned-off.

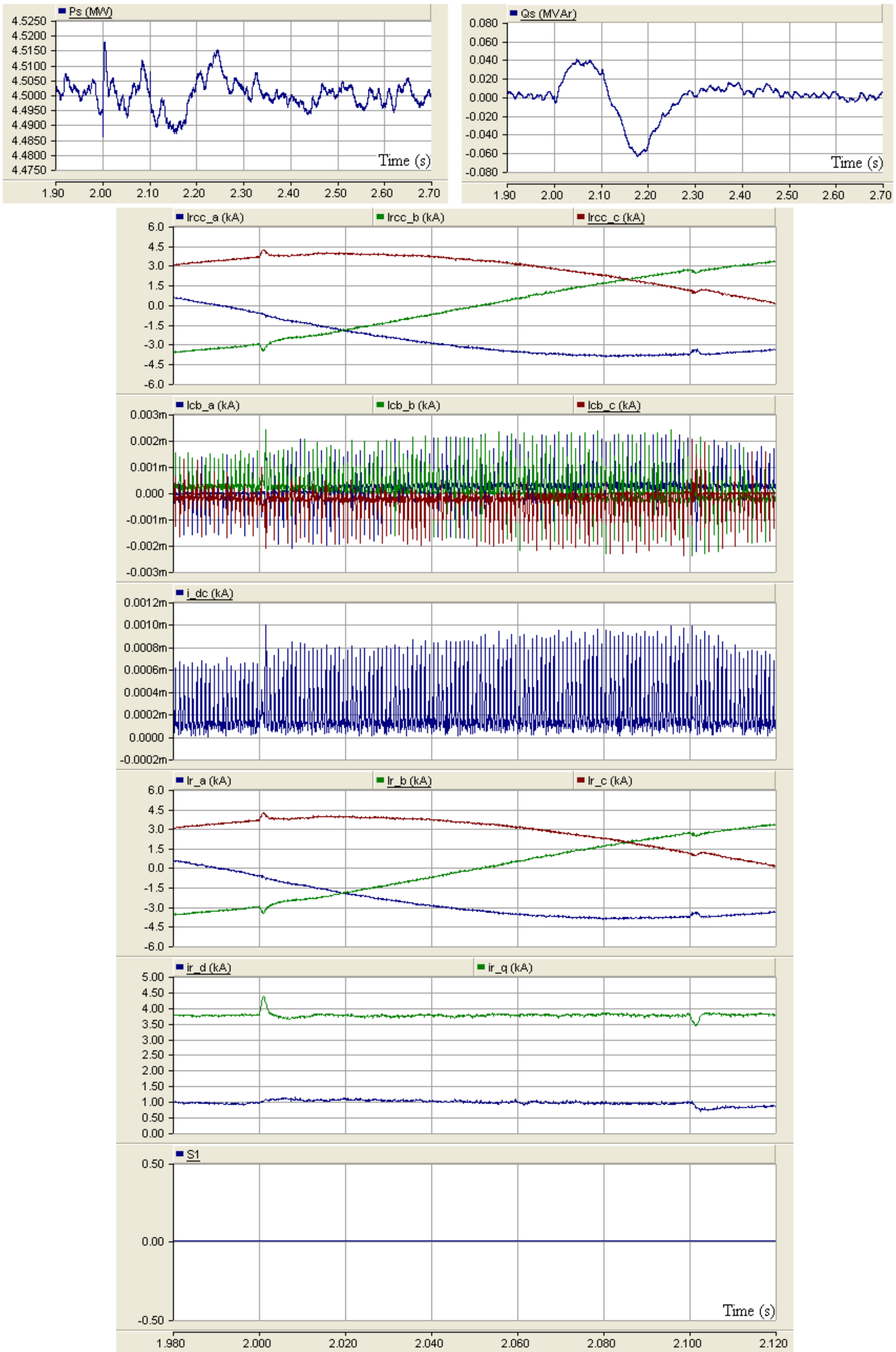

Figure 5.12: Stator active and reactive power, and rotor-side currents during an increase in the DC-link voltage (from 1kV to 1.5kV between t=2s and t=2.1s)

By applying the voltage sag and suspending the crowbar protection during the voltage sag event, the behaviour of the DC-link brake against this voltage sag is summarised in

Figure 5.13. Using only the DC-link brake is not enough to protect the DFIG system. The DC-link voltage excursion is reduced but fluctuations in other quantities remain and indeed are worse for stator active and reactive power.

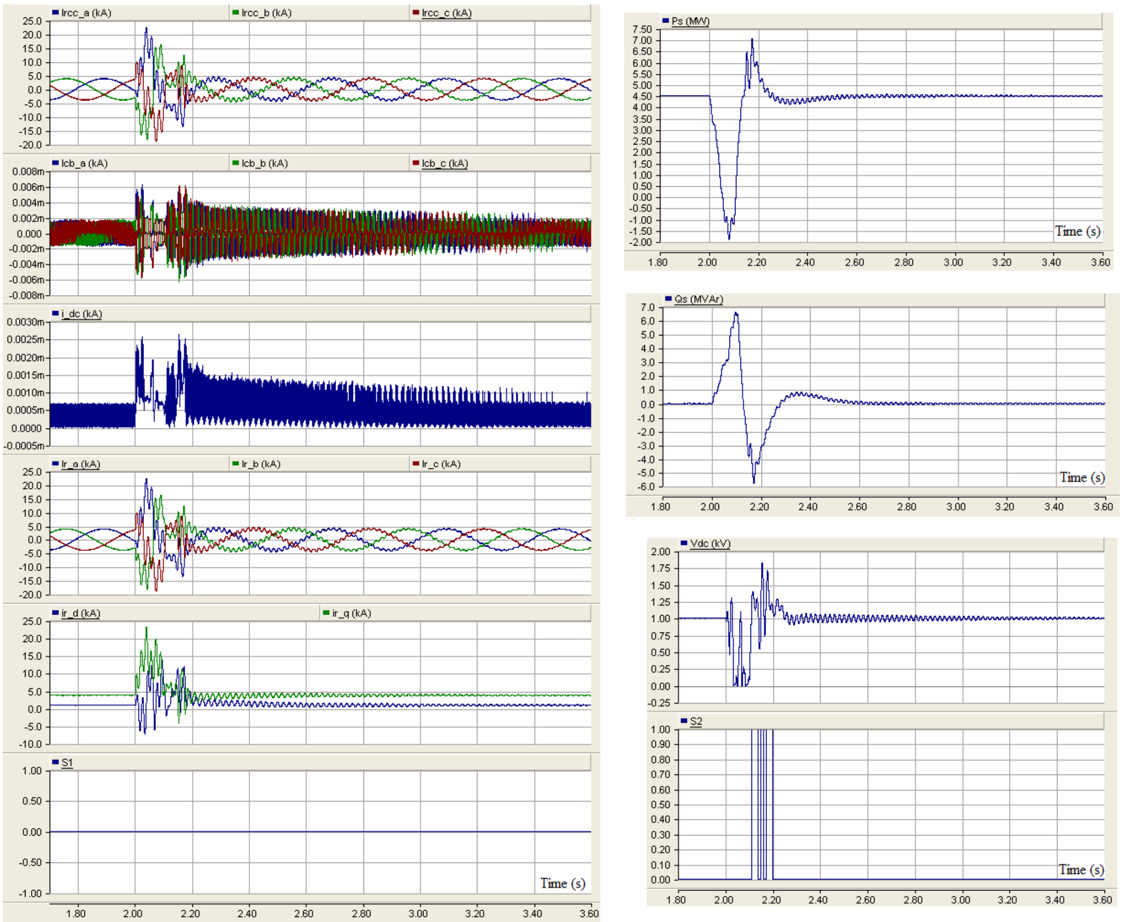

Figure 5.13: Only DC-link brake action taken by introducing voltage sag (the crowbar protection is intentionally suspended)

5.5.1 Three-phase Voltage Sag

i) Applying 0.2pu sag

A 20% three-phase (Phase A, B and C) voltage sag is applied to the network source whose retained voltage is 80% (≈21.56kV phase-peak) during the voltage sag. The voltage sag in the network voltage between 2s and 2.1s is shown on the top-left in Figure 5.14. This 0.2pu voltage sag does not cause over-current in the rotor and over-voltage in the DC-link capacitor. Therefore, the protection devices did not activate. The DFIG system simulated in this research can sustain service under a 0.2pu three-phase voltage sag lasting 100ms without taking any protection action. There was also no need to include a lock-out time block. The simulation results are given in Figures 5.14 and 5.15.

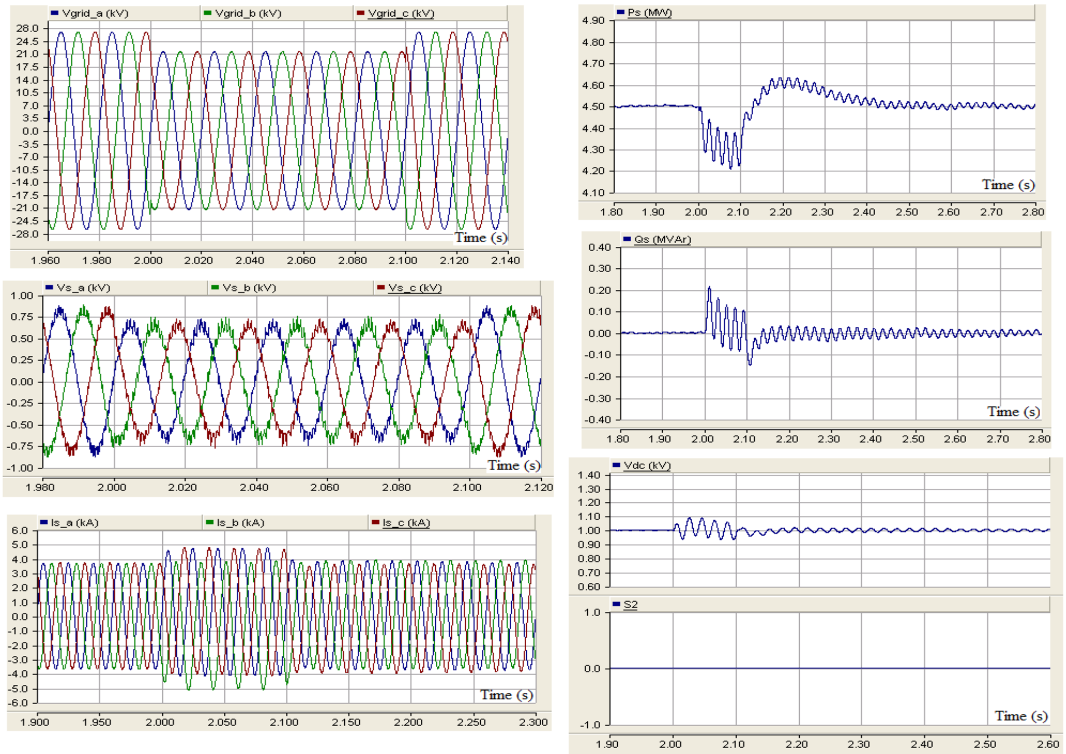

Figure 5.14: 0.2pu three-phase voltage sag

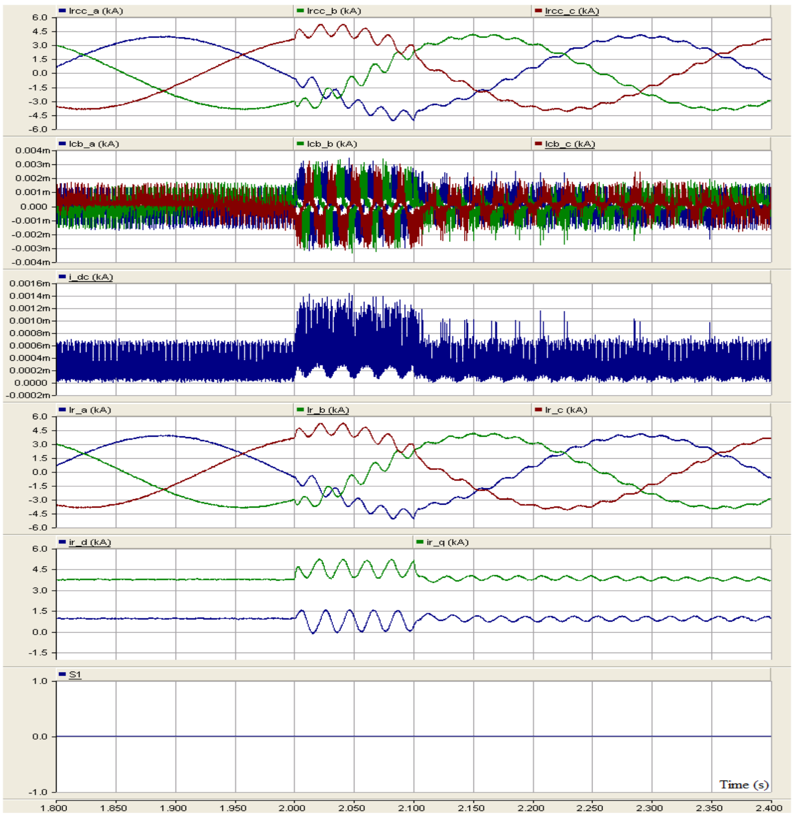

Figure 5.15: Rotor-side currents during a 0.2pu three-phase voltage sag

ii) Applying 0.5pu sag

A more severe (0.5pu) three-phase voltage sag is now applied to the grid voltage in order to see the consequences on the DFIG system. First a single-time over-current in the rotor (at t=2.0186s) and then approximately 26.7ms later a single-time over-voltage in the DC-link occurred. Both protection designs activate once during a 0.5pu three-phase voltage sag. As soon as the rotor-currents and the DC-link voltage exceed their maximum limits, the crowbar and the DC-link brake trigger. Again, they do not activate more than once, a mono-stable (lock-out time) block is not required. The results are demonstrated in Figures 5.16 and 5.17.

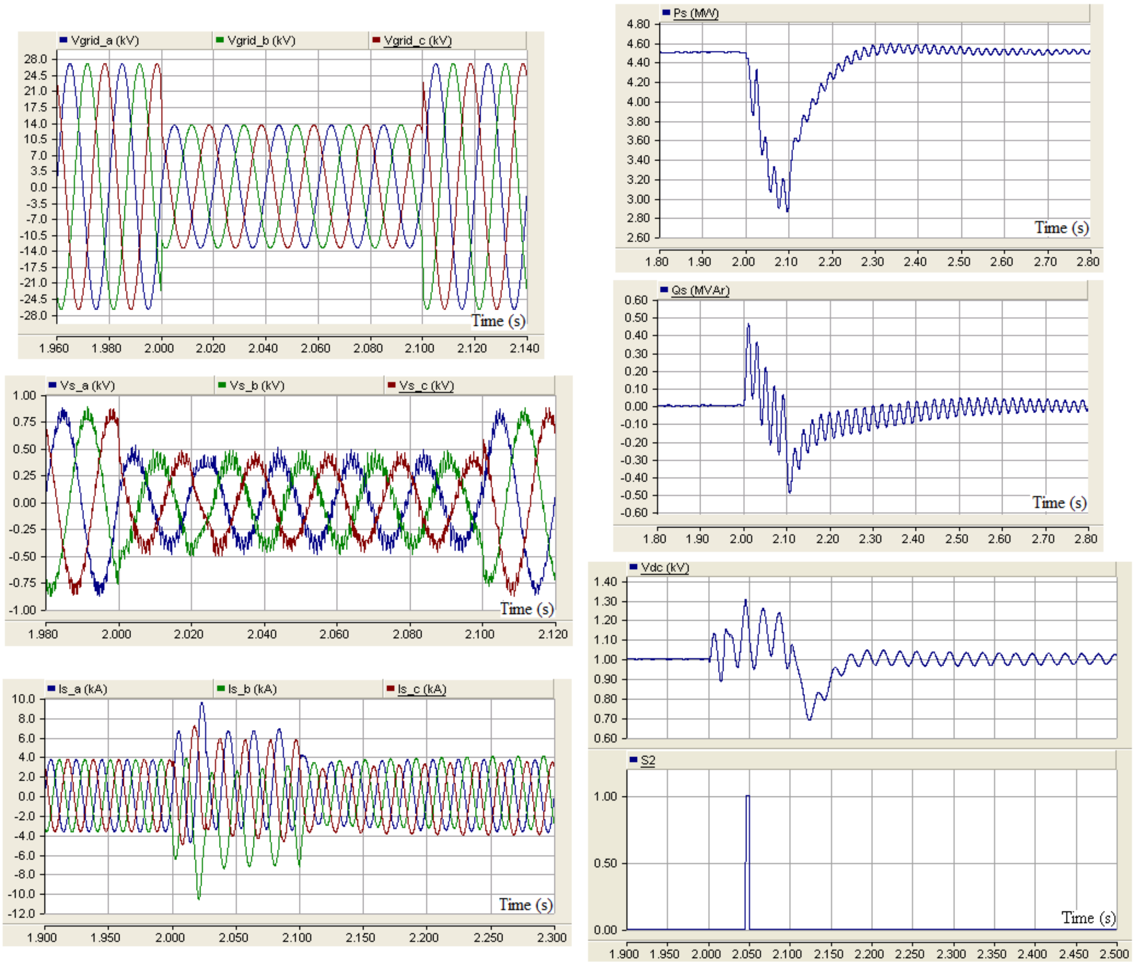

Figure 5.16: 0.5pu three-phase voltage sag

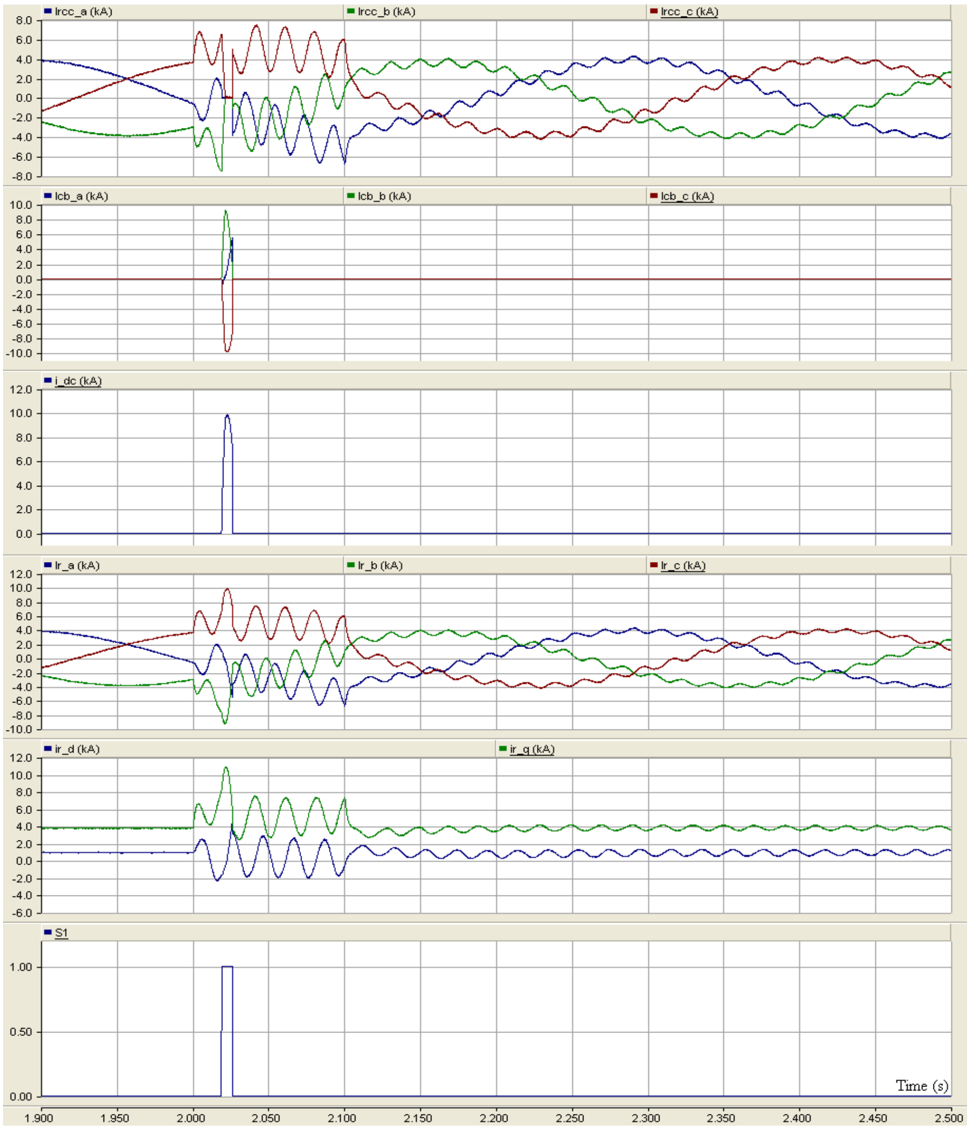

Figure 5.17: Rotor-side currents during a 0.5pu three-phase voltage sag

iii) Applying 0.8pu sag

A further severe voltage sag magnitude of 0.8pu is now applied. The simulation results without a lock-out time for the crowbar circuit are presented in Figure 5.19. Since a lock-out time (mono-stable) block is unused, several switch-on and -off actions of the crowbar protection have been observed. Furthermore, the DC-link brake also takes action twice because the over-voltage in the DC-link capacitor persists during the voltage sag period. After the crowbar is deactivated the stator active and reactive powers reach the steady-state again in approximately 20ms but including the oscillations since the smoothing time constants of the power meters were set to 25ms. The V_{dc} excursion is small enough and slow enough that the GSC outer (voltage) loop can pull the DC-link voltage back to nominal value (i.e. in $1/f_n = 0.1$s).

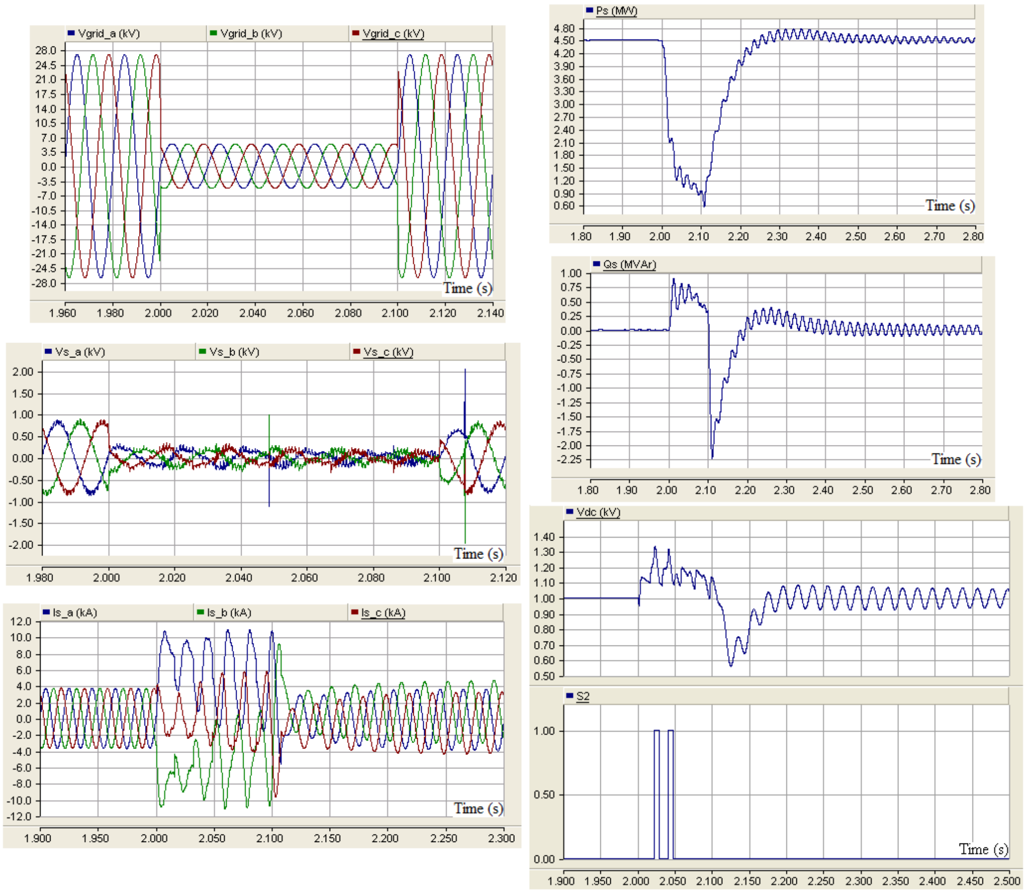

Figure 5.18: 0.8pu three-phase voltage sag excluding a lock-out time block

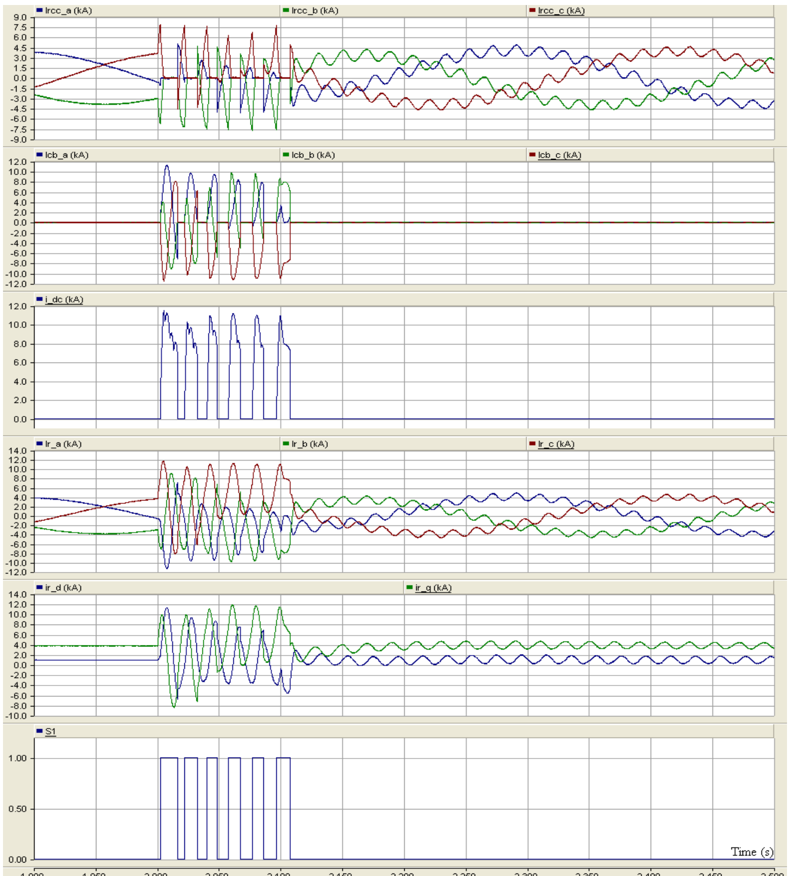

Figure 5.19: Rotor-side currents during a 0.8pu three-phase voltage sag excluding a lock-out time block

Figures 5.20 - 5.21, and 5.22 - 5.23 illustrate the simulation results by using the mono-stable block in the control algorithm circuit of the crowbar. By including this lock-out time block, the switch-on and off actions of the crowbar can be reduced. Thus, further oscillations in the system state can be prevented throughout the voltage sag. This should ease system design. However leaving protection on too long is also undesirable. So, choosing a reasonable time for the mono-stable equipment plays a significant role. The simulation is run with a mono-stable block and the results are given in Figures 5.20 and 5.21 (lock-out time is set to 0.01s).

When the over-current in the rotor is detected by a SR flip-flop, then the set (logic 1) signal is sent to trigger the crowbar switch (S1). A mono-stable is utilised here to enable the crowbar stay ON for a fixed time from the first activation time. After this time passes, if the over-current still takes place in the rotor, the crowbar activates again until the over-current disappears. But using a 0.01s lock-out time, the crowbar switch action is decreased in comparison to the excluding a mono-stable block. As a result of decreasing the crowbar actions, there is no need for DC-link brake to take action since the DC-link voltage does not reach the maximum limit level (see Figure 5.20). Therefore, further overcharging of the DC-link capacitor is avoided. Thus, the protection coordination between the crowbar and the DC-link brake is then maintained.

Further improvements in the crowbar action can be achieved by increasing the lock-out time to a reasonable number which lets the crowbar activate once. The simulation in PSCAD is re-run with a slightly greater lock-out time (=0.045s) and the results are given in Figures 5.22 and 5.23. A significant enhancement in the response of the DC-link voltage can be seen in Figure 5.22. Voltage stressing of the power electronics is undesirable since this is one of the ways that components' life is reduced [100].

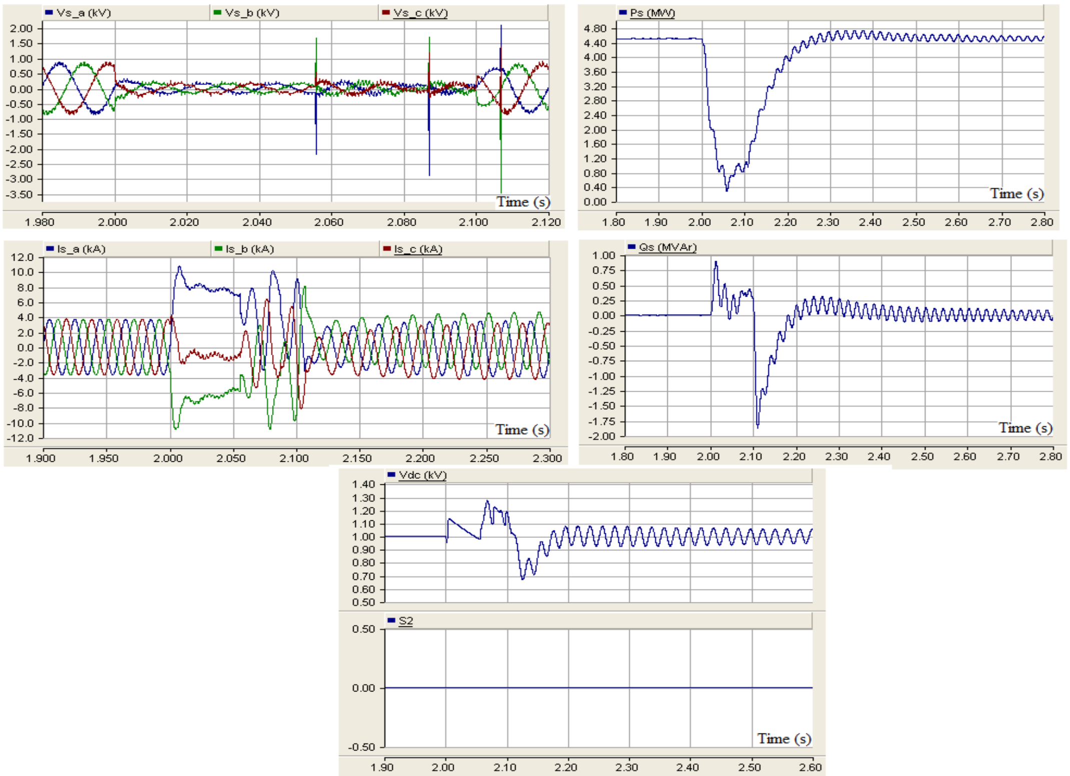

Figure 5.20: 0.8pu three-phase voltage sag including a lock-out time (0.01s) block

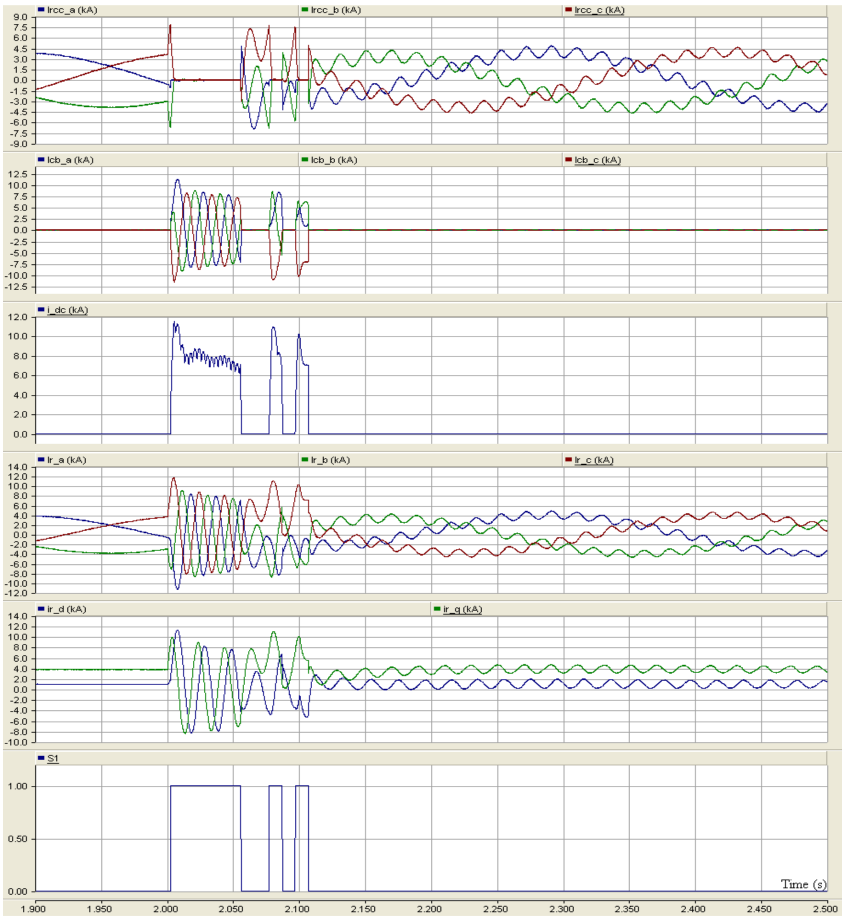

Figure 5.21: Rotor-side currents during a 0.8pu three-phase voltage sag including a lock-out time (0.01s) - Decreasing crowbar switch-on and -off actions

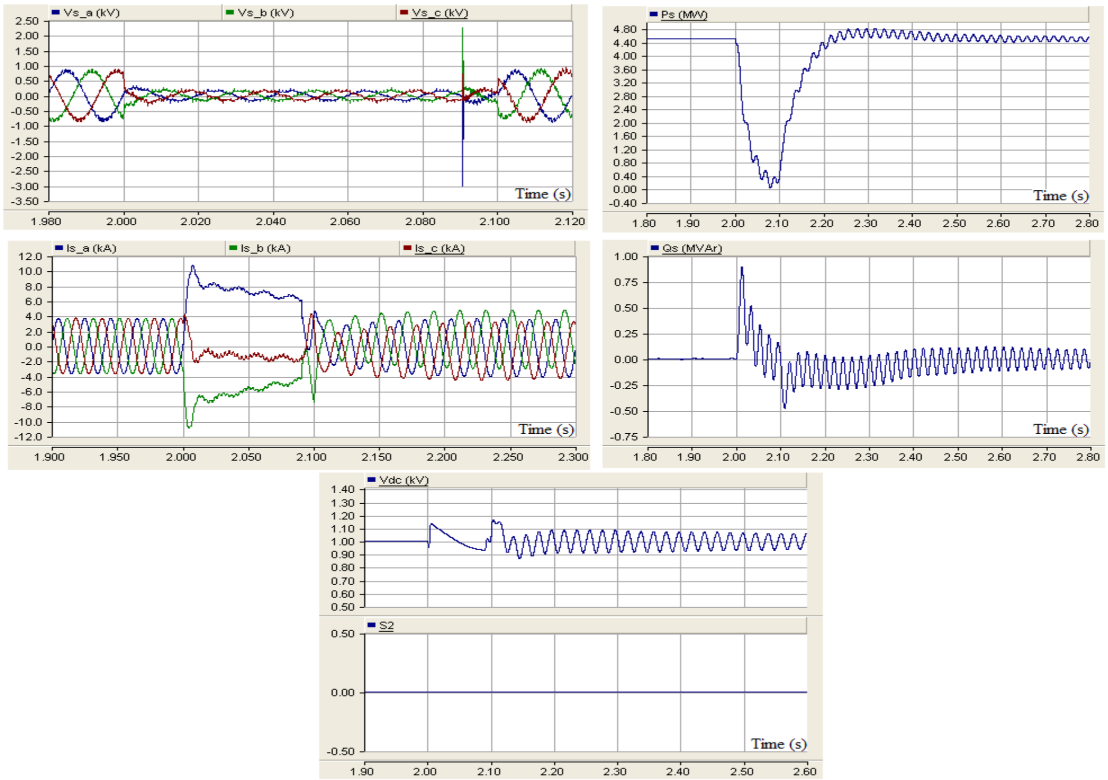

Figure 5.22: 0.8pu three-phase voltage sag including a lock-out time (0.045s) block

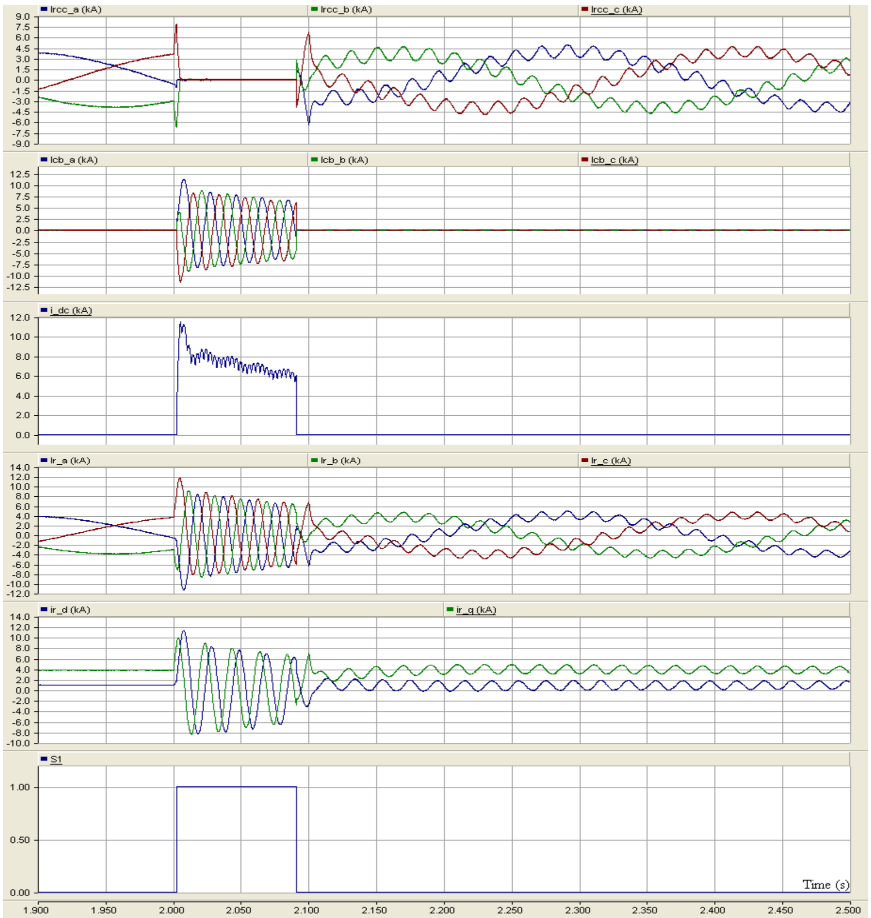

Figure 5.23: Rotor-side currents during a 0.8pu three-phase voltage sag including a lock-out time (0.045s) – Improved results

5.5.2 Two-phase Voltage Sag

i) Applying 0.2pu sag

A 0.2pu two-phase (0.8pu retained voltage in the grid source) voltage sag is applied to Phase A and Phase B while letting Phase C be constant at 1pu. In this sub-section, a two-phase voltage sag is introduced to the network voltage. Since neither any phase rotor-current nor the DC-link voltage exceeds their relay settings, there is no protection action required to switch on these protection schemes. The selected simulation results are depicted in Figures 5.24 and 5.25 and the variations in the quantities' outputs can be regarded as negligible.

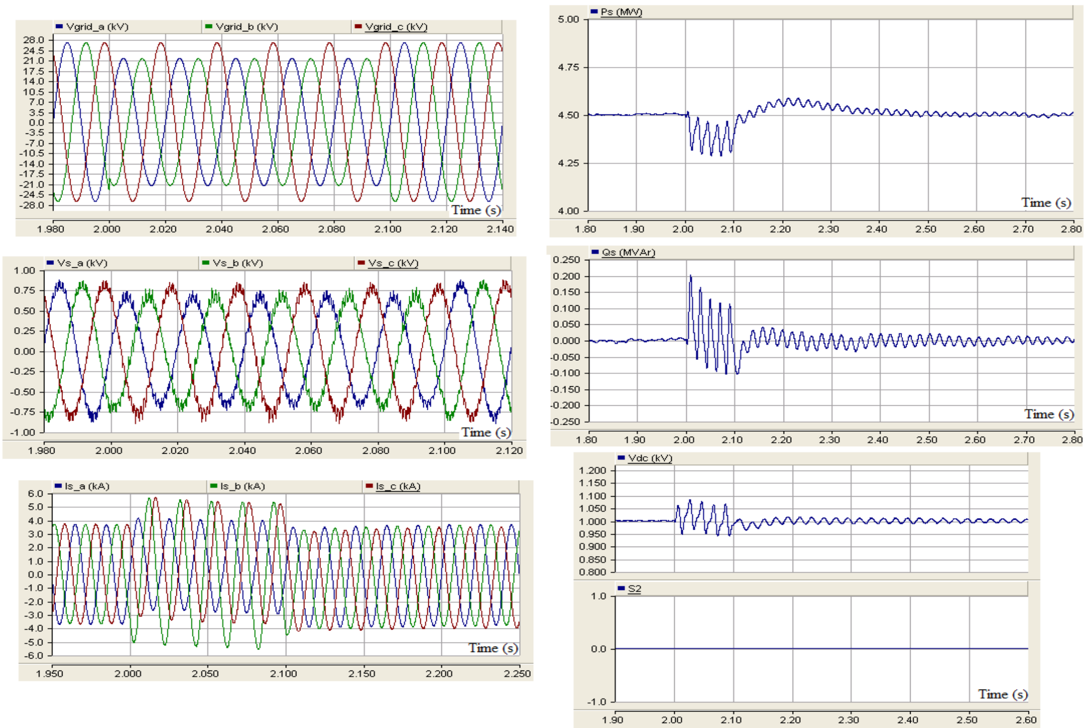

Figure 5.24: 0.2pu two-phase voltage sag

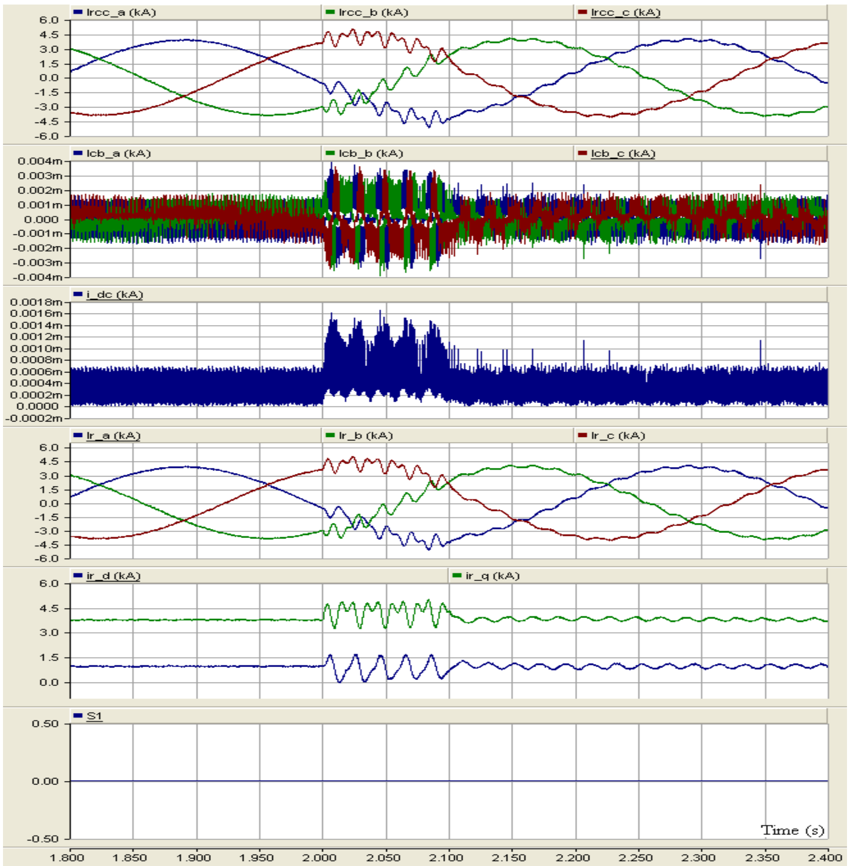

Figure 5.25: Rotor-side currents during a 0.2pu two-phase voltage sag

ii) Applying 0.5pu sag

A 50% two-phase voltage sag is implemented to check that the protection circuits work or not. Both the DC-link brake and the rotor-crowbar circuit switch on once since the DC-link voltage and the rotor-current exceed their upper limits. Again, the crowbar only activates once and there is no need to use a lock-out time which prevents the crowbar making several switch-on and -off actions. The simulation results are displayed in Figures 5.26 and 5.27.

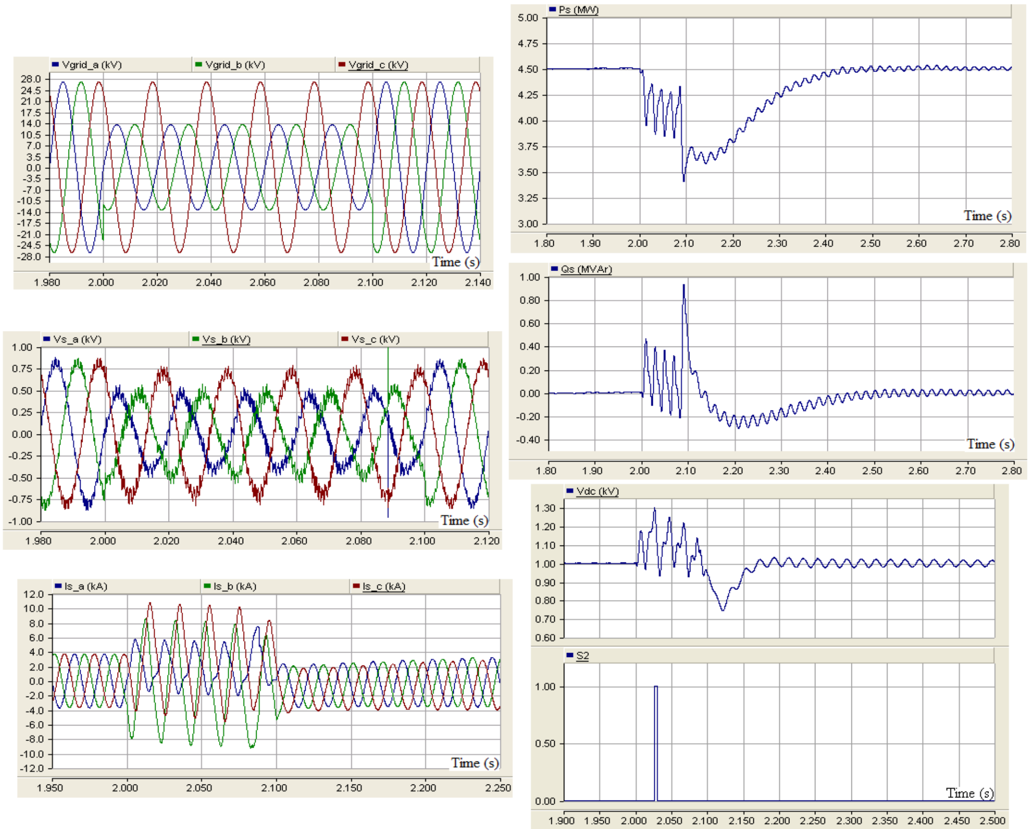

Figure 5.26: 0.5pu two-phase voltage sag

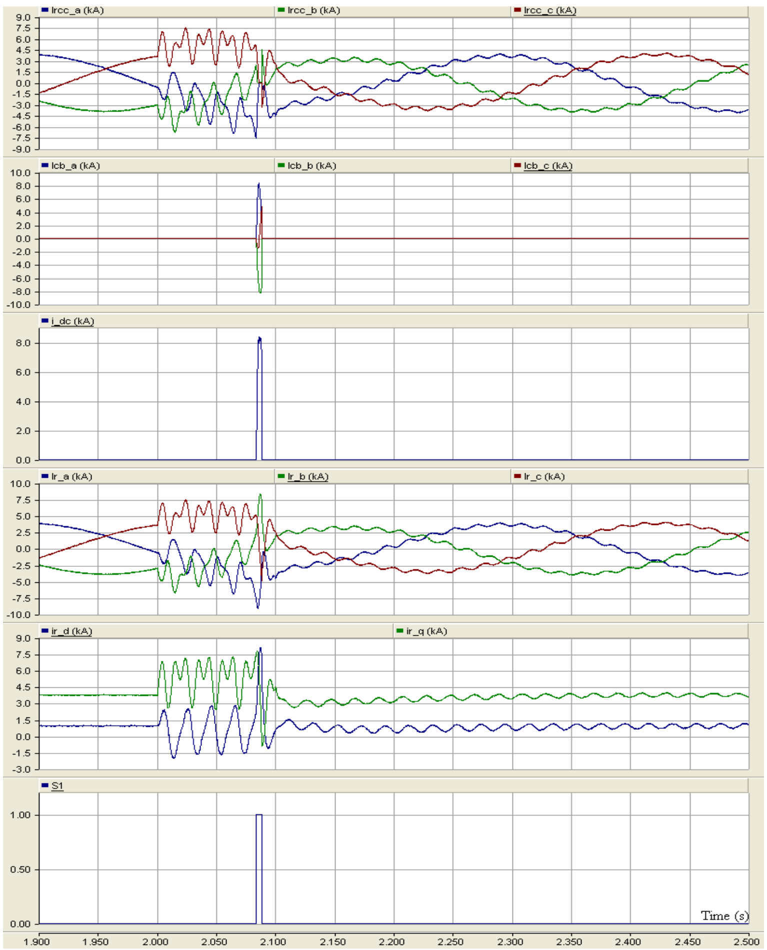

Figure 5.27: Rotor-side currents during a 0.5pu two-phase voltage sag

iii) Applying 0.8pu sag

A more severe (0.8pu) two-phase voltage sag is applied to the network voltage. The simulation file of the DFIG system is run without a mono-stable block. Therefore, the crowbar takes switch-on and -off action for 5 times as seen in Figure 5.29. This causes frequent non-linear changes in system state though. Inserting a lock-out time of 20.5ms to the simulation circuit ensures that the crowbar triggers once (see Figure 5.30). In doing so, there is almost no noticeable improvement seen in the stator active power, but the peak value of the reactive power reduces from 3MVAr to 2MVAr and is pulled back to its reference value (0MVAr) faster. However, a more smooth response occurs in the DC-link voltage. The simulation results can be found in Figures 5.28 to 5.31.

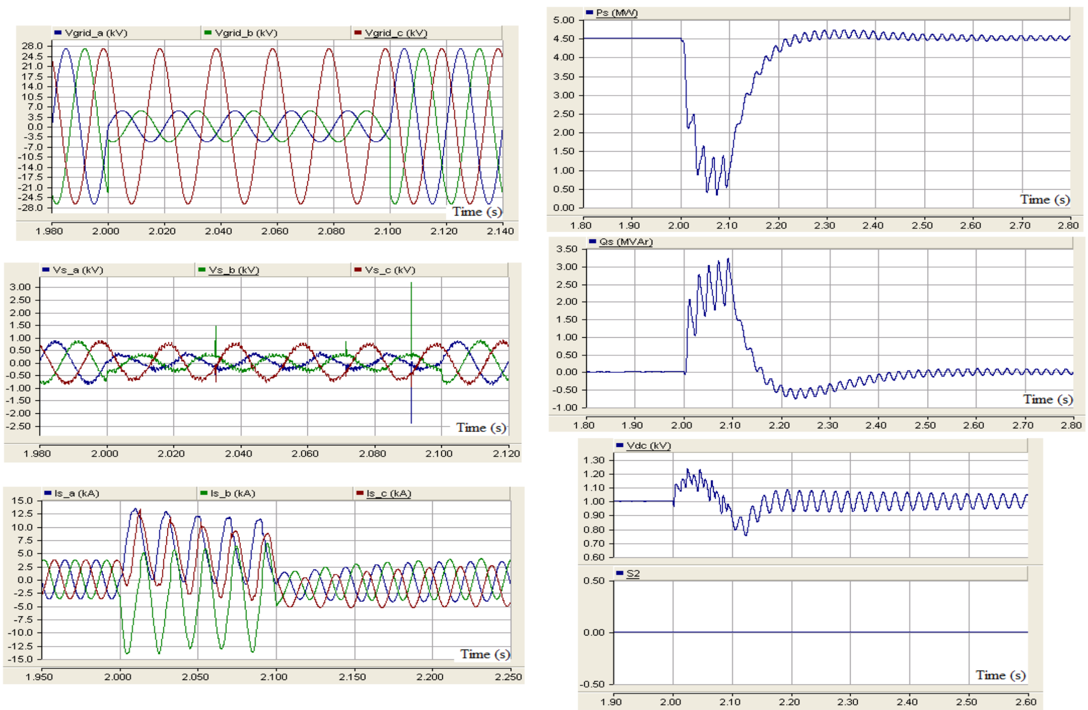

Figure 5.28: 0.8pu two-phase voltage sag excluding a lock-out time block

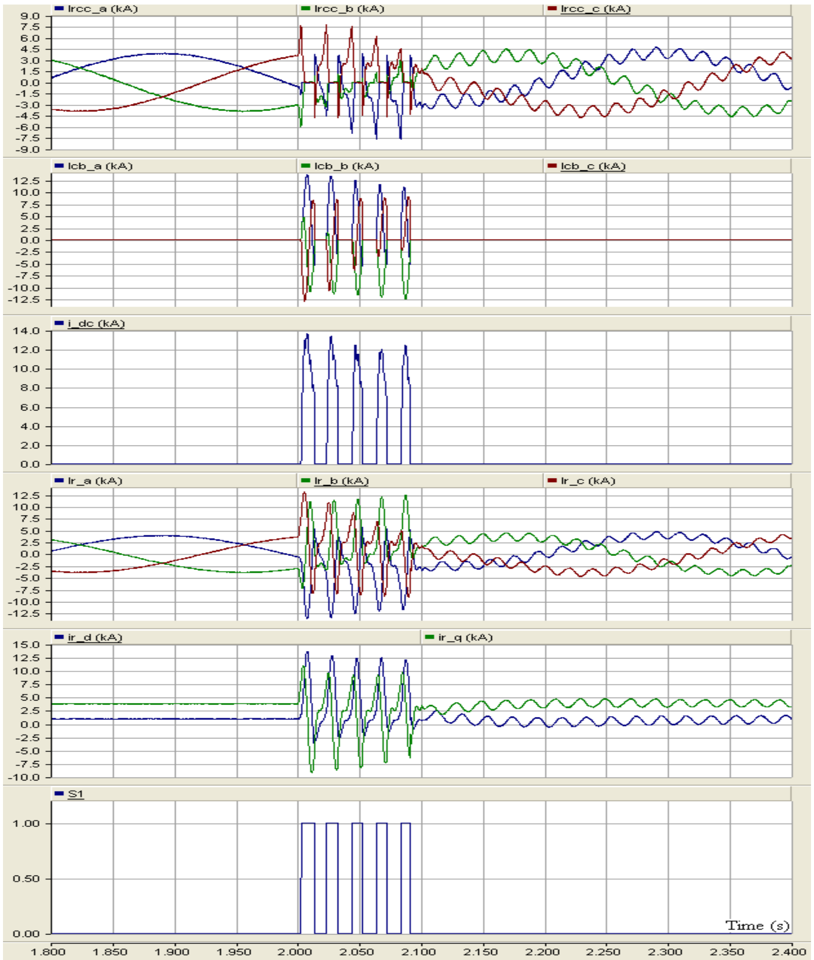

Figure 5.29: Rotor-side currents during a 0.8pu two-phase voltage sag excluding a lock-out time block

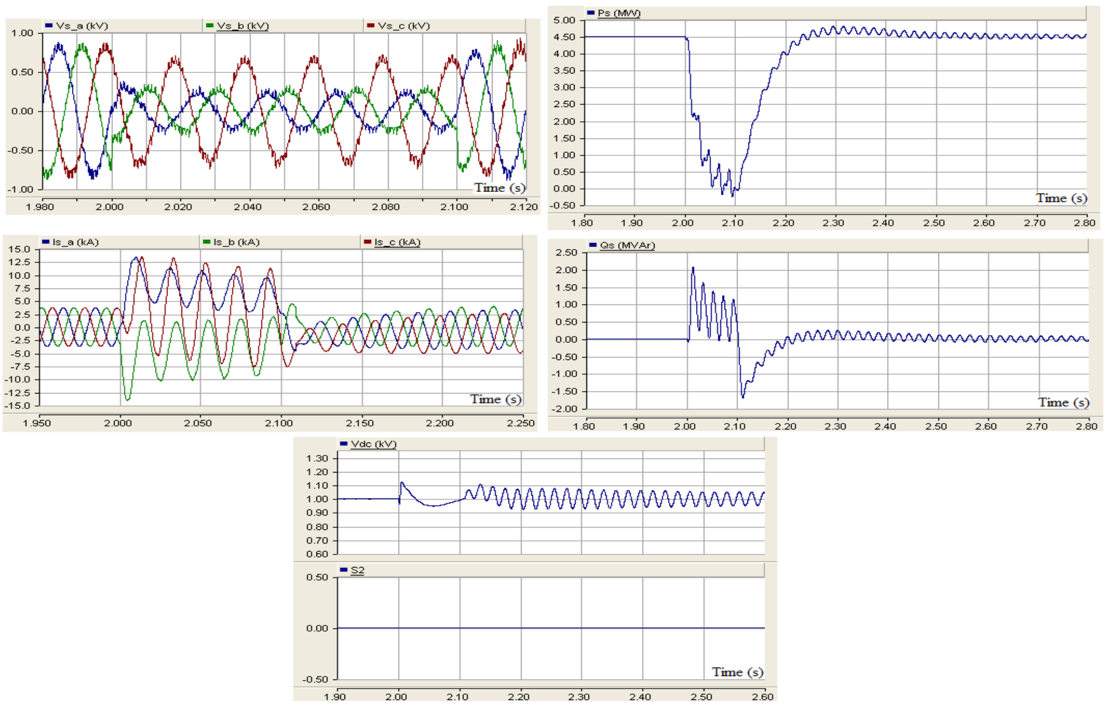

Figure 5.30: 0.8pu two-phase voltage sag including a lock-out time block (0.0205s)

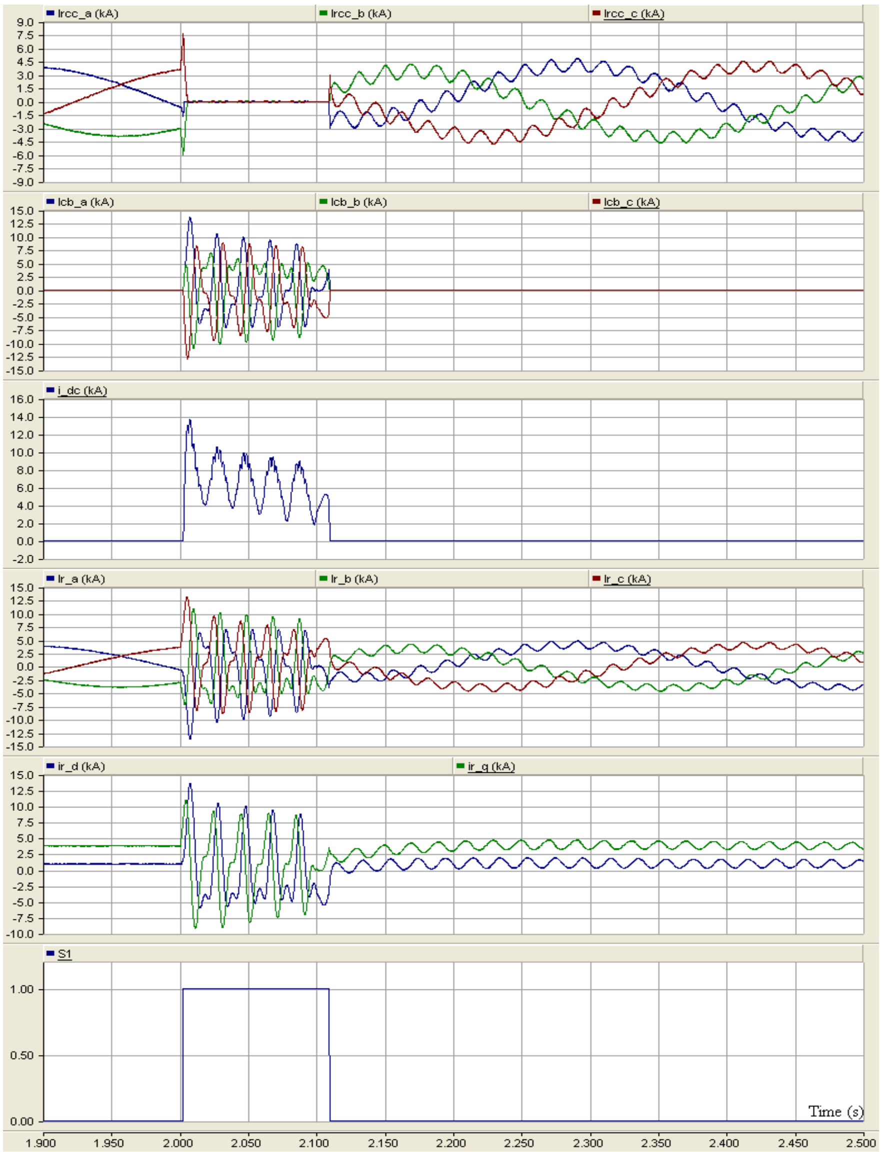

Figure 5.31: Rotor-side currents during a 0.8pu two-phase voltage sag including a lock-out time block (0.0205s) – Improved results

5.5.3 One-phase Voltage Sag

i) Applying 0.2pu sag

A 0.2pu (retained voltage is 0.8pu) one-phase voltage sag is now applied to the grid voltage source. Note that this voltage sag is introduced only to Phase A while keeping Phase B and Phase C at 1pu. The results are given in Figures 5.32 and 5.33. The DFIG system can maintain delivering the service demanded under a 0.2pu one-phase voltage sag without activating the protection devices since the rotor-currents and the DC-link voltage do not exceed the maximum limits. Again, negligible changes occur in the outputs as seen in Figure 5.32.

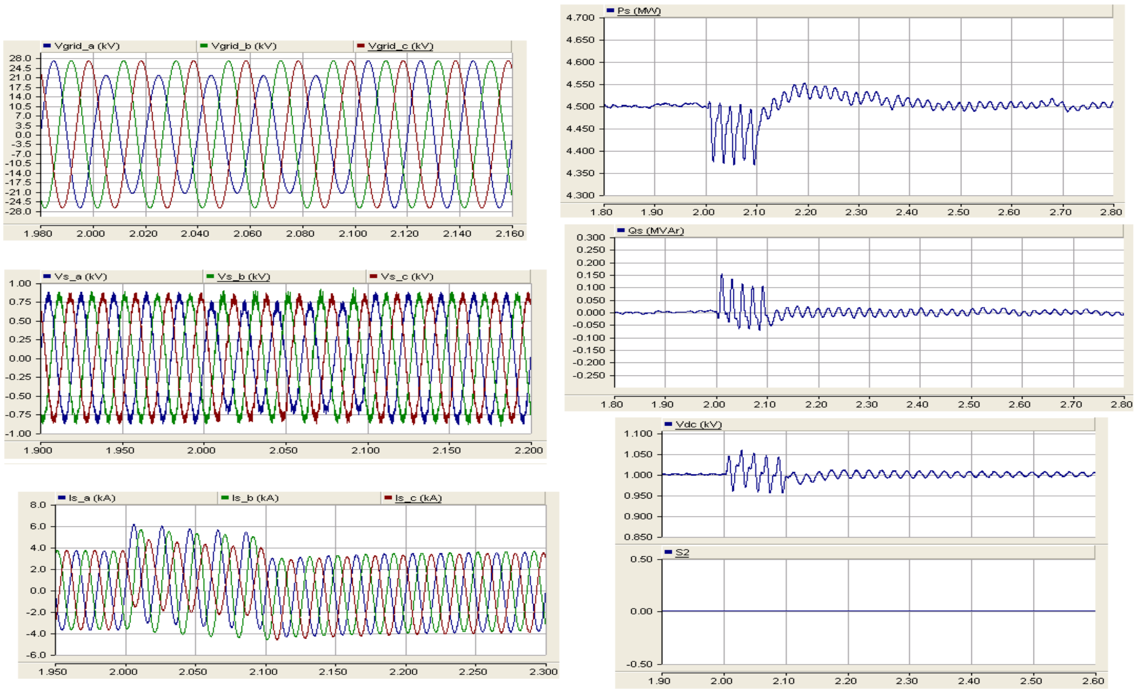

Figure 5.32: 0.2pu one-phase voltage sag

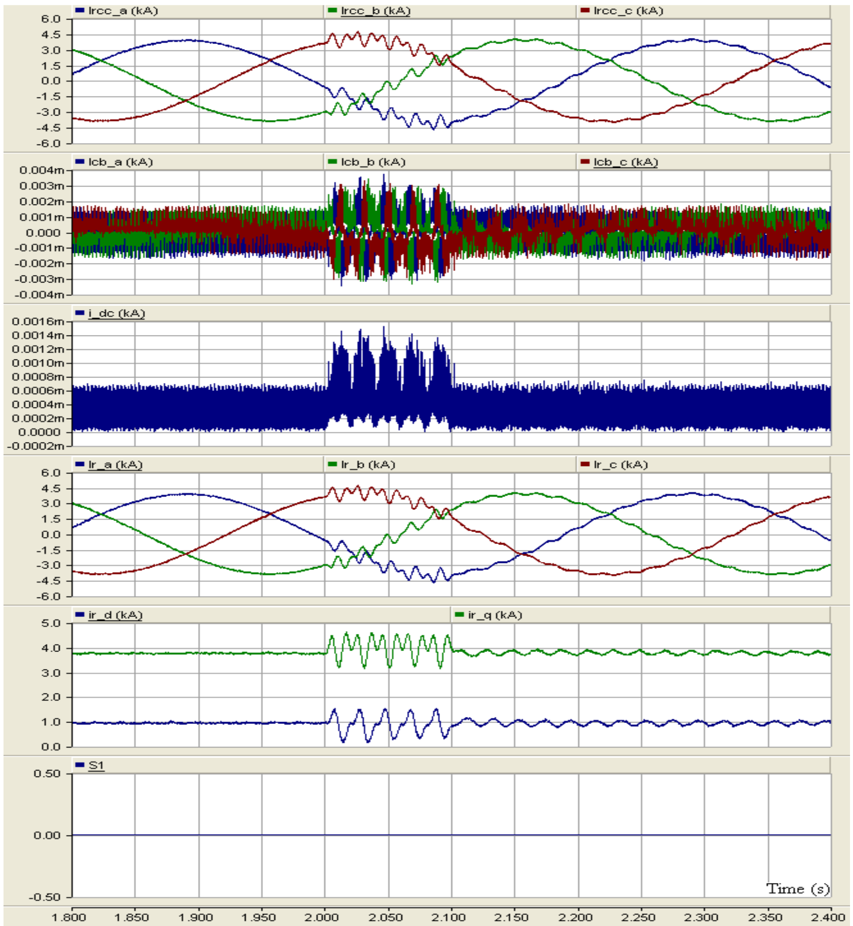

Figure 5.33: Rotor-side currents during a 0.2pu one-phase voltage sag

ii) Applying 0.5pu sag

Now, a 0.5pu one-phase voltage sag is applied. As in the case of the 0.2pu one-phase voltage sag, no over-voltage in the DC-link capacitor and no over-current in the rotor are observed. The DFIG system can accommodate the consequences of a 0.5pu one-phase without taking any precautions. The results are presented in Figures 5.34 and 5.35.

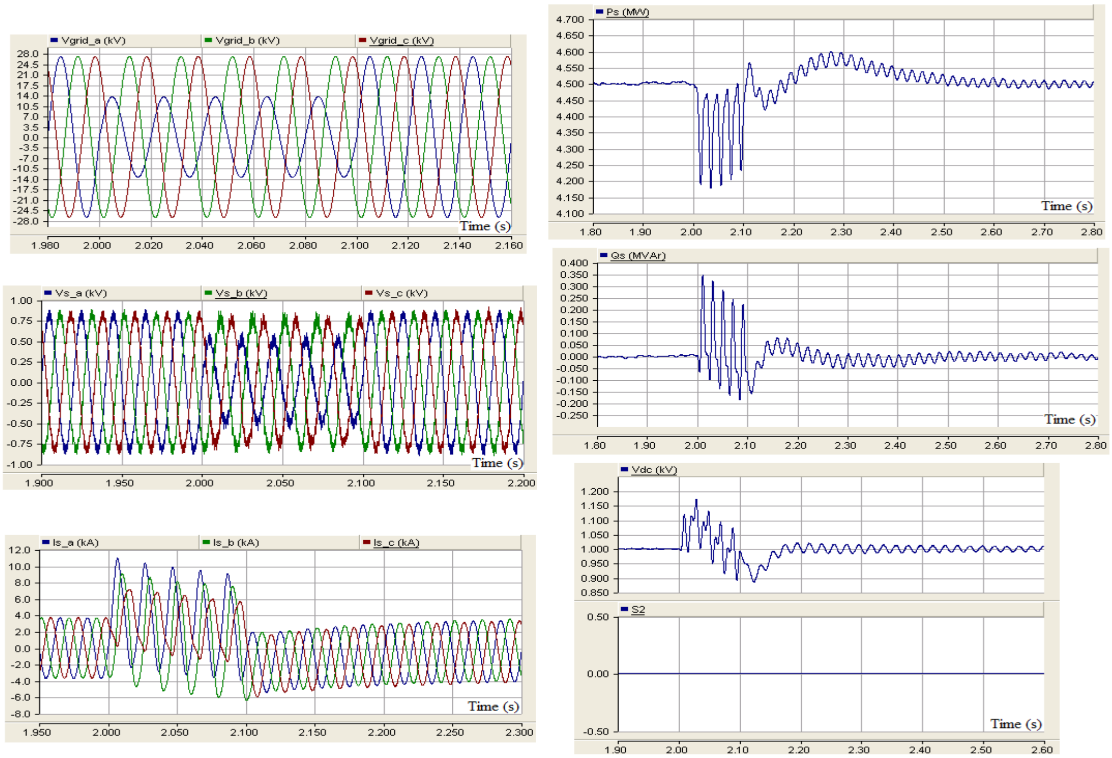

Figure 5.34: 0.5pu one-phase voltage sag

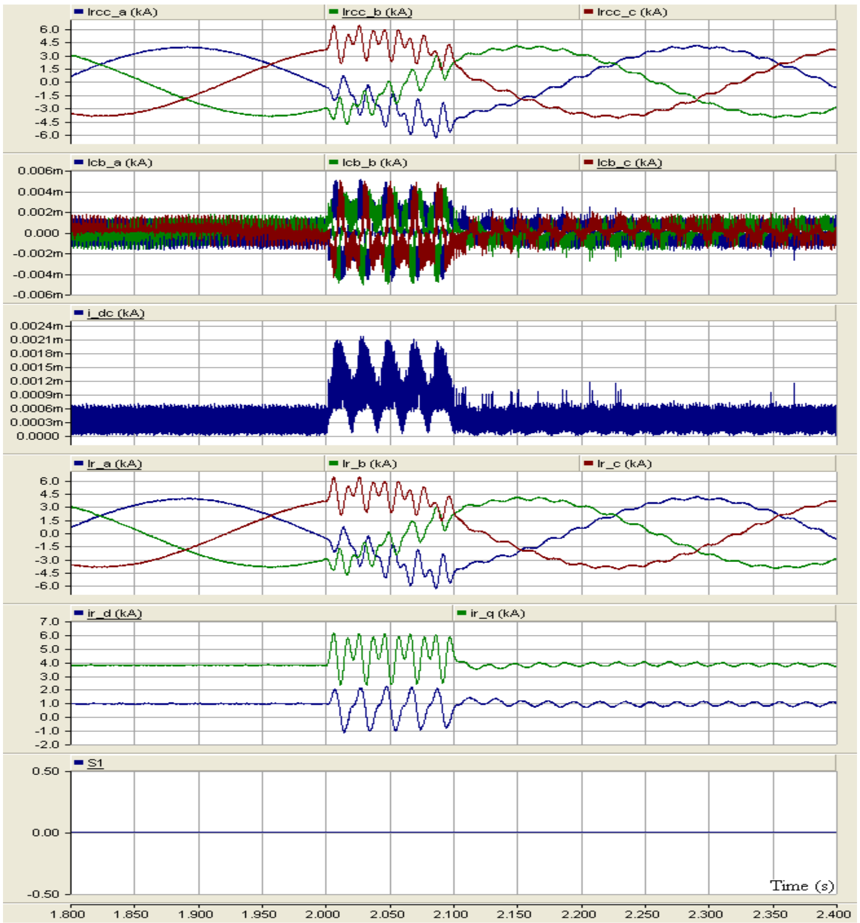

Figure 5.35: Rotor-side currents during a 0.5pu one-phase voltage sag

iii) Applying 0.8pu sag

A more severe one-phase voltage sag (0.8pu) is now carried out. Only over-current in the rotor occurs. Therefore, only the rotor crowbar engages twice during the voltage sag while the DC-link brake remains inactive. The results excluding a mono-stable block are shown in Figures 5.36 and 5.37. A lock out time of 20.2ms is set for the mono-stable block to let the crowbar trigger for one-time (see Figure 5.39). The output results are further improved then.

All types of voltage sag considered in this work are summarised in Table 5.1. The changes in the quantities are given in approximate numbers. 0.8pu voltage sag can be considered as a more severe case in which stator active power drops dramatically even to 0MW. The impacts of the 0.2pu three-, two- and one-phase voltage sags on the system can be regarded as negligible. 0.5pu voltage sag gets worse starting from one-phase type to three-phase type. A detailed mathematical quantification is presented in Table 5.1.

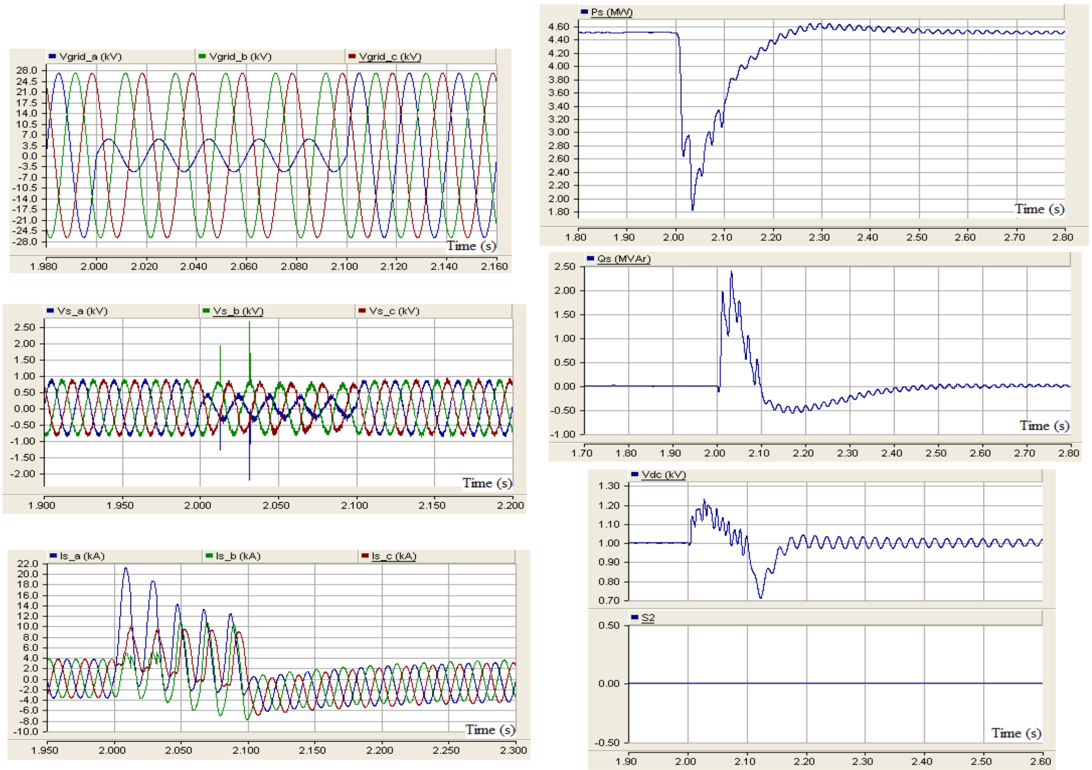

Figure 5.36: 0.8pu one-phase voltage sag excluding a mono-stable

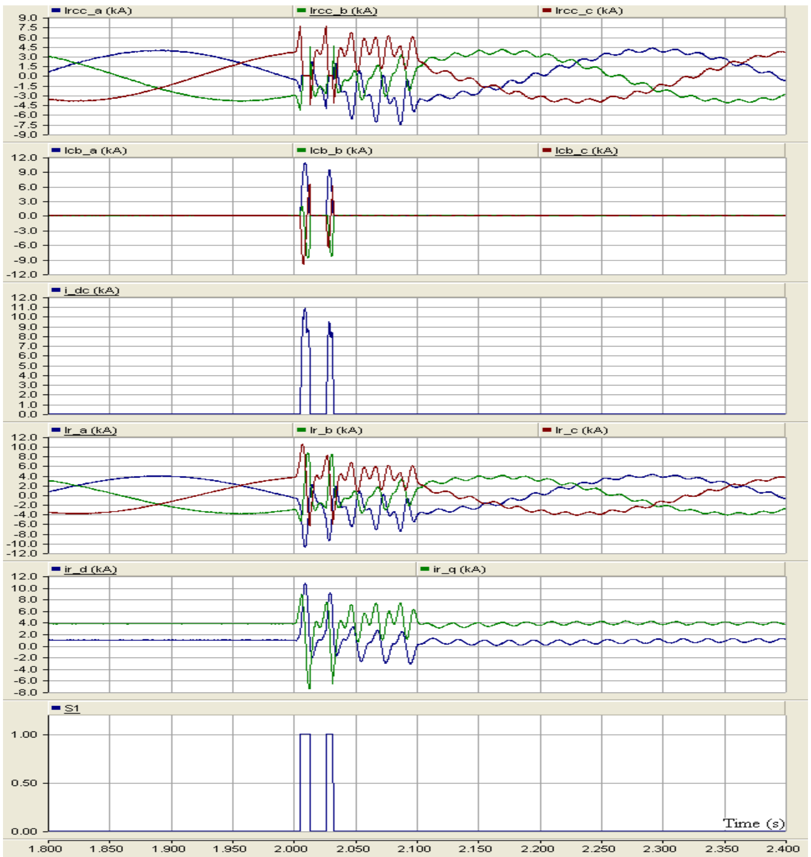

Figure 5.37: Rotor-side currents during a 0.8pu one-phase voltage sag excluding a mono-stable

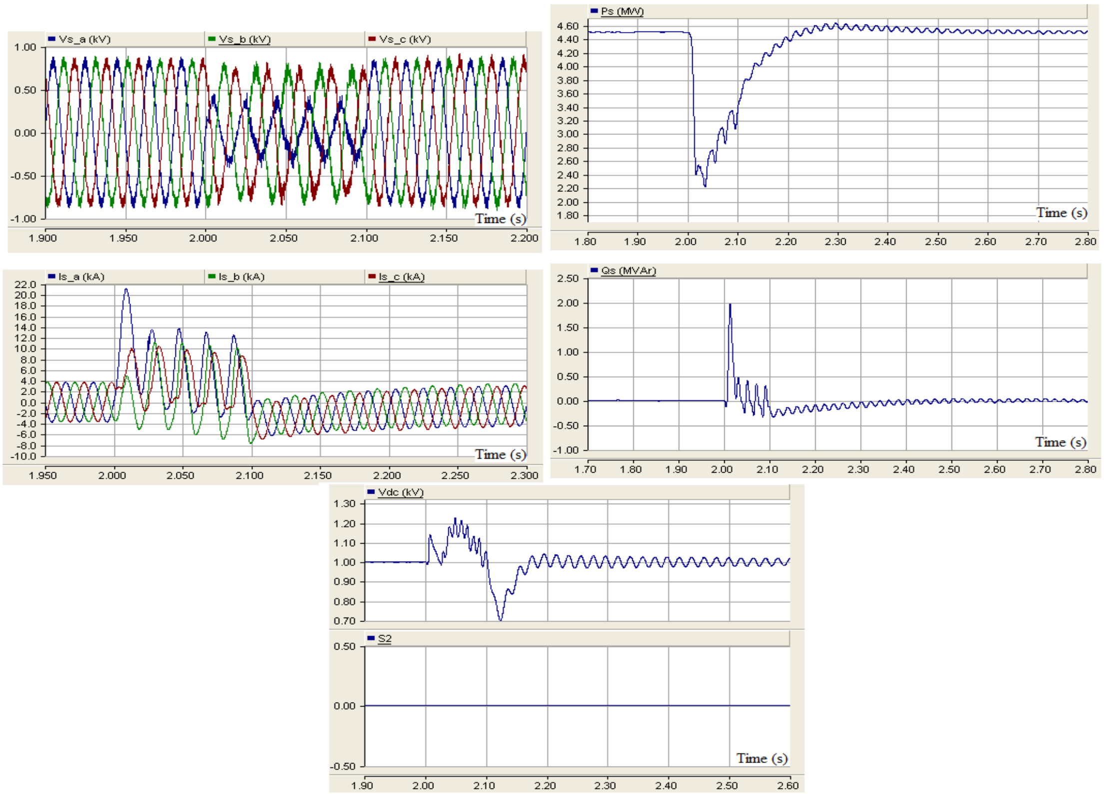

Figure 5.38: 0.8pu one-phase voltage sag including a mono-stable (0.0202s)

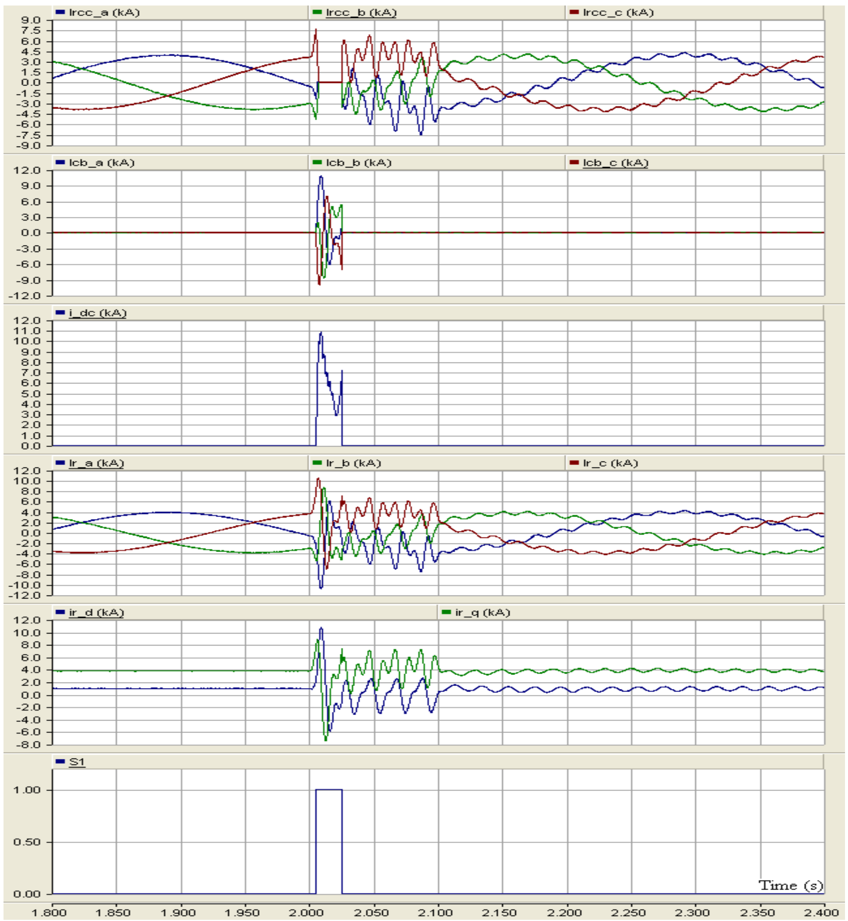

Figure 5.39: Rotor-side currents during a 0.8pu one-phase voltage sag including a mono-stable (0.0202s) – Improved results

Voltage sag type	Voltage sag magnitude and suggested lock-out time		Variation in stator active power (P_s^*=4.5MW)	Variation in stator reactive power (Q_s^*=0MVAr)	Variation in DC-link voltage (V_{dc}^*=1kV)
Three-phase	0.2pu		4.2MW	±0.2MVAr	1.1kV 0.9kV
Three-phase	0.5pu		2.8MW	±0.5MVAr	1.31kV 0.7kV
Three-phase	0.8pu	no lock-out time	0.6MW	+0.8MVAr -2.25MVAr	1.32kV 0.55kV
		10ms of lock-out time	0.4MW	+0.8MVAr -1.8MVAr	1.29kV 0.7kV
		45ms of lock-out time	0MW	+0.8MVAr -0.5MVAr	1.2kV 0.9kV
Two-phase	0.2pu		4.25MW	±0.2MVAr	1.1kV 0.95kV
Two-phase	0.5pu		3.5MW	+0.9MVAr -0.3MVAr	1.31kV 0.75kV
Two-phase	0.8pu	no lock-out time	0.5MW	+3.25MVAr -0.5MVAr	1.25kV 0.75kV
		20.5ms of lock-out time	-0.2MW	+2MVAr -1.6MVAr	1.1kV 0.9kV
One-phase	0.2pu		4.38MW	+0.15MVAr -0.06MVAr	1.05kV 0.95kV
One-phase	0.5pu		4.18MW	+0.35MVAr -0.2MVAr	1.18kV 0.9kV
One-phase	0.8pu	no lock-out time	1.8 MW	+2.4MVAr -0.5MVAr	1.22kV 0.7kV
		20.2ms of lock-out time	2.2MW	+2MVAr -0.25MVAr	1.22kV 0.7kV

Table 5.1: Summary of the effects of the voltage sag types on the DC-link voltage, stator active and reactive power

5.6 Investigation of the Relation between the Rotor Crowbar and the DC-link Brake Protection Actions

In this section, there are two severe voltage sag conditions assessed: 0.8pu three-phase and 0.8pu two-phase voltage sags are applied to the grid voltage. Other voltage sags are presented in Appendix 4. To discover the relation between the protection actions, for each case the stator active and reactive power, the DC-link voltage and the rotor-side currents responses are traced in the orders of not involving any protection, triggering only DC-link brake (crowbar is inactive), activating only crowbar (DC-link brake is suspended) and taking both protection actions. Note that a lock out time of 45ms is used in the crowbar logic circuit for the 0.8pu 3-phase voltage sag, and that of 20.5ms is used for 0.8pu 2-phase voltage sag in order to let the crowbar take only single action during the sag event. The final ‘best’ choice depends on the local optimisation required by the application in the ‘real-world’. The related simulation results of this investigation are given in the following figures.

The 0.8pu 3-phase voltage sag has been considered as the most severe condition in this thesis. Without taking any protection and taking only DC-link brake activation, this exhibits the worst response characteristics in the rotor-side currents, DC-link voltage, stator active and reactive powers as seen in Figures 5.40-5.41 and Figures 5.44-5.45. The stator reactive power fluctuates between approximately +7MVAr and -6MVAr while the stator real power oscillates in the range of +6/+7MW and -2MW. Negative real power means that the DFIG turns into a motor absorbing the real power from the network. It is understood from the related simulation results that activating only the DC-link brake causes the most severe consequences. Employing the crowbar protection is essential to improve the results. The stator active and reactive power output are pulled back to transiently stable conditions (see left-side graphs in Figures 5.42 and 5.43). It also helps the DC-link voltage exhibit less stress, become more stable and stay between the upper and lower limits during the voltage sag period (see right-side graph in Figures 5.42 and 5.43). Note that the DC-link brake did not activate since the DC-link brake is kept between the thresholds. The over-currents in the rotor side also extinguish and drop below the upper threshold value most of the time during the sag incident.

It is noted that less severe consequences occur in the system response under a 0.8pu 2-phase voltage sag. Less oscillations and variations are observed in the quantities. The full simulation results for a 0.8pu 2-phase voltage sag are given from Figure 5.48 to Figure 5.55. The same method utilised for the 0.8pu 3-phase voltage sag applies to the 0.8pu 2-phase voltage sag as well.

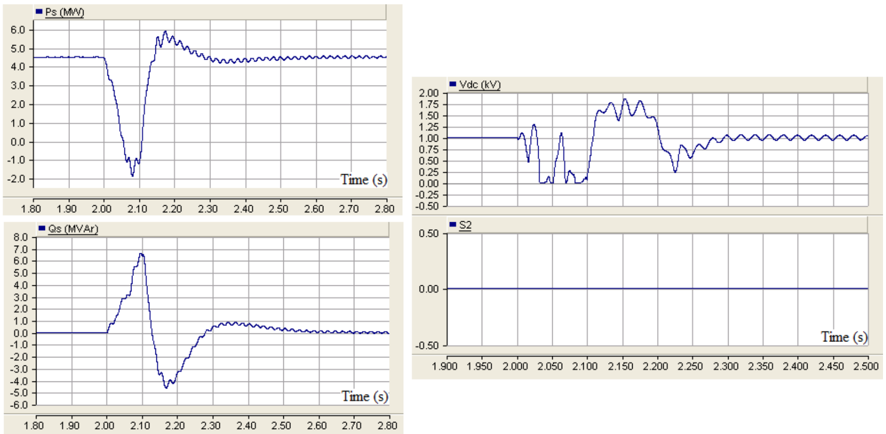

Figure 5.40: The DC-link voltage, stator real and reactive power behaviours during a 0.8pu 3-phase voltage sag in the case of no protection involved

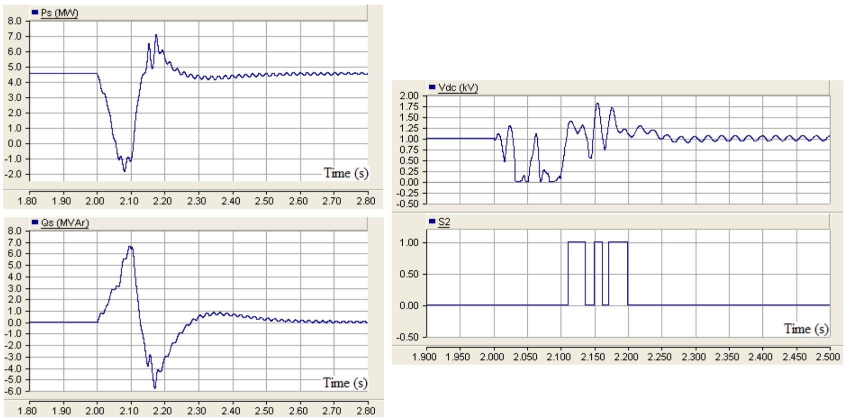

Figure 5.41: The DC-link voltage, stator real and reactive power behaviours during a 0.8pu 3-phase voltage sag by activating only DC-link brake protection

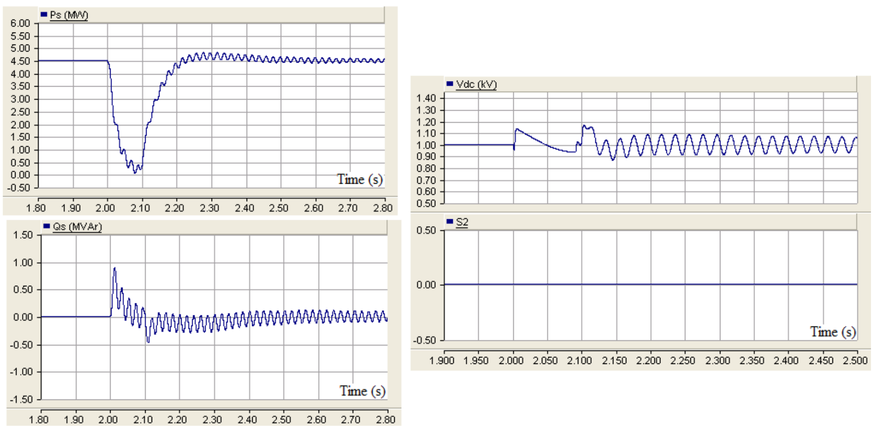

Figure 5.42: The DC-link voltage, stator real and reactive power behaviours during a 0.8pu 3-phase voltage sag by activating only crowbar protection

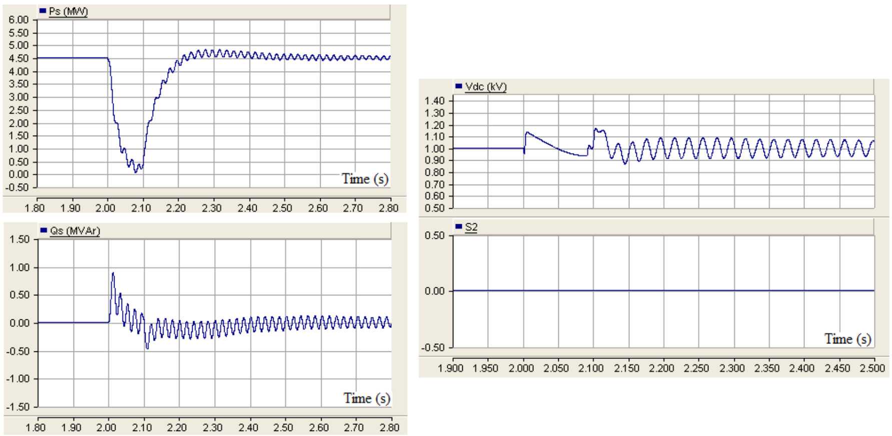

Figure 5.43: The DC-link voltage, stator real and reactive power behaviours during a 0.8pu 3-phase voltage sag by activating both crowbar and DC-link brake protections

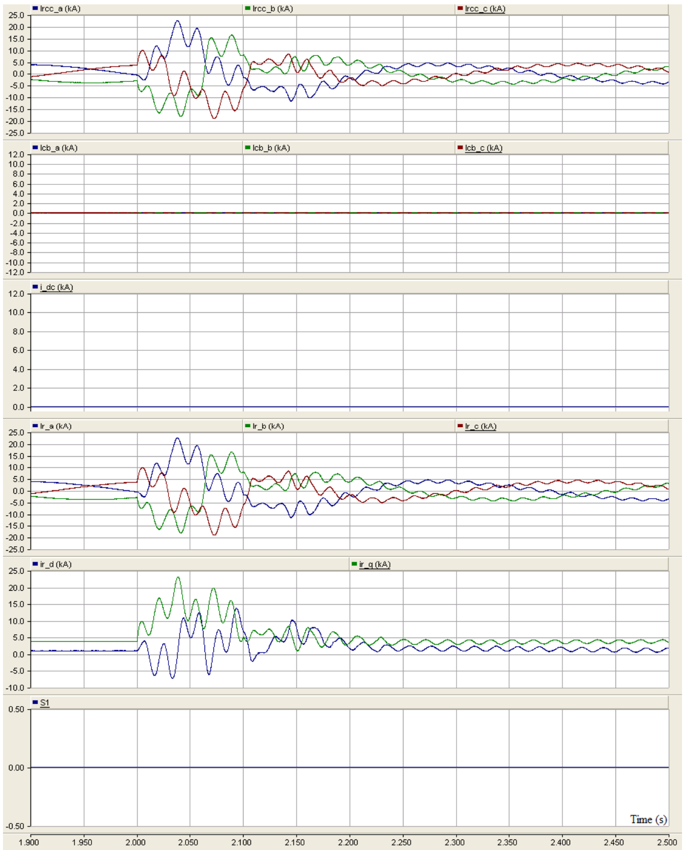

Figure 5.44: Rotor-side currents behaviours during a 0.8pu 3-phase voltage sag in the case of no involving any protection

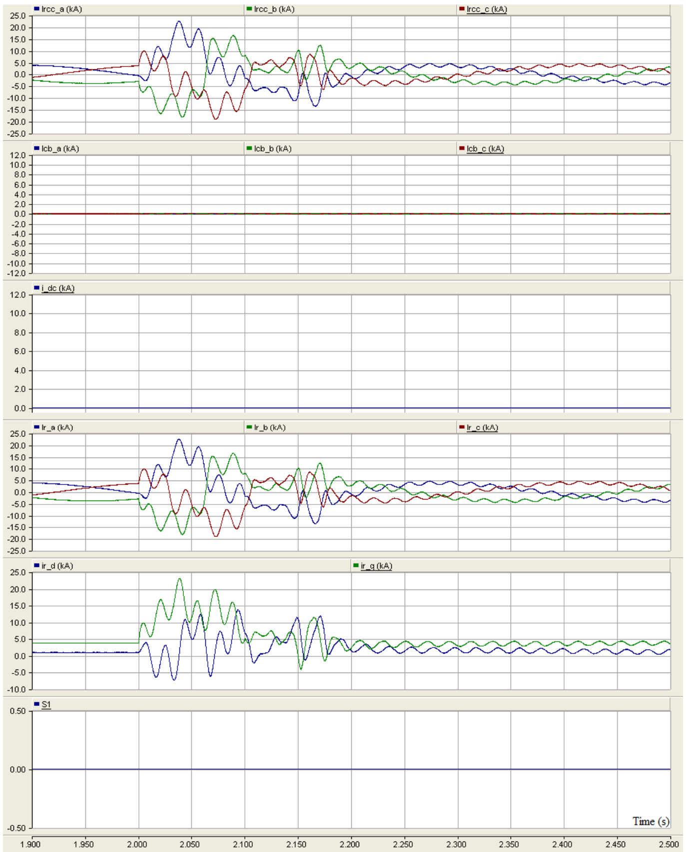

Figure 5.45: Rotor-side currents behaviours during a 0.8pu 3-phase voltage sag by activating only DC-link brake protection

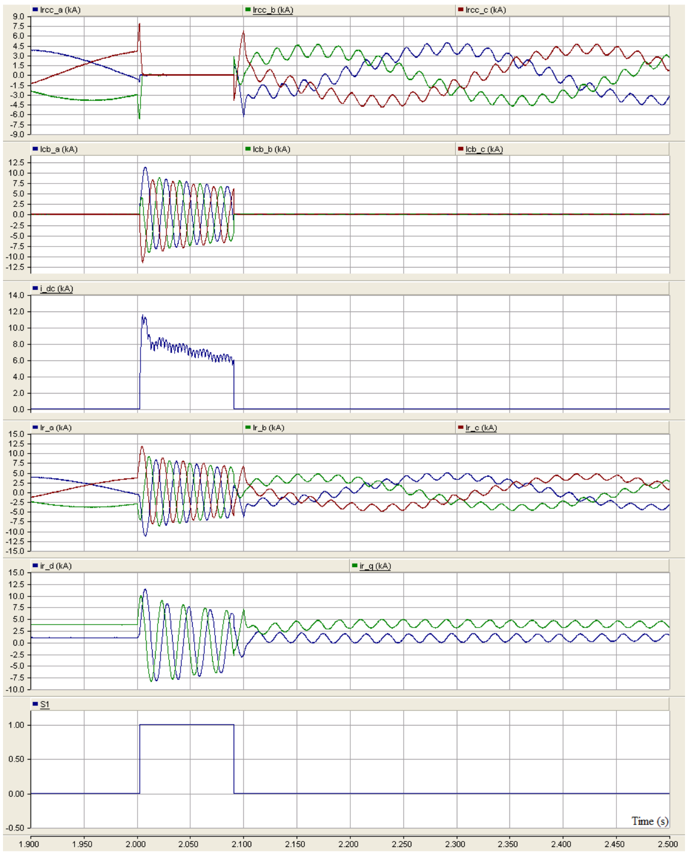

Figure 5.46: Rotor-side currents behaviours during a 0.8pu 3-phase voltage sag by activating only crowbar protection

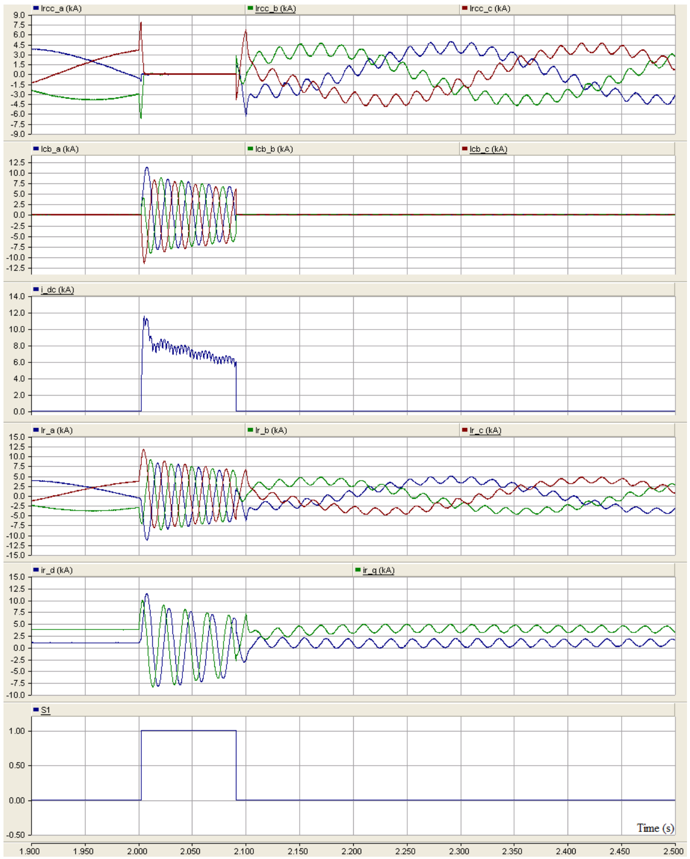

Figure 5.47: Rotor-side currents behaviours during a 0.8pu 3-phase voltage sag by activating both crowbar and DC-link brake protections

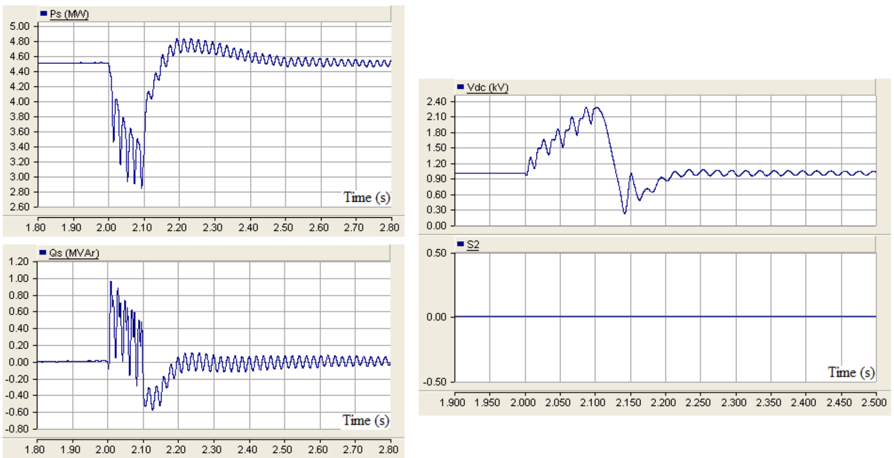

Figure 5.48: The DC-link voltage, stator real and reactive power behaviours during a 0.8pu 2-phase voltage sag in the case of no involving any protection

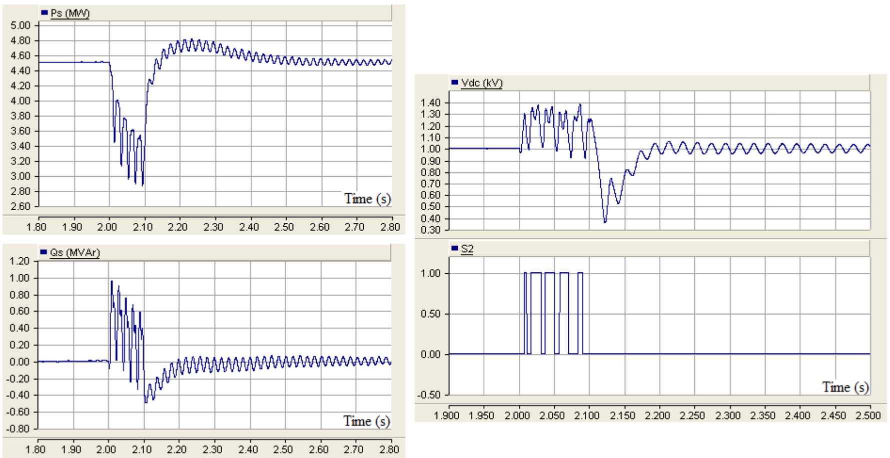

Figure 5.49: The DC-link voltage, stator real and reactive power behaviours during a 0.8pu 2-phase voltage sag by activating only DC-link brake protection

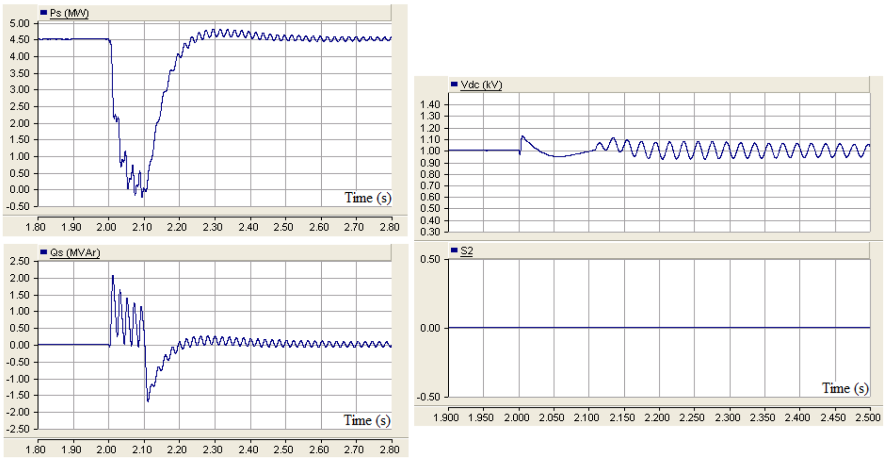

Figure 5.50: The DC-link voltage, stator real and reactive power behaviours during a 0.8pu 2-phase voltage sag by activating only crowbar protection

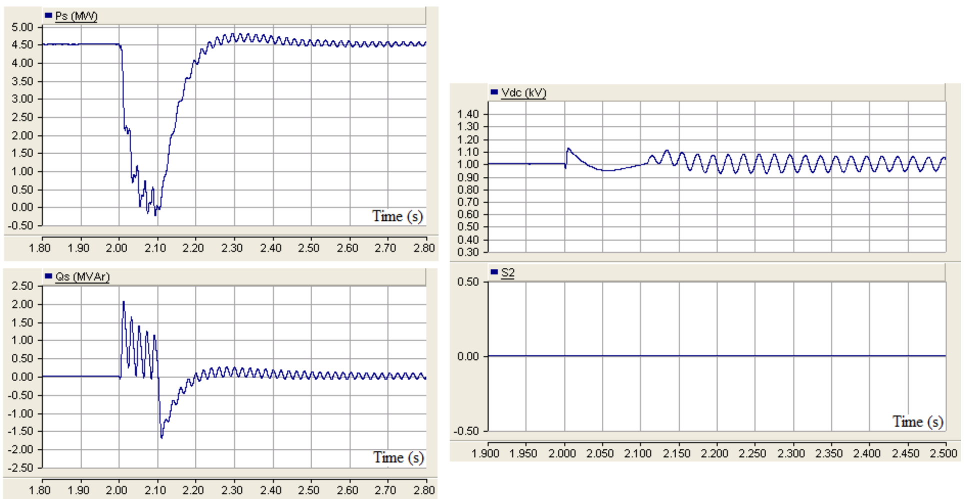

Figure 5.51: The DC-link voltage, stator real and reactive power behaviours during a 0.8pu 2-phase voltage sag by activating both crowbar and DC-link brake protections

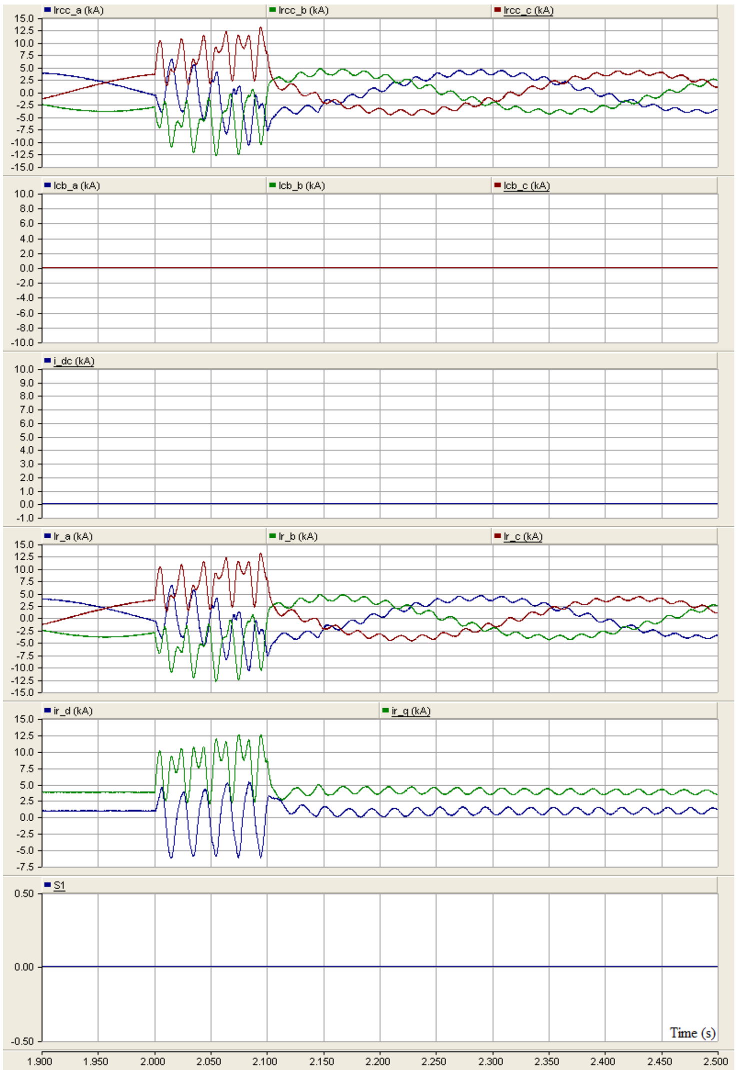

Figure 5.52: Rotor-side currents behaviours during a 0.8pu 2-phase voltage sag in the case of no involving any protection

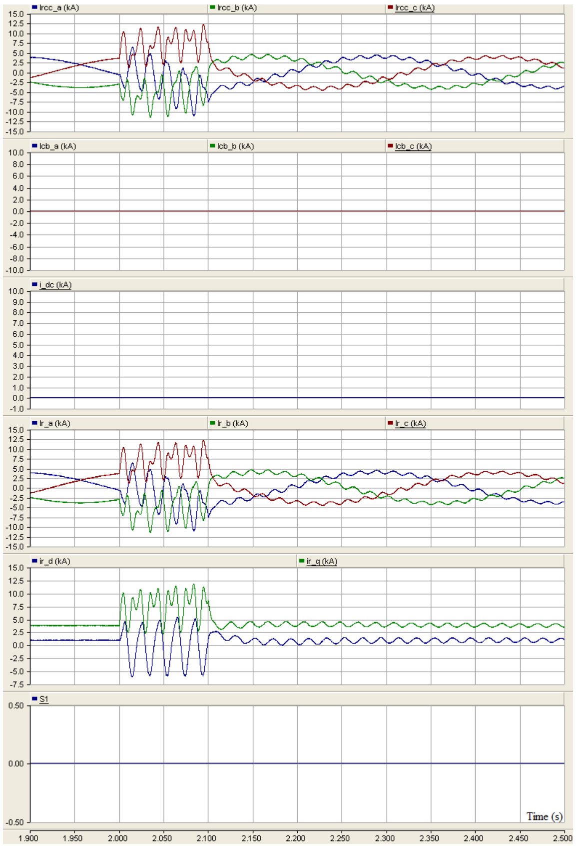

Figure 5.53: Rotor-side currents behaviours during a 0.8pu 2-phase voltage sag by activating only DC-link brake protection

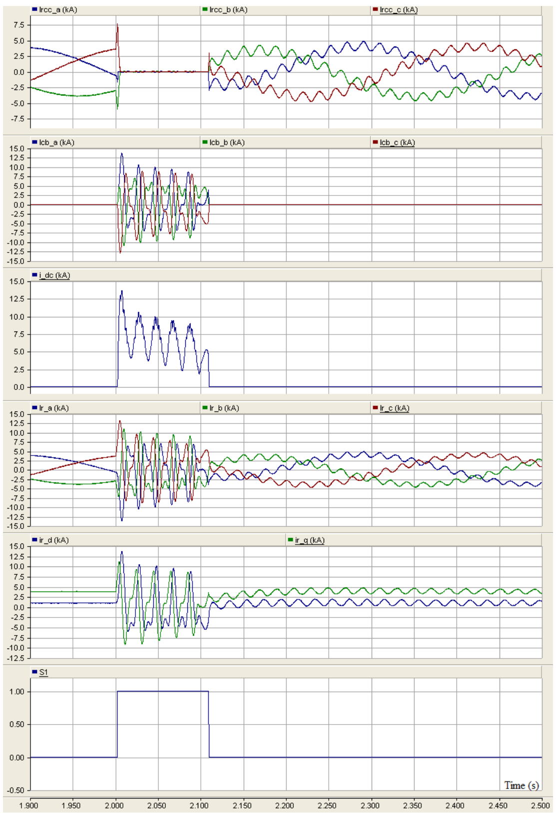

Figure 5.54: Rotor-side currents behaviours during a 0.8pu 2-phase voltage sag by activating only crowbar protection

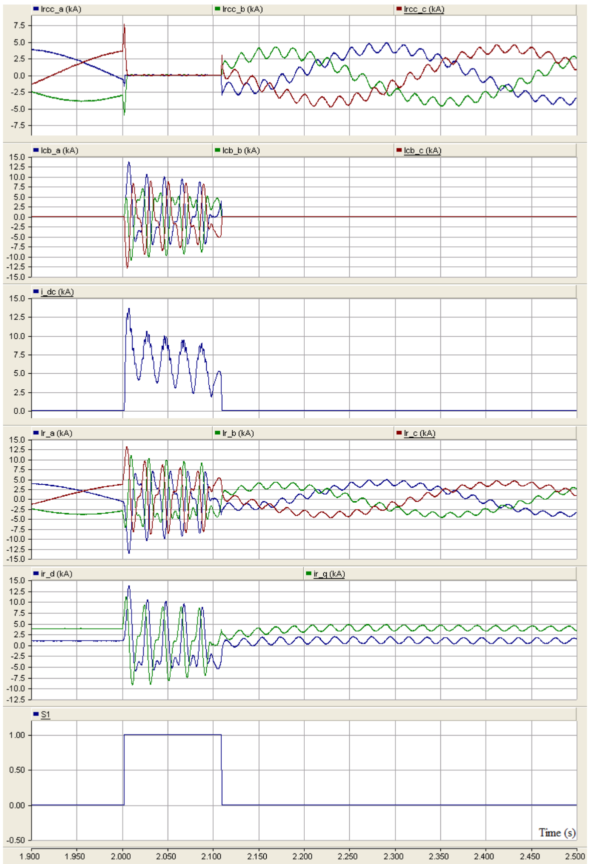

Figure 5.55: Rotor-side currents behaviours during a 0.8pu 2-phase voltage sag by activating both crowbar and DC-link brake protections

5.7 Summary

The rotor crowbar protection and the DC-link brake circuits were designed. The controller algorithms for these protection schemes were shown to work. The control loop segmentation was achieved. The selection of tuning parameters for the controller loops was described. The electrical interaction between these loops was reduced and reasonably minimised to get adequate performance.

Noticeable is the interaction between the DFIG operational control, sag behaviour, the DC-link brake and the crowbar. The link between the protection actions is investigated. If the DC-link protection only activates, the system cannot remain transiently stable, and this is insufficient for more severe dips since it creates severe power oscillations. The crowbar control on its own can guarantee the DC-link optimum voltage control. Activating both the crowbar and the DC-link brake together is a requirement for a good DC-link voltage and stability control.

Chapter 6 Improved RSC Outer (Power) Loop Control

6.1 Introduction

The enhancement of the outer (power) loop control of the rotor-side converter (RSC) is investigated in this chapter. Instead of a PI controller, a PID controller is used to design the power loop control. Other controllers have been suggested of varying complexity however a PID is chosen since controllers must be tuned by field engineers. This type is familiar to them and relatively easy to programme. A sensitivity analysis of the outer loop control is undertaken by varying undamped natural frequency (f_n) and damping ratio (ζ) as well as the K_D parameter. As mentioned earlier in Chapter 5 (see Figure 5.1) the ranges of f_n and ζ for power loop control are set to 0.7 – 1.1 and 1Hz – 2.5Hz, respectively. Appropriate K_D values are also worked through. The effects of varying these parameters on the system control design are examined. The robustness analysis for each selected stator voltage (V_s: 0.8pu, 1pu and 1.2pu) is carried out by manually changing the mutual (magnetising) and stator self-inductances (L_m and L_{ss}) by ±10%.

6.2 Choosing a PI Controller

The conventional control approach for DFIG converters is to use a PI control. First, a PI controller is utilised for the outer (power) loop control of the rotor-side converter. As mentioned in Chapter 3 the stator active and reactive power equations are shown again here (equations 6.1 and 6.2) in order to get the controller equations for tuning process.

$$P_s = -\frac{3}{2}\frac{\sqrt{2}V_s L_m}{L_{ss}} i^e_{r\_q} \tag{6.1}$$

$$Q_s = \frac{3}{2}\frac{\sqrt{2}V_s}{L_{ss}} \Psi^e_s - \frac{3}{2}\frac{\sqrt{2}V_s L_m}{L_{ss}} i^e_{r\_d} \tag{6.2}$$

Neglecting the inner (current) loop by assuming that it is fast, using the above-mentioned power equations and considering a PI controller for the outer (power) loop of the RSC, the state-feedback system-block (SFSB) diagram can be depicted as in Figure 6.1. Note that the full SFSB of the RSC control was given in Chapter 5 (see Figure 5.3).

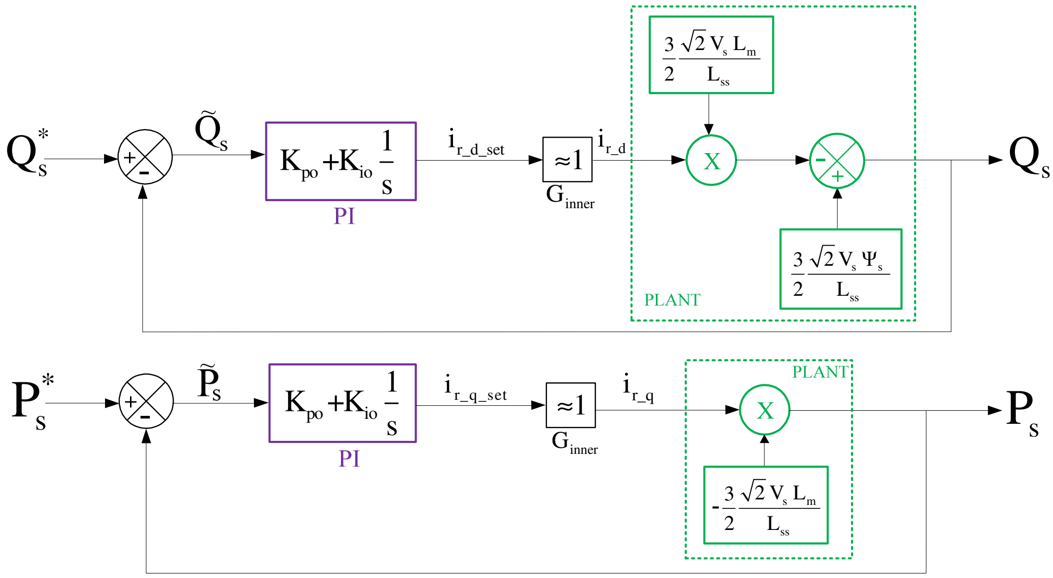

Figure 6.1: Outer (power) loop control of the RSC utilising the PI controller

The full-transfer function (FTF1) of the power loop of the RSC converter employing a PI controller can then be derived as:

$$\mathrm{FTF1}=\frac{Q_s}{Q_s^*}=\frac{P_s}{P_s^*}=\frac{\left(K_{po}+K_{io}\frac{1}{s}\right)\left(\frac{3}{2}\frac{\sqrt{2}V_sL_m}{L_{ss}}\right)}{1+\left(K_{po}+K_{io}\frac{1}{s}\right)\left(\frac{3}{2}\frac{\sqrt{2}V_sL_m}{L_{ss}}\right)}=\frac{\left(sK_{po}+K_{io}\right)}{\left(K_{po}+\frac{2}{3}\frac{L_{ss}}{\sqrt{2}V_sL_m}\right)s+K_{io}} \tag{6.3}$$

Assuming $K_{io}>>K_{po}$, FTF1 can be reduced to

$$\mathrm{STF1}=\frac{K_{io}}{s\left(K_{po}+\frac{2}{3}\frac{L_{ss}}{\sqrt{2}V_sL_m}\right)+K_{io}} \tag{6.4}$$

STF1 (simplified transfer function) can be made to look like a typical first-order transfer function ($\frac{1}{Ts+1}$ [101]) by dividing both the numerator and denominator by K_{io}. Approximating the STF1 to a first-order transfer function (FoTF)

$$\mathrm{FoTF}=\frac{1}{\frac{\left(K_{po}+\frac{2}{3}\frac{L_{ss}}{\sqrt{2}V_sL_m}\right)}{K_{io}}s+1} \tag{6.5}$$

where T, time constant, is equal to

$$T=\frac{K_{po}+\frac{2}{3}\frac{L_{ss}}{\sqrt{2}\,V_s\,L_m}}{K_{io}} \tag{6.6}$$

As seen in equation 6.4, using a PI controller gives us a first-order transfer function in the case considered in this work. The undamped natural frequency (f_n) equation will then be the inverse of T shown in equation 6.6. For a pre-set value of the (f_n), the tuning parameters (K_{po} and K_{io}) should be reasonably calculated by also taking the assumption of $K_{io}>>K_{po}$ into account. Since this control type allows us to only set the bandwidth (in Hz or rad/s) but unfortunately not the damping, it may not be appropriate.

6.3 Choosing a PID Controller

The PI controller is replaced with a PID controller in this research in order to have the ability to set both the bandwidth and the damping. However, the tuning process of PID control is more complicated than that of PI control, and selecting K_D, K_{po}, and K_{io} parameters needs to be done very carefully. In previous systems, K_p and K_i were set to achieve a nominal bandwidth and damping. Now setting three parameters to two design constraints allows a great deal of freedom but also means other factors can and have to be taken into account other than undamped natural frequency and damping ratio to achieve 'good' tuning. The outer (power) loop control of the RSC using a PID controller is illustrated in Figure 6.2. The three degrees of freedom to set two quantities is also unhelpful since it does not give a ‘defined’ problem solution. The user is left with considerable design choices. Two degrees of freedom and two tuning parameters are much easier. This defines a solution but gives the user fewer design choices.

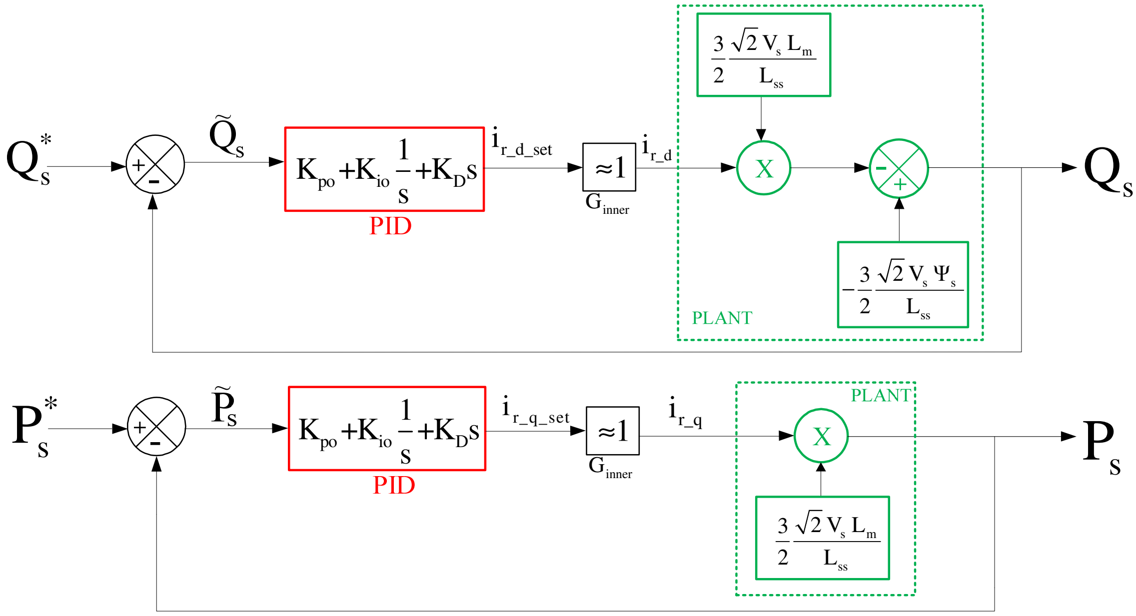

Figure 6.2: Outer (power) loop control of RSC utilising the PID controller

The full-transfer function (FTF2) is

$$FTF2=\frac{Q_s}{Q_s^*}=\frac{P_s}{P_s^*}=\frac{\left(K_{po}+K_{io}\frac{1}{s}+K_D s\right)\left(\frac{3}{2}\frac{\sqrt{2}V_s L_m}{L_{ss}}\right)}{1+\left(K_{po}+K_{io}\frac{1}{s}+K_D s\right)\left(\frac{3}{2}\frac{\sqrt{2}V_s L_m}{L_{ss}}\right)}=\frac{\left(K_D s^2+K_{po}s+K_{io}\right)}{K_D s^2+\left(K_{po}+\frac{2}{3}\frac{L_{ss}}{\sqrt{2}V_s L_m}\right)s+K_{io}}$$

$$=\frac{\left(s^2+s\frac{K_{po}}{K_D}+\frac{K_{io}}{K_D}\right)}{s^2+\frac{\left(K_{po}+\frac{2}{3}\frac{L_{ss}}{\sqrt{2}V_s L_m}\right)}{K_D}s+\frac{K_{io}}{K_D}} \tag{6.7}$$

Neglecting s^2 term from the numerator of equation 6.7, FTF2 turns into STF2:

$$STF2=\frac{\left(s\frac{K_{po}}{K_D}+\frac{K_{io}}{K_D}\right)}{s^2+\frac{\left(K_{po}+\frac{2}{3}\frac{L_{ss}}{\sqrt{2}V_s L_m}\right)}{K_D}s+\frac{K_{io}}{K_D}} \tag{6.8}$$

Assuming $\frac{K_{io}}{K_D}>>\frac{K_{po}}{K_D}$, the simplified transfer function (STF2) is further reduced to the second-order approximated transfer function (SoATF) shown in equation 6.9.

$$\text{SoATF}=\frac{\dfrac{K_{io}}{K_D}}{s^2+\dfrac{\left(K_{po}+\dfrac{2}{3}\dfrac{L_{ss}}{\sqrt{2}\,V_s\,L_m}\right)}{K_D}s+\dfrac{K_{io}}{K_D}} \tag{6.9}$$

To extract the damping ratio (ζ) and the undamped natural frequency (ω_n), the SoATF needs to be equated to $\approx \dfrac{\omega_n^2}{s^2+2\zeta\omega_n s+\omega_n^2}$

$$\omega_n^2=\frac{K_{io}}{K_D}\Rightarrow\omega_n=\sqrt{\frac{K_{io}}{K_D}} \quad (6.10) \quad \text{and} \quad 2\zeta\omega_n=\frac{K_{po}+\dfrac{2}{3}\dfrac{L_{ss}}{\sqrt{2}\,V_s\,L_m}}{K_D}\Rightarrow\zeta=\frac{K_{po}+\dfrac{2}{3}\dfrac{L_{ss}}{\sqrt{2}\,V_s\,L_m}}{2\sqrt{K_{io}K_D}} \quad (6.11)$$

6.4 Tuning Process of the PID Loop for Nominal Operating Point

Around 90-95% of the controller types widely used in the industry are based on the proportional (P) - integral (I) - derivative (D) controllers (PID), which are also known as the "three-term" controllers [102, 103 and 104]. The main drawback of the PID controller is that there is no standardisation of design and tuning process for the PID controllers. The tuning process is also confidential and used within only the patent holders. Moreover, tuning method of the PID is slightly more complex than that of the PI, and needs extra care.

As a reminder, in a standard PID controller, the P-term gain (K_p) is proportional to the error and reduces the steady-state error. The I-term gain (K_i) is proportional to the integral of the error and reduces this offset error down to zero. The D-term gain (K_D) provides an improvement in the closed-loop stability. The future characteristic of the error can also be anticipated by using the derivative action. Therefore, using a PID controller can enhance the system transient response and the system response steady-state errors [105]. The independent effect of these three terms on the overall system response is summarised in a table in [104] and shown in this section (see Table 6.1). In the meantime, a reasonable derivative-term gain should be chosen since increasing it further makes the system too sensitive to noise.

Closed-loop Response	**Rise Time**	**Overshoot**	**Settling Time**	**Steady-state Error**	**Stability**
Increasing K_p	Decreases	Increases	Small Increase	Decreases	Degrades
Increasing K_i	Small Decrease	Increases	Increases	Large Decrease	Degrades
Increasing K_D	Small Decrease	Decreases	Decreases	Minor Change	Improves

Table 6.1: Effects of Independent P, I and D Tuning [104]

Using a PID controller instead of a PI for the power loop of the RSC considered in this research gives the advantage of setting both controller quantities, which are damping and bandwidth. For a given undamped natural frequency (f_n) and damping ratio (ζ), in order to calculate the tuning gains, K_{po} and K_{io}, an appropriate value of K_D should be chosen and then the equations of the f_n and ζ (see equations 6.10 and 6.11) can be used. The data of electrical quantities existing in the related above-mentioned equations are taken from [16] and given in Appendix1.

Considering the nominal values of those quantities, $\frac{2}{3}\frac{L_{ss}}{\sqrt{2}\,V_s\,L_m}$ is equal approximately to 0.852. In order to approximate the full-transfer function (FTF2) shown in equation 6.7 to that in equation 6.9, the assumption of $\frac{K_{io}}{K_D} >> \frac{K_{po}}{K_D}$ was proposed and the s^2 term in the numerator was neglected.

As a rule of thumb $\frac{K_{io}}{K_D}$ should be greater enough than $\frac{K_{po}}{K_D}$ and K_D must be as reasonably small as possible to reduce the noise and so as to ensure that the system response is least influenced by the noise. But, a too small K_D may result in a negative K_{po}. To avoid from entering into a negatively damped region, which is also out of interest, a positive K_{po} should be guaranteed by choosing a reasonable K_D. The tuning gains for selected undamped natural frequency , damping ratio and K_D are presented in Table 6.2 by assuming that is $\frac{K_{io}}{K_D}$ 10 times greater than $\frac{K_{po}}{K_D}$. Note that if the ratio of $\frac{K_{io}}{K_D} >> \frac{K_{po}}{K_D}$ increases further, K_{po} gets too small. Therefore, this ratio should be decided carefully.

$\frac{K_{io}}{K_D} >> \frac{K_{po}}{K_D}$ ≈10 times	f_n=2.5Hz and ζ=1			
	K_{po}	K_{io}	$T_{io}(=1/K_{io})$	K_D
	3.075	30.84s-1	0.0324s	0.125s

Table 6.2: Tuning parameters for power (PID) loop controller of the RSC

6.5 Sensitivity Analysis

The control sensitivity analysis is conducted for the power (outer) loop of the rotor-side converter where the inner loop of the rotor-side and both inner and outer loops of the grid-side converter control are tuned for fixed undamped natural frequency (f_n) and damping ratio (ζ) parameters. In this analysis, the only outer loop tuning parameters of the rotor-side converter control are being varied. In order to investigate the impacts of the PID tuning parameters on the system response, each time only one parameter is varied while others are kept constant at their pre-defined reference values.

The first step of the sensitivity analysis is to vary the f_n from 1Hz to 2.5Hz in case of fixed ζ and K_D. Secondly, the ζ is varied between 0.7 and 1.1 while keeping the f_n and K_D constant. Finally, the K_D is varied from 0.1s to 0.4s for the fixed values of f_n and ζ. In doing so, the reasonable search space for tuning parameters and gains for the PID controller used as the outer (power) loop controller of the RSC is investigated. The sensitivity analysis work is applied to the full transfer function (FTF2), simplified transfer function (STF2) and second-order approximated transfer function (SoATF) of the outer (power) loop PID controller. These functions are illustrated in Table 6.3.

Rotor-side Converter Outer (Power) Loop PID	$\dfrac{\frac{K_{io}}{K_D}}{s^2+\left(\frac{K_{po}+0.852}{K_D}\right)s+\frac{K_{io}}{K_D}}$ SoATF	$\dfrac{s\frac{K_{po}}{K_D}+\frac{K_{io}}{K_D}}{s^2+\left(\frac{K_{po}+0.852}{K_D}\right)s+\frac{K_{io}}{K_D}}$ STF2	$\dfrac{s^2+s\frac{K_{po}}{K_D}+\frac{K_{io}}{K_D}}{s^2+\left(\frac{K_{po}+0.852}{K_D}\right)s+\frac{K_{io}}{K_D}}$ FTF2

Table 6.3: Full (FTF2), simplified (STF2) and second-order approximated (SoATF) transfer functions of the power (outer) loop controller of the RSC

The variation processes for undamped natural frequency (f_n or ω_n), damping ratio (ζ) and derivative time constant (K_D) are contextually given in the tables in Appendix 5 (see Tables A.5.2, A.5.5, A.5.8 to A.5.12). The green coloured operating points are those for which the assumptions made remain true and are utilised in this main chapter. Full representations of this sensitivity analysis, including some red coloured regions as well, which do not ensure the assumptions made, are also documented in Appendix 5.

6.5.1 Varying Undamped Natural Frequency

The undamped natural frequency (f_n) is varied from 1Hz to 2.5Hz with an increment of 0.5Hz, where the damping ratio and the derivative time gain are kept constant at their pre-defined values. The instructions for varying f_n are given in Table A.5.2. The mathematical calculations of those operating points ensuring that $\frac{K_{io}}{K_D} >> \frac{K_{po}}{K_D}$ is greater than 10 are shown as an Excel table in Table 6.4 and they are substituted in the full, simplified and second-order approximated transfer functions presented in Table 6.3.

Varying undamped natural frequency for fixed damping ratio and derivative time constant											
ζ	ω_n (rad/s)	K_d (s)	K_{po}	K_{io} (1/s)	T_{io} (s)	f_n (Hz)	π	Kio / Kd	Kpo / Kd	(Kpo+0.852)/Kd	(Kio/Kd) / (Kpo/Kd)
0.7	6.283	0.1	0.028	3.948	0.253	1	3.142	39.478	0.275	8.795	143.370
0.7	9.425	0.1	0.467	8.883	0.113	1.5	3.142	88.826	4.674	13.194	19.006
0.7	12.566	0.1	0.907	15.791	0.063	2	3.142	157.914	9.072	17.592	17.407
0.7	15.708	0.1	1.347	24.674	0.041	2.5	3.142	246.740	13.470	21.990	18.318
0.8	6.283	0.1	0.153	3.948	0.253	1	3.142	39.478	1.532	10.052	25.769
0.8	9.425	0.1	0.656	8.883	0.113	1.5	3.142	88.826	6.559	15.079	13.544
0.8	12.566	0.1	1.159	15.791	0.063	2	3.142	157.914	11.585	20.105	13.631
0.8	15.708	0.1	1.661	24.674	0.041	2.5	3.142	246.740	16.612	25.132	14.853
0.9	6.283	0.1	0.279	3.948	0.253	1	3.142	39.478	2.789	11.309	14.157
0.9	9.425	0.1	0.844	8.883	0.113	1.5	3.142	88.826	8.444	16.964	10.520
0.9	12.566	0.1	1.410	15.791	0.063	2	3.142	157.914	14.098	22.618	11.201
0.9	15.708	0.1	1.975	24.674	0.041	2.5	3.142	246.740	19.753	28.273	12.491
1	15.708	0.1	2.289	24.674	0.041	2.5	3.142	246.740	22.895	31.415	10.777

Table 6.4: Calculations in Excel for the assessment of varying f_n

As seen from Table 6.4, increasing the f_n increases the K_{po} and K_{io}, and decreases the T_i where the damping ratio and K_D quantities are constant. This relation is also confirmed by the equations of the $\omega_n(=2\pi f_n)$ and damping ratio given below.

$$\text{increasing} \leftarrow \omega_n^2 = \frac{\overset{\text{increases}}{\overset{\uparrow}{K_{io}}}}{\underset{\text{constant}}{\underset{\downarrow}{K_D}}} \qquad \text{constant} \leftarrow \zeta = \frac{\overset{\text{increases}}{\overset{\uparrow}{K_{po}}} + \overset{\text{constant}}{\overset{\uparrow}{\boxed{\frac{2}{3}\frac{L_{ss}}{\sqrt{2}V_s L_m}}}}}{\underset{\text{increasing}}{\underset{\downarrow}{2\omega_n}} K_D \rightarrow \text{constant}}$$

The implementation of the related operating points given in Table 6.4 to the full, simplified and second-order approximated transfer functions is depicted in Table 6.5. In order to choose a 'best' f_n value or values for the power loop, the controller segmentation graph shown in Figure 5.1 (see Chapter 5) should be taken into account. According to this figure, the f_n of 2Hz and 2.5Hz are 5 and 6.25 times faster than the fastest f_n assigned for the pitch controller, 5 and 4 times slower than the current (inner) loop of the rotor-side converter, respectively. These f_n values confirm the assumption made for the cascaded controller loops segmentation.

Rotor-side Converter Outer (Power) Loop PID		$\dfrac{\frac{K_{io}}{K_D}}{s^2+\left(\frac{K_{po}+0.852}{K_D}\right)s+\frac{K_{io}}{K_D}}$	$\dfrac{s\frac{K_{po}}{K_D}+\frac{K_{io}}{K_D}}{s^2+\left(\frac{K_{po}+0.852}{K_D}\right)s+\frac{K_{io}}{K_D}}$	$\dfrac{s^2+s\frac{K_{po}}{K_D}+\frac{K_{io}}{K_D}}{s^2+\left(\frac{K_{po}+0.852}{K_D}\right)s+\frac{K_{io}}{K_D}}$
$\zeta=0.7$ $K_D=0.1s$	$f_n=1Hz$	$\frac{39.5}{s^2+8.8s+39.5}$	$\frac{0.28s+39.5}{s^2+8.8s+39.5}$	$\frac{s^2+0.28s+39.5}{s^2+8.8s+39.5}$
	$f_n=1.5Hz$	$\frac{88.8}{s^2+13.2s+88.8}$	$\frac{4.7s+88.8}{s^2+13.2s+88.8}$	$\frac{s^2+4.7s+88.8}{s^2+13.2s+88.8}$
	$f_n=2Hz$	$\frac{158}{s^2+17.6s+158}$	$\frac{9.1s+158}{s^2+17.6s+158}$	$\frac{s^2+9.1s+158}{s^2+17.6s+158}$
	$f_n=2.5Hz$	$\frac{246.7}{s^2+22s+246.7}$	$\frac{13.5s+246.7}{s^2+22s+246.7}$	$\frac{s^2+13.5s+246.7}{s^2+22s+246.7}$
$\zeta=0.8$ $K_D=0.1s$	$f_n=1Hz$	$\frac{39.5}{s^2+10s+39.5}$	$\frac{1.5s+39.5}{s^2+10s+39.5}$	$\frac{s^2+1.5s+39.5}{s^2+10s+39.5}$
	$f_n=1.5Hz$	$\frac{88.8}{s^2+15s+88.8}$	$\frac{6.56s+88.8}{s^2+15s+88.8}$	$\frac{s^2+6.56s+88.8}{s^2+15s+88.8}$
	$f_n=2Hz$	$\frac{158}{s^2+20s+158}$	$\frac{11.6s+158}{s^2+20s+158}$	$\frac{s^2+11.6s+158}{s^2+20s+158}$
	$f_n=2.5Hz$	$\frac{246.7}{s^2+25.13s+246.7}$	$\frac{16.6s+246.7}{s^2+25.13s+246.7}$	$\frac{s^2+16.6s+246.7}{s^2+25.13s+246.7}$
$\zeta=0.9$ $K_D=0.1s$	$f_n=1Hz$	$\frac{39.5}{s^2+11.3s+39.5}$	$\frac{2.8s+39.5}{s^2+11.3s+39.5}$	$\frac{s^2+2.8s+39.5}{s^2+11.3s+39.5}$
	$f_n=1.5Hz$	$\frac{88.8}{s^2+17s+88.8}$	$\frac{8.45s+88.8}{s^2+17s+88.8}$	$\frac{s^2+8.45s+88.8}{s^2+17s+88.8}$
	$f_n=2Hz$	$\frac{158}{s^2+22.62s+158}$	$\frac{14.1s+158}{s^2+22.62s+158}$	$\frac{s^2+14.1s+158}{s^2+22.62s+158}$
	$f_n=2.5Hz$	$\frac{246.7}{s^2+28.3s+246.7}$	$\frac{19.75s+246.7}{s^2+28.3s+246.7}$	$\frac{s^2+19.75s+246.7}{s^2+28.3s+246.7}$
$\zeta=1$ $K_D=0.1s$	$f_n=1Hz$	$\frac{39.5}{s^2+12.565s+39.5}$	$\frac{4.05s+39.5}{s^2+12.565s+39.5}$	$\frac{s^2+4.05s+39.5}{s^2+12.565s+39.5}$
	$f_n=1.5Hz$	$\frac{88.8}{s^2+18.85s+88.8}$	$\frac{10.33s+88.8}{s^2+18.85s+88.8}$	$\frac{s^2+10.33s+88.8}{s^2+18.85s+88.8}$
	$f_n=2Hz$	$\frac{158}{s^2+25.13s+158}$	$\frac{16.6s+158}{s^2+25.13s+158}$	$\frac{s^2+16.6s+158}{s^2+25.13s+158}$
	$f_n=2.5Hz$	$\frac{246.7}{s^2+31.42s+246.7}$	$\frac{23s+246.7}{s^2+31.42s+246.7}$	$\frac{s^2+23s+246.7}{s^2+31.42s+246.7}$

Table 6.5: Varying f_n - SoATF, STF2 and FTF2

Since the remaining f_n values (1Hz and 1.5Hz) result in relatively slow response and fail to prove the related assumption, they are neglected. The varying operating points of undamped natural frequency for the damping ratios of 1 (excluding at 2.5Hz) and 1.1

are ignored because the ratio of $\frac{K_{io}}{K_D} >> \frac{K_{po}}{K_D}$ is less than 10. Therefore, the damping ratio values of 0.7, 0.8, 0.9 and 1 are of interest for the f_n values of 2Hz and 2.5Hz. The step response curves obtained in MATLAB for these operating points are illustrated in Figures 6.3-6.6. The difference between the bottom graph (step response of the full transfer function - FTF2) of Figures 6.3 to 6.11 and the classic step response is a simulation artefact which would not appear in reality since the actuator output saturates in practice. Further explanation is given in Appendix 5.

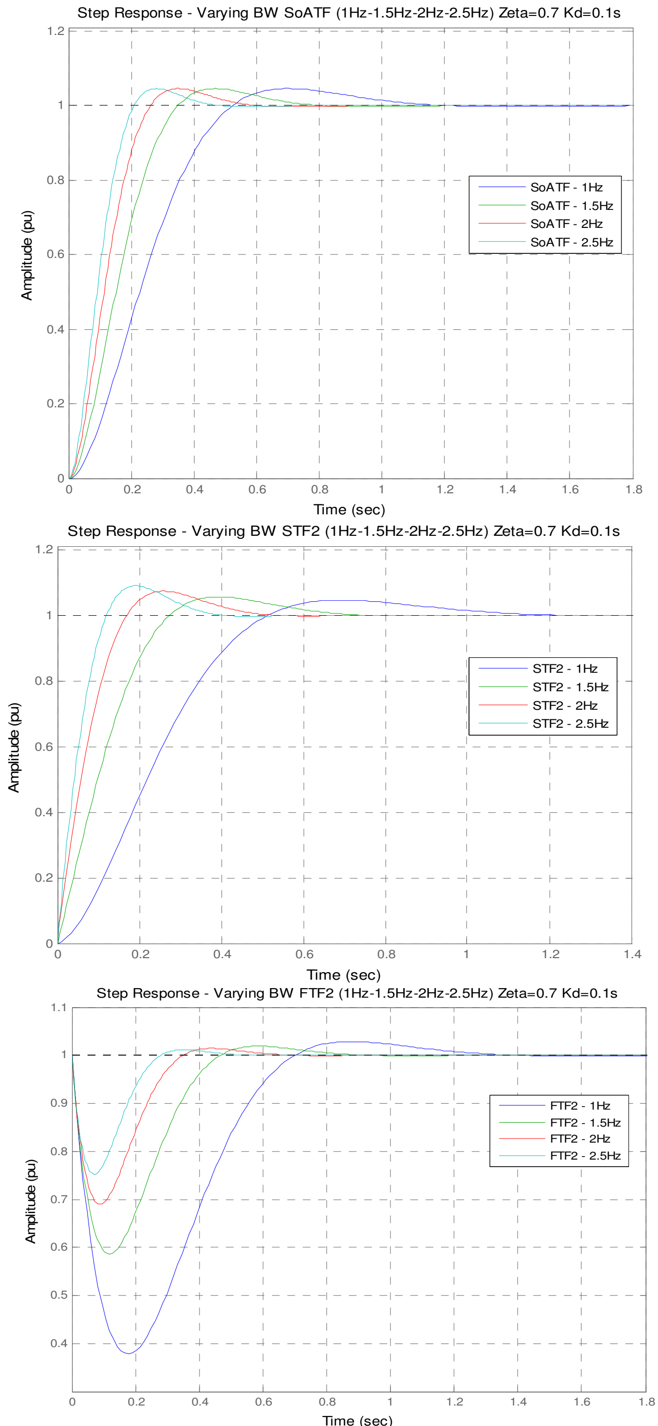

Figure 6.3: Varying f_n – step responses of SoATF, STF2 and FTF2
ζ=0.7 and K_D=0.1s

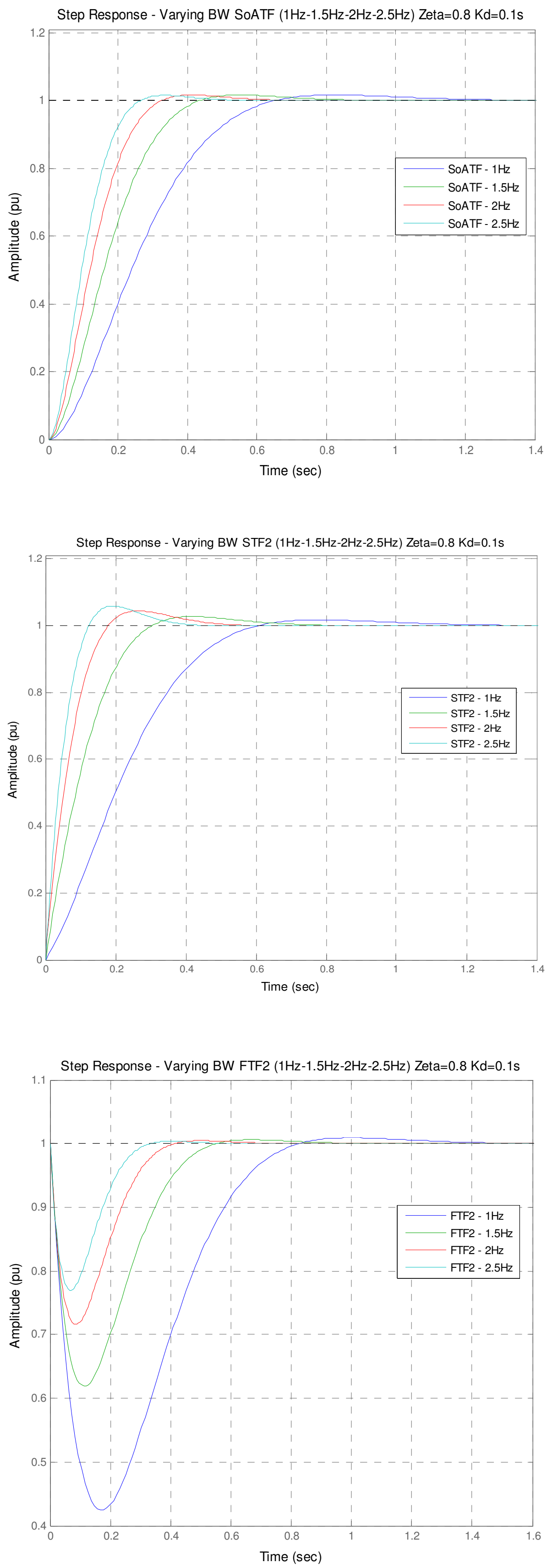

Figure 6.4: Varying f_n – step responses of SoATF, STF2 and FTF2
ζ=0.8 and K_D=0.1s

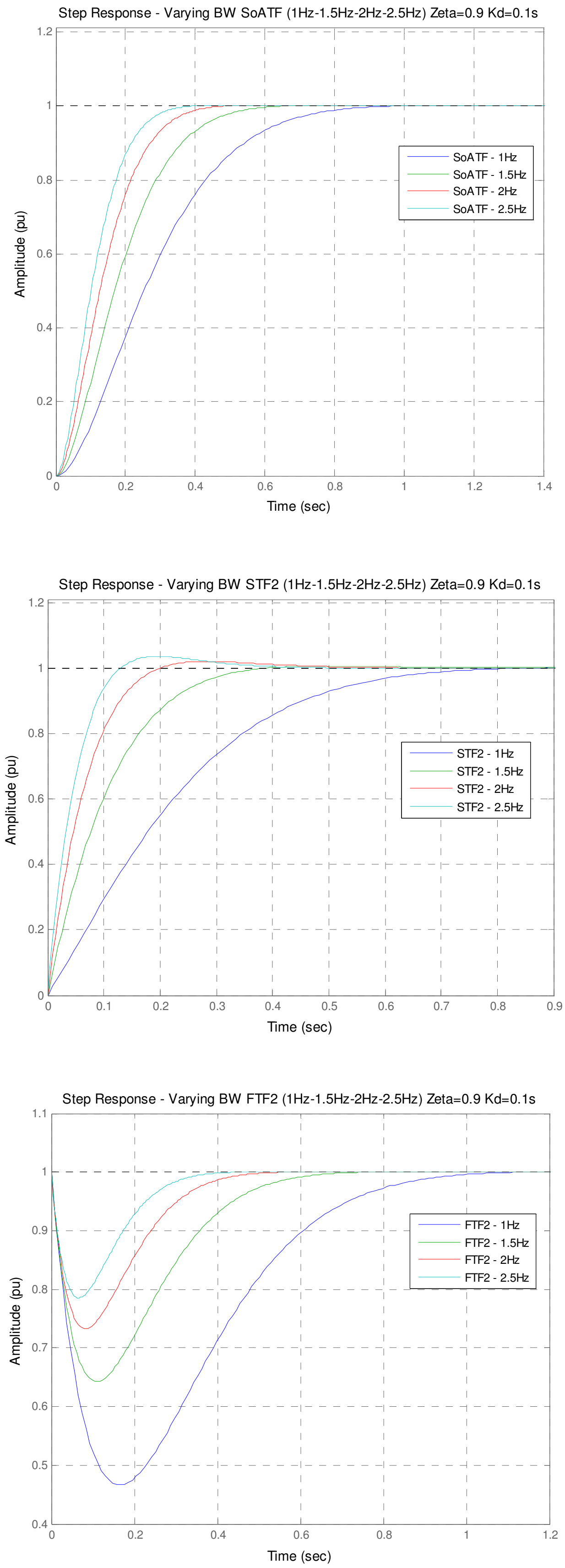

Figure 6.5: Varying f_n – step responses of SoATF, STF2 and FTF2
ζ=0.9 and K_D=0.1s

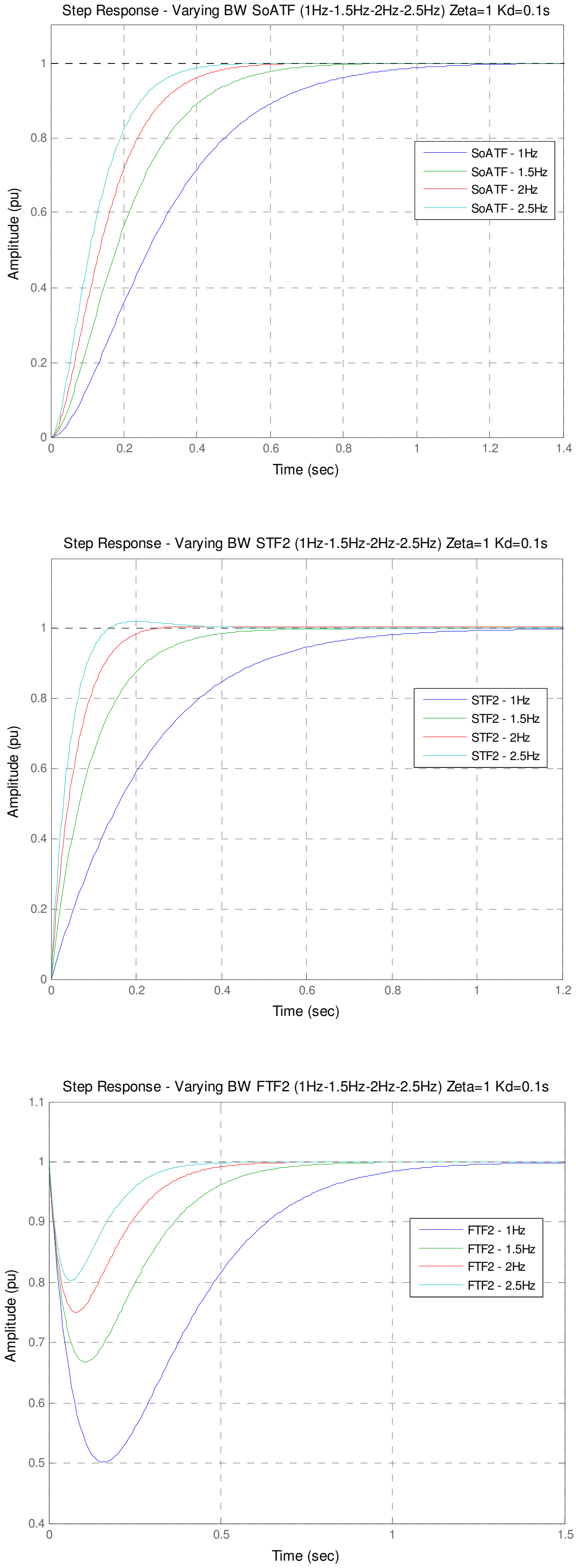

Figure 6.6: Varying f_n – step responses of SoATF, STF2 and FTF2
ζ=1 and K_D=0.1s

6.5.2 Varying Damping Ratio

The sensitivity analysis work for damping ratio variation is carried out by selecting these values of the damping ratio: 0.7, 0.8, 0.9, 1, and 1.1. The damping ratio is increased from 0.7 to 1.1 while holding the undamped natural frequency (f_n) and K_D fixed. The variation process for damping ratio is summarised in Table A.5.5 in Appendix 5. Those rows including green coloured operating points are taken from Table A.5.6 and presented in Table 6.6.

		Varying damping ratio for fixed undamped natural frequency and derivative time constant									
ζ	ω_n (rad/s)	K_d (s)	K_{po}	K_{io} (1/s)	T_{io} (s)	f_n (Hz)	π	Kio / Kd	Kpo / Kd	(Kpo+0.852)/Kd	(Kio/Kd) / (Kpo/Kd)
0.7	6.283	0.1	0.028	3.948	0.253	1	3.142	39.478	0.275	8.795	143.370
0.8	6.283	0.1	0.153	3.948	0.253	1	3.142	39.478	1.532	10.052	25.769
0.9	6.283	0.1	0.279	3.948	0.253	1	3.142	39.478	2.789	11.309	14.157
0.7	9.425	0.1	0.467	8.883	0.113	1.5	3.142	88.826	4.674	13.194	19.006
0.8	9.425	0.1	0.656	8.883	0.113	1.5	3.142	88.826	6.559	15.079	13.544
0.9	9.425	0.1	0.844	8.883	0.113	1.5	3.142	88.826	8.444	16.964	10.520
0.7	12.566	0.1	0.907	15.791	0.063	2	3.142	157.914	9.072	17.592	17.407
0.8	12.566	0.1	1.159	15.791	0.063	2	3.142	157.914	11.585	20.105	13.631
0.9	12.566	0.1	1.410	15.791	0.063	2	3.142	157.914	14.098	22.618	11.201
0.7	15.708	0.1	1.347	24.674	0.041	2.5	3.142	246.740	13.470	21.990	18.318
0.8	15.708	0.1	1.661	24.674	0.041	2.5	3.142	246.740	16.612	25.132	14.853
0.9	15.708	0.1	1.975	24.674	0.041	2.5	3.142	246.740	19.753	28.273	12.491
1	15.708	0.1	2.289	24.674	0.041	2.5	3.142	246.740	22.895	31.415	10.777

Table 6.6: Calculations in Excel for the assessment of varying ζ

Increasing the damping ratio for fixed f_n and K_D increases only K_{po}. This can be seen either in Table 6.6 or from the equations depicted below. The system response speed is not affected by varying the damping ratio since it depends on f_n and the K_D.

$$\underset{\text{constant}}{\omega_n^2} = \frac{\overset{\text{constant}}{K_{io}}}{\underset{\text{constant}}{K_D}} \qquad \underset{\text{increasing}}{\zeta} = \frac{\overset{\text{increases}}{K_{po}} + \overset{\text{constant}}{\boxed{\frac{2}{3}\frac{L_{ss}}{\sqrt{2}V_s L_m}}}}{\underset{\text{constant}}{2\omega_n K_D}}$$

Since the possible 'best' f_n values are determined as 2Hz and 2.5Hz in section 6.5.1, the varying damping ratio process is then only evaluated for these f_n values. In order to get less overshoot, a slightly high damping ratio (i.e. 0.9 or 1) should be chosen.

The data given for 2Hz and 2.5Hz in Table 6.6 are substituted in the second-order approximated (SoATF), simplified (STF2) and full (FTF2) transfer function equations (see Table 6.7).

Rotor-side Converter Outer (Power) Loop PID		$\dfrac{\frac{K_{io}}{K_D}}{s^2+\left(\frac{K_{po}+0.852}{K_D}\right)s+\frac{K_{io}}{K_D}}$	$\dfrac{s\frac{K_{po}}{K_D}+\frac{K_{io}}{K_D}}{s^2+\left(\frac{K_{po}+0.852}{K_D}\right)s+\frac{K_{io}}{K_D}}$	$\dfrac{s^2+s\frac{K_{po}}{K_D}+\frac{K_{io}}{K_D}}{s^2+\left(\frac{K_{po}+0.852}{K_D}\right)s+\frac{K_{io}}{K_D}}$
f_n=2Hz K_D=0.1s	ζ=0.7	$\dfrac{158}{s^2+17.6s+158}$	$\dfrac{9.1s+158}{s^2+17.6s+158}$	$\dfrac{s^2+9.1s+158}{s^2+17.6s+158}$
	ζ=0.8	$\dfrac{158}{s^2+20s+158}$	$\dfrac{11.6s+158}{s^2+20s+158}$	$\dfrac{s^2+11.6s+158}{s^2+20s+158}$
	ζ=0.9	$\dfrac{158}{s^2+22.62s+158}$	$\dfrac{14.1s+158}{s^2+22.62s+158}$	$\dfrac{s^2+14.1s+158}{s^2+22.62s+158}$
	ζ=1	$\dfrac{158}{s^2+25.13s+158}$	$\dfrac{16.6s+158}{s^2+25.13s+158}$	$\dfrac{s^2+16.6s+158}{s^2+25.13s+158}$
	ζ=1.1	$\dfrac{158}{s^2+27.65s+158}$	$\dfrac{19.13s+158}{s^2+27.65s+158}$	$\dfrac{s^2+19.13s+158}{s^2+27.65s+158}$
f_n=2.5Hz K_D=0.1s	ζ=0.7	$\dfrac{246.7}{s^2+22s+246.7}$	$\dfrac{13.5s+246.7}{s^2+22s+246.7}$	$\dfrac{s^2+13.5s+246.7}{s^2+22s+246.7}$
	ζ=0.8	$\dfrac{246.7}{s^2+25.13s+246.7}$	$\dfrac{16.6s+246.7}{s^2+25.13s+246.7}$	$\dfrac{s^2+16.6s+246.7}{s^2+25.13s+246.7}$
	ζ=0.9	$\dfrac{246.7}{s^2+28.3s+246.7}$	$\dfrac{19.75s+246.7}{s^2+28.3s+246.7}$	$\dfrac{s^2+19.75s+246.7}{s^2+28.3s+246.7}$
	ζ=1	$\dfrac{246.7}{s^2+31.42s+246.7}$	$\dfrac{23s+246.7}{s^2+31.42s+246.7}$	$\dfrac{s^2+23s+246.7}{s^2+31.42s+246.7}$
	ζ=1.1	$\dfrac{246.7}{s^2+34.56s+246.7}$	$\dfrac{26.04s+246.7}{s^2+34.56s+246.7}$	$\dfrac{s^2+26.04s+246.7}{s^2+34.56s+246.7}$

Table 6.7: Varying ζ- SoATF, STF2 and FTF2

Considering the assumption, reasonable damping ratios were designated as 0.7-0.8-0.9 (for all f_n values) and 1 (for only 2.5Hz of f_n) in section 6.5.1. However, in order to observe less overshoot, the importance of selecting a higher damping ratio is emphasised in this section. Therefore, the reasonable damping ratios for the tuning process for the power loop of the RSC can be determined as 0.9 (for 2Hz and 2.5Hz) and 1 (for 2.5Hz). Note that the damping ratios of 0.9 and 1 exhibit the less overshoot characteristics than those of 0.7 and 0.8 for the second-order approximated, simplified and full transfer functions shown in Figures 6.7 and 6.8. So far, the 'best' undamped natural frequency and the 'best' damping ratio values are chosen as 2Hz and 2.5Hz; and 0.9 and 1, respectively.

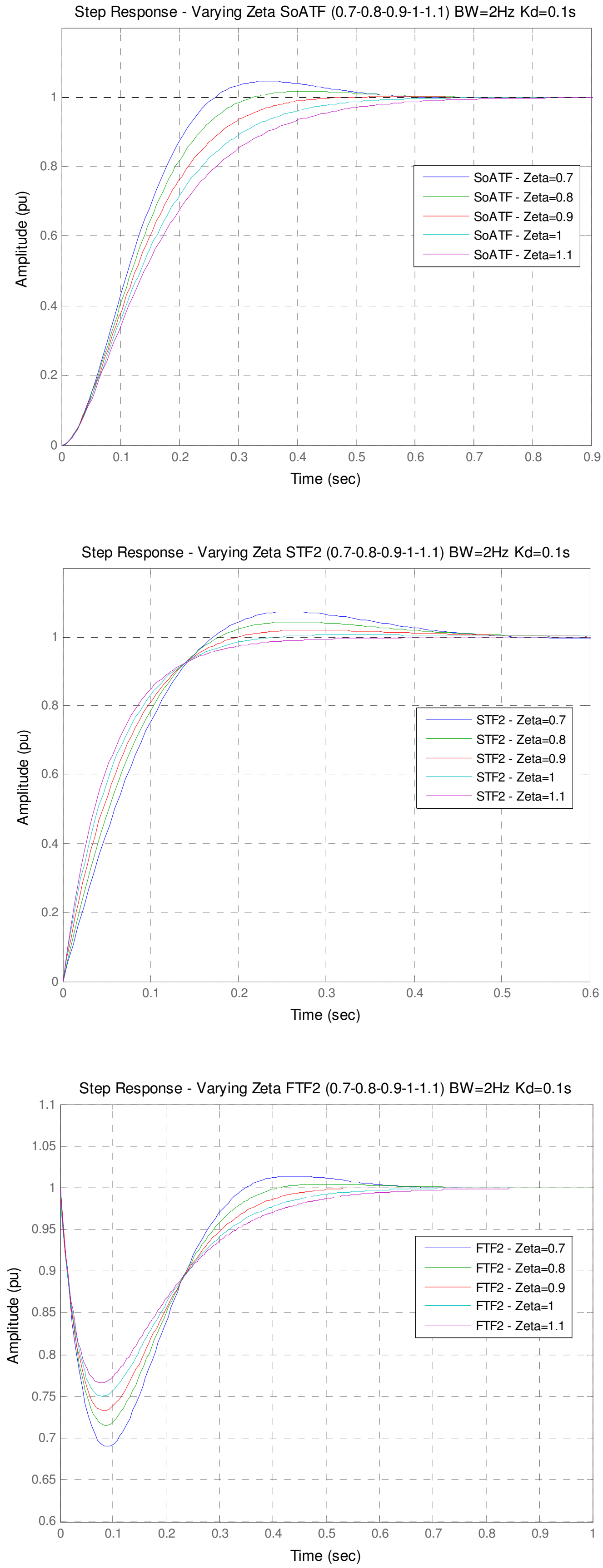

Figure 6.7: Varying ζ – step responses of SoATF, STF2 and FTF2
f_n=2Hz and K_D=0.1s

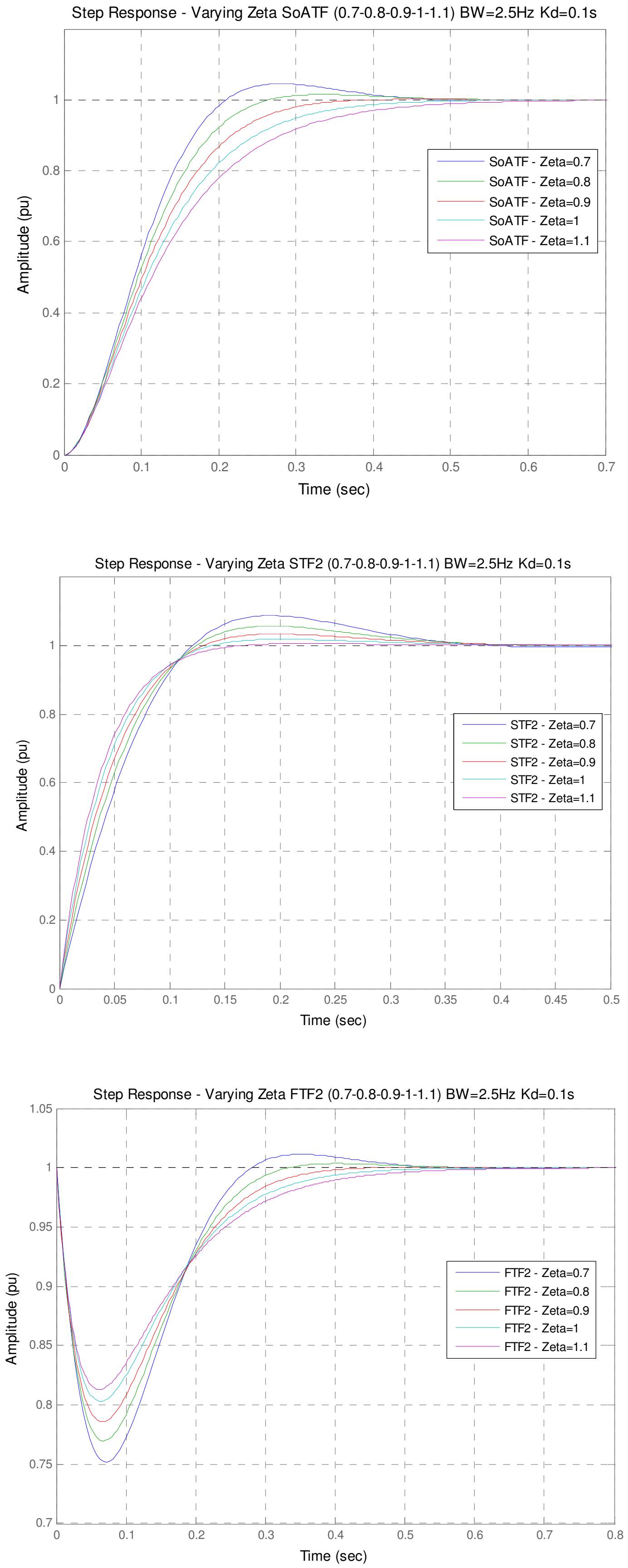

Figure 6.8: Varying ζ– step responses of SoATF, STF2 and FTF2
f_n=2.5Hz and K_D=0.1s

6.5.3 Varying K_D

The effect of varying K_D on the system response is investigated in this section. Four different values of K_D, which are 0.1s, 0.2s, 0.3s and 0.4s, are used for the sensitivity analysis of varying K_D. Varying K_D analysis as context is shown in the related tables in Appendix 5 (see Tables A.5.8 to A.5.12). Again, there green areas are regarded in this section. Related calculations are displayed in Table 6.8.

		Varying derivative time constant for fixed undamped natural frequency and damping ratio									
ζ	ω_n (rad/s)	K_d (s)	K_{po}	K_{io} (1/s)	T_{io} (s)	f_n (Hz)	π	Kio / Kd	Kpo / Kd	(Kpo+0.852)/Kd	(Kio/Kd) / (Kpo/Kd)
0.7	6.283	0.1	0.028	3.948	0.253	1	3.142	39.478	0.275	8.795	143.370
0.7	9.425	0.1	0.467	8.883	0.113	1.5	3.142	88.826	4.674	13.194	19.006
0.7	9.425	0.2	1.787	17.765	0.056	1.5	3.142	88.826	8.934	13.194	9.942
0.7	12.566	0.1	0.907	15.791	0.063	2	3.142	157.914	9.072	17.592	17.407
0.7	12.566	0.2	2.666	31.583	0.032	2	3.142	157.914	13.332	17.592	11.844
0.7	12.566	0.3	4.426	47.374	0.021	2	3.142	157.914	14.753	17.593	10.704
0.7	12.566	0.4	6.185	63.165	0.016	2	3.142	157.914	15.463	17.593	10.213
0.7	15.708	0.1	1.347	24.674	0.041	2.5	3.142	246.740	13.470	21.990	18.318
0.7	15.708	0.2	3.546	49.348	0.020	2.5	3.142	246.740	17.731	21.991	13.916
0.7	15.708	0.3	5.745	74.022	0.014	2.5	3.142	246.740	19.151	21.991	12.884
0.7	15.708	0.4	7.944	98.696	0.010	2.5	3.142	246.740	19.861	21.991	12.423
0.8	6.283	0.1	0.153	3.948	0.253	1	3.142	39.478	1.532	10.052	25.769
0.8	9.425	0.1	0.656	8.883	0.113	1.5	3.142	88.826	6.559	15.079	13.544
0.8	12.566	0.1	1.159	15.791	0.063	2	3.142	157.914	11.585	20.105	13.631
0.8	12.566	0.2	3.169	31.583	0.032	2	3.142	157.914	15.846	20.106	9.966
0.8	15.708	0.1	1.661	24.674	0.041	2.5	3.142	246.740	16.612	25.132	14.853
0.8	15.708	0.2	4.174	49.348	0.020	2.5	3.142	246.740	20.872	25.132	11.821
0.8	15.708	0.3	6.688	74.022	0.014	2.5	3.142	246.740	22.292	25.132	11.068
0.8	15.708	0.4	9.201	98.696	0.010	2.5	3.142	246.740	23.002	25.132	10.727
0.9	6.283	0.1	0.279	3.948	0.253	1	3.142	39.478	2.789	11.309	14.157
0.9	9.425	0.1	0.844	8.883	0.113	1.5	3.142	88.826	8.444	16.964	10.520
0.9	12.566	0.1	1.410	15.791	0.063	2	3.142	157.914	14.098	22.618	11.201
0.9	15.708	0.1	1.975	24.674	0.041	2.5	3.142	246.740	19.753	28.273	12.491
0.9	15.708	0.2	4.803	49.348	0.020	2.5	3.142	246.740	24.014	28.274	10.275
1	15.708	0.1	2.289	24.674	0.041	2.5	3.142	246.740	22.895	31.415	10.777

Table 6.8: Calculations in Excel for the assessment of varying K_D

$$\underset{\text{constant}}{\omega_n^2} = \frac{\overset{\text{increases}}{K_{io}}}{\underset{\text{increasing}}{K_D}} \qquad \underset{\text{constant}}{\zeta} = \frac{\overset{\text{increases}}{K_{po}} + \overset{\text{constant}}{\boxed{\frac{2}{3}\frac{L_{ss}}{\sqrt{2}\,V_s L_m}}}}{2\underset{\text{constant}}{\omega_n}\underset{\text{increasing}}{K_D}}$$

Table 6.8 and the above-shown tuning equations shows that increasing the K_D increases both K_{po} and K_{io} (decreasing the T_{io} which means fast response) where both the damping ratio and the undamped natural frequency stay constant. Further increase in K_D makes the system too sensitive to the noise and also results in too fast response which is not needed for the power loop of the RSC. Therefore, the value of K_D should be selected to be as small as possible. But, in order to let the K_{po} be positive the K_D parameter should be small enough.

Related K_D values in which the assumption is made that the ratio of $\frac{K_{io}}{K_D} >> \frac{K_{po}}{K_D}$ is approximately equal to or greater than 10 times are picked from Tables A.5.15 and A.5.16 and shown in Table 6.8. In sections 6.5.1 and 6.5.2, the possible 'best' values for the undamped natural frequency (f_n) and damping ratio were specified as 2Hz-2.5Hz and 0.9-1, respectively. Considering these operating points, the 'best' values of K_D can be extracted from Table 6.8 as 0.1s and 0.2s. The transfer function table is prepared for f_n values of 2Hz and 2.5Hz, and the damping ratios of 0.9 and 1 (see Table 6.9). The full transfer function table of the variation process of K_D for all f_n and damping ratio values can be found in Appendix 5. The MATLAB traces for above-mentioned operating points are presented in Figures 6.9 to 6.11.

Rotor-side Converter Outer (Power) Loop PID		$\frac{\frac{K_{io}}{K_D}}{s^2+\left(\frac{K_{po}+0.852}{K_D}\right)s+\frac{K_{io}}{K_D}}$	$\frac{s\frac{K_{po}}{K_D}+\frac{K_{io}}{K_D}}{s^2+\left(\frac{K_{po}+0.852}{K_D}\right)s+\frac{K_{io}}{K_D}}$	$\frac{s^2+s\frac{K_{po}}{K_D}+\frac{K_{io}}{K_D}}{s^2+\left(\frac{K_{po}+0.852}{K_D}\right)s+\frac{K_{io}}{K_D}}$
ζ=0.9 f_n=2Hz	K_D=0.1s	$\frac{158}{s^2+22.62s+158}$	$\frac{14.1s+158}{s^2+22.62s+158}$	$\frac{s^2+14.1s+158}{s^2+22.62s+158}$
	K_D=0.2s	$\frac{158}{s^2+22.62s+158}$	$\frac{18.36s+158}{s^2+22.62s+158}$	$\frac{s^2+18.36s+158}{s^2+22.62s+158}$
	K_D=0.3s	$\frac{158}{s^2+22.62s+158}$	$\frac{19.78s+158}{s^2+22.62s+158}$	$\frac{s^2+19.78s+158}{s^2+22.62s+158}$
	K_D=0.4s	$\frac{158}{s^2+22.62s+158}$	$\frac{20.5s+158}{s^2+22.62s+158}$	$\frac{s^2+20.5s+158}{s^2+22.62s+158}$
ζ=0.9 f_n=2.5Hz	K_D=0.1s	$\frac{246.7}{s^2+28.3s+246.7}$	$\frac{19.75s+246.7}{s^2+28.3s+246.7}$	$\frac{s^2+19.75s+246.7}{s^2+28.3s+246.7}$
	K_D=0.2s	$\frac{246.7}{s^2+28.3s+246.7}$	$\frac{24s+246.7}{s^2+28.3s+246.7}$	$\frac{s^2+24s+246.7}{s^2+28.3s+246.7}$
	K_D=0.3s	$\frac{246.7}{s^2+28.3s+246.7}$	$\frac{25.4s+246.7}{s^2+28.3s+246.7}$	$\frac{s^2+25.4s+246.7}{s^2+28.3s+246.7}$
	K_D=0.4s	$\frac{246.7}{s^2+28.3s+246.7}$	$\frac{26.15s+246.7}{s^2+28.3s+246.7}$	$\frac{s^2+26.15s+246.7}{s^2+28.3s+246.7}$
ζ=1 f_n=2.5Hz	K_D=0.1s	$\frac{246.7}{s^2+31.42s+246.7}$	$\frac{23s+246.7}{s^2+31.42s+246.7}$	$\frac{s^2+23s+246.7}{s^2+31.42s+246.7}$
	K_D=0.2s	$\frac{246.7}{s^2+31.42s+246.7}$	$\frac{27.16s+246.7}{s^2+31.42s+246.7}$	$\frac{s^2+27.16s+246.7}{s^2+31.42s+246.7}$
	K_D=0.3s	$\frac{246.7}{s^2+31.42s+246.7}$	$\frac{28.58s+246.7}{s^2+31.42s+246.7}$	$\frac{s^2+28.58s+246.7}{s^2+31.42s+246.7}$
	K_D=0.4s	$\frac{246.7}{s^2+31.42s+246.7}$	$\frac{29.3s+246.7}{s^2+31.42s+246.7}$	$\frac{s^2+29.3s+246.7}{s^2+31.42s+246.7}$

Table 6.9: Varying K_D SoATF, STF2 and FTF2

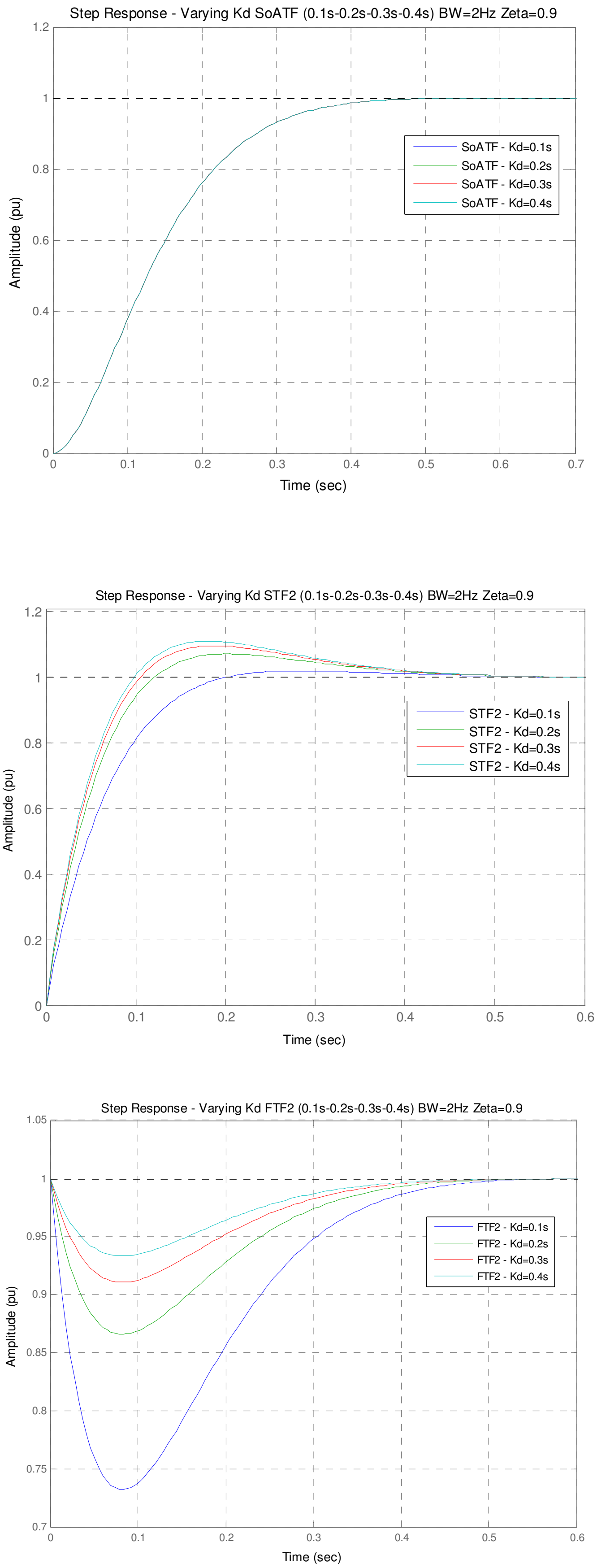

Figure 6.9: Varying K_D – step responses of SoATF, STF2 and FTF2
f_n=2Hz and ζ=0.9

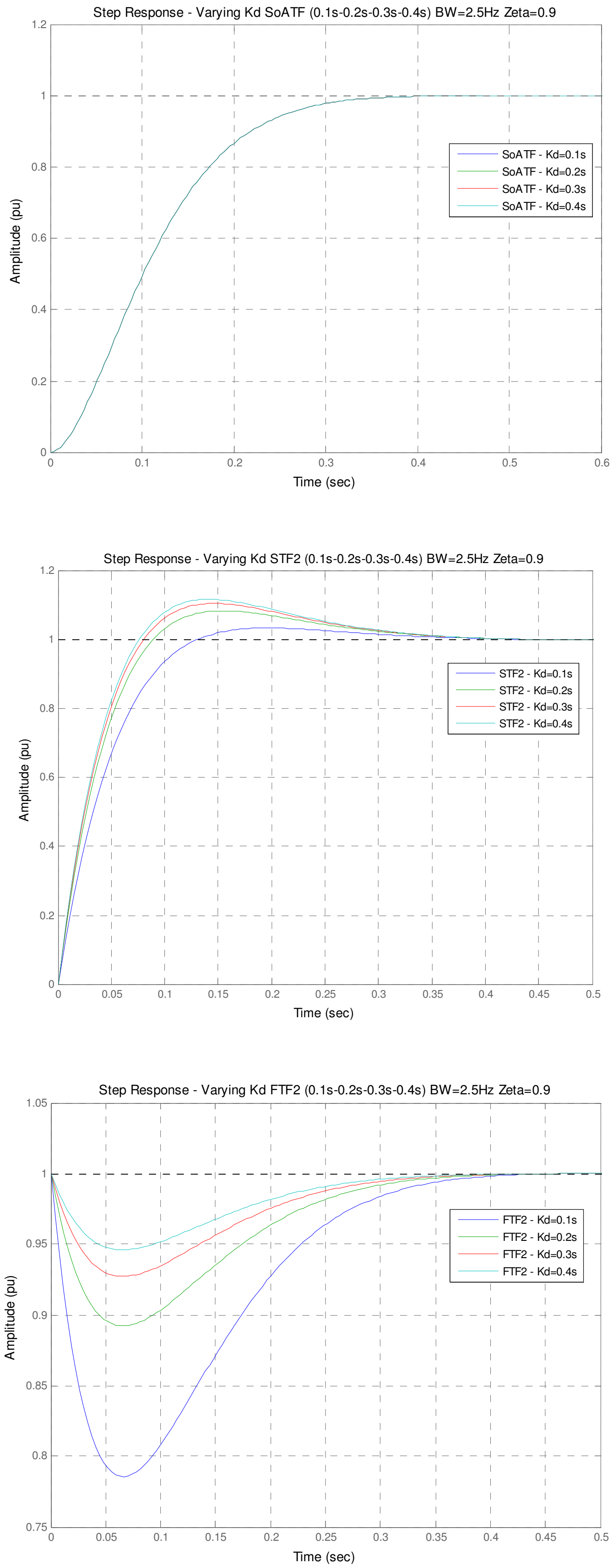

Figure 6.10: Varying K_D – step responses of SoATF, STF2 and FTF2
f_n=2.5Hz and ζ=0.9

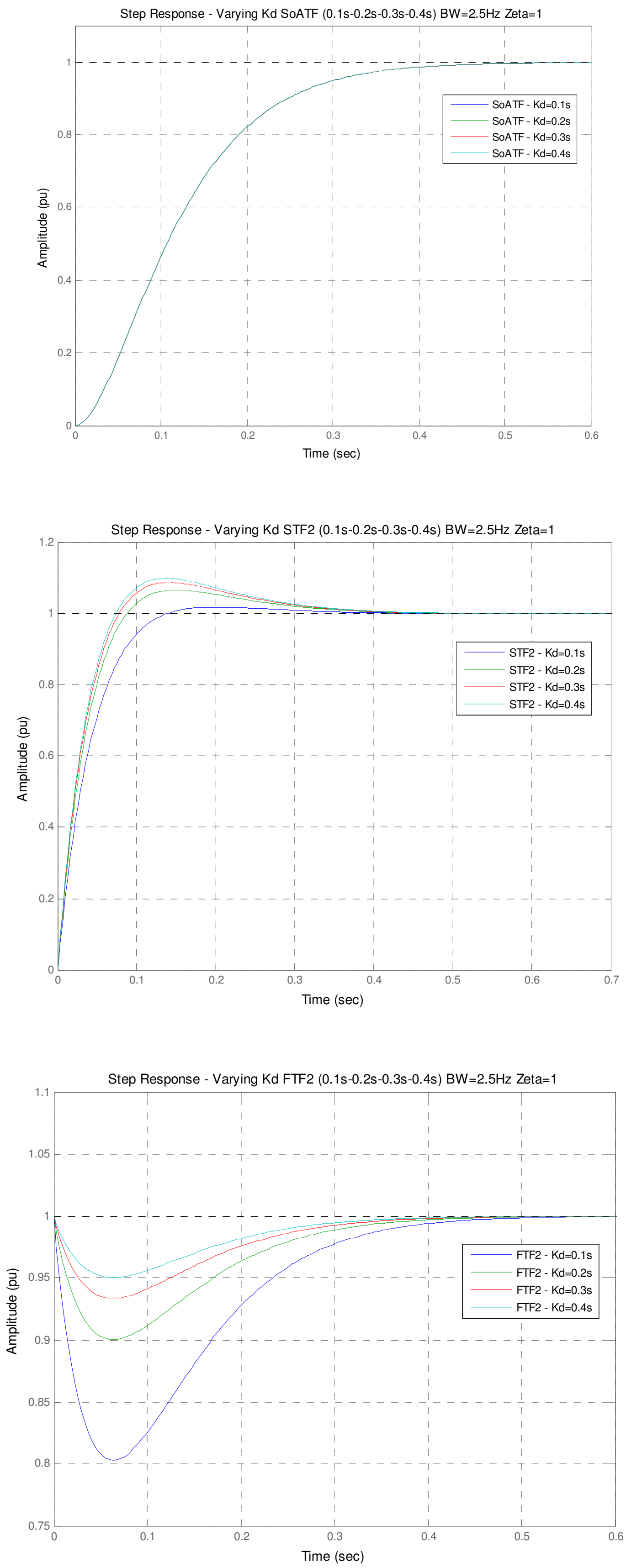

Figure 6.11: Varying K_D – step responses of SoATF, STF2 and FTF2 f_n=2.5Hz and ζ=1

Considering the simplified transfer function step responses shown in the middle of Figures 6.9-6.11, increasing the K_D increases the overshoot. The least overshoot happens at K_D=0.1s. Note that for second-order approximated and full transfer functions increasing K_D does not influence the overshoot. The 'best' tuning parameters for power loop of the RSC so far are extracted and presented in Table 6.10.

	ζ	f_n (or ω_n)	K_D
1.	0.9	2Hz	0.1s
2.	0.9	2.5Hz	0.1s
3.	0.9	2.5Hz	0.2s
4.	1	2.5Hz	0.1s

Table 6.10: The 'best' tuning parameters of the PID loop

The summary of the sensitivity analysis done for varying undamped natural frequency, damping ratio and the derivative time constant is demonstrated in Table 6.11. The relation between the preset parameters, ζ, ω_n and K_D, and the calculated tuning gains, K_{po}, K_{io}, and hence T_{io}, is briefly given in Table 6.11. According to this table, K_{po} is directly related to all preset parameters where K_{io} and T_{io} are related to ω_n and K_D.

ζ	f_n (or ω_n)	K_D	K_{po}	K_{io}	T_{io}
Increasing	Constant	Constant	Increases	Constant	Constant
Constant	Increasing	Constant	Increases	Increases	Decreases
Constant	Constant	Increasing	Increases	Increases	Decreases

Table 6.11: The summary of the effects of varying the tuning parameters

6.5.4 PSCAD Results

Four 'best' tuning parameters are designated for the outer (power) PID loop control of the RSC controller by carrying out the sensitivity analysis. These parameters are now used to implement a circuit built up in PSCAD. A small step change (0.1MW) is applied to the pre-set value of the stator active power of 4.5MW at t=2s. The step change in the stator active power (P_{s_set}), measured stator active power (P_s), the characteristics of the stator active power considering the second-order approximated transfer function (P_s_SoATF), simplified transfer function (P_s_STF2) and full transfer function (P_s_FTF2) are plotted and presented in the same figure for four tuning parameters (See Figures 6.12 to 6.15).

As seen in Figure 6.14, the maximum overshoot happens in the STF2 curve but the percentage of the overshoot is below 2.58%. Although the STF2 does not fully represent the physical system and is an intermediate step between the SoATF and FTF2, it is a usefully system to consider since it offers a 'worst case result' but is still relatively straightforward to simulate. Since the overall system circuits constructed in PSCAD are complex and inherently interact with each other (e.g. sub-system controllers) the PSCAD results are not expected to show same behaviours as the MATLAB results. However, the tendency in both simulation programmes is very similar to each other. Having a look at the figures, the stator active power curves show more oscillations in Figures 6.12-6.13 and 6.15 rather than those in Figure 6.14. Furthermore, in Figure 6.14 the measured stator active power characteristic is more similar to the characteristic in the full transfer function of the stator active power output. The stator active power curves in Figure 6.14 reach the steady-state in 0.4s to 0.5s which means a faster system response than the other ones. Taking these advantages into account, the 'best' tuning parameters for the outer (power) PID loop of the rotor-side converter can be decided as in Figure 6.14 (ζ=0.9, f_n=2.5Hz and K_D=0.2s). The latter section, robustness analysis, will be based on these 'best' tuning parameters.

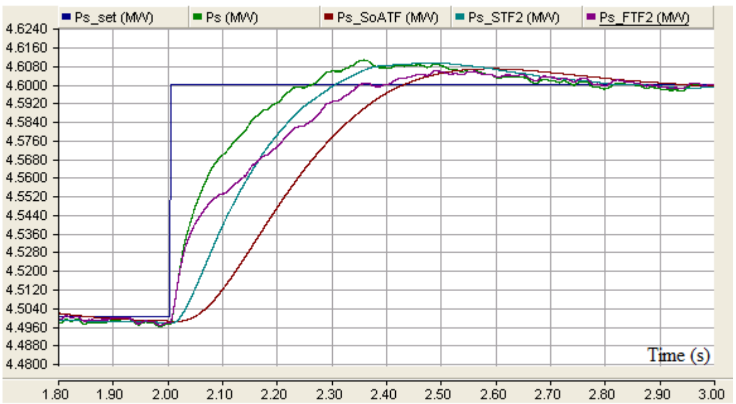

Figure 6.12: The PSCAD results for f_n=2Hz, ζ=0.9 and K_D=0.1s

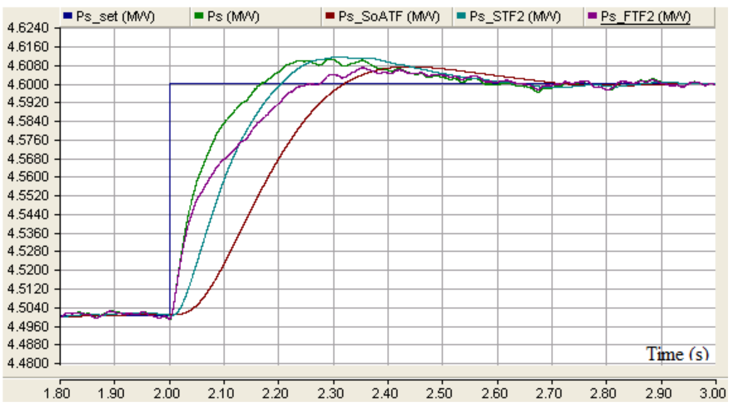

Figure 6.13: The PSCAD results for f_n=2.5Hz, ζ=0.9 and K_D=0.1s

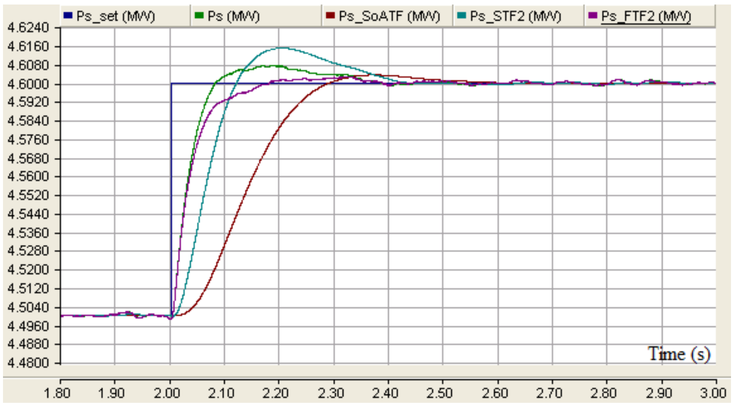

Figure 6.14: The PSCAD results for f_n=2.5Hz, ζ=0.9 and K_D=0.2s

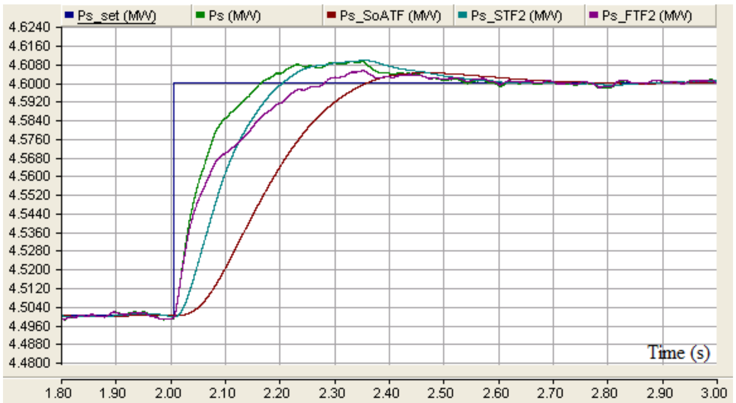

Figure 6.15: The PSCAD results for f_n=2.5Hz, ζ=1 and K_D=0.1s

6.6 Robustness Analysis

The control of the DFIG systems must be robust enough against the change in the electrical parameters and voltage dips due to faults. In this section, a ±20% change applied to the stator voltage while the stator self-inductance and the mutual (or magnetising) inductance are both varied by ±10%. This section will give a robustness analysis of the 'best' tuning parameters found out in Section 6.5 for the power (outer) PID loop controller of the RSC (see Table 6.10). The electrical data of the DFIG system considered in this thesis was given in Appendix 1. The stator self-inductance (L_{ss}) is the sum of the stator leakage inductance (L_s), mutual inductance (L_m) and the positive sequence leakage reactance of the transformer between the windings 1 and 3 (L_{13}). Therefore, this robustness analysis is only feasible where the magnitude of stator self-inductance is greater than that of the mutual inductance. Otherwise (e.g. 1.1Lm and 0.9Lss), to maintain the required stator-self inductance a negative stator leakage inductance should be entered into the DFIG system built in PSCAD, which is physically impossible to realise. Thus, only operating points are of interest ensuring that the stator self-inductance is larger than the magnetising inductance. Possible (green) and impossible (red) operating points are presented in Table 6.12. The mathematical calculations for the robustness analysis are given in Table A.5.23 in Appendix 5. In addition, the calculation of the stator leakage inductance in pu corresponding the changes in the stator self-inductance and the mutual inductance is displayed in Table A.5.25.

L_{ss} / L_m	$0.9L_{ss}$	L_{ss}	$1.1L_{ss}$
$0.9L_m$	3.71268pu 3.557511pu	4.1252pu 3.557511pu	4.53772pu 3.557511pu
L_m	3.71268pu 3.95279pu	4.1252pu 3.95279pu	4.53772pu 3.95279pu
$1.1L_m$	3.71268pu 4.348069pu	4.1252pu 4.348069pu	4.53772pu 4.348069pu

Table 6.12: Operating points for robustness analysis.

6.6.1 V_s=0.8pu (Variations in L_{ss} and L_m by ±10%)

A 20% drop in the stator voltage is assumed and the changes in the inductances are reflected to the system. 6 possible damping ratios are calculated. Since the ratio of L_{ss}/L_m stays same, $\zeta_1=\zeta_4=\zeta_6$. Equation 6.11 also confirms the relation that decreasing the V_s increases the damping ratio where the L_{ss}/L_m is constant. This makes the system more damped then. For a fixed V_s, in case of increase in the L_{ss}/L_m the damping ratio increases too. The calculated damping ratios are demonstrated in Table 6.13.

	L_{ss} / L_m	$0.9L_{ss}$	L_{ss}	$1.1L_{ss}$
V_s=0.8pu=0.8kV L-L RMS	$0.9L_m$	ζ_1=0.934	ζ_2=0.953	ζ_3=0.972
	L_m	N/A	ζ_4=0.934	ζ_5=0.951
	$1.1L_m$	N/A	N/A	ζ_6=0.934

Table 6.13: Calculated damping ratios for V_s=0.8pu

As seen in Table 6.13, the damping ratios are very close to each other. The highest difference, which occurs between ζ_3 and ζ_1 (or $\zeta_4=\zeta_6$), is 4.07%. As this percentage is quite small, it can be neglected. These damping ratios are also simulated in PSCAD and the results are shown in Figure 6.16. The damping ratios , $\zeta_1=\zeta_4=\zeta_6$, which are equal to each other are given in a separate graph in Figure 6.17.

The curves of all six damping ratios seem to be effectively same in Figure 6.16, but the damping ratios of ζ_2, ζ_3 and ζ_5 exhibit oscillatory behaviour. Note that the whole system including other cascaded sub-controllers is simulated in PSCAD. The interaction of these sub-controllers with the outer (power) loop of the RSC can cause the oscillation in the stator active power response in case of larger damping ratios (ζ_2, ζ_3 and ζ_5). Another reason would be that the system tries to act more damped but for a less stator voltage. In Figure 6.17, the curves of the equal damping ratios ($\zeta_1=\zeta_4=\zeta_6$) well matched each other and demonstrate very similar characteristics with less oscillations.

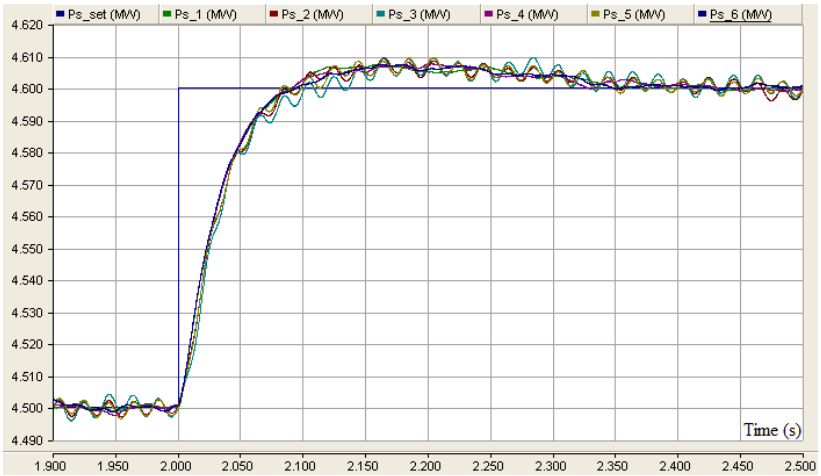

Figure 6.16: PSCAD results for robustness analysis - V_s=0.8pu

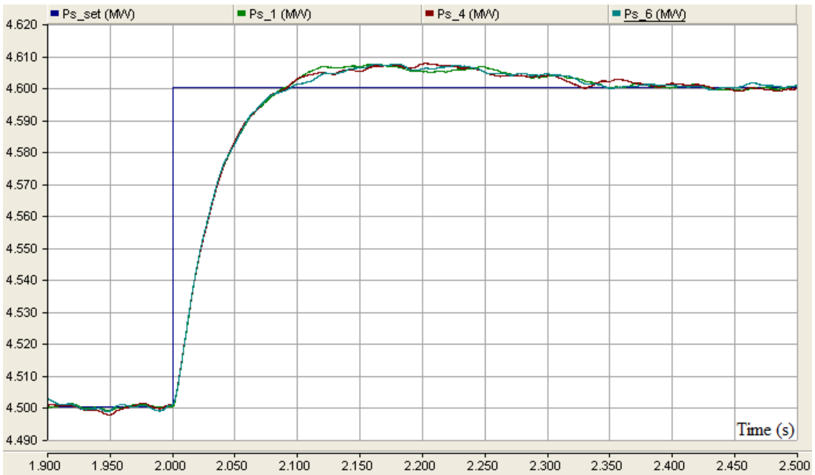

Figure 6.17: PSCAD results of $\zeta_1=\zeta_4=\zeta_6$ for robustness analysis - V_s=0.8pu

6.6.2 V_s=1pu (Variations in L_{ss} and L_m by ±10%)

The effects of change in the stator self-inductance and the mutual inductance are worked out while keeping the stator voltage at its nominal value (1pu). For each of the damping ratios, the system response is investigated in PSCAD. The calculated damping ratios are given in Table 6.14. As in section 6.6.1, the calculated diagonal damping ratios are same, other damping ratios are slightly greater than the diagonal damping ratios. The biggest change is now decreased to 3.33% (it was 4% in section 6.6.1). The stator voltage is now sufficient enough (1pu) to reduce the oscillations which noticeably occurred in the system response. The characteristics system responses corresponding the damping ratios are plotted in Figure 6.18. The diagonal damping ratio curves, which can be assumed to be effectively same, are depicted together in Figure 6.19.

<table>
<tr><td rowspan="4">V_s=1pu=1kV L-L RMS</td><td>L_{ss} / L_m</td><td>$0.9L_{ss}$</td><td>L_{ss}</td><td>$1.1L_{ss}$</td></tr>
<tr><td>$0.9L_m$</td><td>ζ_7=0.9</td><td>ζ_8=0.915</td><td>ζ_9=0.93</td></tr>
<tr><td>L_m</td><td>N/A</td><td>ζ_{nom}=0.9</td><td>ζ_{10}=0.914</td></tr>
<tr><td>$1.1L_m$</td><td>N/A</td><td>N/A</td><td>ζ_{11}=0.9</td></tr>
</table>

Table 6.14: Calculated damping ratios for V_s=1pu

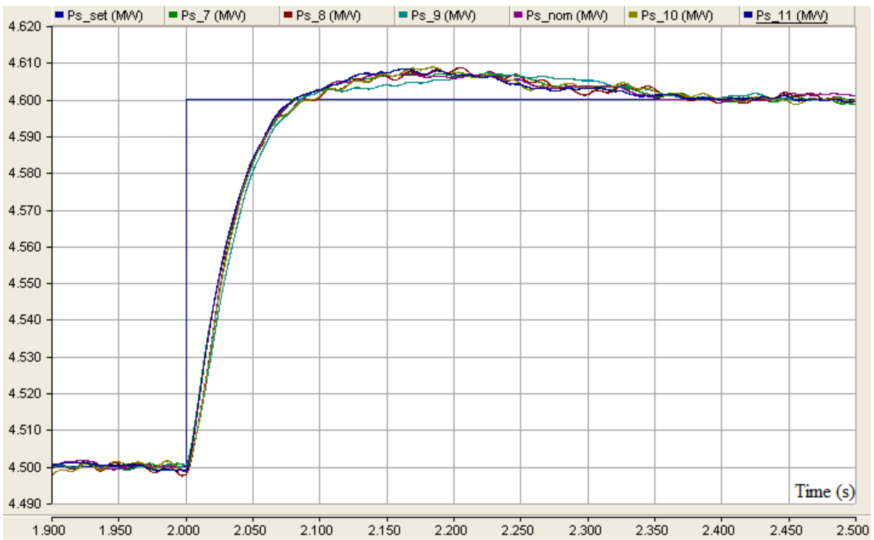

Figure 6.18: PSCAD results for robustness analysis - V_s=1pu

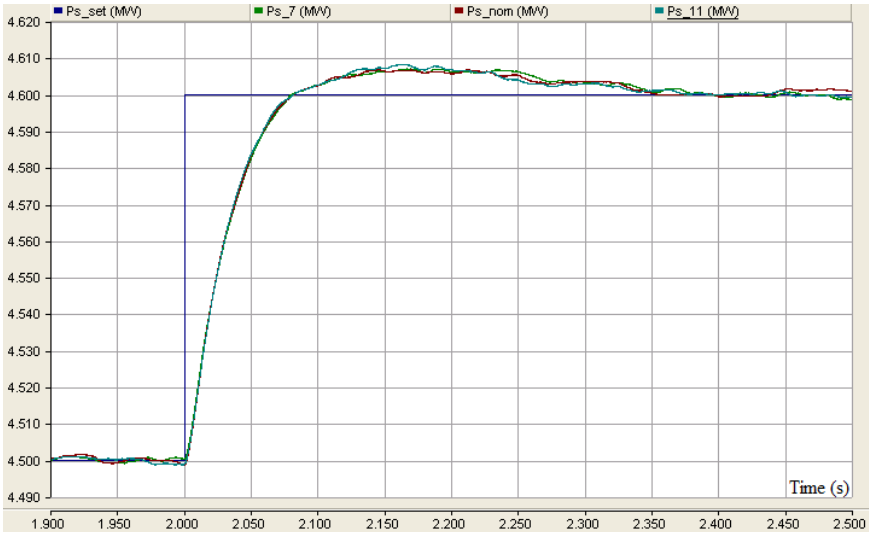

Figure 6.19: PSCAD results of $\zeta_7=\zeta_{nom}=\zeta_{11}$ for robustness analysis - V_s=1pu

6.6.3 V_s=1.2pu (Variations in L_{ss} and L_m by ±10%)

Finally, the stator voltage is increased by 20%. In a similar way to the previous sections, a ±10% change in the inductance values is performed. The resulting damping ratios are calculated and illustrated in Table 6.15. The maximum change between the lowest damping ratio and the highest damping ratio is further reduced to 2.96%. The least damped system response occurs in the case of V_s=1.2pu but with the greatest overshoot. The maximum overshoot is now only 2.44% though. Since the stator voltage is more than adequate, the least oscillations observed in the system response. The PSCAD results are presented in Figures 6.20 and 6.21. The system response for the diagonal damping ratios is almost the same.

V_s=1.2pu=1.2kV L-L RMS	L_{ss} / L_m	**0.9L_{ss}**	**L_{ss}**	**1.1L_{ss}**
	0.9L_m	ζ_{12}=0.877	ζ_{13}=0.89	ζ_{14}=0.903
	L_m	N/A	ζ_{15}=0.877	ζ_{16}=0.889
	1.1L_m	N/A	N/A	ζ_{17}=0.877

Table 6.15: Calculated damping ratios for V_s=1.2pu

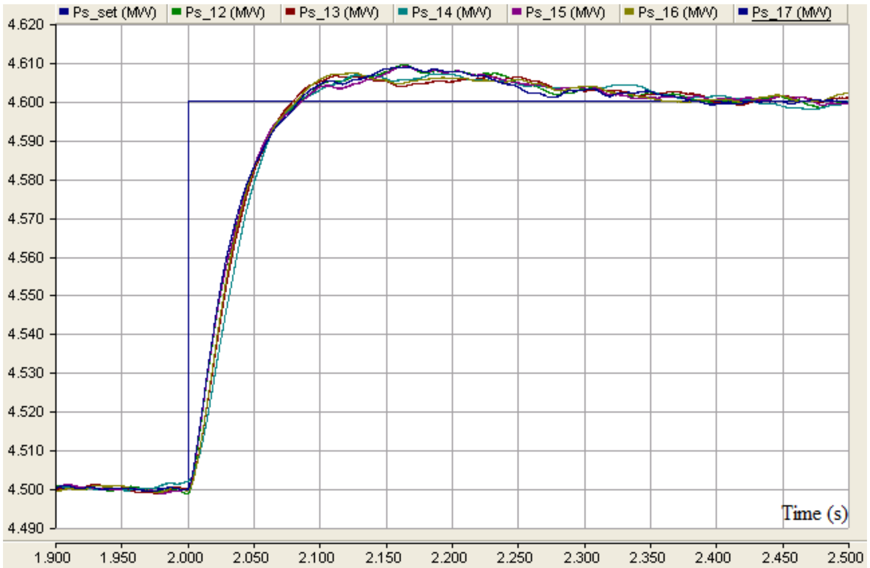

Figure 6.20: PSCAD results for robustness analysis - V_s=1.2pu

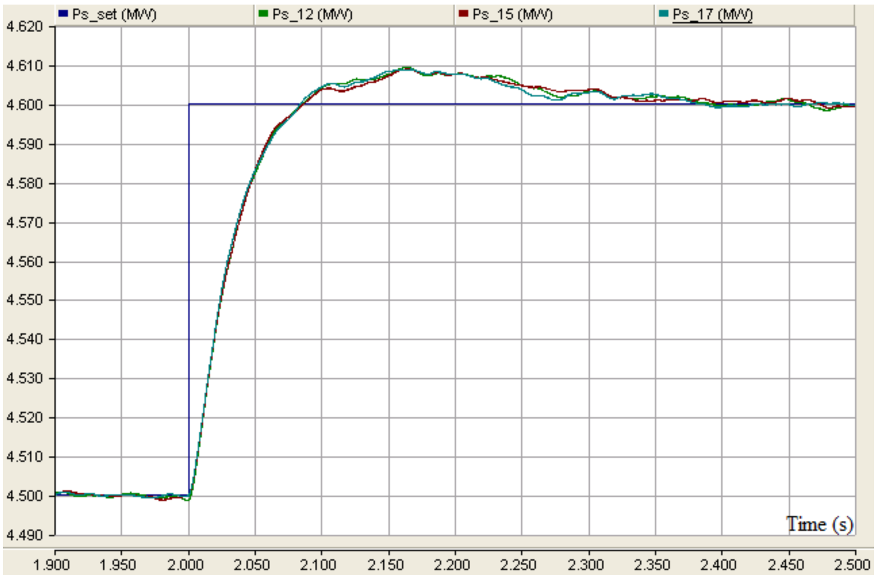

Figure 6.21: PSCAD results of $\zeta_{12}=\zeta_{15}=\zeta_{17}$ for robustness analysis - V_s=1.2pu

The robustness study can tell us that the system is robust enough against the changes in the stator self-inductance and the mutual inductance by ±10%, and ±20% change in the stator voltage. Considering the complexity of the whole system, for the case of V_s=0.8pu the oscillatory behaviour of the system can be regarded as reasonable. Nevertheless, extra care from the point of control may be taken to the operating points of the damping ratio of ζ_2, ζ_3 and ζ_5. If an overall consideration of the robustness analysis is taken into account, the system can be regarded as reasonably robust though.

6.7 Summary

The significant difference between using a PI and more complex (e.g. PID) controller for the power (outer) loop of the RSC controller is emphasised. Related transfer functions (full, simplified and second-order approximated transfer function) of the power loop are derived. The effects of tuning parameters (undamped natural frequency, damping ratio and derivative time constant) are investigated. 'Best' tuning parameters are determined by doing a sensitivity analysis. Finally, the robustness analysis is implemented to these parameters by manually changing the electrical quantities which are stator voltage (V_s), stator self-inductance (L_{ss}), and the mutual inductance (L_m). This chapter demonstrates that a robust system tuning, with more flexibility in the command tracking response shape, can be achieved using a PID tuner and explains how to tune it.

Chapter 7 Conclusions and Further Work

7.1 Conclusions

Conventional energy resources (e.g. fossil fuels) have been significantly run down throughout the globe. Alternative, renewable energy sources have started to be increasingly used to generate green power. Amongst them, wind power is drawing a great deal of attention. As mentioned in related previous chapters, doubly-fed induction generators (DFIGs) are mostly employed in wind conversion systems, since DFIGs have most advantages over other variable speed generator topologies. Therefore, a stand-alone DFIG-based wind turbine is chosen to be investigated in this research project.

A brief background study of research on wind power theory, mechanical and electrical components of a typical wind turbine and general knowledge of wind turbine generator topologies was presented. A comprehensive literature review of the most recent and significant references on DFIG modelling, control and protection was added. Dynamic modelling discussion, machine equations and equations for the transformation from the *abc* frame to the *dq* plane (Clarke and Park) were provided. The use of common control techniques for the current (inner) loop of the rotor-side and grid-side converters were discussed and shown to sufficiently work. Moreover, the drive-train modelling and pitch control methods were documented at a basic level of knowledge.

The DC-link voltage control for the DFIG system considered in this thesis was further developed by undertaking a comprehensive analysis. Previous published work only undertakes a simplified analysis. In addition this approach was extended by a thorough investigation of the methods used to derive controller parameters. The full transfer function of the grid-side converter (including inner-current and outer-voltage loops) was derived. The mathematical analysis for the simplifications of the full transfer function to transfer function (by ignoring inner-current loop) and simplified transfer function (by neglecting the term including the K_s parameter in the denominator of the transfer function) was undertaken. These simplifications were verified against the MATLAB results. By applying simplifications, the complexity of the inner (current) loop for the grid-side converter was then avoided. In addition, the computational time for tuning parameters of the controller was significantly decreased. Reasonable assumptions were made in order to drive the equations of the all transfer functions illustrated in Chapter 4 (see section 4.5).

The operating point sensitivity analysis of the DC-link voltage, and *d*-components of the grid voltage and current was carried out. It was concluded that increasing the DC-link voltage decreases the bandwidth, increasing the *d*-component of the grid-voltage increases the bandwidth. The mathematical calculations were well-matched with the MATLAB graphs. The PSCAD results also support this. Note that the grid-side converter was simulated by itself to get rid of the other sub-system dynamics interference. Moreover, it was impossible to manually change the operating point of the *d*-component of the grid-current due to the nature of simulation circuit. According to the equation of the undamped natural frequency, varying the *d*-component of the grid-current does not change the bandwidth. In fact, considering the full and transfer functions and since the system has complexity, changing the *d*-component of the grid-current has impact on the bandwidth, but this is not significant. However, regarding the simplified transfer function for all operating points of the *d*-component of the grid-current, the bandwidth stays constant.

A sensitivity analysis was also undertaken to find out the relation between the damping ratio and varying the operating points of the DC-link voltage, and *d*-components of the grid voltage and current. For the damping ratio assessment, the forward-path transfer function was used to read the approximate damping ratios on the Bode diagrams in MATLAB. To conclude, increasing the DC-link voltage decreases the damping ratio, increasing the *d*-component of the grid-voltage increases the damping ratio and varying the *d*-component of the grid-current has no significant effect on the damping ratio. The mathematical calculations, the MATLAB results and the PSCAD results are all consistent with each other.

In order to test how stiff the DC-link voltage is to the disturbance input current and the *d*-component of the grid voltage, dynamic stiffness analyses were conducted. Note that the disturbance inputs were taken into account which have been neglected in the literature. The dynamic stiffness analysis results were summarised in Chapter 4 (see Table 4.8). The mathematical analysis matched the MATLAB results well. With reference to the dynamic stiffness analysis of the disturbance input current with respect to the DC-link voltage, increasing the DC-link voltage decreases the stiffness of the system in case of low and mid- frequencies and has no effective change on the stiffness at high frequency. Increasing the *d*-component of the grid-voltage results in a more stiff system in case of low and mid- frequencies and again no effective change occurs in the stiffness at high frequency. Varying the *d*-component of the grid-current does not reflect effective change onto the stiffness at low and high frequencies, for the mid-frequency increasing the *d*-component of the grid-current increases the system stiffness.

For the dynamic stiffness analysis of the *d*-component of the grid-voltage with respect to the DC-link voltage, increasing the DC-link voltage decreases the stiffness at mid- and high frequencies while having no effective change at low frequency. Increasing the *d*-component of the grid-voltage gives more stiff system at low and mid- frequencies and does not effectively influence the stiffness of the system at high frequency. Increasing the *d*-component of the grid-current makes the system less stiff at all low, mid- and high frequencies.

The electrical sub-system interaction between the current, voltage and power loop controllers of the power converters was significantly alleviated by designing the controller loops segmentation which was maintained by specifying the undamped natural frequencies of the loops four to ten times slower than the next faster loop. The GB grid code fault ride-through requirements were briefly summarised. A rotor crowbar circuit against over-current and a DC-link brake against over-voltage protection schemes were described in detail. Their control algorithms were further enhanced. Moreover, the protection coordination between the rotor-crowbar and the DC-link brake was achieved. The relationship between the actions of these protection devices were investigated. The protection control was integrated with the overall system control. The magnitudes of 0.8pu (retained voltage 0.2pu), 0.5pu (retained voltage 0.5pu) and 0.2pu (retained voltage 0.8pu) balanced three-phase, two-phase and single-phase voltage sags were introduced the network voltage for a duration of 100ms in order to verify that the proposed protection circuits work sufficiently enough. Even for more severe voltage sags, by activating both the rotor-crowbar circuit and the DC-link brake together gives a good DC-link voltage control, improves the overall system stability and results in an adequate performance of the DFIG.

Finally, an improved power (outer) loop of the rotor-side converter was developed. Contrary to the use of a traditional PI controller, a PID controller was utilised. Therefore, controlling both the damping and bandwidth was achieved. A sensitivity analysis for tuning process of the outer (power) loop control was performed by each time varying only one quantity. The ranges of the undamped natural frequency, damping ratio and the derivative time constant were determined as 1Hz-1.5Hz-2Hz-2.5Hz, 0.7-0.8-0.9-1-1.1, and 0.1s-0.2s-0.3s-0.4s, respectively. By carrying out the sensitivity analysis, four possible 'best' tuning parameter operating points were found. To do so, the overshoot and settling time characteristics and the step-response characteristics of the full, simplified, second-order approximated transfer function and the measured power curves in both PSCAD and MATLAB results were considered. Then, these four operating points were tested by undertaking a robustness analysis to clarify of which operating points is the 'best'. The robustness analysis for each selected stator voltage (V_s:0.8pu, 1pu and 1.2pu) was done by manually changing the values of the mutual (magnetising) and stator self-inductances by ±10% located in the DFIG model built up in PSCAD. The mathematical analysis and the results of the robustness analysis simulated in PSCAD matched each other reasonably. For fixed values of the mutual (magnetising) and stator self-inductances, increasing the stator voltage decreases the damping ratio but gives less oscillatory system response. Extra care should be taken in case of low stator voltage (in this case 0.8kV) since it results in more oscillatory characteristic of the system response. However, regarding the complexity of the system considered in this research, this is unavoidable and could be considered reasonable. In three operating points of the stator voltage, in case the ratio of the stator self-inductance over the mutual inductance keeps constant (see diagonal damping ratios) better characteristics of the step response occur from the point of less oscillatory view.

7.2 Suggestions for Further Work

In this thesis, a stand-alone DFIG-based wind turbine system is considered. It would be worthwhile to build up and simulate an offshore wind farm by aggregating the desired number of DFIGs in order to investigate that the methodology developed and applied to the single DFIG works sufficiently for larger collections of turbines. Another further step will be to develop a complete model of the wind turbine including turbine mechanical dynamics and a blade pitching control mechanism at a simulation level in PSCAD/EMTDC. However, the simulation penalty adding extra complexity to the system should be taken into account.

Investigation of the behaviour of the DFIG-based wind turbine system and fault-ride through capability of the DFIG during and after unbalanced voltage sags (e.g. applying voltage sags with the magnitude of 0.8pu to Phase A, 0.5pu to Phase B and 0.2pu to Phase C) will be another expansion of this work.

The connection types of the possible offshore wind farm constituted in the simulation programme to the shore, will be the focus of the further research. Traditional AC connection method or contemporary HVDC connection (nowadays this is a promising connection technology) will be investigated and compared with each other. A wind farm model including synchronous aggregation of wind turbines and an HVDC link to shore (DC) and appropriate HVDC modelling will be designed as a further line of research. The effect of synchronous aggregation modelling of the wind-turbines and that of the communication control delays on the selection of the control strategies for the wind-farm will be evaluated within the framework of this research.

In order to validate the related further research projections, a small-scaled test rig would ideally be built up in a laboratory. Thus, the theoretical work could then be experimentally justified.

Lastly, there is considerable scope for novel controllers. The initial work focused on the well-known (and thus easy for industry to adopt) PID controller. More complex controllers with better performance would be worth investigating.

References

[1] A. D. Hansen, F. Lov, F. Blaabjerg, and L. H. Hansen, "Review of contemporary wind turbine concepts and their market penetration," Wind Engineering, vol. 28, pp. 247-263, 2004.

[2] T. Burton, D. Sharpe, N. Jenkins, and E. Bossanyi, Wind Energy Handbook. UK: John Wiley and Sons Ltd., 2001.

[3] “Wind Energy - The Facts, Volume 1 and 2" coordinated by the European Wind Energy Association (EWEA), http://www.wind-energy-the-facts.org/en/downloads.html

[4] A. R. Jha, “Wind Turbine Technology”, CRC Press, Taylor & Francis Group, 2011.

[5] T. Ackermann (editor), “Wind Power in Power Systems”, John Wiley & Sons Ltd., 2005.

[6] G. M. Master, “Renewable and Efficient Electric Power Systems”, John Wiley & Sons Inc., 2004.

[7] Global Wind Energy Council (GWEC), “Global Wind Report – Annual market update 2010”, April 2011.

http://www.gwec.net/fileadmin/images/Publications/GWEC_annual_market_update_2010_-_2nd_edition_April_2011.pdf

[8] European Wind Energy Association (EWEA) Report, “Pure Power”, July 2011.
http://www.ewea.org/fileadmin/ewea_documents/documents/publications/reports/Pure_Power_III.pdf

[9] European Wind Energy Association (EWEA), “EU Energy Policy after 2020”.
http://www.ewea.org/fileadmin/ewea_documents/documents/campaigns/2010_campaign/EU_energy_policy_post_2020.pdf

[10] O. Anaya-Lara, N. Jenkins, J. Ekanayake, P. Cartwright, and M. Hughes, “Wind Energy Generation – Modelling and Control”, John Wiley & Sons, Ltd., Chichester. 2009.

[11] M. R. Khadraoui, and M. Elleuch, "Comparison between OptiSlip and Fixed Speed Wind Energy Conversion Systems", 5th International Multi-Conference on Systems, Signals and Devices, IEEE SSD 2008.

[12] J. Twidell, and T. Weir, "Renewable Energy Resources", 2nd ed., Taylor & Francis Group, 2006.

[13] V. Akhmatov, Analysis of Dynamic Behaviour of Electrical Power Systems with Large Amount of Wind Power, PhD thesis, Ørsted DTU, Technical University of Denmark, 2003.

[14] J. F. Manwell, J. G. McGowan, and A. L. Rogers, "Wind Energy Explained - Theory, Design, and Application", John Wiley & Sons, Ltd., 2002.

[15] M. R. Patel, "Wind and Solar Power Systems", CRC Press, 2006.

[16] S. Chondrogiannis, "Technical Aspects of Offshore Wind Farms Employing Doubly-Fed Induction Generators", PhD Thesis, University of Manchester, 2007.

[17] E. Hau, "Wind Turbines - Fundamentals, Technologies, Applications, Economics" 2nd ed., Springer-Verlag, 2006.

[18] Vestas Wind Systems A/S, "V90-3.0 MW An efficient way to more power" http://www.ceoe.udel.edu/windpower/docs/ProductbrochureV90_3_0_UK.pdf Accessed on 15 October 2011).

[19] W. Leonhard, "Control of Electric Drives", (Springer Verlag, Berlin, 1996, 2nd edn.)

[20] I. Boldea, "Variable Speed Generators" Handbook, 2006

[21] P. C. Krause, O. Wasynczuk, and S. D. Sudhoff, " Analysis of Electric Machinery and Drive System", 2nd ed., John Wiley & Sons, Inc., 2002.

[22] S. Heier, "Grid Integration of Wind Energy Conversion Systems", John Wiley & Sons, Ltd., 1998.

[23] ABB HVDC Reference Projects in Europe, BorWin1, http://www.abb.com/industries/ap/db0003db004333/a8e328849ac67b66c125774a00243367.aspx (Accessed on 19 October 2011).

[24] C. Barker, "HVDC – Connecting to the future", Alstom Grid, 2010.

[25] G. Pannell, "Grid Fault Ride Through for Wind Turbine Doubly-Fed Induction Generators", EngD Thesis, Newcastle University, 2008.

[26] E. Acha, V. G. Agelidis, O. Anaya-Lara, and T. J. E. Miller, "Power Electronic Control in Electrical Systems", Newnes Power Engineering Series, 2002.

[27] N. Mohan, T. M. Undeland, and W. P. Robbins, "Power Electronics - Converters, Applications, and Design", 3rd Ed. (Intr. Ed.), John Wiley & Sons, Inc., 2003.

[28] T. Kimoto, "SiC Technologies for Future Energy Electronics", Symposium on VLSI Technology (VLSIT) 2010. DOI: 10.1109/VLSIT.2010.5556137

[29] J. M. Park, “Novel Power Devicesfor Smart Power Applications”, PhD Dissertation, ausgeführt zum Zwecke der Erlangung des akademischen Grades eines Doktors der technischen Wissenschaften, eingereicht an der Technischen Universität Wien Fakultät für Elektrotechnik und Informationstechnik, October 2004. [Online] Available on http://www.iue.tuwien.ac.at/phd/park/diss.html#CHILD_LINKS [Accessed on 21 October 2011]

[30] L. H. Hansen, L. Helle, F. Blaabjerg, E. Ritchie, S. Munk-Nielsen, H. Bindner, P. Sorensen, and B. Bak-Jensen, " Conceptual survey of Generators and Power Electronics for Wind Turbines", Risø National Laboratory, Denmark, 2001.

[31] M. A. Boost, and P. D. Ziogas, "State-of-the-Art Carrier PWM Techniques: A Critical Evaluation", IEEE Transactions on Industry Applications, Vol. 24, No. 2, pp. 271-280, 1988.

[32] M. A. Patel, A. R. Patel, D. R. Vyas, and K. M. Patel, "Use of PWM Techniques for Power Quality Improvement", International Journal on Recent Trends in Engineering, Vol. 1, No. 4, pp. 99-102, Academy Publisher, ACEEE, 2009.

[33] C. Fitzer, “Digital Signal Processing for the Control of a Dynamic Voltage Restorer”, PhD Thesis, UMIST, 2002.

[34] S. R. Bowes, and Y.-S. Lai, "The Relationship between Space-Vector Modulation and Regular-Sampled PWM", IEEE Transactions on Industrial Electronics, Vol. 44, No. 5, pp. 670-679, 1997.

[35] V. Akhmatov, “Variable-Speed Wind Turbines with Doubly-Fed Induction Generators – Part I: Modelling in Dynamic Simulation Tool”, Wind Engineering, Vol. 26, No. 2, pp. 85-108, 2002.

[36] V. Akhmatov, “Variable-Speed Wind Turbines with Doubly-Fed Induction Generators – Part II: Power System Stability”, Wind Engineering, Vol. 26, No. 3, pp. 171-188, 2002.

[37] V. Akhmatov, “Variable-Speed Wind Turbines with Doubly-Fed Induction Generators – Part III: Model with the Back-to-Back Converters”, Wind Engineering, Vol. 27, No. 2, pp. 79-91, 2003.

[38] V. Akhmatov, “Variable-Speed Wind Turbines with Doubly-Fed Induction Generators – Part IV: Uninterrupted Operation Features at Grid Faults with Converter Control Coordination”, Wind Engineering, Vol. 27, No. 6, pp. 519-529, 2003.

[39] J. G. Slootweg, "Wind Power Modelling and Impact on Power System Dynamics", PhD Thesis, Delft University of Technology (TU Delft, the Netherlands), 2003.

[40] M. A. Pöller, “Doubly-fed induction machine models for stability assessment of wind farms,” in Proc. IEEE Bologna Power Tech, Italy, June 2003.

[41] J. B. Ekanayake, L. Holdsworth, and N. Jenkins, “Comparison of 5th order and 3rd order machine models for doubly fed induction generator (DFIG) wind turbines,” Electric Power Systems Research, vol. 67, pp. 207–215, Dec. 2003.

[42] P. Sørensen, A. D. Hansen, T. Lund, and H. Bindner, "Reduced models of doubly fed induction generator system for wind turbine simulations," Wind Energy, vol. 9, pp. 299-311, 2006.

[43] J. Kretschmann, H. Wrede, S. Mueller-Engelhardt, and I. Erlich, "Enhanced Reduced Order Model of Wind Turbines with DFIG for Power System Stability Studies," IEEE PECon, Malaysia, 2006.

[44] F. Mei, "Small-Signal Modelling and Analysis of Doubly-Fed Induction Generators in Wind Power Applications" PhD Thesis, Imperial College London, University of London, 2008.

[45] A. Perdana, "Dynamic Models of Wind Turbines A Contribution towards to Establishment of Standardised Models of Wind Turbines for Power System Stability Studies ", PhD thesis, Chalmers University of Technology, 2008.

[46] J. G. Slootweg, H. Polinder and W. L. Kling, “Representing Wind Turbine Electrical Generating Systems in Fundamental Frequency Simulations”, IEEE Transactions on Energy Conversion, Vol. 18, No. 4, December 2003.

[47] L. Holdsworth, J. B. Ekanayake, and N. Jenkins, “Power System Frequency Response from Fixed Speed and Doubly Fed Induction Generator-based Wind Turbines”, Wind Energy, Vol. 7, Iss. 1, pp. 21-35, 2004.

[48] A. Petersson, "Analysis, Modelling and Control of Doubly-Fed Induction Generators for Wind Turbines," PhD Thesis, Division of Electric Power Engineering, Chalmers University of Technology, Sweden, 2005.

[49] B. Hopfensperger, "Field Oriented Control of Single and Cascaded Doubly-Fed Induction Machines", PhD Thesis, Newcastle University, 1998.

[50] B. Hopfensperger, D. Atkinson, and R. A. Lakin, “Stator Flux Oriented Control of a Cascaded Doubly-fed Induction Machine,” IEE Proceedings Electric Power Applications, Vol. 146, Iss. 6, pp. 597–605, 1999.

[51] B. Hopfensperger, D. Atkinson, and R. A. Lakin, “Stator flux oriented control of a cascaded doubly-fed induction machine with and without position encoder,” IEE Proc. Electr. Power Appl., vol. 147, no. 4, pp. 241-250, July 2000.

[52] S. Williamson, and R. C. Healey, "Space vector represantation of advanced motor models for vector controlled induction motors", IEE Proc. Electric Power Applications, Vol. 143, No. 1, pp. 69-77, 1996.

[53] R. W De Doncker, F. Profumo, M. Pastorelli, and P. Ferraris, "Comparison of Universal Field Oriented (UFO) Controllers in Different Reference Frames", IEEE Transactions on Power Electronics, Vol. 10, No. 2, pp. 205-13, 1995.

[54] L. Xu and W. Cheng, “Torque and reactive power control of a doubly fed induction machine by position sensorless scheme,” IEEE Trans. Ind. Appl.., vol. 31, no. 3, pp. 636–642, May/June 1995.

[55] D. W. Novotny, and T. A. Lipo, "Vector Control and Dynamics of AC Drives", Oxford Science Publications, 1998.

[56] L. Xu and P. Cartwright, "Direct active and reactive power control of DFIG for wind energy generation," IEEE Transactions on Energy Conversion, vol. 21, pp. 750-758, 2006.

[57] R. Datta and V. T. Ranganathan, "Direct power control of grid-connected wound rotor induction machine without rotor position sensors," Power Electronics, IEEE Transactions on, vol. 16, pp. 390-399, 2001.

[58] S. Arnalte, J. C. Burgos, and J. L. Rodriguez-Amenedo, "Direct Torque Control od a Doubly-Fed Induction Generator for Variable Speed Wind Turbines", Electric Pwoer Components and Systems, Vol. 30, Iss. 2, pp. 199-216, 2002.

[59] R. Todd, "High Power Wind Energy Conversion Systems", EngD Thesis, University of Manchester, 2006.

[60] R. Pena, J.C. Clare, G.M. Asher, “Doubly Fed Induction Generator using back-to-back PWM Converters and its Application to Variable Speed Wind-Energy Generation”, IEE Proc.-Electr. Power Appl., Vol. 143, No:3, May 1996.

[61] S. Seman, J. Niiranen, S. Kanerva, A. Arkkio, and J. Saitz, “Performance Study of a Doubly Fed Wind-Power Induction Generator under Network Disturbances”, IEEE Transactions on Energy Conversion, Vol. 21, No. 4, pp. 883-890, 2006.

[62] J. Morren and S. W. H. de Haan, "Ridethrough of Wind Turbines with Doubly-Fed Induction Generator During a Voltage Dip," IEEE Transactions on Energy Conversion, Vol. 20, No. 2 pp. 435-441, June 2005.

[63] X. Dawei, R. Li, P. J. Tavner, and S. Yang, "Control of a Doubly Fed Induction Generator in a Wind Turbine During Grid Fault Ride-Through," IEEE Transaction on Energy Conversion, , Vol. 21, No. 3pp. 652-662, September 2006.

[64] J. Niiranen, "Experiences on voltage dip ride through factory testing of synchronous and doubly fed generator drives," 11th European Conference on Power Electronics and Applications (EPE), Dresden, Germany, September, 2005.

[65] S. Seman, J. Niiranen, and A. Arkkio, "Ride-Through Analysis of Doubly Fed Induction Wind-Power Generator Under Unsymmetrical Network Disturbance," IEEE Transactions on Power Systems, , vol. 21, pp. 1782-1789, 2006.

[66] B. I. Naess, J. Eek, T. M. Undeland, and T. Gjengedal, "Ride Through Solutions for Doubly Fed Induction Generators," 4th World Wind Energy Conference & Renewable Energy Exhibition, Australia, 2005.
http://www.elkraft.ntnu.no/eno/Papers2005/Bjarne-Australia.pdf

[67] L. Holdsworth, I. Charalambous, J. B. Ekanayake, and N. Jenkins, "Power System Fault Ride Through Capabilities of Induction Generator based Wind Turbines", Wind Engineering, Vol. 28, No. 4, pp. 399-412, 2004.

[68] S. Foster, L. Xu, and B. Fox, “Behaviour and Protection of Doubly-Fed Induction Generators during Network Faults”, IEEE Power & Energy Society General Meeting, PES 2009.

[69] S. Foster, L. Xi, and B. Fox, “Coordinated Reactive Power Control for Facilitating Fault Ride Through of Doubly Fed Induction Generator- and Fixed Speed Induction Generator-Based Wind Farms”, IET Renewable Power Generation, Vol. 4, Iss. 2, pp. 128-138, March 2010.

[70] O. Anaya-Lara, X. Wu, P. Cartwright, J. B. Ekanayake, and N. Jenkins, “Performance of Doubly Fed Induction Generator (DFIG) During Network Faults”, Wind Engineering, Vol. 29, No. 1, pp. 49-66, 2005.

[71] G. Pannell, D. Atkinson, R. Kemsley, L. Holdsworth, P. Taylor, and O. Moja, "DFIG Control Performance under Fault Conditions for Offshore Wind Applications," 18th International Conference and Exhibition on Electricity Distribution, Italy, CIRED 2005.

[72] M. Rodriguez, G. Abad, I. Sarasola, and A. Gilabert, “Crowbar Control Algorithms for Doubly Fed induction Generator during Voltage Dips”, European Conference on Power Electronics and Applications, 2005.

[73] I. Erlich, H. Wrede, and C. Feltes, “Dynamic Behaviour of DFIG-Based Wind Turbines during Grid Faults”, Power Conversion Conference – Nagoya, pp. 1195-1200, PCC 2007.

[74] C. Zhan, C. D. Barker, “Fault Ride-Through Capability Investigation of a Doubly-Fed Induction Generator with an Additional Series-Connected Voltage Source

Converter”, 8th IEE International Conference on AC and DC Power Transmission, pp. 79-84, ACDC 2006.

[75] A. D. Hansen, G. Michalke, “Fault Ride-Through Capability of DFIG Wind Turbines”, Renewable Energy, Vol. 32, Iss. 9, pp. 1594-1610, July 2007.

[76] G. Pannel, D. J. Atkinson, and B. Zahawi, “Analytical Study of Grid-Fault Response of Wind Turbine Doubly Fed Induction Generator", IEEE Transactions on Energy Conversion, Vol. 25, No. 4, pp. 1081-1091, December 2010.

[77] G. Pannel, D. J. Atkinson, and B. Zahawi, “Minimum-Threshold Crowbar for a Fault-Ride-Through Grid-Code-Compliant DFIG Wind Turbine”, IEEE Transactions on Energy Conversion, Vol. 25, No. 3, pp. 750-759, September 2010.

[78] R. Datta and V. T. Ranganathan, “Variable-speed wind power generation using doubly fed wound rotor induction machine-a comparison with alternative schemes,” IEEE Trans. on Energy Conversion, vol. 17, no. 3, pp. 414–421, Sept. 2002.

[79] S. Muller, M. Deicke, and R. W. De Doncker, “Doubly fed induction generator systems for wind turbines,” IEEE Ind. Applicat. Mag., pp. 26-33, May/June 2002.

[80] M. Barnes, MSc Modules, University of Manchester, 2010.

[81] R. Todd, M. Barnes, and A. C. Smith, "Design Study of Doubly-Fed Induction Generators for a 2MW Wind Turbine", Wind Engineering, Vol. 33, No. 5, pp. 497-508, 2009.

[82] J. W. Park, K. W. Lee, and H. J. Lee, "Control of Active Power in a Doubly-Fed Induction Generator Taking into Account the Rotor Side Apparent Power", 35th Annual IEEE Power Electronics Speacilaists Conference, pp. 2060-2064, 2004.

[83] S. M. Muyeen, J. Tamura, and T. Murata, "Stability Augmentation of a Grid-connected Wind Farm", Springer, 2009.

[84] M. Kayikci, "The Influence of Wind Plant Control on Transient Performance of the Network", PhD Thesis, University of Manchester, 2007.

[85] A. D. Hansen, G. Michalke, P. Sorensen, T. Lund, and F. Iov, "Co-ordinated Voltage Control of DFIG Wind Turbines in Uninterrupted Operation during Grid Faults", Wind Energy, Vo. 10, Issue 1, pp. 51-68, 2007.

[86] A. D. Hansen, C. Jauch, P. Sorensen, F. Iov, and F. Blaabjerg, "Dynamic Wind Turbine Models in Power System Simulation Tool DIgSILENT", Riso-R-1400(EN), 2003.

[87] B. C. Kuo, and F. Golnaraghi, "Automatic Control Systems", 8th ed., John Wiley & Sons, Inc, 2003.

[88] C. L. Phillips, and R. D. Harbor, "Feedback Control Systems", 4th ed., Prentice Hall, 2000.

[89] F. Golnaraghi, and B. C. Kuo, "Automatic Control Systems", 9th ed., John Wiley & Sons, Inc., 2010.

[90] G. Abad, J. Lopez, M. A. Rodriguez, L. Marroyo, and G. Iwanski, “Doubly Fed Induction Machine – Modeling and Control for Wind Energy Generation”, IEEE Press, John Wiley & Sons Inc., 2011.

[91] M. H. Hansen, A. Hansen, T. J. Larsen, S. Oye, P. Sorensen and P. Fuglsang, “Control Design for a Pitch-Regulated Variable-Speed Wind Turbine, Riso-R-1500(EN), Riso National Laboratory, Denmark, January 2005.

[92] J. Niiranen, “Voltage Dip Ride Through of a Doubly-Fed Generator Equipped with an Active Crowbar”, Proc. of Nordic Wind Power Conference NWPC, March 2004.

[93] F. Koch, F. Shewarega, and I. Erlich, "Alternative Models of the Doubly-fed Induction Machine of Power System Dynamic Analysis" presented at International Conference on New and Renewable Energy Technologies for Sustainable Development, Evora, Portugal, 2004.

[94] T. Sun, Z. Chen, and F. Blaabjerg, "Voltage recovery of grid-connected wind turbines with DFIG after a short-circuit fault," presented at Power Electronics Specialists Conference, PESC 04, IEEE 35th Annual, 2004.

[95] P. Zhou, and Y. He, “Control Strategy of an Active Crowbar for DFIG Wind Turbine under Grid Voltage Dips”, Proceeding of International Conference on Electrical Machines and Systems 2007, Oct. 8~11, Seoul, Korea.

[96] P. Zhou, Y. He, D. Sun, and J. G. Zhu, “Control and Protection of a DFIG-based Wind Turbine under Unbalanced Grid Voltage Dips”, Industry Applications Society Annual Meeting, IAS ’08, IEEE, 2008.

[97] M. M. Mano, and C. R. Kime, "Logic and Computer Design Fundamentals", 2nd ed., Prentice Hall, 2000.

[98] J. Morren, S.W.H de Haan, “Short-Circuit of Wind Turbines with DFIG”, IEEE Trans. on Energy Conversion, vol.22, no.1, March 2007.

[99] The Grid Code, Issue 4, Revision 10, 3 January 2012, National Grid Electricity Transmission plc, available on http://www.nationalgrid.com/NR/rdonlyres/67374C36-1635-42E8-A2B8-B7B8B9AF2408/51019/Z_CompleteGridCode_I4R10.pdf

[100] MIL-HDBK-217F, Notice 2, Military Handbook: Reliability Prediction of Electronic Equipment, 28/02/1995. [Accessed at http://www.everyspec.com/MIL-

HDBK/MIL-HDBK+(0200+-+0299)/MIL-HDBK-217F_NOTICE-2_14590/ on 12th March 2012]

[101] K. Ogata, “Modern Control Engineering”, 5th ed., Pearson, 2010.

[102] K. Astrom, and T. Hagglund, "PID Controllers: Theory, Design and Tuning", 2nd ed., ISA (The Instrumentation, Systems, and Automation Society), 1995.

[103] W. S. Levine, "Control System Fundamentals", editor, 2nd edition, CRC Press, 2011.

[104] K. H. Ang, G. Chong, and Y. Li, "PID Control System Analysis, Design, and Technology", IEEE Transactions on Control Systems Technology, vol. 13, no. 4, pp. 559-576, July 2005.

[105] Z. Gajic, M. Lelic, “Modern Control Systems”, Prentice Hall, 1996.

Appendix 1 Data of Electrical Components

Electrical Generator (DFIG) Data:

Rating	4.5 MVA
Stator Voltage (L-L, RMS)	1 kV
L_s	0.09241 pu
L_r	0.09955 pu
L_m	3.95279 pu
R_s	0.00488 pu
R_r	0.00549 pu

3-winding Transformer:

Rating	4.5 MVA
V_1 (L-L, RMS)	1 kV
V_2 (L-L, RMS)	0.4 kV
V_3 (L-L, RMS)	33 kV
L_{12}	0.08 pu
L_{13}	0.08 pu
L_{23}	0.001 pu
No load losses	0.01 pu
Copper losses	0.01 pu

Frequency Converter:

C_{base}		0.014324 F
C_{dc_link}		3.5 pu
V_{dc}		1 kV
Grid-side converter	$L_{coupling\_grid}$	1 pu (per 0.4 kV base
	$R_{coupling\ \_grid}$	0.017 pu (per 0.4 kV base)
Rotor-side converter	$L_{coupling\ \_rotor}$	0.2 pu (per 1 kV base)
	$R_{coupling\ \_rotor}$	0 pu (per 1 kV base)

Stator self-inductance:

$L_{ss} = L_s + L_m + L_{13} = 0.09241\text{pu}+3.95279\text{pu}+0.08\text{pu}= 4.1252$ pu

Rotor self-inductance:

$L_{rr} = L_r + L_m = 0.09955\text{pu}+3.95279\text{pu}= 4.05234$ pu

Total coupling inductance to grid-side:

$L_{gsc} = L_{coupling\_grid} + L_{23} = 1\text{pu}+0.08\text{pu}= 1.08$ pu (per 0.4 kV base)

Coupling resistance to grid-side:

$R_{gsc} = R_{coupling\_grid} = 0.017$ pu (per 0.4 kV base)

Coupling inductance to rotor:

$L_{rsc} = L_{coupling\_rotor} = 0.2$ pu (per 1 kV base)

Coupling resistance to rotor:

$R_{rsc} = R_{coupling\_rotor} = 0$ pu

DC-link Capacitor:

C_{dc_link}=3.5 pu

Appendix 2 Layout of the DFIG System in PSCAD/EMTDC

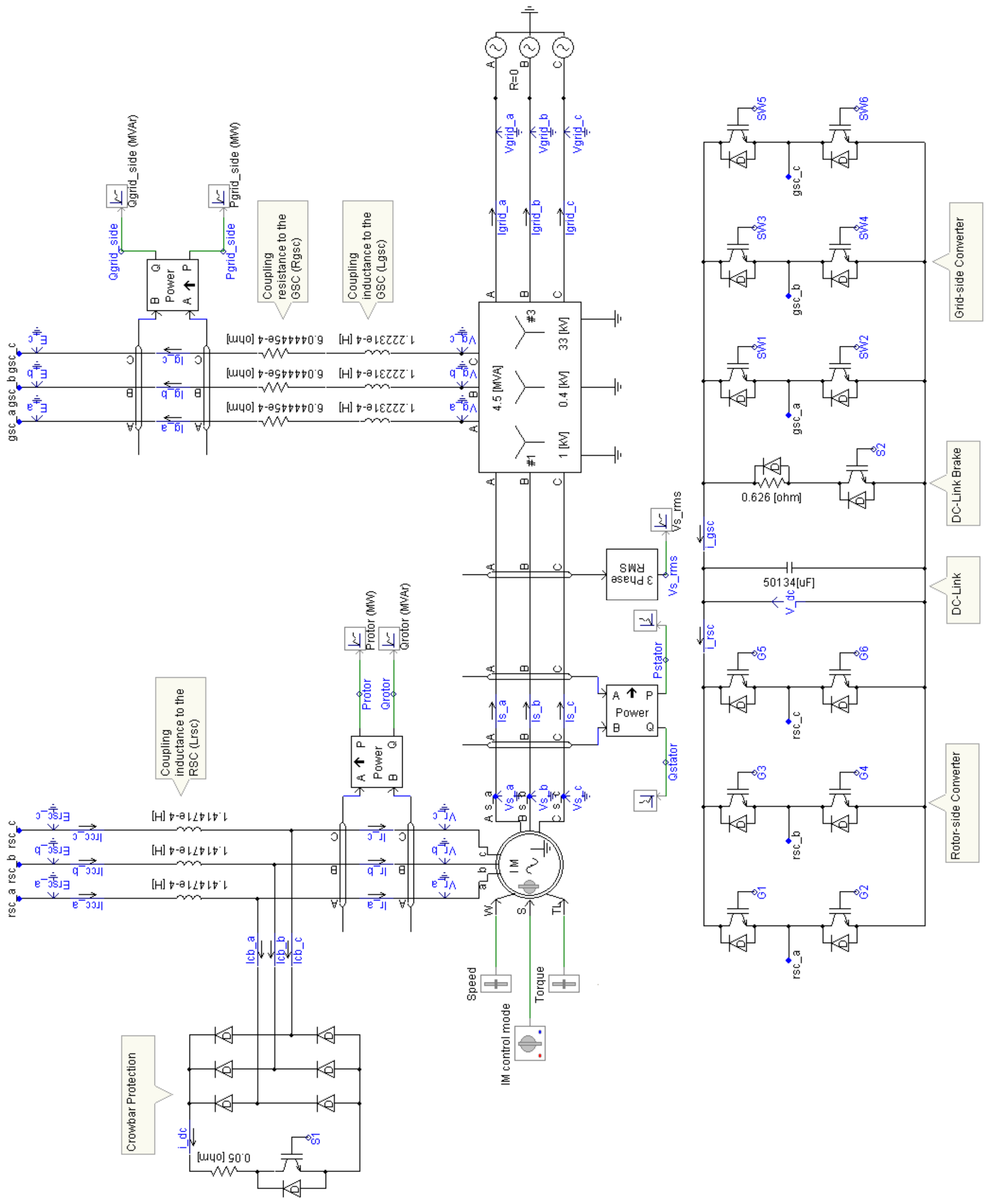

Figure A.2.1: Overall DFIG system layout

Appendix 3 Operating Point Sensitivity Analysis and Dynamic Stiffness Assessment of DC-link Voltage Control

A.3.1 V_{dco} Sensitivity

A.3.1.1 Mathematical Calculations

i) $V_{dco}= V_{dco\_min}$=700V (0.7kV)

The first step is to calculate new K_v and K_s values, since both of them vary with the change in V_{dc}.

$$K_v = \frac{v_{g\_do\_nom}}{v_{dco}} = \frac{0.3266\text{kV}}{0.7\text{kV}} \approx 0.467 \quad \text{and} \quad K_s = \frac{i_{g\_do\_nom}}{v_{dco}} = \frac{2.75568\text{kA}}{0.7\text{kV}} \approx 3.937\ (\text{A/V})$$

Substituting K_{pv}, K_{iv}, K_{pi}, K_{ii}, K_v and K_s parameters in equations a-h, these equations can be re-written as follows:

$$\text{a) FTF}=\frac{\Delta V_{dc}}{\Delta V^*_{dc}}=\frac{4.3508s^2+6351.4622s+276286.9971}{6.12793\text{x}10^{-6}s^4+0.0349894s^3+55.2441s^2+9043.6405s+276286.9971}$$

$$\text{b) TF}=\frac{\Delta V_{dc}}{\Delta V^*_{dc}}=\frac{6.3001s+282.7446}{0.050134s^2+9.0552s+282.7446}$$

$$\text{c) STF}=\frac{\Delta V_{dc}}{\Delta V^*_{dc}}=\frac{6.3001s+282.7446}{0.050134s^2+6.3001s+282.7446}$$

$$\text{d) SoATF}=\frac{\Delta V_{dc}}{\Delta V^*_{dc}}=\frac{5639.7774}{s^2+180.6197s+5639.7774}$$

$$\text{e) SSoATF}=\frac{\Delta V_{dc}}{\Delta V^*_{dc}}=\frac{5639.7774}{s^2+125.665s+5639.7774} \approx \frac{\omega^2_{no}}{s^2+2\zeta\omega_{no}s+\omega^2_{no}} \Rightarrow \omega_{no\_max}=75.1\text{rad/s or } f_{no\_max}=11.95\text{Hz} \Rightarrow \zeta_{o\_max}=0.837$$

$$\text{f) FpTF=G(s).H(s)}=\frac{6.3001s+282.7446}{0.050134s^2+2.7551s}$$

$$\text{g) DS1}=\left|\frac{\Delta i_n}{\Delta V_{dc}}\right|=\left|\frac{0.050134s^2+9.0552s+282.7446}{s}\right|$$

$$\text{h) DS2}=\left|\frac{\Delta v_{g\_d}}{\Delta V_{dc}}\right|=\left|\frac{0.00849s^2+1.5335s+47.8821}{s}\right|$$

ii) V_{dco}=800V (0.8kV)

$$K_v = \frac{v_{g\_do\_nom}}{v_{dco}} = \frac{0.3266\text{kV}}{0.8\text{kV}} \approx 0.408 \quad \text{and} \quad K_s = \frac{i_{g\_do\_nom}}{v_{dco}} = \frac{2.75568\text{kA}}{0.8\text{kV}} \approx 3.445 \text{ (A/V)}$$

Substituting K_{pv}, K_{iv}, K_{pi}, K_{ii}, K_v and K_s parameters in equations a-h, these equations will transform into:

$$\text{a) FTF}=\frac{\Delta V_{dc}}{\Delta V_{dc}^{*}}=\frac{3.807s^2+5557.5294s+241751.1224}{6.12793\text{x}10^{-6}s^4+0.0349105s^3+54.254s^2+7618.7284s+241751.1224}$$

$$\text{b) TF}=\frac{\Delta V_{dc}}{\Delta V_{dc}^{*}}=\frac{5.5126s+247.4015}{0.050134s^2+7.622s+247.4015}$$

$$\text{c) STF}=\frac{\Delta V_{dc}}{\Delta V_{dc}^{*}}=\frac{5.5126s+247.4015}{0.050134s^2+5.5126s+247.4015}$$

$$\text{d) SoATF}=\frac{\Delta V_{dc}}{\Delta V_{dc}^{*}}=\frac{4934.8052}{s^2+152.0316s+4934.8052}$$

$$\text{e) SSoATF}=\frac{\Delta V_{dc}}{\Delta V_{dc}^{*}}=\frac{4934.8052}{s^2+109.9568s+4934.8052}\approx\frac{\omega_{no}^2}{s^2+2\zeta\omega_{no}s+\omega_{no}^2} \quad \Rightarrow \omega_{no}=70.248\text{rad/s or } f_{no}=11.18\text{Hz} \quad \Rightarrow \zeta_o=0.783$$

$$\text{f) FpTF=G(s).H(s)}=\frac{5.5126s+247.4015}{0.050134s^2+2.1094s}$$

$$\text{g) DS1}=\left|\frac{\Delta i_n}{\Delta V_{dc}}\right|=\left|\frac{0.050134s^2+7.622s+247.4015}{s}\right|$$

$$\text{h) DS2}=\left|\frac{\Delta v_{g\_d}}{\Delta V_{dc}}\right|=\left|\frac{0.0097s^2+1.4752s+47.8821}{s}\right|$$

iii) V_{dco}=900V (0.9kV)

$$K_v = \frac{v_{g\_do\_nom}}{v_{dco}} = \frac{0.3266\text{kV}}{0.9\text{kV}} \approx 0.363 \quad \text{and} \quad K_s = \frac{i_{g\_do\_nom}}{v_{dco}} = \frac{2.75568\text{kA}}{0.9\text{kV}} \approx 3.062\,(\text{A/V})$$

Substituting K_{pv}, K_{iv}, K_{pi}, K_{ii}, K_v and K_s parameters in equations a-h, these equations turn into:

a) $\text{FTF}=\dfrac{\Delta V_{dc}}{\Delta V_{dc}^{*}}=\dfrac{3.384s^2+4940.0262s+214889.8866}{6.12793\text{x}10^{-6}s^4+0.0348564s^3+53.525s^2+6568.6278s+214889.8866}$

b) $\text{TF}=\dfrac{\Delta V_{dc}}{\Delta V_{dc}^{*}}=\dfrac{4.9001s+219.9125}{0.050134s^2+6.5667s+219.9125}$

c) $\text{STF}=\dfrac{\Delta V_{dc}}{\Delta V_{dc}^{*}}=\dfrac{4.9001s+219.9125}{0.050134s^2+4.9001s+219.9125}$

d) $\text{SoATF}=\dfrac{\Delta V_{dc}}{\Delta V_{dc}^{*}}=\dfrac{4386.4935}{s^2+130.9837s+4386.4935}$

e) $\text{SSoATF}=\dfrac{\Delta V_{dc}}{\Delta V_{dc}^{*}}=\dfrac{4386.4935}{s^2+97.7394s+4386.4935}\approx\dfrac{\omega_{no}^2}{s^2+2\zeta\omega_{no}s+\omega_{no}^2} \Rightarrow \omega_{no}=66.23\text{rad/s or } f_{no}=10.54\text{Hz} \Rightarrow \zeta_o=0.738$

f) $\text{FpTF=G(s).H(s)}=\dfrac{4.9001s+219.9125}{0.050134s^2+1.6667s}$

g) $\text{DS1}=\left|\dfrac{\Delta i_n}{\Delta V_{dc}}\right|=\left|\dfrac{0.050134s^2+6.5667s+219.9125}{s}\right|$

h) $\text{DS2}=\left|\dfrac{\Delta v_{g\_d}}{\Delta V_{dc}}\right|=\left|\dfrac{0.01092s^2+1.4298s+47.8821}{s}\right|$

iv) $V_{dco}= V_{dco\_nom}$=1000V (1kV)

$$K_v=\frac{v_{g\_do\_nom}}{v_{dco\_nom}}=\frac{0.3266\text{kV}}{1\text{kV}}\approx 0.327 \quad \text{and} \quad K_s=\frac{i_{g\_do\_nom}}{v_{dco\_nom}}=\frac{2.75568\text{kA}}{1\text{kV}}\approx 2.756\ (\text{A/V})$$

Substituting K_{pv}, K_{iv}, K_{pi}, K_{ii}, K_v and K_s parameters in equations a-h, these equations turn into:

$$\text{a) FTF}=\frac{\Delta V_{dc}}{\Delta V_{dc}^*}=\frac{3.0456s^2+4446.0235s+193400.8979}{6.12793\text{x}10^{-6}s^4+0.0348177s^3+52.9677s^2+5765.1909s+193400.8979}$$

$$\text{b) TF}=\frac{\Delta V_{dc}}{\Delta V_{dc}^*}=\frac{4.4101s+197.9212}{0.050134s^2+5.7601s+197.9212}$$

$$\text{c) STF}=\frac{\Delta V_{dc}}{\Delta V_{dc}^*}=\frac{4.4101s+197.9212}{0.050134s^2+4.4101s+197.9212}$$

$$\text{d) SoATF}=\frac{\Delta V_{dc}}{\Delta V_{dc}^*}=\frac{3947.8442}{s^2+114.8933s+3947.8442}$$

$$\text{e) SSoATF}=\frac{\Delta V_{dc}}{\Delta V_{dc}^*}=\frac{3947.8442}{s^2+87.9655s+3947.8442}\approx\frac{\omega_{no}^2}{s^2+2\zeta\omega_{no}s+\omega_{no}^2} \quad \Rightarrow \omega_{n\_nom}=62.83\text{rad/s or } f_{n\_nom}=10\text{Hz} \Rightarrow \zeta_{nom}=0.7$$

$$\text{f) FpTF=G(s).H(s)}=\frac{4.4101s+197.9212}{0.050134s^2+1.35s}$$

$$\text{g) DS1}=\left|\frac{\Delta i_n}{\Delta V_{dc}}\right|=\left|\frac{0.050134s^2+5.7601s+197.9212}{s}\right|$$

$$\text{h) DS2}=\left|\frac{\Delta v_{g\_d}}{\Delta V_{dc}}\right|=\left|\frac{0.01213s^2+1.3935s+47.8821}{s}\right|$$

v) V_{dco}= 1100V (1.1kV)

$$K_v = \frac{v_{g\_do\_nom}}{v_{dco}} = \frac{0.3266kV}{1.1kV} \approx 0.297 \quad \text{and} \quad K_s = \frac{i_{g\_do\_nom}}{v_{dco}} = \frac{2.75568kA}{1.1kV} \approx 2.505 \text{ (A/V)}$$

Substituting K_{pv}, K_{iv}, K_{pi}, K_{ii}, K_v and K_s parameters in equations a-h, these equations turn into:

a) $FTF=\frac{\Delta V_{dc}}{\Delta V_{dc}^*}=\frac{2.7687s^2+4041.8396s+175818.9981}{6.12793x10^{-6}s^4+0.034789s^3+52.5289s^2+5132.0605s+175818.9981}$

b) $TF=\frac{\Delta V_{dc}}{\Delta V_{dc}^*}=\frac{4.0091s+179.9284}{0.050134s^2+5.1248s+179.9284}$

c) $STF=\frac{\Delta V_{dc}}{\Delta V_{dc}^*}=\frac{4.0091s+179.9284}{0.050134s^2+4.0091s+179.9284}$

d) $SoATF=\frac{\Delta V_{dc}}{\Delta V_{dc}^*}=\frac{3588.9493}{s^2+102.223s+3588.9493}$

e) $SSoATF=\frac{\Delta V_{dc}}{\Delta V_{dc}^*}=\frac{3588.9493}{s^2+79.9686s+3588.9493}\approx\frac{\omega_{no}^2}{s^2+2\zeta\omega_{no}s+\omega_{no}^2}\Rightarrow\omega_{no}=59.906\text{rad/s or } f_{no}=9.535\text{Hz}\Rightarrow\zeta_o=0.666$

f) $FpTF=G(s).H(s)=\frac{4.0091s+179.9284}{0.050134s^2+1.1157s}$

g) $DS1=\left|\frac{\Delta i_n}{\Delta V_{dc}}\right|=\left|\frac{0.050134s^2+5.1248s+179.9284}{s}\right|$

h) $DS2=\left|\frac{\Delta v_{g\_d}}{\Delta V_{dc}}\right|=\left|\frac{0.01334s^2+1.3638s+47.8821}{s}\right|$

vi) V_{dco}= 1200V (1.2kV)

$$K_v = \frac{v_{g\_do\_nom}}{v_{dco}} = \frac{0.3266kV}{1.2kV} \approx 0.273 \quad \text{and} \quad K_s = \frac{i_{g\_do\_nom}}{v_{dco}} = \frac{2.75568kA}{1.2kV} \approx 2.296 \text{ (A/V)}$$

Substituting K_{pv}, K_{iv}, K_{pi}, K_{ii}, K_v and K_s parameters in equations a-h, these equations turn into:

a) $\text{FTF}=\frac{\Delta V_{dc}}{\Delta V_{dc}^*}=\frac{2.538s^2+3705.0196s+161167.415}{6.12793x10^{-6}s^4+0.0347672s^3+52.175s^2+4621.1081s+161167.415}$

b) $\text{TF}=\frac{\Delta V_{dc}}{\Delta V_{dc}^*}=\frac{3.6751s+164.9344}{0.050134s^2+4.6126s+164.9344}$

c) $\text{STF}=\frac{\Delta V_{dc}}{\Delta V_{dc}^*}=\frac{3.6751s+164.9344}{0.050134s^2+3.6751s+164.9344}$

d) $\text{SoATF}=\frac{\Delta V_{dc}}{\Delta V_{dc}^*}=\frac{3289.8702}{s^2+92.0045s+3289.8702}$

e) $\text{SSoATF}=\frac{\Delta V_{dc}}{\Delta V_{dc}^*}=\frac{3289.8702}{s^2+73.3046s+3289.8702}\approx\frac{\omega_{no}^2}{s^2+2\zeta\omega_{no}s+\omega_{no}^2} \Rightarrow \omega_{no}=57.357\text{rad/s or } f_{no}=9.1287\text{Hz} \Rightarrow \zeta_o=0.639$

f) $\text{FpTF=G(s).H(s)}=\frac{3.6751s+164.9344}{0.050134s^2+0.9375s}$

g) $\text{DS1}=\left|\frac{\Delta i_n}{\Delta V_{dc}}\right|=\left|\frac{0.050134s^2+4.6126s+164.9344}{s}\right|$

h) $\text{DS2}=\left|\frac{\Delta v_{g\_d}}{\Delta V_{dc}}\right|=\left|\frac{0.01455s^2+1.3391s+47.8821}{s}\right|$

vii) $V_{dco} = V_{dco\_max} = 1300V$ (1.3kV)

$$K_v = \frac{v_{g\_do\_nom}}{v_{dco}} = \frac{0.3266kV}{1.3kV} \approx 0.252 \quad \text{and} \quad K_s = \frac{i_{g\_do\_nom}}{v_{dco}} = \frac{2.75568kA}{1.3kV} \approx 2.12\ (A/V)$$

Substituting K_{pv}, K_{iv}, K_{pi}, K_{ii}, K_v and K_s parameters in equations a-h, these equations turn into:

$$\text{a) FTF} = \frac{\Delta V_{dc}}{\Delta V^*_{dc}} = \frac{2.3427s^2 + 3420.0181s + 148769.9215}{6.12793x10^{-6}s^4 + 0.0347503s^3 + 51.8839s^2 + 4200.5905s + 148769.9215}$$

$$\text{b) TF} = \frac{\Delta V_{dc}}{\Delta V^*_{dc}} = \frac{3.3924s + 152.2471}{0.050134s^2 + 4.1912s + 152.2471}$$

$$\text{c) STF} = \frac{\Delta V_{dc}}{\Delta V^*_{dc}} = \frac{3.3924s + 152.2471}{0.050134s^2 + 3.3924s + 152.2471}$$

$$\text{d) SoATF} = \frac{\Delta V_{dc}}{\Delta V^*_{dc}} = \frac{3036.8032}{s^2 + 83.5994s + 3036.8032}$$

$$\text{e) SSoATF} = \frac{\Delta V_{dc}}{\Delta V^*_{dc}} = \frac{3036.8032}{s^2 + 67.6658s + 3036.8032} \approx \frac{\omega^2_{no}}{s^2 + 2\zeta\omega_{no}s + \omega^2_{no}} \Rightarrow \omega_{no\_min} = 55.107 rad/s \text{ or } f_{no\_min} = 8.77Hz \Rightarrow \zeta_{o\_min} = 0.614$$

$$\text{f) FpTF} = G(s).H(s) = \frac{3.3924s + 152.2471}{0.050134s^2 + 0.7988s}$$

$$\text{g) DS1} = \left|\frac{\Delta i_n}{\Delta V_{dc}}\right| = \left|\frac{0.050134s^2 + 4.1912s + 152.2471}{s}\right|$$

$$\text{h) DS2} = \left|\frac{\Delta v_{g\_d}}{\Delta V_{dc}}\right| = \left|\frac{0.01577s^2 + 1.3181s + 47.8821}{s}\right|$$

A.3.1.2 MATLAB Results

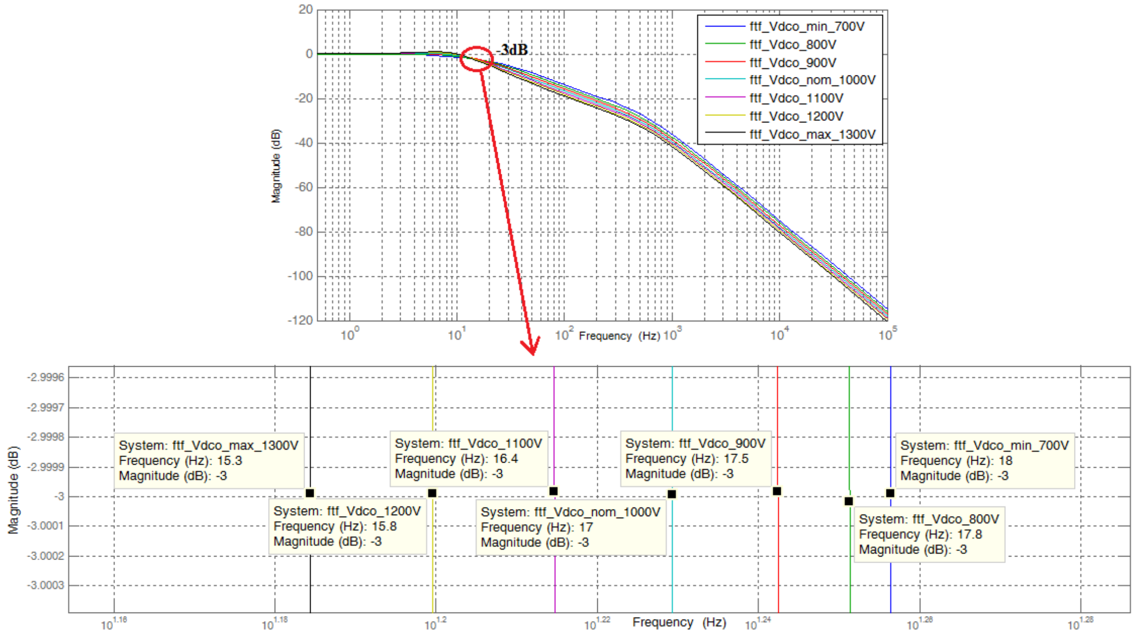

Figure A.3.1: Full transfer function and bandwidths representation

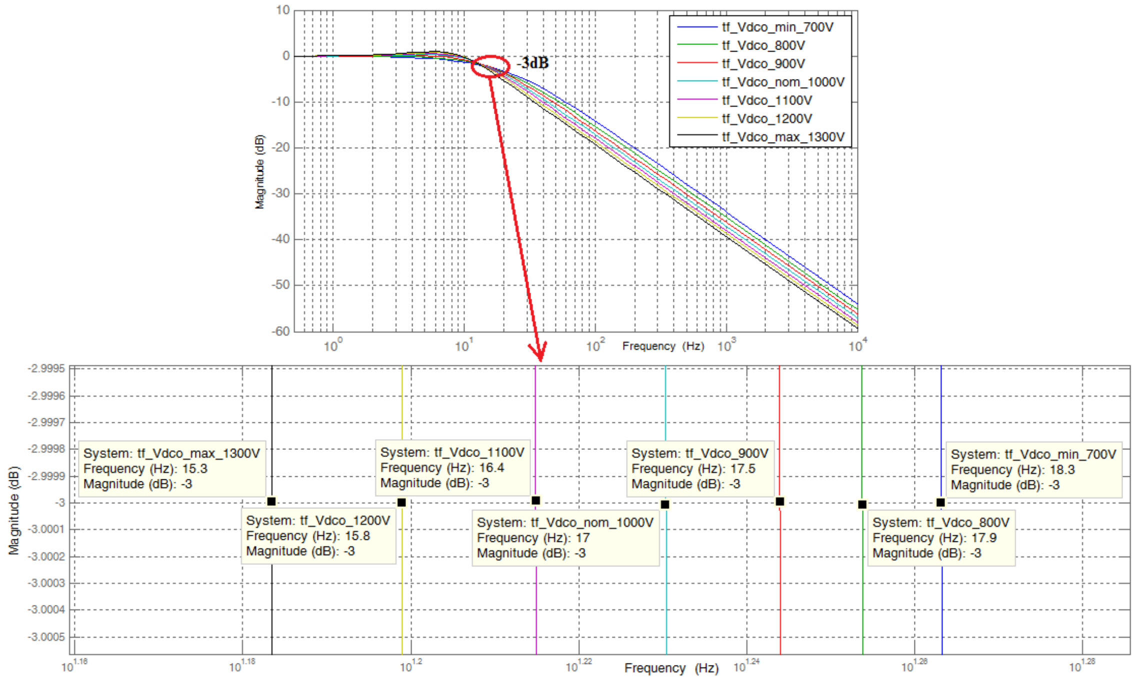

Figure A.3.2: Transfer function and bandwidths representation

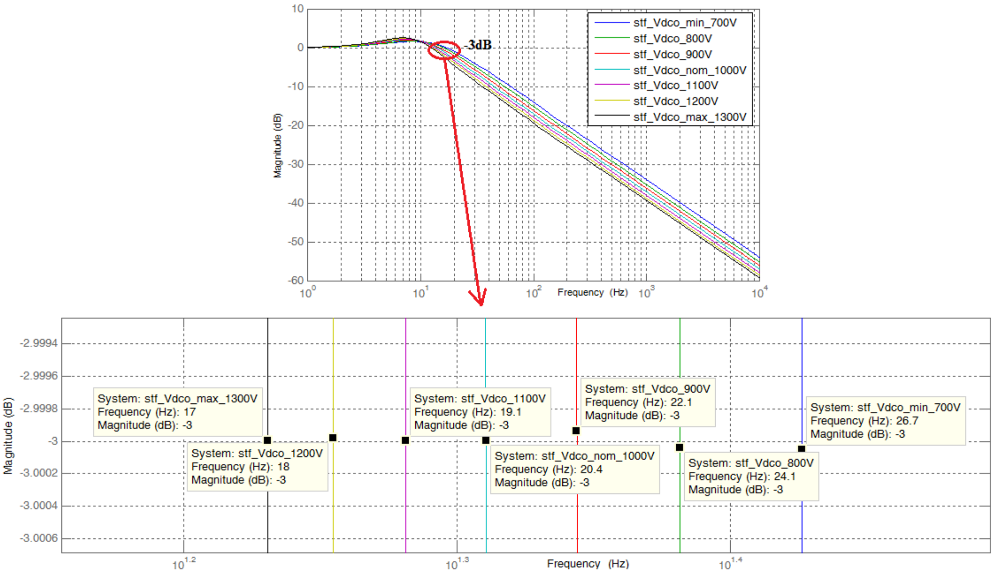

Figure A.3.3: Simplified transfer function and bandwidths representation

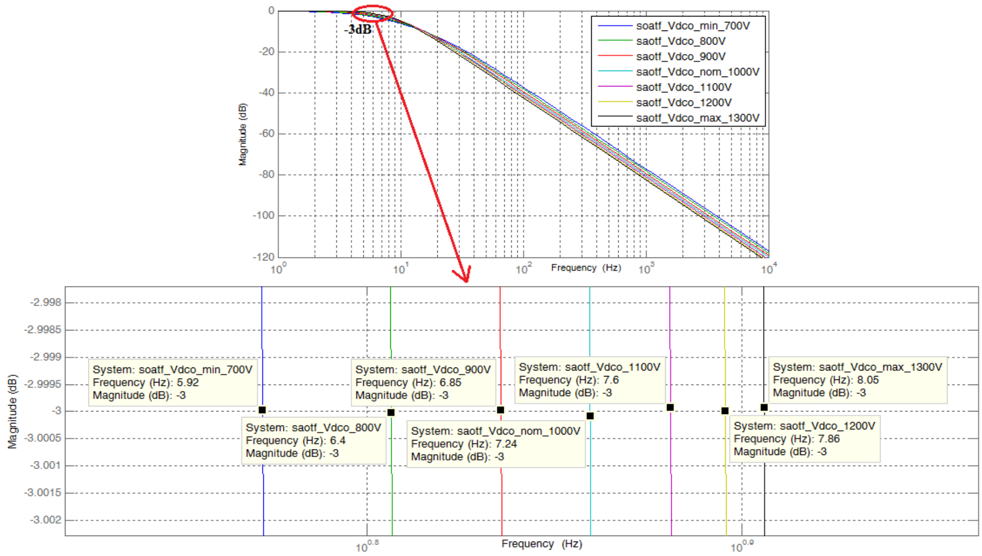

Figure A.3.4: Second-order approximated transfer function and bandwidths representation

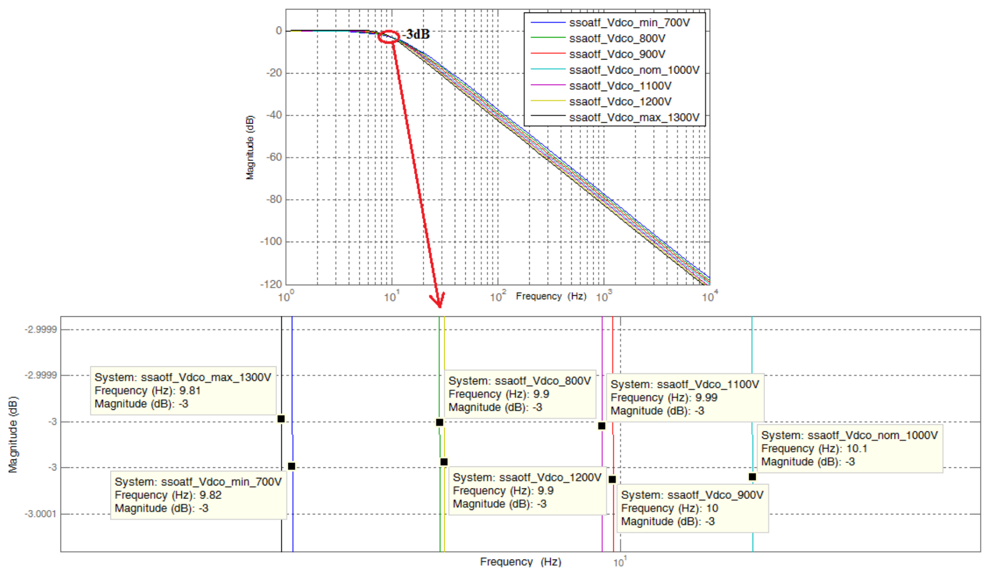

Figure A.3.5: Simplified second-order approximated transfer function and bandwidths representation

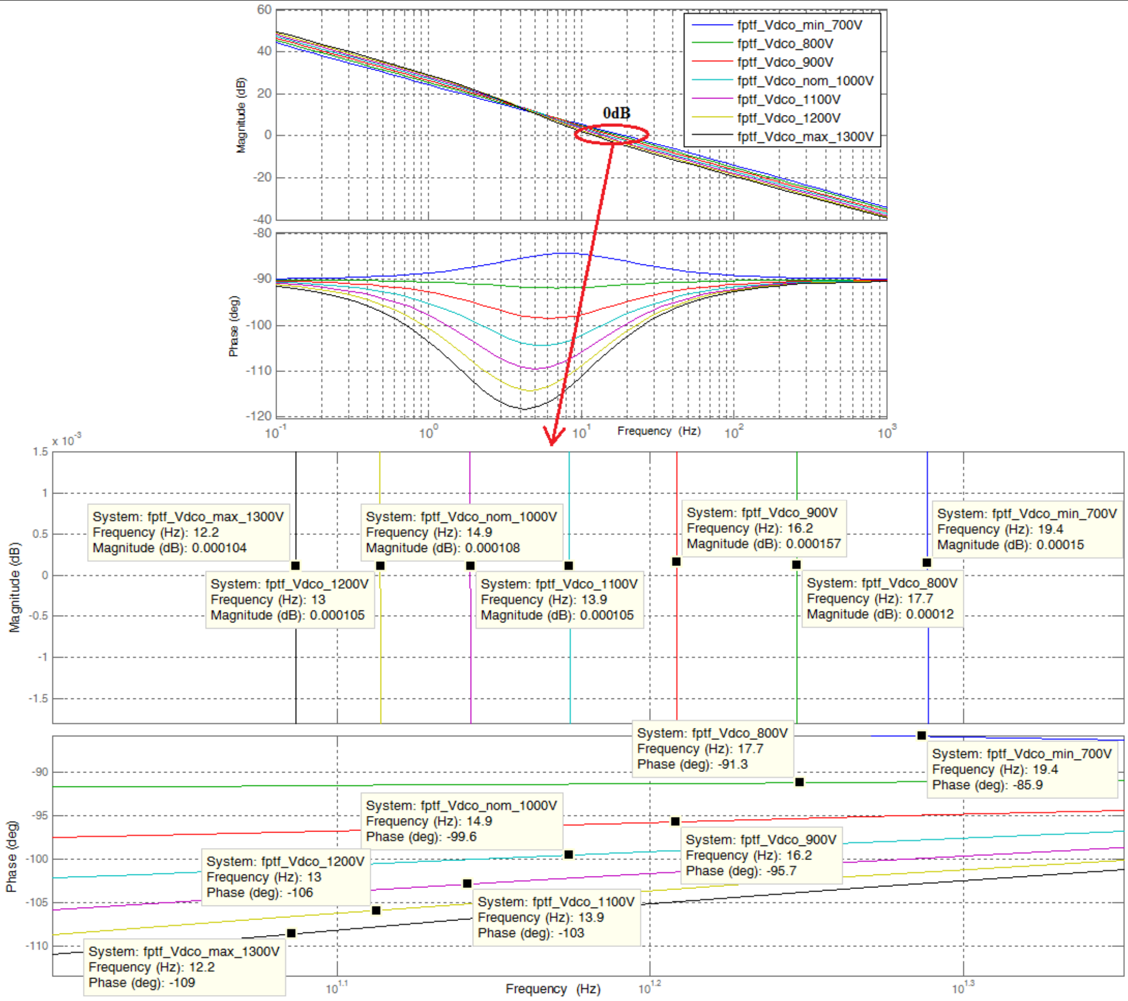

Figure A.3.6: Forward-path transfer function and damping ratios representation

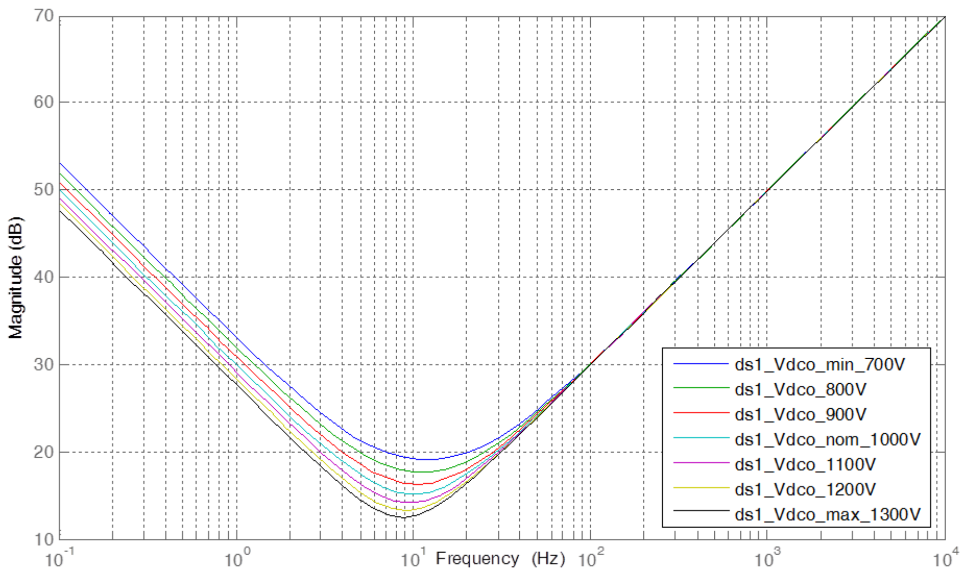

Figure A.3.7: Dynamic stiffness analysis of $\Delta i_n/\Delta V_{dc}$ (DS1)

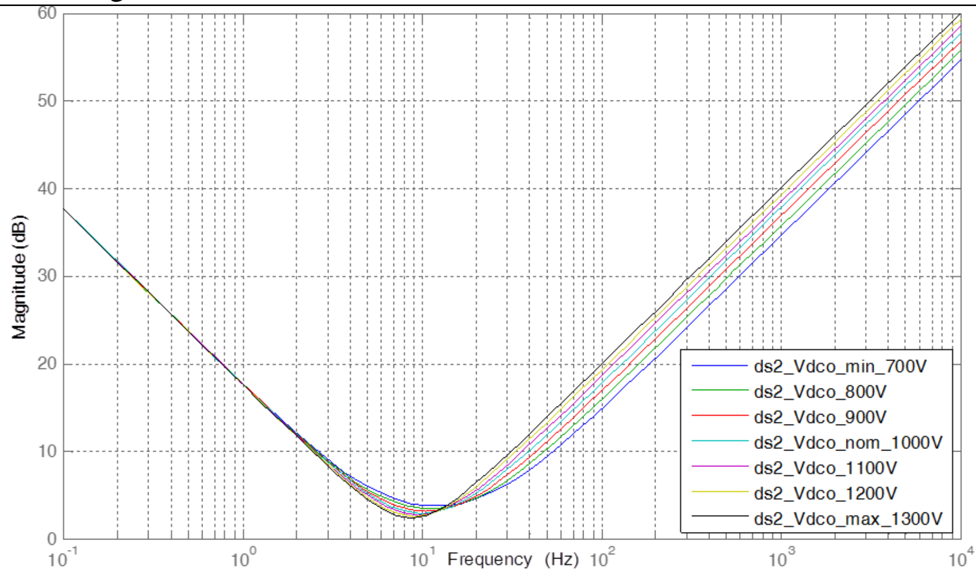

Figure A.3.8: Dynamic stiffness analysis of $\Delta v_{g\_d}/\Delta V_{dc}$ (DS2)

A.3.2 v_{g_do} Sensitivity

A.3.2.1 Mathematical Calculations

i) $v_{g\_do} = v_{g\_do\_min}$=228.62V (0.22862kV)

$$K_v = \frac{v_{g\_do}}{v_{dco\_nom}} = \frac{0.22862\text{kV}}{1\text{kV}} \approx 0.229 \quad \text{and} \quad K_s = \frac{i_{g\_do\_nom}}{v_{dco\_nom}} = \frac{2.75568\text{kA}}{1\text{kV}} \approx 2.756\ (\text{A/V})$$

a) $\text{FTF}=\frac{\Delta V_{dc}}{\Delta V_{dc}^{*}}=\frac{2.1319s^2+3112.2165s+135380.6286}{6.12793\text{x}10^{-6}s^4+0.0347682s^3+51.7741s^2+4035.6336s+135380.6286}$

b) $\text{TF}=\frac{\Delta V_{dc}}{\Delta V_{dc}^{*}}=\frac{3.087s+138.5449}{0.050134s^2+4.032s+138.5449}$

c) $\text{STF}=\frac{\Delta V_{dc}}{\Delta V_{dc}^{*}}=\frac{3.087s+138.5449}{0.050134s^2+3.087s+138.5449}$

d) $\text{SoATF}=\frac{\Delta V_{dc}}{\Delta V_{dc}^{*}}=\frac{2763.4909}{s^2+80.4253s+2763.4909}$

e) $\text{SSoATF}=\frac{\Delta V_{dc}}{\Delta V_{dc}^{*}}=\frac{2763.4909}{s^2+61.5758s+2763.4909}\approx\frac{\omega_{no}^2}{s^2+2\zeta\omega_{no}s+\omega_{no}^2}\Rightarrow\omega_{no\_min}=52.57\text{rad/s or } f_{no\_min}=8.367\text{Hz}\Rightarrow\zeta_{o\_min}=0.586$

f) $\text{FpTF=G(s).H(s)}=\frac{3.087s+138.5449}{0.050134s^2+0.945s}$

g) $\text{DS1}=\left|\frac{\Delta i_n}{\Delta V_{dc}}\right|=\left|\frac{0.050134s^2+4.032s+138.5449}{s}\right|$

h) $\text{DS2}=\left|\frac{\Delta v_{g\_d}}{\Delta V_{dc}}\right|=\left|\frac{0.01213s^2+0.9755s+33.5175}{s}\right|$

ii) v_{g_do}=261.28V (0.26128kV)

$$K_v = \frac{v_{g\_do}}{v_{dco\_nom}} = \frac{0.26128\text{kV}}{1\text{kV}} \approx 0.261 \quad \text{and} \quad K_s = \frac{i_{g\_do\_nom}}{v_{dco\_nom}} = \frac{2.75568\text{kA}}{1\text{kV}} \approx 2.756\ (\text{A/V})$$

a) $\text{FTF}=\frac{\Delta V_{dc}}{\Delta V_{dc}^{*}}=\frac{2.4365s^2+3556.8188s+154720.7184}{6.12793\text{x}10^{-6}s^4+0.0347847s^3+52.1719s^2+4612.1527s+154720.7184}$

b) $\text{TF}=\frac{\Delta V_{dc}}{\Delta V_{dc}^{*}}=\frac{3.528s+158.337}{0.050134s^2+4.608s+158.337}$

c) $\text{STF}=\frac{\Delta V_{dc}}{\Delta V_{dc}^{*}}=\frac{3.528s+158.337}{0.050134s^2+3.528s+158.337}$

d) $\text{SoATF}=\frac{\Delta V_{dc}}{\Delta V_{dc}^{*}}=\frac{3158.2754}{s^2+91.9147s+3158.2754}$

e) $\text{SSoATF}=\frac{\Delta V_{dc}}{\Delta V_{dc}^{*}}=\frac{3158.2754}{s^2+70.3724s+3158.2754}\approx\frac{\omega_{no}^2}{s^2+2\zeta\omega_{no}s+\omega_{no}^2}\Rightarrow\omega_{no}=56.2\text{rad/s or } f_{no}=8.944\text{Hz}\Rightarrow\zeta_{o}=0.626$

f) $\text{FpTF=G(s).H(s)}=\frac{3.528s+158.337}{0.050134s^2+1.08s}$

g) $\text{DS1}=\left|\frac{\Delta i_n}{\Delta V_{dc}}\right|=\left|\frac{0.050134s^2+4.608s+158.337}{s}\right|$

h) $\text{DS2}=\left|\frac{\Delta v_{g\_d}}{\Delta V_{dc}}\right|=\left|\frac{0.01213s^2+1.1148s+38.3057}{s}\right|$

iii) v_{g_do}=293.94 (0.29394kV)

$$K_v=\frac{v_{g\_do}}{v_{dco\_nom}}=\frac{0.29394kV}{1kV}\approx 0.294 \text{ and } K_s=\frac{i_{g\_do\_nom}}{v_{dco\_nom}}=\frac{2.75568kA}{1kV}\approx 2.756\ (A/V)$$

a) $FTF=\frac{\Delta V_{dc}}{\Delta V_{dc}^*}=\frac{2.741s^2+4001.4212s+174060.8082}{6.12793x10^{-6}s^4+0.0348012s^3+52.5698s^2+5188.6718s+174060.8082}$

b) $TF=\frac{\Delta V_{dc}}{\Delta V_{dc}^*}=\frac{3.9691s+178.1291}{0.050134s^2+5.1841s+178.1291}$

c) $STF=\frac{\Delta V_{dc}}{\Delta V_{dc}^*}=\frac{3.9691s+178.1291}{0.050134s^2+3.9691s+178.1291}$

d) $SoATF=\frac{\Delta V_{dc}}{\Delta V_{dc}^*}=\frac{3553.0598}{s^2+103.404s+3553.0598}$

e) $SSoATF=\frac{\Delta V_{dc}}{\Delta V_{dc}^*}=\frac{3553.0598}{s^2+79.1689s+3553.0598}\approx\frac{\omega_{no}^2}{s^2+2\zeta\omega_{no}s+\omega_{no}^2}\Rightarrow \omega_{no}=59.607rad/s \text{ or } f_{no}=9.487Hz\Rightarrow\zeta_o=0.664$

f) $FpTF=G(s).H(s)=\frac{3.9691s+178.1291}{0.050134s^2+1.215s}$

g) $DS1=\left|\frac{\Delta i_n}{\Delta V_{dc}}\right|=\left|\frac{0.050134s^2+5.1841s+178.1291}{s}\right|$

h) $DS2=\left|\frac{\Delta v_{g\_d}}{\Delta V_{dc}}\right|=\left|\frac{0.01213s^2+1.2542s+43.0939}{s}\right|$

iv) v_{g_do}= $v_{g\_do\_nom}$=326.6V (0.3266kV)

$$K_v=\frac{v_{g\_do\_nom}}{v_{dco\_nom}}=\frac{0.3266kV}{1kV}\approx 0.326 \text{ and } K_s=\frac{i_{g\_do\_nom}}{v_{dco\_nom}}=\frac{2.75568kA}{1kV}\approx 2.756\ (A/V)$$

a) $FTF=\frac{\Delta V_{dc}}{\Delta V_{dc}^*}=\frac{3.0456s^2+4446.0235s+193400.8979}{6.12793x10^{-6}s^4+0.0348177s^3+52.9677s^2+5765.1909s+193400.8979}$

b) $TF=\frac{\Delta V_{dc}}{\Delta V_{dc}^*}=\frac{4.4101s+197.9212}{0.050134s^2+5.7601s+197.9212}$

c) $STF=\frac{\Delta V_{dc}}{\Delta V_{dc}^*}=\frac{4.4101s+197.9212}{0.050134s^2+4.4101s+197.9212}$

d) $SoATF=\frac{\Delta V_{dc}}{\Delta V_{dc}^*}=\frac{3947.8442}{s^2+114.8933s+3947.8442}$

e) $SSoATF=\frac{\Delta V_{dc}}{\Delta V_{dc}^*}=\frac{3947.8442}{s^2+87.9655s+3947.8442}\approx\frac{\omega_{no}^2}{s^2+2\zeta\omega_{no}s+\omega_{no}^2}\Rightarrow \omega_{n\_nom}=62.83rad/s \text{ or } f_{n\_nom}=10Hz\Rightarrow\zeta_o=0.7$

f) $FpTF=G(s).H(s)=\frac{4.4101s+197.9212}{0.050134s^2+1.35s}$

g) $DS1=\left|\frac{\Delta i_n}{\Delta V_{dc}}\right|=\left|\frac{0.050134s^2+5.7601s+197.9212}{s}\right|$

h) $DS2=\left|\frac{\Delta v_{g\_d}}{\Delta V_{dc}}\right|=\left|\frac{0.01213s^2+1.3935s+47.8821}{s}\right|$

v) v_{g_do}=359.26V (0.35926kV)

$$K_v=\frac{v_{g\_do\_nom}}{v_{dco\_nom}}=\frac{0.35926kV}{1kV}\approx 0.36 \quad \text{and} \quad K_s=\frac{i_{g\_do\_nom}}{v_{dco\_nom}}=\frac{2.75568kA}{1kV}\approx 2.756\ (A/V)$$

a) $FTF=\frac{\Delta V_{dc}}{\Delta V_{dc}^{*}}=\frac{3.3501s^2+4890.6259s+212740.9877}{6.12793x10^{-6}s^4+0.0348342s^3+53.3656s^2+6341.71s+212740.9877}$

b) $TF=\frac{\Delta V_{dc}}{\Delta V_{dc}^{*}}=\frac{4.8511s+217.7133}{0.050134s^2+6.3361s+217.7133}$

c) $STF=\frac{\Delta V_{dc}}{\Delta V_{dc}^{*}}=\frac{4.8511s+217.7133}{0.050134s^2+4.8511s+217.7133}$

d) $SoATF=\frac{\Delta V_{dc}}{\Delta V_{dc}^{*}}=\frac{4342.6286}{s^2+126.3826s+4342.6286}$

e) $SSoATF=\frac{\Delta V_{dc}}{\Delta V_{dc}^{*}}=\frac{4342.6286}{s^2+96.762s+4342.6286}\approx\frac{\omega_{no}^2}{s^2+2\zeta\omega_{no}s+\omega_{no}^2} \Rightarrow \omega_{no}=65.9rad/s\ or\ f_{no}=10.488Hz \Rightarrow \zeta_o=0.734$

f) $FpTF=G(s).H(s)=\frac{4.8511s+217.7133}{0.050134s^2+1.485s}$

g) $DS1=\left|\frac{\Delta i_n}{\Delta V_{dc}}\right|=\left|\frac{0.050134s^2+6.3361s+217.7133}{s}\right|$

h) $DS2=\left|\frac{\Delta v_{g\_d}}{\Delta V_{dc}}\right|=\left|\frac{0.01213s^2+1.5329s+52.6703}{s}\right|$

vi) v_{g_do}=391.92V (0.39192kV)

$$K_v=\frac{v_{g\_do\_nom}}{v_{dco\_nom}}=\frac{0.39192kV}{1kV}\approx 0.392 \quad \text{and} \quad K_s=\frac{i_{g\_do\_nom}}{v_{dco\_nom}}=\frac{2.75568kA}{1kV}\approx 2.756\ (A/V)$$

a) $FTF=\frac{\Delta V_{dc}}{\Delta V_{dc}^{*}}=\frac{3.6547s^2+5335.2283s+232081.0775}{6.12793x10^{-6}s^4+0.0348507s^3+53.7634s^2+6918.2291s+232081.0775}$

b) $TF=\frac{\Delta V_{dc}}{\Delta V_{dc}^{*}}=\frac{5.2921s+237.5055}{0.050134s^2+6.9121s+237.5055}$

c) $STF=\frac{\Delta V_{dc}}{\Delta V_{dc}^{*}}=\frac{5.2921s+237.5055}{0.050134s^2+5.2921s+237.5055}$

d) $SoATF=\frac{\Delta V_{dc}}{\Delta V_{dc}^{*}}=\frac{4737.413}{s^2+137.872s+4737.413}$

e) $SSoATF=\frac{\Delta V_{dc}}{\Delta V_{dc}^{*}}=\frac{4737.413}{s^2+105.5586s+4737.413}\approx\frac{\omega_{no}^2}{s^2+2\zeta\omega_{no}s+\omega_{no}^2} \Rightarrow \omega_{no}=68.83rad/s\ or\ f_{no}=10.954Hz \Rightarrow \zeta_o=0.767$

f) $FpTF=G(s).H(s)=\frac{5.2921s+237.5055}{0.050134s^2+1.62s}$

g) $DS1=\left|\frac{\Delta i_n}{\Delta V_{dc}}\right|=\left|\frac{0.050134s^2+6.9121s+237.5055}{s}\right|$

h) $DS2=\left|\frac{\Delta v_{g\_d}}{\Delta V_{dc}}\right|=\left|\frac{0.01213s^2+1.6722s+57.4585}{s}\right|$

vii) $v_{g\_do} = v_{g\_do\_max}$=424.58V (0.42458kV)

$$K_v = \frac{v_{g\_do\_nom}}{v_{dco\_nom}} = \frac{0.42458kV}{1kV} \approx 0.425 \quad \text{and} \quad K_s = \frac{i_{g\_do\_nom}}{v_{dco\_nom}} = \frac{2.75568kA}{1kV} \approx 2.756\ (A/V)$$

a) $FTF = \frac{\Delta V_{dc}}{\Delta V_{dc}^*} = \frac{3.9592s^2+5779.8306s+251421.1673}{6.12793x10^{-6}s^4+0.0348672s^3+54.1613s^2+7494.7482s+251421.1673}$

b) $TF = \frac{\Delta V_{dc}}{\Delta V_{dc}^*} = \frac{5.7331s+257.2976}{0.050134s^2+7.4881s+257.2976}$

c) $STF = \frac{\Delta V_{dc}}{\Delta V_{dc}^*} = \frac{5.7331s+257.2976}{0.050134s^2+5.7331s+257.2976}$

d) $SoATF = \frac{\Delta V_{dc}}{\Delta V_{dc}^*} = \frac{5132.1974}{s^2+149.3613s+5132.1974}$

e) $SSoATF = \frac{\Delta V_{dc}}{\Delta V_{dc}^*} = \frac{5132.1974}{s^2+114.3551s+5132.1974} \approx \frac{\omega_{no}^2}{s^2+2\zeta\omega_{no}s+\omega_{no}^2} \Rightarrow \omega_{no\_max} = 71.64 rad/s \text{ or } f_{no\_max} = 11.4Hz \Rightarrow \zeta_{o\_max} = 0.798$

f) $FpTF = G(s).H(s) = \frac{5.7331s+257.2976}{0.050134s^2+1.755s}$

g) $DS1 = \left|\frac{\Delta i_n}{\Delta V_{dc}}\right| = \left|\frac{0.050134s^2+7.4881s+257.2976}{s}\right|$

h) $DS2 = \left|\frac{\Delta v_{g\_d}}{\Delta V_{dc}}\right| = \left|\frac{0.01213s^2+1.8116s+62.2467}{s}\right|$

A.3.2.2 MATLAB Results

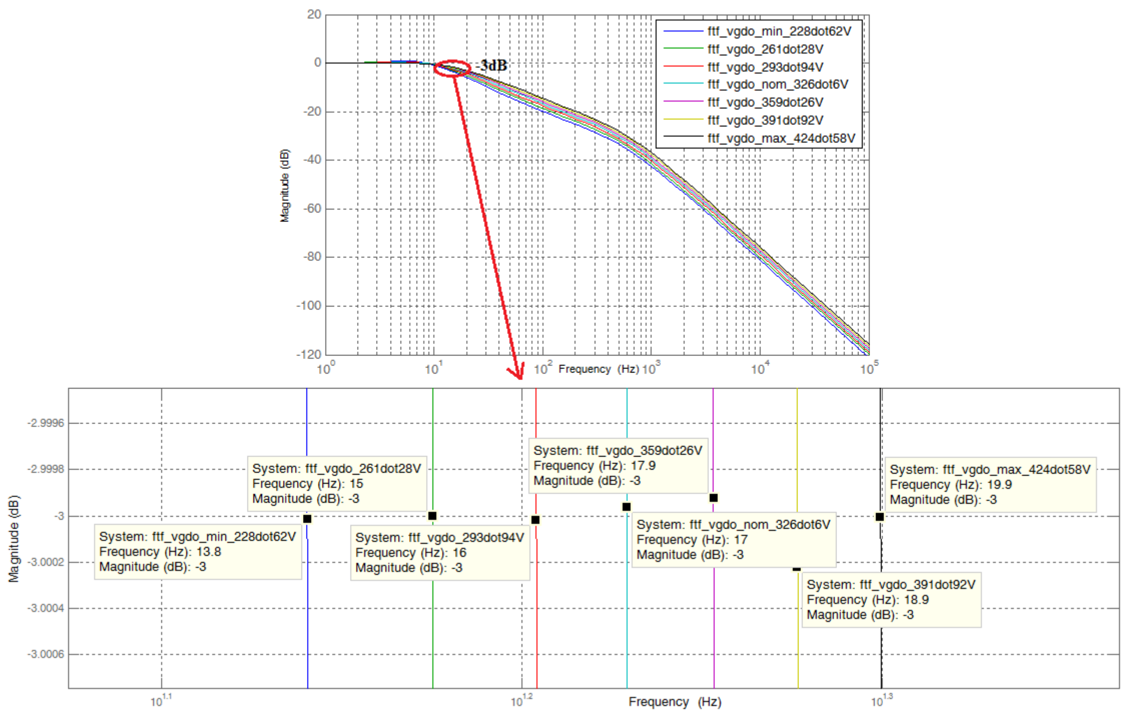

Figure A.3.9: Full transfer function and bandwidths representation

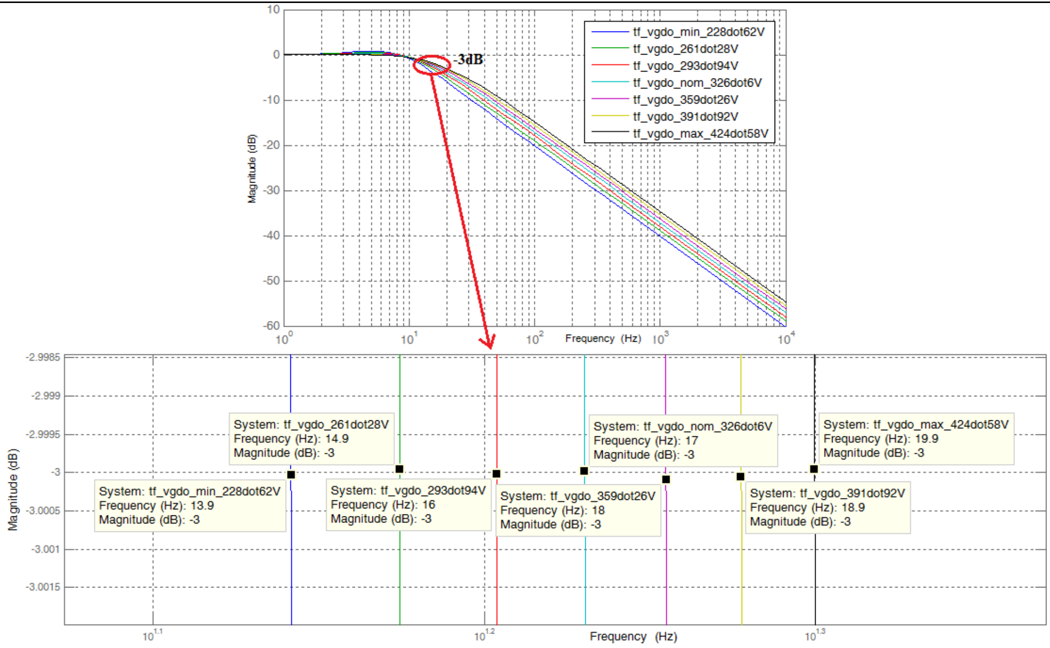

Figure A.3.10: Transfer function and bandwidths representation

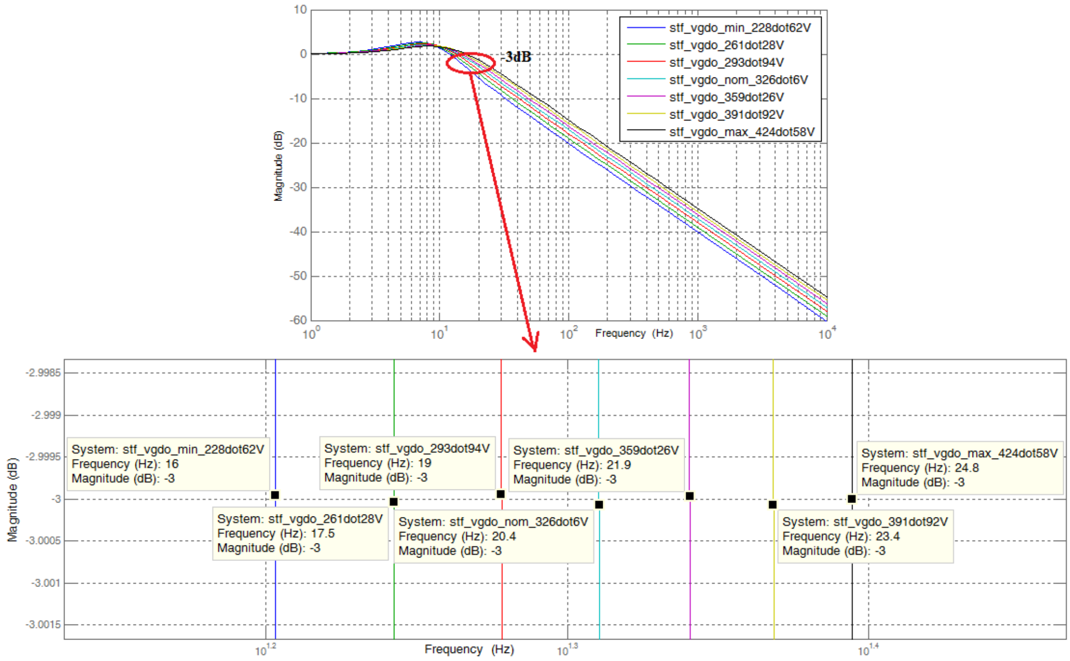

Figure A.3.11: Simplified transfer function and bandwidths representation

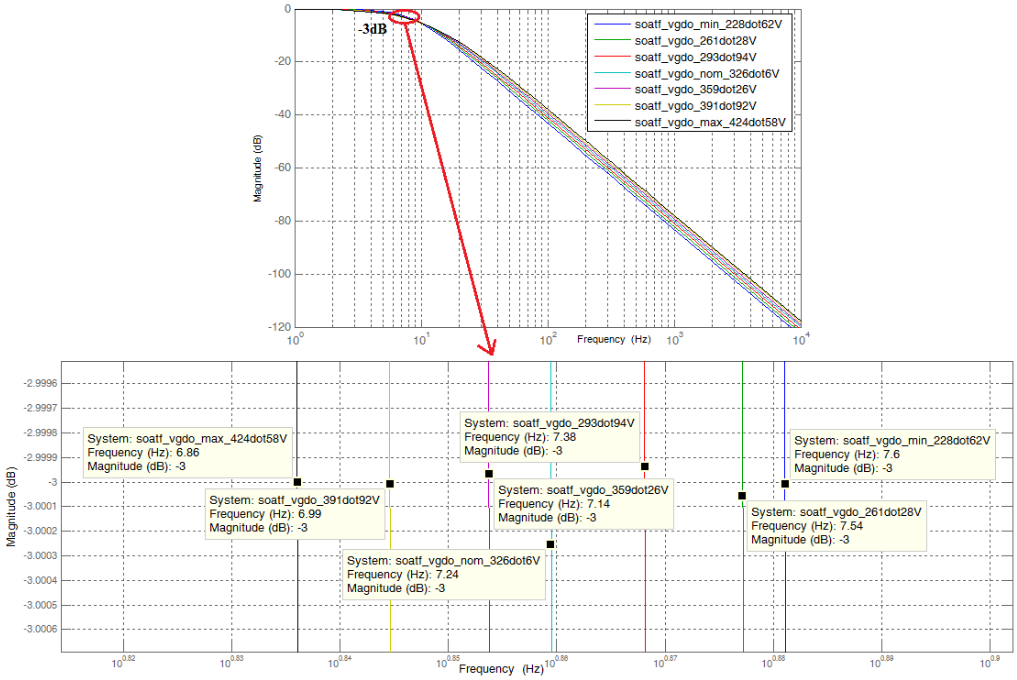

Figure A.3.12: Second-order approximated transfer function and bandwidths representation

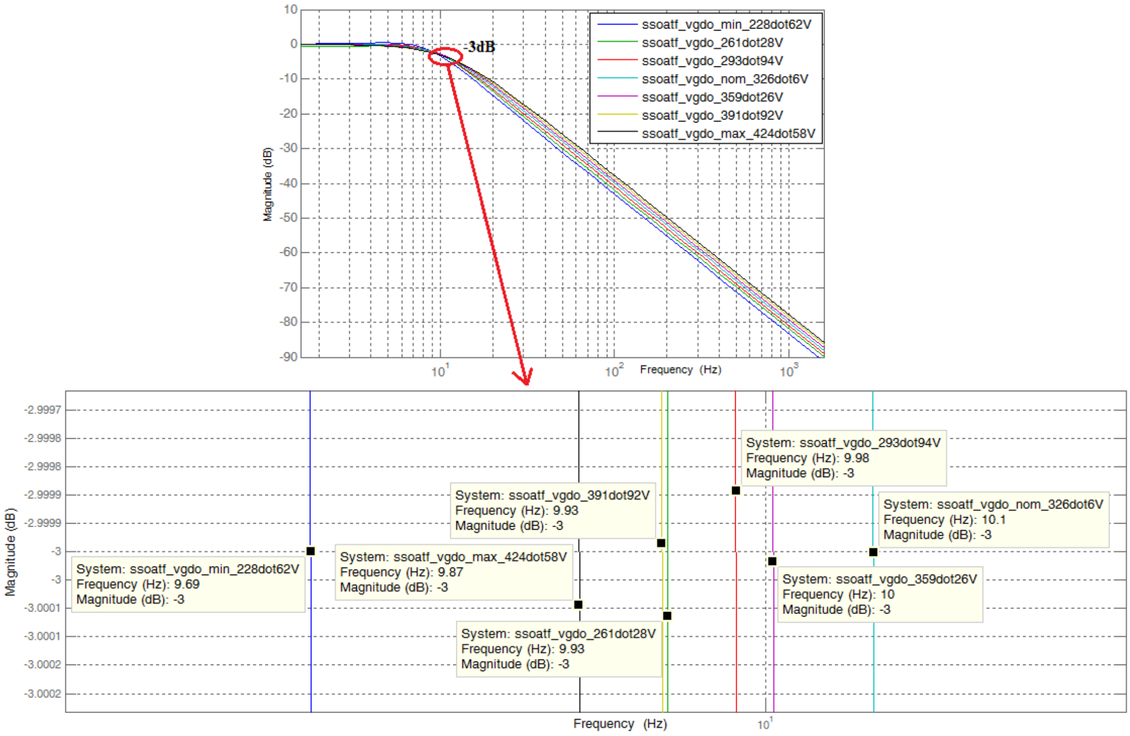

Figure A.3.13: Simplified second-order approximated transfer function and bandwidths representation

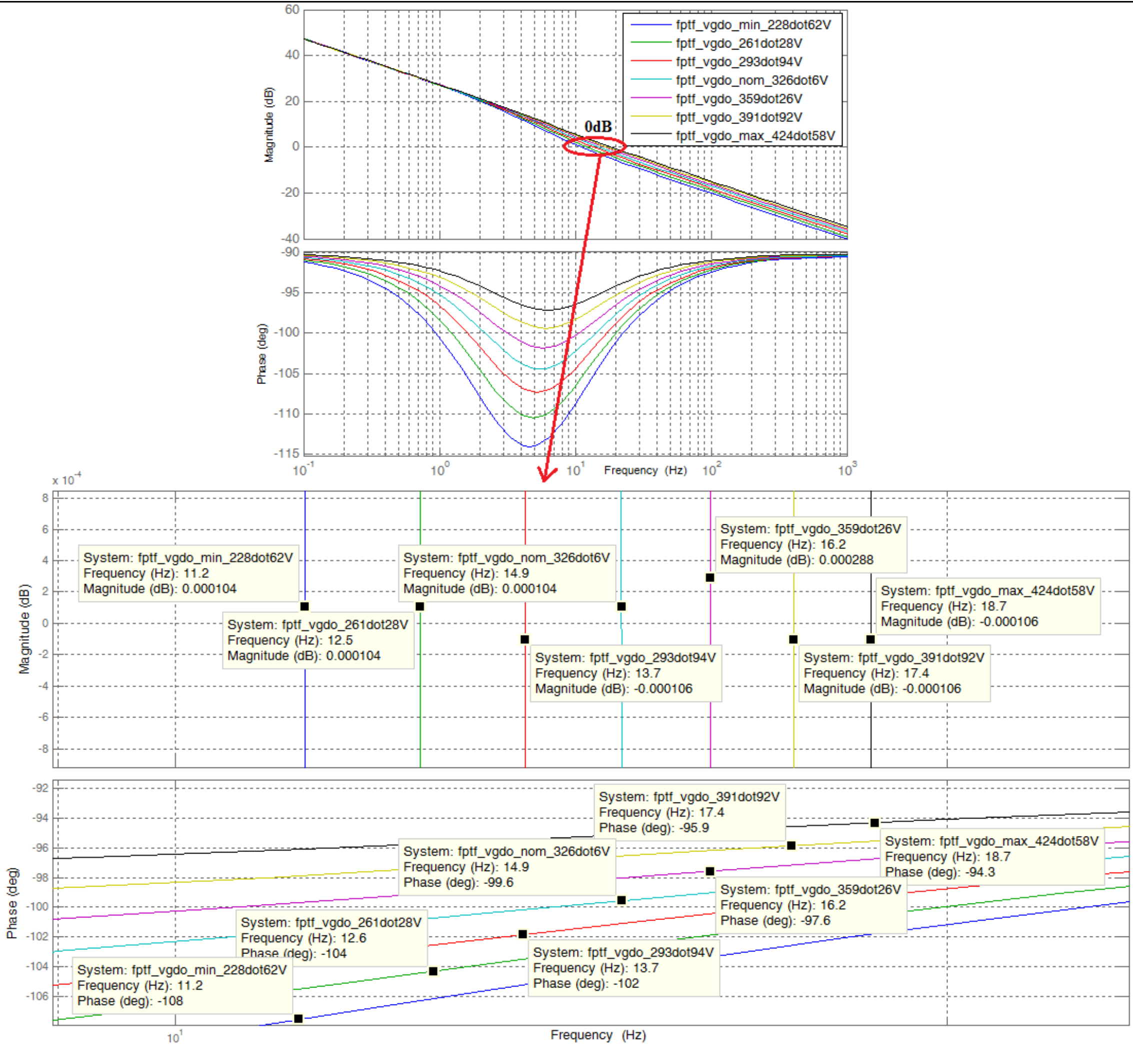

Figure A.3.14: Forward-path transfer function and damping ratios representation

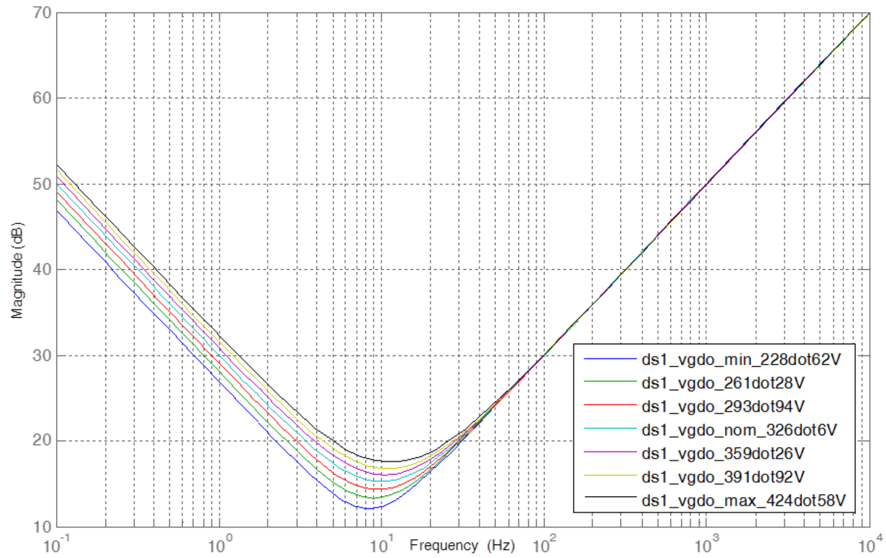

Figure A.3.15: Dynamic stiffness analysis of $\Delta i_n/\Delta V_{dc}$ (DS1)

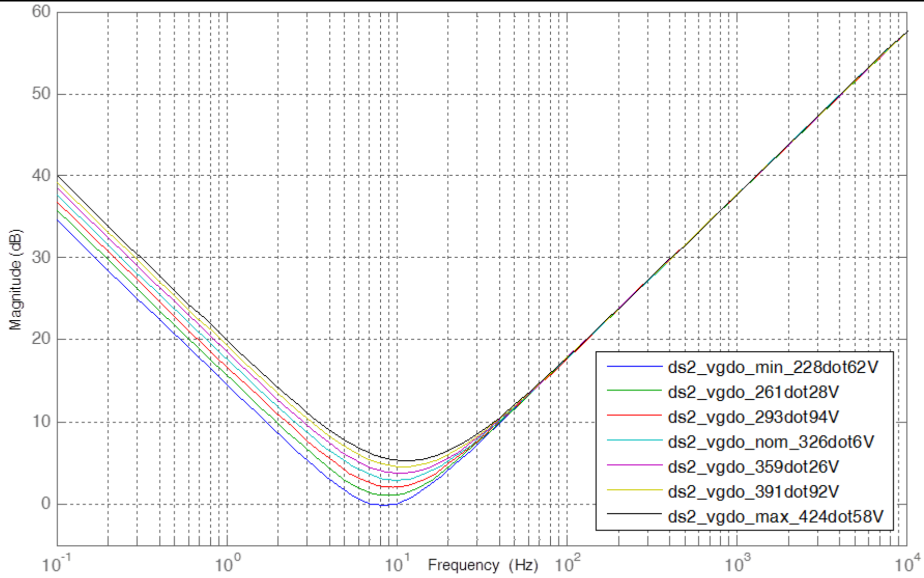

Figure A.3.16: Dynamic stiffness analysis of $\Delta v_{g\_d}/\Delta V_{dc}$ (DS2)

A.3.3 i_{g_do} Sensitivity

A.3.3.1 Mathematical Calculations

Since only i_{g_do} varies the K_s varies as well, but the K_v stays constant. As there is no K_s parameter in STF and SSoATF, so these two functions (*c* and *e*) are same for all seven operating points of i_{g_d}.

$$\text{c) STF}=\frac{\Delta V_{dc}}{\Delta V_{dc}^{*}}=\frac{4.4101s+197.9212}{0.050134s^2+4.4101s+197.9212}$$

$$\text{e) SSoATF}=\frac{\Delta V_{dc}}{\Delta V_{dc}^{*}}=\frac{3947.8442}{s^2+87.9655s+3947.8442}\approx\frac{\omega_{no}^2}{s^2+2\zeta\omega_{no}s+\omega_{no}^2}\quad\Rightarrow f_{n\_nom}=10\text{Hz}\quad\Rightarrow\zeta_{nom}=0.7$$

i) i_{g_do}= $i_{g\_do\_min}$=1928.97A (≈1.929kA)

$$K_s=\frac{i_{g\_do}}{v_{dco\_nom}}=\frac{1.929\text{kA}}{1\text{kV}}=1.929\ (\text{A/V})\ \text{ and }\ K_v=\frac{v_{g\_do\_nom}}{v_{dco\_nom}}=\frac{0.3266\text{kV}}{1\text{kV}}\approx 0.327$$

$$\text{a) FTF}=\frac{\Delta V_{dc}}{\Delta V_{dc}^{*}}=\frac{3.0456s^2+4446.0235s+193400.8979}{6.12793\text{x}10^{-6}s^4+0.0347682s^3+52.6877s^2+5369.4407s+193400.8979}$$

$$\text{b) TF}=\frac{\Delta V_{dc}}{\Delta V_{dc}^{*}}=\frac{4.4101s+197.9212}{0.050134s^2+5.3551s+197.9212}$$

$$\text{d) SoATF}=\frac{\Delta V_{dc}}{\Delta V_{dc}^{*}}=\frac{3947.8442}{s^2+106.815s+3947.8442}$$

$$\text{f) FpTF}=G(s).H(s)=\frac{4.4101s+197.9212}{0.050134s^2+0.945s}$$

$$\text{g) DS1}=\left|\frac{\Delta i_n}{\Delta V_{dc}}\right|=\left|\frac{0.050134s^2+5.3551s+197.9212}{s}\right|$$

$$\text{h) DS2}=\left|\frac{\Delta v_{g\_d}}{\Delta V_{dc}}\right|=\left|\frac{0.01733s^2+1.8507s+68.403}{s}\right|$$

ii) i_{g_do}=2204.54A (≈2.205kA)

$$K_s = \frac{i_{g\_do}}{v_{dco\_nom}} = \frac{2.205kA}{1kV} \approx 2.205\ (A/V) \ \text{ and } \ K_v = \frac{v_{g\_do\_nom}}{v_{dco\_nom}} = \frac{0.3266kV}{1kV} \approx 0.327$$

a) $\text{FTF}=\frac{\Delta V_{dc}}{\Delta V_{dc}^{*}}=\frac{3.0456s^2+4446.0235s+193400.8979}{6.12793x10^{-6}s^4+0.0347847s^3+52.7811s^2+5501.3574s+193400.8979}$

b) $\text{TF}=\frac{\Delta V_{dc}}{\Delta V_{dc}^{*}}=\frac{4.4101s+197.9212}{0.050134s^2+5.4901s+197.9212}$

d) $\text{SoATF}=\frac{\Delta V_{dc}}{\Delta V_{dc}^{*}}=\frac{3947.8442}{s^2+109.5077s+3947.8442}$

f) $\text{FpTF}=G(s).H(s)=\frac{4.4101s+197.9212}{0.050134s^2+1.08s}$

g) $\text{DS1}=\left|\frac{\Delta i_n}{\Delta V_{dc}}\right|=\left|\frac{0.050134s^2+5.4901+197.9212}{s}\right|$

h) $\text{DS2}=\left|\frac{\Delta v_{g\_d}}{\Delta V_{dc}}\right|=\left|\frac{0.01516s^2+1.6602s+59.8526}{s}\right|$

iii) i_{g_do}=2480.11A (≈2.48kA)

$$K_s = \frac{i_{g\_do}}{v_{dco\_nom}} = \frac{2.48kA}{1kV} \approx 2.48\ (A/V) \ \text{ and } \ K_v = \frac{v_{g\_do\_nom}}{v_{dco\_nom}} = \frac{0.3266kV}{1kV} \approx 0.327$$

a) $\text{FTF}=\frac{\Delta V_{dc}}{\Delta V_{dc}^{*}}=\frac{3.0456s^2+4446.0235s+193400.8979}{6.12793x10^{-6}s^4+0.0348012s^3+52.8744s^2+5633.2742s+193400.8979}$

b) $\text{TF}=\frac{\Delta V_{dc}}{\Delta V_{dc}^{*}}=\frac{4.4101s+197.9212}{0.050134s^2+5.6251s+197.9212}$

d) $\text{SoATF}=\frac{\Delta V_{dc}}{\Delta V_{dc}^{*}}=\frac{3947.8442}{s^2+112.2005s+3947.8442}$

f) $\text{FpTF}=G(s).H(s)=\frac{4.4101s+197.9212}{0.050134s^2+1.215s}$

g) $\text{DS1}=\left|\frac{\Delta i_n}{\Delta V_{dc}}\right|=\left|\frac{0.050134s^2+5.6251s+197.9212}{s}\right|$

h) $\text{DS2}=\left|\frac{\Delta v_{g\_d}}{\Delta V_{dc}}\right|=\left|\frac{0.01348s^2+1.512s+53.2023}{s}\right|$

iv) $i_{g\_do} = i_{g\_do\_nom}$=2755.68A (≈2.756kA)

$$K_s = \frac{i_{g\_do\_nom}}{v_{dco\_nom}} = \frac{2.756kA}{1kV} \approx 2.756\ (A/V) \ \text{ and } \ K_v = \frac{v_{g\_do\_nom}}{v_{dco\_nom}} = \frac{0.3266kV}{1kV} \approx 0.327$$

a) $FTF = \frac{\Delta V_{dc}}{\Delta V_{dc}^*} = \frac{3.0456s^2 + 4446.0235s + 193400.8979}{6.12793x10^{-6}s^4 + 0.0348177s^3 + 52.9677s^2 + 5765.1909s + 193400.8979}$

b) $TF = \frac{\Delta V_{dc}}{\Delta V_{dc}^*} = \frac{4.4101s + 197.9212}{0.050134s^2 + 5.7601s + 197.9212}$

d) $SoATF = \frac{\Delta V_{dc}}{\Delta V_{dc}^*} = \frac{3947.8442}{s^2 + 114.8933s + 3947.8442}$

f) $FpTF = G(s).H(s) = \frac{4.4101s + 197.9212}{0.050134s^2 + 1.35s}$

g) $DS1 = \left|\frac{\Delta i_n}{\Delta V_{dc}}\right| = \left|\frac{0.050134s^2 + 5.7601s + 197.9212}{s}\right|$

h) $DS2 = \left|\frac{\Delta v_{g\_d}}{\Delta V_{dc}}\right| = \left|\frac{0.01213s^2 + 1.3935s + 47.8821}{s}\right|$

v) i_{g_do}=3031.24A (≈3.031kA)

$$K_s = \frac{i_{g\_do\_nom}}{v_{dco\_nom}} = \frac{3.031kA}{1kV} \approx 3.031\ (A/V) \ \text{ and } \ K_v = \frac{v_{g\_do\_nom}}{v_{dco\_nom}} = \frac{0.3266kV}{1kV} \approx 0.327$$

a) $FTF = \frac{\Delta V_{dc}}{\Delta V_{dc}^*} = \frac{3.0456s^2 + 4446.0235s + 193400.8979}{6.12793x10^{-6}s^4 + 0.0348342s^3 + 53.061s^2 + 5897.1076s + 193400.8979}$

b) $TF = \frac{\Delta V_{dc}}{\Delta V_{dc}^*} = \frac{4.4101s + 197.9212}{0.050134s^2 + 5.8951s + 197.9212}$

d) $SoATF = \frac{\Delta V_{dc}}{\Delta V_{dc}^*} = \frac{3947.8442}{s^2 + 117.5861s + 3947.8442}$

f) $FpTF = G(s).H(s) = \frac{4.4101s + 197.9212}{0.050134s^2 + 1.485s}$

g) $DS1 = \left|\frac{\Delta i_n}{\Delta V_{dc}}\right| = \left|\frac{0.050134s^2 + 5.8951s + 197.9212}{s}\right|$

h) $DS2 = \left|\frac{\Delta v_{g\_d}}{\Delta V_{dc}}\right| = \left|\frac{0.01103s^2 + 1.2965s + 43.5292}{s}\right|$

vi) i_{g_do}=3306.81A (≈3.307kA)

$$K_s=\frac{i_{g\_do\_nom}}{v_{dco\_nom}}=\frac{3.307kA}{1kV}\approx 3.307\ (A/V)\ \text{ and }\ K_v=\frac{v_{g\_do\_nom}}{v_{dco\_nom}}=\frac{0.3266kV}{1kV}\approx 0.327$$

a) $\text{FTF}=\frac{\Delta V_{dc}}{\Delta V_{dc}^*}=\frac{3.0456s^2+4446.0235s+193400.8979}{6.12793x10^{-6}s^4+0.0348507s^3+53.1543s^2+6029.0244s+193400.8979}$

b) $\text{TF}=\frac{\Delta V_{dc}}{\Delta V_{dc}^*}=\frac{4.4101s+197.9212}{0.050134s^2+6.0301s+197.9212}$

d) $\text{SoATF}=\frac{\Delta V_{dc}}{\Delta V_{dc}^*}=\frac{3947.8442}{s^2+120.2789s+3947.8442}$

f) $\text{FpTF}=G(s).H(s)=\frac{4.4101s+197.9212}{0.050134s^2+1.62s}$

g) $\text{DS1}=\left|\frac{\Delta i_n}{\Delta V_{dc}}\right|=\left|\frac{0.050134s^2+6.0301s+197.9212}{s}\right|$

h) $\text{DS2}=\left|\frac{\Delta v_{g\_d}}{\Delta V_{dc}}\right|=\left|\frac{0.01011s^2+1.2157s+39.9017}{s}\right|$

vii) i_{g_do}= $i_{g\_do\_max}$=3582.38A (≈3.582kA)

$$K_s=\frac{i_{g\_do\_nom}}{v_{dco\_nom}}=\frac{3.582kA}{1kV}\approx 3.582\ (A/V)\ \text{ and }\ K_v=\frac{v_{g\_do\_nom}}{v_{dco\_nom}}=\frac{0.3266kV}{1kV}\approx 0.327$$

a) $\text{FTF}=\frac{\Delta V_{dc}}{\Delta V_{dc}^*}=\frac{3.0456s^2+4446.0235s+193400.8979}{6.12793x10^{-6}s^4+0.0348672s^3+53.2476s^2+6160.9411s+193400.8979}$

b) $\text{TF}=\frac{\Delta V_{dc}}{\Delta V_{dc}^*}=\frac{4.4101s+197.9212}{0.050134s^2+6.1651s+197.9212}$

d) $\text{SoATF}=\frac{\Delta V_{dc}}{\Delta V_{dc}^*}=\frac{3947.8442}{s^2+122.9717s+3947.8442}$

f) $\text{FpTF}=G(s).H(s)=\frac{4.4101s+197.9212}{0.050134s^2+1.755s}$

g) $\text{DS1}=\left|\frac{\Delta i_n}{\Delta V_{dc}}\right|=\left|\frac{0.050134s^2+6.1651s+197.9212}{s}\right|$

h) $\text{DS2}=\left|\frac{\Delta v_{g\_d}}{\Delta V_{dc}}\right|=\left|\frac{0.00933s^2+1.1473s+36.8324}{s}\right|$

A.3.3.2 MATLAB Results

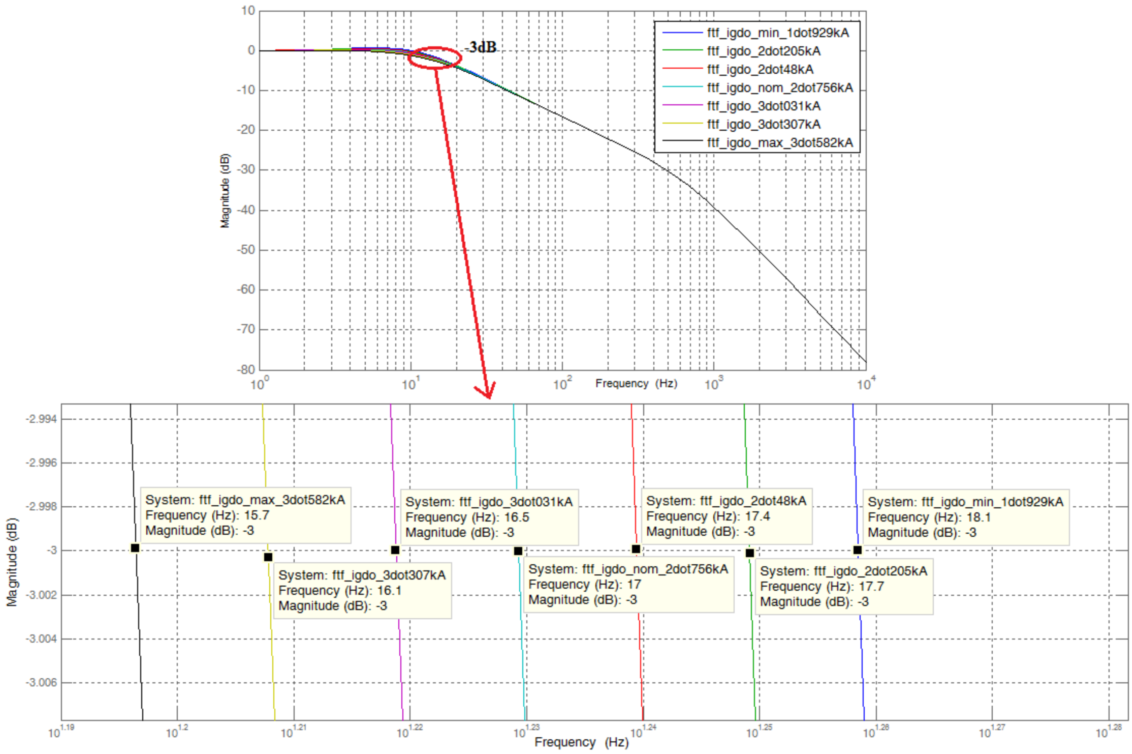

Figure A.3.17: Full transfer function and bandwidths representation

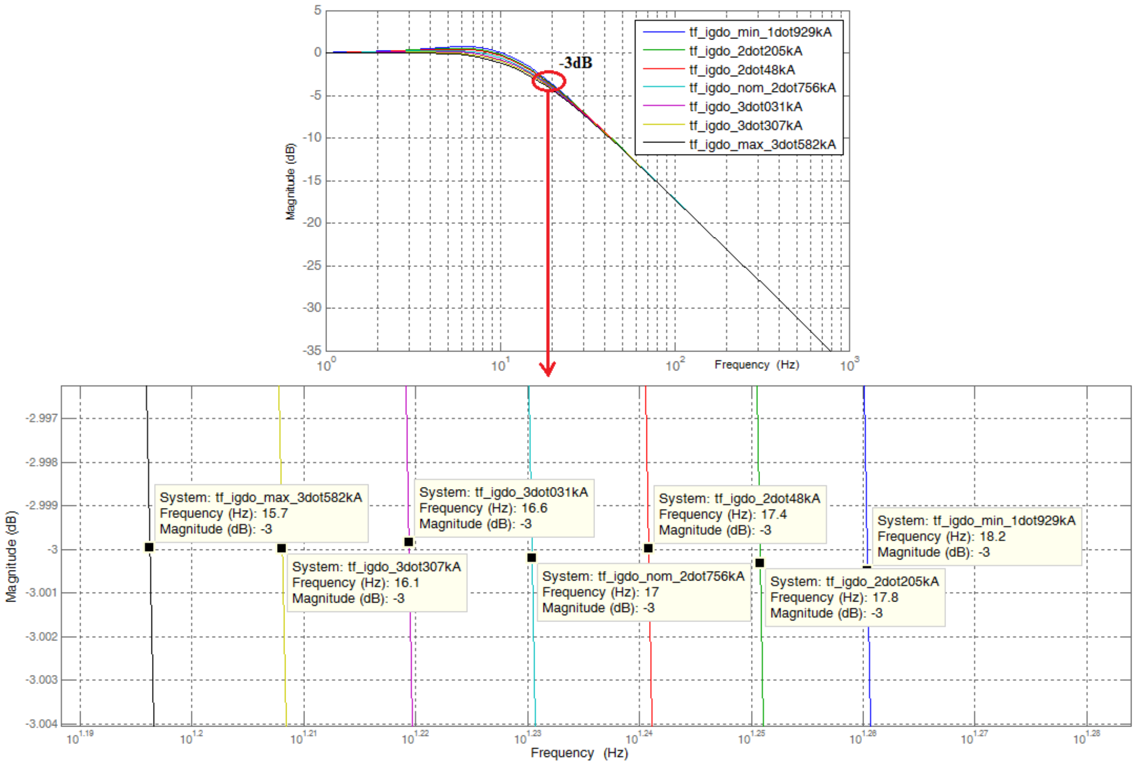

Figure A.3.18: Transfer function and bandwidths representation

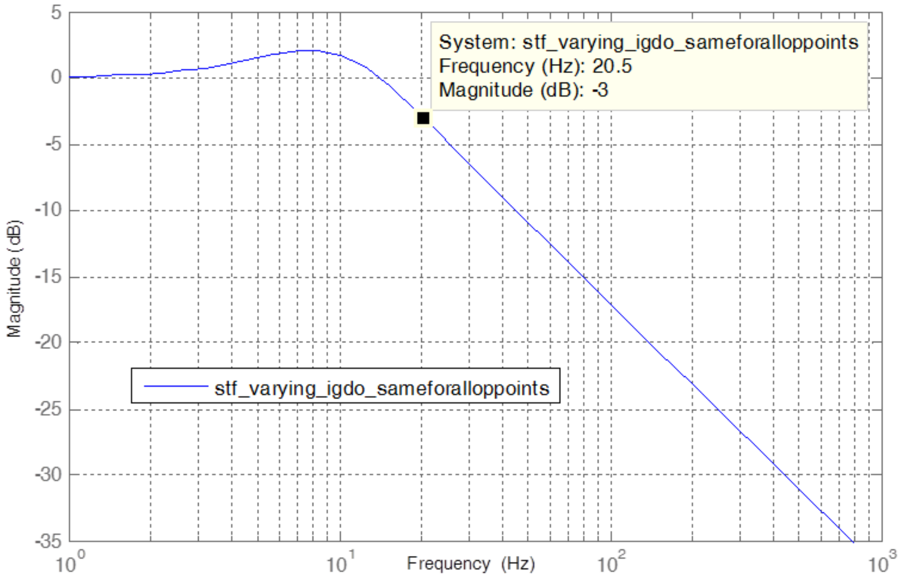

Figure A.3.19: Simplified transfer function and bandwidth representation

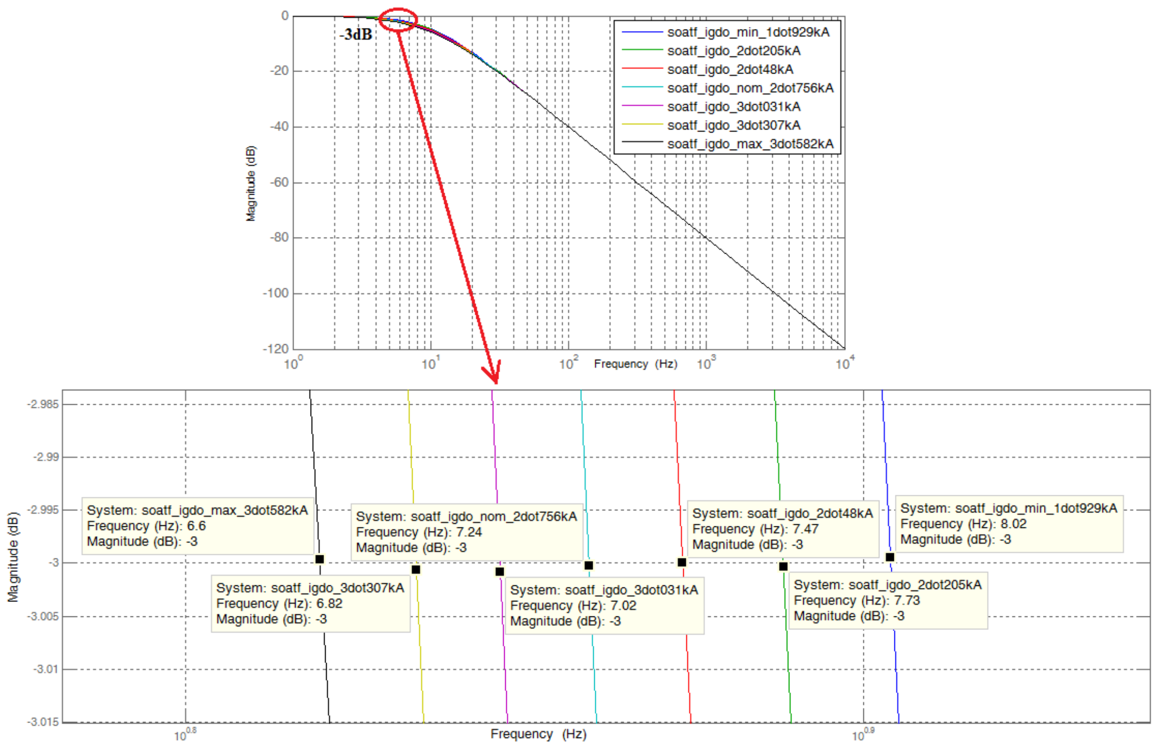

Figure A.3.20: Second-order approximated transfer function and bandwidths representation

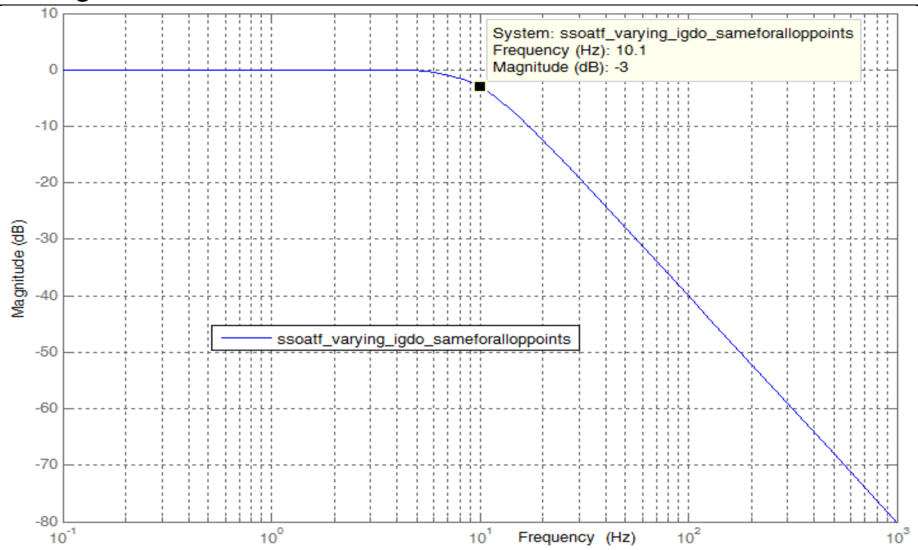

Figure A.3.21: Simplified second-order approximated transfer function and bandwidths representation

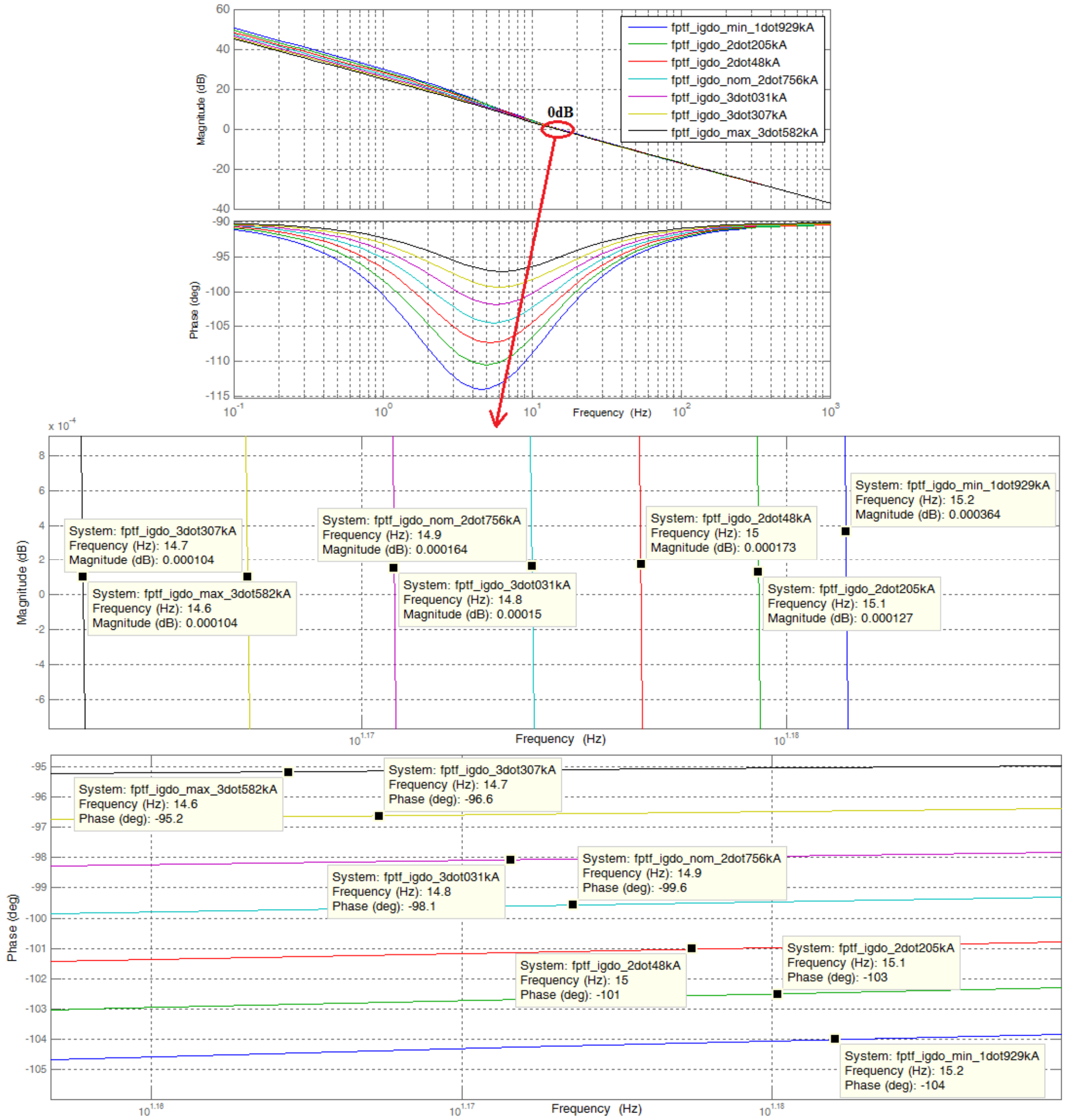

Figure A.3.22: Forward-path transfer function and damping ratios representation

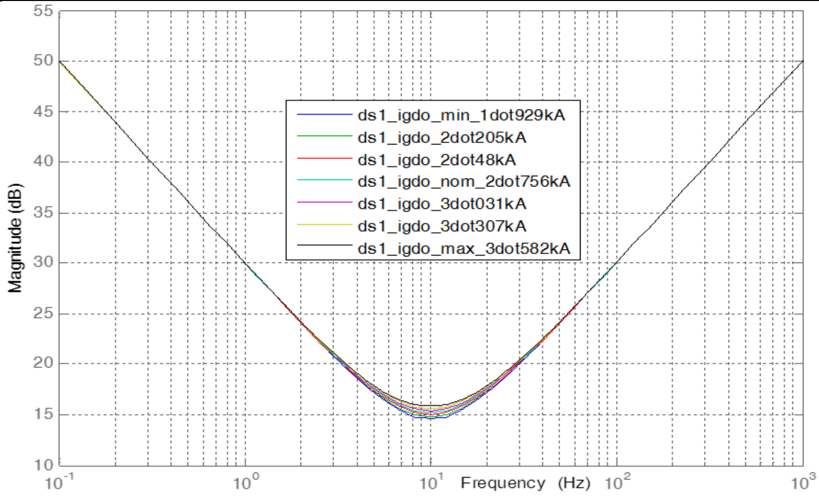

Figure A.3.23: Dynamic stiffness analysis of $\Delta i_n/\Delta V_{dc}$ (DS1)

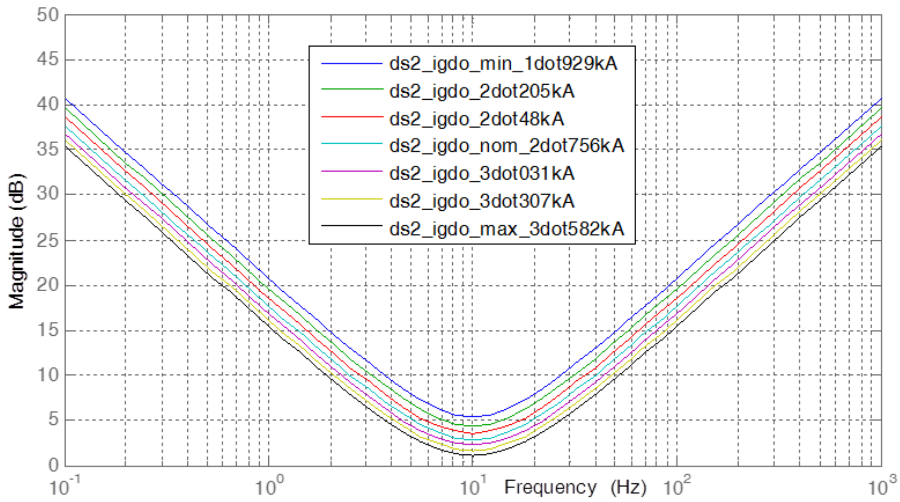

Figure A.3.24: Dynamic stiffness analysis of $\Delta v_{g\_d}/\Delta V_{dc}$ (DS2)

A.3.4 PSCAD Simulation Circuit

The grid-side converter circuit was set up in PSCAD on its own to investigate the sensitivity analyses for the voltage (outer) loop control. Thus, the interaction between the other sub-systems of the whole system is avoided and the behaviour of the voltage loop was not influenced. The simulation circuit is depicted in Figure A.3.25. Some example graphs of the voltage loop sensitivity investigation with the inclusion of full system are shown in Figures A.3.26 and A.3.27. The interference of the other sub-systems to the sensitivity analyses can be clearly seen in these figures.

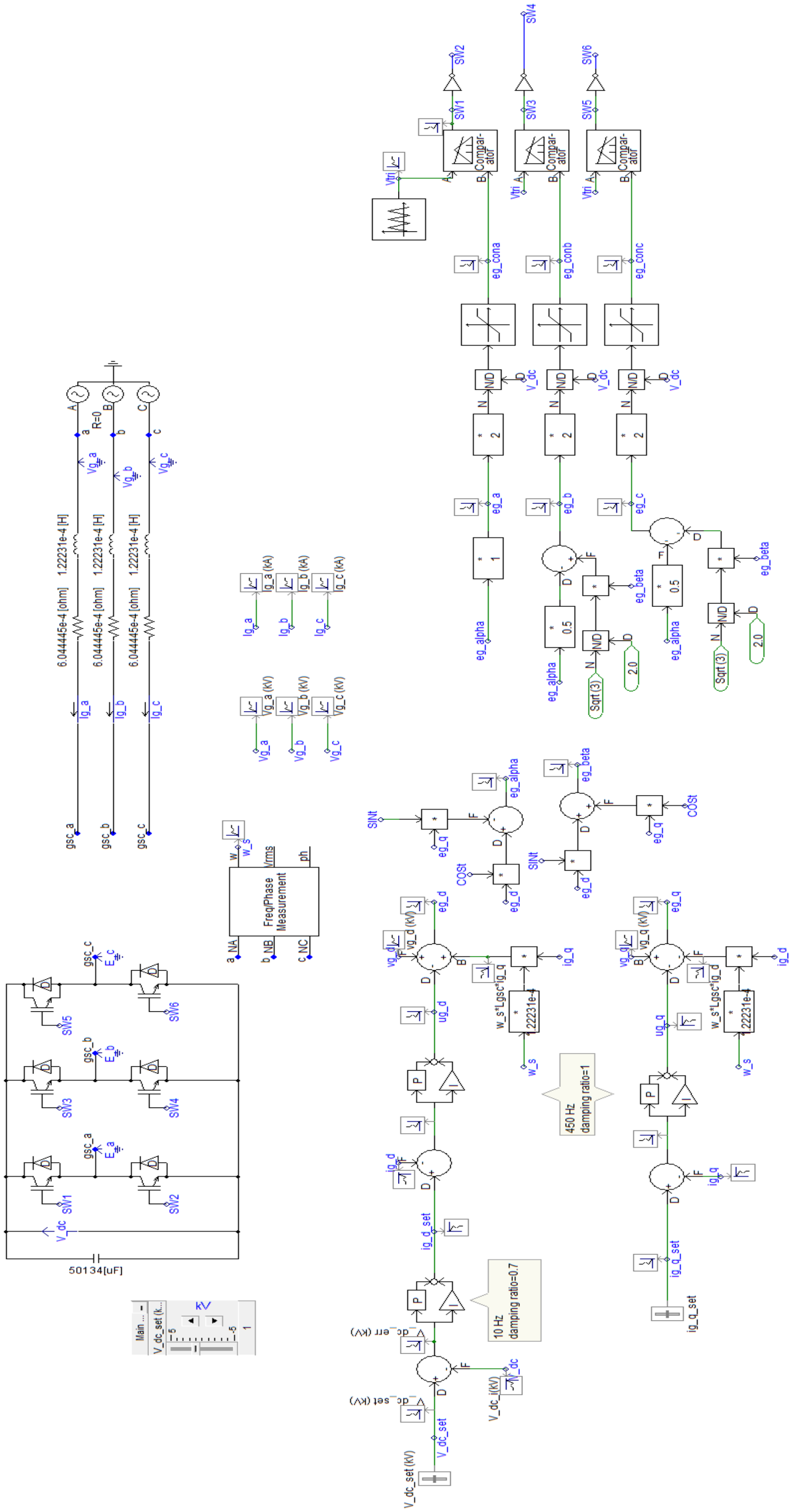

Figure A.3.25: The simulation circuit of the grid-side converter in PSCAD

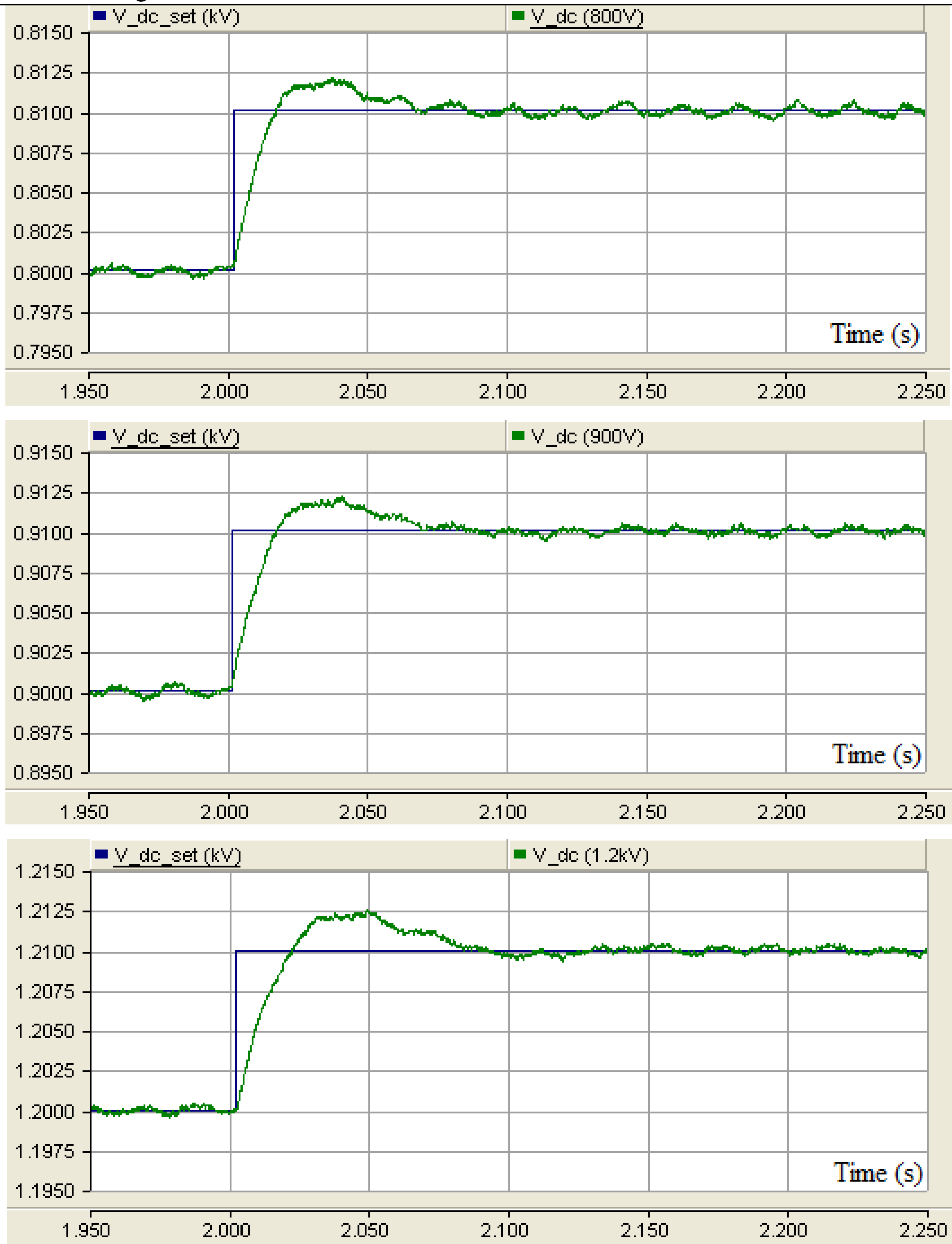

Figure A.3.26: Examples of the simulation result for the full system - Varying V_{dco}

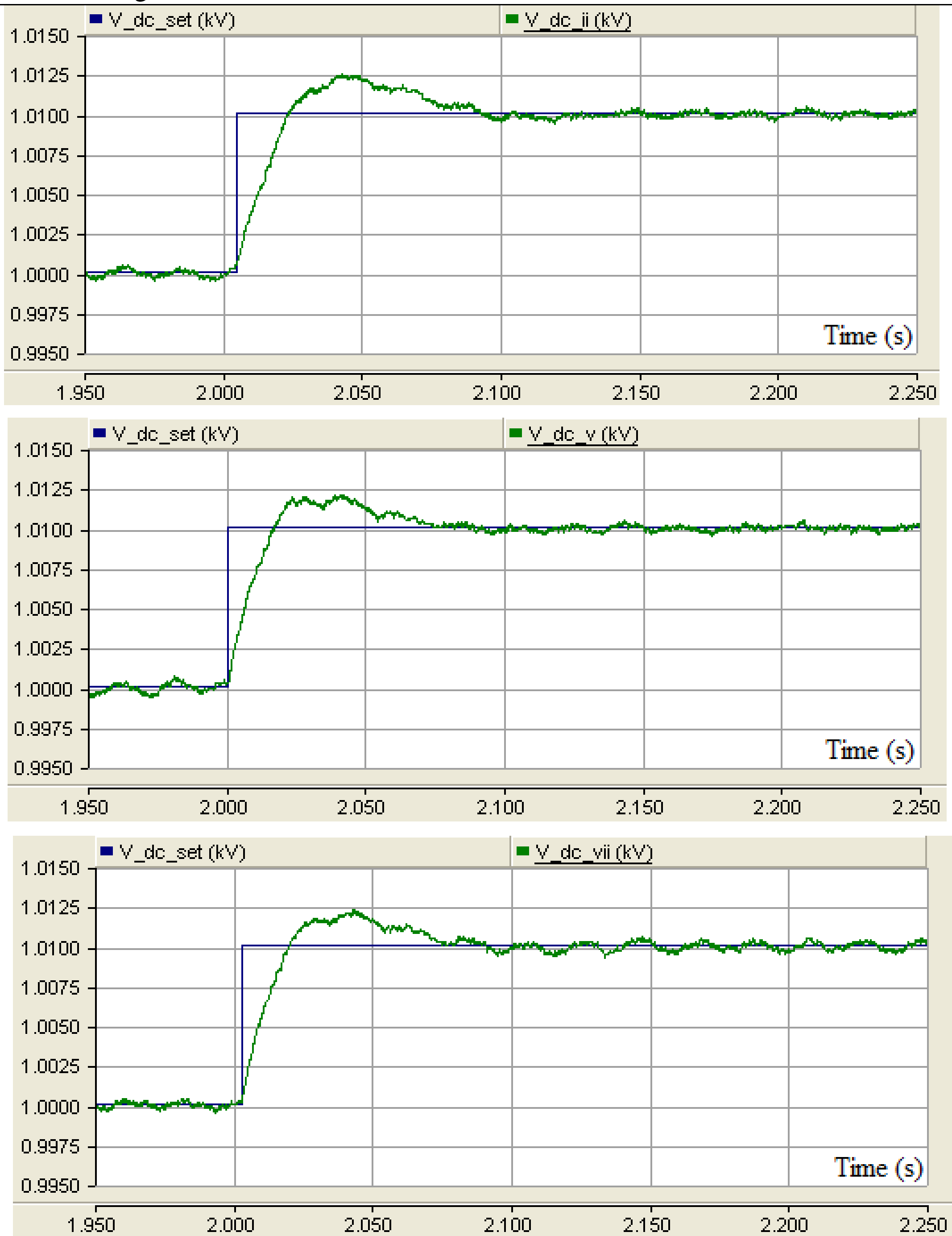

Figure A.3.27: Examples of the simulation result for the full system - Varying v_{g_do}

Appendix 4 Investigation of Protection Coordination

The differences between the inclusion and exclusion of the protection schemes at start-up are summarised in Figure A.4.1. The simulation file constructed in PSCAD was run with the set values of 4.5 MW stator active power and of 1 MVAr stator reactive power while the DC-link voltage was set to 1 kV. As seen in Figure A.4.1 enabling the protection systems at start-up causes distortion in the system quantities (currents, powers and voltages). Therefore a time block is added to the simulation file in PSCAD to avoid triggering the protection circuits at start-up. Thus, the nature of the start-up transients is not distorted.

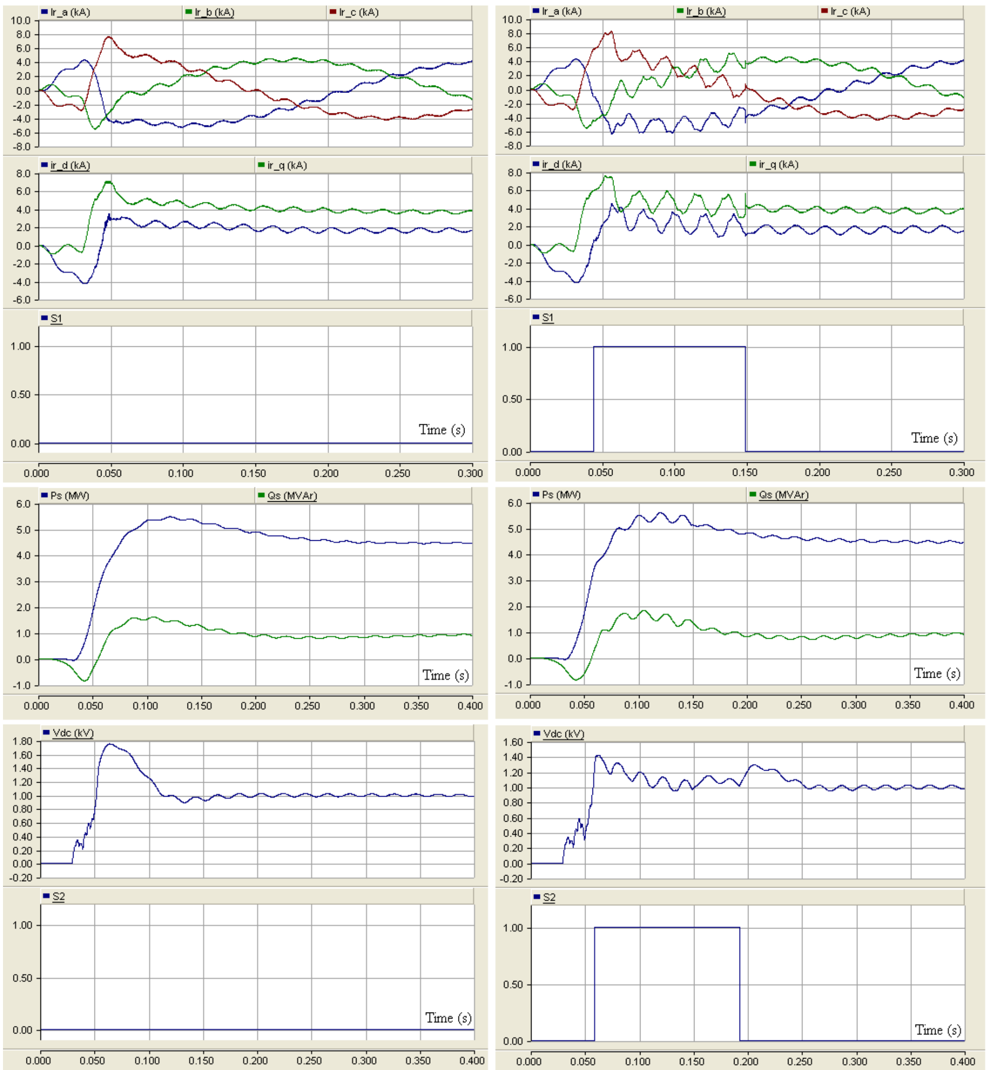

a. Exclusion of the protection at start-up   b. Inclusion of the protection at start-up

Figure A.4.1: The effect of protection devices on the system at start-up

For both crowbar circuit and DC-link brake, SR flip-flops are used with a low initial state of output ($Q_{initial}$=0). The active clock trigger edge of these flip-flops is determined as the positive edge (0-to-1 transition). These edge-triggered flip-flops only work during a transition of the clock signal. If any phase rotor current exceeds the threshold value the state input of S will immediately be 1 and so will the output state (Q). Then this signal is conveyed to the crowbar switch and lets this switch trigger. When all phase rotor currents are below the threshold value at the same time, then the S and R inputs will be returned to 0 and 1, respectively. So, the crowbar will be deactivated and resumed. The SR flip-flop existing in the PSCAD library is designed with NOR gates. Therefore, a typical logic diagram of a SR flip-flop with only NOR gates and its truth table taken from [97] is illustrated in Figure A.4.2.

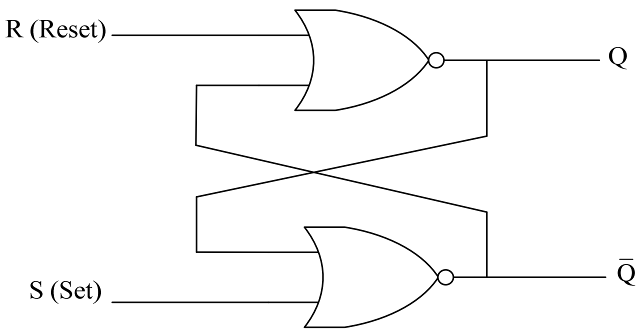

S	R	Q	$\bar{Q}$	
1	0	1	0	Set state
0	0	1	0	
0	1	0	1	Reset state
0	0	0	1	
1	1	0	0	Undefined

Figure A.4.2: SR Flip-Flop with NOR gates and its function table

A.4.1 Estimation of the DC-link Brake Resistor

In this work, the converter power rating is set to 30% of the rated DFIG power. This assumption then reflects on the calculation of the DC-link brake resistor. During the grid faults, the over-voltage occurs in the DC-link capacitor which activates the DC-link brake. The rectified (DC) current flows through the DC-link brake resistor during the DC-link brake activation. This resistor should withstand the heating in case of high rectified current. Therefore, the brake power is then defined as twice (choosing larger brake power gives less brake resistance due to the nature of the equation) the converter power because of protection concerns of sinking both converter powers (worst case). The maximum limit of the DC-link voltage is considered to calculate the DC-link brake resistor.

$P_{brake} \;\; = 2 \text{ x } P_{converter}$

$P_{converter} = 30\% \text{ Rated Power } (S_{base})$

$P_{brake} \;\; = 2 \text{ x } 30\% \; S_{base} = 2.7MW$

$$P_{brake} = \frac{V_{dc}^2}{R_{brake}} = \frac{V_{dc,max}^2}{R_{brake}} \;\Rightarrow\; R_{brake} = \frac{V_{dc,max}^2}{P_{brake}} = \frac{(1.3kV)^2}{2.7MW} \approx 0.626\Omega$$

A.4.2 The Relation Between Protection Actions

First, a 0.5pu 3-phase voltage sag is introduced to the external grid voltage. The same methodology used for the investigation of the relation between the crowbar and the DC-link brake actions applies in this appendix section. Then, a 0.5pu 2-phase voltage sag is tried. Finally, a 0.8pu 1-phase voltage sag is applied in which a lock out time of 20.2ms is used for the crowbar control algorithm. The simulation results are added in the following.

In case of a less severe voltage sag of a 0.5pu 3-phase voltage sag, for all states (no protection taken, only DC-link brake action taken, only crowbar activation, and both of them involved) the behaviour of the stator reactive power stays effectively same (see lower left graph in Figures A.4.3 to A.4.6). In Figures A.4.7 and A.4.8, the over-currents persist in the rotor during the voltage sag period which can cause over-heating in the passive elements of the rotor circuit. To prevent the components over-heating, it is then essential to let the crowbar take action to keep the rotor-currents below their maximum threshold values (approx. 7.5kA). Although the stator active power (see upper left graph in Figures A.4.3 to A.4.6) does not drop below approximately 3.5MW during the fault in the cases of taking no protection action and/or only DC-link brake activation, the larger overshoot happens in the stator active power response and it takes a bit longer to reach transiently steady-state. Note that the rotor over-currents persist as well. Therefore, triggering only the DC-link brake during the voltage sag will not be a good idea in terms of fault ride-through capability. Taking the crowbar action into consideration enables the stator real power reach the steady-state quicker causing no overshoot (see upper left graph in Figures A.4.5 and A.4.6). Moreover, it eases the stress on the DC-link voltage (see right graph in Figure A.4.6). As seen in Figures A.4.9 and A.4.10, once the crowbar triggers due to a single occurring over-current in the rotor, in the rest of the voltage sag duration the over-current will be eliminated. Using both protection devices is then highly desirable in the fault ride-through technique considered in this work.

For the same magnitude of the voltage sag applied to the network voltage, the worst case happens in the 3-phase voltage sag incident. The least severe voltage sag occurs in the case of single-phase. The overall DFIG system response improves in case of a 0.5pu 2-phase voltage sag. Related simulation results are presented in the following figures. Even if the voltage sag magnitude is 0.8pu, since this voltage sag is applied to one phase better response results can be observed in the relevant figures. In all cases, using both protection devices provides better performance in the riding through the fault. This advantage should be taken though.

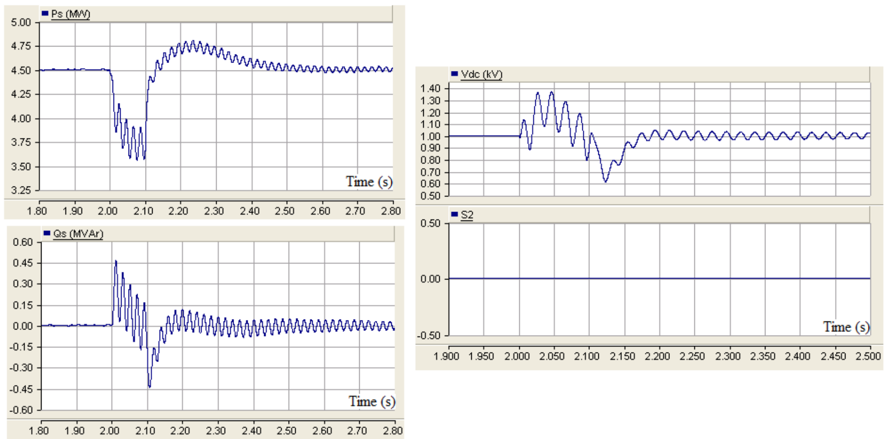

Figure A.4.3: The DC-link voltage, stator real and reactive power behaviours during a 0.5pu 3-phase voltage sag in the case of no involving any protection

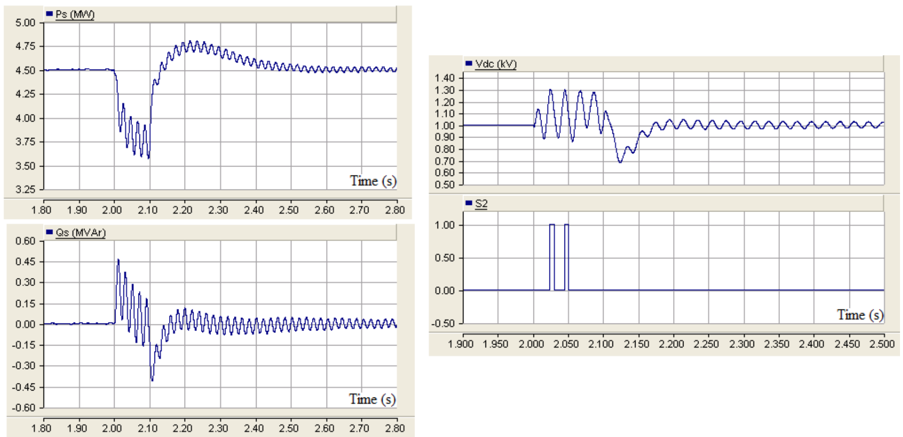

Figure A.4.4: The DC-link voltage, stator real and reactive power behaviours during a 0.5pu 3-phase voltage sag by activating only DC-link brake protection

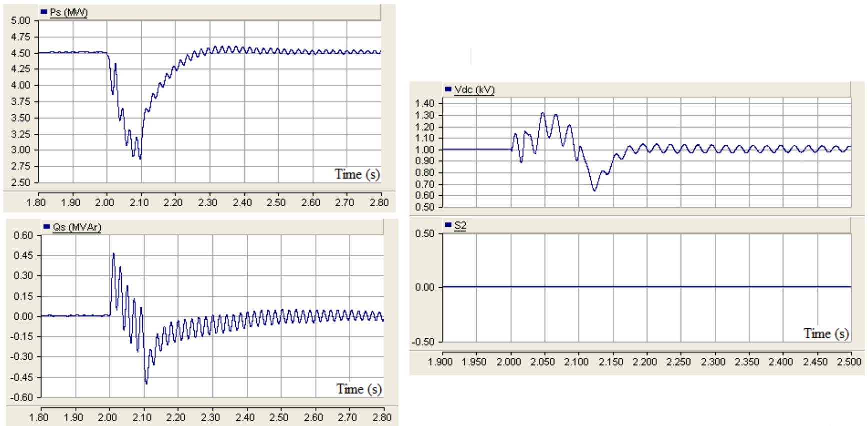

Figure A.4.5: The DC-link voltage, stator real and reactive power behaviours during a 0.5pu 3-phase voltage sag by activating only crowbar protection

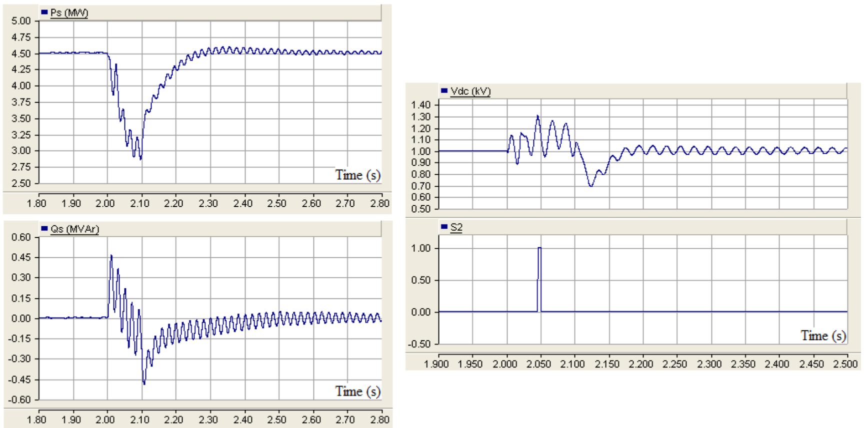

Figure A.4.6: The DC-link voltage, stator real and reactive power behaviours during a 0.5pu 3-phase voltage sag by activating both crowbar and DC-link brake protections

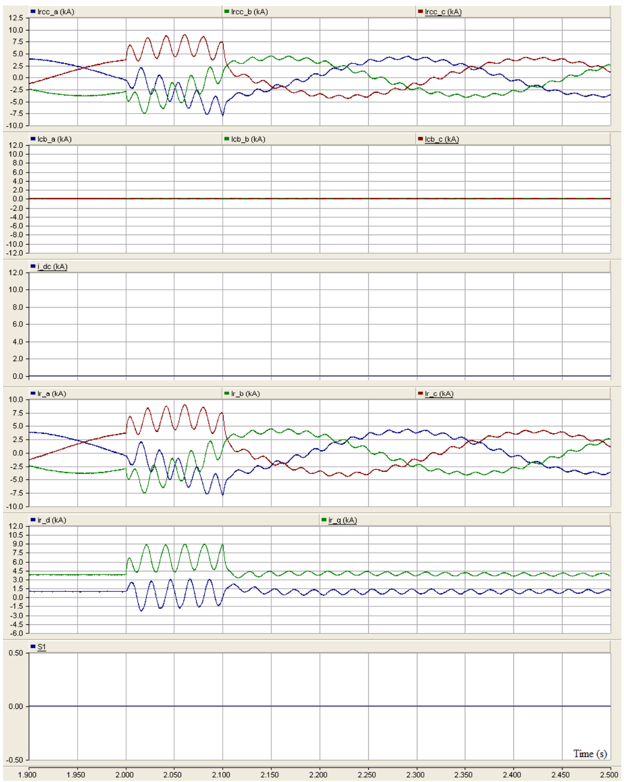

Figure A.4.7: Rotor-side currents behaviours during a 0.5pu 3-phase voltage sag in the case of no involving any protection

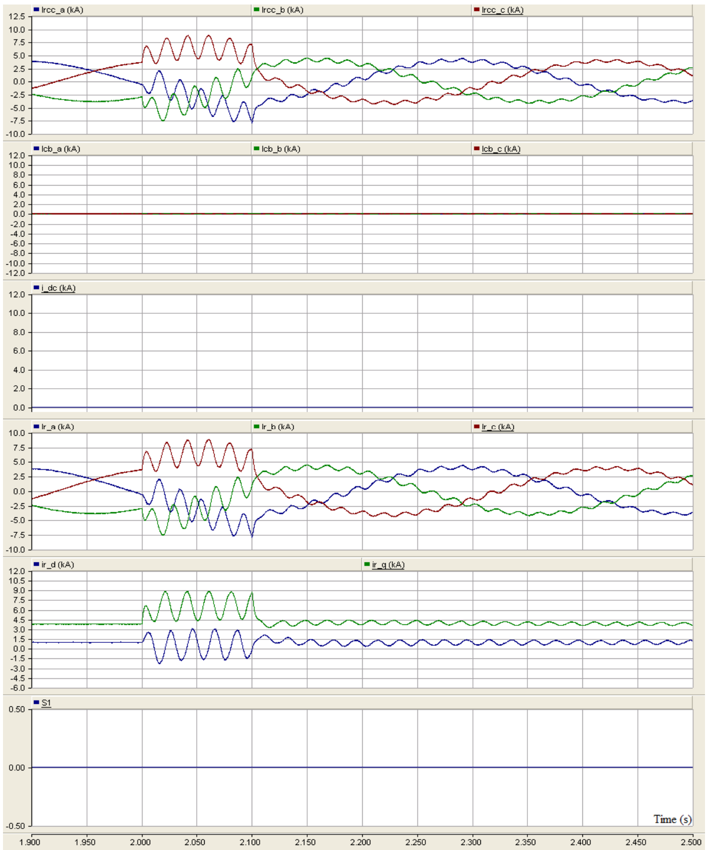

Figure A.4.8: Rotor-side currents behaviours during a 0.5pu 3-phase voltage sag by activating only DC-link brake protection

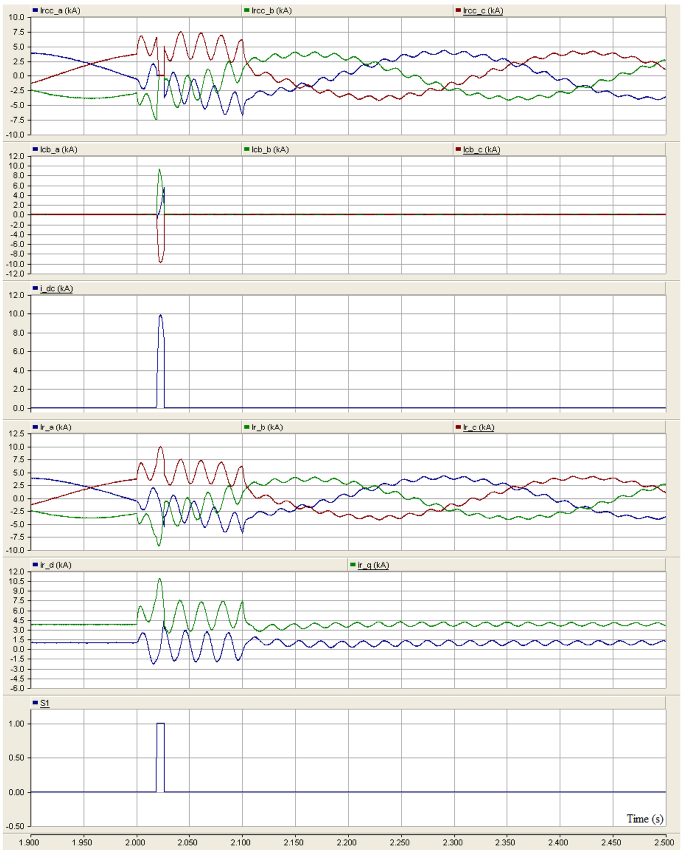

Figure A.4.9: Rotor-side currents behaviours during a 0.5pu 3-phase voltage sag by activating only crowbar protection

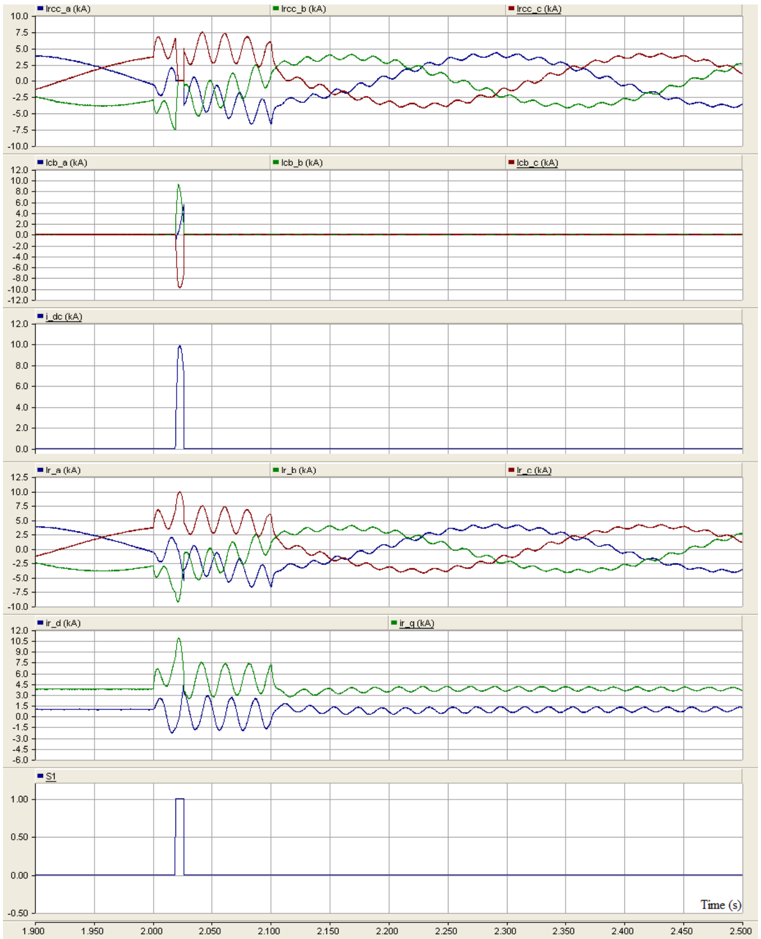

Figure A.4.10: Rotor-side currents behaviours during a 0.5pu 3-phase voltage sag by activating both crowbar and DC-link brake protections

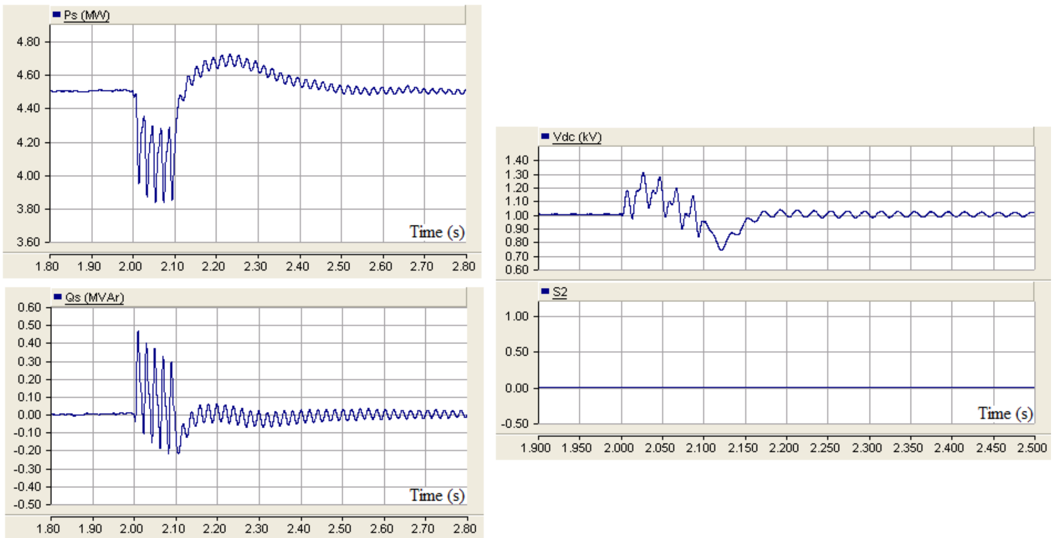

Figure A.4.11: The DC-link voltage, stator real and reactive power behaviours during a 0.5pu 2-phase voltage sag in the case of no involving any protection

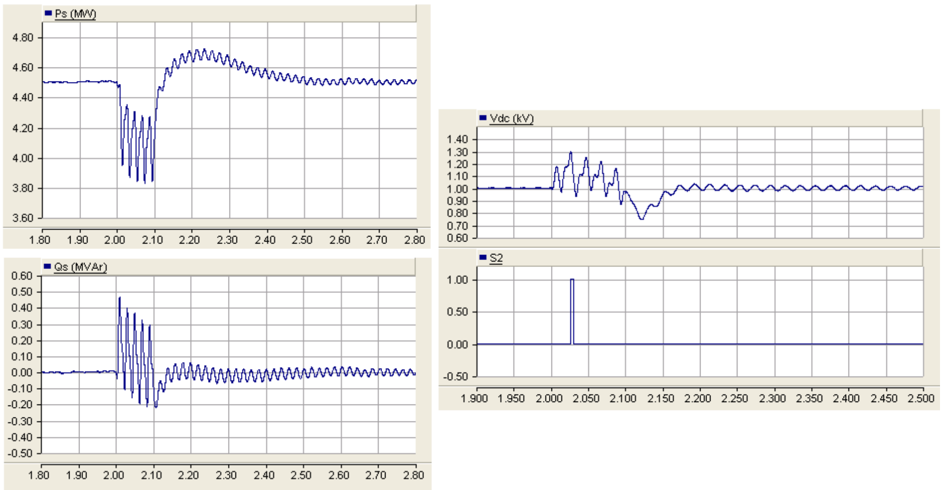

Figure A.4.12: The DC-link voltage, stator real and reactive power behaviours during a 0.5pu 2-phase voltage sag by activating only DC-link brake protection

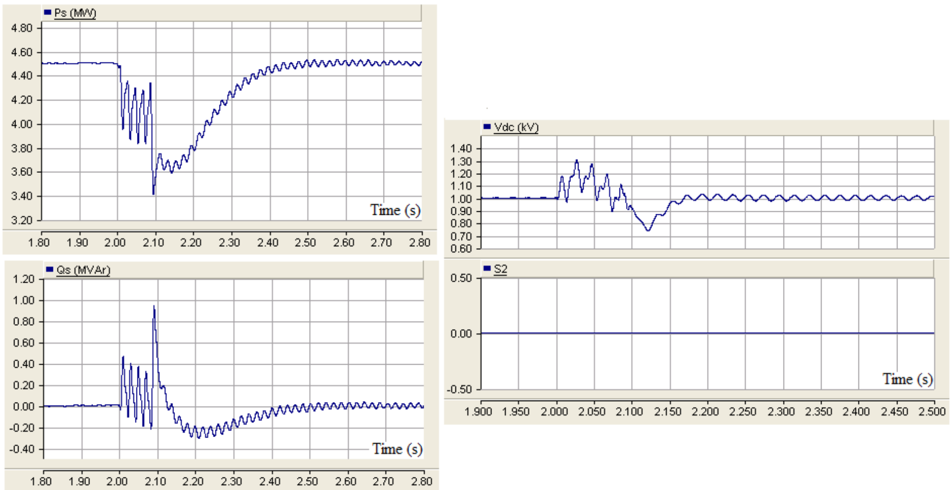

Figure A.4.13: The DC-link voltage, stator real and reactive power behaviours during a 0.5pu 2-phase voltage sag by activating only crowbar protection

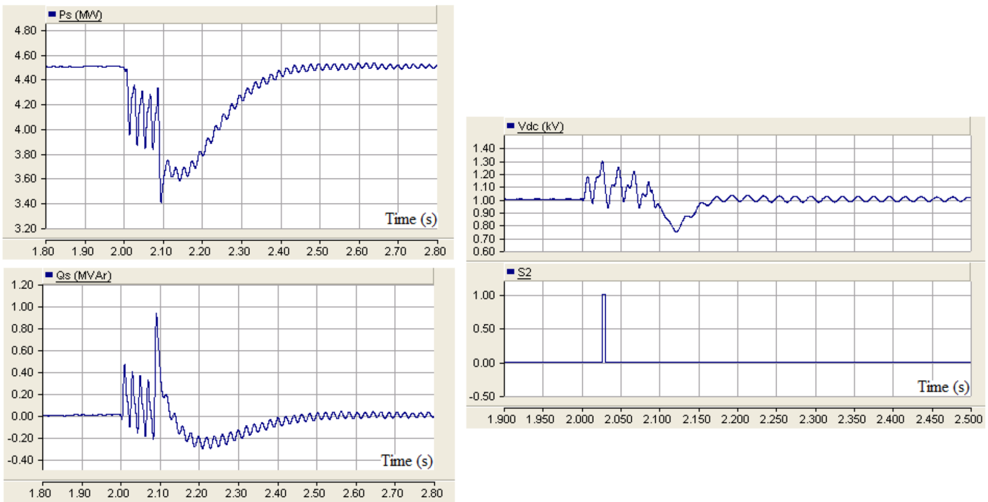

Figure A.4.14: The DC-link voltage, stator real and reactive power behaviours during a 0.5pu 2-phase voltage sag by activating both crowbar and DC-link brake protections

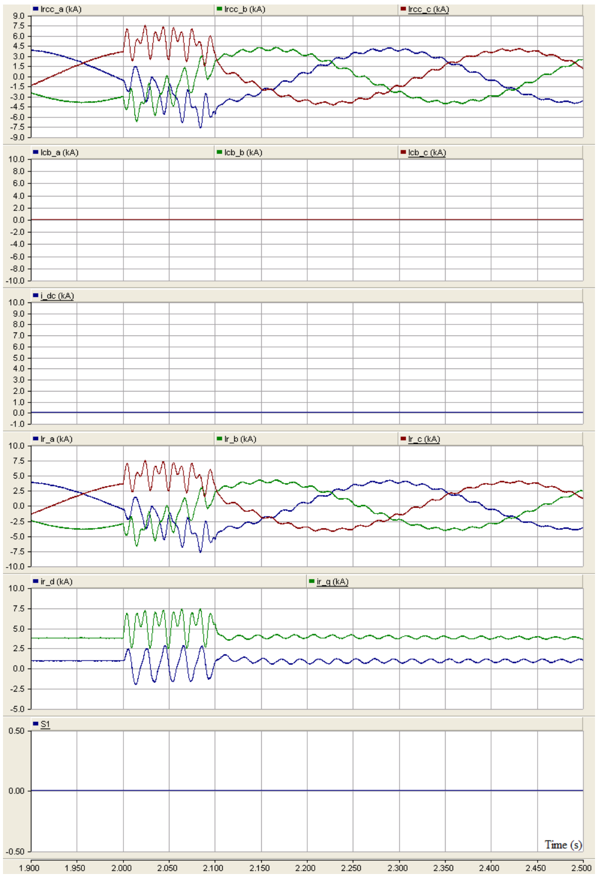

Figure A.4.15: Rotor-side currents behaviours during a 0.5pu 2-phase voltage sag in the case of no involving any protection

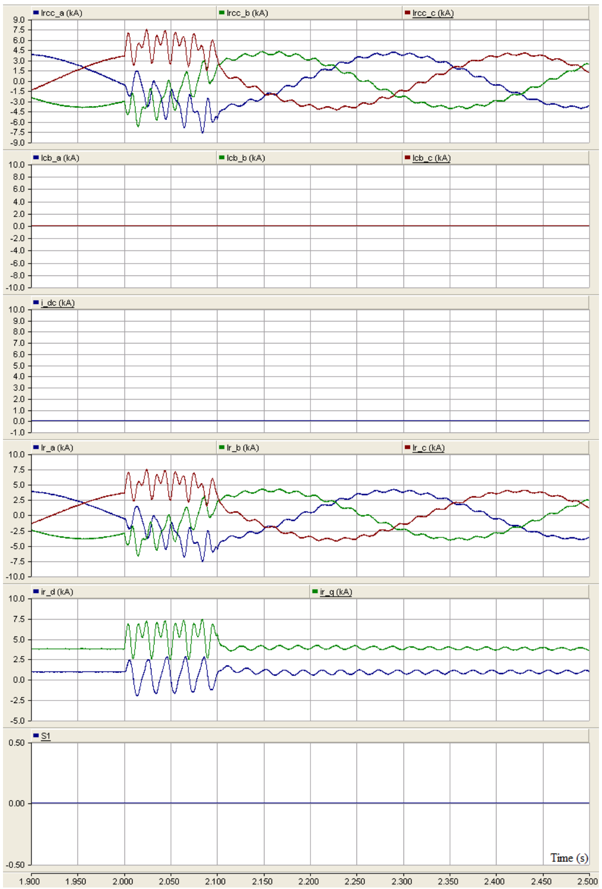

Figure A.4.16: Rotor-side currents behaviours during a 0.5pu 2-phase voltage sag by activating only DC-link brake protection

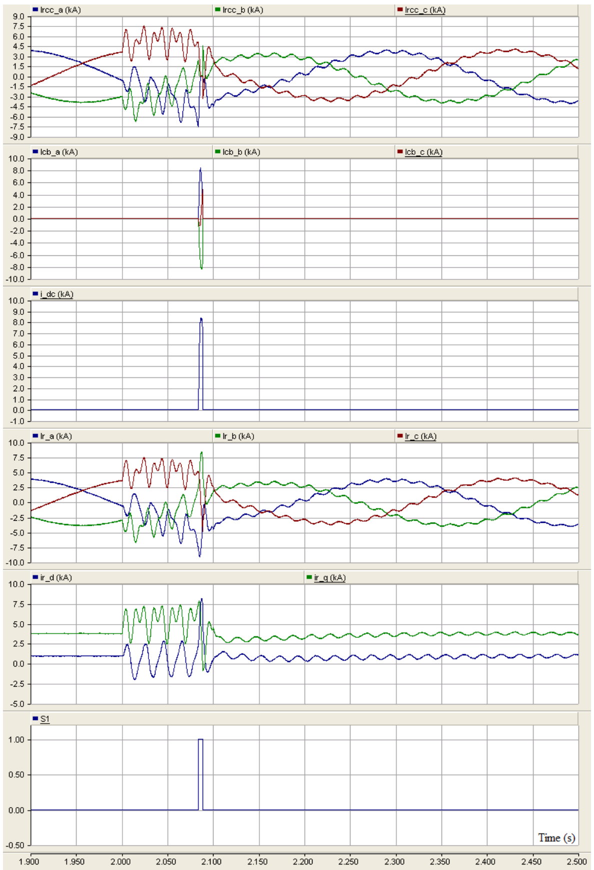

Figure A.4.17: Rotor-side currents behaviours during a 0.5pu 2-phase voltage sag by activating only crowbar protection

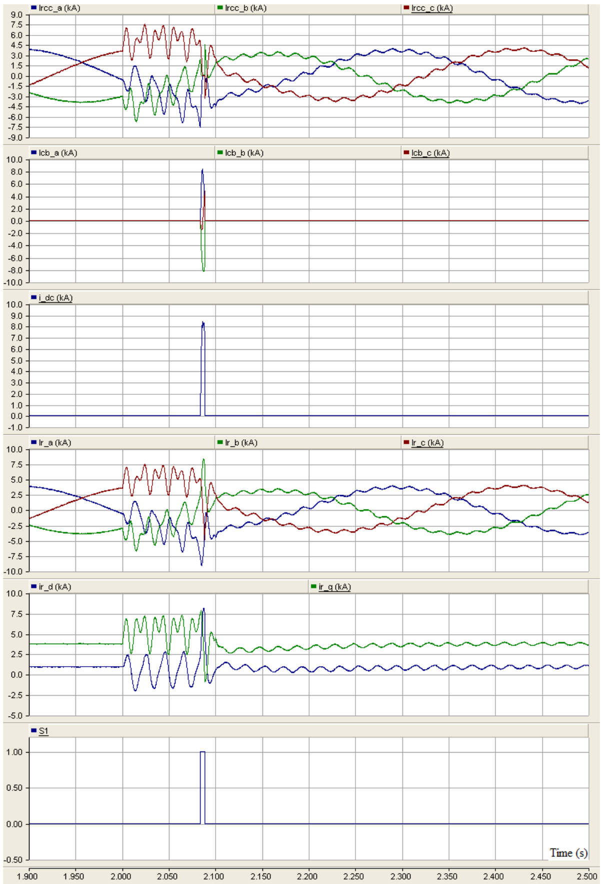

Figure A.4.18: Rotor-side currents behaviours during a 0.5pu 2-phase voltage sag by activating both crowbar and DC-link brake protections

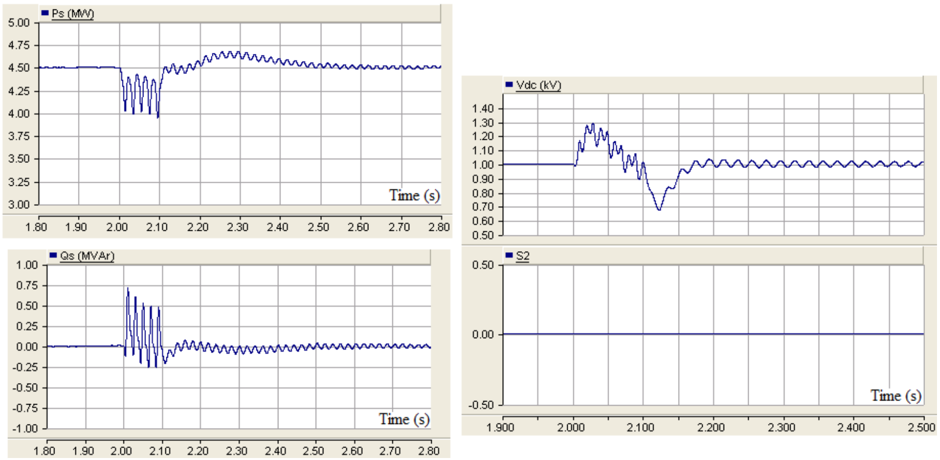

Figure A.4.19: The DC-link voltage, stator real and reactive power behaviours during a 0.8pu 1-phase voltage sag in the case of no involving any protection

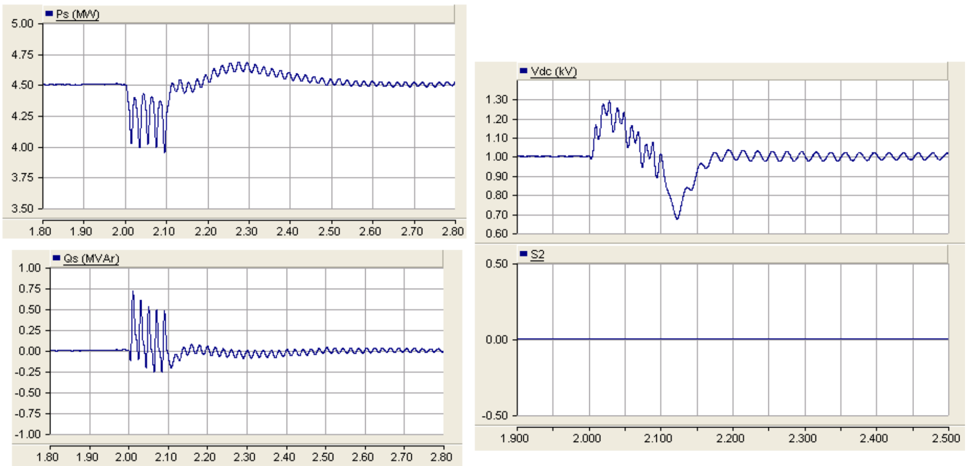

Figure A.4.20: The DC-link voltage, stator real and reactive power behaviours during a 0.8pu 1-phase voltage sag by activating only DC-link brake protection

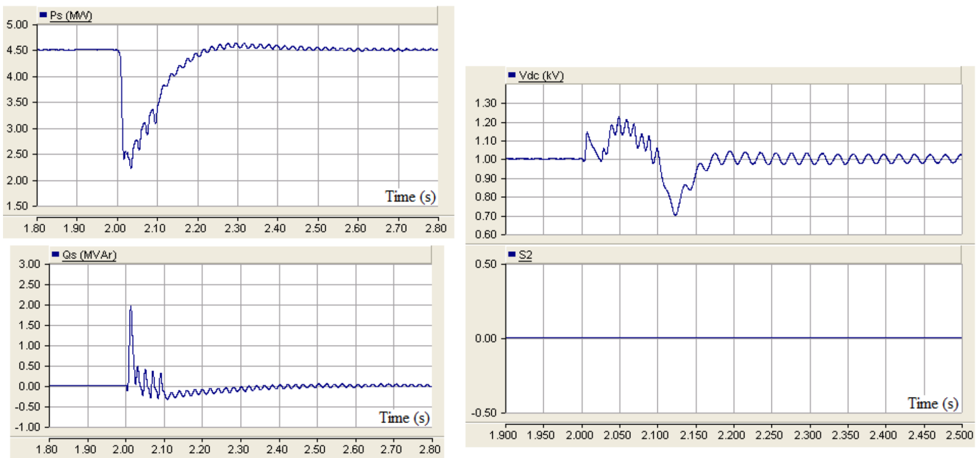

Figure A.4.21: The DC-link voltage, stator real and reactive power behaviours during a 0.8pu 1-phase voltage sag by activating only crowbar protection

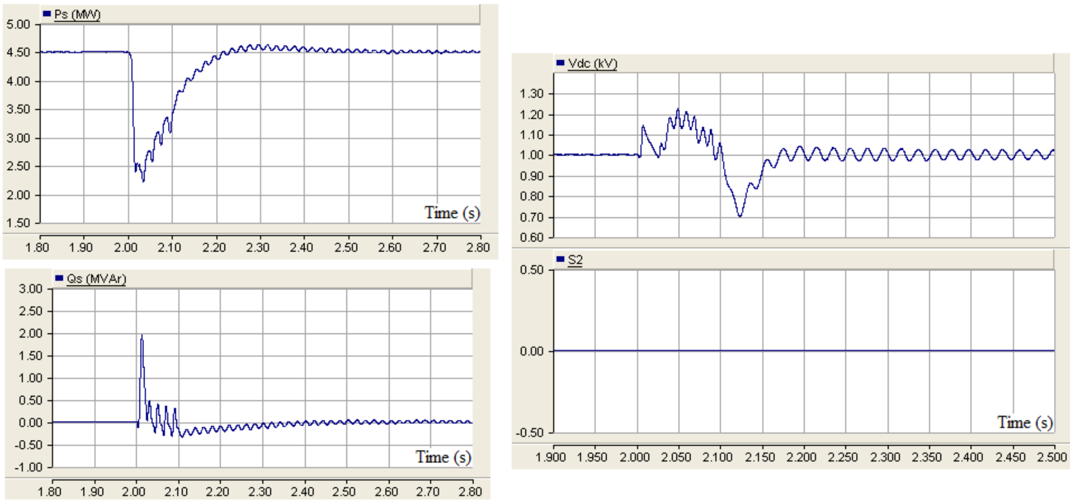

Figure A.4.22: The DC-link voltage, stator real and reactive power behaviours during a 0.8pu 1-phase voltage sag by activating both crowbar and DC-link brake protections

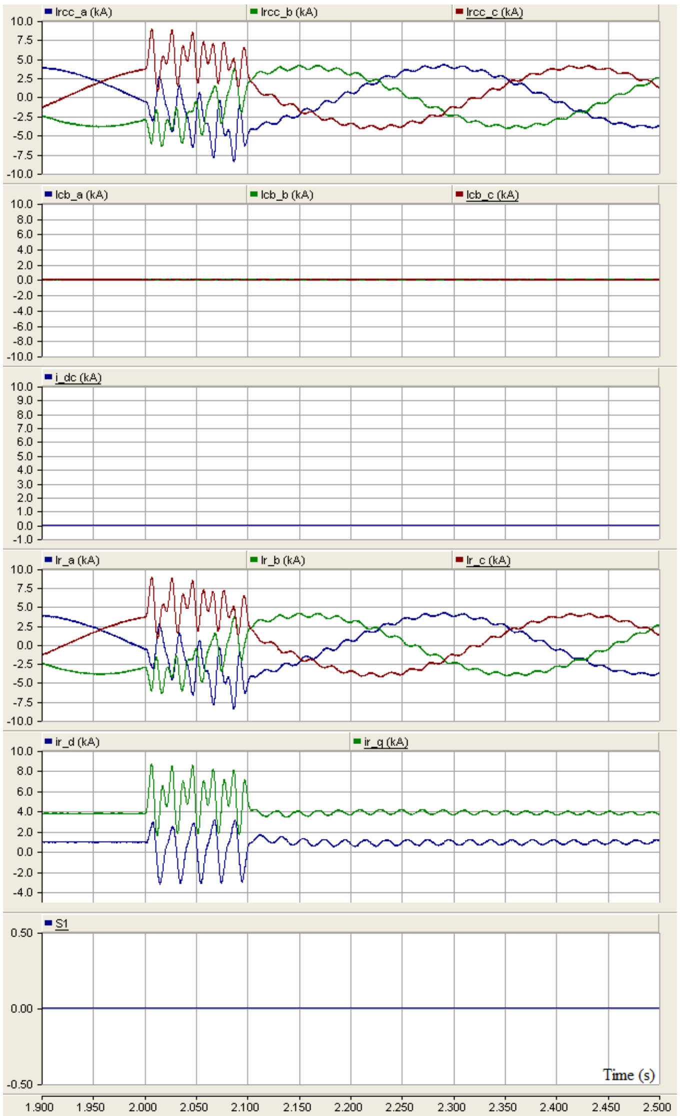

Figure A.4.23: Rotor-side currents behaviours during a 0.8pu 1-phase voltage sag in the case of no involving any protection

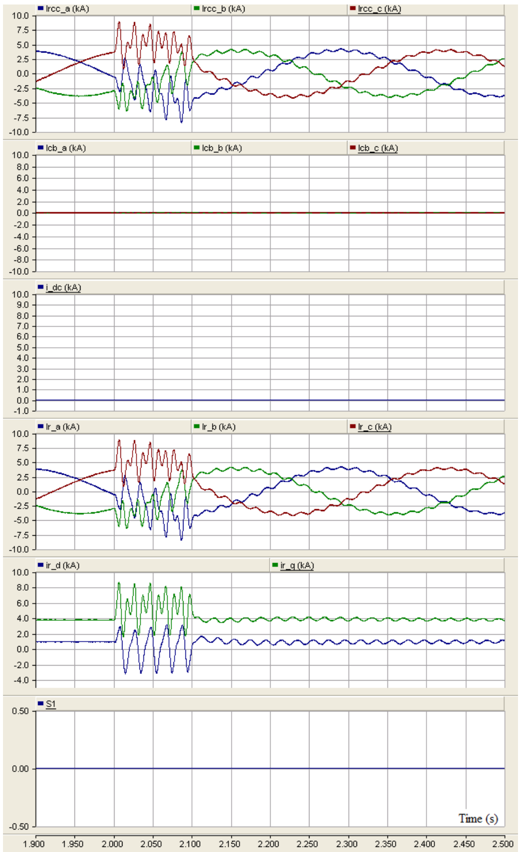

Figure A.4.24: Rotor-side currents behaviours during a 0.8pu 1-phase voltage sag by activating only DC-link brake protection

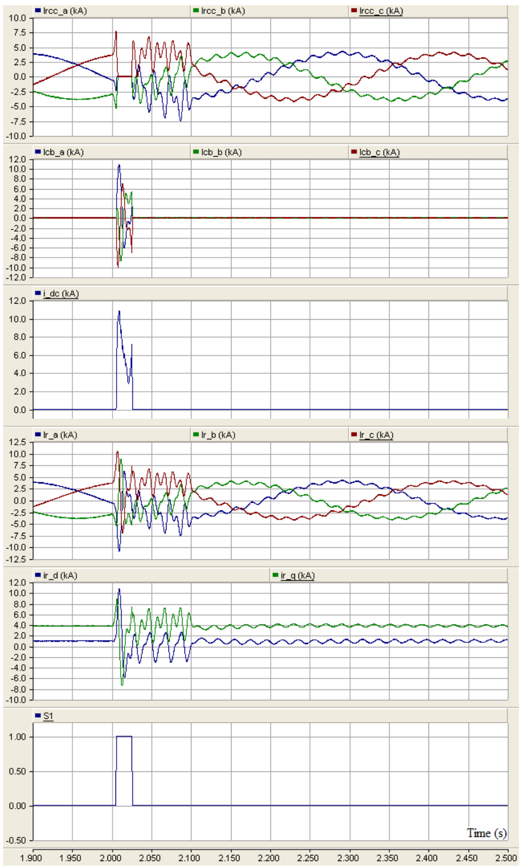

Figure A.4.25: Rotor-side currents behaviours during a 0.8pu 1-phase voltage sag by activating only crowbar protection

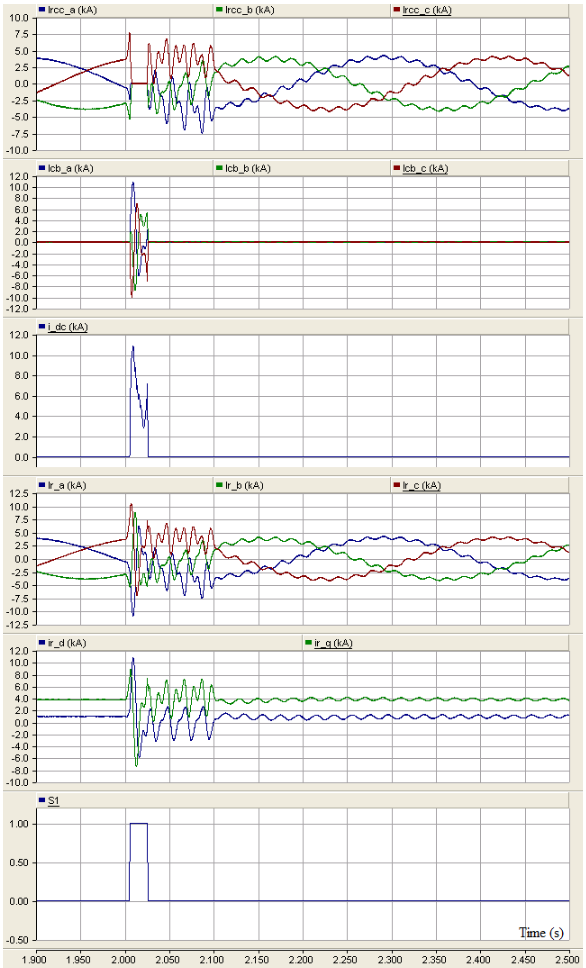

Figure A.4.26: Rotor-side currents behaviours during a 0.8pu 1-phase voltage sag by activating both crowbar and DC-link brake protections

Appendix 5 Sensitivity and Robustness Analyses of RSC Power Loop Control

A.5.1 Sensitivity Analysis

The sensitivity analysis is carried out by varying one tuning parameter each time while other two parameters are held constant at their pre-defined values. First, the variation process is summarised as context in the table. Then, the calculations are done and given in the Excel form. Considering the assumption made ($\frac{K_{io}}{K_D} >> \frac{K_{po}}{K_D}$ is equal to or greater than 10 times), the green coloured operating regions, in which the assumptions made are realised, shown in the Excel tables are picked and worked out. The data existing in the Excel forms are applied to the transfer functions illustrated in Table A.5.1. Finally, related simulation results are obtained and compared each other and as well as with the mathematical calculations.

Rotor-side Converter Outer (Power) Loop PID	$\dfrac{\frac{K_{io}}{K_D}}{s^2+\left(\frac{K_{po}+0.852}{K_D}\right)s+\frac{K_{io}}{K_D}}$	$\dfrac{s\frac{K_{po}}{K_D}+\frac{K_{io}}{K_D}}{s^2+\left(\frac{K_{po}+0.852}{K_D}\right)s+\frac{K_{io}}{K_D}}$	$\dfrac{s^2+s\frac{K_{po}}{K_D}+\frac{K_{io}}{K_D}}{s^2+\left(\frac{K_{po}+0.852}{K_D}\right)s+\frac{K_{io}}{K_D}}$

Table A.5.1: Full (FTF2), simplified (STF2) and second-order approximated (SoATF) transfer functions of the power (outer) loop controller of the RSC

A.5.1.1 Varying Undamped Natural Frequency

The variation process of the undamped natural frequency (f_n) while the damping ratio and K_D are fixed is presented in Table A.5.2.

f_n	Damping Ratio (ζ)	Derivative Gain (K_D)
1Hz	0.7	0.1s
1.5Hz	0.7	0.1s
2Hz	0.7	0.1s
2.5Hz	0.7	0.1s
1Hz	0.8	0.1s
1.5Hz	0.8	0.1s
2Hz	0.8	0.1s
2.5Hz	0.8	0.1s
1Hz	0.9	0.1s
1.5Hz	0.9	0.1s
2Hz	0.9	0.1s
2.5Hz	0.9	0.1s
1Hz	1	0.1s
1.5Hz	1	0.1s
2Hz	1	0.1s
2.5Hz	1	0.1s
1Hz	1.1	0.1s
1.5Hz	1.1	0.1s
2Hz	1.1	0.1s
2.5Hz	1.1	0.1s

Table A.5.2: Varying undamped natural frequency for constant damping ratio and K_D

Varying undamped natural frequency for fixed damping ratio and derivative time constant											
ζ	ω_n (rad/s)	K_d (s)	K_{po}	K_{io} (1/s)	T_{io} (s)	f_n (Hz)	π	Kio / Kd	Kpo / Kd	(Kpo+0.852)/Kd	(Kio/Kd) / (Kpo/Kd)
0.7	6.283	0.1	0.028	3.948	0.253	1	3.142	39.478	0.275	8.795	143.370
0.7	9.425	0.1	0.467	8.883	0.113	1.5	3.142	88.826	4.674	13.194	19.006
0.7	12.566	0.1	0.907	15.791	0.063	2	3.142	157.914	9.072	17.592	17.407
0.7	15.708	0.1	1.347	24.674	0.041	2.5	3.142	246.740	13.470	21.990	18.318
0.8	6.283	0.1	0.153	3.948	0.253	1	3.142	39.478	1.532	10.052	25.769
0.8	9.425	0.1	0.656	8.883	0.113	1.5	3.142	88.826	6.559	15.079	13.544
0.8	12.566	0.1	1.159	15.791	0.063	2	3.142	157.914	11.585	20.105	13.631
0.8	15.708	0.1	1.661	24.674	0.041	2.5	3.142	246.740	16.612	25.132	14.853
0.9	6.283	0.1	0.279	3.948	0.253	1	3.142	39.478	2.789	11.309	14.157
0.9	9.425	0.1	0.844	8.883	0.113	1.5	3.142	88.826	8.444	16.964	10.520
0.9	12.566	0.1	1.410	15.791	0.063	2	3.142	157.914	14.098	22.618	11.201
0.9	15.708	0.1	1.975	24.674	0.041	2.5	3.142	246.740	19.753	28.273	12.491
1	6.283	0.1	0.405	3.948	0.253	1	3.142	39.478	4.045	12.565	9.759
1	9.425	0.1	1.033	8.883	0.113	1.5	3.142	88.826	10.328	18.848	8.600
1	12.566	0.1	1.661	15.791	0.063	2	3.142	157.914	16.612	25.132	9.506
1	15.708	0.1	2.289	24.674	0.041	2.5	3.142	246.740	22.895	31.415	10.777
1.1	6.283	0.1	0.530	3.948	0.253	1	3.142	39.478	5.302	13.822	7.446
1.1	9.425	0.1	1.221	8.883	0.113	1.5	3.142	88.826	12.213	20.733	7.273
1.1	12.566	0.1	1.912	15.791	0.063	2	3.142	157.914	19.125	27.645	8.257
1.1	15.708	0.1	2.604	24.674	0.041	2.5	3.142	246.740	26.036	34.556	9.477

Table A.5.3: The mathematical calculations in Excel table for the case of varying undamped natural frequency

The f_n variation process for fixed damping ratio of 1.1 and K_D of 0.1s is disregarded since all four operating points of the f_n are in red colour.

Rotor-side Converter Outer (Power) Loop PID		$\frac{\frac{K_{io}}{K_D}}{s^2+\left(\frac{K_{po}+0.852}{K_D}\right)s+\frac{K_{io}}{K_D}}$	$\frac{s\frac{K_{po}}{K_D}+\frac{K_{io}}{K_D}}{s^2+\left(\frac{K_{po}+0.852}{K_D}\right)s+\frac{K_{io}}{K_D}}$	$\frac{s^2+s\frac{K_{po}}{K_D}+\frac{K_{io}}{K_D}}{s^2+\left(\frac{K_{po}+0.852}{K_D}\right)s+\frac{K_{io}}{K_D}}$
$\zeta=0.7$ $K_D=0.1s$	$f_n=1Hz$	$\frac{39.5}{s^2+8.8s+39.5}$	$\frac{0.28s+39.5}{s^2+8.8s+39.5}$	$\frac{s^2+0.28s+39.5}{s^2+8.8s+39.5}$
	$f_n=1.5Hz$	$\frac{88.8}{s^2+13.2s+88.8}$	$\frac{4.7s+88.8}{s^2+13.2s+88.8}$	$\frac{s^2+4.7s+88.8}{s^2+13.2s+88.8}$
	$f_n=2Hz$	$\frac{158}{s^2+17.6s+158}$	$\frac{9.1s+158}{s^2+17.6s+158}$	$\frac{s^2+9.1s+158}{s^2+17.6s+158}$
	$f_n=2.5Hz$	$\frac{246.7}{s^2+22s+246.7}$	$\frac{13.5s+246.7}{s^2+22s+246.7}$	$\frac{s^2+13.5s+246.7}{s^2+22s+246.7}$
$\zeta=0.8$ $K_D=0.1s$	$f_n=1Hz$	$\frac{39.5}{s^2+10s+39.5}$	$\frac{1.5s+39.5}{s^2+10s+39.5}$	$\frac{s^2+1.5s+39.5}{s^2+10s+39.5}$
	$f_n=1.5Hz$	$\frac{88.8}{s^2+15s+88.8}$	$\frac{6.56s+88.8}{s^2+15s+88.8}$	$\frac{s^2+6.56s+88.8}{s^2+15s+88.8}$
	$f_n=2Hz$	$\frac{158}{s^2+20s+158}$	$\frac{11.6s+158}{s^2+20s+158}$	$\frac{s^2+11.6s+158}{s^2+20s+158}$
	$f_n=2.5Hz$	$\frac{246.7}{s^2+25.13s+246.7}$	$\frac{16.6s+246.7}{s^2+25.13s+246.7}$	$\frac{s^2+16.6s+246.7}{s^2+25.13s+246.7}$
$\zeta=0.9$ $K_D=0.1s$	$f_n=1Hz$	$\frac{39.5}{s^2+11.3s+39.5}$	$\frac{2.8s+39.5}{s^2+11.3s+39.5}$	$\frac{s^2+2.8s+39.5}{s^2+11.3s+39.5}$
	$f_n=1.5Hz$	$\frac{88.8}{s^2+17s+88.8}$	$\frac{8.45s+88.8}{s^2+17s+88.8}$	$\frac{s^2+8.45s+88.8}{s^2+17s+88.8}$
	$f_n=2Hz$	$\frac{158}{s^2+22.62s+158}$	$\frac{14.1s+158}{s^2+22.62s+158}$	$\frac{s^2+14.1s+158}{s^2+22.62s+158}$
	$f_n=2.5Hz$	$\frac{246.7}{s^2+28.3+246.7}$	$\frac{19.75s+246.7}{s^2+28.3s+246.7}$	$\frac{s^2+19.75s+246.7}{s^2+28.3s+246.7}$
$\zeta=1$ $K_D=0.1s$	$f_n=1Hz$	$\frac{39.5}{s^2+12.565s+39.5}$	$\frac{4.05s+39.5}{s^2+12.565s+39.5}$	$\frac{s^2+4.05s+39.5}{s^2+12.565s+39.5}$
	$f_n=1.5Hz$	$\frac{88.8}{s^2+18.85s+88.8}$	$\frac{10.33s+88.8}{s^2+18.85s+88.8}$	$\frac{s^2+10.33s+88.8}{s^2+18.85s+88.8}$
	$f_n=2Hz$	$\frac{158}{s^2+25.13s+158}$	$\frac{16.6s+158}{s^2+25.13s+158}$	$\frac{s^2+16.6s+158}{s^2+25.13s+158}$
	$f_n=2.5Hz$	$\frac{246.7}{s^2+31.42s+246.7}$	$\frac{23s+246.7}{s^2+31.42s+246.7}$	$\frac{s^2+23s+246.7}{s^2+31.42s+246.7}$
$\zeta=1.1$ $K_D=0.1s$	$f_n=1Hz$	$\frac{39.5}{s^2+13.8s+39.5}$	$\frac{5.3s+39.5}{s^2+13.8s+39.5}$	$\frac{s^2+5.3s+39.5}{s^2+13.8s+39.5}$
	$f_n=1.5Hz$	$\frac{88.8}{s^2+20.74s+88.8}$	$\frac{12.21s+88.8}{s^2+20.74s+88.8}$	$\frac{s^2+12.21s+88.8}{s^2+20.74s+88.8}$
	$f_n=2Hz$	$\frac{158}{s^2+27.65s+158}$	$\frac{19.13s+158}{s^2+27.65s+158}$	$\frac{s^2+19.13s+158}{s^2+27.65s+158}$
	$f_n=2.5Hz$	$\frac{246.7}{s^2+34.56s+246.7}$	$\frac{26.04s+246.7}{s^2+34.56s+246.7}$	$\frac{s^2+26.04s+246.7}{s^2+34.56s+246.7}$

Table A.5.4: Varying f_n – SoATF, STF2, FTF2

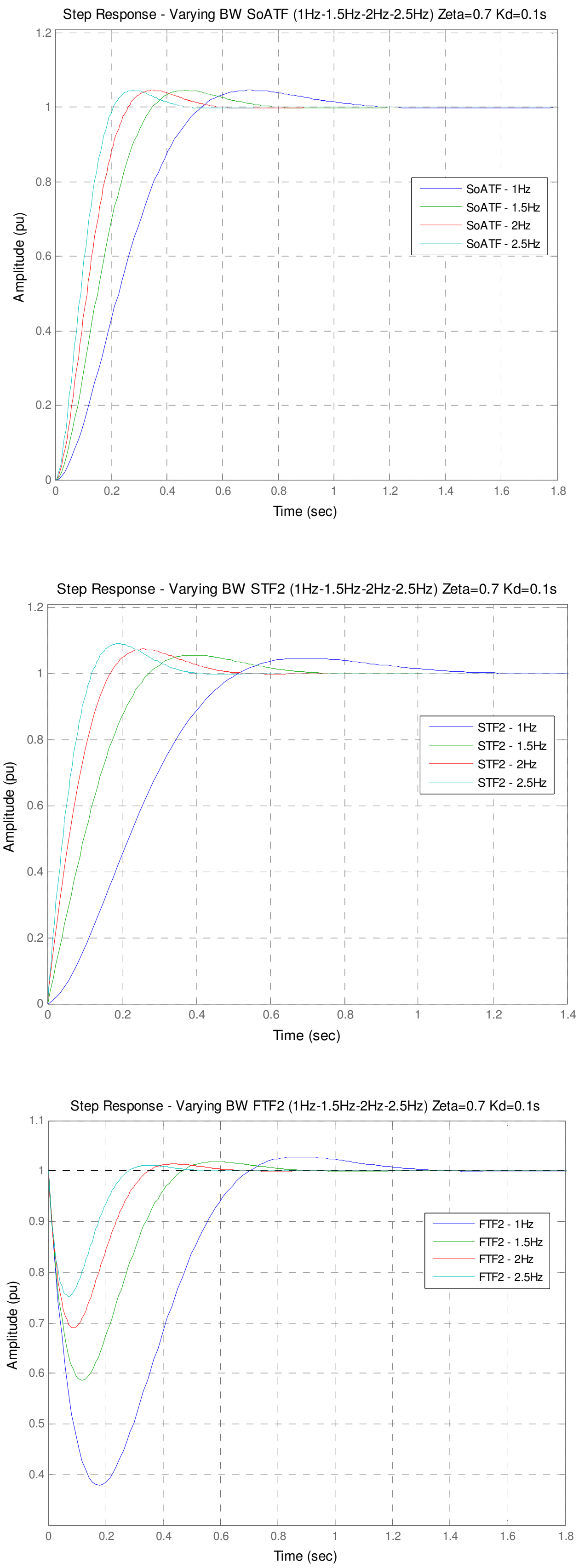

Figure A.5.1: Varying f_n – step responses of SoATF, STF2 and FTF2 ζ=0.7 and K_D=0.1s

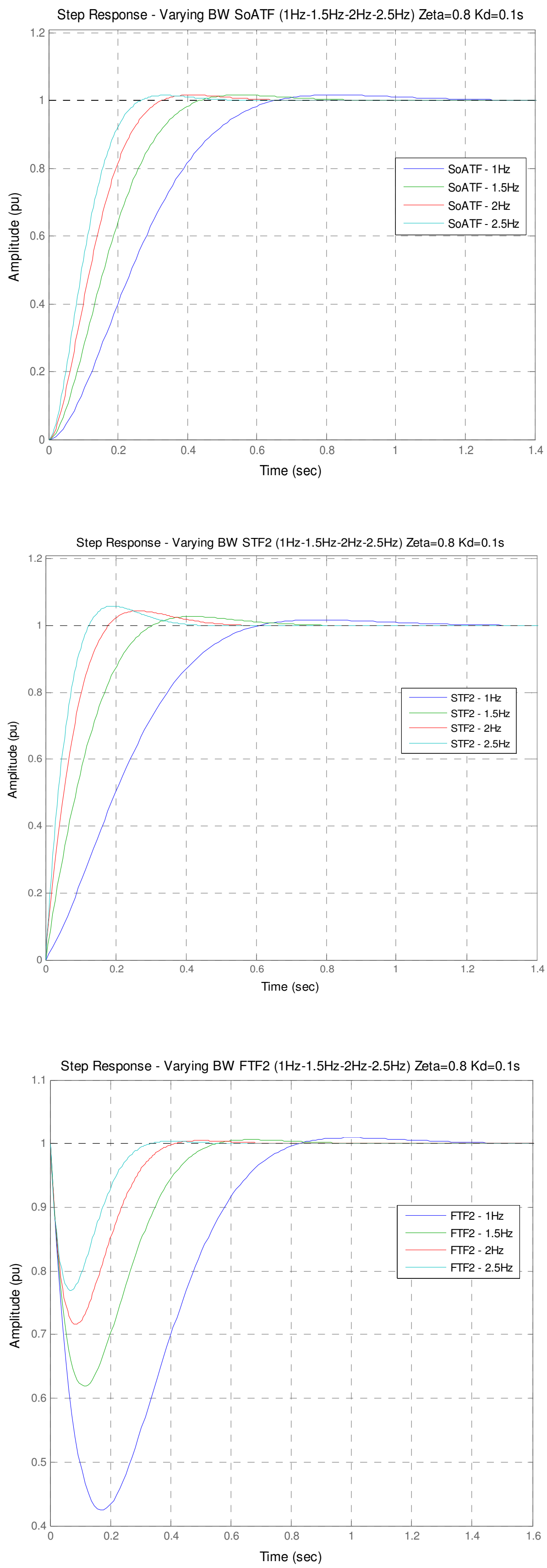

Figure A.5.2: Varying f_n – step responses of SoATF, STF2 and FTF2
ζ=0.8 and K_D=0.1s

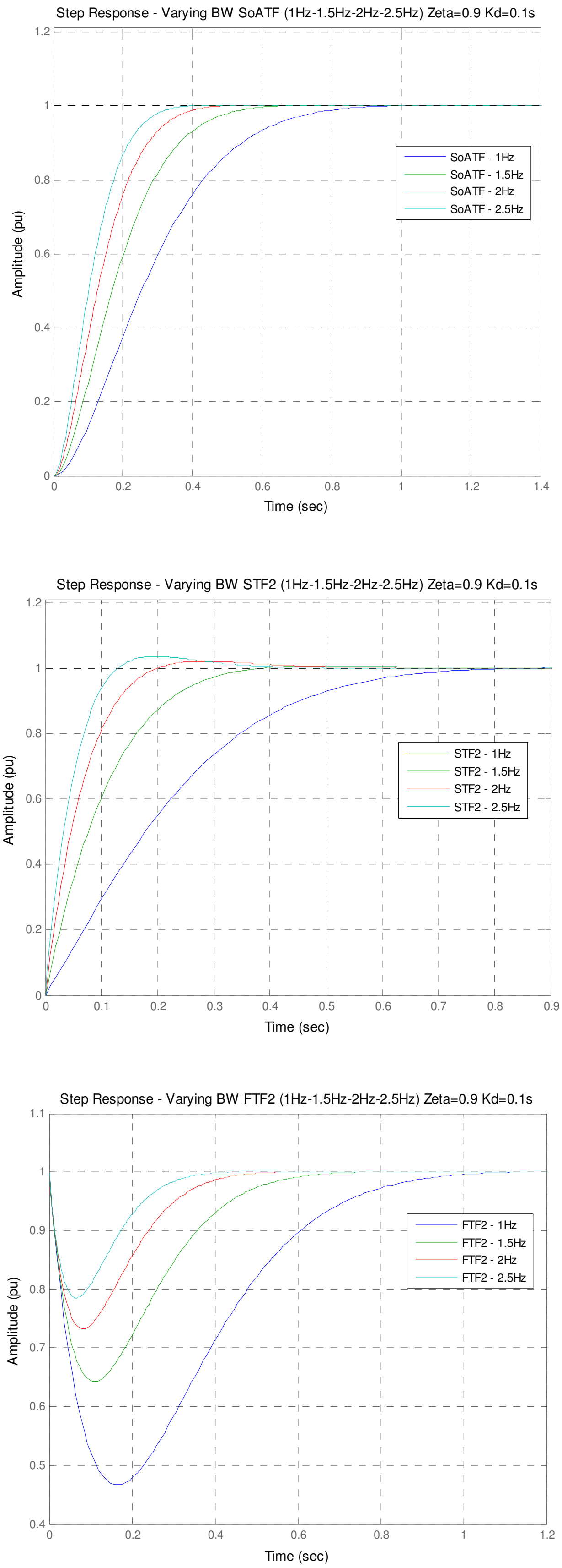

Figure A.5.3: Varying f_n – step responses of SoATF, STF2 and FTF2
ζ=0.9 and K_D=0.1s

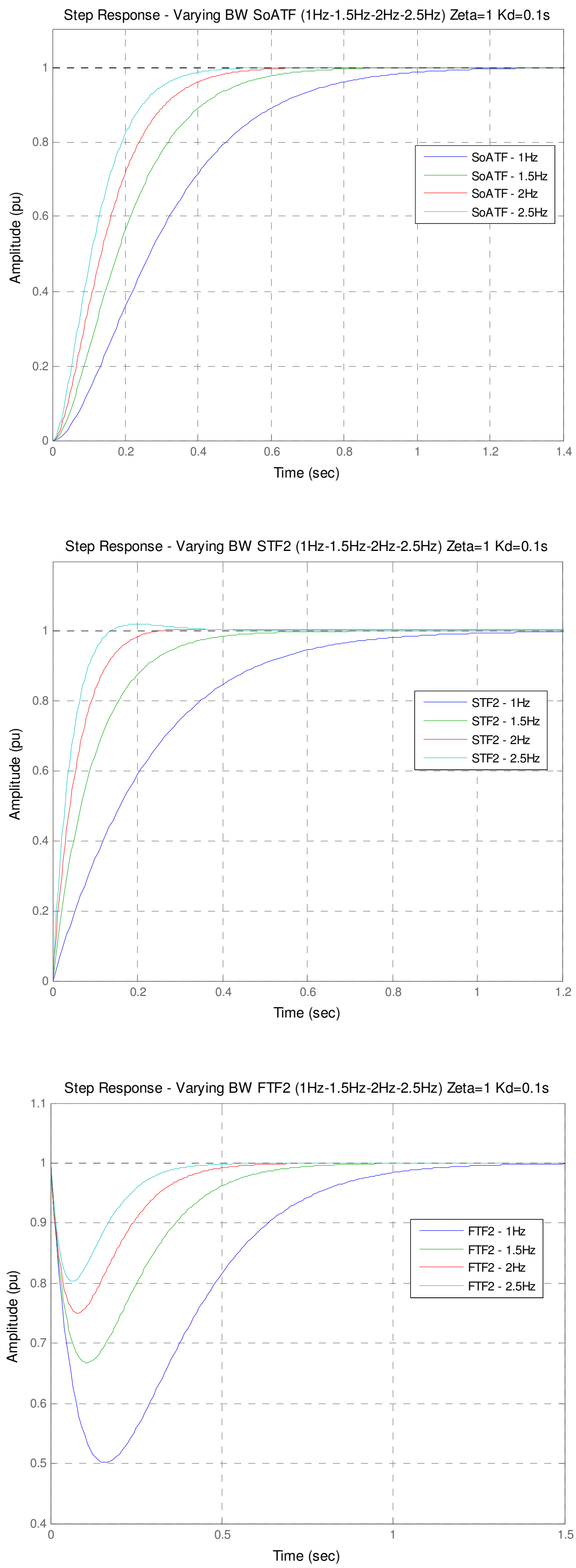

Figure A.5.4: Varying f_n – step responses of SoATF, STF2 and FTF2
ζ=1 and K_D=0.1s

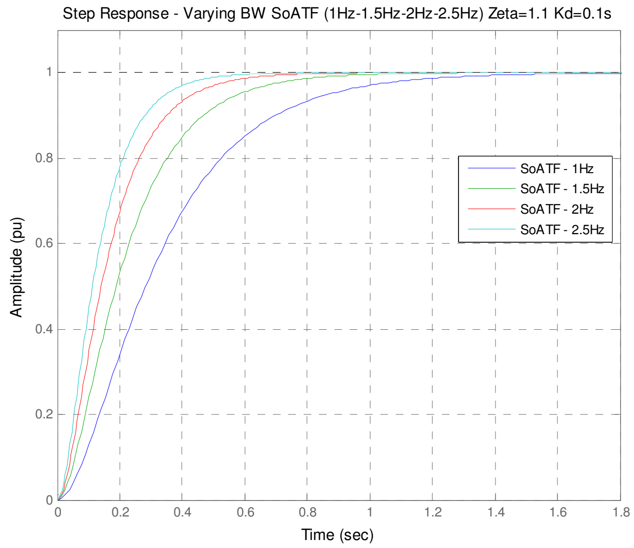

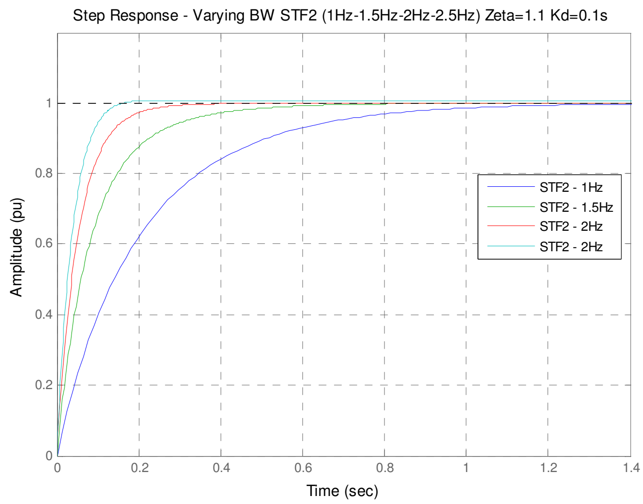

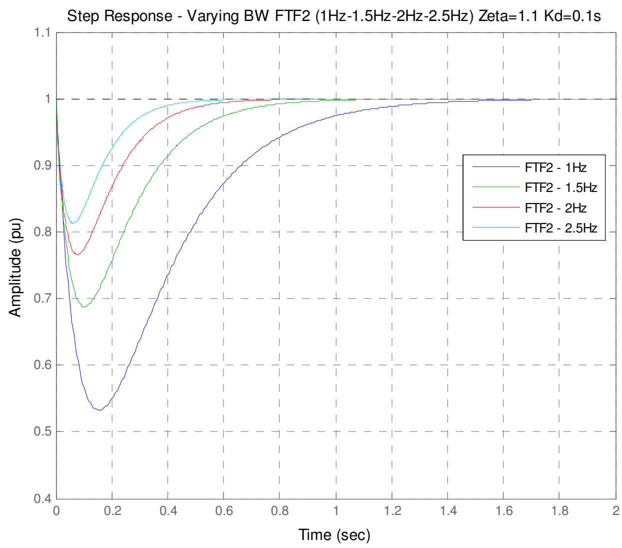

Figure A.5.5: Varying f_n – step responses of SoATF, STF2 and FTF2 ζ=1.1 and K_D=0.1s

A.5.1.2 Varying Damping Ratio

The range of variation damping ratio for the fixed f_n and K_D is given below in Table A.5.5.

Damping Ratio (ζ)	f_n	Derivative Gain (K_D)
0.7	1Hz	0.1s
0.8	1Hz	0.1s
0.9	1Hz	0.1s
1	1Hz	0.1s
1.1	1Hz	0.1s
0.7	1.5Hz	0.1s
0.8	1.5Hz	0.1s
0.9	1.5Hz	0.1s
1	1.5Hz	0.1s
1.1	1.5Hz	0.1s
0.7	2Hz	0.1s
0.8	2Hz	0.1s
0.9	2Hz	0.1s
1	2Hz	0.1s
1.1	2Hz	0.1s
0.7	2.5Hz	0.1s
0.8	2.5Hz	0.1s
0.9	2.5Hz	0.1s
1	2.5Hz	0.1s
1.1	2.5Hz	0.1s

Table A.5.5: Varying damping ratio for constant f_n and K_D

Varying damping ratio for fixed undamped natural frequency and derivative time constant											
ζ	ω_n (rad/s)	K_d (s)	K_{po}	K_{io} (1/s)	T_{io} (s)	f_n (Hz)	π	Kio / Kd	Kpo / Kd	(Kpo+0.852)/Kd	(Kio/Kd) / (Kpo/Kd)
0.7	6.283	0.1	0.028	3.948	0.253	1	3.142	39.478	0.275	8.795	143.370
0.8	6.283	0.1	0.153	3.948	0.253	1	3.142	39.478	1.532	10.052	25.769
0.9	6.283	0.1	0.279	3.948	0.253	1	3.142	39.478	2.789	11.309	14.157
1	6.283	0.1	0.405	3.948	0.253	1	3.142	39.478	4.045	12.565	9.759
1.1	6.283	0.1	0.530	3.948	0.253	1	3.142	39.478	5.302	13.822	7.446
0.7	9.425	0.1	0.467	8.883	0.113	1.5	3.142	88.826	4.674	13.194	19.006
0.8	9.425	0.1	0.656	8.883	0.113	1.5	3.142	88.826	6.559	15.079	13.544
0.9	9.425	0.1	0.844	8.883	0.113	1.5	3.142	88.826	8.444	16.964	10.520
1	9.425	0.1	1.033	8.883	0.113	1.5	3.142	88.826	10.328	18.848	8.600
1.1	9.425	0.1	1.221	8.883	0.113	1.5	3.142	88.826	12.213	20.733	7.273
0.7	12.566	0.1	0.907	15.791	0.063	2	3.142	157.914	9.072	17.592	17.407
0.8	12.566	0.1	1.159	15.791	0.063	2	3.142	157.914	11.585	20.105	13.631
0.9	12.566	0.1	1.410	15.791	0.063	2	3.142	157.914	14.098	22.618	11.201
1	12.566	0.1	1.661	15.791	0.063	2	3.142	157.914	16.612	25.132	9.506
1.1	12.566	0.1	1.912	15.791	0.063	2	3.142	157.914	19.125	27.645	8.257
0.7	15.708	0.1	1.347	24.674	0.041	2.5	3.142	246.740	13.470	21.990	18.318
0.8	15.708	0.1	1.661	24.674	0.041	2.5	3.142	246.740	16.612	25.132	14.853
0.9	15.708	0.1	1.975	24.674	0.041	2.5	3.142	246.740	19.753	28.273	12.491
1	15.708	0.1	2.289	24.674	0.041	2.5	3.142	246.740	22.895	31.415	10.777
1.1	15.708	0.1	2.604	24.674	0.041	2.5	3.142	246.740	26.036	34.556	9.477

Table A.5.6: The mathematical calculations in Excel table for the case of varying damping ratio

Rotor-side Converter Outer (Power) Loop PID		$\frac{\frac{K_{io}}{K_D}}{s^2+\left(\frac{K_{po}+0.852}{K_D}\right)s+\frac{K_{io}}{K_D}}$	$\frac{s\frac{K_{po}}{K_D}+\frac{K_{io}}{K_D}}{s^2+\left(\frac{K_{po}+0.852}{K_D}\right)s+\frac{K_{io}}{K_D}}$	$\frac{s^2+s\frac{K_{po}}{K_D}+\frac{K_{io}}{K_D}}{s^2+\left(\frac{K_{po}+0.852}{K_D}\right)s+\frac{K_{io}}{K_D}}$
f_n=1Hz K_D=0.1s	ζ=0.7	$\frac{39.5}{s^2+8.8s+39.5}$	$\frac{0.28s+39.5}{s^2+8.8s+39.5}$	$\frac{s^2+0.28s+39.5}{s^2+8.8s+39.5}$
	ζ=0.8	$\frac{39.5}{s^2+10s+39.5}$	$\frac{1.5s+39.5}{s^2+10s+39.5}$	$\frac{s^2+1.5s+39.5}{s^2+10s+39.5}$
	ζ=0.9	$\frac{39.5}{s^2+11.3s+39.5}$	$\frac{2.8s+39.5}{s^2+11.3s+39.5}$	$\frac{s^2+2.8s+39.5}{s^2+11.3s+39.5}$
	ζ=1	$\frac{39.5}{s^2+12.565s+39.5}$	$\frac{4.05s+39.5}{s^2+12.565s+39.5}$	$\frac{s^2+4.05s+39.5}{s^2+12.565s+39.5}$
	ζ=1.1	$\frac{39.5}{s^2+13.8s+39.5}$	$\frac{5.3s+39.5}{s^2+13.8s+39.5}$	$\frac{s^2+5.3s+39.5}{s^2+13.8s+39.5}$
f_n=1.5Hz K_D=0.1s	ζ=0.7	$\frac{88.8}{s^2+13.2s+88.8}$	$\frac{4.7s+88.8}{s^2+13.2s+88.8}$	$\frac{s^2+4.7s+88.8}{s^2+13.2s+88.8}$
	ζ=0.8	$\frac{88.8}{s^2+15s+88.8}$	$\frac{6.56s+88.8}{s^2+15s+88.8}$	$\frac{s^2+6.56s+88.8}{s^2+15s+88.8}$
	ζ=0.9	$\frac{88.8}{s^2+17s+88.8}$	$\frac{8.45s+88.8}{s^2+17s+88.8}$	$\frac{s^2+8.45s+88.8}{s^2+17s+88.8}$
	ζ=1	$\frac{88.8}{s^2+18.85s+88.8}$	$\frac{10.33s+88.8}{s^2+18.85s+88.8}$	$\frac{s^2+10.33s+88.8}{s^2+18.85s+88.8}$
	ζ=1.1	$\frac{88.8}{s^2+20.74s+88.8}$	$\frac{12.21s+88.8}{s^2+20.74s+88.8}$	$\frac{s^2+12.21s+88.8}{s^2+20.74s+88.8}$
f_n=2Hz K_D=0.1s	ζ=0.7	$\frac{158}{s^2+17.6s+158}$	$\frac{9.1s+158}{s^2+17.6s+158}$	$\frac{s^2+9.1s+158}{s^2+17.6s+158}$
	ζ=0.8	$\frac{158}{s^2+20s+158}$	$\frac{11.6s+158}{s^2+20s+158}$	$\frac{s^2+11.6s+158}{s^2+20s+158}$
	ζ=0.9	$\frac{158}{s^2+22.62s+158}$	$\frac{14.1s+158}{s^2+22.62s+158}$	$\frac{s^2+14.1s+158}{s^2+22.62s+158}$
	ζ=1	$\frac{158}{s^2+25.13s+158}$	$\frac{16.6s+158}{s^2+25.13s+158}$	$\frac{s^2+16.6s+158}{s^2+25.13s+158}$
	ζ=1.1	$\frac{158}{s^2+27.65s+158}$	$\frac{19.13s+158}{s^2+27.65s+158}$	$\frac{s^2+19.13s+158}{s^2+27.65s+158}$
f_n=2.5Hz K_D=0.1s	ζ=0.7	$\frac{246.7}{s^2+22s+246.7}$	$\frac{13.5s+246.7}{s^2+22s+246.7}$	$\frac{s^2+13.5s+246.7}{s^2+22s+246.7}$
	ζ=0.8	$\frac{246.7}{s^2+25.13s+246.7}$	$\frac{16.6s+246.7}{s^2+25.13s+246.7}$	$\frac{s^2+16.6s+246.7}{s^2+25.13s+246.7}$
	ζ=0.9	$\frac{246.7}{s^2+28.3+246.7}$	$\frac{19.75s+246.7}{s^2+28.3s+246.7}$	$\frac{s^2+19.75s+246.7}{s^2+28.3s+246.7}$
	ζ=1	$\frac{246.7}{s^2+31.42s+246.7}$	$\frac{23s+246.7}{s^2+31.42s+246.7}$	$\frac{s^2+23s+246.7}{s^2+31.42s+246.7}$
	ζ=1.1	$\frac{246.7}{s^2+34.56s+246.7}$	$\frac{26.04s+246.7}{s^2+34.56s+246.7}$	$\frac{s^2+26.04s+246.7}{s^2+34.56s+246.7}$

Table A.5.7: Varying damping ratio – SoATF, STF2, FTF2

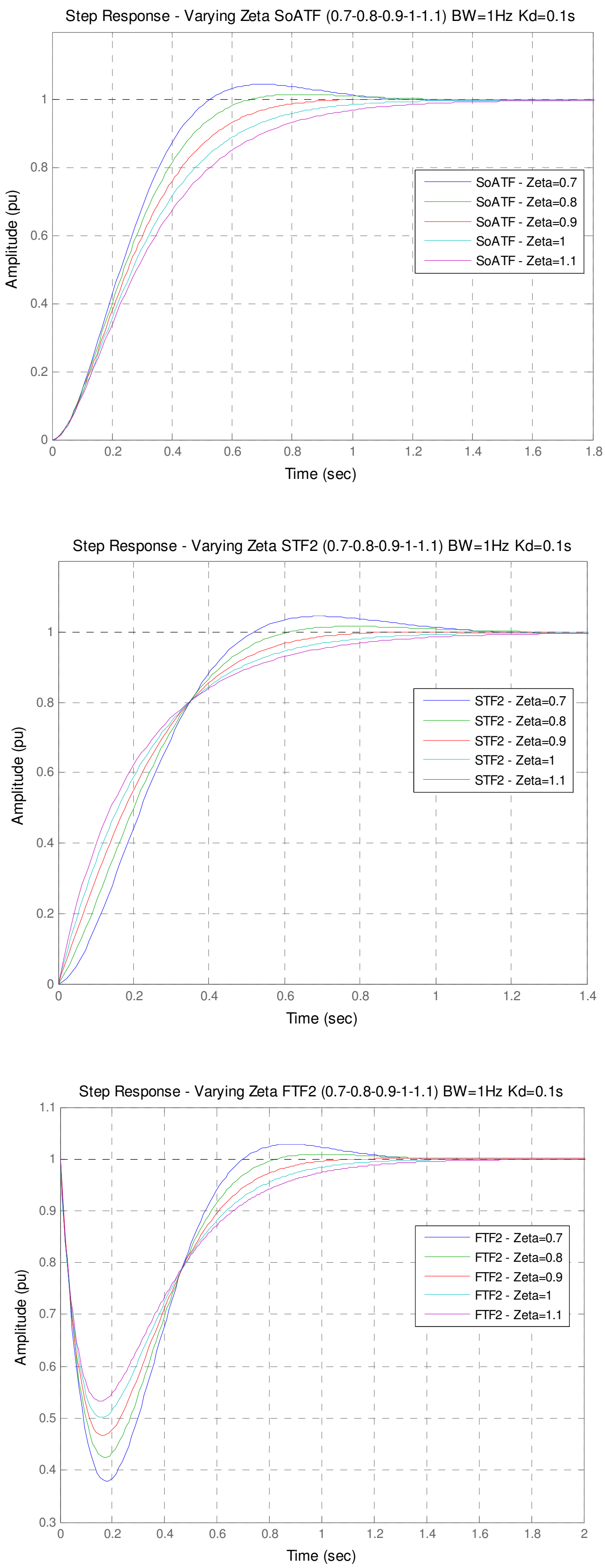

Figure A.5.6: Varying damping ratio – step responses of SoATF, STF2 and FTF2 f_n=1Hz and K_D=0.1s

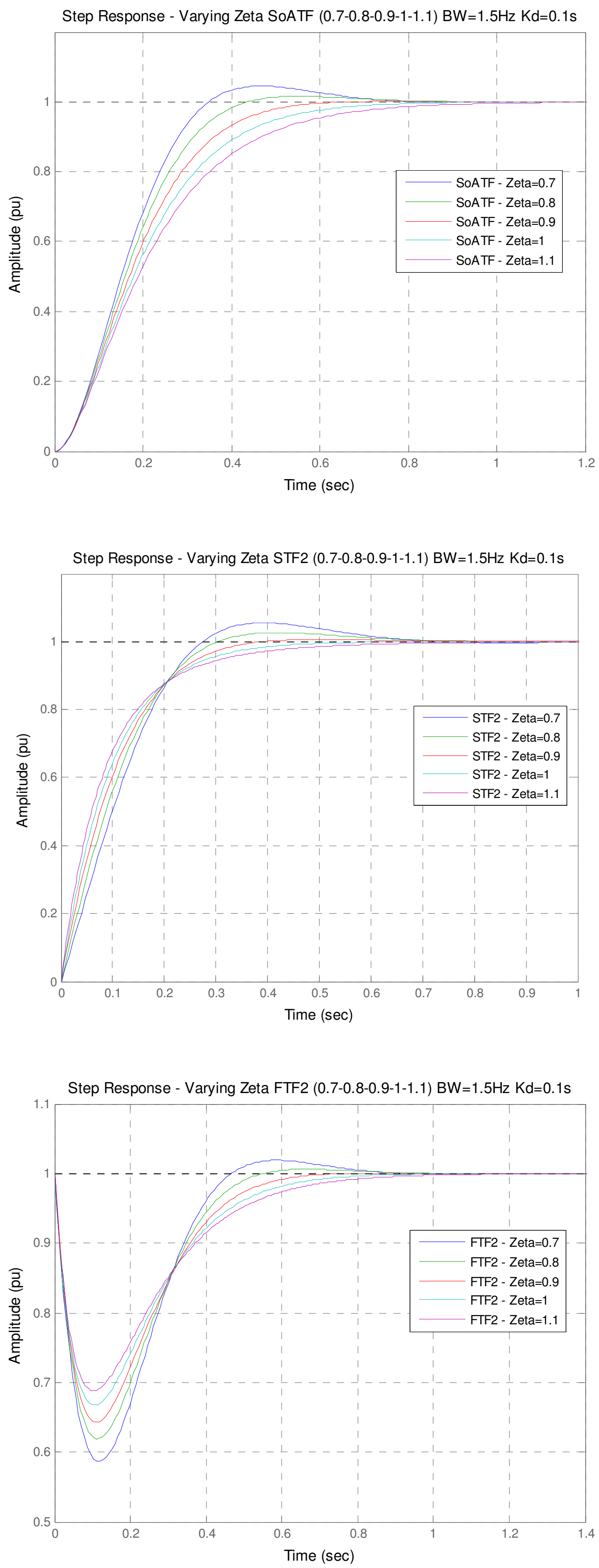

Figure A.5.7: Varying damping ratio – step responses of SoATF, STF2 and FTF2
f_n=1.5Hz and K_D=0.1s

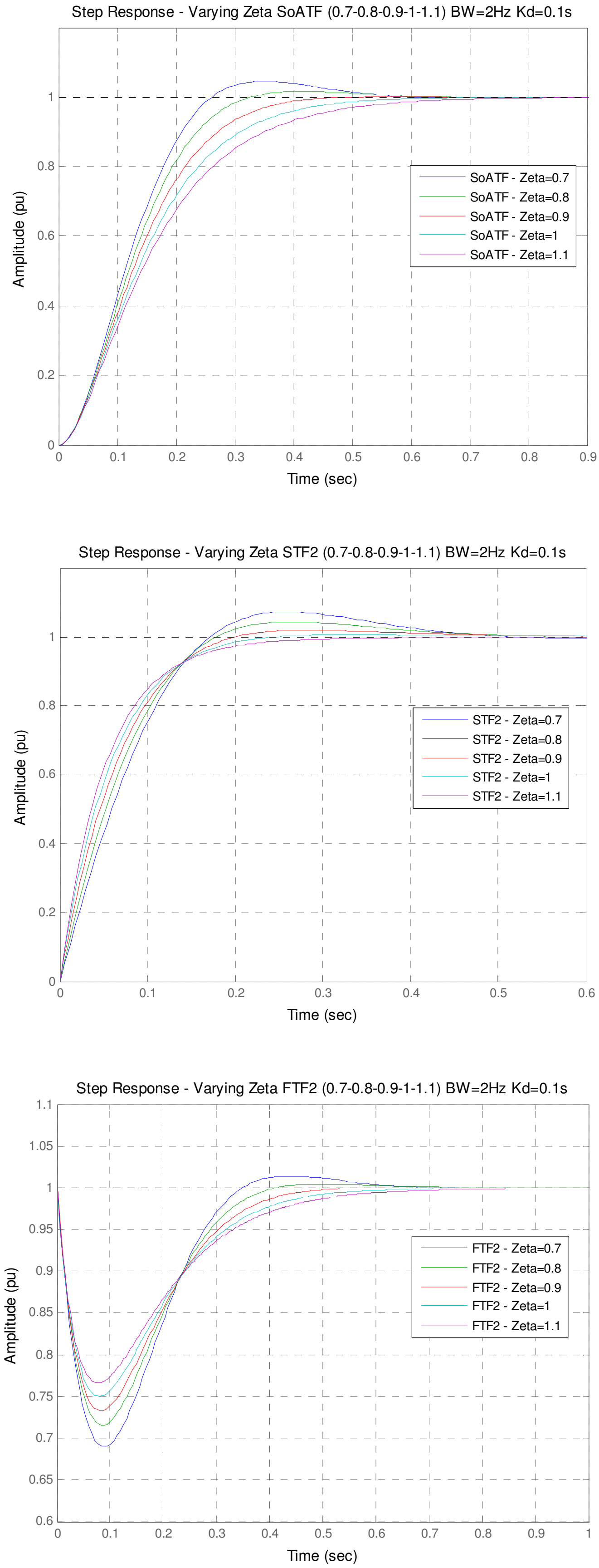

Figure A.5.8: Varying damping ratio – step responses of SoATF, STF2 and FTF2 f_n=2Hz and K_D=0.1s

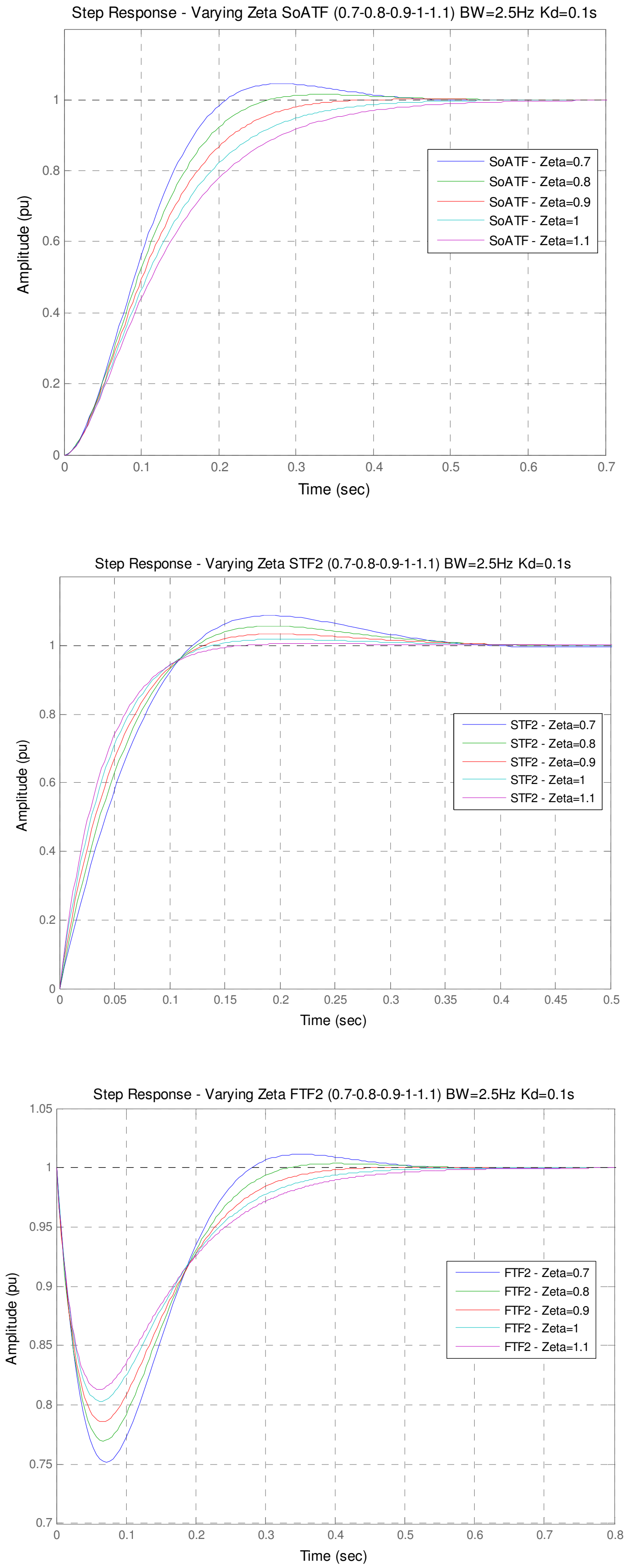

Figure A.5.9: Varying damping ratio – step responses of SoATF, STF2 and FTF2 f_n=2.5Hz and K_D=0.1s

A.5.1.3 Varying K_D

The analysis of varying K_D is presented in Tables A.5.8 to A.5.12.

Derivative Gain (K_D)	Damping Ratio (ζ)	f_n
0.1s	0.7	1Hz
0.2s	0.7	1Hz
0.3s	0.7	1Hz
0.4s	0.7	1Hz
0.1s	0.7	1.5Hz
0.2s	0.7	1.5Hz
0.3s	0.7	1.5Hz
0.4s	0.7	1.5Hz
0.1s	0.7	2Hz
0.2s	0.7	2Hz
0.3s	0.7	2Hz
0.4s	0.7	2Hz
0.1s	0.7	2.5Hz
0.2s	0.7	2.5Hz
0.3s	0.7	2.5Hz
0.4s	0.7	2.5Hz

Table A.5.8: Varying K_D for constant f_n and damping ratio (0.7)

Derivative Gain (K_D)	Damping Ratio (ζ)	f_n
0.1s	0.8	1Hz
0.2s	0.8	1Hz
0.3s	0.8	1Hz
0.4s	0.8	1Hz
0.1s	0.8	1.5Hz
0.2s	0.8	1.5Hz
0.3s	0.8	1.5Hz
0.4s	0.8	1.5Hz
0.1s	0.8	2Hz
0.2s	0.8	2Hz
0.3s	0.8	2Hz
0.4s	0.8	2Hz
0.1s	0.8	2.5Hz
0.2s	0.8	2.5Hz
0.3s	0.8	2.5Hz
0.4s	0.8	2.5Hz

Table A.5.9: Varying K_D for constant f_n and damping ratio (0.8)

Derivative Gain (K_D)	Damping Ratio (ζ)	f_n
0.1s	0.9	1Hz
0.2s	0.9	1Hz
0.3s	0.9	1Hz
0.4s	0.9	1Hz
0.1s	0.9	1.5Hz
0.2s	0.9	1.5Hz
0.3s	0.9	1.5Hz
0.4s	0.9	1.5Hz
0.1s	0.9	2Hz
0.2s	0.9	2Hz
0.3s	0.9	2Hz
0.4s	0.9	2Hz
0.1s	0.9	2.5Hz
0.2s	0.9	2.5Hz
0.3s	0.9	2.5Hz
0.4s	0.9	2.5Hz

Table A.5.10: Varying K_D for constant f_n and damping ratio (0.9)

Derivative Gain (K_D)	Damping Ratio (ζ)	f_n
0.1s	1	1Hz
0.2s	1	1Hz
0.3s	1	1Hz
0.4s	1	1Hz
0.1s	1	1.5Hz
0.2s	1	1.5Hz
0.3s	1	1.5Hz
0.4s	1	1.5Hz
0.1s	1	2Hz
0.2s	1	2Hz
0.3s	1	2Hz
0.4s	1	2Hz
0.1s	1	2.5Hz
0.2s	1	2.5Hz
0.3s	1	2.5Hz
0.4s	1	2.5Hz

Table A.5.11: Varying K_D for constant f_n and damping ratio (1)

Derivative Gain (K_D)	Damping Ratio (ζ)	f_n
0.1s	1.1	1Hz
0.2s	1.1	1Hz
0.3s	1.1	1Hz
0.4s	1.1	1Hz
0.1s	1.1	1.5Hz
0.2s	1.1	1.5Hz
0.3s	1.1	1.5Hz
0.4s	1.1	1.5Hz
0.1s	1.1	2Hz
0.2s	1.1	2Hz
0.3s	1.1	2Hz
0.4s	1.1	2Hz
0.1s	1.1	2.5Hz
0.2s	1.1	2.5Hz
0.3s	1.1	2.5Hz
0.4s	1.1	2.5Hz

Table A.5.12: Varying K_D for constant f_n and damping ratio (1.1)

The K_D variation process for fixed damping ratio of 1 and f_n of 1Hz-1.5Hz-2Hz, and that for fixed damping ratio of 1.1 and f_n of 1Hz-1.5Hz-2Hz-2.5Hz are disregarded since they are all in red colour which means that they disprove the assumption made in section A.5.1.

Varying derivative time constant for fixed undamped natural frequency and damping ratio											
ζ	ω_n (rad/s)	K_d (s)	K_{po}	K_{io} (1/s)	T_{io} (s)	f_n (Hz)	π	Kio / Kd	Kpo / Kd	(Kpo+0.852)/Kd	(Kio/Kd) / (Kpo/Kd)
0.7	6.283	0.1	0.028	3.948	0.253	1	3.142	39.478	0.275	8.795	143.370
0.7	6.283	0.2	0.907	7.896	0.127	1	3.142	39.478	4.536	8.796	8.704
0.7	6.283	0.3	1.787	11.844	0.084	1	3.142	39.478	5.956	8.796	6.628
0.7	6.283	0.4	2.666	15.791	0.063	1	3.142	39.478	6.666	8.796	5.922
0.7	9.425	0.1	0.467	8.883	0.113	1.5	3.142	88.826	4.674	13.194	19.006
0.7	9.425	0.2	1.787	17.765	0.056	1.5	3.142	88.826	8.934	13.194	9.942
0.7	9.425	0.3	3.106	26.648	0.038	1.5	3.142	88.826	10.354	13.194	8.579
0.7	9.425	0.4	4.426	35.531	0.028	1.5	3.142	88.826	11.064	13.194	8.028
0.7	12.566	0.1	0.907	15.791	0.063	2	3.142	157.914	9.072	17.592	17.407
0.7	12.566	0.2	2.666	31.583	0.032	2	3.142	157.914	13.332	17.592	11.844
0.7	12.566	0.3	4.426	47.374	0.021	2	3.142	157.914	14.753	17.593	10.704
0.7	12.566	0.4	6.185	63.165	0.016	2	3.142	157.914	15.463	17.593	10.213
0.7	15.708	0.1	1.347	24.674	0.041	2.5	3.142	246.740	13.470	21.990	18.318
0.7	15.708	0.2	3.546	49.348	0.020	2.5	3.142	246.740	17.731	21.991	13.916
0.7	15.708	0.3	5.745	74.022	0.014	2.5	3.142	246.740	19.151	21.991	12.884
0.7	15.708	0.4	7.944	98.696	0.010	2.5	3.142	246.740	19.861	21.991	12.423

Table A.5.13: The mathematical calculations in Excel table for the case of varying K_D (ζ=0.7)

		Varying derivative time constant for fixed undamped natural frequency and damping ratio									
ζ	ω_n (rad/s)	K_d (s)	K_{po}	K_{io} (1/s)	T_{io} (s)	f_n (Hz)	π	Kio / Kd	Kpo / Kd	(Kpo+0.852)/Kd	(Kio/Kd) / (Kpo/Kd)
0.8	6.283	0.1	0.153	3.948	0.253	1	3.142	39.478	1.532	10.052	25.769
0.8	6.283	0.2	1.159	7.896	0.127	1	3.142	39.478	5.793	10.053	6.815
0.8	6.283	0.3	2.164	11.844	0.084	1	3.142	39.478	7.213	10.053	5.473
0.8	6.283	0.4	3.169	15.791	0.063	1	3.142	39.478	7.923	10.053	4.983
0.8	9.425	0.1	0.656	8.883	0.113	1.5	3.142	88.826	6.559	15.079	13.544
0.8	9.425	0.2	2.164	17.765	0.056	1.5	3.142	88.826	10.819	15.079	8.210
0.8	9.425	0.3	3.672	26.648	0.038	1.5	3.142	88.826	12.239	15.079	7.257
0.8	9.425	0.4	5.180	35.531	0.028	1.5	3.142	88.826	12.949	15.079	6.860
0.8	12.566	0.1	1.159	15.791	0.063	2	3.142	157.914	11.585	20.105	13.631
0.8	12.566	0.2	3.169	31.583	0.032	2	3.142	157.914	15.846	20.106	9.966
0.8	12.566	0.3	5.180	47.374	0.021	2	3.142	157.914	17.266	20.106	9.146
0.8	12.566	0.4	7.190	63.165	0.016	2	3.142	157.914	17.976	20.106	8.785
0.8	15.708	0.1	1.661	24.674	0.041	2.5	3.142	246.740	16.612	25.132	14.853
0.8	15.708	0.2	4.174	49.348	0.020	2.5	3.142	246.740	20.872	25.132	11.821
0.8	15.708	0.3	6.688	74.022	0.014	2.5	3.142	246.740	22.292	25.132	11.068
0.8	15.708	0.4	9.201	98.696	0.010	2.5	3.142	246.740	23.002	25.132	10.727

Table A.5.14: The mathematical calculations in Excel table for the case of varying K_D (ζ=0.8)

	Varying derivative time constant for fixed undamped natural frequency and damping ratio										
ζ	ω_n (rad/s)	K_d (s)	K_{po}	K_{io} (1/s)	T_{io} (s)	f_n (Hz)	π	Kio / Kd	Kpo / Kd	(Kpo+0.852)/Kd	(Kio/Kd) / (Kpo/Kd)
0.9	6.283	0.1	0.279	3.948	0.253	1	3.142	39.478	2.789	11.309	14.157
0.9	6.283	0.2	1.410	7.896	0.127	1	3.142	39.478	7.049	11.309	5.600
0.9	6.283	0.3	2.541	11.844	0.084	1	3.142	39.478	8.469	11.309	4.661
0.9	6.283	0.4	3.672	15.791	0.063	1	3.142	39.478	9.179	11.309	4.301
0.9	9.425	0.1	0.844	8.883	0.113	1.5	3.142	88.826	8.444	16.964	10.520
0.9	9.425	0.2	2.541	17.765	0.056	1.5	3.142	88.826	12.704	16.964	6.992
0.9	9.425	0.3	4.237	26.648	0.038	1.5	3.142	88.826	14.124	16.964	6.289
0.9	9.425	0.4	5.934	35.531	0.028	1.5	3.142	88.826	14.834	16.964	5.988
0.9	12.566	0.1	1.410	15.791	0.063	2	3.142	157.914	14.098	22.618	11.201
0.9	12.566	0.2	3.672	31.583	0.032	2	3.142	157.914	18.359	22.619	8.601
0.9	12.566	0.3	5.934	47.374	0.021	2	3.142	157.914	19.779	22.619	7.984
0.9	12.566	0.4	8.196	63.165	0.016	2	3.142	157.914	20.489	22.619	7.707
0.9	15.708	0.1	1.975	24.674	0.041	2.5	3.142	246.740	19.753	28.273	12.491
0.9	15.708	0.2	4.803	49.348	0.020	2.5	3.142	246.740	24.014	28.274	10.275
0.9	15.708	0.3	7.630	74.022	0.014	2.5	3.142	246.740	25.434	28.274	9.701
0.9	15.708	0.4	10.458	98.696	0.010	2.5	3.142	246.740	26.144	28.274	9.438

Table A.5.15: The mathematical calculations in Excel table for the case of varying K_D (ζ=0.9)

	Varying derivative time constant for fixed undamped natural frequency and damping ratio										
ζ	ω_n (rad/s)	K_d (s)	K_{po}	K_{io} (1/s)	T_{io} (s)	f_n (Hz)	π	Kio / Kd	Kpo / Kd	(Kpo+0.852)/Kd	(Kio/Kd) / (Kpo/Kd)
1	6.283	0.1	0.405	3.948	0.253	1	3.142	39.478	4.045	12.565	9.759
1	6.283	0.2	1.661	7.896	0.127	1	3.142	39.478	8.306	12.566	4.753
1	6.283	0.3	2.918	11.844	0.084	1	3.142	39.478	9.726	12.566	4.059
1	6.283	0.4	4.174	15.791	0.063	1	3.142	39.478	10.436	12.566	3.783
1	9.425	0.1	1.033	8.883	0.113	1.5	3.142	88.826	10.328	18.848	8.600
1	9.425	0.2	2.918	17.765	0.056	1.5	3.142	88.826	14.589	18.849	6.089
1	9.425	0.3	4.803	26.648	0.038	1.5	3.142	88.826	16.009	18.849	5.548
1	9.425	0.4	6.688	35.531	0.028	1.5	3.142	88.826	16.719	18.849	5.313
1	12.566	0.1	1.661	15.791	0.063	2	3.142	157.914	16.612	25.132	9.506
1	12.566	0.2	4.174	31.583	0.032	2	3.142	157.914	20.872	25.132	7.566
1	12.566	0.3	6.688	47.374	0.021	2	3.142	157.914	22.292	25.132	7.084
1	12.566	0.4	9.201	63.165	0.016	2	3.142	157.914	23.002	25.132	6.865
1	15.708	0.1	2.289	24.674	0.041	2.5	3.142	246.740	22.895	31.415	10.777
1	15.708	0.2	5.431	49.348	0.020	2.5	3.142	246.740	27.155	31.415	9.086
1	15.708	0.3	8.573	74.022	0.014	2.5	3.142	246.740	28.576	31.416	8.635
1	15.708	0.4	11.714	98.696	0.010	2.5	3.142	246.740	29.286	31.416	8.425

Table A.5.16: The mathematical calculations in Excel table for the case of varying K_D (ζ=1)

Varying derivative time constant for fixed undamped natural frequency and damping ratio											
ζ	ω_n (rad/s)	K_d (s)	K_{po}	K_{io} (1/s)	T_{io} (s)	f_n (Hz)	π	Kio / Kd	Kpo / Kd	(Kpo+0.852)/Kd	(Kio/Kd) / (Kpo/Kd)
1.1	6.283	0.1	0.530	3.948	0.253	1	3.142	39.478	5.302	13.822	7.446
1.1	6.283	0.2	1.912	7.896	0.127	1	3.142	39.478	9.562	13.822	4.128
1.1	6.283	0.3	3.295	11.844	0.084	1	3.142	39.478	10.983	13.823	3.595
1.1	6.283	0.4	4.677	15.791	0.063	1	3.142	39.478	11.693	13.823	3.376
1.1	9.425	0.1	1.221	8.883	0.113	1.5	3.142	88.826	12.213	20.733	7.273
1.1	9.425	0.2	3.295	17.765	0.056	1.5	3.142	88.826	16.474	20.734	5.392
1.1	9.425	0.3	5.368	26.648	0.038	1.5	3.142	88.826	17.894	20.734	4.964
1.1	9.425	0.4	7.442	35.531	0.028	1.5	3.142	88.826	18.604	20.734	4.775
1.1	12.566	0.1	1.912	15.791	0.063	2	3.142	157.914	19.125	27.645	8.257
1.1	12.566	0.2	4.677	31.583	0.032	2	3.142	157.914	23.385	27.645	6.753
1.1	12.566	0.3	7.442	47.374	0.021	2	3.142	157.914	24.806	27.646	6.366
1.1	12.566	0.4	10.206	63.165	0.016	2	3.142	157.914	25.516	27.646	6.189
1.1	15.708	0.1	2.604	24.674	0.041	2.5	3.142	246.740	26.036	34.556	9.477
1.1	15.708	0.2	6.059	49.348	0.020	2.5	3.142	246.740	30.297	34.557	8.144
1.1	15.708	0.3	9.515	74.022	0.014	2.5	3.142	246.740	31.717	34.557	7.779
1.1	15.708	0.4	12.971	98.696	0.010	2.5	3.142	246.740	32.427	34.557	7.609

Table A.5.17: The mathematical calculations in Excel table for the case of varying K_D (ζ=1.1)

Rotor-side Converter Outer (Power) Loop PID		$\dfrac{\frac{K_{io}}{K_D}}{s^2+\left(\frac{K_{po}+0.852}{K_D}\right)s+\frac{K_{io}}{K_D}}$	$\dfrac{s\frac{K_{po}}{K_D}+\frac{K_{io}}{K_D}}{s^2+\left(\frac{K_{po}+0.852}{K_D}\right)s+\frac{K_{io}}{K_D}}$	$\dfrac{s^2+s\frac{K_{po}}{K_D}+\frac{K_{io}}{K_D}}{s^2+\left(\frac{K_{po}+0.852}{K_D}\right)s+\frac{K_{io}}{K_D}}$
ζ=0.7 f_n=1Hz	K_D=0.1s	$\frac{39.5}{s^2+8.8s+39.5}$	$\frac{0.28s+39.5}{s^2+8.8s+39.5}$	$\frac{s^2+0.28s+39.5}{s^2+8.8s+39.5}$
	K_D=0.2s	$\frac{39.5}{s^2+8.8s+39.5}$	$\frac{4.536s+39.5}{s^2+8.8s+39.5}$	$\frac{s^2+4.536s+39.5}{s^2+8.8s+39.5}$
	K_D=0.3s	$\frac{39.5}{s^2+8.8s+39.5}$	$\frac{5.96s+39.5}{s^2+8.8s+39.5}$	$\frac{s^2+5.96s+39.5}{s^2+8.8s+39.5}$
	K_D=0.4s	$\frac{39.5}{s^2+8.8s+39.5}$	$\frac{6.67s+39.5}{s^2+8.8s+39.5}$	$\frac{s^2+6.67s+39.5}{s^2+8.8s+39.5}$
ζ=0.7 f_n=1.5Hz	K_D=0.1s	$\frac{88.8}{s^2+13.2s+88.8}$	$\frac{4.7s+88.8}{s^2+13.2s+88.8}$	$\frac{s^2+4.7s+88.8}{s^2+13.2s+88.8}$
	K_D=0.2s	$\frac{88.8}{s^2+13.2s+88.8}$	$\frac{8.94s+88.8}{s^2+13.2s+88.8}$	$\frac{s^2+8.94s+88.8}{s^2+13.2s+88.8}$
	K_D=0.3s	$\frac{88.8}{s^2+13.2s+88.8}$	$\frac{10.35s+88.8}{s^2+13.2s+88.8}$	$\frac{s^2+10.5s+88.8}{s^2+13.2s+88.8}$
	K_D=0.4s	$\frac{88.8}{s^2+13.2s+88.8}$	$\frac{11.06s+88.8}{s^2+13.2s+88.8}$	$\frac{s^2+11.06s+88.8}{s^2+13.2s+88.8}$
ζ=0.7 f_n=2Hz	K_D=0.1s	$\frac{158}{s^2+17.6s+158}$	$\frac{9.1s+158}{s^2+17.6s+158}$	$\frac{s^2+9.1s+158}{s^2+17.6s+158}$
	K_D=0.2s	$\frac{158}{s^2+17.6s+158}$	$\frac{13.33s+158}{s^2+17.6s+158}$	$\frac{s^2+13.33s+158}{s^2+17.6s+158}$
	K_D=0.3s	$\frac{158}{s^2+17.6s+158}$	$\frac{14.75s+158}{s^2+17.6s+158}$	$\frac{s^2+14.75s+158}{s^2+17.6s+158}$
	K_D=0.4s	$\frac{158}{s^2+17.6s+158}$	$\frac{15.46s+158}{s^2+17.6s+158}$	$\frac{s^2+15.46s+158}{s^2+17.6s+158}$
ζ=0.7 f_n=2.5Hz	K_D=0.1s	$\frac{246.7}{s^2+22s+246.7}$	$\frac{13.5s+246.7}{s^2+22s+246.7}$	$\frac{s^2+13.5s+246.7}{s^2+22s+246.7}$
	K_D=0.2s	$\frac{246.7}{s^2+22s+246.7}$	$\frac{17.73s+246.7}{s^2+22s+246.7}$	$\frac{s^2+17.73s+246.7}{s^2+22s+246.7}$
	K_D=0.3s	$\frac{246.7}{s^2+22s+246.7}$	$\frac{19.15s+246.7}{s^2+22s+246.7}$	$\frac{s^2+19.15s+246.7}{s^2+22s+246.7}$
	K_D=0.4s	$\frac{246.7}{s^2+22s+246.7}$	$\frac{19.86s+246.7}{s^2+22s+246.7}$	$\frac{s^2+19.86s+246.7}{s^2+22s+246.7}$

Table A.5.18: Varying K_D – SoATF, STF2, FTF2 (ζ=0.7)

Rotor-side Converter Outer (Power) Loop PID		$\dfrac{\frac{K_{io}}{K_D}}{s^2+\left(\frac{K_{po}+0.852}{K_D}\right)s+\frac{K_{io}}{K_D}}$	$\dfrac{s\frac{K_{po}}{K_D}+\frac{K_{io}}{K_D}}{s^2+\left(\frac{K_{po}+0.852}{K_D}\right)s+\frac{K_{io}}{K_D}}$	$\dfrac{s^2+s\frac{K_{po}}{K_D}+\frac{K_{io}}{K_D}}{s^2+\left(\frac{K_{po}+0.852}{K_D}\right)s+\frac{K_{io}}{K_D}}$
ζ=0.8 f_n=1Hz	K_D=0.1s	$\frac{39.5}{s^2+10s+39.5}$	$\frac{1.5s+39.5}{s^2+10s+39.5}$	$\frac{s^2+1.5s+39.5}{s^2+10s+39.5}$
	K_D=0.2s	$\frac{39.5}{s^2+10s+39.5}$	$\frac{5.79s+39.5}{s^2+10s+39.5}$	$\frac{s^2+5.79s+39.5}{s^2+10s+39.5}$
	K_D=0.3s	$\frac{39.5}{s^2+10s+39.5}$	$\frac{7.2s+39.5}{s^2+10s+39.5}$	$\frac{s^2+7.2s+39.5}{s^2+10s+39.5}$
	K_D=0.4s	$\frac{39.5}{s^2+10s+39.5}$	$\frac{7.9s+39.5}{s^2+10s+39.5}$	$\frac{s^2+7.9s+39.5}{s^2+10s+39.5}$
ζ=0.8 f_n=1.5Hz	K_D=0.1s	$\frac{88.8}{s^2+15s+88.8}$	$\frac{6.56s+88.8}{s^2+15s+88.8}$	$\frac{s^2+6.56s+88.8}{s^2+15s+88.8}$
	K_D=0.2s	$\frac{88.8}{s^2+15s+88.8}$	$\frac{10.82s+88.8}{s^2+15s+88.8}$	$\frac{s^2+10.82s+88.8}{s^2+15s+88.8}$
	K_D=0.3s	$\frac{88.8}{s^2+15s+88.8}$	$\frac{12.24s+88.8}{s^2+15s+88.8}$	$\frac{s^2+12.24s+88.8}{s^2+15s+88.8}$
	K_D=0.4s	$\frac{88.8}{s^2+15s+88.8}$	$\frac{12.95s+88.8}{s^2+15s+88.8}$	$\frac{s^2+12.95s+88.8}{s^2+15s+88.8}$
ζ=0.8 f_n=2Hz	K_D=0.1s	$\frac{158}{s^2+20s+158}$	$\frac{11.6s+158}{s^2+20s+158}$	$\frac{s^2+11.6s+158}{s^2+20s+158}$
	K_D=0.2s	$\frac{158}{s^2+20s+158}$	$\frac{15.85s+158}{s^2+20s+158}$	$\frac{s^2+15.85s+158}{s^2+20s+158}$
	K_D=0.3s	$\frac{158}{s^2+20s+158}$	$\frac{17.27s+158}{s^2+20s+158}$	$\frac{s^2+17.27s+158}{s^2+20s+158}$
	K_D=0.4s	$\frac{158}{s^2+20s+158}$	$\frac{17.98s+158}{s^2+20s+158}$	$\frac{s^2+17.98s+158}{s^2+20s+158}$
ζ=0.8 f_n=2.5Hz	K_D=0.1s	$\frac{246.7}{s^2+25.13s+246.7}$	$\frac{16.6s+246.7}{s^2+25.13s+246.7}$	$\frac{s^2+16.6s+246.7}{s^2+25.13s+246.7}$
	K_D=0.2s	$\frac{246.7}{s^2+25.13s+246.7}$	$\frac{20.87s+246.7}{s^2+25.13s+246.7}$	$\frac{s^2+20.87s+246.7}{s^2+25.13s+246.7}$
	K_D=0.3s	$\frac{246.7}{s^2+25.13s+246.7}$	$\frac{22.3s+246.7}{s^2+25.13s+246.7}$	$\frac{s^2+22.3s+246.7}{s^2+25.13s+246.7}$
	K_D=0.4s	$\frac{246.7}{s^2+25.13s+246.7}$	$\frac{23s+246.7}{s^2+25.13s+246.7}$	$\frac{s^2+23s+246.7}{s^2+25.13s+246.7}$

Table A.5.19: Varying K_D – SoATF, STF2, FTF2 (ζ=0.8)

Rotor-side Converter Outer (Power) Loop PID		$\frac{\frac{K_{io}}{K_D}}{s^2+\left(\frac{K_{po}+0.852}{K_D}\right)s+\frac{K_{io}}{K_D}}$	$\frac{s\frac{K_{po}}{K_D}+\frac{K_{io}}{K_D}}{s^2+\left(\frac{K_{po}+0.852}{K_D}\right)s+\frac{K_{io}}{K_D}}$	$\frac{s^2+s\frac{K_{po}}{K_D}+\frac{K_{io}}{K_D}}{s^2+\left(\frac{K_{po}+0.852}{K_D}\right)s+\frac{K_{io}}{K_D}}$
ζ=0.9 f_n=1Hz	K_D=0.1s	$\frac{39.5}{s^2+11.3s+39.5}$	$\frac{2.8s+39.5}{s^2+11.3s+39.5}$	$\frac{s^2+2.8s+39.5}{s^2+11.3s+39.5}$
	K_D=0.2s	$\frac{39.5}{s^2+11.3s+39.5}$	$\frac{7.05s+39.5}{s^2+11.3s+39.5}$	$\frac{s^2+7.05s+39.5}{s^2+11.3s+39.5}$
	K_D=0.3s	$\frac{39.5}{s^2+11.3s+39.5}$	$\frac{8.47s+39.5}{s^2+11.3s+39.5}$	$\frac{s^2+8.47s+39.5}{s^2+11.3s+39.5}$
	K_D=0.4s	$\frac{39.5}{s^2+11.3s+39.5}$	$\frac{9.18s+39.5}{s^2+11.3s+39.5}$	$\frac{s^2+9.18s+39.5}{s^2+11.3s+39.5}$
ζ=0.9 f_n=1.5Hz	K_D=0.1s	$\frac{88.8}{s^2+17s+88.8}$	$\frac{8.45s+88.8}{s^2+17s+88.8}$	$\frac{s^2+8.45s+88.8}{s^2+17s+88.8}$
	K_D=0.2s	$\frac{88.8}{s^2+17s+88.8}$	$\frac{12.7s+88.8}{s^2+17s+88.8}$	$\frac{s^2+12.7s+88.8}{s^2+17s+88.8}$
	K_D=0.3s	$\frac{88.8}{s^2+17s+88.8}$	$\frac{14.13s+88.8}{s^2+17s+88.8}$	$\frac{s^2+14.13s+88.8}{s^2+17s+88.8}$
	K_D=0.4s	$\frac{88.8}{s^2+17s+88.8}$	$\frac{14.84s+88.8}{s^2+17s+88.8}$	$\frac{s^2+14.84s+88.8}{s^2+17s+88.8}$
ζ=0.9 f_n=2Hz	K_D=0.1s	$\frac{158}{s^2+22.62s+158}$	$\frac{14.1s+158}{s^2+22.62s+158}$	$\frac{s^2+14.1s+158}{s^2+22.62s+158}$
	K_D=0.2s	$\frac{158}{s^2+22.62s+158}$	$\frac{18.36s+158}{s^2+22.62s+158}$	$\frac{s^2+18.36s+158}{s^2+22.62s+158}$
	K_D=0.3s	$\frac{158}{s^2+22.62s+158}$	$\frac{19.78s+158}{s^2+22.62s+158}$	$\frac{s^2+19.78s+158}{s^2+22.62s+158}$
	K_D=0.4s	$\frac{158}{s^2+22.62s+158}$	$\frac{20.5s+158}{s^2+22.62s+158}$	$\frac{s^2+20.5s+158}{s^2+22.62s+158}$
ζ=0.9 f_n=2.5Hz	K_D=0.1s	$\frac{246.7}{s^2+28.3+246.7}$	$\frac{19.75s+246.7}{s^2+28.3s+246.7}$	$\frac{s^2+19.75s+246.7}{s^2+28.3s+246.7}$
	K_D=0.2s	$\frac{246.7}{s^2+28.3+246.7}$	$\frac{24s+246.7}{s^2+28.3s+246.7}$	$\frac{s^2+24s+246.7}{s^2+28.3s+246.7}$
	K_D=0.3s	$\frac{246.7}{s^2+28.3+246.7}$	$\frac{25.4s+246.7}{s^2+28.3s+246.7}$	$\frac{s^2+25.4s+246.7}{s^2+28.3s+246.7}$
	K_D=0.4s	$\frac{246.7}{s^2+28.3+246.7}$	$\frac{26.15s+246.7}{s^2+28.3s+246.7}$	$\frac{s^2+26.15s+246.7}{s^2+28.3s+246.7}$

Table A.5.20: Varying K_D – SoATF, STF2, FTF2 (ζ=0.9)

Rotor-side Converter Outer (Power) Loop PID		$\frac{\frac{K_{io}}{K_D}}{s^2+\left(\frac{K_{po}+0.852}{K_D}\right)s+\frac{K_{io}}{K_D}}$	$\frac{s\frac{K_{po}}{K_D}+\frac{K_{io}}{K_D}}{s^2+\left(\frac{K_{po}+0.852}{K_D}\right)s+\frac{K_{io}}{K_D}}$	$\frac{s^2+s\frac{K_{po}}{K_D}+\frac{K_{io}}{K_D}}{s^2+\left(\frac{K_{po}+0.852}{K_D}\right)s+\frac{K_{io}}{K_D}}$
ζ=1 f_n=1Hz	K_D=0.1s	$\frac{39.5}{s^2+12.565s+39.5}$	$\frac{4.05s+39.5}{s^2+12.565s+39.5}$	$\frac{s^2+4.05s+39.5}{s^2+12.565s+39.5}$
	K_D=0.2s	$\frac{39.5}{s^2+12.565s+39.5}$	$\frac{8.3s+39.5}{s^2+12.565s+39.5}$	$\frac{s^2+8.3s+39.5}{s^2+12.565s+39.5}$
	K_D=0.3s	$\frac{39.5}{s^2+12.565s+39.5}$	$\frac{9.73s+39.5}{s^2+12.565s+39.5}$	$\frac{s^2+9.73s+39.5}{s^2+12.565s+39.5}$
	K_D=0.4s	$\frac{39.5}{s^2+12.565s+39.5}$	$\frac{10.44s+39.5}{s^2+12.565s+39.5}$	$\frac{s^2+10.44s+39.5}{s^2+12.565s+39.5}$
ζ=1 f_n=1.5Hz	K_D=0.1s	$\frac{88.8}{s^2+18.85s+88.8}$	$\frac{10.33s+88.8}{s^2+18.85s+88.8}$	$\frac{s^2+10.33s+88.8}{s^2+18.85s+88.8}$
	K_D=0.2s	$\frac{88.8}{s^2+18.85s+88.8}$	$\frac{14.6s+88.8}{s^2+18.85s+88.8}$	$\frac{s^2+14.6s+88.8}{s^2+18.85s+88.8}$
	K_D=0.3s	$\frac{88.8}{s^2+18.85s+88.8}$	$\frac{16s+88.8}{s^2+18.85s+88.8}$	$\frac{s^2+16s+88.8}{s^2+18.85s+88.8}$
	K_D=0.4s	$\frac{88.8}{s^2+18.85s+88.8}$	$\frac{16.72s+88.8}{s^2+18.85s+88.8}$	$\frac{s^2+16.72s+88.8}{s^2+18.85s+88.8}$
ζ=1 f_n=2Hz	K_D=0.1s	$\frac{158}{s^2+25.13s+158}$	$\frac{16.6s+158}{s^2+25.13s+158}$	$\frac{s^2+16.6s+158}{s^2+25.13s+158}$
	K_D=0.2s	$\frac{158}{s^2+25.13s+158}$	$\frac{20.87s+158}{s^2+25.13s+158}$	$\frac{s^2+20.87s+158}{s^2+25.13s+158}$
	K_D=0.3s	$\frac{158}{s^2+25.13s+158}$	$\frac{22.23s+158}{s^2+25.13s+158}$	$\frac{s^2+22.23s+158}{s^2+25.13s+158}$
	K_D=0.4s	$\frac{158}{s^2+25.13s+158}$	$\frac{23s+158}{s^2+25.13s+158}$	$\frac{s^2+23s+158}{s^2+25.13s+158}$
ζ=1 f_n=2.5Hz	K_D=0.1s	$\frac{246.7}{s^2+31.42s+246.7}$	$\frac{23s+246.7}{s^2+31.42s+246.7}$	$\frac{s^2+23s+246.7}{s^2+31.42s+246.7}$
	K_D=0.2s	$\frac{246.7}{s^2+31.42s+246.7}$	$\frac{27.16s+246.7}{s^2+31.42s+246.7}$	$\frac{s^2+27.16s+246.7}{s^2+31.42s+246.7}$
	K_D=0.3s	$\frac{246.7}{s^2+31.42s+246.7}$	$\frac{28.58s+246.7}{s^2+31.42s+246.7}$	$\frac{s^2+28.58s+246.7}{s^2+31.42s+246.7}$
	K_D=0.4s	$\frac{246.7}{s^2+31.42s+246.7}$	$\frac{29.3s+246.7}{s^2+31.42s+246.7}$	$\frac{s^2+29.3s+246.7}{s^2+31.42s+246.7}$

Table A.5.21: Varying K_D – SoATF, STF2, FTF2 (ζ=1)

Rotor-side Converter Outer (Power) Loop PID		$\dfrac{\frac{K_{io}}{K_D}}{s^2+\left(\frac{K_{po}+0.852}{K_D}\right)s+\frac{K_{io}}{K_D}}$	$\dfrac{s\frac{K_{po}}{K_D}+\frac{K_{io}}{K_D}}{s^2+\left(\frac{K_{po}+0.852}{K_D}\right)s+\frac{K_{io}}{K_D}}$	$\dfrac{s^2+s\frac{K_{po}}{K_D}+\frac{K_{io}}{K_D}}{s^2+\left(\frac{K_{po}+0.852}{K_D}\right)s+\frac{K_{io}}{K_D}}$
ζ=1.1 f_n=1Hz	K_D=0.1s	$\dfrac{39.5}{s^2+13.8s+39.5}$	$\dfrac{5.3s+39.5}{s^2+13.8s+39.5}$	$\dfrac{s^2+5.3s+39.5}{s^2+13.8s+39.5}$
	K_D=0.2s	$\dfrac{39.5}{s^2+13.8s+39.5}$	$\dfrac{9.56s+39.5}{s^2+13.8s+39.5}$	$\dfrac{s^2+9.56s+39.5}{s^2+13.8s+39.5}$
	K_D=0.3s	$\dfrac{39.5}{s^2+13.8s+39.5}$	$\dfrac{11s+39.5}{s^2+13.8s+39.5}$	$\dfrac{s^2+11s+39.5}{s^2+13.8s+39.5}$
	K_D=0.4s	$\dfrac{39.5}{s^2+13.8s+39.5}$	$\dfrac{11.7s+39.5}{s^2+13.8s+39.5}$	$\dfrac{s^2+11.7s+39.5}{s^2+13.8s+39.5}$
ζ=1.1 f_n=1.5Hz	K_D=0.1s	$\dfrac{88.8}{s^2+20.74s+88.8}$	$\dfrac{12.21s+88.8}{s^2+20.74s+88.8}$	$\dfrac{s^2+12.21s+88.8}{s^2+20.74s+88.8}$
	K_D=0.2s	$\dfrac{88.8}{s^2+20.74s+88.8}$	$\dfrac{16.48s+88.8}{s^2+20.74s+88.8}$	$\dfrac{s^2+16.48s+88.8}{s^2+20.74s+88.8}$
	K_D=0.3s	$\dfrac{88.8}{s^2+20.74s+88.8}$	$\dfrac{17.9s+88.8}{s^2+20.74s+88.8}$	$\dfrac{s^2+17.9s+88.8}{s^2+20.74s+88.8}$
	K_D=0.4s	$\dfrac{88.8}{s^2+20.74s+88.8}$	$\dfrac{18.6s+88.8}{s^2+20.74s+88.8}$	$\dfrac{s^2+18.6s+88.8}{s^2+20.74s+88.8}$
ζ=1.1 f_n=2Hz	K_D=0.1s	$\dfrac{158}{s^2+27.65s+158}$	$\dfrac{19.13s+158}{s^2+27.65s+158}$	$\dfrac{s^2+19.13s+158}{s^2+27.65s+158}$
	K_D=0.2s	$\dfrac{158}{s^2+27.65s+158}$	$\dfrac{23.4s+158}{s^2+27.65s+158}$	$\dfrac{s^2+23.4s+158}{s^2+27.65s+158}$
	K_D=0.3s	$\dfrac{158}{s^2+27.65s+158}$	$\dfrac{24.8s+158}{s^2+27.65s+158}$	$\dfrac{s^2+24.8s+158}{s^2+27.65s+158}$
	K_D=0.4s	$\dfrac{158}{s^2+27.65s+158}$	$\dfrac{25.5s+158}{s^2+27.65s+158}$	$\dfrac{s^2+25.5s+158}{s^2+27.65s+158}$
ζ=1.1 f_n=2.5Hz	K_D=0.1s	$\dfrac{246.7}{s^2+34.56s+246.7}$	$\dfrac{26.04s+246.7}{s^2+34.56s+246.7}$	$\dfrac{s^2+26.04s+246.7}{s^2+34.56s+246.7}$
	K_D=0.2s	$\dfrac{246.7}{s^2+34.56s+246.7}$	$\dfrac{30.3s+246.7}{s^2+34.56s+246.7}$	$\dfrac{s^2+30.3s+246.7}{s^2+34.56s+246.7}$
	K_D=0.3s	$\dfrac{246.7}{s^2+34.56s+246.7}$	$\dfrac{31.7s+246.7}{s^2+34.56s+246.7}$	$\dfrac{s^2+31.7s+246.7}{s^2+34.56s+246.7}$
	K_D=0.4s	$\dfrac{246.7}{s^2+34.56s+246.7}$	$\dfrac{32.43s+246.7}{s^2+34.56s+246.7}$	$\dfrac{s^2+32.43s+246.7}{s^2+34.56s+246.7}$

Table A.5.22: Varying K_D – SoATF, STF2, FTF2 (ζ=1.1)

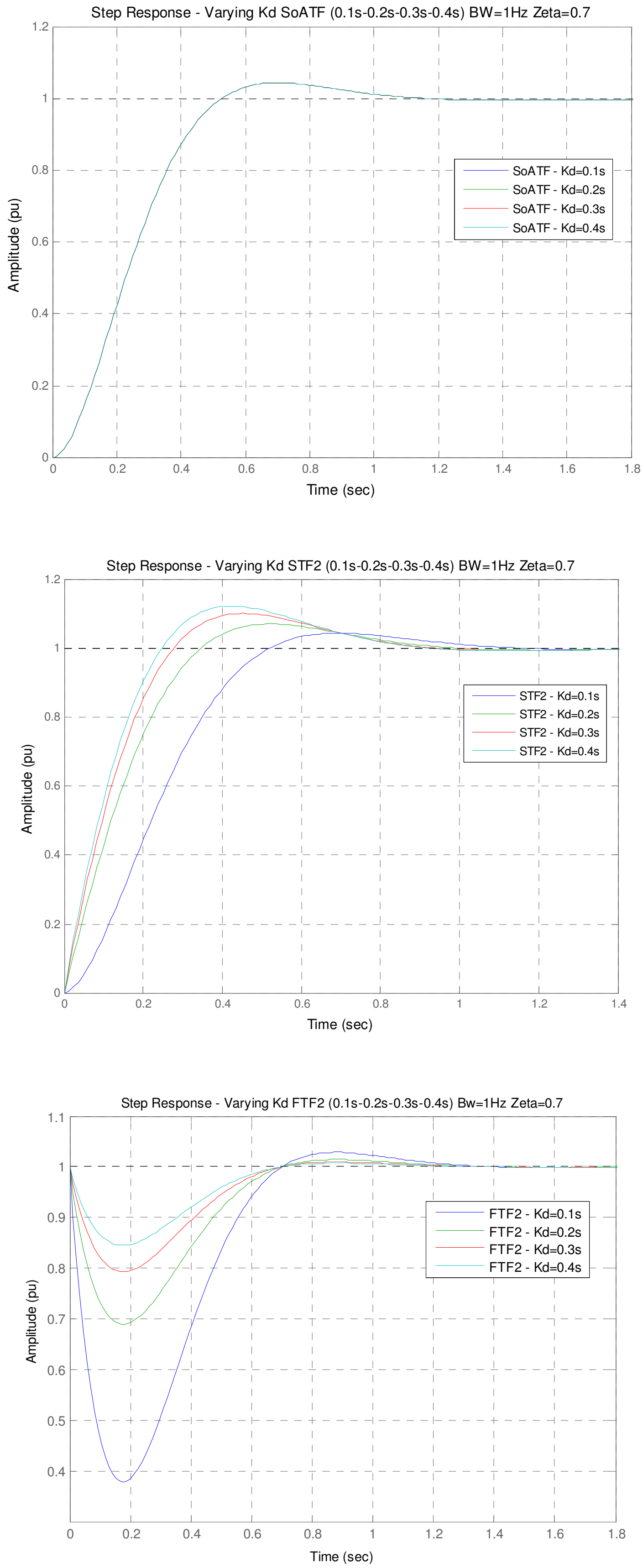

Figure A.5.10: Varying K_D – step responses of SoATF, STF2 and FTF2 f_n=1Hz and ζ=0.7

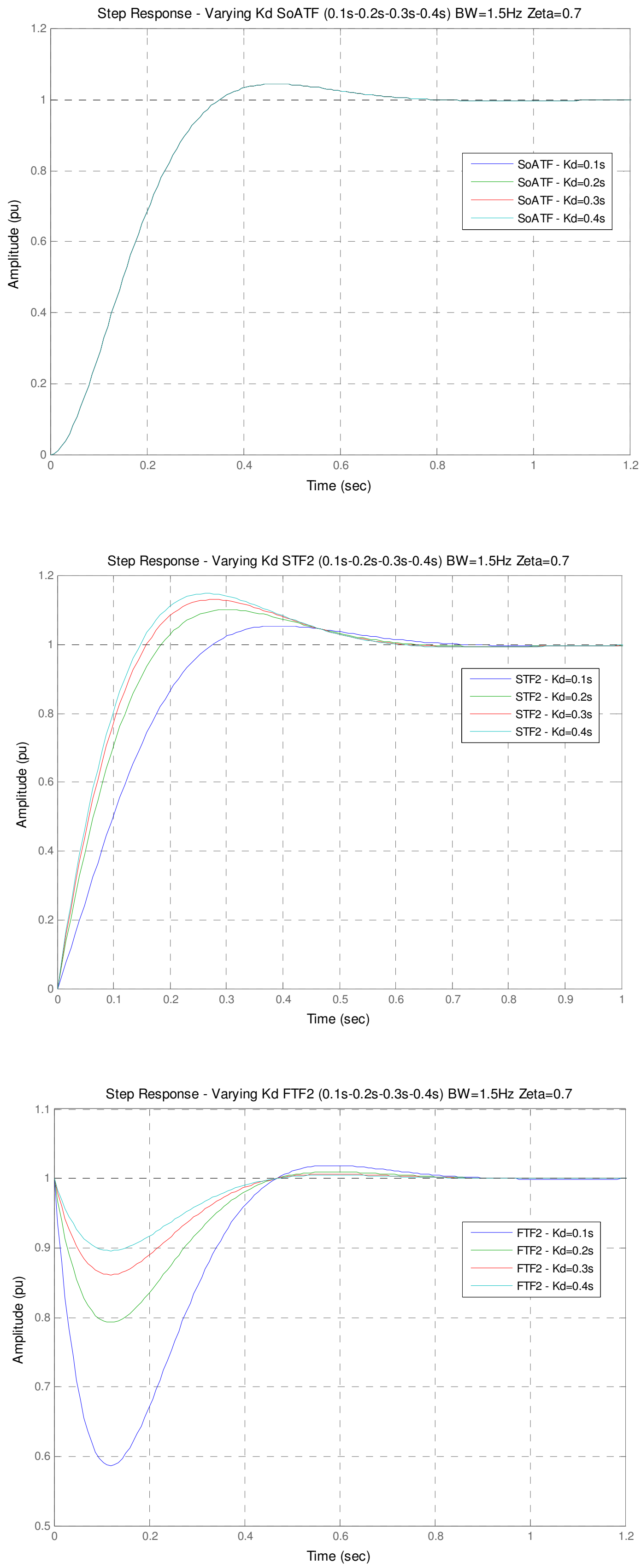

Figure A.5.11: Varying K_D – step responses of SoATF, STF2 and FTF2
f_n=1.5Hz and ζ=0.7

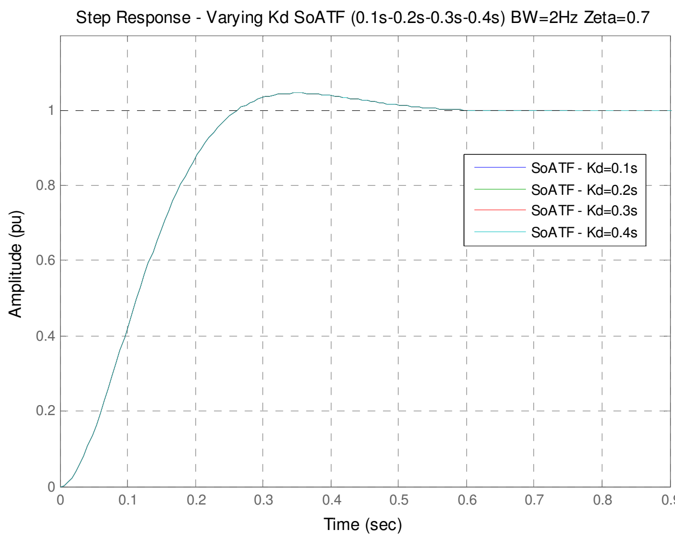

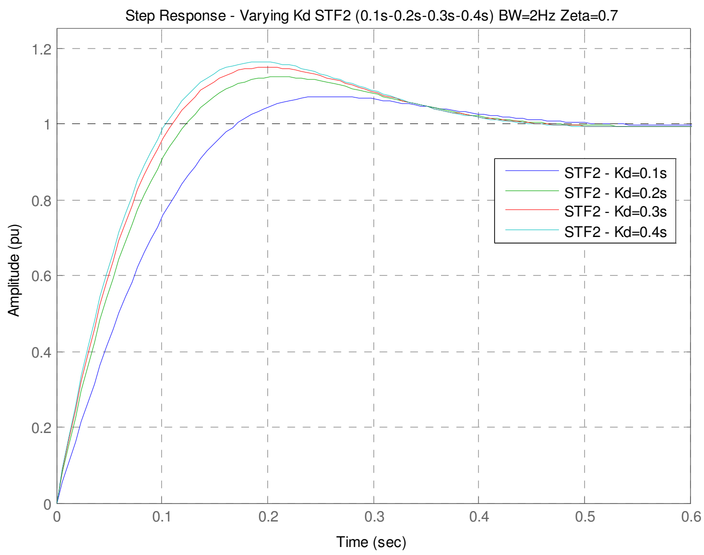

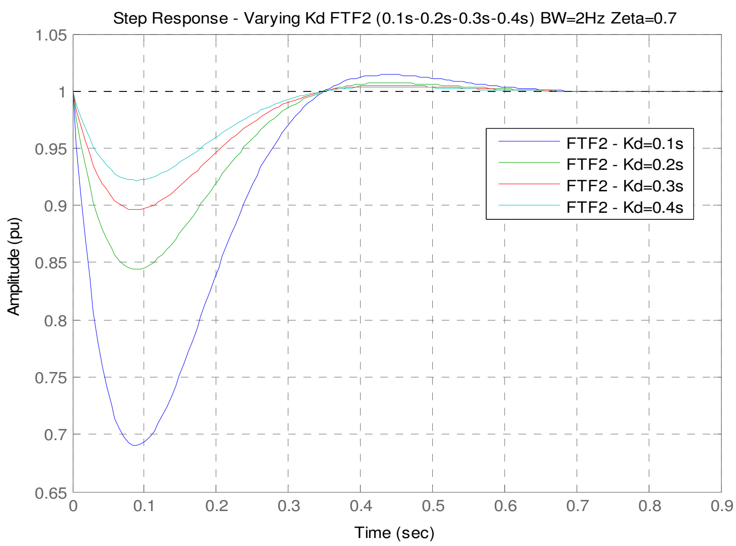

Figure A.5.12: Varying K_D – step responses of SoATF, STF2 and FTF2
f_n=2Hz and ζ=0.7

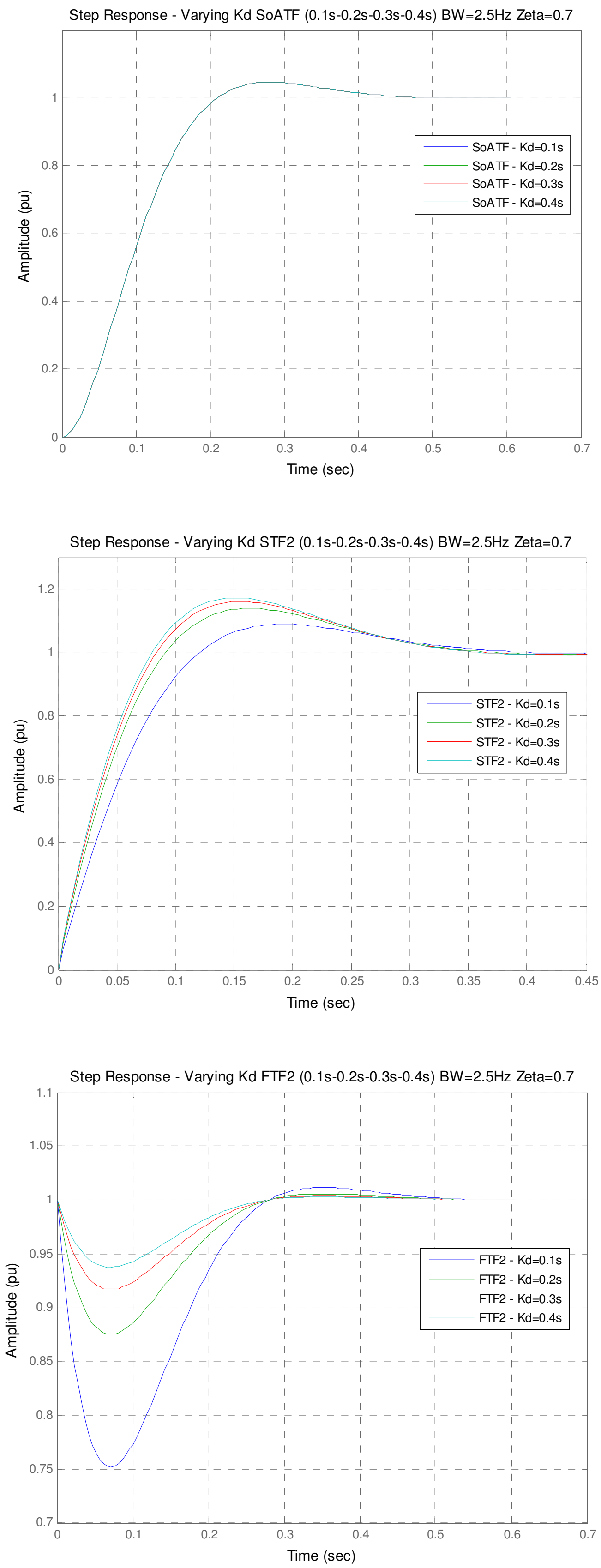

Figure A.5.12: Varying K_D – step responses of SoATF, STF2 and FTF2
f_n=2.5Hz and ζ=0.7

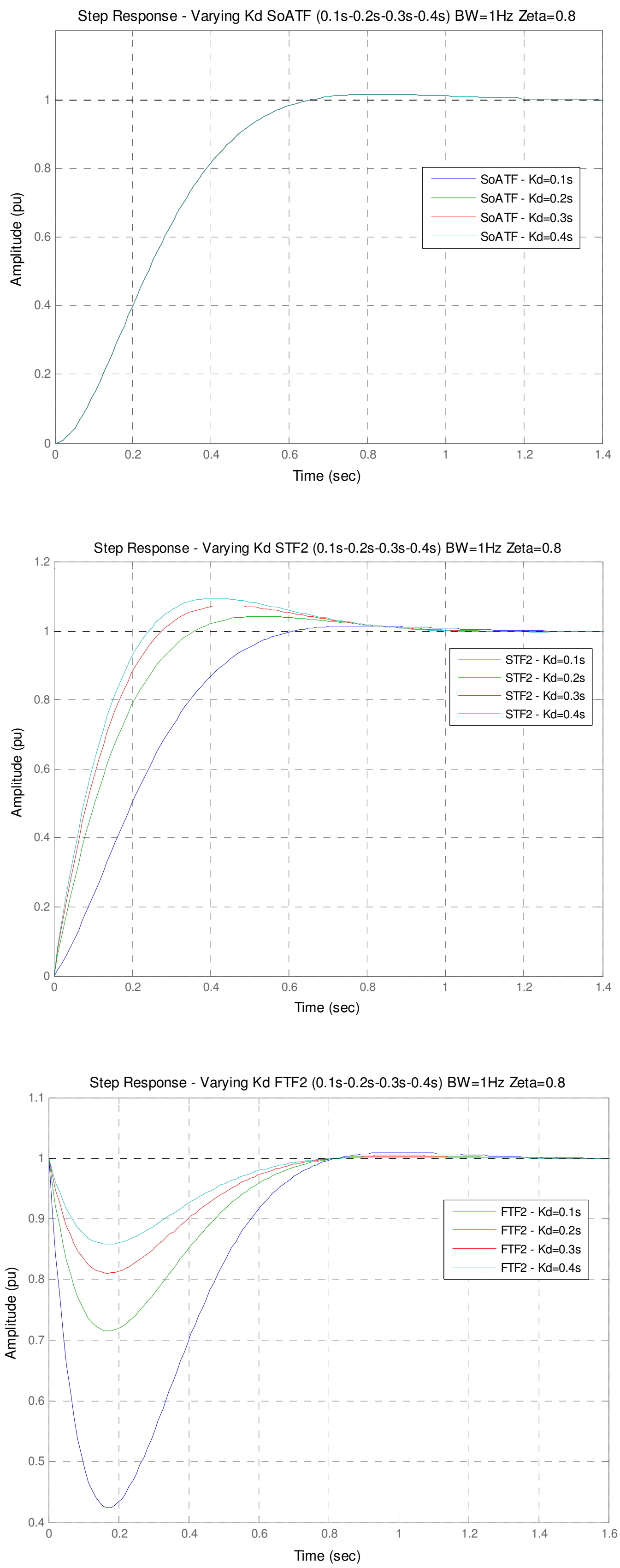

Figure A.5.13: Varying K_D – step responses of SoATF, STF2 and FTF2
f_n=1Hz and ζ=0.8

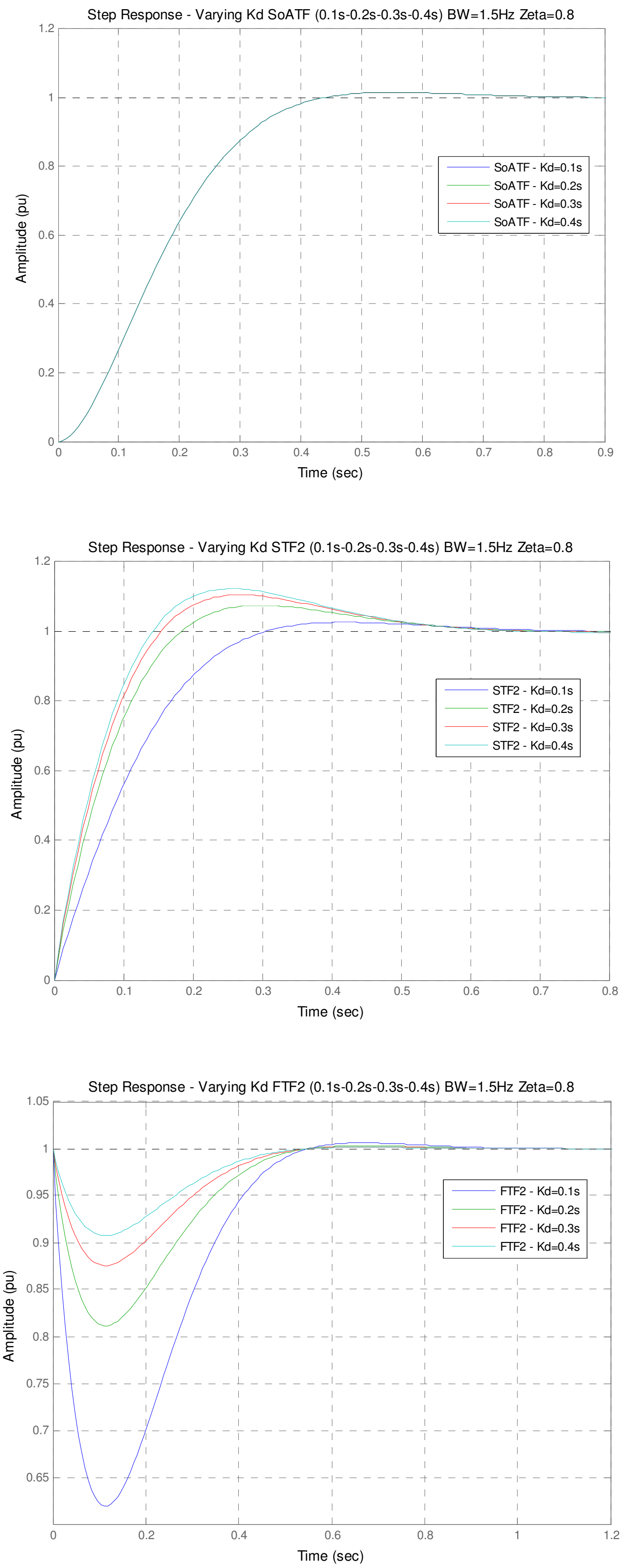

Figure A.5.14: Varying K_D – step responses of SoATF, STF2 and FTF2
f_n=1.5Hz and ζ=0.8

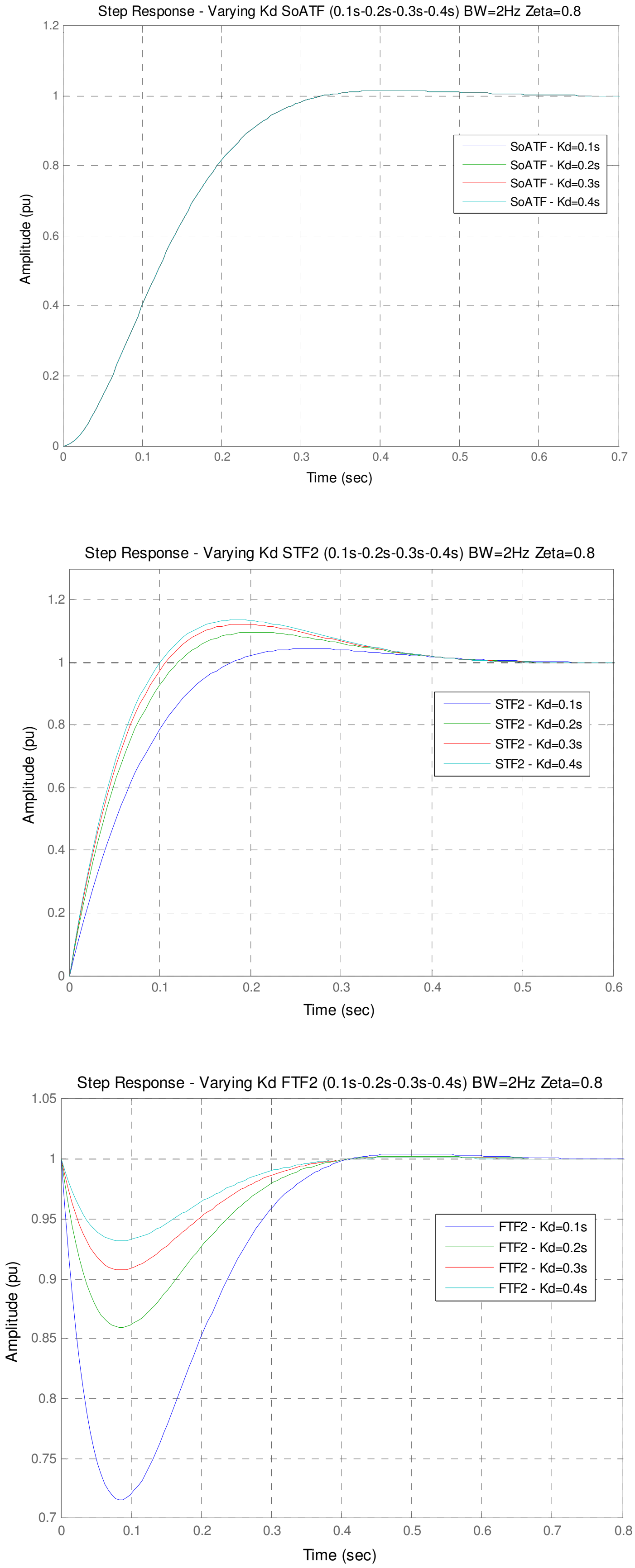

Figure A.5.15: Varying K_D – step responses of SoATF, STF2 and FTF2 f_n=2Hz and ζ=0.8

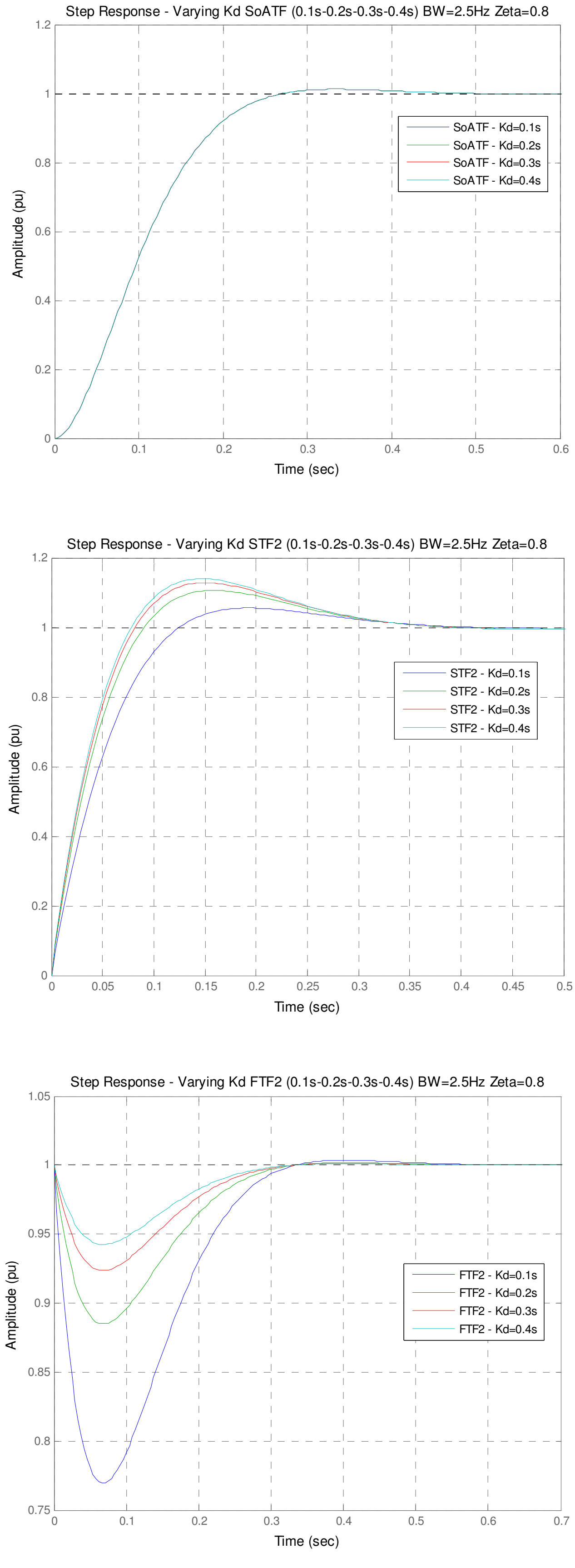

Figure A.5.16: Varying K_D – step responses of SoATF, STF2 and FTF2
f_n=2.5Hz and ζ=0.8

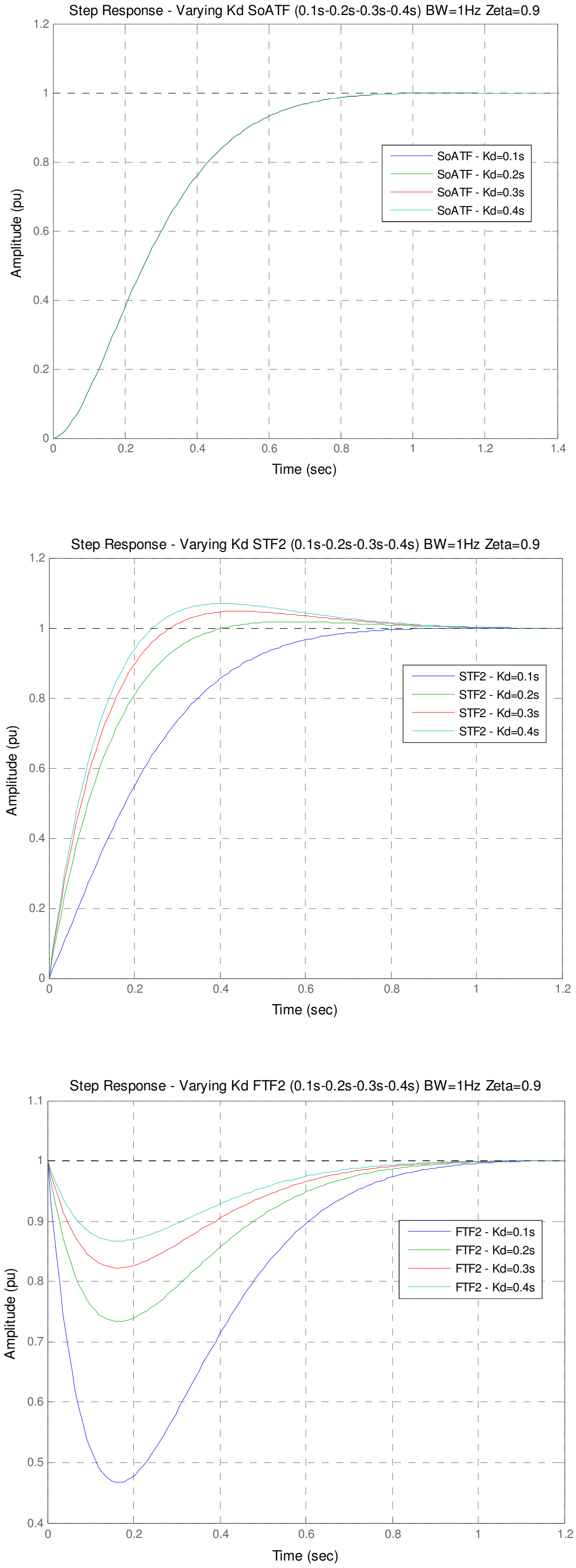

Figure A.5.17: Varying K_D – step responses of SoATF, STF2 and FTF2
f_n=1Hz and ζ=0.9

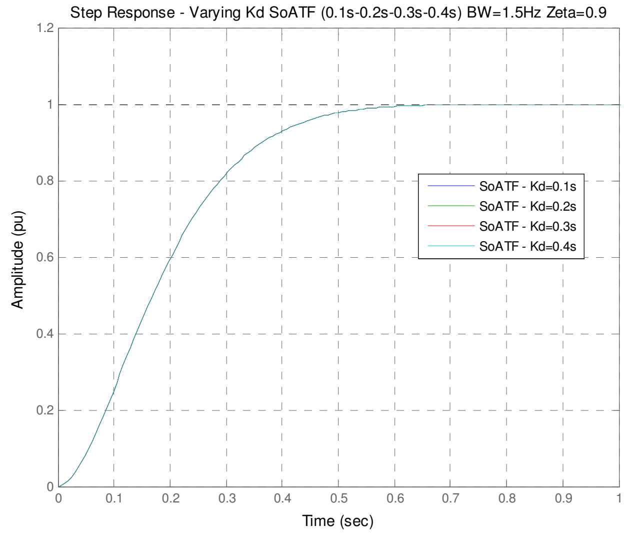

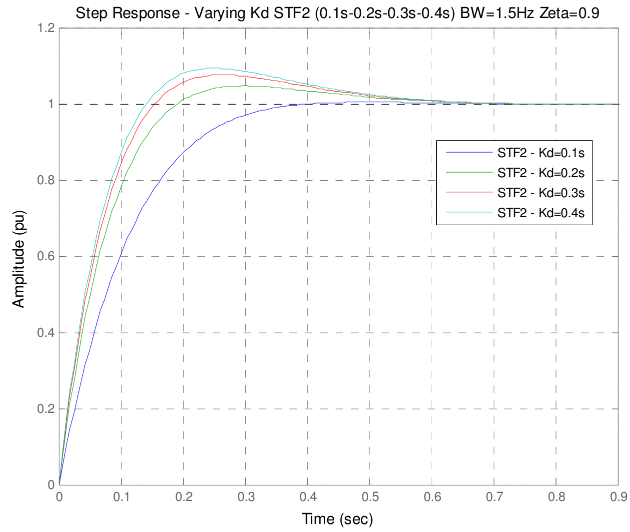

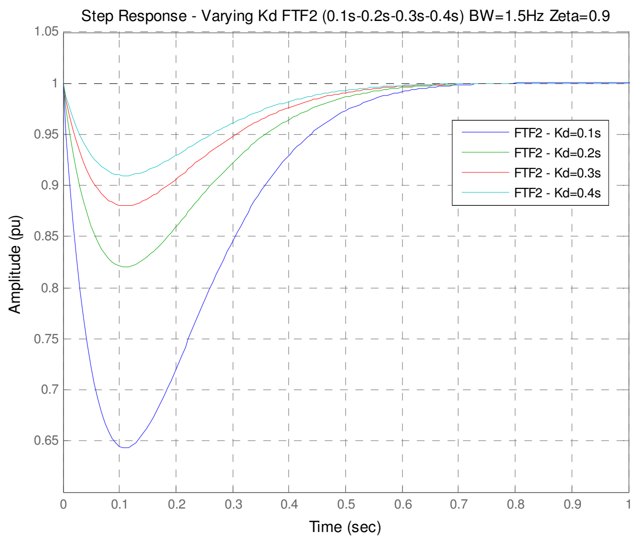

Figure A.5.18: Varying K_D – step responses of SoATF, STF2 and FTF2
f_n=1.5Hz and ζ=0.9

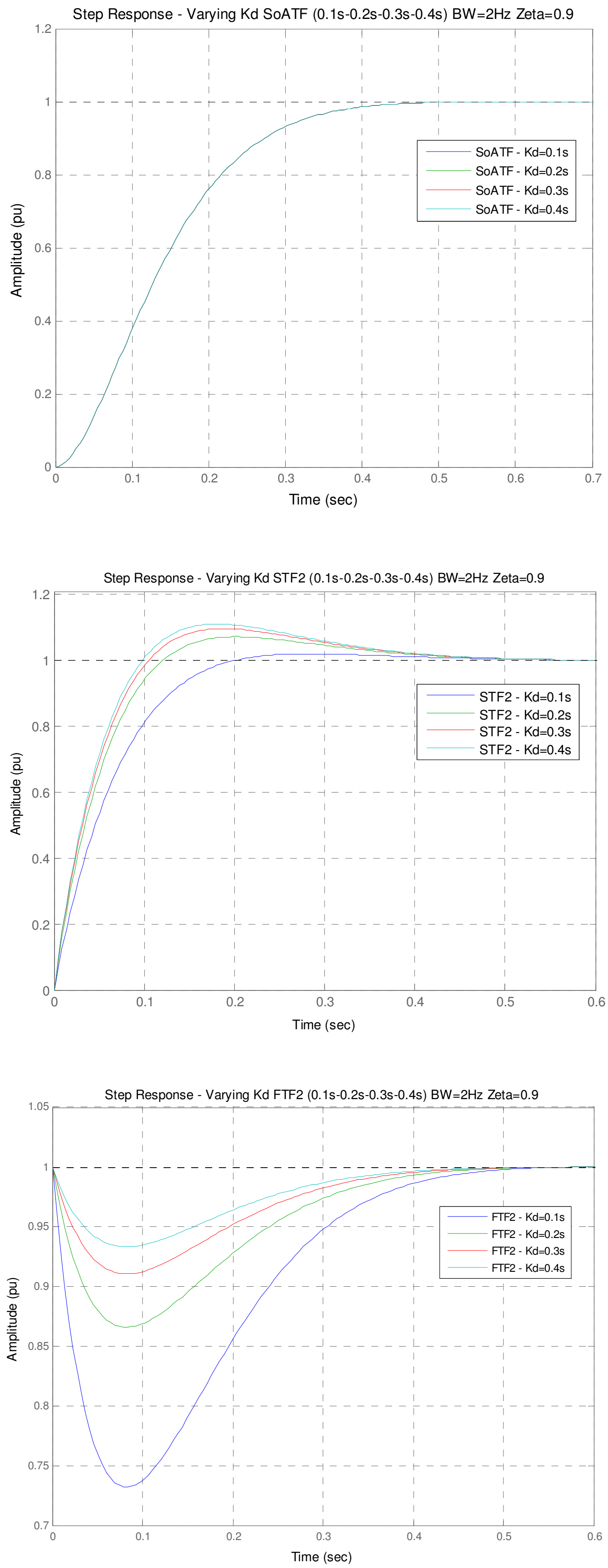

Figure A.5.19: Varying K_D – step responses of SoATF, STF2 and FTF2
f_n=2Hz and ζ=0.9

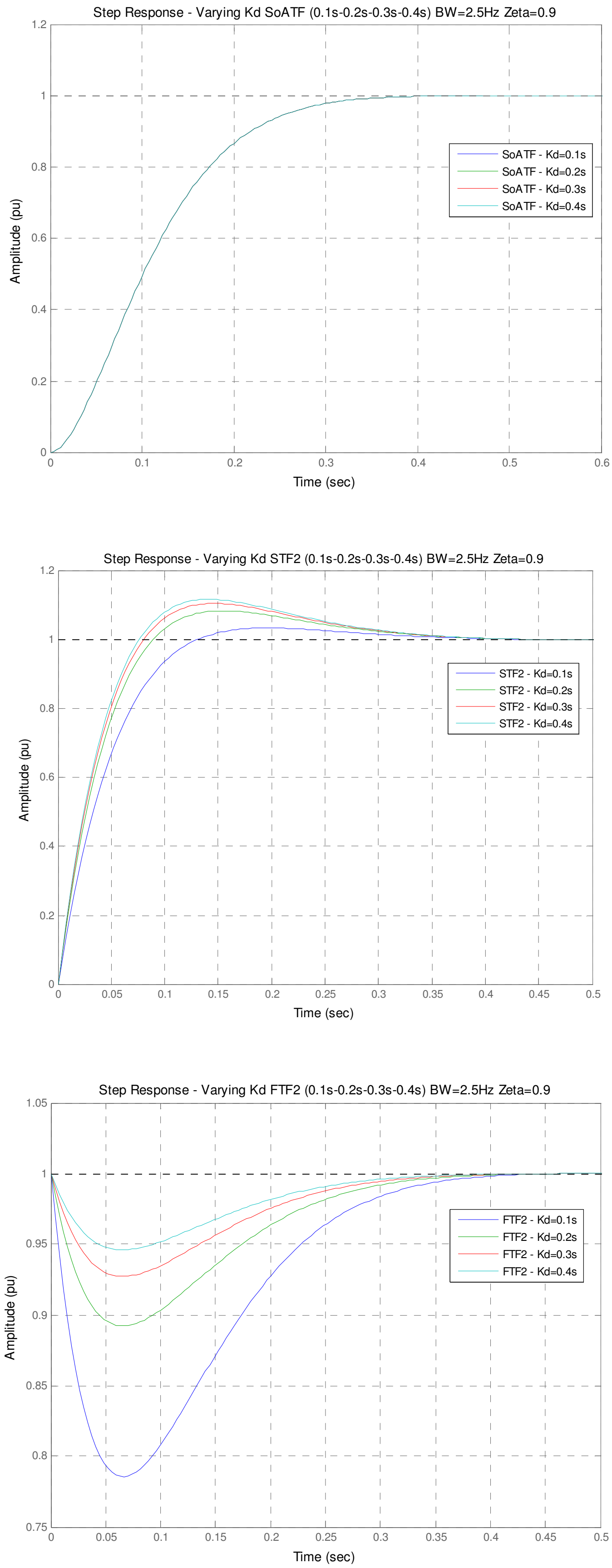

Figure A.5.20: Varying K_D – step responses of SoATF, STF2 and FTF2
f_n=2.5Hz and ζ=0.9

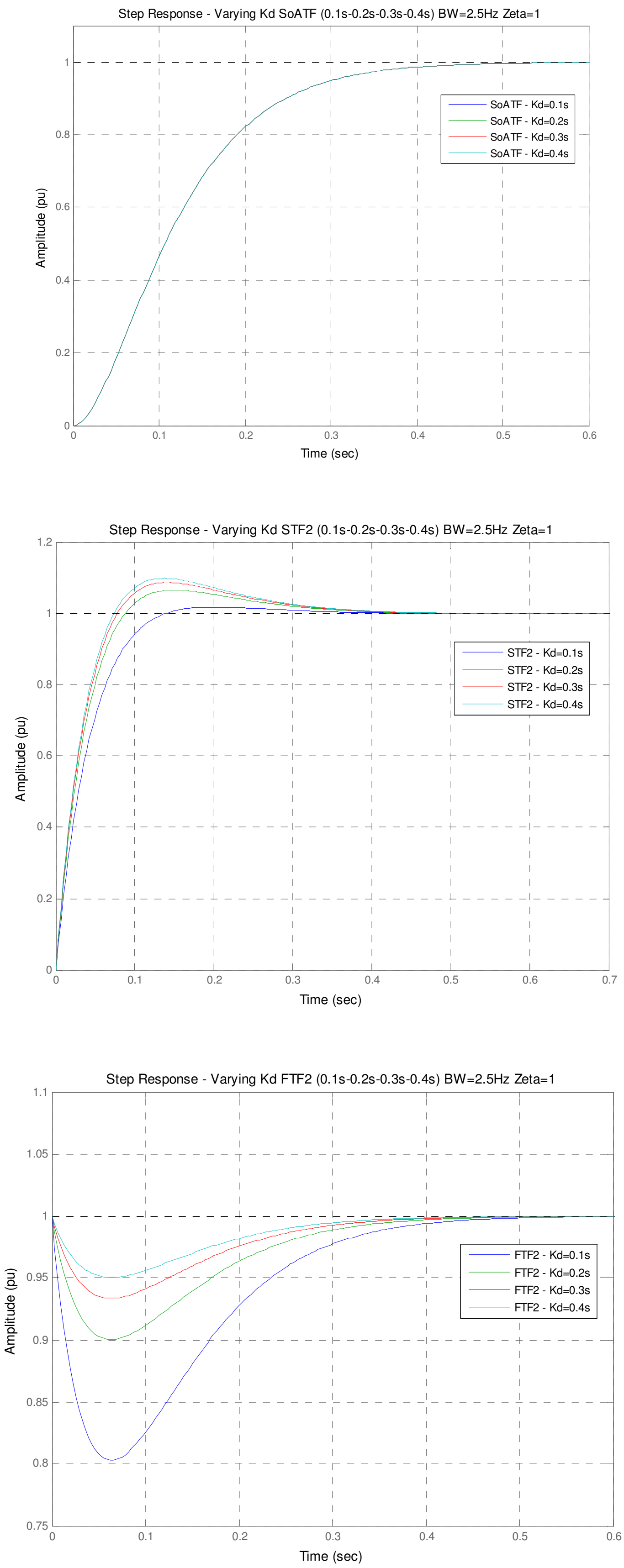

Figure A.5.21: Varying K_D – step responses of SoATF, STF2 and FTF2 f_n=2.5Hz and ζ=1

The difference between the lower graph (step response of the full transfer function - FTF2) of Figures A.5.1 to A.5.21 and the classic step response is, in fact, originating from a mathematical artefact which also reflects to the simulation results.

The complex *s*-plane includes a real (σ) and an imaginary (ω) components which can be denoted as $s=\sigma+j\omega$. "It should be noted that *s* has a unit of 1/second" [A.5.1]. As seen in Figure A.5.22, at t=0s the step responses of second-order approximated transfer function (SoATF) and the simplified transfer function (STF2) arise from 0, which matches the classic step response characteristic, while that of the full-transfer function (FTF2) starts to fall from the point of 1. In order to investigate this, the FTF2 and STF2 are re-written in the parenthesis of s^2 and *s*, respectively, and the SoATF is taken and shown here as it is.

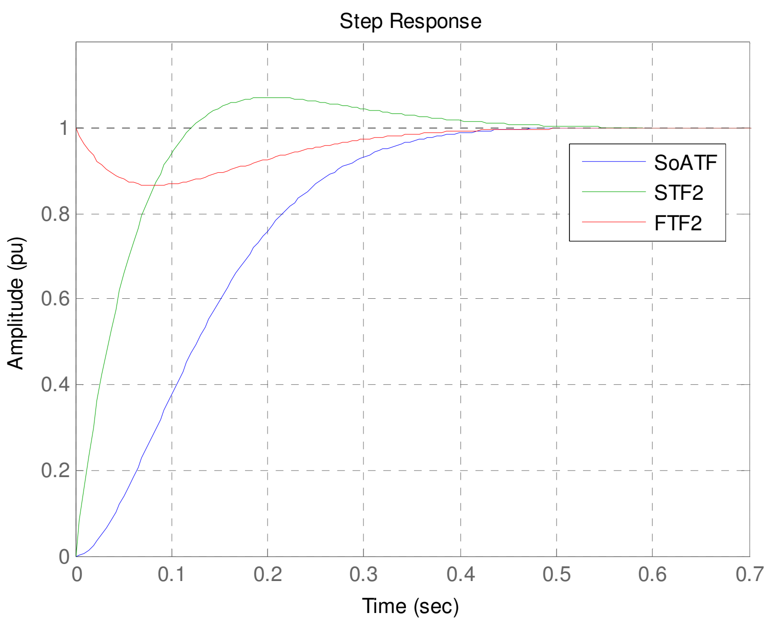

Figure A.5.22: The step response curves of SoATF, STF2 and FTF2

Since *s* has a unit of 1/second, t=0s needs to be converted to that in s^{-1} which results in complex infinity ($\tilde{\infty}$=1/0) [A.5.2]. "Complex infinity represents a quantity with infinite magnitude, but undetermined complex phase" [A.5.3]. If the *s* existing in the transfer functions is replaced with an infinite number (∞), the magnitudes of the SoATF and STF2 will then be 0, while that of FTF2 is 1.

[A.5.1] D. Xue, Y.Q. Chen, and D. P. Atherton, "Linear Feedback Control - Analysis and Design with MATLAB", Society for Industrial and Applied Mathematics (SIAM), 2007.

[A.5.2] http://www.wolframalpha.com/input/?i=1/0

[A.5.3] http://reference.wolfram.com/mathematica/ref/ComplexInfinity.html

$$\mathrm{FTF2}=\frac{\left(s^2+s\frac{K_{po}}{K_D}+\frac{K_{io}}{K_D}\right)}{s^2+\frac{\left(K_{po}+\frac{2}{3}\frac{L_{ss}}{\sqrt{2}\,V_s\,L_m}\right)}{K_D}s+\frac{K_{io}}{K_D}}=\frac{\cancel{s^2}\left(1+\cancelto{0}{\frac{K_{po}}{sK_D}}+\cancelto{0}{\frac{K_{io}}{s^2K_D}}\right)}{\cancel{s^2}\left(1+\cancelto{0}{\frac{\left(K_{po}+\frac{2}{3}\frac{L_{ss}}{\sqrt{2}\,V_s\,L_m}\right)}{sK_D}}+\cancelto{0}{\frac{K_{io}}{s^2K_D}}\right)}\Rightarrow\left|\mathrm{FTF2}\right|=1$$

$$\mathrm{STF2}=\frac{\left(s\frac{K_{po}}{K_D}+\frac{K_{io}}{K_D}\right)}{s^2+\frac{\left(K_{po}+\frac{2}{3}\frac{L_{ss}}{\sqrt{2}\,V_s\,L_m}\right)}{K_D}s+\frac{K_{io}}{K_D}}=\frac{\cancel{s}\left(\frac{K_{po}}{K_D}+\cancelto{0}{\frac{K_{io}}{sK_D}}\right)}{\cancel{s}\left(\overset{\infty}{\uparrow}{s}+\frac{\left(K_{po}+\frac{2}{3}\frac{L_{ss}}{\sqrt{2}\,V_s\,L_m}\right)}{K_D}+\cancelto{0}{\frac{K_{io}}{sK_D}}\right)}\Rightarrow\left|\mathrm{STF2}\right|=0$$

$$\mathrm{SoATF}=\frac{\frac{K_{io}}{K_D}}{\overset{\infty}{\uparrow}{s^2}+\frac{\left(K_{po}+\frac{2}{3}\frac{L_{ss}}{\sqrt{2}\,V_s\,L_m}\right)}{K_D}\overset{\infty}{\uparrow}{s}+\frac{K_{io}}{K_D}}\Rightarrow\left|\mathrm{SoATF}\right|=0$$

A.5.2 Robustness Analysis

The mathematical calculations for the robustness analysis is depicted in Table A.5.23.

Robustness Analysis for Power (Outer) PID Loop of the RSC																
0.8*Vs (kV)	Lm(mH)	Ls(mH)	L13(mH)	Lss(mH)	fn(Hz)	wn(rad/s)	Kd(s)	Kp	Ki(1/s)	Ti(s)	ζ	zeta name	Lm(pu)	Ls(pu)	L13(pu)	Lss(pu)
0.462	2.516	0.053	0.057	2.626	2.5	15.708	0.2	4.803	49.348	0.02026	0.934	ζ1	3.5575	0.0752	0.08	3.713
0.462	2.516	0.345	0.057	2.918	2.5	15.708	0.2	4.803	49.348	0.02026	0.953	ζ2	3.5575	0.4877	0.08	4.125
0.462	2.516	0.637	0.057	3.210	2.5	15.708	0.2	4.803	49.348	0.02026	0.972	ζ3	3.5575	0.9002	0.08	4.538
0.462	2.796	x	0.057	x	2.5	15.708	0.2	4.803	49.348	0.02026	x	x	3.9528	x	0.08	x
0.462	2.796	0.065	0.057	2.918	2.5	15.708	0.2	4.803	49.348	0.02026	0.934	ζ4	3.9528	0.0924	0.08	4.125
0.462	2.796	0.357	0.057	3.210	2.5	15.708	0.2	4.803	49.348	0.02026	0.951	ζ5	3.9528	0.5049	0.08	4.538
0.462	3.076	x	0.057	x	2.5	15.708	0.2	4.803	49.348	0.02026	x	x	4.3481	x	0.08	x
0.462	3.076	x	0.057	x	2.5	15.708	0.2	4.803	49.348	0.02026	x	x	4.3481	x	0.08	x
0.462	3.076	0.078	0.057	3.210	2.5	15.708	0.2	4.803	49.348	0.02026	0.934	ζ6	4.3481	0.1097	0.08	4.538
Vs (kV)	Lm(mH)	Ls(mH)	L13(mH)	Lss(mH)	fn (Hz)	wn (rad/s)	Kd(s)	Kp	Ki(1/s)	Ti(s)	ζ	zeta name	Lm(pu)	Ls(pu)	L13(pu)	Lss(pu)
0.577	2.516	0.053	0.057	2.626	2.5	15.708	0.2	4.803	49.348	0.02026	0.9	ζ7	3.5575	0.0752	0.08	3.713
0.577	2.516	0.345	0.057	2.918	2.5	15.708	0.2	4.803	49.348	0.02026	0.915	ζ8	3.5575	0.4877	0.08	4.125
0.577	2.516	0.637	0.057	3.210	2.5	15.708	0.2	4.803	49.348	0.02026	0.93	ζ9	3.5575	0.9002	0.08	4.538
0.577	2.796	x	0.057	x	2.5	15.708	0.2	4.803	49.348	0.02026	x	x	3.9528	x	0.08	x
0.577	2.796	0.065	0.057	2.918	2.5	15.708	0.2	4.803	49.348	0.02026	0.9	ζnom	3.9528	0.0924	0.08	4.125
0.577	2.796	0.357	0.057	3.210	2.5	15.708	0.2	4.803	49.348	0.02026	0.914	ζ10	3.9528	0.5049	0.08	4.538
0.577	3.076	x	0.057	x	2.5	15.708	0.2	4.803	49.348	0.02026	x	x	4.3481	x	0.08	x
0.577	3.076	x	0.057	x	2.5	15.708	0.2	4.803	49.348	0.02026	x	x	4.3481	x	0.08	x
0.577	3.076	0.078	0.057	3.210	2.5	15.708	0.2	4.803	49.348	0.02026	0.9	ζ11	4.3481	0.1097	0.08	4.538
1.2*Vs (kV)	Lm(mH)	Ls(mH)	L13(mH)	Lss(mH)	fn (Hz)	wn (rad/s)	Kd(s)	Kp	Ki(1/s)	Ti(s)	ζ	zeta name	Lm(pu)	Ls(pu)	L13(pu)	Lss(pu)
0.693	2.516	0.053	0.057	2.626	2.5	15.708	0.2	4.803	49.348	0.02026	0.877	ζ12	3.5575	0.0752	0.08	3.713
0.693	2.516	0.345	0.057	2.918	2.5	15.708	0.2	4.803	49.348	0.02026	0.89	ζ13	3.5575	0.4877	0.08	4.125
0.693	2.516	0.637	0.057	3.210	2.5	15.708	0.2	4.803	49.348	0.02026	0.903	ζ14	3.5575	0.9002	0.08	4.538
0.693	2.796	x	0.057	x	2.5	15.708	0.2	4.803	49.348	0.02026	x	x	3.9528	x	0.08	x
0.693	2.796	0.065	0.057	2.918	2.5	15.708	0.2	4.803	49.348	0.02026	0.877	ζ15	3.9528	0.0924	0.08	4.125
0.693	2.796	0.357	0.057	3.210	2.5	15.708	0.2	4.803	49.348	0.02026	0.889	ζ16	3.9528	0.5049	0.08	4.538
0.693	3.076	x	0.057	x	2.5	15.708	0.2	4.803	49.348	0.02026	x	x	4.3481	x	0.08	x
0.693	3.076	x	0.057	x	2.5	15.708	0.2	4.803	49.348	0.02026	x	x	4.3481	x	0.08	x
0.693	3.076	0.078	0.057	3.210	2.5	15.708	0.2	4.803	49.348	0.02026	0.877	ζ17	4.3481	0.1097	0.08	4.538

Table A.5.23: Mathematical calculations for robustness analysis

The electrical data of the DFIG system considered in this thesis was given in Appendix 1. As a reminder, the nominal values of the stator leakage-reactance, mutual inductance, stator self-inductance and the positive sequence leakage reactance of the transformer between the windings 1 and 3 in pu (per unit) are 0.09241pu, 3.95279pu, 4.1252pu and 0.08pu, respectively. ±10% change reflected to the stator self-inductance and the mutual inductance is presented in Table A.5.24. Only green operating areas are of interest, since the parameters in red areas are not physically feasible.

L_{ss} / L_m	**$0.9L_{ss}$**	**L_{ss}**	**$1.1L_{ss}$**
$0.9L_m$	3.71268pu 3.557511pu	4.1252pu 3.557511pu	4.53772pu 3.557511pu
L_m	3.71268pu 3.95279pu	4.1252pu 3.95279pu	4.53772pu 3.95279pu
$1.1L_m$	3.71268pu 4.348069pu	4.1252pu 4.348069pu	4.53772pu 4.348069pu

Table A.5.24: Operating points for robustness analysis

The stator leakage inductance is calculated by subtracting the sum of the mutual inductance and the positive sequence leakage reactance of the transformer between the windings 1 and 3 from the stator self-inductance and shown in pu in Table A.5.25.

$$L_{ss} = L_s + L_m + L_{13} \quad \rightarrow \quad L_s = L_{ss} - (L_m + L_{13})$$

L_{ss} / L_m	**$0.9L_{ss}$**	**L_{ss}**	**$1.1L_{ss}$**
$0.9L_m$	L_s 0.075169pu	L_s 0.487689pu	L_s 0.900209pu
L_m	N/A	L_s 0.09241pu	L_s 0.50493pu
$1.1L_m$	N/A	N/A	L_s 0.109651pu

Table A.5.25: The stator leakage inductance in pu corresponding the change in stator self- and mutual inductances

MODELLING AND ANALYSIS OF DFIG WIND TURBINE SYSTEM IN PSCAD/EMTDC

T. Lei*, M. Ozakturk*, M. Barnes*

**Power Conversion Group, University of Manchester – M1 0QD, UK*
Ting.lei-2@postgrad.manchester.ac.uk

Keywords: PSCAD/EMTDC, DFIG Modelling, Converter Control, Pitch Control, Mathematical Model

Abstract

Wind turbine technology is currently driven by offshore development, which requires more reliable, multi-megawatts turbines. Models with different levels of detail have been continuously explored for years. This paper presents a 4.5MW doubly-fed induction generator wind turbine model established in PSCAD/EMTDC with two control levels, the wind turbine control and the DFIG control. Two converter models, a detailed and a simplified model are discussed. Mathematical representations of the closed-loop control systems are developed and verified against the PSCAD/EMTDC model. Simulation studies show good correspondence between the two results. In addition, the dynamic response of a 2-mass shaft model to a wind step is also simulated to examine the effect of torsional oscillations. This model can be employed to evaluate the control scheme, mechanical and electrical dynamics and the fault ride-through capability.

1 Introduction

The trend of future wind turbine installations moving offshore is stimulating the need for high reliability, ever larger wind turbines in order to minimize cost. Two wind turbine concepts currently used are considered to be suitable for the multi-megawatts offshore installations – the doubly-fed induction generator (DFIG) wind turbine (WT) and the permanent magnet synchronous generator (PMSG) wind turbine [7]. Currently the former has the largest market share with a capacity up to 5 MW. Increasingly comprehensive studies should be carried out to evaluate the control strategies and system dynamic behaviour. These studies require accurate models.

DFIG WTs have been investigated for many years [3-6, 9-13]. In most of these, the converters are simplified as controllable voltage or current sources with only fundamental frequency components, which makes it impossible to implement a detailed study of power converter. The drive-train dynamics and the induced torsional oscillations are neglected. However, these oscillations may cause power converter problems and also affect the transient stability.

In this paper, a PSCAD/EMTDC based DFIG WT model with two control levels is provided. The DFIG control level involves the rotor-side converter (RSC) control and the grid-side converter (GSC) control. The WT control level involves the pitch control and the optimum torque tracking [5]. Mathematic models of RSC control, GSC control pitch control systems with a lumped-mass shaft are provided and validated against the PSCAD/EMTDC simulations. Two converter representations, with and without IGBT switches are used here which are referred to as the full switched model (FSM) and the switch-averaged model (SAM). The latter is used to demonstrate the WT response to wind steps. The 2-mass shaft model is discussed and the effect of shaft torsional oscillations is observed by including a multi-mass model in the program. This model can be used to evaluate the DFIG WT behaviour as well as its interaction with the network.

The paper is structured as follows. Section 2 discusses the component models and equations. Section 3 and 4 then elaborate the two level control systems and the corresponding mathematical representations. The simulations results are shown in section 5 and the conclusions are given in section 6.

2 System modelling

A schematic diagram of the DFIG WT and its overall control systems are illustrated in figure 1. The turbine rotor is connected to the DFIG through a shaft system. The generator rotor is fed from the grid through a back-to-back converter which handles only the slip power (up to 30% of the total).

2.1 Aerodynamic modelling

The aerodynamic model of the turbine rotor is generally the same for all WT concepts [1]. The aerodynamic power or torque extracted from the wind can be derived as:

$$P_a = \frac{\rho}{2}\pi R_a^2 C_p(\lambda,\beta) v_w^3 \tag{1}$$

$$T_a = \frac{\rho}{2}\pi R_a^3 \frac{C_p(\lambda,\beta)}{\lambda^3} v_w^2 \tag{2}$$

with ρ the air density [kg/m^3], R_a the radius of the rotor [m], v_w the wind speed upstream the rotor [m/s] and ω_r the rotor speed [rad/s]. The power coefficient C_p is a function of the tip speed ratio λ and the pitch angle β [deg], for which the numerical approximation in [12] is used:

$$\lambda = \frac{\omega_r R_a}{v_w} \tag{3}$$

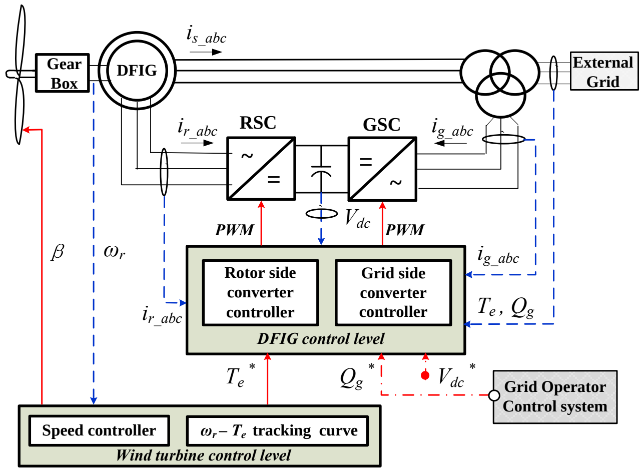

Figure 1: DFIG WT model and its overall control systems

$$\frac{1}{\lambda_i} = \frac{1}{\lambda + 0.08\beta} - \frac{0.035}{\beta^3 + 1} \tag{4}$$

$$C_p(\lambda, \beta) = 0.22\left(\frac{116}{\lambda_i} - 0.4\beta - 5\right)e^{-\frac{12.5}{\lambda i}} \tag{5}$$

The turbine aerodynamic model is assembled with the build-in functions in the PSCAD/EMTDC program.

2.2 Induction generator modelling

In this paper, the generation convention is considered for DFIG modelling, where positive power is from the generator to the grid. The set of machine equations are given by [12].

$$\begin{aligned}
\bar{v}_s &= -R_s\bar{\iota}_s + \frac{d\bar{\psi}_s}{dt} + j\omega_s\bar{\psi}_s \\
\bar{v}_r &= -R_r\bar{\iota}_r + \frac{d\bar{\psi}_r}{dt} + j(\omega_s - \omega_r)\bar{\psi}_r \\
\bar{\psi}_s &= -L_s\bar{\iota}_s - L_m\bar{\iota}_r \\
\bar{\psi}_r &= -L_r\bar{\iota}_r - L_m\bar{\iota}_s
\end{aligned} \tag{6}$$

with v the voltage [kV], R the resistance [Ω], i the current [kA], ω_s the synchronous electric speed [rad/s], ψ the flux linkage [Wb], L_m the mutual inductance between stator and rotor windings [H]. The subscripts s and r denote the stator and rotor quantities.

2.3 Back-to-back converter modelling

Two VSIs are connected back to back via a DC link to comprise the converter, which enables bidirectional power flow. In figure 2, the FSM has all the IGBT switches are presented with a PWM frequency set to 4.5 kHz. A chopper circuit is connected in parallel with the DC circuit to protect the capacitor. The FSM provides a deeper insight of the converter dynamics over a short time scale.

In the SAM, the converter is presented as two current-controlled voltage sources coupled through a DC-link. The DC dynamics are based on the power unbalance between the RSC and GSC, which results in two disturbances from the VSIs feeding into the DC-link. The SAM is suitable for inspecting the mechanical dynamics in over a longer time scale without the disturbance from the switching noise

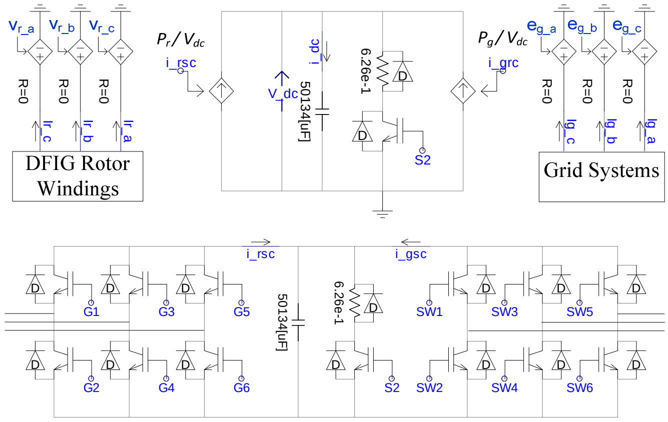

Figure 2: Two converter models (upper: FSM, down: SAM)

2.4 Shaft system modelling

The shaft system has been presented as six, three, two, and lumped-mass models [8], among which the lumped and 2-mass shaft models are often used to study the electric behaviours of the DFIG. It is suggested in [1] that for a generator with shaft stiffness lower than 3pu/el.rad, a 2- mass shaft model should be considered.

PSCAD/EMTDC provides the standard models of the wound rotor induction machine and the multi-mass shaft. They can be interfaced as shown in figure 3. The performance of the 2-mass shaft model is shown in figure 14. If not specified, the analysis refers to the lumped shaft model with a SAM converter in the paper.

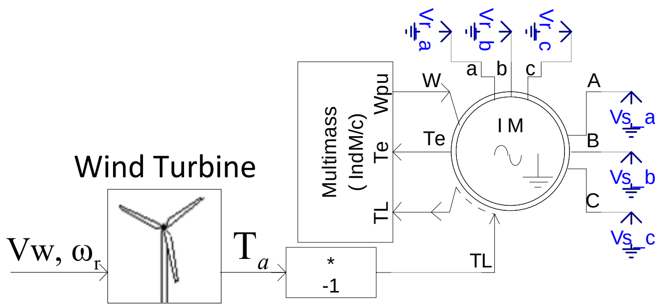

Figure 3: Turbine rotor, 2-mass shaft and DFIG model arrangements in PSCAD/EMTDC

3 DFIG control

The control system has been shown in figure 1, in which two control levels are identified based on different bandwidths. The DFIG control is achieved by the RSC control and the GSC control. The RSC is used to provide decoupled control of the active and reactive power whilst the grid-side converter (GSC) is mainly used to ensure a constant voltage on the DC-link [6, 10].

3.1 RSC control

Stator-flux orientation is used for the RSC control in which the stator flux is collinear with the d-axis, and the other rotor quantities are converted to this frame. The dependence of the electric torque and the stator reactive power on the rotor current dq components is shown as in equations (7) and (8).

$$T_e = -\frac{3}{2}\frac{L_m}{L_s}\psi_s i_{r\_q} \tag{7}$$

$$Q_s = -\frac{3}{2}\frac{\sqrt{2}V_s}{L_s}\psi_s - \frac{3}{2}\frac{\sqrt{2}V_s L_m}{L_s} i_{r\_d} \tag{8}$$

where V_s is the stator phase voltage in rms.

According to equation (6), the voltage to be applied to the RSC can be expressed as a function of the rotor current. Equations (9) and (10) show the relationship in the dq frame.

$$v_{r\_d}^* = -R_r i_{r\_d} + \omega_{slip}\left(L_r - \frac{L_m^2}{L_s}\right) i_{r\_q} \tag{9}$$

$$v_{r\_q}^* = -R_r i_{r\_q} - \omega_{slip}\left(L_r - \frac{L_m^2}{L_s}\right) i_{r\_d} + \omega_{slip}\frac{L_m}{L_s}\psi_s \tag{10}$$

where $\omega_{slip} = \omega_s - \omega_r$

The mathematical model of RSC control is depicted as in figure 4, where the control of reactive power and electric torque are decoupled by adding the feed-forward compensation after the PI controllers. The hat is used to distinguish the estimated variables from the real system parameters. An outer loop control could be added, by measuring the electric torque or reactive power from the grid and comparing with the reference values (see figure 1).

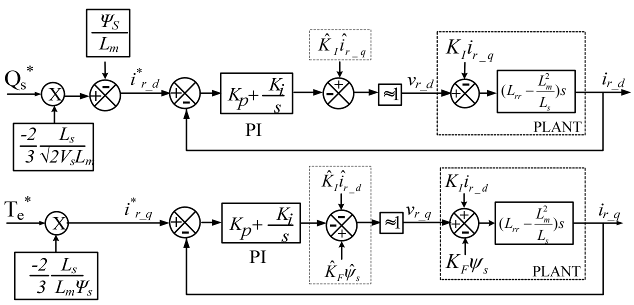

Figure 4: Decoupled control loops of the RSC

3.2 GSC control

In GSC control, the q-component controls the dc-link voltage and the d-component controls the reactive power. Positive current is considered from the grid to the converter. Thus the voltage equations in the dq frame are expressed as:

$$v_{g\_d} = R_{gsc} i_{g\_d} + \frac{L_{gsc} di_{g\_d}}{dt} - \omega_s L_{gsc} i_{g\_q} + e_{g\_d} \tag{11}$$

$$v_{g\_q} = R_{gsc} i_{g\_q} + L_{gsc}\frac{di_{g\_q}}{dt} - \omega_s L_{gsc} i_{g\_d} + e_{g\_q} \tag{12}$$

Similar with the RSC control, current control of the GSC also has two independent control loops, as shown in figure 5.

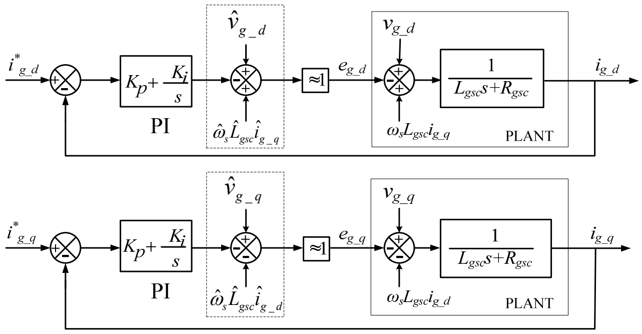

Figure 5: Current (inner) control loops of the GSC

Aligning the q-axis to the grid voltage vector, i.e. $v_{g\_d} = 0$, and thus:

$$Q_g = \frac{3}{2} v_{g\_q} i_{g\_d} \tag{13}$$

$$P_r = \frac{3}{2} v_{g\_q} i_{g\_q} = V_{dc} i_{gsc} \tag{14}$$

The dc dynamics shown in figure 2 can be described as

$$C\frac{dV_{dc}}{dt} = i_{gsc} - i_{rsc} \tag{15}$$

Substituting equation (14) into (15) and undertaking partial differentiation and taking only terms of interest delivers

$$C\Delta\dot{V}_{dc} = -\Delta i_{rsc} - 1.5K_V K_G \Delta V_{dc} + 1.5K_V \Delta i_{g\_q} \tag{16}$$

$$K_V = \frac{V_{g\_q0}}{V_{dc0}} \text{ and } K_G = \frac{i_{g\_q0}}{V_{dc0}}$$

where the subscript '0' denotes a constant operating point value. The DC-link voltage (V_{dc}) control is cascaded with the q-loop of the GSC current control, as depicted in figure 6.

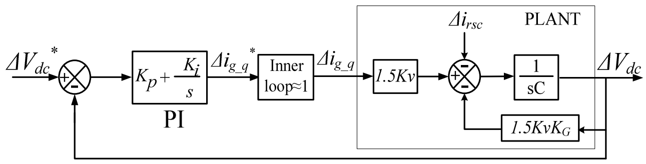

Figure 6: Small signal model DC-link (outer) control loop

4 Wind turbine control

As shown in figure 1, in the wind turbine control level, the system measures the rotor speed and uses it to generate reference signals both to the pitch system of the wind turbine and to the DFIG control level. This control is mainly separated by two operating regions. At lower wind speeds, the pitch angle remains at the optimum value (0 degrees) and the optimum torque is tracked according to a pre-defined curve [1] characterised by

$$T^{opt} = K_{opt}\,\omega_r^2 \tag{17}$$

At higher wind speeds, the pitch control is activated to remove excessive power extracted from wind. The two control modes sometimes work together to regulate the wind turbine in the high wind region [5, 8]. However, in order to make the mathematical analysis straightforward, the model presented here considers the design with two controllers operating independently. In PSCAD/EMTDC library, the non-linear transfer function is employed to generate the torque-speed look-up table.

The pitch controller is constructed as in figure 7, where the actuator introduces a lag between the actual pitch angle and the commanded pitch from the PI controller. The pitch controller is designed with a loop bandwidth of 0.25 Hz, actuator time constant $\tau = 0.2$s and pitch rate limit 3rad/s. System response to wind steps are shown in figure 13.

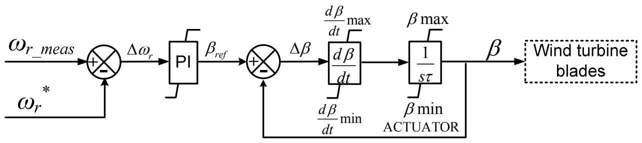

Figure 7: General pitch controller with an actuator

The full non-linear wind turbine control model is depicted in figure 8, where J_t is the total rotational inertia. The wind speed v_w acts as the external disturbance experienced by turbine rotor and the generator torque T_g is treated as an internal disturbance signal on the shaft system, and it is constant (rated value) for the higher wind speed region.

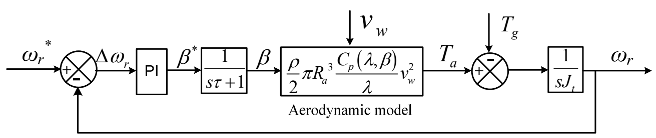

Figure 8: Full model of the WT pitch control system

A linear system model is required in order to evaluate its control performance. Linearization of different mass systems has been performed in [14] and this methodology is applied in [15] to design the PI controller.

At a particular operating point, $\omega_{r0}, \beta_0, v_{w0}$, the disturbance function of the rotor speed and wind perturbation is given by:

$$\frac{d\Delta\omega_r}{dt} = \frac{\gamma_0}{J_t}\Delta\omega_r + \frac{\zeta_0}{J_t}\Delta\beta + \frac{\eta_0}{J_t}\Delta v_w \tag{24}$$

where $\gamma = \partial T_a/\partial \omega_r$, $\zeta = \partial T_a/\partial \beta$. $\eta = \partial T_a/\partial v_w$.

Therefore, the linear model of pitch control without the actuator is shown in figure 9.

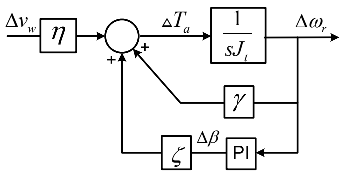

Figure 9: Linear model of the pitch control system

5 Simulation results

The DFIG WT is connected to the grid through a step-up transformer. Parameters used in the model are tabulated in the appendix.

The performances of FSM and SAM are compared as shown in figure 10. The DFIG is set to the speed control mode with a nominal rotor speed. The simulation results from giving a power step at 0.3s, which is accompanied by a grid q-current component step. Harmonics are presented in the FSM.

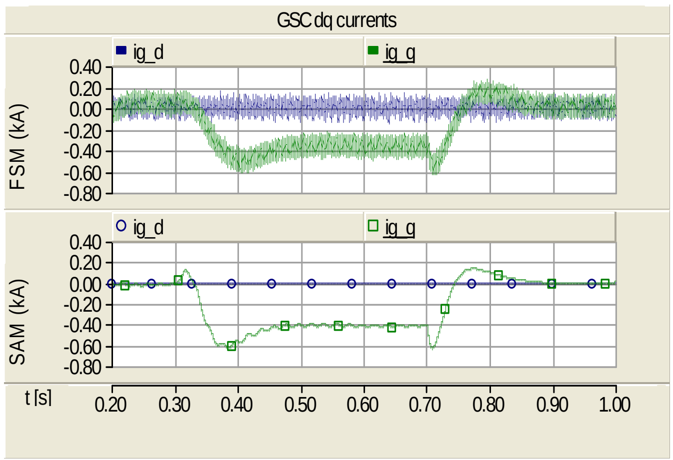

Figure 10: Comparison of FSM and SAM performances

Responses from the mathematical models are compared with PSCAD/EMTDC simulations (figure 11-13). The actual waveforms ($i_{r\_d,q}$, $i_{g\_d,q}$, $V_{\_dc}$) are obtained by varying the control signals, which are the electric torque and reactive power in the RSC control and the DC voltage in the GSC control. The theoretical outputs 'tf' from the 2nd order transfer functions are obtained by changing the 'set' signals. The two results match very well indicating that the mathematical model of DFIG control is accurate.

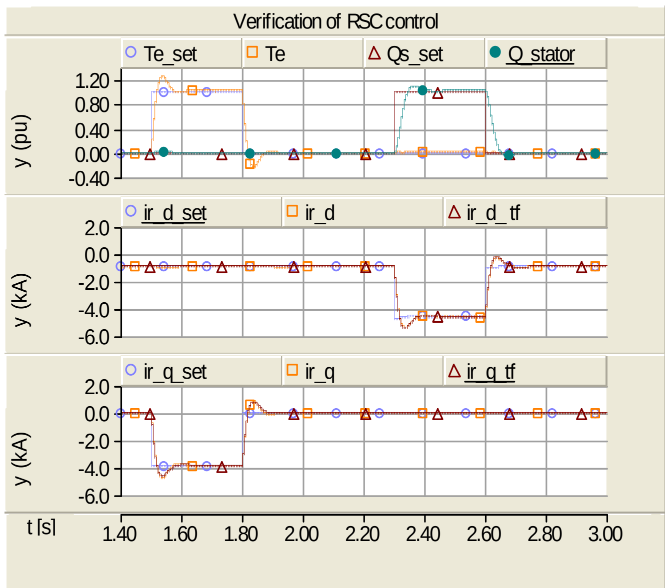

Figure 11: Mathematical verification of the RSC control (using a 1 pu step on T_e and Q_{stator} respectively)

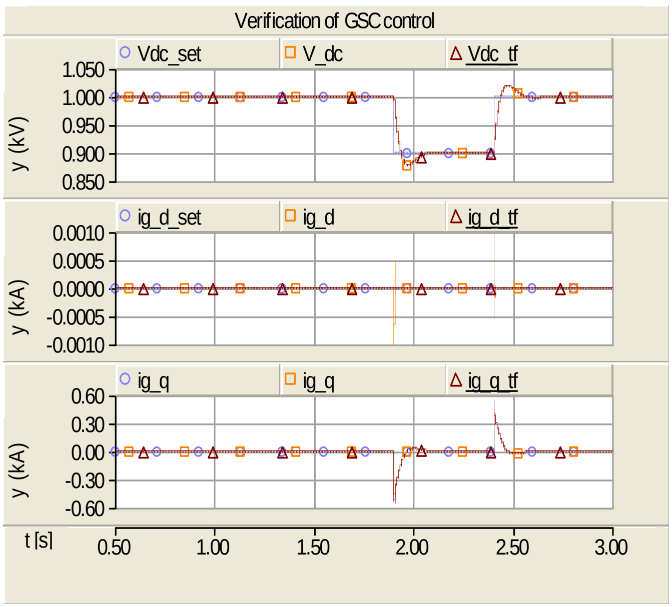

Figure 12: Mathematical verification of the GSC control (using a 1kV step at the DC-link voltage)

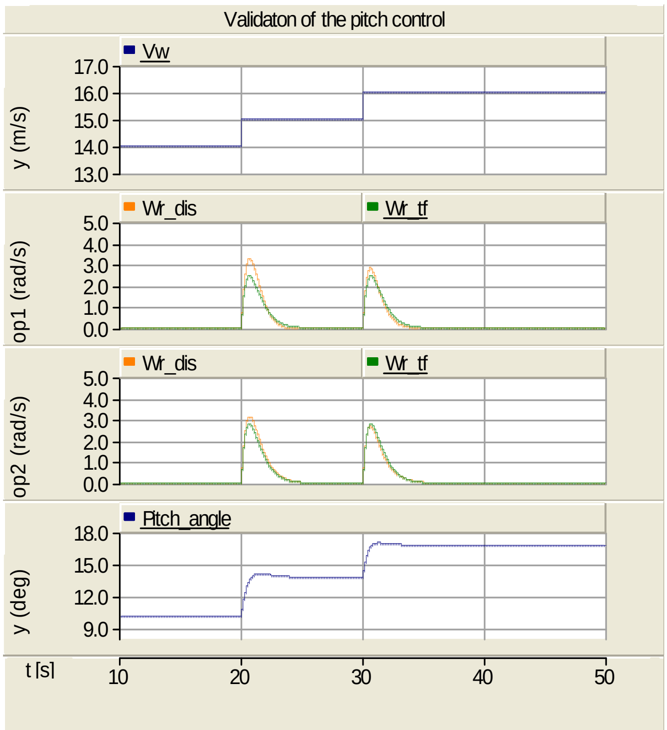

Figure 13: Mathematical verification of the pitch control (using 1m/s wind steps, at two operating points: Op1: 14/ms and Op2: 15m/s)

Figure 13 shows the rotor disturbance, ω_{r_dis} to a 1m/s wind step at two specific operating points. The DFIG is switched to torque control mode after initiation. Op1, and Op2 indicate the models that are linearised at v_w=14m/s and 15m/s respectively. For the same operating point, the PI gains are derived from the linear model and applied into PSCAD simulations. The results show better correspondence at higher wind speeds, e.g. the curves mach exactly in Op2 at a wind step from 15m/s, corresponding to its operating point.

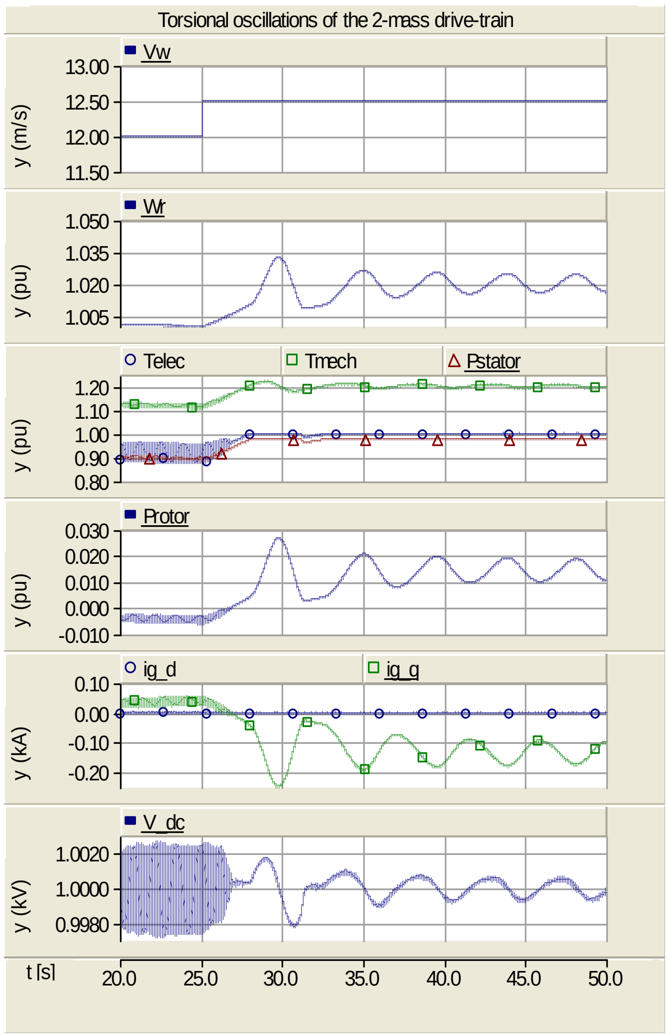

Figure 14: Torsional oscillations of the rotor speed, torque and currents using a 2-mass shaft model

The response of a 2-mass WT model to a wind step is shown in figure 14, where the wind increases from just below the rated speed to above rated speed. As is seen in the figure, the system experiences high frequency disturbances near the synchronous speed. Following by the transient in the wind speed, significant torsional effects occurred, which is shown as fluctuations in the rotor speed, mechanical torque, rotor power, grid current and DC voltages. However, the elastic shaft has little impact on the electric torque and stator power. This is reasonable due to the smoothing effect of the converter.

5 Conclusions

With future WTs moving offshore, very large size turbines will be installed making their reliability critical. Comprehensive studies on the WT behaviours and control systems are needed in order to improve their design and operation. This paper presents a complete DFIG WT model and its overall control systems. The interaction of the WT control level with the DFIG control level has been presented in the paper. Two converter models, a full switched model with IGBTs and a switched-averaged model are compared. The former is suitable for detailed studies whilst the latter is recommended for investigating mechanical responses over a longer time scale. The 2-mass shaft model should be included in the model since fluctuations of the electrical or mechanical parameters are induced, which may impose significant stresses on power electronics and affect the power system stability. Mathematical models of the RSC control, GSC control and pitch control systems are developed and their responses are consistent with the PSCAD/EMTDC simulations. These models can be used to adjust the PI gains and evaluate the control performance more accurately.

This model is useful to WT manufacturers, operators as well as researchers in relevant fields.

Acknowledgements

The authors would like to thank the Engineering and Physical Sciences Research Council for supporting this work through grant EP/H018662/1 - Supergen 'Wind Energy Technologies'.

References

[1] V. Akhmatov, "Analysis of Dynamic Behaviour of Electrical Power Systems with Large Amount of Wind Power", PhD thesis, Ørsted DTU, Technical University of Denmark, (2003).

[2] E. A. Bossany, "The design of closed loop controllers for wind turbines", *Wind Energy*, **Vol. 3**, pp. 149-163, (2000).

[3] S. Chondrogiannis. "Technical aspects of offshore wind farms employing doubly-fed induction generators", PhD Thesis, University of Manchester, (2007).

[4] J. B. Ekanayake, L. Holdsworth, X. Wu, and N. Jenkins. "Dynamic modeling of doubly fed induction generator wind turbines", *IEEE Transaction on Power Systems*, **Vol. 18**, (2003).

[5] A. D. Hansen, P. Sorensen, F. Lov, F. Blaabjerg, "Control of variable speed wind turbines with doubly-fed induction generators", *Wind Engineering*, **Vol. 28**, pp 411-434, (2004).

[6] B. Hopfensperger, D. J. Atkinson, R. A. Lakin. "Stator-flux-oriented control of a doubly-fed induction machine with and without position encoder", *IEE Proceedings on Electric Power Applications*, **Vol. 147**, pp. 241-250, (2000).

[7] H. Li, Z. Chen. "Overview of different wind generator systems and their comparisons", *IET Renewable Power Generation*, **Vol. 2**, pp. 123-138, (2008).

[8] S. M. Muyeen, M. H. Ali, R. Takahashi, T. Murata, J. Tamura, Y. Tomaki, A. Sakahara, and E. Sasano, "Comparative study on transient stability analysis of wind turbine generator system using different drive train models", *IET Renewable Power Generation*, **Vol. 1**, pp. 131-141, June (2007).

[9] G. Pannell. "Grid Fault Ride Through for Wind Turbine Doubly-Fed Induction Generators", PhD Thesis, Newcastle University, (2008).

[10] R. Peña, J. C. Clare, and G. M. Asher. "Doubly fed induction generator using back-to-back PWM converters and its application to variable speed wind-energy generation", *IEEE Proceedings on Elecric Power Appication*, **Vol. 143**, pp. 231–241, (1996).

[11] J. G. Slootweg, S. W. H. de Haan, H. Polinder, and W. L. Kling, "General Model for Representing Variable Speed Wind Turbines in Power System Dynamics Simulation", *IEEE Transactions on Power Systems*, **Vol. 18**, pp. 144-151, (2003).

[12] J. G. Slootweg, H. Polinder, and W. L. Kling, "Dynamic modelling of a wind turbine with doubly fed induction generator", *IEEE proceedings on Power Engineering Society*, Vancouver, BC, Canada, (2001).

[13] R. Todd, "High Power Wind Energy Conversion Systems", EngD Thesis, University of Manchester, (2006).

[14] A. D. Wright, "Modern Control Design for Flexible Wind Turbines", NREL, Report No. TP-500-35816, Golden, CO: National Renewable Energy Laboratory, (2004).

[15] A. D. Wright, L. J. Fingersh, "Advanced control design for wind turbines-part 1: Control design, implementation, and initial tests", NREL, Report No. TP-500-42437, (2008).

Appendix

Parameters that are used in the DFIG WT model:

Rating		4.5 MVA	
Rated wind speed		12m/s	
Cut-in wind speed		3.5m/s	
Rotor diameter		112m	
Gear box ratio		1:100	
$H_{turbine}$		3 sec	
$H_{generator}$		0.5sec	
Spring constant (K)		0.6pu/el.rad	
Generator self-damping		0.032 pu	
Turbine self-damping		0.022 pu	
Mutual damping		1 pu	
Stator Voltage (L-L, RMS)		1 kV	
Stator/rator turns ratio		1	
L_s	0.09241 pu	R_s	0.00488 pu
L_r	0.09955 pu	C_{dc_link}	3.5 pu
L_m	3.95279 pu	V_{dc}	1 kV